Passive and active flow control studies using hybrid RANS/LES methods

Wei Wang

Supervised by Professor Ning Qin

Department of Mechanical Engineering

The University of Sheffield

This thesis is submitted to The University of Sheffield in partial fulfilment
of the requirement for the degree of

Doctor of Philosophy

September 2013

To my parents, my brother, and my husband.

Acknowledgements

First and foremost, I would like to sincerely thank my supervisor, Professor Ning Qin, for his advice, support and guidance during the past four years. I have benefited a lot from his profound knowledge, illuminating suggestions, and scientific attitude. His valuable experiences and thorough knowledge on various CFD related topics influence me to become an independent scientific researcher. I deeply appreciate all of these.

I wish to express my appreciation to Dr. Franck Nicolleau for our cooperation in the study of flow through fractal orifice pipes. I would also like to thank Dr. Hongwei Zheng for his help in understanding the in-house code during the early stage of my PhD research, which laid the foundation of my four years study. I appreciate discussions with Dr. Mohammed Mohammed and Dr. Yibin Wang on numerical methods and mesh generations. I also thank Dr. Spiridon Siouris and Palma Garcia for our collaboration in the MARS project. I am here to say thank you to all of the people in our Aerodynamics Group.

I am grateful for the support of the MARS project on the investigation on active flow control, and the Leverhulme Trust for the support of study on the flow through fractal orifices. I also acknowledge the support of the EPSRC UK Turbulence Consortium, which supports the high performance computing and provides the opportunities to communicate with other groups in annual conferences. I appreciate the computing resources and the corresponding supporting teams, namely, Greengrid, Iceberg, HECTOR and N8. I want to acknowledge the three years' financial support from the China Scholarship Council.

Last but not the least, I wish to devote my greatest gratitude to my whole families and friends for their enthusiastic support over the years. Especially, I would like to express my deep appreciation to my parents and my husband for their love and encouragement. Their support is the driving force in my pursuing an academic career.

Abstract

Turbulent flow control of three types of flow is numerically studied using hybrid RANS/LES approaches. Flow control effect and control mechanisms are studied through both instantaneous and statistically-averaged flow properties. Behaviours of hybrid RANS/LES methods in these three types of flow are also investigated.

Flow over a backward facing step is investigated, with piezoelectric actuators implemented on the step to control flow separation and recirculation. The simulation results agree well with the experiments. For the controlled flow, a slightly reduced primary recirculation between two adjacent actuators was observed. In the exploring study of actuators with a control velocity similar to the free stream flow, counter-rotating vortex pairs are generated, interacting with the separated shear layer. The primary recirculation becomes much smaller, and the recovered flow has a smaller skin friction.

Pitched and skewed jet vortex generators are applied to the NACA0015 aerofoil to study their control effect on the trailing edge separation induced by a gradual adverse pressure gradient. Both the simulation and experiments show that after a certain time, the originally separated flow is forced to be attached by the blowing jets. The lift coefficient is enhanced and the drag coefficient is reduced. When the jets are switched off, the fully attached flow recovers to the originally separated flow. The jet-removal process has about 70% longer transient time than the jet-deployment process.

Flow through fractal orifices in pipes is studied to investigate the passive control effect of the orifice geometries in flow mixing and decay. The simulation results are in good agreement with the available experimental data. With a higher fractal level, the vena contracta velocity decreases and the unrecoverable pressure loss becomes smaller. The higher level fractal orifices generate more organized vortices, maintaining a high turbulent kinetic energy for a longer distance and a slower decay. Axis-switching is observed for all these fractal orifices.

Contents

List of Figures

List of Tables

Nomenclature

Roman Symbols

a Speed of sound

$\mathbf{A}$ $= A_i, (i = 1, 2, 3)$ Vector of a surface area

A_a The maximum displacement (magnitude) of the apex on an oscillating surface

$\mathbf{A}_c$ Conservative Jacobian matrix

C A constant number

c Chord length of an aerofoil

C_d Drag coefficient

C_f Coefficient of skin friction

C_L Lift coefficient

C_p Coefficient of pressure

c_p Specific heat capacity at constant pressure

C_{SGS} A coefficient to scale the grid-spacing in a SGS model

C_μ Momentum coefficient in jets flow control

c_v Specific heat capacity at constant volume

D Drag force, or diameter of a pipe

d Diameter of a circular orifice in a pipe

d_{w} Wall distance, the distance from a point to the nearest wall

NOMENCLATURE

E Specific total energy

e Specific internal energy

f Frequency

$\mathbf{F_c}$ Vector of convective flux

$\mathbf{F_d}$ Vector of dissipation flux in the Roe scheme

$\mathbf{F_v}$ Vector of viscous flux

H Specific total enthalpy, or height of the step in BFS

h Specific internal enthalpy

K A multiplier

k Turbulence kinetic energy

L Lift force

L_e Entrance length in pipe flow

l_{hyb} Hybrid length scale of turbulence and RANS average

l_{RANS} RANS length scale

l_{turb} Turbulence length scale

L_z Length of a span

M Mach number

$\mathbf{n}$ $= n_i, (i = 1, 2, 3)$ Normal vector of a surface

N_{face} Face number

n_r A random number with magnitude less than a unity

N_z Cell number along a span

O Order of magnitudes

p Fluid static pressure

$\mathbf{A}_p$ Primary Jacobian matrix

Pr   Prandtl number

p^* Normalized pressure drop

$\mathbf{Q}$ Vector of primary variables, $\mathbf{Q} = (p, u_1, u_2, u_3, T)^T$

$\mathbf{q}$ $= q_i, (i = 1, 2, 3)$ Heat flux vector

$\mathbf{R}$ Residual vector in the N-S equations

$\mathbf{r}$ A displacement vector form one point to another

R The ideal gas constant for air, $R = 287.04$ J Kg^{-1} K^{-1}, or Radius of a geometry

Re Reynolds number

Re_τ Friction Reynolds number

r_p Pressure recovery rate

$\mathbf{S}$ $= S_{ij}$ Rate of strain tensor, or a vector of the source term in the N-S equations

St Strouhal number, $St = fL/U$

T Fluid absolute temperature

t Physical time

T_0 The reference temperature in the Suntherland's law, $T_0 = 288.15$ K, or a time interval

Δt Physical time interval

Δt^* Dimensionless time step, $\Delta t^* = \Delta t/(L/U_\infty)$

T_{ft} Flow-through time period

$\mathbf{u_g}$ Velocity vector on a moving surface

$\mathbf{u}$ $= u_i = (u, v, w)^T, (i = 1, 2, 3)$, instantaneous velocity components in Cartesian coordinates

U_∞ Free stream velocity

u_n Magnitude of a real normal velocity of a surface of a control volume, $u_n = (\mathbf{u} - \mathbf{u_g}) \cdot \mathbf{n}$

NOMENCLATURE

U_r $= U_{\text{ref}}$ Reference velocity

u_τ Friction velocity, $u_\tau = \sqrt{\nu(\partial u/\partial y)}$

V_a The maximum velocity (magnitude) of the apex on an oscillating surface

VR Velocity ratio of the control velocity to the free stream flow

$\mathbf{W}$ Vector of conserved variables, $\mathbf{W} = (\rho, \rho u_1, \rho u_2, \rho u_3, \rho e,)^T$

X_R Reattachment length towards the step

$\mathbf{x}$ $= x_i = (x, y, z)^T, (i = 1, 2, 3)$, Cartesian coordinates

Greek Symbols

α Thermal diffusivity, or angle of attach of an aerofoil

Δ Grid spacing in a SGS model

δ Boundary layer thickness

δ_{ij} Kronecker's delta symbol

$\Delta\tau$ Pseudo time step

Δx_i $i = 1, 2, 3$, characteristic length of a control volume

γ Heat capacity ratio, $\gamma = c_p/c_v$

$\boldsymbol{\Gamma}$ The transformation matrix in the preconditioning

$\boldsymbol{\Gamma_{nc}}$ A transition format of the transformation matrix in the preconditioning

κ The von Karman constant, $\kappa = 0.41$, or thermal conductivity coefficient, or wave number

λ Bulk elasticity or second coefficient of viscosity, or spacial interval between two adjacent jets

$\boldsymbol{\Lambda}$ $= \lambda_k, (k = 1, 2, ...5)$ Diagonal matrix of eigenvalues

Λ_c Spectral radii of the convective flux

Λ_v Spectral radii of the viscous flux

μ Dynamic viscosity

μ_0 The reference viscosity in the Suntherland's law, $\mu_0 = 1.7895 \times 10^{-5}$ m^{-1} Kg s^{-1}

ν Kinematic viscosity

$\boldsymbol{\Omega}$ $= \Omega_i, (i = 1, 2, 3)$ Vorticity vector

Ω Control volume

ϕ An arbitrary flow variable

Ψ A low-Reynolds number correction in DES and its variations

ρ Fluid density

τ Pseudo time, or $= \tau_{ij}$, Reynolds stress tensor

Θ A replacement of ρ_p in the preconditioning

θ_p Pitch angle

θ_s Skew angle

ε Coefficients in the backward Euler's discretization

$\varepsilon_{i,j,k}$ The Levi-Civita symbol

Superscripts

$+$ Dimensionless distance, $y^+ \equiv u_\tau y / \nu$

L The left side of a surface

M Modelled variables

m Time step of the pseudo time

mol   The modelled variables

n Time step of the physical time

$'$ Flow fluctuation

R The right side of a surface, or the Reynolds Averaged variable

NOMENCLATURE

res   The resolved variables

S Sub-grid scale filtered variable

T Transposition of a vector or a matrix

tot   The total variables, which is the sum of the resolved and modelled values.

Subscripts

e variables at the edge of the velocity boundary layer (99% of the freestream velocity)

exp   Experimental data

i $i = 1, 2, 3$, variables in the directions of the Cartesian coordinates, x, y, z

j $j = 1, 2, 3$, variables in the directions of the Cartesian coordinates, x, y, z

jet   Variables in the jets flow control

l variables for laminar flow

m   Measured variables in experiments

m $m = 1, 2, 3$, variables in the directions of the Cartesian coordinates, x, y, z

rms   Root mean square of a variable

t variables for turbulent flow

Other Symbols

$\hat{\cdot}$ Roe averaged values

$\langle \cdot \rangle$ Spatial filtered, or resolved

$\bar{\cdot}$ Time averaged

$\tilde{\cdot}$ Modified variables in the S-A model

Acronyms

2D   Two Dimensional

3D   Three Dimensional

ALE   Arbitrary Lagranigan-Eulerian

APL-UniMan The Aero-Physics Laboratory of The University of Manchester

AUSM Advection Upstream Splitting Method

BFS   Backward Facing Step

C   The circular orifice

CFD   Computational Fluid Dynamics

CFL   Courant-Friedrichs-Lewy condition or number

CGCL   Continuous Geometric Conservation Law

DDES   Delayed Detached Eddy Simulation

DES   Detached Eddy Simulation

DGCL   Discrete Geometric Conservation Law

DG-DES The name of our in-house CFD solver

DNS   Direct Numerical Simulations

F0   The triangular orifice, the zero-level of snowflake fractal orifice

F1   The first-level of snowflake fractal orifice

F2   The second-level of snowflake fractal orifice

F3   The third-level of snowflake fractal orifice

FCSD   Flexible Composite Surface Deturbulator

GCL   Geometric Conservation Law

GIS   Grid-Induced Separation

IDDES Improved Delayed Detached Eddy Simulation

ILES   Implicit Large Eddy Simulation

LES   Large Eddy Simulation

NOMENCLATURE

LLM   Log-Law Mismatch

LNS   Limited Numerical Scales

MSD   Modelled Reynolds Stress Depletion

NLES Numerical Large Eddy Simulation

N-S   Navier-Stokes

OS   Oscillating Surface

PANS Partially-Averaged Navier-Stokes

PRNS Partially-Resolved Numerical Simulation

PSD   Power Spectral Density

RANS Reynolds-Averaged Navier-Stokes

SA-ILES Implicit Large Eddy Simulation with Spalart-Allmaras wall modelling

SAS   Scale-Adaptive Simulation

SCL   Surface Conservation Law

SGS   Sub-grid Scale

SHUS Simple High-resolution Upwind Scheme

SLAU Simple Low-dissipation Scheme of AUSM-family

SST   Shear Stress Transport Model

TKE   Turbulence kinetic energy

URANS Unsteady Reynolds-Averaged Navier-Stokes

VLES Very Large Eddy Simulation

WMLES Wall-Modelled Large Eddy Simulation

ZNMF Zero Net Mass Flux

Chapter 1

Introduction

1.1 Background and motivations

Actively or passively changing a flow field to a desired state is of immense technological importance. The purposes of manipulation of a flow field include, but not limited to, drag reduction, flow separation control, laminar-turbulent transition control, noise and vibration reduction (Gad-el Hak [2007]). Drag reduction and flow separation control are directly related to more effective transport of air, less environmental impact and increased safety in the aerospace industry. Changing or manipulating a flow field is so-called "flow control" in fluid dynamics, which is usually realized by flow control devices in a beneficial way for overall efficiency of the fluid dynamical systems (Kral [1999]). Flow control is an effective and powerful tool for improving existing fluid dynamical systems.

Since Prandtl's boundary layer control in 1904 (Prandtl [1904]), the subject of flow control has evolved into various control methods and numerous applications to fluid flows. Flow control devices can be classified into passive and active flow control methods. Passive flow control includes changing the object geometries, installing new devices to generate vortex or to break up large eddies, and so on. Active flow control has external energy introduced into flows to change original flow fields. Most of the control devices involve interacting with the boundary layer flow, to change flow properties near the wall. One popular flow control device is a vortex generator, which can be implemented through either passive or active methods. Vortex generators have been utilized on some commercial aircraft, for example, the Boeing aircraft B737 and B767. The vortex generators installed on wing upper surface or on the engine nacelles generate vortex, which interacts with the boundary layer behind the device by introducing high momentum flow from the outside of the boundary layer down to the wall surface displacing low momentum flow. Through energizing the boundary layer, vortex

1

generators can delay, control or even remove separation of the boundary layer, to improve lift and reduce drag. Apart from interaction with the boundary layer flow, some control devices directly force the generation of turbulence, for example, changing the geometry of the orifice in flow meters to affect flow mixing downstream. Both active and passive flow control have obtained promising control effects in recent decades.

In spite of the positive progress, there is a lack of thorough understanding of the interaction between various flow control devices and their manipulated flow fields. A deeper understanding can potentially improve the effectiveness of flow control. With the development of computer technology, Large Eddy Simulation (LES) has been successfully applied to complex unsteady flows at industry-relevant Reynolds numbers. In order to reduce the required mesh resolution for the boundary layer flows, Reynolds-averaged Navier-Stokes (RANS) simulation can be used in the near-wall field in the LES study, which is the hybrid RANS/LES method. Both LES and hybrid RANS/LES modelling techniques have been widely applied to complex unsteady turbulent flows, and these modelling methods have achieved reasonably good simulation results for various types of flows. These turbulence modelling techniques are also credible tools to study the interaction between control devices and their manipulated flow field without using high-cost direct numerical simulations in computational fluid dynamics (CFD). However, it is also recognized that the feasibility of LES-based simulation approaches for flow control can be further improved in terms of turbulence modelling, flow-control devices modelling and other related numerical issues in order to enable robust analysis of unsteady flow control problems with realistic configurations. These aspects will be systematically addressed in the present work.

Numerical investigations on flow control can provide an overall understanding of the controlled flow fields in the context of the experiments. In addition, numerical study can also explore more control device and parameters, which may inspire optimization of their control configurations and even inventions of novel control devices. Hence, this research focuses on investigating performances of various control devices and improving understandings of control mechanisms by numerical simulations of complex unsteady flow fields.

1.2   Aims and objectives

The general objective of this thesis is to study effects and mechanisms of flow control methods applied to three typical flow fields.

(1) The first one is turbulent flow over a backward facing step, which has a geometry-induced abrupt separation. Piezoelectric actuators are installed on the step before

flow separation. The oscillating motion of the actuators is expected to manipulate the boundary layer before flow separation, then to make further changes to the flow-recirculation downstream of the step.

(2) The second case is flow over a NACA0015 aerofoil at an angle of attack 11° with a mild trailing edge separation caused by the adverse pressure gradient. Fluidic jet vortex generators are implemented upstream of the separation point to control flow separation, which aims to affect the lift and drag coefficients. The above two control devices both belong to active flow control.

(3) The last case is a passive flow control, which studies pipe flow through orifices with fractal snowflake geometries. Four levels of fractal snowflakes will be simulated and compared in vortex generation, flow mixing and decay.

The main aims of the numerical investigation on all these three typical flow and corresponding flow control methods are summarized as follows:

- To validate turbulence modelling techniques in three classic types of flows.

- To implement numerically various control devices in the in-house CFD solver and to conduct computational simulations to extract reliable flow physics, including the first and second order flow statistics.

- To investigate the controlled flow dynamics and the interaction between the control devices and the manipulated flow field.

- To explore key control parameters and strategies for efficient flow control of dynamic fluid-structures.

1.3 Outline of the thesis

Different hybrid RANS/LES turbulence modelling techniques have their "biased" applications to flow fields with different characteristics. In present work, three typical flow fields with different separation-mechanisms are studied. Under such a circumstance, a solitary chapter about flow validations may jeopardize the consistency of each studied flow type. It seems to be a more logical and natural way to organize this thesis by inserting the validation part in front of the detailed study of each baseline and flow control case. Corresponding to this arrangement, the outline of this thesis is briefly described as follows.

1.3. Outline of the thesis

Chapter 1 presents an introduction to flow control and turbulence modelling techniques for complex turbulent flow. Three typical flow cases with their control methods are briefly introduced. The study objectives are also described in this chapter.

Chapter 2 is a review on the published literatures and the state of the art in research on turbulent flow properties, turbulence modelling methods and flow control techniques. Turbulence modelling techniques documented in this chapter include RANS, LES, implicit LES and various hybrid RANS/LES. In the part of flow control, firstly a review of general flow control strategies and their control effect are summarized, then comprehensive reviews of the flow control devices in both experiments and numerical simulations are presented, especially piezoelectric actuators, jet vortex generators and fractal geometries.

Chapter 3 briefly introduces the in-house CFD solver, which covers the basic equations in fluid dynamics and discretization techniques in numerical simulation. Improvements of the previous in-house CFD solver and the newly added portion are presented in details, which includes the low-dissipation numerical schemes for the large eddy simulations, the hybrid RANS/LES methods based on the Spalart-Allmaras turbulence model, and the numerical realization of control methods in the in-house CFD solver, and so on.

Chapter 4 presents the numerical simulation of flow over a backward facing step at a step-height based Reynolds number of 64 000. Flow control with piezoelectric actuators with oscillating surface in this case is investigated. Firstly, a classical test case of a backward facing step is validated to study the mesh resolution, the numerical methods and the turbulence modelling in this abrupt separated turbulent flow. Then, flow over the backward facing step with experiments carried out by our partners in the Aero-Physics Laboratory of the University of Manchester is numerically simulated both for the baseline flow and the oscillating surface controlled flow. The numerical results are compared with the available experimental data, enabling their reliable assessment. After that, more flow properties, which are not easy to be obtained from experiments, are revealed to discuss flow control effects and mechanisms. Finally, an exploring study on the flow control parameters is carried out, and the influences of the oscillation magnitudes are discussed to identify a promising control configuration.

Chapter 5 gives the numerical simulation of flow control with jet vortex generators in NACA0015 at the angle of attack 11° and Reynolds number about one million. Firstly, the application of different hybrid RANS/LES modelling techniques to this mild separation aerofoil is discussed. Then, the numerical simulation results of both the baseline flow and the controlled flow are compared with experimental data to ensure the reliability of simulations. After that, the manipulated flow field by jet vortex generators is compared with the baseline

flow field to investigate flow control effect and mechanisms. Finally, the flow dynamics during the transition process of deploying jets and removing jets are presented to obtain further understandings of the flow control mechanisms.

Chapter 6 presents the numerical simulation of flow through fractal orifices in pipes at the pipe-diameter based Reynolds number of 38 900. Flow through a circular orifice pipe is validated firstly to investigate the application of hybrid RANS/LES models in this wall-bounded abruptly separated flow. After that, orifices with four snowflake fractal levels are simulated and compared with each other to study the influences of the fractal scaling effects on the pressure drop, velocity field, turbulence kinetic energy and the energy spectra.

Chapter 7 summarizes the main achievements and conclusions in the present work. Finally, recommendations for future work are suggested.

Chapter 2

Literature Review

2.1 Introduction

For numerical investigations on turbulent flow control, there are two primary issues. One is the numerical methods with turbulence modelling, which tackles numerical realization of flow control in complex turbulent flows. The other is the flow features and mechanisms of flow control. The aim of this chapter is to present a brief introduction of a new horizon of turbulent flow modelling techniques and flow control methods.

In the review of turbulent flow modelling, firstly, the characteristics of turbulent flow are described. Then, the main turbulence modelling techniques are summarized. Feature of each modelling technique and its potential applications are discussed and compared. As the hybrid RANS/LES method is chosen as the primary modelling technique in the current study, details on the development of these hybrid methods, the improvements in the hybrid modelling, the potential problems and attempts to conquer these existing issues are discussed and summarized.

In the review of flow control, a brief description of general flow control methods is given. Passive flow control with fractal-geometry, the active flow control with piezoelectric actuators and jet vortex generators is presented in details. For each flow control method, three main parts are provided, the original concept of this control method, the status of experiments and CFD simulations, and the potential applications.

Overall, this literature review summarizes the turbulence modelling techniques, the development of flow control methods, and the numerical implementation of the turbulence modelling in flow control methods.

2.2 The nature of turbulence

This study focuses on the flow control of turbulent flows, so the characteristics of turbulence are essential. This section will briefly introduce basic features of turbulence.

Turbulent flow widely exists in nature and engineering applications. It might be smoke from a chimney, stirring coffee, running water, vapour above boiling water, a trail of streaks of condensed water vapour or wakes of an aircraft. Turbulent flow is highly nonlinear and random in nature. Even though turbulent flow is common in nature, easily generated in experiments, and simulated with numerical methods, there is no accurate definition of turbulence. Most definitions of turbulent flow are based on characteristic descriptions. Observing flow through a water jet shown in Figure 2.1, the main acknowledged characteristics of turbulent flow are listed as follows (Sagaut *et al.* [2006]).

Figure 2.1: Two-dimensional image of an axisymmetric water jet, obtained by the laser-induced fluorescence technique. (Prasad and Sreenivasan [1990])

Continuum. Turbulence is a continuum phenomenon. Even the smallest turbulent scales are much larger than molecular scales. Besides flow motion, vortices distribution is also continuous but irregular.

Irregularity. Turbulent flow is irregular and can never be reproduced in details, which makes it impossible to deterministically describe turbulent flow motions as functions of time and space coordinates. That is why most of the popular research is based on statistical methods.

Three dimensionality of the vorticity fluctuations. Turbulent flow is non-linear in its convection process, which makes flow unsteady, three dimensional and rotational with a non-zero vorticity. Vorticity dynamics plays an essential role in turbulent flows. Vortex

generation, stretching and shedding are all significant mechanisms in turbulence. The energy cascade of turbulence is also related to the stretching and thinning of the vortices.

Diffusivity. Velocity fluctuations in turbulent flow spread to its surroundings via convection and diffusivity. The diffusivity of turbulence is the main feature of turbulent flow, which contributes to the mixing enhancement, mass and heat transfer. Thus, it is one of the most important properties concerned in engineering applications.

Multi-scales. Turbulent fluctuations exist over a wide range of time and spatial scales. Turbulent flows can be viewed as a superposition of an entire hierarchy of eddies with a range of length scales. The length scales of these eddies range from the size similar to the object size to the smallest size conditioned by viscous dissipation. In addition, turnover time of the entire hierarchy eddies is also multi-scales.

Cascading. The largest eddies are anisotropic, while the smallest ones show isotropic characteristics (at least at high Reynolds numbers). The largest eddies extract energy from the mean flow motion. As they break up, energy is transferred to the smaller eddies. These smaller eddies undergo a similar process. Eventually, they are small enough for viscous dissipation to become the principal mechanism, and finally turbulence kinetic energy is irreversibly converted into thermal energy.

Above characteristics of turbulent flows play important roles in turbulence modelling and flow control on turbulence. The main objective of turbulence modelling is to accurately model turbulence convection, diffusion, dissipation and the interaction between different scales. Flow control mostly focuses on the manipulation of vorticity to achieve desired flow status. Details of turbulence modelling and flow control of turbulence will be reviewed in the following sections.

2.3 Flow simulation

2.3.1 Direct numerical simulation

The turbulent flow, no matter how complex behaviour it has, is the consequence of a fairly simple set of equations from classical physics, the Navier-Stokes (N-S) equations. In these equations, the flow variables are functions of both space and time (Moin and Mahesh [1998]). However, there are no analytical solutions to even the simplest turbulent flow, due to "strong non-linearity, a large number of degrees of freedom, sensitivity to small differences in flow conditions, the existence of viscosity, a lack of firm universal phenomenology, and many other factors" (Ishihara *et al.* [2009]). Therefore, the N-S equations can only be solved numerically. The simplest simulation approach is the direct numerical simulation (DNS).

The mathematical equations in DNS are completely closed, without any empirical inputs.

The objective of DNS is to resolve the whole spectra of both the length and the time scales of turbulence during a sufficient time interval. Therefore, DNS must have a domain large enough to contain the largest turbulent eddies with a length scale of the characteristic length of the object l_0, and it is also required to accurately represent the length scales down to the Kolmogorov length scale η. In other words, in a computational domain with a size larger than the object in a fluid, the mesh resolution for DNS should be fine enough to accurately capture most of the dissipation, which occurs down to the Kolmogorov length scale. Take a case with homogenous isotropic turbulence for example, for DNS, the numerical elements in one spatial direction should have a number of $l_0/\eta \sim Re^{3/4}$, and for a 3D space, the number of cell is about $Re^{9/4}$. Besides, the number of computational time steps scales with $\tau_0/\tau_\eta \sim Re^{1/2}$. If the Reynolds number is doubled, the mesh cells will increase by a factor of 4.8 and the number of time steps increases by a factor of 1.5. With an algorithm requiring $N\log N$ operations in each direction, the total computational cost will increase by a factor of 11 with a doubled Reynolds number. Take the Lockheed Martin F-22 Raptor for example, its Reynolds number is about 4.5×10^8, with the chord length around 10.0 m and a cruising Mach number of 1.82. At this Reynolds number, computational cost for this high Reynolds number with DNS is far beyond the current most powerful computers. Therefore, the huge computational cost makes DNS limited to a small Reynolds number range.

In the practical point of view, solving the whole spectra of turbulent flow may be not necessary, as most of the turbulence kinetic energy is carried by eddies with large scales (Sagaut *et al.* [2006]). Engineers are more interested in how turbulence fluctuations extract energy from the mean flow and how the turbulent flow cascades in large scales, rather than how the smallest scales of turbulence cascade and dissipate. If the turbulence fluctuations with small scales can be accurately modelled, and their interactions with the large scales can be accurately superposed on the mean flows or eddies with large scales, most requirements for current industrial applications are satisfied. Therefore, turbulence modelling techniques have been widely applied in numerical simulations to get rid of the high computational cost.

2.3.2 Reynolds-averaged numerical simulation

A turbulent flow field with fluctuations has an infinite number of spatial and temporal scales (degrees of freedom), which make it impossible to resolve all scales with affordable sources. Reynolds [1895] proposed to decompose an instantaneous flow quantity into its time-averaged and fluctuating components. This treatment reduces degrees of freedom in a turbulent flow field and lays the groundwork for turbulence modelling techniques. This

2.3. Turbulence modelling

treatment is the Reynolds average approach.

The essence of the Reynolds average is an ensemble average. With reasonable assumptions, the most popular definition of the Reynolds average, based on a long time average, is expressed as

$$\overline{\phi(x_j)} = \frac{1}{T_0} \lim_{T_0 \to \infty} \int_t^{t+T_0} \phi(x_j, \tau) d\tau, \tag{2.1}$$

where ϕ is a variable of both space and time, and T_0 is a long time interval. The strategy of the Reynolds average is the Reynolds decomposition, which decomposes flow variables into mean and fluctuating quantities. Take a velocity vector for example, the real instantaneous velocity $u_i(x_j, t)$ can be decomposed into

$$u_i(x_j, t) = \overline{u_i(x_j)} + u_i^{'}(x_j, t), \tag{2.2}$$

where $\overline{u_i(x_j)}$ is Reynolds (or time) averaged velocity, and $u_i^{'}(x_j, t)$ is the fluctuation superposed on the mean velocity. For steady flows, the Reynolds averaged variables are independent on time ($\partial/\partial t = 0$). For unsteady flows, it is assumed that the variation of the Reynolds averaged variable during the time interval T_0 is negligible. This assumption makes Reynolds average valid in the scenarios, where time scales associated with the turbulent fluctuations are much smaller than the physical time steps in simulations, and the time step is also much smaller than the important global unsteady time scales forced in the flow (Anderson *et al.* [1984]), such as flapping time intervals in a flapping wing.

When the variables in the N-S equations are substituted by the decomposed variables in Eq. (2.2), the N-S equations become equations to solve the Reynolds averaged variables, which are the Reynolds Averaged Navier-Stokes equations. These equations solve the mean flows and lose the flow perturbations. The assumption behind the RANS equations is that the time-dependent turbulent (chaotic) flow fluctuations can be separated from the mean flows. The interaction between the mean flows and the fluctuations is realized by modelling additional terms, so-called Reynolds stresses, which come from the Reynolds average of the convection terms in the N-S equations. In RANS equations, the convection terms are the velocity-uncorrelated terms $\bar{u}_i \bar{u}_j$ rather than the velocity-correlated terms $\overline{u_i u_j}$, therefore, the Reynolds average of the convective term introduces an additional terms (Reynolds stresses)

$$\overline{u_i^{'} u_j^{'}} = \overline{u_i u_j} - \bar{u}_i \bar{u}_j, \tag{2.3}$$

which need to be modelled. Most of investigations on RANS concentrate on how to model these Reynolds stresses accurately for different flow types. There are numerous turbulence

models for RANS, which can be roughly categorized as algebraic zero-equation models, one-equation models, two-equation models, full Reynolds Stress Models and non-linear stress-stain models. Each type includes many turbulence models. A comprehensive description of developments of RANS models are summarized in Wilcox [2006].

If the integration time T_0 in Eq. (2.1) is similar to the characteristic time of the flow, the time differential terms $\partial/\partial t$ cannot be assumed to be zero any more. The RANS equations with $\partial/\partial t \neq 0$ is unsteady RANS (URANS). A detailed definition of URANS is given by Merzari *et al.* [2009], based on the ensemble averaging over different realisations of the flow fields. URANS is regarded as a generalized filter in both time and space with characteristic filter spatial scales and filter temporal scales (Merzari *et al.* [2009]). (In practical situations of numerical simulations, the ensemble average is assumed to be equivalent to a time-average.) Following this interpretation, URANS can only resolve the fluctuations of time scales larger than the characteristic filter scales. Figure 2.2 cited from Spalart [2009] compares the resolved vorticity in flows around a cylinder with RANS and URANS (both 2D and 3D). RANS modelled all the fluctuations and a steady solution was achieved (see Figure 2.2(a)), 2D URANS captured flow shedding with steady flow features in the spanwise (see Figure 2.2(b)) and 3D URANS resolved flow fluctuations with characteristic length and time scales (see Figure 2.2(c)), and some 3D fluctuations in the spanwise direction were also resolved.

Although URANS can resolve some large eddies, the current RANS turbulence models do not have good performances on flows with high adverse pressure gradients. There are some improvements on URANS. A recent development of URANS is so-called Scale-Adaptive Simulation (SAS) (Menter and Egorov [2010], Egorov *et al.* [2010]). SAS introduces the von Karman length scale to the source terms of the underlying two-equation turbulence model. Thus, SAS allows the turbulence models to resolve the flow dynamics without a spatial filter and to react more dynamically to resolved scales in the flow field, which cannot be handled by the standard URANS models. Figure 2.3 shows that SAS-URANS can resolve much more small turbulence structures than URANS.

2.3.3 Large-eddy simulation

DNS aims to resolve all the spectra of turbulent flow, while RANS intends to model all the spectra. Large eddy simulation is a technique intermediate between RANS and DNS. LES was designed to resolve large eddies containing most of the turbulence kinetic energy and momentum, and to model interactions between the resolved flows and flows with length scales smaller than the grid scales (usually called sub-grid scale (SGS)). LES is similar to
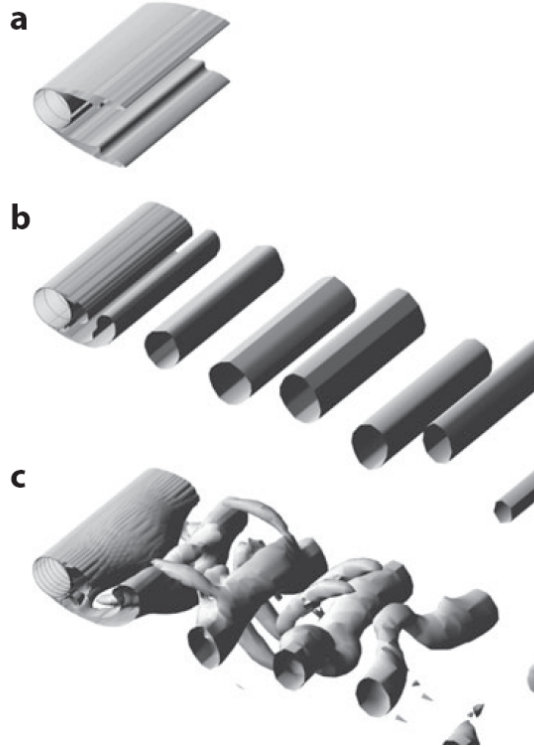
Figure 2.2: Vorticity iso-surfaces of flow over a circular cylinder at $Re_D = 5 \times 10^4$ with laminar separation. (a) RANS, (b) 2D URANS and (c) 3D URANS. (Spalart [2009])

DNS in that LES provides three dimensional, time-dependent solutions of N-S equations, therefore, LES also requires computational grids with high resolutions. However, as the smallest resolved flow in LES is determined by the grid-spacings which may be thousands of times larger than the Kolmogorov's length scale, LES can deal with flows at relatively high Reynolds numbers.

Spatial filter is employed in LES. As a result, flow variables are decomposed into a low-pass term (large length scales) $\langle u_i(x_j, t) \rangle$ which will be resolved and a filtered term (small length scales) $u'(x_j, t)$ which will be modelled. The decomposition is expressed as

$$u_i(x_j, t) = \langle u_i(x_j, t) \rangle + u_i'(x_j, t). \tag{2.4}$$

When a spatial filter function is applied to the N-S equations (often defined as a convolution product), the filtered N-S equations are achieved, which simulate the filtered flow fields. The effect of the sub-grid scale flow on the resolved flow is reproduced in the momentum
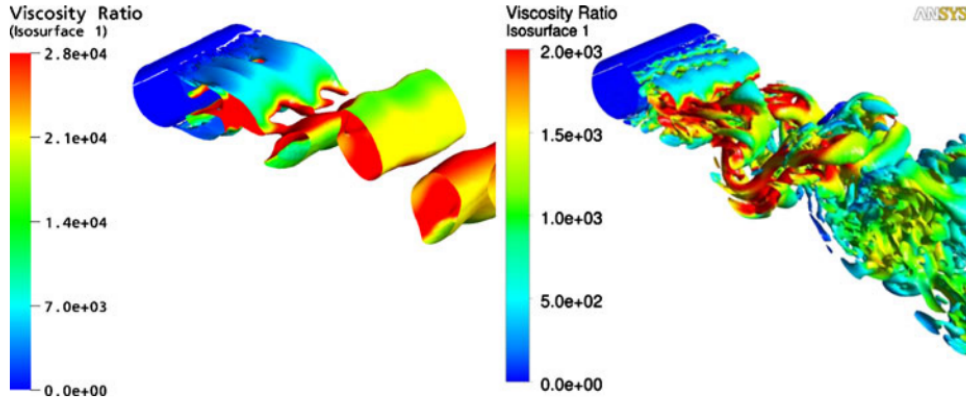
Figure 2.3: Q-criterion iso-surfaces (coloured with the eddy viscosity ratio) by a circular cylinder at $Re_D = 3.6 \times 10^6$. Left: URANS, Right: SAS-URANS. (Menter and Egorov [2010])

equations via modelling the sub-grid scale stresses τ_{ij}^{S}, which read

$$\tau_{ij}^{\mathrm{S}} = \langle u_i u_j \rangle - \langle u_i \rangle \langle u_j \rangle. \tag{2.5}$$

A crucial issue for LES is in what range the spatial filter should be for both an accurate resolution and an affordable computation cost. A commonly accepted rule is that the spatial filter or the grid is sufficiently fine to resolve about 80% of total turbulence kinetic energy (Sagaut *et al.* [2006]). This rule brings about another issue for LES in wall-bounded flows. As there are numerous small turbulent structures of cascading length scales in the boundary layers, simulating 80% of the turbulence kinetic energy in the boundary layer requires a "quasi-DNS" mesh resolution (Baggett [1998]), which is still unaffordable with current computational sources for flows at high Reynolds numbers. Therefore, the wall-modelled LES (WMLES) becomes an alternative, which models most of kinetic energy in the near-wall region and resolve most of the turbulent structures in other regions. The techniques of wall-modelling will be presented in the next section, together with the hybrid RANS/LES methods. Herein the sub-grid scale model will be focused.

The main task of a SGS model is to dissipate a proper amount of energy from the resolved scales through the sub-grid scale dissipation. The firstly used SGS model is the Smagorinksy model (Smagorinsky [1963]). As the Smagorinsky constant employed by the Smagorinksy model is estimated from isotropic homogenous flows, this model is overly dissipative for most of real flows. Thus, it is only used for simple flow. A dynamic Smagorinsky model

2.3. Turbulence modelling

(Germano *et al.* [1991]) was proposed to solve this problem. The dynamic Smagorinksy model has two spatial filters and uses the overlapping of these two filters to calculate the Smagorinsky coefficient dynamically based on local transient flow fields. The most significant contribution of this dynamic Smagorinsky model is the introduction of the Germano-identity. Most follow-up research on the dynamic SGS models adopts the concept of the Germano-identity. In the past decade, many SGS models were proposed and investigated. Wall-adapting local eddy-viscosity model (Nicoud and Ducros [1999]) introduces a spatial filter associated with the wall distance and the cell volume to guarantee a zero turbulent viscosity for laminar shear flows. Kim and Menon [1997] and Kim [2004] proposed a dynamic kinetic energy sub-grid-scale model, which uses the transport of the sub-grid-scale kinetic energy to realize a better modelling. Vreman [2004] proposed an eddy viscosity sub-grid scale model (Vreman's model), which guarantees theoretically zero sub-grid scale dissipation for various laminar shear flows. Park and Choi [2006] realized a dynamic procedure of the Vreman's model using the Germano-identity, and this dynamic procedure was based on the global equilibrium between dissipation in the sub-grid scale and the viscous dissipation. In this method, the constant model coefficient in Vreman's model, is still globally constant in space but varies in time, which makes this model more suitable for complex flows. Different from employing two-level test filters by Park and Choi [2006], You and Moin [2007] proposed a dynamic procedure for the Vreman's model with only a single-level test filter. This method has the potential to be used in complex geometries, because there is no any *ad hoc* spatial and temporal averaging or clipping of the model coefficient. In all above mentioned dynamic SGS models, the dynamic coefficients are averaged in space to avoid possible singularity, because the model dynamic coefficients highly depends on instantaneous flow fields, which may contain some negative eddy viscosity, leading to a computational instability. However, the global average is not applicable to complex inhomogeneous flows. In order to conquer this issue, the Lagrangian average was introduced to SGS models. Instead of averaging over directions of statistical homogeneity, the averaging over flow pathlines in the Lagrangian average makes the dynamic SGS models available to be applied to inhomogeneous flows in complex geometries. Dynamic SGS models with the Lagrangian average are the Lagrangian dynamic SGS models (Meneveau *et al.* [1996]). Actually, all above mentioned SGS models can be converted to a Lagrangian SGS model with the Lagrangian average. The main issue in the Lagrangian average is the time scale over which the averaging is performed, and in other words, is how to determine the Lagrangian time scale. Initially, Meneveau *et al.* [1996] adopted a characteristic Lagrangian time scale, which is determined by the relevant Lagrangian autocorrelation functions. A very recent improvement on the Lagrangian average

is a dynamic estimation of the Lagrangian time scale (Vreman and Mahesh [2012]).

Besides models specially designed for LES, some RANS turbulence models can also be used a SGS model by minor modifications (usually by introducing a grid-spacing term). For example, with a grid-spacing scale replacing the wall distance in the model, the Spalart-Allmaras (S-A) model can also work as a SGS model (Spalart *et al.* [1997]). The direct transformation from RANS models to SGS models makes a hybrid RANS/LES easier to implement.

2.3.4 Hybrid RANS/LES numerical simulation

The main obstacle for LES is its prohibitive computational cost in its application to wall-bounded flows at high Reynolds numbers. Baggett [1998] calculated that the number of mesh cells required by LES for a turbulent boundary layer scales with $N \sim Re_\tau{}^2$. A natural idea to conquer this issue is to introduce a URANS method to model the near-wall region. All the SGS models with a wall-modelling treatment can be generally denoted as WM-LES. Approaches, implementing both RANS and LES, are termed as hybrid RANS/LES approaches. Hybrid RANS/LES models have made noticeable advances in the recent years. These models combine the advantages of LES in accurately resolving complex turbulent flows and the merits of RANS in modelling the near-wall region to avoid very high mesh resolution for flows at high Reynolds numbers. Sagaut and Deck [2009] claimed that the hybrid RANS/LES approach is the main strategy to reduce the computational cost, compared with LES, when attached boundary layers have a significant impact on the global flow. Much effort has been invested in this field and numerous hybrid RANS/LES models have been proposed.

The first proposal of a hybrid RANS/LES approach was made by Schumann [1975], who applied a mixing length eddy viscosity to model the near-wall region in a large eddy simulation with the Smagorinsky model. However, the most cited pioneer work in the hybrid RANS/LES approaches is Detached Eddy Simulation (DES) (Spalart *et al.* [1997]) and Very Large Eddy Simulation (VLES) (Speziale [1998]).

The idea of VLES is to introduce a resolution-control function to re-scale a conventional RANS model, and a SGS model is achieved by damping the Reynolds stresses via this control function. The resolution-control function proposed by Speziale [1998] depends on the ratio of a physical turbulence length scale and a grid-spacing scale. Following the idea of VLES in Speziale [1998], Batten *et al.* [2004] proposed a limited numerical scales approach (labelled as LNS), in which the control function is determined by the product of the characteristic length scale and the velocity scale calculated from a SGS model and the

corresponding product from a RANS turbulence model. Liu and Shih [2006] proposed a spatially-resolved numerical simulation (labelled as PRNS), in which the control function is based on a temporal filter with a fixed filter width, and this temporal filter defines the length scales of resolved structures. Hsieh *et al.* [2010] proposed a control function based on the turbulence energy spectrum, in which a cut-off wave number separates turbulent flows into resolved (from integral length scale to the cut-off length scale) and modelled parts (from the cut-off length scale to the Kolmogorov length scale). Han and Krajnovic [2012] considered the advantages of both the control function designed by Speziale [1998] and that by Hsieh *et al.* [2010] to propose a control function based on turbulence kinetic energy. Most investigation on developments of the VLES focuses on designing a better and proper control function, which can realize an accurate simulation of a seamless transition between RANS and LES for complex turbulent flows.

Another popular hybrid RANS/LES type is DES and its variations. DES introduces a turbulence length scale associated with the grid-spacing to replace the wall distance in the source term of a RANS turbulence model (for example, the S-A model or the SST model), realizing a sub-grid scale modelling. The branches developing from DES are mainly the Delayed Detached Eddy Simulation (DDES) (Spalart *et al.* [2006]) and the improved DDES (IDDES) (Shur *et al.* [2008]). The initial intention of DES (Spalart *et al.* [1997]) was to treat the near-wall region with RANS and to deal with outer regions with LES. In DES, the interface between RANS and LES in DES is pre-determined by grid-spacing and wall distances. Because of this high dependence on mesh resolutions, the interface in DES may lay in a very inner region of the boundary layer for cases with a fine mesh. This is far from the original intention, which expects RANS to cover the whole attached boundary layer. In addition, when an earlier-trigged LES penetrates into the attached boundary layer with an "ambiguous" mesh resolution, the modelled Reynolds stresses in DES will decrease, whereas the resolved stresses are still deficient to balance the reduction of modelled Reynolds stresses due to limitations of grid resolutions. This situation leads to a modelled Reynolds stress depletion (MSD) (Spalart [2009]). The MSD problem usually gives rise to a spurious buffer layer, a log-layer mismatch (LLM) with an under-estimation of skin friction and a grid-induced separation (GIS) (Menter and Kuntz [2004]). In principle, these problems can be avoided by extending the RANS mode to cover the whole attached boundary layer (Menter *et al.* [2003]). By following this strategy, DDES, with a blending function associated with instantaneous flow fields, was proposed to extend the RANS mode from the near wall region to the whole attached boundary layer (Spalart *et al.* [2006]). This blending function takes transient flow fields into consideration to realize a dynamic interface between RANS

and LES. DDES obtained improved results over DES for flows with thick boundary layers (Spalart *et al.* [2006]). However, it was argued by Travin *et al.* [2006] that DDES is sensitive to initial flow fields and still suffers from the LLM problem due to its inheritance from DES, therefore, the wall modelled LES was recommended as an alternative. Later, an improved version of DDES named IDDES (Shur *et al.* [2008]) was proposed to overcome problems mentioned above. Several empirical functions were introduced in IDDES to realize a transition between DDES and WMLES. The transition depends on the initial turbulence content, and IDDES can recover from a disordered initial flow field. A very recent study on IDDES is re-calibration of the empiric constants in the blending function to optimize the formula in SST-based IDDES (Gritskevich *et al.* [2012]). Deck [2012] summarized the main issues in DES and its variations.

For the hybrid RANS/LES approaches, including both the VLES branches and DES branches, the fundamental challenges lie in defining the interface between two methods (Regions near the interface is usually named as the "grey" region.) and realizing a reasonable production and transport of turbulence kinetic energy between RANS and LES. There are numerous approaches proposed to tackle these issues.

One approach is to introduce a non-commutativity error as an additional term in the time-filter and the spatial-filter. Hamba [2003], Hamba [2006] and Hamba [2009] developed an additional filter to define two velocities at the interface to remove inconsistency in the velocity equations due to a rapid variation in the filter width. This additional filter is considered as a finite difference approximation of extra terms deriving from non-commutativity between the hybrid filter and the spatial derivatives.

Another interesting development on blending techniques is to perform a weight average of temporal and spatial filters. Germano [2004] proposed a hybrid filter to combine RANS and LES, but Rajamani and Kim [2010] argued that the missing of the Germano stress term in this approach made it inadequate to match secondary quantities such as the Reynolds stresses at the interface, and they prompted the necessity to have a Germano stress-like term in the Reynolds stresses in order to achieve a more accurate total Reynolds stress at the interface. However, these added terms have to be modelled in practical application, arising more difficulties. Sánchez-Rocha and Menon [2009] re-derived the N-S equations using a hybrid filter and the newly derived hybrid equations involves additional terms that play a fundamental role in compensating for the turbulence which is neither modelled nor resolved in the transition region between RANS and LES.

Adding forcing to the momentum equation is another way to treat the simulation of transition regions between RANS and LES. Piomelli *et al.* [2003] introduced a backscatter

17

model based on stochastic forcing to generate Reynolds stresses-carrying eddies at the transition region to compensate for dramatically decreased turbulent viscosity. However, it is difficult to determine to what extent the magnitude of stochastic forcing may not change the original physical flow field. In order to obtain physical structures of turbulence, Davidson and Dahlström [2005] used a forcing field from a DNS database. Keating and Piomelli [2006] applied a dynamic stochastic forcing, whose magnitude was adjusted based on an assumption that the resolved and modelled Reynolds stress should be approximately equal in the RANS/LES transition region. Davidson [2009] proposed a dissipative scale-similarity SGS model, which can work as a usual dissipative SGS model in the forward scatter mode or as a forcing model to simulate the generation of resolved turbulence. Therefore, this method can dampen the resolved fluctuations (forward scatter) or stimulate the growth of resolved turbulence (back scatter).

A more recent approach to realize a consistent formulation for hybrid RANS/LES is to apply an Eulerian temporal filtering (Fadai-Ghotbi *et al.* [2010]), in which the temporal filter width can be implicitly fixed by grid spacings, enabling local refinements based on the sensitivity of the dissipate rate of RANS to the cut-off frequency. Besides, there are other methods proposed to tackle this issue. In order to remedy the insufficient momentum transfer from the LES mode to the RANS mode, Wang *et al.* [2012a] proposed a pressure-sink method to enhance the momentum transfer from the outer boundary layer to the inner boundary layer by introducing a small pressure gradient in the wall-normal direction. Simulations on wall-bounded supersonic flow gave improved results. In order to reduce the computational cost for LES in a large flow system, zonal RANS/LES methods are also usually considered. The most popular treatment is to manually set up a LES region in regions which are interested and to leave other regions with RANS. The zonal approach is often hampered by the same difficulties in hybrid RANS/LES, which is how to transfer flow information properly between RANS and LES. Details about zonal RANS/LES methods can be found in Jakirlić *et al.* [2009], which will not be reviewed in details.

Although there are numerous hybrid RANS/LES treatments, all these models can be generally classified into either a model with a hard-interface or a model with a soft-interface (Fröhlich and von Terzi [2008]). The hard-interface means the interface between RANS and LES is stationary, such as DES. Models with soft-interfaces adjust the interfaces according to transient flow fields. Classic examples of the latter are the delayed DES and its improved version IDDES. The hybrid RANS/LES models can also be divided into another two categories according to coupling mechanisms between RANS and LES modes. Approaches with an explicit coupling usually involve additional terms or extra coupling/forcing conditions

at interfaces, such as the method proposed by Piomelli *et al.* [2003]. Because of the additional coupling conditions at the interface, flow information can be exchanged between the time-averaged RANS and the spatial-filtered LES, thus these approaches can release the problem of "grey" regions (Spalart [2009]) near the interfaces. Implicit coupling is a weak RANS/LES coupling method. It employs the same turbulence model for both RANS and LES, and it usually has an automatic switching between these two modes. The implicit coupling does not require additional *ad hoc* transport conditions or any treatments at interfaces. Therefore, turbulence models with implicit couplings become popular in practical CFD solvers, which are also focused on in this study.

2.4 Flow control

Flow control usually means manipulating flow passively or actively to alter a natural flow state into a more desired state. Take flow around an aircraft for example, popular manipulations of flows include delaying/advancing transition, postponing/promoting separation, augmenting/suppressing turbulence, and so on. The goals are to increase lift, to reduce skin friction and pressure drag, to augment turbulence, to enhance heat transfer, to suppress noise and so on (Jahanmiri [2010]).

For real flows, some of the flow control goals conflict with each other, and currently there is no a single device for flow control which can realize all these goals simultaneously. Inter-relations between conventional goals in flow control are summarized in Figure 2.4, in which the upper three terms (flow transition, separation and reattachment) are three primary flow features to be controlled, and the lower two terms (drag and lift) are two common control objectives.

According to energy expenditure, flow control methods can be classified into passive flow control and active flow control. Passive flow control means manipulating flows without external energy expenditure. Active flow control has external energy or auxiliary power introduced into original flows. For active flow control, if the input steady/unsteady energy is given in advance without considering instantaneous flow fields, it is a predetermined active flow control, for example, oscillating surface driven by a piezoelectric actuator with a fixed oscillating frequency and magnitude setup beforehand. On the contrary, if the input energy is continuously adjusted depending on some flow properties measured in real time by sensors, it is interactive flow control. The control loop for interactive flow control can either be an open loop (feed-forward control) or a closed loop (feed-back control). These flow control methods can be briefly summarized as shown in Figure 2.5.

2.4. Flow control
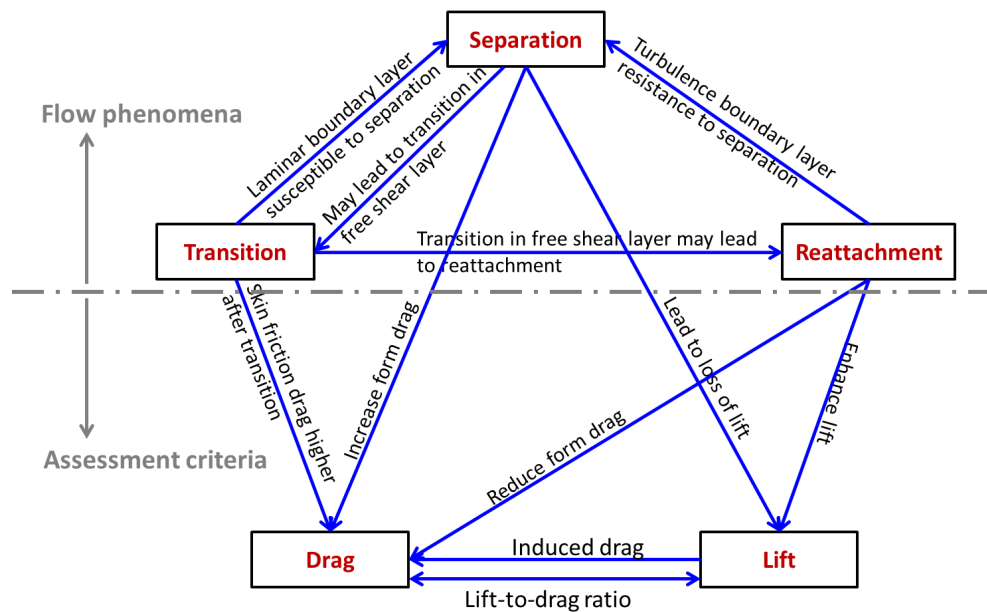
Figure 2.4: Interrelation between flow control goals (Jahanmiri [2010])

Table 2.1: Flow phenomena most commonly studied in flow control

Boundary layers	Vortex flows	Jets, mixing layers, wakes
Separation control	Forebody vortex control	Mixing enhancement
Drag reduction	Blade-vortex interaction	Jet vectoring
Noise suppression	Wing-tip vortex dynamics	Noise suppression
Virtual surface shaping	Vortex geneartion/alleviation	Wake modification

Main flow phenomena involved in flow control are usually separated into three categories: the laminar and turbulent boundary layer flow control, vortex flow control, wakes and mixing layer flow control. The most commonly studied flow phenomena are summarized in Table 2.1.

To successfully apply either passive or active flow control, a common procedure is as follows.

- Step 1: to specify a primary control objective.

- Step 2: to identify the flow phenomenon/physics to be controlled.

- Step 3: to select/design an appropriate control strategy.

- Step 4: to determine a range of operation for the key control parameters.
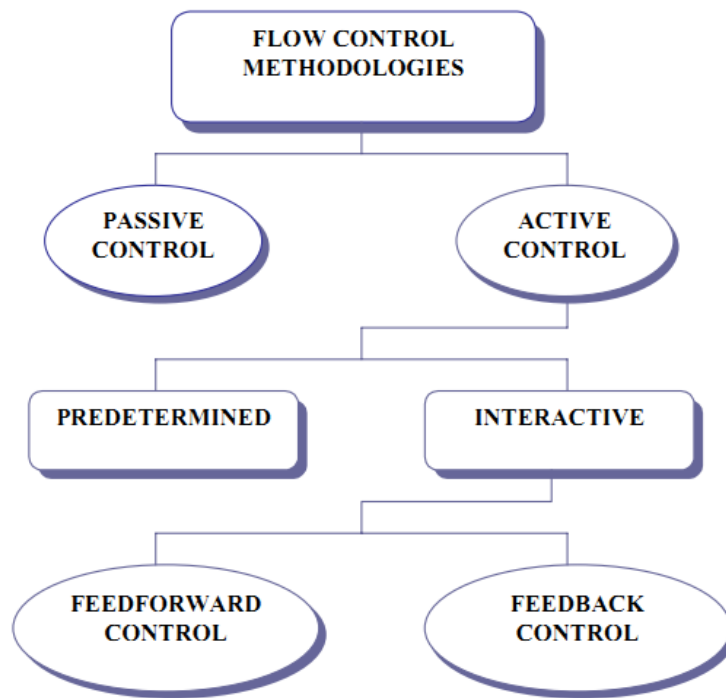
Figure 2.5: Classification of flow control (Jahanmiri [2010])

Following these procedures, the review of the controlled methods involved in the current study will be given in the following sections. Even with the best intentions and efforts, it is by no means a complete review of these flow control methods. A more general and comprehensive review on flow control methods, not limited to the three particular control methods studied in this thesis, can be found in a recently published book by Gad-el Hak [2007].

2.4.1 Passive flow control

2.4.1.1 A review

Techniques for passive flow control include modifications of flow objects, mounting additional mechanical devices, and so on. Design-modification and geometry-shaping have wide latitude. Modifications on geometries may include creating various bumps, cavities, fences, riblets, surface roughness, trips and so on (Neumann and Wengle [2003]; Oyewola [2012]). An example of geometry-shaping is aerodynamic optimization design of aerofoils. Mounted mechanical devices mainly include large-eddy break-up devices and vortex generators. For instance, in order to enhance the mixing process in the separated shear layer, Neumann

and Wengle [2003] simulated flows over a backward facing step with a thin fence positioned upstream of the step. A diagram of this control device is shown in Figure 2.6. Their DNS and LES results showed that the secondary recirculation zone had a considerably reduction and the mean reattachment length was reduced by 13%. Lee and Setoguchi [2008] installed triangular bumps and rectangular cavities near the leading edge of a backward facing step to reduce pressure oscillation. Lin [2002] and Lu *et al.* [2011] summarized different types of passive control devices, which will not be discussed in details here. The geometric change of orifices in pipes will be focussed on in this study.
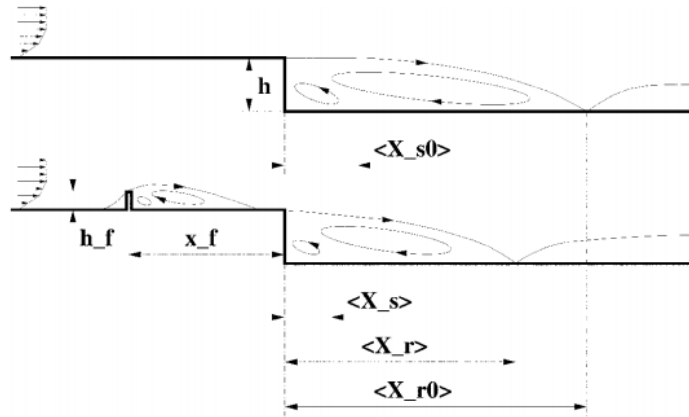
Figure 2.6: Schematic view of the baseline flow in BFS (Top) and passively controlled BFS flow (Bottom) (Neumann and Wengle [2003])

2.4.1.2   Orifice with fractal geometries

Opening slots or orifices is a basic procedure for pulsed jets or synthetic jets active flow control. A potential and simplified example is flow blowing through a jet slot into an ambient atmosphere. If it is further assumed that the ambient atmosphere is wall-bounded in a pipe, then this example becomes flow through an orifice in a pipe. A passive flow control with flow through orifices with various geometries is interesting and worthy. On the one hand, it can investigate influences of jet geometries in jets active control. On the other hand, it is also an important case in studying fractal-geometry forced/scaled turbulent flows. This thesis will explore flow through snowflake fractal orifices. A review on jets flow, orifice flow, and fractal geometries will be addressed in this subsection.

Flow control with jets through various geometries of slots. For active flow control with jets, geometry of the jet exit (or orifice exit) is an important parameter. A pioneer work was done by Liscinsky *et al.* [1996], who studied the flow mixing effect in flow

injected into a constant velocity cross flow through circular, square, elliptical and rectangular orifices with the same geometric area. After that, jets with different geometries in cross flows are widely investigated (El-Askary *et al.* [2012]; Kawai and Lele [2009]). Furthermore, jets control devices with different geometric slots are also widely studied recently (Most of them are experimental investigations.). Watson *et al.* [2003] compared a rectangular orifice and a circular orifice in flow control with a synthetic jet. It was found that with the same exit area, rectangular synthetic jets produced higher level of turbulent entrainment. Iio *et al.* [2006] studied vortex generating from pulsating jets with a rectangular nozzle, and found that the vortices originating from the short side of the rectangular moved faster than those from the longer edge of the rectangular jet. Uruba *et al.* [2007] applied blowing/suction with orifices of the rectangle and serrated shapes near the step foot of the backward facing step and found the shape of the orifice is of great important in entrainment of fluids in the recirculation zone in the blowing control mechanism, while it gave little influences in the suction control mechanisms. Nastase and Meslem [2007] applied lobed nozzles to jet flows. Their experimental data shows flows through the lobed jets have enhanced mixing compared with the circular jet of the same volume rate and flow area.

Flow through orifices with various shapes in pipes. Besides orifice geometry as a flow control parameter of flow control with jets, flow through orifices with various shapes in a pipe is also an active investigation topic. There are numerous potential applications of flows forced through different kinds of orifices in engineering applications, such as optimal flow meters, industrial mixing, combustion, cooling in nuclear power stations and flow control devices. Investigations on orifice flow in a pipe have potential benefits for designing flow control devices. Recently, there are a few experimental studies on this topic. Gutmark and Grinstein [1999] and Mi *et al.* [2010] studies flows through classical non-circular orifice jets, which both found that the notched jets had a higher rate of mixing than the circular counterpart. England *et al.* [2010] studied a triangular oscillating jet nozzle, which found the angle of deflection in the triangular jets strongly influenced flow spread and decay. The above mentioned changes of slots' geometries are mainly basic geometry, like triangular, rectangular, ellipse, and so forth.

Flow through orifices with fractal orifices. Mandelbrot and Blumen [1989] defined fractal geometry as "a workable geometric middle ground between the excessive geometric order of Euclid and the geometric chaos of general mathematics". In recent years, fractal geometry is used to generate turbulence, to investigate the interaction between the fractal geometry and the multi-scales of turbulence. In this study, orifice geometry is our investigating objective. Experiments of flows through orifices with fractal perimeters were carried

23

out to study flow behaviours introduced by fractal boundary geometries (Nicolleau [2013]; Nicolleau *et al.* [2011]). Numerical studies of the fractal orifices with experiments carried out by Nicolleau *et al.* [2011] will be researched in this thesis. The fractal geometry of the orifice follows the Koch snowflake (Von Koch [1904]), and the first four iterations is shown in Figure 2.7. A DES study of the snowflake fractal orifice (only the first fractal level F1 in Figure 2.7) was carried out by Zheng *et al.* [2012], which studied the application of different numerical methods in this type of flow and validated the DES method in simulating wall-bounded forced turbulent flows. Geurts [2012] numerically studied both laminar and turbulent flow through the fractal orifices (all these four levels in Figure 2.7), using direct numerical simulation with a volume penalization immersed boundary method. In their study, the Reynolds number for the laminar flow is $Re = 1$ and $Re = 4300$ for turbulent flow, and the thickness of the orifice plate is 0.3125 times of the pipe diameter. This thick orifice plate at such a low Reynolds number only generates turbulent flow with very weak fluctuations, as shown in their DNS results. A study on flows through fractal orifices at an industry-interested Reynolds number is meaningful and desirable, which will be focused on in this study.
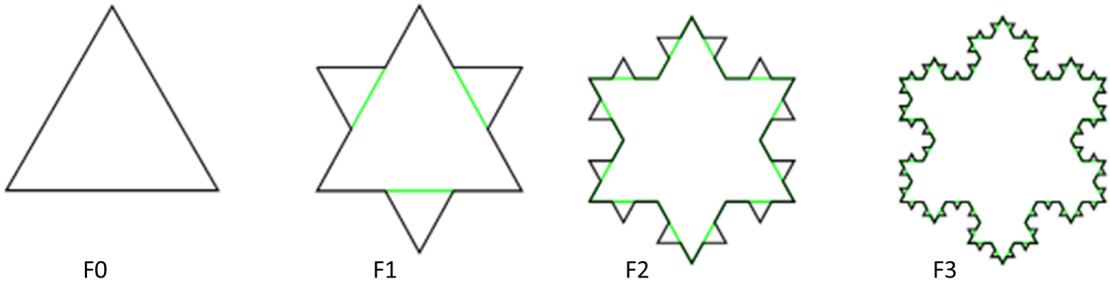
Figure 2.7: The first four iterations of the Koch snowflake

Flow through other fractal objects. Besides above two literatures, there is lack of research on the fractal snowflake orifices. Nevertheless, other fractal geometries in an open free stream flow have been investigated by several research groups. Traditional attempts at understanding the multi-scale facet of turbulence rely on turbulent flows generated by simple geometries, such as flat plates, pipes and steps. In the recent decade, new approaches to generate turbulent flows have emerged. In these approaches, turbulent flows are generated by multi-scale/fractal objects. The properties of turbulent flows, such as the turbulence evolution, its dissipation, decay and the cascade process, were better understood by studying the interaction between the flow intrinsic multi-scales and the boundary geometric scales of the fractal objects. Further understanding of flows through fractal objects will provide

some guidelines to design novel flow control devices. Most of the fractal geometries are two dimensional, such as regular grids with different blockage ratio (Geipel *et al.* [2010]; Hurst and Vassilicos [2007]; Keylock *et al.* [2012]; Krogstad and Davidson [2011]; Laizet *et al.* [2010]; Nagata *et al.* [2008]; Suzuki *et al.* [2010]; Valente and Vassilicos [2012]), fractal square grids (Gomes-Fernandes *et al.* [2012]; Hurst and Vassilicos [2007]; Laizet *et al.* [2010]; Laizet and Vassilicos [2011]; Mazellier and Vassilicos [2010]; Nagata *et al.* [2008]; Seoud and Valente [2007]; Suzuki *et al.* [2010]; Valente and Vassilicos [2011, 2012]), "I"-shape branches (Hurst and Vassilicos [2007]; Laizet *et al.* [2010]), Sierpinski triangle and Sierpinski carpet patterns (Kang and Dennis [2011]), snowflake and polygon fractals in pipes (Geurts [2012]; Nicolleau [2013]; Nicolleau *et al.* [2011]). A few three dimensional fractal objects have also been investigated recently, such as "I"-shape branches developed in the three-dimensional space (Staicu *et al.* [2003]), three-dimensional tree-like elements in a boundary layer (Bai *et al.* [2012]; Chester and Meneveau [2007]; Chester *et al.* [2007]). Most of the research focuses on experiments, and few numerical simulations were reported.

The study on fractal geometry in the above literatures are mostly about nature of turbulence cascading, turbulence production, and scaling of the dissipation scales, which may be beyond the scope of this study, due to the modelling of the short waves turbulence by hybrid RANS/LES and incapability of resolving a whole spectra of turbulence scales. In addition, fractal orifice in a pipe flow behaves quite different from fractal geometry in a free stream, therefore, some conclusions drawn in above literatures about turbulent flow properties will not be repeated herein.

2.4.2 Active flow control

2.4.2.1 A review

Theoretically, any spectra range in turbulent spectra can be controlled, provided that there are proper control devices. However, the control effects in different spectra ranges with the same control device vary widely. Each control device has its own targeted control range, and they should be carefully chosen or designed to control these spectra ranges for given control objectives. The method of triple decomposition of flow signals (Hussain and Reynolds [1970]) is a useful tool to analyse active flow control. The triple decomposition reads

$$\phi(x_j, t) = \overline{\phi(x_j)} + \widetilde{\phi(x_j, t)} + \phi^{'}(x_j, t), \tag{2.6}$$

where $\overline{\phi(x_j)}$ is the global mean value, $\widetilde{\phi(x_j, t)}$ is the statistical contribution of a organized motion and $\phi^{'}(x_j, t)$ is the random component (disordered turbulence). The first two terms

can be merged to one phase-averaged value as shown in

$$\widetilde{\widetilde{\phi(x_j,t)}} = \overline{\phi(x_j)} + \widetilde{\phi(x_j,t)}. \tag{2.7}$$

Figure 2.8 displays these three components of a turbulence signal. From the perspective of flow control, all of these three components can be manipulated by some kinds of control devices. Flow control with brute force techniques (for example a fluidic vortex generator with a high control velocity ratio) usually have sufficient amplitude to directly modify the mean flow structures represented by $\overline{\phi(x_j)}$. However, for these control methods, the input control energy is usually similar to or even larger than the studied flow. Therefore, the control efficiency is very low. More effective approaches usually manipulate the phase averaged value $\widetilde{\phi(x_j,t)}$, which seek to leverage flow properties/instabilities using small-amplitude perturbations (Cattafesta and Sheplak [2011]). The above two control strategies are the conventional methods for active flow control, which manipulate the large-scale coherent structures, consequently followed by altering the fine scales through turbulence cascading. Direct manipulation of a random turbulence signal $\phi'(x_j,t)$ is also possible. For example, an oscillating surface with micro magnitudes in the boundary layer is an example, which influences flows at the smallest scales (within the sub-layer of a boundary layer). If the control effect is obvious for this micro-manipulation, this control strategy will be of the highest efficiency as a result of the least input energy. However, as stated in Cattafesta and Sheplak [2011], effective small-amplitude forcing remains an elusive goal because of the lack of sufficient bandwidth and control authority of the actuators.

As active flow control usually has an external forcing with a determined frequency, a natural control strategy is to manipulate the flow with a similar frequency to the original flow period. Thus, the phase averaged wave in Figure 2.8 may be results of the interaction between periodic flow dynamics and the input control forcing. Considering the external forcing with frequencies, simulation of controlled flow usually requires to resolve flow time-scales smaller than the forcing time scales. Apparently, RANS lacks this capability. Thus, LES or hybrid RANS/LES or DNS is the primary simulation method for flow control.

According to the function of control actuators, active flow control can be classified into four main categories, shown in Figure 2.9. "Fluidic" in Figure 2.9 usually means fluidic vortex generators, in which fluid is injected into or sucked from the main flow. Pulsed/synthetic jet is a typical representative. The fluidic jet vortex generators on the NACA0015 aerofoil, which will be studied in this thesis, belong to this type. This control method usually manipulates the mean flow structures or at least the periodic flow structures. Thus, the flow
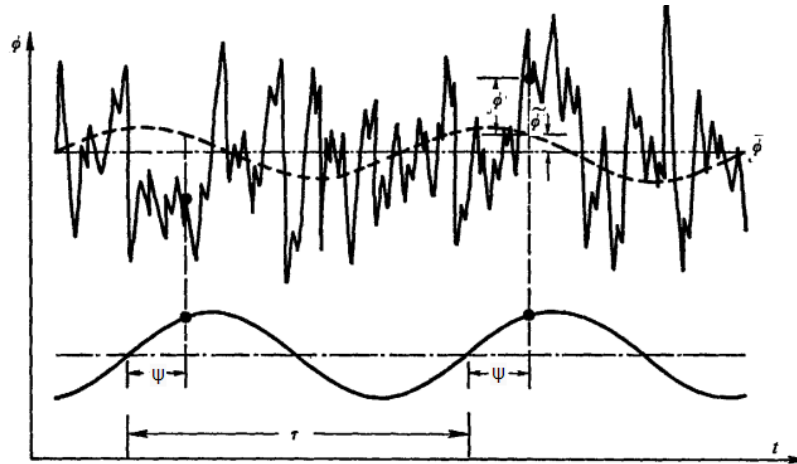
Figure 2.8: The triple decomposition of a turbulence signal, cited from Hussain and Reynolds [1970]. Upper solid curve: a turbulence signal, upper dash line: $\bar{\phi}$ phase averaged signal and the lower curve: an organized wave.

control effect is obvious and efficient. Another category involves a moving/oscillating part of the domain boundary. Rather than blowing or sucking fluid into/from the whole flow domain, the moving/oscillating part of the domain boundary aims to induce local fluid motion (Cattafesta and Sheplak [2011]). The third classification is plasma actuators, which have gained popularity in recent years due to their solid-state nature and fast time response. Moreau [2007] gave a comprehensive review of the plasma actuators.

Recent developments of micro-electro-mechanical systems and advances in manufacturing control actuators and measurement sensors intensify research on active flow control strategies. Three very recent reviews about active flow control are given by Jahanmiri [2010], Cattafesta and Sheplak [2011] and Wang *et al.* [2012b]. Rumsey [2009] summarized the challenges in numerical simulations of flow control, especially for synthetic jets flow control. Back to our objectives, flow control with oscillating surfaces and fluidic jet vortex generators will be given detailed descriptions in the following sections.

2.4.2.2 Oscillating surface on the domain boundary

Piezoelectric actuators become popular in the recent decade to locally manipulate a flow field via its oscillating motion because of their lightweight, fast time response, no-contact, reliability and low cost. Piezoelectric actuators are based on a mutual transformation between the mechanical and the electrical state, which is the piezoelectric effect. By controlling the voltage amplitude and frequency of the applied electricity, membranes of the piezoelectric

2.4. Flow control
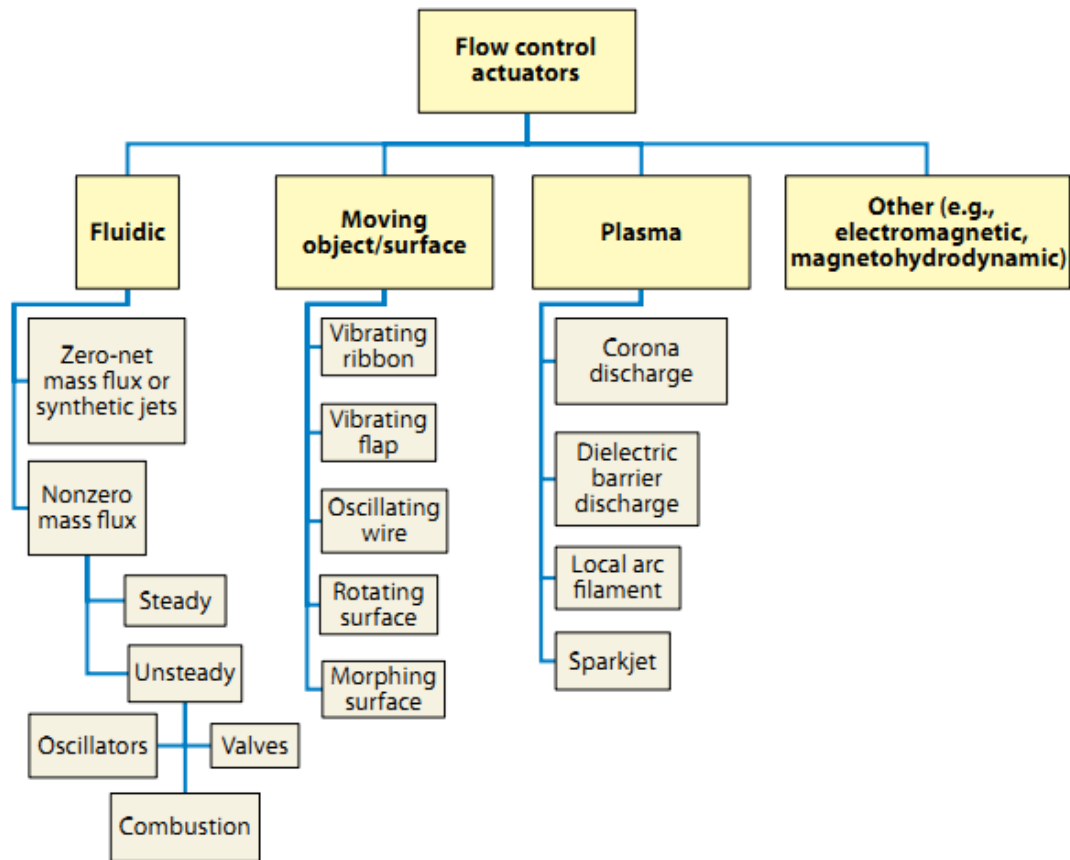
Figure 2.9: A typical classification of flow control actuators. (Cattafesta and Sheplak [2011])

actuators have corresponding mechanical motions. If these motions are applied into a flow field, thus to modify their surrounding flow properties, a desirable flow field may be produced. The most common applications of piezoelectric actuators on the flow boundary are piezoelectric flaps, piezoelectric oscillating surface and micro jets, which will be addressed respectively.

Application of piezoelectric actuators to form a micro jet by the oscillation motion will be not addressed in details herein, because it has some kinds of similarity to the jets vortex generator in the next section, which will be delicately addressed then.

Figure 2.10 shows a typical example of applications of piezoelectric flaps. The piezoelectric actuators are installed in chambers opened in the surface of an object, then the piezoelectric actuators are fixed in one side and free in the other side to realize a flapping motion. Cattafesta *et al.* [1997] carried out experiments to study the control effect of piezoelectric flaps in noise attenuation by exciting shear layer instabilities incommensurate with the Rossiter resonance mechanism. Cattafesta *et al.* [2001] discussed theoretical

modelling, experimental validation, and optimal design of piezoelectric unimorph and bi-morph flap actuators. Later, Mathew *et al.* [2006] carried out a study on the optimization of the piezoelectric flaps for noise-suppression. Cattafesta *et al.* [2003] and Cattafesta *et al.* [2008] summarized the application of piezoelectric flaps to suppress oscillations caused by flow over open cavities. The above mentioned applications of piezoelectric flaps are mainly for suppressing the cavity noise. Apart from noise-suppression, piezoelectric flaps are also used in aerofoils to control flow separation. Seifert *et al.* [1998] experimentally controlled the flow separation via piezoelectric flaps by exciting the turbulent boundary layer upstream of separation with actuators interacting directly with the attached boundary layer. Heinz [2010] investigated the piezoelectric actuators attached at the trailing edge of an aerofoil to realize a movable flap using 2D incompressible RANS, and the results show a substantial drag reduction.
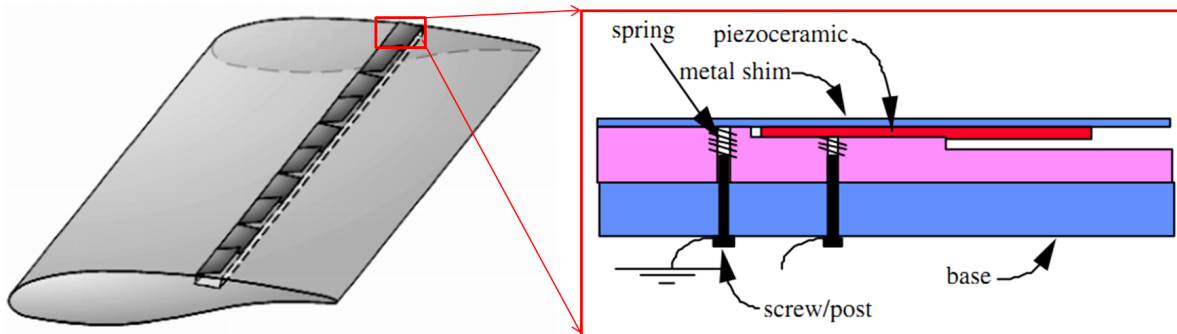
Figure 2.10: Piezoelectric actuator as oscillating flap

Another application of piezoelectric actuators, which is also what we will study in this thesis, is the motion introduced by oscillating surfaces of piezoelectric actuators. This application is very novel and lack of literatures. An example of a piezoelectric oscillating surface is shown in Figure 2.11, cited from Amir and Kontis [2008]. The experimental study was carried out by the Aero-Physics Laboratory of The University of Manchester (APL-UniMan, for short). Piezoelectric actuators were installed on the upper surface of a NACA0015 aerofoil to replace the original solid surface. In their experiments, in order to mount these diaphragms, circular slots were created by CNC machining, and Araldite super glue was used to glue the diaphragms. Their experiments showed that actuators operating at a near leading edge position ($0.25c$) are more effective than those operating at $0.5c$ with an increase of 47% increment of the maximum lift-to-drag ratio. They also observed that below the angle of attack 12°, the control effect is less effective. However, when the incidence angle is larger than 12°, the oscillating motion of piezoelectric actuators significantly changes the

boundary layer thickness, mean flow field and turbulence intensity. The main mechanism is the oscillating surface enhances the flow momentum in the boundary layer and suppress the turbulent intensity, and furthermore, to eliminate the flow separation.
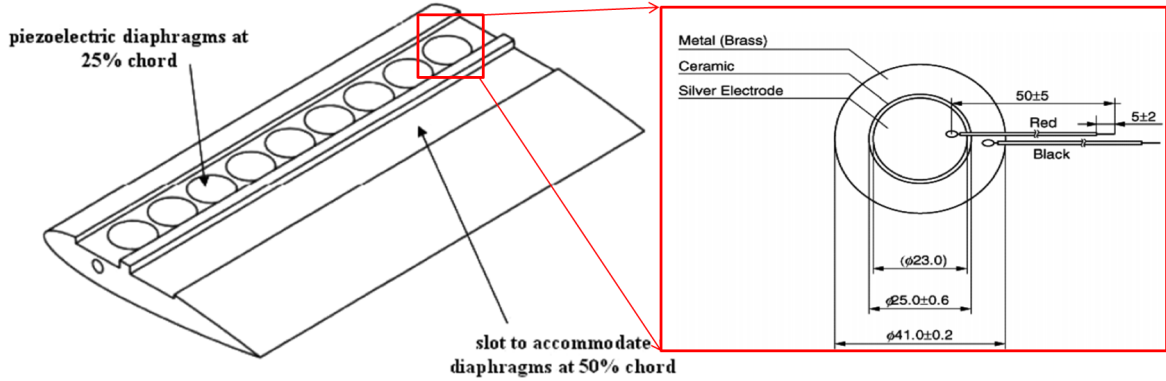
Figure 2.11: Piezoelectric actuator as oscillating surface.

Except for the application of piezoelectric actuators as oscillating surfaces on the aerofoil shown in Amir and Kontis [2008], there are no other literatures on the applications of oscillating surface of piezoelectric actuators. Nevertheless, a very similar flow control device is so-called "Flexible Composite Surface Deturbulator" (FCSD) (Sinha and Ravande [2006a]), shown in Figure 2.12. The FCSD is a micro-structured compliant wall. Through the interaction between the compliant wall and the laminar/turbulent boundary layer with zero-pressure gradient, the FSCD approach can reduce the overall aerodynamic drag by maintaining a thin layer of separated flow near the surface and by attenuating turbulent mixing in this shear layer (Sinha and Hyvärinen [2008]; Sinha and Ravande [2006b]).

All current documented piezoelectric oscillating surface and the FCSD approach are applied to an adverse or zero pressure gradient flow. The micro-motion of the oscillating surface can manipulate the thin boundary layer flow, then to affect the flow separation and lift-to-drag coefficient, and finally to achieve improvements on the aerofoil performance. The control effect of piezoelectric oscillating surfaces on thick attached boundary layer is still unknown. A novel application of the piezoelectric oscillating surface will be carried out by APL-UniMan group (experimentally) and our group (numerically), which is to study the oscillating surface flow control of the thick boundary layer before flow separated from a sharp step edge in a backward facing step.
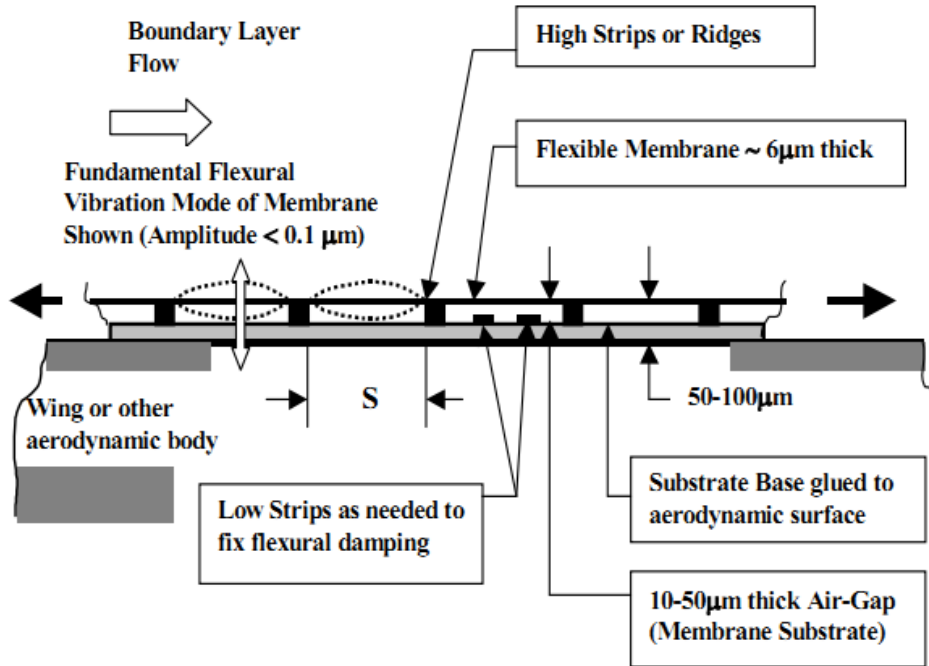
Figure 2.12: Schematic of the SINHA Flexible Composite Surface (FCSD). (Sinha and Ravande [2006a])

2.4.2.3 Fluidic flow control

As shown in Figure 2.9, fluidic vortex generators can be classified into zero-net mass flux (ZNMF) actuators and nonzero mass flux actuators. The ZNMF actuators, by definition, alternately ingest and expel fluid in an oscillatory manner through an orifice/slot only using the working fluid without any external mass source/sink (Cattafesta and Sheplak [2011]). One of the most popular zero-net mass flux actuator devices is the synthetic jet. On the contrary, the non-zero mass flux actuators require external fluid source/sink to provide steady and/or unsteady forcing via combinations of valves (Siauw *et al.* [2009]), natural fluidic oscillators (Travnivcek *et al.* [2003]), or combustion-driven devices (Crittenden *et al.* [2001]). These two kinds of fluidic vortex generators will be separately described in this section. The ZNMF actuators will be briefly introduced. The fluidic vortex generator with nonzero-net mass flux, which will be studies in this study, will be reviewed in details.

(1) Fluidic jets with zero-net mass flux

The terminology "synthetic" in synthetic jets usually means "zero-net mass flux" (Glezer [2011]). Without external mass injection, synthetic jets generate and transfer discrete vor-

tical structures to a flow system, in the means of actuators integrated in the boundary of working flow.

A synthetic jet actuator usually consists of a cavity with an oscillatory element on one side and an orifice/slot exit on the other side. The moving element oscillates about its equilibrium position, alternately expelling or ingesting fluid from or into the cavity through the orifice/slot. According to the oscillatory motion in a synthetic jet, there are mainly three types of synthetic jets, which are jets driven by acoustic power or electrodynamic actuation (Nani and Smith [2012]; Sawant *et al.* [2012]), jets driven by piezoelectric diaphragms (Mane *et al.* [2005]), and jets driven by electromechanical pistons (Gilarranz *et al.* [2005]; Thomas and Abraham [2010]).

Figure 2.13 demonstrates the formation and evolution of synthetic jets with piezoelectric membranes to drive oscillation motions. The jet is synthesized by the time-harmonic formation and subsequent interaction of a train of vortex pairs that are formed at the edge of the orifice by the motion of a diaphragm mounted in a sealed cavity (Smith and Glezer [1998]). An examples of synthetic jets driven by electrodynamic actuation is shown in Figure 2.14(a). Figure 2.14(b) displays an examples of synthetic jets with electromechanically driven pistons.
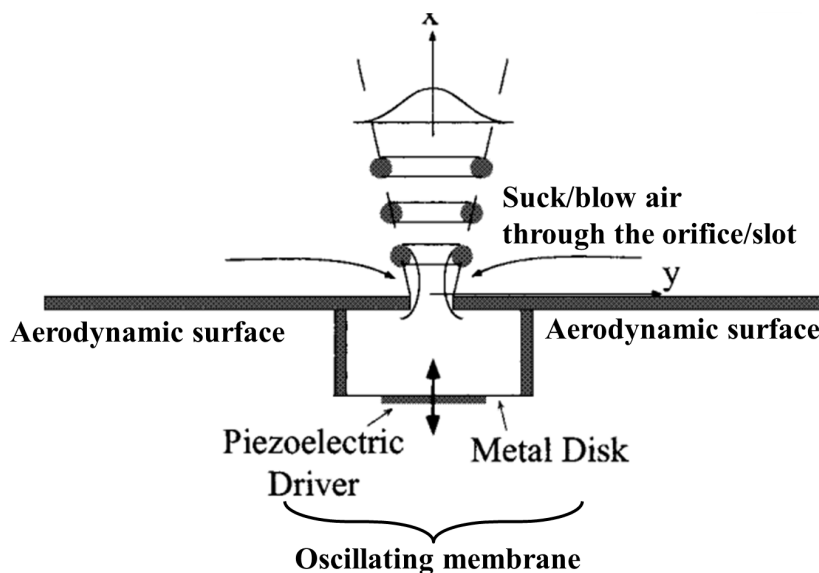
Figure 2.13: Schematic diagrams of synthetic jet with piezoelectric diaphragm. (Smith and Glezer [1998])

Experimental investigations on the synthetic jets are well documented. A comprehensive review on the synthetic jets was given by Glezer and Amitay [2002], then Glezer [2011]
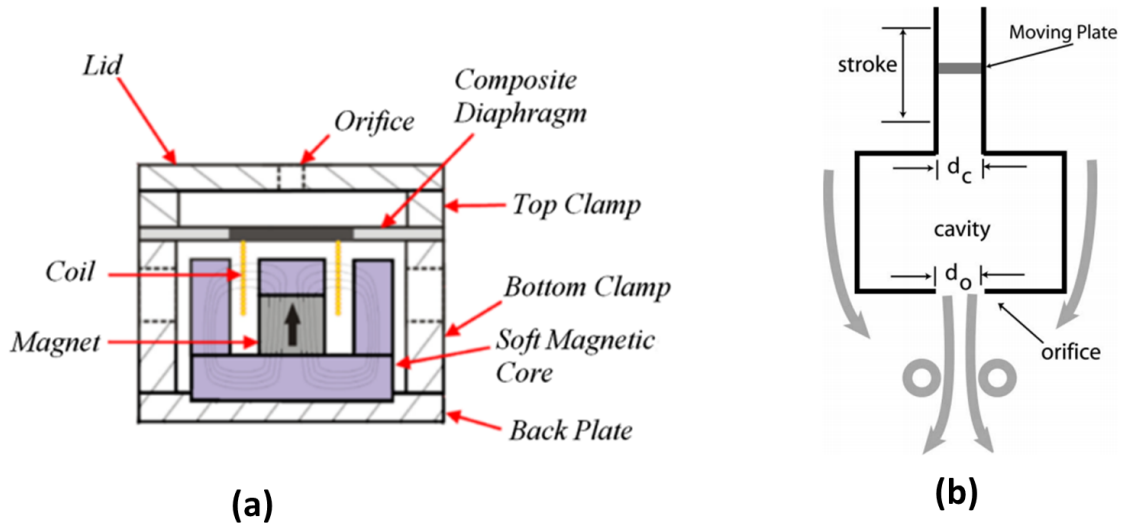
Figure 2.14: Schematic diagrams of synthetic jet with (a) electrodynamic actuators (Sawant *et al.* [2012]) and (b) electromechanically driven pistons (Thomas and Abraham [2010])

summarized the recent developments in the last decade. Leschziner and Lardeau [2011] addressed the achievements and challenges in the development of simulations of synthetic jets. Literatures on numerical simulations of synthetic jets will be summarized in the following.

An early numerical investigation of synthetic jets was carried out by Kral *et al.* [1997]. In Kral *et al.* [1997], a two dimensional and incompressible RANS simulation was conducted, and the synthetic jet was modelled by specifying velocity profiles measured in experiments, which means the modelling of the cavity was omitted. Ignoring the jet cavity may sacrifice the accuracy of the curvature of the diaphragm when the oscillating amplitude is not very small. Therefore, for the first time, Mittal *et al.* [2001] modelled the diaphragm as a moving boundary in a realistic manner in order to compute the internal cavity flow accurately in a two dimensional RANS configuration. Lee and Goldstein [2002] carried out a DNS simulation of an array of synthetic jets driven by pistons in a two-dimensional configuration, which observed the lip and depth of the cavity plays important roles in generating vortices. Kamnis and Kontis [2004] validated different RANS turbulence models in simulating synthetic jets by specifying a velocity boundary condition. Their two-dimensional simulation results show the Spalart-Allmaras model predicted more accurate results than the $k-\varepsilon$ and $k-\omega$ models. With a few of previous studies in 2D, a three-dimensional DNS simulation of synthetic jets with the cavity flow was carried out by Ravi *et al.* [2004] to investigate the 3D jet flow in quiescent and cross flows. Xia and Qin [2005] firstly applied the DES modelling method to study the synthetic jets with cavities using the dynamic grid techniques. Later, Xia and Qin

[2008] and Qin and Xia [2008] studied a cubic-root filter in DES and dissipation-controlled Roe scheme applied in an isolated synthetic jet, and the flow control mechanism was also investigated in these two literatures. You and Moin [2006] and You and Moin [2007] carried out a large eddy simulation of the separation control with synthetic jets in NACA0015, involving a small slot across the span connected to a cavity inside of the aerofoil to product the oscillatory synthetic jets. Dandois *et al.* [2007] simulated the synthetic jets with the cavity using both DNS and LES in a rounded ramp, which observed that the synthetic frequency similar to the natural shedding frequency can suppressed the flow separation most effectively. Similarly, Hong [2012] studied synthetic jets flow control on the boundary layer laminar-separation, and it is observed that the synthetic jets were most effective in eliminating the laminar separation bubbles when the forcing frequency was in the lower range of the T-S instability. Sawant *et al.* [2012] employed the lumped-element electrotechnical model to study an electrodynamic ZNMF actuators and achieved promising results.

Generally speaking, the main trend in simulation of synthetic jets is to accurately simulate the whole cavity to provide a realizable control effect with LES or DNS. Meanwhile, the control frequencies, amplitudes and geometries of the orifice/slot are also hot research areas.

(2) Fluidic jets with nonzero-net mass flux

As the classification shown in Figure 2.9, there are two main categories for the nonzero-net mass flux. One is a steady fluidic source/sink, and the other is an unsteady forcing. Herein the steady suction, steady blowing and unsteady periodic actuation will be respectively introduced.

(a) Steady suction

Steady suction is one of the earliest studied flow control methods, which was firstly investigated by Prandtl [1904] in the boundary layer control. The most popular application of steady suction is to control the laminar boundary layer. Boundary-layer suction has been known for decades to delay laminar/turbulent transition by significantly enhancing the stability of the boundary-layer flow. Several typical literatures on experiments are Kosin [1965], Maddalon *et al.* [1990], Wright and Nelson [2000], Ovenden and Smith [2005] and Chen *et al.* [2013].

The main idea of steady suction is to redirect the high momentum fluid from the free shear layer towards the near-wall region with decelerated fluid. In order to maintain laminar flow on a swept wing or a tailplane as far downstream as possible, it has been proposed to combine surface suction, applied in the leading-edge region, with extended regions of

favourable pressure gradients, attained by profile shaping. As stated by Messing and Kloker [2010], for two-dimensional boundary layers, the effect of suction is to make the wall-normal streamwise-velocity profile fuller by sucking a high-momentum fluid to the wall. For three-dimensional boundary layers, it is the reduction of the cross flow that decreases the cross flow-related, dominantly inviscid instability that is typically strongest in the front part of a swept wing and leads to early laminar breakdown. Figure 2.15 demonstrates an example of steady suction for laminar flow control.
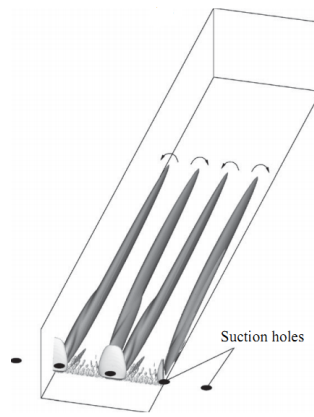
Figure 2.15: Schematic diagrams of steady suction with discrete orifices for laminar flow control. (Messing and Kloker [2010])

In the aspect of numerical simulations, recent studies focus on direct numerical simulation of laminar flow with steady suction flow control to investigate flow control mechanisms. Messing and Kloker [2010] studied the effect of discrete suction orifices on the disturbance evolution in a laminar three-dimensional boundary layer with favourable pressure gradient. They found steady suction with discrete orifices could excite unsteady cross flow modes even with the orifice spacing smaller than the chordwise wavelengths of unstable modes, and the unstable steady vortex mode results in strong corssflow vortices invoking turbulence by secondary instability. Friederich and Kloker [2011] studied a single suction hole in a Blasius boundary layer using DNS. Their results show that the pinpoint suction in the swept-wing laminar boundary layer flow can delay cross flow transition, and weaken the growth of secondary instabilities which are responsible for the final laminar breakdown.

Steady suction to control turbulent flow separation or reattachment is scarcely used, due to its mechanical complexity, additional weight and large energy requirements, which can make any performance benefits gained from the steady suction devices negligible.

(b) Steady/continous blowing

2.4. Flow control

Steady or continuous blowing is usually achieved by a blower or compressor to pump air continuously into a boundary layer. Figure 2.16 shows flow features with a steady blowing devices with a pitched and skewed angle. Blowing a small amount of air from high-pressure engine sources into the near-wall region upstream of a separated flow may sufficiently energise the boundary layer to overcome the downstream adverse pressure gradient and to avoid flow separation (Luedke *et al.* [2005]). In order to suppress the flow separation induced by an adverse pressure gradient, a steady blowing flow control has been studied both experimentally and numerically in recent decades.
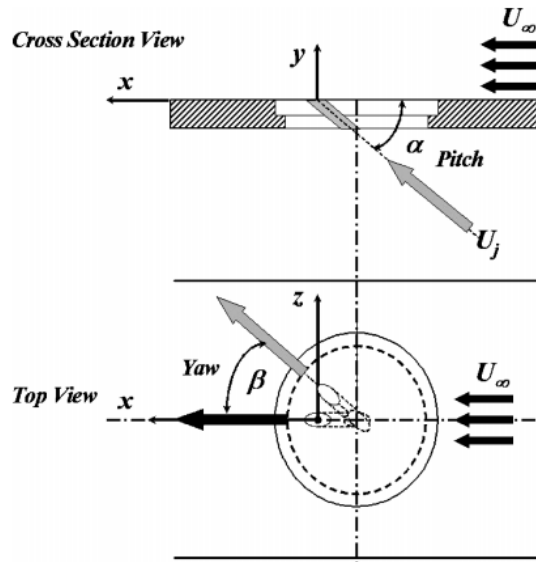
Figure 2.16: Flow features of steady blowing with jets into a cross flow. (Milanovic and Zaman [2004])

The study on steady blowing to control flow separation dates back to 1960s. Thomas [1965] experimentally investigated the effect of steady blowing on stability of the boundary layer against separation for a wing at a subsonic speed. Later, Grin [1967] carried out an experimental study of blowing flow control at the Mach number of 2.5, in which the blowing flow increased the fullness of the velocity profile and led to a considerable increase of the critical pressure ratio in the interaction between the shock and the boundary layer. After a long time silence, the steady blowing as a flow control has been gaining renewed emphasis since 1990s. Compton and Johnston [1992] carried out an experimental studies of pitched and skewed jets blowing in a turbulent boundary layer, and found that blowing jets can produce longitudinal vortices, similar to weak vortices produced by a solid vortex generator, but different from a strong vortex from a larger solid vortex generators. Zhang [2003] studied

the evolution of co-rotating vortices generated by inclined jets experimentally, which found the blowing-forced streamwise vortices have two types. With a small jet speed, weak vortices were generated close to the wall and featured with diametrically opposed, secondary, near-wall flows in between the vortices. When the jet speed is times of the free stream flow, strong vortices were generated with significant spanwise movement, accompanied by high levels of turbulence with distinct normal and shear stress distribution. Both these two types of vortices are products of complex flow process, including horseshoe vortices in front of the jet exits, recirculating flow to the lee side of the jets, counter-rotating vortices from the rolling up of vortex sheet around the jets, strong and induced spanwise flow. Weaver *et al.* [2004] experimentally applied strong steady blowing to a Boeing-Vertol VR-7 aerofoil. The experiments showed the steady blowing prevented the bursting of the leading edge separation bubbles, the lift was increased significantly, stall was averted, and the shape of the momentum response showed a positive damping in pitch. Luedke *et al.* [2005] carried out both an experimental study on the steady blowing in the separated flow of a hump diffuser, in which the two most important control parameters, the blowing momentum coefficient and the velocity ratio, were investigated. They found the pitch angle of 45° provided the most effective control in removing the flow separation and increasing the pressure recovery. A RANS study was also performed by Luedke *et al.* [2005] using the commercial CFD solver CFX 5.6, in which the $k-\omega$ model predicts better near-wall flow properties than the $k-\epsilon$ and SST models. Zha *et al.* [2007] experimentally studied the influences of injection slot sizes, which found that smaller injection slot size provides a higher maximum lift and reduction of drag. This phenomenon was explained to be caused by large negative thrust produced by the higher momentum coefficient. Actually, they found there is a limit of jet mass flow rate to maintain the stability of the flow, which depends on cases. Goodarzi *et al.* [2012] also found such a critical value of mass flux in their RANS simulation of blowing jets on NACA0015, but no further investigation on this critical value. Goodarzi *et al.* [2012] carried out a RANS study with the S-A model to study influences of jet locations, jet velocity ratios, and jet angles of steady blowing in NACA0015. Their results show that jets near the trailing edge will effectively increase lift coefficients, while the drag coefficient also increases, and vice versa. Tilly and Sousa [2008] experimentally studied the Kelvin-Helmholtz instability of the laminar boundary layer with a steady flow blowing, and discovered that the blowing jets introduce a decrease in Strouhal number, similar to the case of von Karman vortex shedding. In addition, the relation between the unsteadiness and the blowing rate has been proposed and verified. Angland *et al.* [2012] used steady blowing jets on the surface of a cylinder to reduce the source of noise in experiments and achieved positive results.

The control effect of steady blowing in delaying turbulent flow separation is very promising. Nevertheless, there are some drawbacks of the steady blowing. The high pressure air, blowing into the boundary layer, usually comes from aircraft engines or external compressors. Thus, the extraction of this high pressure air may result in a penalty on overall aircraft performance and efficiency. Improvements on the efficiency of air blowing and minimization of flow-mass required to achieve a net positive impact are desirable. A natural operation is to alter a steady continuous blowing to a periodic blowing.

(c) Periodic blowing

The most popular flow control device of periodic blowing is pulsed jets. In contrast with steady blowing, pulsed jets have significant advantages because of high efficiencies (Greenblatt and Wygnanski [2000]). An unsteady pulsed jet can operate in a periodic manner with an excitation frequency related to the natural period of flow. Intermittent excitation of jets reduces the required mass flow rates without jeopardizing performance benefits (Bons *et al.* [2002]). An inevitable cost of a pulsed jet is the requirement on the external flow source. Therefore, the duty cycle of pulsed jets is a significant parameter to be optimized in order to improve control efficiency and energy cost.

Among the pulsed jets, pulsing jet vortex generators have been extensively studied. The concept is to mimic conventional vortex generators in a fluidic way by skewing and pitching the jet axis (Cattafesta and Sheplak [2011]). Conventional vortex generators always add parasitic drag, while the pulsed jet vortex generators can be deployed only when they are required. Devices for steady or unsteady jets have few differences, and the main differences come from the control of jets, especially the frequency control. Figure 2.17 display a typical configuration of pitched and skewed jets.

Extensive experimental investigations have been carried out in the last decade. Johnston and Nishi [1990] carried out experiments to confirm the effect of pulsing jets in reduction and elimination of stalled regions (defined as zones of detached or separated flow sometimes followed by reattachment), which found pulsed jets generated longitudinal vortices in the boundary layer downstream of the jet holes, mixing with the cross-stream to suppress the stalled regions. Experiments conducted by Tilmann *et al.* [2003] found the velocity ratio in fluidic jet vortex generator is the primary control parameter. Too small a blowing velocity did not have any appreciable effect, while too high a jet velocity may force the resultant vortices out of the boundary layer with a great loss in effectiveness. This conclusion is similar to Zha *et al.* [2007] and Goodarzi *et al.* [2012] in the study of steady jets. Ortmanns and Kähler [2004] experimentally studied the response of pulsed jets as a function of different angles in a turbulent boundary layer, which found that the skew angle is essential
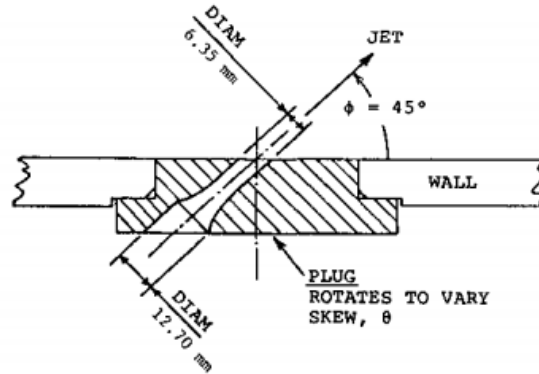
Figure 2.17: Schematic diagrams of an unsteady blowing jets with pitched and skewed angles. (Johnston and Nishi [1990])

for transferring high momentum to the near-wall region. When there is a strong tangential blowing to the wall, there is no spiral motion of the base flow and less efficiency. They also found that the momentum patterns by pulsed jets became very similar to the steady jets shortly after opening the valves, but during the process of jets on-off, a strong spanwise modulation of the base flow was observed. Scholz *et al.* [2006] applied pulsed jets to an aerofoil to prevent a turbulent leading edge stall in experiments. Among the three control parameters (the control frequency, duty-cycle and actuation amplitude), the duty cycle was found to be the major control parameter in this case. Iio *et al.* [2006] experimentally studied pulsed jets with rectangular nozzles, which found vortices originated from the short side of the rectangular nozzle moved faster than those from the longer side. Kostas *et al.* [2007] gave a comprehensive experimental investigation of pulsed jets on a bump, including the co-rotating and counter-rotating, duty cycles, and pulse frequencies. The skin friction measurements showed the wall shear stress was dependent on the net mass flow injected by the actuators. When the control frequency is too high, a quasi-steady flow structure was found to develop far downstream of the injection location. Hasegawa and Kumagai [2008] developed an active separation feedback control system with pulsed jets, which successfully controlled the flow separation. Siauw *et al.* [2009] studied the flow control effect of pulsing jet flow control in NACA0015, in which a trailing edge separation was forced to be attached. A statistical relationship between pressure and velocities during the transient process of attachment/separation was established to investigate the separation criterion based on coherent structures during the process of flow separation. Siauw *et al.* [2010] investigated the transition process during pulsed jet flow control. The studied on the transient dynamics of flow separation control shows that the transient behaviour associated with the formation

and shedding of a starting vortex, and the jets-on to jets-off process has a more gradual process of separation dynamics than the process of jets-off to jets-on. Prince *et al.* [2012] compared the control effects of steady blowing jets and pulsed jets. The results showed that for pulsed jets there were not well-defined vortex formed, but had a "train" of discrete vortical structures, which locally promoted significant levels of mixing.

In addition to experimental studies, there are also some numerical investigations on the pulsed jet flow control. Zhang *et al.* [1996] addressed some numerical issues in simulating streamwise vortices produced by pulsed jets in a turbulent boundary layer on a flat plate. They found that a correct upstream boundary condition including accurate distribution of turbulent kinetic energy is essential for developing streamwise vortices, and the assumption of 1/7 th law did not provide reliable predictions. However, the development of streamwise vortices by jets was not sensitive to the jet inlet condition (top hat or fully developed). This conclusion is essential for numerical investigation, as it is difficult to accurately simulate the inlet conditions of jets. Deng *et al.* [2007] performed a DNS investigation on pulsed jets applied to NACA0012 at an angle of attack 4°. With pulsed jets, the separation zone and the drag were both reduced, while the lift maintained approximately the same level as in the baseline flow. The skew angle was found to be primary control parameters due to the fact that skew angles determine the generation of non-symmetric 3D perturbations containing 3D unstable modes for the early transition. Jewkes and Chung [2010] studied the formation of different fluidic vortices generated by different pitched and skewed angles in pulsed jets. A clear vortical "shell" was observed in a low velocity ratio perpendicular pulsed jet, which is not found in other pitch and skew angles. Sau and Mahesh [2010] performed a wide range of optimizations of pulsed jets penetration and spread in laminar cross-flows using DNS. Behaviours of a single vortex ring in the cross-flow generated by pulsing jets were explained, and they suggested that the parameters of pulsed jets forcing penetration should be determined according to a classification map of ring parameters in Sau and Mahesh [2008]. Laval *et al.* [2010] also widely investigated the control parameters in pulsed jets applied to a 2D bump in a converging-diverging channel using LES. The main conclusions are the pitch angle has no significant effect compared with the skew angle, which has been already confirmed by previous literatures. A high jet velocity can increase the control robustness, but with a low energy efficiency. For the optimal pulsing frequency, the low range is found to improve the control efficiency, while the high control frequency may have a negative effect. During the low frequency range, low values of the duty cycle were observed to reduce the mass flux rate consumption as well as for continuous jets. Bobonea [2012] numerically studied the impact of different slot/orifice geometries of pulsed jets applied on wind turbine

aerofoils using URANS, but the conclusions are unclear.

In spite of some numerical investigations of the pulsed jets in parameter optimization and formation of vortices, conclusions sometimes varies, dependent on different cases, and the key control parameters are also different in different cases. In addition, few literatures report a numerical study of an industry-interested Reynolds number and there is a lack of the transition process during employing pulsed jets. These aspects will be addressed in this study.

2.5   Summary

Promising turbulence simulation techniques for unsteady complex turbulent flow are DNS, LES and hybrid RANS/LES. DNS, which resolves the whole spectra of turbulent flow, can only be applied to flows with low Reynolds numbers, limited by the current computer technology. It is popularly used in the investigation of flow mechanisms at a scaled Reynolds number rather than industry interested flows. Both LES and hybrid RANS/LES are extensively applied to simulate complex turbulence at high Reynolds numbers. In contrast, hybrid RANS/LES methods reduce the requirements on the mesh resolution in the near-wall region, which gains intensive and continuous attentions. Our research focuses on industry-interested flow control at a relatively high Reynolds number, and therefore hybrid RANS/LES method is determined to be the primary methodology.

The main issue in the hybrid RANS/LES method is the transition between the RANS region and the LES region. In spite of a few investigations on this aspect, it seems no one hybrid method can adapt to all kinds of turbulent flow. Results predicted by different hybrid methods in different flows may vary. In this study, three typical and entirely different types of turbulent flow are studied (the turbulent flow separated from a sharp step edge, the turbulent flow separated due to adverse pressure gradient on a smooth surface, and a wall bounded turbulent flow separated from sharp edges), and therefore the validation of different hybrid RANS/LES methods in different flow types is rewarding and meaningful.

With proper turbulence modelling techniques, the flow control simulation will be carried out. For passive flow control, the main control method is realized by changing objects' geometries, which introduces less difficulty to the numerical implementations. The challenge in the fractal orifice flow control is the mesh generation, and determination of proper mesh resolutions. Because the turbulence structures generated from a scaling geometry will also be scaled. For the piezoelectric oscillating surface on the boundary layer, only very few experiments were carried out, and to the author's knowledge, there is no numerical simula-

tion on this particular subject. For pulsed jets flow control, there is some research both on experiments and simulations. We will focus on applications of hybrid RANS/LES methods in this flow control case and the dynamic process during the flow control.

The status of each concerned flow control method is summarized, and the challenges are also presented. The research orientation and emphasises in the current study are also identified in this literature review.

Chapter 3

Governing Equations and Numerical Methods

3.1   Introduction

Fluid dynamics exist in numerous areas, such as machinery, aeronautics, aviation, hydrology, meteorology and chemistry. In order to describe fluid dynamics, there are three primary directions: experiments, mathematical descriptions and numerical simulations. In contrast with numerical simulations, experiments (e.g. wind tunnel experiments) are expensive, lengthy and sometimes impossible. From the physical viewpoint, the equations describing fluid flows, heat and mass transfer can be simply derived from the conservation laws of classical physics. These conservation laws are conservation of mass, conservation of momentum (Newton's second law of motion) and conservation of energy (first law of thermodynamics). Additional equations may be introduced for different phenomena, for example, the second law of thermodynamics for the entropy transport or Maxwell's equations for the electromagnetic field. However, due to highly non-linearity, analytical solutions of a fluid system are scarcely possible, except for very simple ideal conditions. Therefore, the numerical simulation of flow fields is a vital research tool.

Although the equations describing fluid dynamics were developed simultaneously in the early 1800s by George Stokes and Claude-Louis Navier, from the mathematical point of view, until now we do not even know whether a solution exists for all fluids. For most situations, there are no algebraic solutions for these equations. Expensive experiments and underlying difficulties in mathematical solutions of complicated partial differential equations promote the development of CFD. CFD refers to numerical methods to solve the fundamental nonlinear differential equations with predefined geometries and boundary conditions. CFD

is a virtual modelling technique with powerful visualization capabilities. It costs much less than experiments and can obtain reliable qualitative and quantitative properties of complex flows using modern computers. Since the concept of "computer experiments" was elaborated by Harlow and Fromm [1965], CFD is now widely used both in industry and academia. In industry, CFD is used to obtain flow properties both in the pre-design stage and in the stage of posteriori. In academia, CFD is a very important tool to investigate flow properties and to understand physics of fluids. There are many CFD techniques, and the finite volume method has the broadest applications. The other CFD methods include finite element method, finite difference method, spectral method, boundary element method, vorticity-based method, Lattice gas/lattice Boltzmann methods, and so forth. In this study, the in-house CFD solver with the finite volume method, Dynamic-Grid Detached Eddy Simulation (DG-DES), is used.

DG-DES is a density based CFD solver with the cell-centred finite volume method, which can deal with compressible or incompressible, viscous or inviscid flows with both structured and unstructured meshes. The turbulence modelling techniques in DG-DES are mainly the Spalart-Allmaras model based RANS, URANS, DES and its variations. In order to implement flow control, dynamic grid techniques are also included in DG-DES. DG-DES has been applied to various flows. Xia [2005] developed the main framework of the in-house solver DG-DES and verified most of the primary numerical methods and turbulence models for subsonic and supersonic flows. Xia and Qin [2005], Xia [2005], Qin and Xia [2008] and Xia and Qin [2008] studied the synthetic jet flow control using DG-DES with dynamic grid techniques, and the combination of DES and moving meshes was investigated for complex turbulent flows. Durrani [2009] implemented DDES into DG-DES and investigated the numerical simulation of flapping wings with dynamic grid techniques with DG-DES. Later, DG-DES was used to study the application of DES and DDES to a mild-separation aerofoil (Durrani and Qin [2011]) and a massively separated flow around a cylinder (Durrani and Qin [2012]). Using DG-DES, Mohamed [2011] studied flow control with synthetic jet actuation in a wall-mounted hump and investigated the post-stall flow control of NACA0015 with synthetic jets actuators. Zheng *et al.* [2012] used DG-DES to study flow through an orifice with the shape of hexagram, and investigated the low dissipation numerical schemes in complex turbulent flows using DES.

With these developments and application of DG-DES in various flows and flow control with synthetic jets, DG-DES is regarded as a reliable CFD solver. New development and more flow control methods implemented into DG-DES will be carried out in this study. Details of basic numerical methods in DG-DES can be found in above literatures. Besides

basic numerical description of DG-DES, this section will focus on the new developments of DG-DES in the recent years, which are mainly the improvements of low dissipation numerical schemes, implementation and development of state of the art in hybrid RANS/LES turbulence modelling techniques and enrichment of more flow control methods.

This chapter is organized as follows. Firstly, the underlying assumptions in the numerical solver DG-DES will be expressed. Then, the governing equations of fluid dynamics, with or without moving boundaries, are presented in their integral forms with above listed assumptions. Next, discretization of the time term, the inviscid terms and the viscous terms of the N-S equations are described. After that, a wall boundary condition with a non-zero velocity is addressed. Dynamic grid techniques, to be used for flow control, are discussed and a simple dynamic grid method based on geometry similarity is proposed and tested. Finally, turbulence modelling techniques and equations are given in details.

3.2 Assumptions in the CFD solver DG-DES

The scope of application of the in-house solver DG-DES is mainly on aerodynamics, therefore there are some underlying assumptions, which will be addressed as follows.

The fluid motion under consideration all belongs to nonrelativistic mechanics. The fluid moves at velocities considerably smaller than the speed of light. The mass and energy are non-interchangeable, so they can be expressed independently in the equations.

The fluid is assumed to be a continuum. The continuum assumption ensures the fluid is continuous and indefinitely divisible. This assumption allows differential calculus to be applied on elements which are reasonably small for macroscopic phenomena and much larger than the scale of atoms and molecules. This assumption guarantees that the derivatives of all dependent variables exist.

The fluid media is assumed to be Newtonian and isotropic. For Newtonian fluid, the stress tensor is linearly related with the stain rate. The Newton shear formula is expressed as

$$\tau_{ijkm} = \alpha_{i,j,k,m} \frac{\partial u_k}{\partial x_m}, \tag{3.1}$$

where $i, j, k, m = 1, 2, 3$, and $\alpha_{i,j,k,m}$ is a fourth-rank tensor, including 3^4 empirical coefficients, which are constant for Newtonian fluid. If the fluid is further assumed to be isotropic (no preferred directions), the 81 linear coefficients reduces to only two coefficients. The

3.2. Assumptions in the CFD solver DG-DES

Newton shear formula for isotropic fluid reads

$$\tau_{ij} = \mu \left(\frac{\partial u_i}{\partial x_j} + \frac{\partial u_j}{\partial x_i} \right) + \lambda \left(\frac{\partial u_l}{\partial x_l} \right), \tag{3.2}$$

where μ is the coefficient of dynamic viscosity (shear), and λ is the bulk elasticity, or "second" coefficient of viscosity (dilatational).

The fluid is assumed to be classical thermodynamic ideal gas and calorically perfect gas. Ideal gas has an underlying assumption that all collisions are elastic and all motion is frictionless, which means there is no energy loss in the motion or collision of molecules in ideal gas. The ideal gas assumption provides an additional equation, the equation of state of a classic ideal gas, which reads

$$\rho = \frac{p}{RT}, \tag{3.3}$$

where $R = 287.04 \ \text{J kg}^{-1} \ \text{K}^{-1}$ is the ideal gas constant for air. From the ideal gas assumption, there are other conclusions to be drawn. The specific internal energy e and enthalpy h of an ideal gas depend only on the temperature, which means $e = e(T)$ and $h = h(T)$. If the ideal gas is further assumed to be calorically perfect gas, the specific heat capacity becomes constant. The main three parameters for heat capacity are the specific heat capacity at constant volume c_v, the specific heat capacity at constant pressure c_p and the heat capacity ratio (the adiabatic index) $\gamma = c_p/c_v$. For a perfect gas, the specific internal energy e and enthalpy h read

$$e = c_v T, \tag{3.4}$$

$$h = c_p T. \tag{3.5}$$

Flows at subsonic and low supersonic Mach number with a temperature under 1000 K can usually be assumed to be calorically perfect gas.

The fluid is assumed to be Fourier fluid. This assumption ensures the heat flux is proportional to the temperature gradient. The Fourier's law of heat conduction reads

$$q_j = -\kappa \frac{\partial T}{\partial x_j}, \tag{3.6}$$

where q_j is the heat flux transferred in the j direction due to molecular thermal conduction, and κ is the thermal conductivity coefficient.

All descriptions of N-S equations and their discretization in this thesis are based on the above assumptions.

3.3 Governing equations

3.3.1 Unsteady Navier-Stokes equations

The integral form of the governing equations is addressed firstly for the finite volume method. For a given control volume domain Ω with the surface boundary $\partial\Omega$, the three dimensional governing equations are expressed as

$$\frac{\partial}{\partial t}\int_\Omega \mathbf{W} d\Omega + \oint_{\partial\Omega} (\mathbf{F_c} - \mathbf{F_v}) \cdot \mathbf{n} dA = \int_\Omega \mathbf{S} d\Omega, \tag{3.7}$$

where t is time, $\mathbf{n} = (n_1, n_2, n_3)^T$ is the normal vector of the surface boundary $\partial\Omega$, and A is the surface area. The vector of conserved variables $\mathbf{W}$, the convective flux $\mathbf{F_c}$ and the viscous flux $\mathbf{F_v}$ are given in

$$\mathbf{W} = \begin{pmatrix} \rho \\ \rho\mathbf{u} \\ \rho e \end{pmatrix} = \begin{pmatrix} \rho \\ \rho u_1 \\ \rho u_2 \\ \rho u_3 \\ \rho e \end{pmatrix}, \tag{3.8}$$

$$\mathbf{F_c} \cdot \mathbf{n} = \begin{pmatrix} \rho \cdot \mathbf{u} \cdot \mathbf{n} \\ \rho \cdot \mathbf{u} \cdot \mathbf{u} \cdot \mathbf{n} + p\mathbf{n} \\ (\rho e + p) \cdot \mathbf{u} \cdot \mathbf{n} \end{pmatrix} = \begin{pmatrix} \rho \\ \rho u_1 \\ \rho u_2 \\ \rho u_3 \\ \rho e \end{pmatrix} \cdot \mathbf{u} \cdot \mathbf{n} + \begin{pmatrix} 0 \\ n_1 \\ n_2 \\ n_3 \\ \mathbf{u} \cdot \mathbf{n} \end{pmatrix} \cdot p, \tag{3.9}$$

$$\mathbf{F_v} \cdot \mathbf{n} = \begin{pmatrix} 0 \\ \tau \cdot \mathbf{n} \\ \tau \cdot (\mathbf{u} \cdot \mathbf{n}) - \nabla q \cdot \mathbf{n} \end{pmatrix} = \begin{pmatrix} 0 \\ \tau_{11}n_1 + \tau_{12}n_2 + \tau_{13}n_3 \\ \tau_{21}n_1 + \tau_{22}n_2 + \tau_{23}n_3 \\ \tau_{31}n_1 + \tau_{32}n_2 + \tau_{33}n_3 \\ \Phi_1 n_1 + \Phi_2 n_1 + \Phi_3 n_3 \end{pmatrix}, \tag{3.10}$$

where $\mathbf{u} = u_i$ denotes the velocity vector in the Cartesian coordinate system ($i = 1$, 2 or 3 for x, y or z direction), the symbols ρ, p and e are respectively for the density, pressure and internal energy of the flow. The symbol Φ in Eq. 3.10 represents

$$\begin{pmatrix} \Phi_1 \\ \Phi_2 \\ \Phi_3 \end{pmatrix} = \begin{pmatrix} u_1\tau_{11} + u_2\tau_{12} + u_3\tau_{13} - q_1 \\ u_1\tau_{21} + u_2\tau_{22} + u_3\tau_{23} - q_2 \\ u_1\tau_{31} + u_2\tau_{32} + u_3\tau_{33} - q_3 \end{pmatrix}, \tag{3.11}$$

47

3.3. Governing equations

where the heat flux q_j is given in Eq. (3.6). Normally, the thermal conductivity coefficient κ in Eq. (3.6) can be related with the molecular viscosity μ through the Prandtl number Pr,

$$\kappa = \frac{c_p}{\text{Pr}}\mu. \tag{3.12}$$

The symbol $\tau = [\tau_{ij}]$ is the viscous stress tensor, given in Eq. (3.2), which can be expanded and expressed as

$$\tau = \begin{bmatrix} \lambda\nabla\mathbf{u} + 2\mu\frac{\partial u_1}{\partial x_1} & \mu(\frac{\partial u_1}{\partial x_2} + \frac{\partial u_2}{\partial x_1}) & \mu(\frac{\partial u_1}{\partial x_3} + \frac{\partial u_3}{\partial x_1}) \\ \mu(\frac{\partial u_1}{\partial x_2} + \frac{\partial u_2}{\partial x_1}) & \lambda\nabla\mathbf{u} + 2\mu\frac{\partial u_2}{\partial x_2} & \mu(\frac{\partial u_2}{\partial x_3} + \frac{\partial u_3}{\partial x_2}) \\ \mu(\frac{\partial u_1}{\partial x_3} + \frac{\partial u_3}{\partial x_1}) & \mu(\frac{\partial u_2}{\partial x_3} + \frac{\partial u_3}{\partial x_2}) & \lambda\nabla\mathbf{u} + 2\mu\frac{\partial u_3}{\partial x_3} \end{bmatrix}. \tag{3.13}$$

The relation between the coefficient of dynamic (molecular) viscosity μ and the "second" coefficient of viscosity λ is given by the Stokes' hypothesis,

$$\lambda = -\frac{2}{3}\mu. \tag{3.14}$$

On the assumption of idea gas, the molecular viscosity is only dependent on the temperature T. In this study, the Sutherland's law is used to calculate the molecular viscosity at a given temperature, which reads

$$\mu = \mu_0 \frac{T_0 + C}{T + C}\left(\frac{T}{T_0}\right)^{3/2}, \tag{3.15}$$

where μ_0 is reference viscosity at the reference temperature T_0, and C is the Sutherland's constant. For an ideal air, $T_0 = 288.15$ K, $\mu_0 = 1.7894 \times 10^{-5}$ m^{-1} kg s^{-1} and $C = 110.4$.

The five governing equations given in Eq. (3.7) contain six variables (p, u_1, u_2, u_3, T and ρ). To close these equations, the state equation given in Eq. (3.3) is necessary. In addition to the expressions of the specific internal energy and enthalpy in Eq. (3.4) and Eq. (3.5), some other gas properties are also stated here. The specific kinematic energy k, the specific total energy E and the specific total enthalpy H are respectively expressed as

$$k = \frac{1}{2}\left(u_1^2 + u_2^2 + u_3^2\right), \tag{3.16}$$

$$E = e + k = c_v T + k, \tag{3.17}$$

$$H = h + k = c_p T + k = E + \frac{p}{\rho}. \tag{3.18}$$

The speed of sound a is expressed as (for ideal gas)

$$a = \sqrt{\gamma R T}. \tag{3.19}$$

3.3.2 Arbitrary Lagrangian-Euler formulation

The above governing equations are the most common forms of fluid dynamics with fixed boundaries. When the boundaries in flows moves during the simulation, the Arbitrary Lagrangian-Euler (ALE) formulation is introduced to tackle this issue.

Algorithms of continuum mechanics usually make use of two classical descriptions of motion: the Lagrangian description and the Eulerian description. For the Lagrangian algorithm, each individual node of the computational mesh follows the associated media particle during motion. The Lagrangian description makes it easier to track free surfaces and interfaces between different media. The weakness is it cannot follow large distortions of the computational domain. For the Eulerian algorithm, the computational mesh is fixed and the continuum moves with respect to the grid. It can treat with large distortions in the continuum motions, but it is more difficult to deal with the moving and deforming boundaries. Arbitrary Lagranigan-Eulerian description was proposed to combine the advantages of both the Lagrangian and the Eulerian approaches. In the ALE description, the computational mesh can move with the continuum in a normal Lagrangian approach, and it can also be treated in an Eulerian fashion in numerical computations (Donea *et al.* [2004]).

One of the objectives of this study is to study flow control with moving/deforming boundary surfaces. In cases with moving/deforming boundaries, the element volume Ω and element boundary surface $\partial\Omega$ are both time-dependent, and therefore the ALE approach is adopted to describe the dynamics.

The N-S equations will be re-addressed for the ALE. The time-derivative term in Eq. (3.7) can be expanded as

$$\frac{\partial}{\partial t} \int_{\Omega(t)} \mathbf{W(t)} d\Omega = \int_{\Omega(t)} \frac{\partial \mathbf{W(t)}}{\partial t} d\Omega + \int_{\Omega(t)} \mathbf{W(t)} \frac{\partial d\Omega(t)}{\partial t}. \tag{3.20}$$

Define $\mathbf{u_g} = (u_{1g}, u_{2g}, u_{3g})^T$ as the velocity of a moving surface $\partial\Omega(t)$, then the second term of the right hand side in Eq. (3.20) becomes

$$\int_{\Omega(t)} \mathbf{W(t)} \frac{\partial d\Omega(t)}{\partial t} = - \int_{\partial\Omega(t)} \mathbf{W(t)} \cdot \mathbf{u_g} \cdot \mathbf{n} dA. \tag{3.21}$$

Substituting Eq. (3.20) and Eq. (3.21) into the N-S equations Eq. (3.7), the N-S equations

for the ALE are obtained, shown as

$$\int_{\Omega} \frac{\partial \mathbf{W}}{\partial t} d\Omega + \oint_{\partial \Omega} [\mathbf{F_c} - (\mathbf{W} \cdot \mathbf{u_g})] \cdot \mathbf{n} dA - \oint_{\partial \Omega} \mathbf{F_v} \cdot \mathbf{n} dA = \int_{\Omega} \mathbf{S} d\Omega. \tag{3.22}$$

The convective flux $\mathbf{F_c}$ expressed in Eq. (3.9) becomes to a new format (the same symbol $\mathbf{F_c}$ is used for simplicity),

$$\mathbf{F_c} \cdot \mathbf{n} = \begin{pmatrix} \rho \\ \rho u_1 \\ \rho u_2 \\ \rho u_3 \\ \rho e \end{pmatrix} \cdot (\mathbf{v} - \mathbf{u_g}) \cdot \mathbf{n} + \begin{pmatrix} 0 \\ n_1 \\ n_2 \\ n_3 \\ \mathbf{u} \cdot \mathbf{n} \end{pmatrix} \cdot p. \tag{3.23}$$

Comparing Eq. (3.7) with Eq. (3.22), the time-derivative term changes from a differential format in Eq. (3.7) to a integral format in Eq. (3.22). This change make the finite volume method more easier to be discretized. When $\mathbf{u_g} = \mathbf{0}$, the ALE N-S equations restore back to the mostly-used Eulerian equations (Eq. (3.7)), with

$$\frac{\partial}{\partial t} \int_{\Omega(t)} \mathbf{W(t)} d\Omega = \int_{\Omega(t)} \frac{\partial \mathbf{W}(t)}{\partial t} d\Omega. \tag{3.24}$$

When $\mathbf{u_g} \neq \mathbf{0}$, the N-S equations are solved in the format of the ALE N-S equations (Eq. (3.22)).

3.4   Temporal discretization

There are two main methods in solving the governing equations. One is the pressure-based solver, which uses pressure correction techniques to solve the equations in a segregated manner. This method is suitable for incompressible flows at low Reynolds numbers. The other is the density-based solver, which employs time-marching procedures implicitly or explicitly to solve the governing equations. The density-based schemes were initially developed for compressible flow. Considering flow problems of mixed compressible/incompressible type, preconditioning techniques have been developed to solve nearly incompressible flow with density-based solvers. The CFD solver DG-DES used in this study employs a density based method for all-speed flows. The preconditioning techniques in DG-DES for incompressible flow can be found in Durrani [2009].

3.4.1 Dual time stepping

Multiplying the time derivative by a preconditioning matrix changes the time behaviour of a flow system and accelerates the convergence to a steady state. In addition, the preconditioning also destroys the time accuracy of the governing equations. For steady-state flows, this is not essential. For unsteady flow, the preconditioning should be properly and carefully applied to a time marching approach with less accuracy deterioration. The dual time stepping method is a common choice for unsteady flows, as both the preconditioning and local time stepping can be applied to accelerate the convergence with good time accuracy.

The dual time stepping method was firstly proposed by Jameson [1991] to calculate time-dependent flows. The main objective is to solve the problem of time stiffness caused by disparities in characteristic times, as time-steps dictated by numerical stability are much smaller than that required by an accuracy consideration. The dual time stepping has a pseudo time step and a physical time step. All acceleration techniques are implemented within pseudo time steps, not affecting the original physical time derivative. The physical time step can be determined by flow physics, not necessary to consider the limitations of numerical stability. When the pseudo-time step converges to a steady state in each physical times step, the physical time marches.

The N-S equation with the dual-time stepping is expressed as

$$\frac{\partial}{\partial t} \int_{\Omega} \mathbf{W} d\Omega + \frac{\partial}{\partial \tau} \int_{\Omega} \mathbf{W} d\Omega + \oint_{\partial \Omega} (\mathbf{F_c} - \mathbf{F_v}) \cdot \mathbf{n} dA = \int_{\Omega} \mathbf{S} d\Omega. \tag{3.25}$$

where t is physical time and τ is pseudo time. Re-arranging the dual time stepping N-S equations, it is obtained as follows

$$\frac{\partial}{\partial \tau} \int_{\Omega} \mathbf{W} d\Omega = - \left[\frac{\partial}{\partial t} \int_{\Omega} \mathbf{W} d\Omega + \oint_{\partial \Omega} (\mathbf{F_c} - \mathbf{F_v}) \cdot \mathbf{n} dA \right] + \int_{\Omega} \mathbf{S} d\Omega. \tag{3.26}$$

Theoretically, the pseudo time term (the left hand side of Eq. (3.26)) should approach to zero at each time step before the physical time marches, after that, the original N-S equations are recovered. This principle introduces the procedure for dual time stepping method: within each physical time step the N-S equations (the right hand side of Eq. (3.26)) should achieve to a steady state in each pseudo time step, then the physical time step marches.

In order to reduce the destroy on the physical time with preconditioning techniques, the preconditioning matrix multiplies the pseudo time derivative term rather than the physical time. Following the preconditioning procedure in the above section, the preconditioned N-S

equation with the dual-time stepping is

$$\frac{\partial}{\partial t}\int_{\Omega}\mathbf{W}d\Omega + \mathbf{\Gamma}\frac{\partial}{\partial \tau}\int_{\Omega}\mathbf{Q}d\Omega + \oint_{\partial\Omega}(\mathbf{F_c} - \mathbf{F_v})\cdot\mathbf{n}dA = \int_{\Omega}\mathbf{S}d\Omega. \tag{3.27}$$

The in-house code DG-DES was designed for both steady and unsteady flows. A multi-stage time discretization is applied to the preconditioned dual-time N-S equations.

3.4.2 Physical time discretization

In the dual-time stepping procedure, the physical time step is the outer iteration, and the pseudo time step is the inner iteration. By treating the physical time term as part of the residual, Eq. (3.27) is re-arranged as

$$\mathbf{\Gamma}\frac{\partial}{\partial \tau}\int_{\Omega}\mathbf{Q}d\Omega = -\mathbf{R} - \frac{\partial}{\partial t}\int_{\Omega}\mathbf{W}d\Omega, \tag{3.28}$$

where $\mathbf{R}$ is the residual, expressed as

$$\mathbf{R} = \oint_{\partial\Omega}(\mathbf{F_c} - \mathbf{F_v})\cdot\mathbf{n}dA - \int_{\Omega}\mathbf{S}d\Omega. \tag{3.29}$$

Applying the ALE with Eq. (3.23) involving the surface moving speed to the N-S equations, Eq. (3.28) becomes

$$\mathbf{\Gamma}\int_{\Omega}\frac{\partial}{\partial \tau}\mathbf{Q}d\Omega = -\mathbf{R} - \int_{\Omega}\frac{\partial}{\partial t}\mathbf{W}d\Omega. \tag{3.30}$$

Substituting the integral in time terms with summation, Eq(3.30) is semi-discretized as

$$\mathbf{\Gamma}\frac{\partial(\mathbf{Q}\Omega)}{\partial \tau} = -\mathbf{R} - \frac{\partial(\mathbf{W}\Omega)}{\partial t}. \tag{3.31}$$

Solving the pseudo time marching with the dependent variables $\mathbf{Q}$ in Eq. (3.31) makes the solving of unsteady N-S equations become a steady problem within each physical time steps. Most time stepping methods for steady problems can be directly applied to solve Eq. (3.31). Applying the second-order backward Euler's method to the physical time term, Eq. (3.31) becomes

$$\left[\mathbf{\Gamma}\frac{\partial(\mathbf{Q}\Omega)}{\partial \tau}\right]^{n} = -\mathbf{R}^{n} - \frac{\varepsilon_0(\mathbf{W}\Omega)^{n} + \varepsilon_1(\mathbf{W}\Omega)^{n-1} + \varepsilon_2(\mathbf{W}\Omega)^{n-2}}{\Delta t}, \tag{3.32}$$

where the superscripts n, $n-1$ and $n-2$ denote the current time step, the last time step and the previous step of the last step. ε_0, ε_1 and ε_2 are coefficients determined by the time

Table 3.1: Coefficients for the temporal accuracy

Accuracy order	ε_0	ε_1	ε_2
1st	1	0	1
2nd	3/2	-2	1/2

accuracy, listed in Table 3.1.

Fixing the physical time step n, the pseudo time derivative can be resolved using explicit or implicit time stepping techniques designed for steady flows. Even with moving surfaces, the control volume is independent of the pseudo time within each physical time step. Applying an explicit scheme to the pseudo time term, we obtain

$$\left[\mathbf{\Gamma}^m \frac{(\Delta\mathbf{Q})^m \Omega}{\Delta\tau} \right]^n = -\mathbf{R}^{m-1,n} - \frac{\varepsilon_0(\mathbf{W}\Omega)^{m,n} + \varepsilon_1(\mathbf{W}\Omega)^{n-1} + \varepsilon_2(\mathbf{W}\Omega)^{n-2}}{\Delta t}, \tag{3.33}$$

where the superscript m and $m-1$ denote the current and last pseudo time step.

When Δt approaches to zero, the right hand side of Eq. (3.32) will dramatically increase, which will cause numerical instability. That is the reason why the discretization of the physical time step in Eq. (3.32) will be implicitly treated. Melson *et al.* [1993] analysed the stability problem of different treatments of the physical time term and addressed the implicit treatment can remedy the numerical instability when a small time step Δt is specified according to the time accuracy requirement. As the primary variables $\mathbf{Q}$ are dependent variables, the unknown $(\mathbf{W})^n$ in Eq. (3.33) can be reconstructed by $\mathbf{Q}$ with the Taylor expansion, which reads

$$\mathbf{W}^{m,n} = \mathbf{W}^{m-1,n} + \left(\frac{\partial\mathbf{W}}{\partial\mathbf{Q}} \right)^{m,n} \cdot (\Delta\mathbf{Q})^{m,n}. \tag{3.34}$$

Substitute Eq. (3.34) into Eq. (3.33), and it is obtained as follows

$$\begin{aligned}
\mathbf{\Gamma}^{m,n} \frac{(\Delta\mathbf{Q})^{m,n}\Omega^n}{\Delta\tau} = & -\mathbf{R}^{m-1,n} - \left\{ \varepsilon_0 \frac{\mathbf{W}^{m-1,n}\Omega^n}{\Delta t} + \varepsilon_0 \left(\frac{\partial\mathbf{W}}{\partial\mathbf{Q}} \right)^{m,n} \cdot \left[\frac{(\Delta\mathbf{Q})^{m,n}}{\Delta t} \right] \Omega^n \right. \\
& \left. + \varepsilon_1 \frac{(\mathbf{W}\Omega)^{n-1}}{\Delta t} + \varepsilon_2 \frac{(\mathbf{W}\Omega)^{n-2}}{\Delta t} \right\}.
\end{aligned} \tag{3.35}$$

Rearrange the above equation by using the associativity of matrix product, and it becomes

$$\left[\mathbf{\Gamma}^{m,n} + \varepsilon_0 \frac{\Delta \tau}{\Delta t} \left(\frac{\partial \mathbf{W}}{\partial \mathbf{Q}} \right)^{m,n} \right] \Omega^n \frac{(\Delta \mathbf{Q})^{m,n}}{\Delta \tau} = - \mathbf{R}^{m-1,n} - \left[\varepsilon_0 \frac{\mathbf{W}^{m-1,n}\Omega^n}{\Delta t} \right.$$
$$\left. + \varepsilon_1 \frac{(\mathbf{W}\Omega)^{n-1}}{\Delta t} + \varepsilon_2 \frac{(\mathbf{W}\Omega)^{n-2}}{\Delta t} \right]. \tag{3.36}$$

Eq. (3.36) has the denominator Δt in both left and right hand sides to remove the potential singularity caused by its possible small values, which allows the physical time step Δt to adopt a much smaller value without any numerical instability.

For simplicity, two symbols $\mathbf{\Gamma}^*$ and $\mathbf{R}^*$ are introduced as,

$$\mathbf{\Gamma}^* = \mathbf{\Gamma}^{m,n} + \varepsilon_0 \frac{\Delta \tau}{\Delta t} \left(\frac{\partial \mathbf{W}}{\partial \mathbf{Q}} \right)^{m,n}, \tag{3.37}$$

$$\mathbf{R}^* = -\mathbf{R}^{m-1,n} - \left[\varepsilon_0 \frac{\mathbf{W}^{m-1,n}\Omega^n}{\Delta t} + \varepsilon_1 \frac{(\mathbf{W}\Omega)^{n-1}}{\Delta t} + \varepsilon_2 \frac{(\mathbf{W}\Omega)^{n-2}}{\Delta t} \right]. \tag{3.38}$$

If the determinant of $\mathbf{\Gamma}^*$ is not zero, Eq. (3.36) is rearranged as

$$\frac{(\Delta \mathbf{Q})^{m,n}}{\Delta \tau} = \frac{1}{\Omega^n} \mathbf{\Gamma}^{*-1} \cdot \mathbf{R}^*. \tag{3.39}$$

3.4.3   Pseudo time stepping

The pseudo time stepping is known as the inner iteration within a fixed physical time step. A multi-stage Runge-Kutta scheme for an ordinary equation system (Jameson *et al.* [1981]) can be applied to realize the pseudo time marching. Applying the p-stage Runge-Kutta scheme to Eq. (3.39), the Runge-Kutta iteration within the pseudo time step m can be expressed as

$$\mathbf{Q}^{(i)} = \mathbf{Q}^{(0)} - \alpha_i \Delta \tau \frac{1}{\Omega^n} \mathbf{\Gamma}^{*-1} \cdot \mathbf{R}^*, \tag{3.40}$$

where

$$\mathbf{Q}^{(0)} = \mathbf{Q}^{m-1}, \tag{3.41}$$

and α_i is the multi-stage coefficient for the i-th stage, which can be tuned to increase the maximum time step or to improve the numerical stability (Blazek [2001]). In this study, the α_i adopts the function given by Jameson *et al.* [1981],

$$\alpha_i = \frac{1}{p - i + 1}. \tag{3.42}$$

Other definitions of α_i can be found in Blazek [2001], Berland *et al.* [2006] and Swanson *et al.* [2007] to satisfy different spatial discretization schemes, different dissipation rates, convergence rates and so on. Eq. (3.40) describes the p-stage Runge-Kutta time stepping for the pseudo time inner iteration from the step $m-1$ to m, and the achieved **Q** in the m-th step is

$$\mathbf{Q}^m = \mathbf{Q}^{(p)}. \tag{3.43}$$

In current study, the fourth-order Runge-Kutta scheme is used ($p = 4$).

From above analysis of the dual time stepping, the inner iteration within a pseudo time step should approach to a steady state before the next physical time marches. However, for unsteady flow (especially with control devices), it may take even hundreds of time steps of the inner iteration before the residual reduces to an acceptable order (Dwight [2006]). Therefore, in this study a criterion to judge the convergence of the inner iteration is used to make the inner iterations as few as possible with acceptable time accuracy. The criterion is to choose the smaller one between a given inner iteration step number and the step number satisfying $\varepsilon < \epsilon$, where ϵ is a small number of 10^{-4}. ε is a re-defined residual for the dual time stepping, expressed as

$$\varepsilon = \frac{\sum_{i=1}^{\text{cellnum}} \parallel \phi^{m,n} - \phi^{m-1,n} \parallel_2}{\sum_{i=1}^{\text{cellnum}} \parallel \phi^{m,n} - \phi^n \parallel_2}, \tag{3.44}$$

where ϕ is a flow variable, which adopts the density ρ in this study.

3.4.4 Determination of time steps

Physical time step

The physical time is implicitly discretized, so that the physical time step is less sensitive to the numerical stability. Thus, it can be determined only concerning the flow physics. Generally, a smaller physical time step results in a faster convergence rate in the pseudo time and a longer computational time. However, a physical time step larger than the characteristic time of the flow usually damps out unsteady flow information.

For flows with dominating frequencies, such as vortex shedding frequency, the physical time step should be small enough to capture this periodic motion. For flows without distinct periodic motion, the physical time step is usually determined by the characteristic time of flow. For flows with flow control devices, the physical time step is also required to be small enough to resolve the flow control frequencies and controlled flow motions.

Pseudo time step

As the explicit temporal scheme is used in the pseudo time stepping, the numerical stability restricts the pseudo time step via the Courant-Friedrichs-Lewy (CFL) condition (Blazek [2001]). The pseudo time step $\Delta\tau$ can be determined for a control volume from the approximate relation

$$\Delta\tau = \frac{\text{CFL} \cdot \Omega}{\Lambda_c + C\Lambda_v}, \tag{3.45}$$

where CFL is the CFL number, Λ_c is the spectral radii of the convective flux, Λ_v is the viscous spectral radii, and C is a multiplier. C is usually set to be $C = 4$ for central difference schemes, $C = 2$ for the first order upwind schemes and $C = 1$ for the second order upwind schemes.

For unstructured mesh, Λ_c is defined as (Mavriplis and Jameson [1990]; Vijayan and Kallinderis [1994]),

$$\Lambda_c = \sum_{i=1}^{N_{\text{face}}} \left[|(\mathbf{u} - \mathbf{u_g}) \cdot \mathbf{n}_i + a_i| \cdot A_i \right]. \tag{3.46}$$

where c_i is the sound speed.

The viscous spectral radii Λ_v in Xia [2005] did not take the turbulence modelling into account. Herein, the viscous spectral radii in equations with a turbulence modelling (Blazek [2001]) is used, which reads

$$\Lambda_v = \sum_{i=1}^{N_{\text{face}}} \left[\max\left(\frac{4}{3\rho}, \frac{\gamma}{\rho} \right) \left(\frac{\mu_l}{Pr_l} + \frac{\mu_t}{Pr_t} \right) \frac{A_i^2}{\Omega} \right], \tag{3.47}$$

where μ_l and μ_t denote the laminar and turbulent dynamic viscosity, respectively. Pr_l and Pr_t are the laminar and turbulent Prandtl numbers. In this study, $Pr_l = 0.72$ and $Pr_t = 0.9$. A CFL number around 1.0 is used for calculations.

3.5   Finite volume spatial discretization

The solver DG-DES has a finite volume method with the co-located grid and cell-centred scheme for unstructured grid data architecture, which can handle complex geometries. The co-located grid and cell-centred scheme mean that the control volume is each individual mesh cell, and the conservative and primary variables are stored at the same locations (the centroid of each mesh cell). DG-DES contains several upwind schemes for the convective flux calculation and the central difference schemes for the viscous flux calculation.

3.5.1 Discretisation of inviscid flux: the Roe-family flux splitting scheme

3.5.1.1 Roe's flux difference splitting scheme

Roe's flux difference splitting scheme (Roe [1981]) is a classical and popular shock-capturing upwind scheme in the computation of compressive flows. It is a Godunov-type scheme (Godnunov [1959]) based on the approximate solution of a Riemann problem at each interaface separating pair of neighbouring cells of the spatial discretization (LeVeque [1999]). In Roe's scheme, the original convective flux $\mathbf{F_c}$ at the interface shown in Eq. (3.23) changes to a modified numerical expression $\tilde{\mathbf{F}}$, which is usually written as the sum of a central term $\tilde{\mathbf{F}}_\mathbf{c}$ and a numerical dissipation term $\tilde{\mathbf{F}}_\mathbf{d}$ with the conservative variables $\mathbf{W}$ (Weiss and Smith [1995]), shown as

$$\mathbf{F_c} \xrightarrow{\text{numerically expressed}} \tilde{\mathbf{F}} = \tilde{\mathbf{F}}_\mathbf{c} + \tilde{\mathbf{F}}_\mathbf{d}. \tag{3.48}$$

Generally, the central term $\tilde{\mathbf{F}}_\mathbf{c}$ is calculated by averaging the fluxes at the "left" and "right" sides of the cell face, shown as

$$
\begin{aligned}
\tilde{\mathbf{F}}_\mathbf{c} \cdot \mathbf{n} &= \frac{1}{2} \left(\mathbf{F_c}^\mathrm{L} + \mathbf{F_c}^\mathrm{R} \right) \cdot \mathbf{n} \\
&= \frac{1}{2} \left[u_n{}^\mathrm{L} \cdot \begin{pmatrix} \rho \\ \rho u_1 \\ \rho u_2 \\ \rho u_3 \\ \rho H \end{pmatrix}^\mathrm{L} + u_n{}^\mathrm{R} \cdot \begin{pmatrix} \rho \\ \rho u_1 \\ \rho u_2 \\ \rho u_3 \\ \rho H \end{pmatrix}^\mathrm{R} \right] + \frac{1}{2} \left[p^\mathbf{L} \cdot \begin{pmatrix} 0 \\ n_1 \\ n_2 \\ n_3 \\ 0 \end{pmatrix}^\mathrm{L} + p^\mathbf{R} \cdot \begin{pmatrix} 0 \\ n_1 \\ n_2 \\ n_3 \\ 0 \end{pmatrix}^\mathrm{R} \right]
\end{aligned} \tag{3.49}
$$

The numerical dissipation term $\tilde{\mathbf{F}}_\mathbf{d}$ can be expressed as

$$\tilde{\mathbf{F}}_\mathbf{d} = -\frac{1}{2}|\mathbf{A_c}|\Delta\mathbf{W}, \tag{3.50}$$

where $\mathbf{A_c}$ is the conservative Jacobian, and $\Delta(\cdot) = (\cdot)^R - (\cdot)^L$ is the difference of variables at the right and left side. As the primary variables are selected as the dependent variables, $\Delta\mathbf{W}$ can be transformed as

$$\Delta\mathbf{W} = \frac{\partial\mathbf{W}}{\partial\mathbf{Q}} \cdot \Delta\mathbf{Q}. \tag{3.51}$$

Denote

$$\mathbf{A_p} = |\mathbf{A_c}| \cdot \frac{\partial\mathbf{W}}{\partial\mathbf{Q}}, \tag{3.52}$$

3. Finite volume spatial discretization

then the numerical dissipation term becomes

$$\tilde{\mathbf{F}}_{\mathbf{d}} = -\frac{1}{2}\mathbf{A_p}\Delta\mathbf{Q}. \tag{3.53}$$

The primary Jacobian $\mathbf{A_p}$ can be expressed as

$$\mathbf{A_p} = \hat{\mathbf{R}}^{\text{Roe}}\left|\hat{\mathbf{\Lambda}}^{\text{Roe}}\right|\left(\hat{\mathbf{R}}^{\text{Roe}}\right)^{-1}, \tag{3.54}$$

where $\hat{\cdot}$ stands for the Roe averaged values at the interface, $\hat{\mathbf{R}}^{\text{Roe}}$ is the right eigenvector matrix of $\partial\mathbf{F}/\partial\mathbf{Q}$, and $\hat{\mathbf{\Lambda}}^{\text{Roe}}$ is the diagonal matrix consisting of the five eigenvalues

$$\hat{\lambda}_{1,2,3} = \hat{u}_n, \quad \hat{\lambda}_4 = \hat{u}_n + \hat{a}, \quad \hat{\lambda}_5 = \hat{u}_n - \hat{a}, \tag{3.55}$$

where $u_n = (\mathbf{u} - \mathbf{u_g})\cdot\mathbf{n}$ is the normal velocity on the surface. The numerical dissipation term $\tilde{\mathbf{F}}_{\mathbf{d}}$ can be expanded and rewritten in the following form (Liu and Vinokur [1989]),

$$\tilde{\mathbf{F}}_{\mathbf{d}} = -\frac{1}{2}\left[|\hat{\lambda}_1|\cdot\begin{pmatrix}\Delta\rho\\\Delta(\rho u_1)\\\Delta(\rho u_2)\\\Delta(\rho u_3)\\\Delta(\rho E)\end{pmatrix} + \delta U\cdot\begin{pmatrix}\hat{\rho}\\\hat{\rho}\hat{u}_1\\\hat{\rho}\hat{u}_2\\\hat{\rho}\hat{u}_3\\\hat{\rho}\hat{H}\end{pmatrix} + \delta p\cdot\begin{pmatrix}0\\n_1\\n_2\\n_3\\\hat{u}_n\end{pmatrix}\right]. \tag{3.56}$$

Define $\hat{\lambda}^+$ and $\hat{\lambda}^-$ as

$$\hat{\lambda}^+ = \frac{1}{2}\left(|\hat{\lambda}_4| + |\hat{\lambda}_5|\right) = \begin{cases}\hat{a}, & \text{if subsonic}\\\hat{u}_n, & \text{if supersonic}\end{cases}, \tag{3.57}$$

and

$$\hat{\lambda}^- = \frac{1}{2}\left(|\hat{\lambda}_4| - |\hat{\lambda}_5|\right) = \begin{cases}\hat{u}_n, & \text{if subsonic}\\\hat{a}, & \text{if supersonic}\end{cases}, \tag{3.58}$$

then δU and δp can be given as

$$\delta U = \frac{\hat{\lambda}^+ - |\hat{\lambda}_1|}{\hat{\rho}\hat{a}^2}\cdot\Delta p + \frac{\hat{\lambda}^-}{\hat{a}}\cdot\Delta u_n, \tag{3.59}$$

$$\delta p = \frac{\hat{\lambda}^-}{\hat{a}}\cdot\Delta p + \left(\hat{\lambda}^+ - |\hat{\lambda}_1|\right)\cdot\hat{\rho}\cdot\Delta u_n. \tag{3.60}$$

Eq. (3.56) is a sum of three terms. The first term represents the basic upwind dissipation, in which $|\hat{\lambda}_1|$ has the effect of upwinding the convective variables (Weiss and Smith [1995]). The second term introduces a pressure-derivative smoothing term (δU) to the interface velocity to ensure the velocity-pressure coupling. The third term is a modification to the interface pressure, which decides the accuracy (Li *et al.* [2009]).

In Eq. (3.56), all variables are on the interface of a left and a right control volume. The Roe averaging is applied to obtain these interface variables, which are defined as

$$
\begin{aligned}
\hat{\rho} &= \sqrt{\rho^L + \rho^R}, \\
\hat{\mathbf{u}} &= \frac{\sqrt{\rho^L}\mathbf{u^L} + \sqrt{\rho^R}\mathbf{u^R}}{\sqrt{\rho^L} + \sqrt{\rho^R}}, \\
\hat{H} &= \frac{\sqrt{\rho^L}H^L + \sqrt{\rho^R}H^L}{\sqrt{\rho^L} + \sqrt{\rho^R}}.
\end{aligned}
\tag{3.61}
$$

The Roe-averaged temperature $\hat{T}$, energy $\hat{E}$ and sound speed $\hat{a}$ can be respectively calculated via the Eq. (3.17), Eq. (3.18) and Eq. (3.19).

The main pitfall of the Roe's approximate Riemann solver is that it may violate the entropy condition. The entropy condition is an additional criterion, which states that hyperbolic conservation laws should be satisfied for the governing equations in order to converge necessarily to a physically unique weak solution (LeVeque [1999]). When one of the eigenvalues (Eq. (3.55)) is zero, the dissipation term $\tilde{\mathbf{F}}_{\mathbf{d}}$ will disappear, which will cause unphysical numerical oscillating. This phenomenon usually occurs in computational domains where expansions are observed through sonic regions, i.e. sonic expansion. In order to remedy the deficiencies of approximate Riemann solvers to satisfy the entropy condition, a correction of the eigenvalues so-called "entropy fix" was first proposed by Harten [1983] and Harten and Hyman [1983]. Afterwards, different forms of entropy fix for Roe's approximate Riemann solver have developed (LeVeque [1999]). The entropy fix in Kermani and Plett [2001] is used for the in-house solver DG-DES, which maps the eigenvalues to

$$
\hat{\lambda}_{(new)} = \begin{cases} \frac{\hat{\lambda}^2 + \epsilon^2}{2\epsilon}, & \text{if } |\hat{\lambda}| < \epsilon \\ \hat{\lambda}, & \text{otherwise} \end{cases},
\tag{3.62}
$$

where the small number ϵ is set to be

$$
\epsilon = K \max(\lambda^{\mathrm{R}} - \lambda^{\mathrm{L}}, 0).
\tag{3.63}
$$

3. Finite volume spatial discretization

This modification of the most popular entropy fix (Harten and Hyman [1983]) involves a multiplier K ($K = 2$ in this study) to allow the expansion-shock to totally diffuse into the computational domain and completely disappear to obtain more consistent solutions with the physical solutions (Kermani and Plett [2001]).

Details about the Roe-type schemes for all speed flows can be found in Li *et al.* [2009].

3.5.1.2   The Roe scheme with low dissipation

When the upwind schemes are applied to LES, one of the most desired properties is a low dissipation. However, the numerical dissipation of upwind schemes has a possibility to exceed turbulence dissipation within sub-grid scale filters. Upwind schemes usually produce too much dissipation for turbulent flows. Even though excessive dissipation does not result in an unstable or meaningless solution, it prevents simulation results from taking full advantages of the fine grid provided and it also may stop the energy cascade before the SGS eddy viscosity does (Strelets [2001]). One solution is to use high-order centred or compact schemes. However, they do not have sufficient numerical stability for complex flows with LES. Numerical stability and dissipation propose a contradictory demand on numerical schemes for applying LES to complex flows.

The numerical dissipation can be reduced by introducing an control/blending function/factor to the numerical dissipation term (Bui [2000]). The convective flux in the Roe scheme $\tilde{\mathbf{F}}$ in (Eq. (3.48)) becomes

$$\tilde{\mathbf{F}}_{\mathrm{lowdissip}} = \tilde{\mathbf{F}}_{\mathbf{c}} + \varepsilon_{\mathrm{dissip}}\tilde{\mathbf{F}}_{\mathbf{d}}, \tag{3.64}$$

where $\varepsilon_{\mathrm{dissip}}$ is a blending dissipation factor between 0 and 1. The Eq. (3.64) can be rearranged as

$$
\begin{aligned}
\tilde{\mathbf{F}}_{\mathrm{lowdissip}} &= (1 - \varepsilon_{\mathrm{dissip}})\tilde{\mathbf{F}}_{\mathbf{c}} + \varepsilon_{\mathrm{dissip}}\tilde{\mathbf{F}}_{\mathbf{c}} + \tilde{\mathbf{F}}_{\mathbf{d}} \\
&= (1 - \varepsilon_{\mathrm{dissip}})\tilde{\mathbf{F}}_{\mathbf{c}} + \varepsilon_{\mathrm{dissip}}\tilde{\mathbf{F}}.
\end{aligned}
\tag{3.65}
$$

Eq. (3.65) is a blending of the central difference and the original upwind Roe scheme. When $\varepsilon_{\mathrm{dissip}} = 0$, it becomes to a pure central difference, and $\varepsilon_{\mathrm{dissip}} = 1$ corresponds to a full Roe scheme. As previously stated, a small $\varepsilon_{\mathrm{dissip}}$ can cause numerical instability, while a large $\varepsilon_{\mathrm{dissip}}$ produces too much numerical dissipation for turbulent flows. Lin *et al.* [1997] found $\varepsilon_{\mathrm{dissip}} = 0.1$ provided good turbulent solutions and numerical stability in their in-house CFD solver. Bui [2000] stated that the finer the grids, the smaller the minimum value of $\varepsilon_{\mathrm{dissip}}$ can be used. Xia [2005] also used such a priori to determine the value of $\varepsilon_{\mathrm{dissip}}$.

There is some progress in the recent years in determining the value $\varepsilon_{\text{dissip}}$, which is implemented into DG-DES. Travin *et al.* [2002] suggested a blending dissipation factor $\varepsilon_{\text{dissip}}$ depending on the flow fields and grid spacings for the SST-based hybrid RANS/LES methods. Strelets [2001] applied this method to massively separated flows, and Hasse *et al.* [2009] applied this blending dissipation factor to a simplified engine with SST-based DES. The blending dissipation factor has to ensure the upwind scheme used for flows in the irrigational region, the RANS region and the LES regions with coarse grids. The blending dissipation factor reads

$$\varepsilon_{\text{dissip}} = \varepsilon_{\text{max}} \tanh\left(A^{C_{\text{H1}}}\right), \tag{3.66}$$

where the function A is

$$A = C_{\text{H2}} \cdot \max\left(\frac{C_{\text{DES}}\Delta}{g \cdot l_{\text{turb}}} - 0.5, 0\right). \tag{3.67}$$

l_{turb} is the turbulent length scale, defined as (for SST),

$$l_{\text{turb}} = \frac{\sqrt{k}}{C_{\mu}\omega} \tag{3.68}$$

The parameter g is introduced to guarantee the dominance of the upwind scheme in the irrotational flows (with $|\mathbf{S}| > 0$ and $|\mathbf{\Omega}| \ll 0$), which reads

$$g = \max\left[\tanh(B^4), 10^{-10}\right], \tag{3.69}$$

where

$$B = C_{\text{H3}}|\cdot\mathbf{\Omega}| \cdot \frac{\max\left(|\mathbf{S}|, |\mathbf{\Omega}|\right)}{\max\left(\frac{|\mathbf{S}|^2 + |\mathbf{\Omega}|^2}{2}, 10^{-10}\right)}. \tag{3.70}$$

In order to ensure the consistency with the zonal RANS/LES, the final blending dissipation factor is

$$\varepsilon_{\text{dissip}}^* = \max(\varepsilon_{\text{dissip}}, F_{\text{SST}}), \tag{3.71}$$

where F_{SST} is the blending function in SST-DES (Travin *et al.* [2002]). The constants are: $\varepsilon_{\text{max}} = 1.0$, $C_{\text{H1}} = 3.0$, $C_{\text{H2}} = 1.0$ and $C_{\text{H3}} = 2.0$.

3.5.2 Discretisation of inviscid flux: Simple Low-Dissipation Scheme of AUSM-family

Advection Upstream Splitting Method (AUSM) is an alternative widely-used upwind scheme, which was proposed by Liou and Steffen [1993]. An improved AUSM named AUSM$^+$

3. Finite volume spatial discretization

was proposed in Liou [1996], which has positivity preserving of scalar quantities, and is free of "carbuncle phenomenon" and oscillations at slowing moving shock. Afterwards, an AUSM for all-speed flow, named AUSM$^+$-up, was proposed in Liou [2006] to tackle the low Mach number limit. Later, Shima [1997] proposed a Simple High-resolution Upwind Scheme (SHUS) based on the AUSM-family schemes, which replaces the mass flux of AUSM$^+$ with the one from the Roe scheme but with the arithmetic averaged values rather than the Roe averaged ones. Shima and Kitamura [2009] improved SHUS to give more reliable solutions both for low and high speed flows. This all-speed AUSM with a low dissipation was compared with P-Roe, A-Roe, AUSM$^+$-up and SHUS in Kitamura *et al.* [2011].

As a upwind scheme, AUSM family can also realize a low dissipation scheme for LES or hybrid RANS/LES by blending this upwind scheme with the central difference schemes, just as discussed in Section 3.5.1.2. However, there are other methods to reach such an aim. Shima and Kitamura [2009] modified the mass flux function and the pressure function in the AUSM$^+$-up to reduce the numerical dissipation in regimes with low Mach numbers. Meanwhile, it also improves the numerical robustness for high Mach number regimes. This all-speed low dissipation scheme is named as Simple Low-Dissipation Scheme of AUSM-family (SLAU). It is noted that the SLAU scheme does not have a time-derivative preconditioning for all speed flows, which may have slow convergence.

The mass flux in SLAU is

$$\dot{m}_{\frac{1}{2}} = \frac{1}{2}\left(\rho u_n{}^{\mathrm{L}} + |\rho \bar{u}_n{}^{\mathrm{L}}|\right) + \frac{1}{2}\left(\rho u_n{}^{\mathrm{R}} + |\rho \bar{u}_n{}^{\mathrm{R}}|\right) - \frac{1}{2}\cdot\frac{\chi}{\bar{a}}\cdot(p^{\mathrm{R}} - p^{\mathrm{L}}) \tag{3.72}$$

where

$$\chi = (1 - \tilde{M})^2, \tag{3.73}$$

with

$$\tilde{M} = \min\left(1.0, \frac{1}{\bar{a}}\sqrt{\frac{\mathbf{u}^{\mathrm{L}}\cdot\mathbf{u}^{\mathrm{L}} + \mathbf{u}^{\mathrm{R}}\cdot\mathbf{u}^{\mathrm{R}}}{2}}\right). \tag{3.74}$$

The averaged velocity $|\bar{u}_n|$ is a density weighed velocity, which is given as

$$|\bar{u}_n| = \frac{\rho^{\mathrm{L}}|\bar{u}_n|^{\mathrm{L}} + \rho^{\mathrm{R}}|\bar{u}_n|^{\mathrm{R}}}{\rho^{\mathrm{L}} + \rho^{\mathrm{R}}}. \tag{3.75}$$

The averaged velocity $|\bar{u}_n|$ at the left and right sides of an interface is an blending value, which reads

$$|\bar{u}_n|^{\pm} = (1 - g)\bar{u}_n + g|u_n|^{\pm}, \tag{3.76}$$

where the blending function g is given as

$$g = -\max\left[\min\left(M^+, 0\right), -1.0\right] \cdot \min\left[\max\left(M^-, 0\right), 1.0\right], \tag{3.77}$$

with the Mach number

$$M^\pm = \frac{u_n^\pm}{\bar{a}} \tag{3.78}$$

and the averaged sound speed

$$\bar{a} = \frac{a^{\mathrm{L}} + a^{\mathrm{R}}}{2}. \tag{3.79}$$

The modified pressure flux is given as

$$\begin{aligned}
\tilde{p} = & \frac{1}{2}\left(p\mathrm{L}^+p^{\mathrm{R}}\right) + \frac{1}{2}\left(\left. f_p^{\mathrm{L}}\right|_\alpha - \left. f_p^{\mathrm{R}}\right|_\alpha\right) \cdot \left(p\mathrm{L}^-p^{\mathrm{R}}\right) + \\
& \frac{1-\chi}{2}\left(\left. f_p^{\mathrm{L}}\right|_\alpha + \left. f_p^{\mathrm{R}}\right|_\alpha - 1.0\right) \cdot \left(p\mathrm{L}^+p^{\mathrm{R}}\right),
\end{aligned} \tag{3.80}$$

where the parameter α is $\alpha = 0$.

The SLAU scheme is free from restrictions of specifying reference velocities/Mach numbers, which is desirable for flows without uniform flows, such as the turbo-pump internal flows Kitamura *et al.* [2011].

3.5.3 Discretisation of viscous flux

The discretisation of the viscous flux Eq. (3.10) is mainly about the calculation of flow variables at the interface. The central difference scheme can be used to obtain the variables on the interface of the left and right cells. The variables on the interface (the subscript $\frac{1}{2}$ denotes the interface) are

$$\phi_{\frac{1}{2}} = \frac{1}{2}\left(\phi^{\mathrm{L}} + \phi^{\mathrm{R}}\right), \tag{3.81}$$

where ϕ stands for all flow variables stored at cell centres, such as p, u_1, u_2, u_3, T and the their gradients.

The above central difference is an arithmetic average. In order to increase the accuracy, a weighted average of variables stored in the cell-centres of the left and right cells can also be applied. For meshes with good quality, the arithmetic average can be adopted, as it requires less calculation. For unstructured skewed grids, the volume weighted interface variables can provide more accurate solutions.

DG-DES stores all flow variables at cell-centres. Methods to estimate variable gradients in a cell, approaches to estimation of variables on the face, and techniques to realize a high

order flux reconstruction are all given in Xia and Qin [2005].

3.6   Boundary conditions

The surface of an object in flows represents a natural physical boundary, while the truncation of a physical domain into a computational domain leads to artificial boundaries, where the values of physical variables have to be described properly as boundary conditions. Applying boundary conditions properly is crucial to achieve accurate numerical solutions. Blazek [2001] described boundary conditions widely used in CFD. The ordinary boundary conditions in DG-DES was given in Xia [2005]. Flow control devices will introduce new boundary conditions, which will be discussed.

3.6.1   Boundary conditions for moving wall

For both synthetic jets simulating the cavity and the oscillating surface in piezoelectric actuator flow control, a moving/oscillating wall is involved to be simulated. This introduces a non-zero velocity to the original no-slip wall. According to the no-penetration condition of a solid wall, the boundary velocity $\mathbf{u_b}$ for a moving wall can be calculated by

$$(\mathbf{u_b} - \mathbf{u_g}) \cdot \mathbf{n} = 0. \tag{3.82}$$

The pressure can be obtained through the condition that the pressure gradient normal to the wall is zero. The temperature depends on an adiabatic wall or a isothermal wall.

3.6.2   Turbulent inflow boundary conditions

For RANS or URANS, flow variables on the boundaries are assumed to vary very slowly with time in comparison with the numerical time step. Thus, these quantities on boundaries are set to be constant, independent of time. However, for LES, the grid-filtered variables always contain some time-varying components, stochastically varying on all scales down to the filer scales and the temporal scales of the simulation (Tabor and Baba-Ahmadi [2010]). Therefore, for LES, turbulent fluctuations have to be present at inlets, and there are some methods developed to generate stochastic fluctuations in the grid scale, which can represent turbulence.

Tabor and Baba-Ahmadi [2010] listed several principles in designing a turbulence generator at inlet. Simply, a turbulence generator at inlets has to be capable of produc-

ing anisotropic, inhomogeneous turbulence with a controllable degree of auto and cross-correlations of velocities with respect to time and space as well as satisfying the mass conservation. A natural method is to generate inflow conditions by running a separate and precursor calculation of an equilibrium flow to generate a "library" of turbulent data which can be introduced at the main computation at each time. This method is usually called the precursor simulation method. For inlets near the characteristic objects or inlets influenced by downstream flows, this method may not be a good representation of turbulence. In addition, this method involves large precursor calculations. Lund *et al.* [1998] proposed two turbulence inflow methods. One is the random fluctuation inflow generation method, which recovers a random fluctuation satisfying known Reynolds stress, but cannot represent auto and across correlations. Thus, it damps quickly. The other is the recycling-rescaling method, which re-scales flow properties at some distance downstream of the inlet and then recycles these instantaneous flow properties to the inlet. Jarrin *et al.* [2006] tested this method in flat plate flows and showed that 10 or more time of boundary layer thickness downstream is required to obtain a reasonable turbulence boundary layer. Based on a vortex method (Sergent [2002]), Jarrin *et al.* [2006] proposed a synthetic-eddy-method, which generates vortex with various sizes to realize both time and spatial correlation. Later, Poletto *et al.* [2011] developed Jarrin *et al.* [2006]'s method and proposed a divergence free synthetic eddy method. Shur *et al.* [2011] used an overlapped RANS/LES region to produce turbulent content. Besides, there are other methods, like synthetic turbulence method (Badry and Badarudin [2007]) and spectra method (Gusakov and Kosolapova [2011]). All these methods require fairly long development lengths before realistic turbulence is established. For cases with a short inlet length with velocity profile specified, such as a backward facing step or a fuse or nozzle, all these methods may be not suitable.

In this study, if a turbulence inlet is used, the random fluctuation inflow generation method (Lund *et al.* [1998]) is adopted. Although the fluctuation may damp out in a long distance due to lack of spatial corrections, for cases with short inlet distance, it still has popular usage. This method is described as follows.

The instantaneous velocity component $u_i, (i = 1, 2, 3)$ is given as

$$u_i = \bar{u}_i + C_i n_i u_i^{'}, \tag{3.83}$$

where $\bar{u}_i$ is an given time-averaged inlet velocity profile, n_i is a random number with a magnitude less than a unity and acting in the direction of the velocity component, and C_r is a parameter which relates the amplitudes of fluctuations to the location of the inlet boundary relative to the wall. C_r might also be related to some geometrically-related parameters such

as the non-dimensional distance from the wall y^+, to reflect the increase in eddy sizes moving away from the wall region. If the turbulence kinetic energy at the inlet is known, the fluctuations $u_i^{'}$ is given by (Ferziger and Peric [2002])

$$u_i^{'} = \sqrt{\frac{2}{3}k}. \tag{3.84}$$

This simulation of the fluctuations implies isotropic turbulence generated at inlet. If Reynolds stresses are known at inlet, the instantaneous velocity component u_i is written as

$$u_i = \bar{u}_i + C_i n_j u_{ij}^{'}, \tag{3.85}$$

where C_i usually takes the value of a unit, n_j stands for three sequences of random numbers, which has zero mean, unit variance and zero covariance with the other two distributions. The magnitude of the fluctuations are related with the Reynolds stress tensor τ^{R} via

$$
\begin{aligned}
u_{11}^{'} &= \sqrt{\tau_{11}^{\mathrm{R}}}, \\
u_{12}^{'} = u_{21}^{'} &= \frac{\tau_{21}^{\mathrm{R}}}{u_{11}^{'}}, \\
u_{13}^{'} = u_{31}^{'} &= \frac{\tau_{31}^{\mathrm{R}}}{u_{11}^{'}}, \\
u_{22}^{'} &= \sqrt{\tau_{22}^{\mathrm{R}} - u_{12}^{'}{}^2}, \\
u_{23}^{'} = u_{32}^{'} &= \frac{\tau_{32}^{\mathrm{R}} - u_{12}^{'} u_{13}^{'}}{u_{22}^{'}}, \\
u_{33}^{'} &= \sqrt{\tau_{33}^{\mathrm{R}} - u_{13}^{'}{}^2 - u_{23}^{'}{}^2}.
\end{aligned}
\tag{3.86}
$$

3.7 Dynamic grid techniques

Simulations of flow control are carried out in this study. For flow control with oscillating surfaces or synthetic jets, a moving wall is usually involved. The moving wall will compel the grids in the computational domain or at least domains surrounding the moving wall to move and deform. ALE physically takes the velocity of the moving grid into the N-S equations. There are still several questions to be answered. One of the most important issues is how the surrounding grids move according to the moving/deforming boundaries. This issue is highly related with adaptive grid generation and deformation techniques. It is not the key point of this study, thus only a brief introduction will be given. Another issue is how to calculate the moving speed of each cell ($\mathbf{u_g}$ in above sections), which will be discussed in

details.

3.7.1 Discretisation of geometric conservation law

During simulations of a mesh deformation, Geometric Conservation Law (GCL) has to be complied with to solve the ALE (Thomas and Lombard [1979]). The basic requirement is that any ALE computational method should be able to predict exactly the solution of a uniform flow. Another statement is that no disturbances should be introduced by any arbitrary mesh motion for a uniform flow (Mavriplis and Yang [2006]). Assuming a uniform field of density and velocity, the continuity equation of the mass conservation reduces to

$$\frac{\partial}{\partial t} \int_{\Omega} d\Omega - \oint_{\partial\Omega} \mathbf{u_g} \cdot \mathbf{n} dA = 0. \tag{3.87}$$

This equation states the Continuous Geometric Conservation Law (CGCL). Another formula is the Surface Conservation Law (SCL), which means for a closed surface,

$$\oint_{\partial\Omega} \mathbf{n} dA = 0. \tag{3.88}$$

Intergrading Eq. (3.87) in time from t^n to t^{n+1} obtains the Discrete Geometric Conservation Law (DGCL), shown below

$$\varepsilon_0 \Omega^n + \varepsilon_1 \Omega^{n-1} + \varepsilon_2 \Omega^{n-2} = \int_{t^n}^{t^{n+1}} \left(\oint_{\partial\Omega} \mathbf{u_g} \cdot \mathbf{n} dA \right) dt, \tag{3.89}$$

where n is the time step sequence. DGCL states that the change in volume of each control volume within an arbitrarily small time interval must be equal to the volume swept by the cell boundary during this time interval (Lesoinne and Farhat [1996]).

The volumes at each time step can be calculated exactly via the instant mesh node positions. This puts forward some restrictions that the right hand side of Eq. (3.89) must be exactly computed, which is not easy for numerical calculations. GCL is highly related with the continuity equation (the mass conservation law) in the governing equations. Therefore, the same discretisation method has to be used to ensure the self-consistent of each cell. Otherwise, grid motion induced numerical oscillation may happen (Thomas and Lombard [1979]). In order to satisfy DGCL, various methods were proposed. Lesoinne and Farhat [1996] stated that for first-order time-integration schemes, the face averaged moving velocity is

$$(\mathbf{u_g})^n = \frac{(\mathbf{x_c})^n - (\mathbf{x_c})^{n-1}}{\Delta t}, \tag{3.90}$$

where $\mathbf{x_c}$ is the position vector of a face centre; n and $n-1$ stand for the current and last step. The second order time accuracy can be obtained similarly. This formula by Lesoinne and Farhat [1996] is also the method used in DG-DES.

There are several issues to be noticed. Firstly, both GCL and SCL are neither isolated from the N-S questions nor additional conditions to the N-S questions. Theoretically, the N-S equations are sufficient to describe the motion of fluid dynamics. DGCL is more meaningful to the discretized N-S equations. Secondly, the links between DGCL, the numerical stability and accuracy of ALE schemes are still debated issues in literatures (Farhat *et al.* [2001]; Kamakoti and Shyy [2004]; Mavriplis and Yang [2006]). Thirdly, in the convective flux, the velocity $\mathbf{u}$ is stored at the cell centre, while the calculated $\mathbf{u_g}$ is for each face of the cell. However, $(u - u_g)$ is treated as a whole in the discretisation of the convective flux. This treatment does not cause numerical instability, but the influence on the accuracy of solutions is controversial.

3.7.2 Dynamic grid method

For flow problems with boundary (geometric) deformation or relative motion of multiple bodies, dynamic grid methods are essential to move the mesh in the computational domain according to the movement of boundaries/bodies. In the scope of this study, the term "dynamic grid" is defined as: *moving mesh nodes to dynamically cover the computational domain due to any boundary moving or deforming without changing mesh topology* (Xia [2005]). Therefore, mesh coarsening or refinement is not considered in this study.

3.7.2.1 Literatures on dynamic grid methods

For unstructured meshes, Batina [1990] used a spring analogy to the moving of mesh nodes. The basic concept is to replace the connectivity of nodes with a network of springs or elastic solids inserted between each two neighbouring grid nodes. The movement of the boundaries/bodies will spread around through these springs. Later, numerous dynamic grid methods have emerged and a summary was given in Darbandi and Fouladi [2011].

In addition to the spring tension analogy method, a novel and effective dynamic grid method was proposed by Liu *et al.* [2006] in our Aerodynamic Group, which is the Delaunay graph mapping method. This method successfully realized a global grid-movements based on moving boundaries (Xia [2005]). The basic idea of the Delaunay graph mapping method is firstly to map a fine viscous mesh to a coarse mesh by Delaunay mapping, then to move the mapped graph (only containing the boundary nodes of the original mesh) via the desired
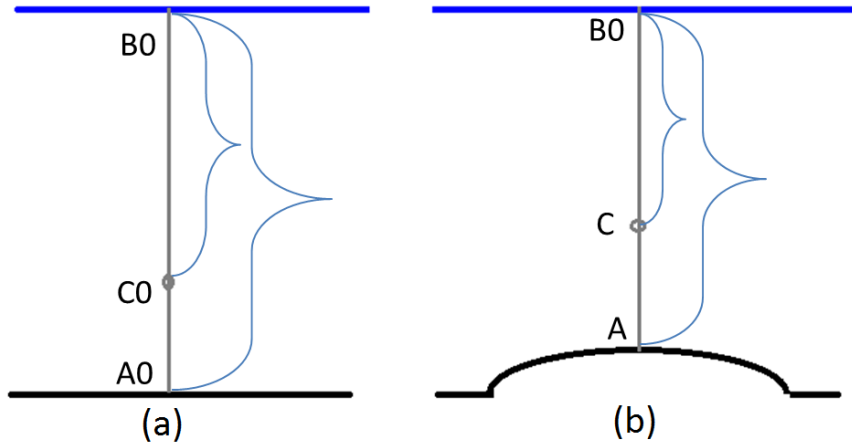
Figure 3.1: Demonstration of the geometry similarity for the moving mesh. The top line where the node B_0 locates is the defined reduced domain range. (a) The original geometry (b) The deformed geometry. The bottom line where the nodes A_0 and its new position A locate is the moving boundary. C is an arbitrary node with the original position C_0.

movement of the boundaries, finally to restore the moved graph to the original mesh with movements.

Both the spring tension analogy and the Delaunay graph mapping method involve moving all nodes located in the computational domain during each step of boundary movements. They both belongs to a complete domain strategy. Darbandi and Fouladi [2011] proposed a reduce-domain strategy, which only moves the grids in a small region close to the moving boundary. However, their method is still time-consuming in updating the time-dependent moving grids.

3.7.2.2 A simple dynamic grid method with a reduced moving domain

When the movement of the boundaries is small, compared with the characteristic length, such as the movement of piezoelectric actuators with the magnitude of micrometers, a complete domain strategy of dynamic grid methods is not necessary, in addition these methods cost much computational resource. According to the current objectives in flow control with oscillating surface of piezoelectric actuators, a simple dynamic grid method with a reduced domain is proposed.

Figure 3.1 shows the basic principle of the geometry similarity. Although Figure 3.1 shows a movement shrinking the moving domain, this method can also realize the expansion of the moving domain.

3. Dynamic grid techniques

The main procedures to apply this simple method to realize the movements of a given domain are given as follows. Firstly, define a reduced moving zone. According to the problem studied, specify the principle direction where the boundary moves. Define a surface/line perpendicular to the moving direction, which usually has a height of at least five times of the maximum deformed length in the same direction to release enough space to spread boundary's motion to the moving zone. Thus, the length of domain in the moving direction is determined. With a small moving distance, it is assumed that there is no grid movement in the other directions, except for the forced moving direction. Secondly, define the movement of the boundary, according to given control devices. Thirdly, obtain each nodes' new position in the principle direction using the geometry similarity. The nodes' coordinates at the other two principle directions do not change. Take an arbitrary node "C" in the moving zone for an example and assume the moving direction is the y-direction, then with a moved boundary layer the new position of the node "C" (y_C) can be calculated with the geometry similarity equation as follows

$$\frac{y_{B0} - y_{A0}}{y_{B0} - y_{C0}} = \frac{y_{B0} - y_A}{y_{B0} - y_C}. \tag{3.91}$$

An example of an oscillating surface on the boundary wall is demonstrated in Figure 3.2. The moving mesh zone is below $y = 1.9$. Figure 3.2 (b) is an enlarged view of meshes around the junction of the moving boundary and the fixed boundary. The geometry similarity grantees no intersections/collapses of fine mesh. The equations for grid movement in 3D deformation of the boundary will be given in 4, where the oscillating surface is realized by this dynamic grid method.

This simple dynamic grid method with a reduced domain reduces the computational cost, and assures the robust of grid movements. Admittedly, there are some limitations of this dynamic grid method. Firstly, it is difficult to be generalized to complex geometries, or cases with complex boundary deformation. Secondly, high mesh quality is preferable in the moving domain. Pour unstructured grids may cause robustness problems. Nevertheless, considering that meshes fitting the boundaries usually have good qualities, the moving domain around the moving surface usually has good mesh qualities. Thirdly, the orthogonality of the fitting meshes around the moving boundary cannot be maintained. Considering the small boundary movement, the damage on the orthogonality of the fitting meshes is usually very small and acceptable.

Even with these pitfalls, the geometry similarity method is a good choice for simple geometry and small boundary deformation. All moving nodes are updated simultaneously, not relying on its surrounding nodes but directly on the moving boundary, which is free from iterations from one node's motion to another. All the moving grids are constrained in the

(a)   (b)
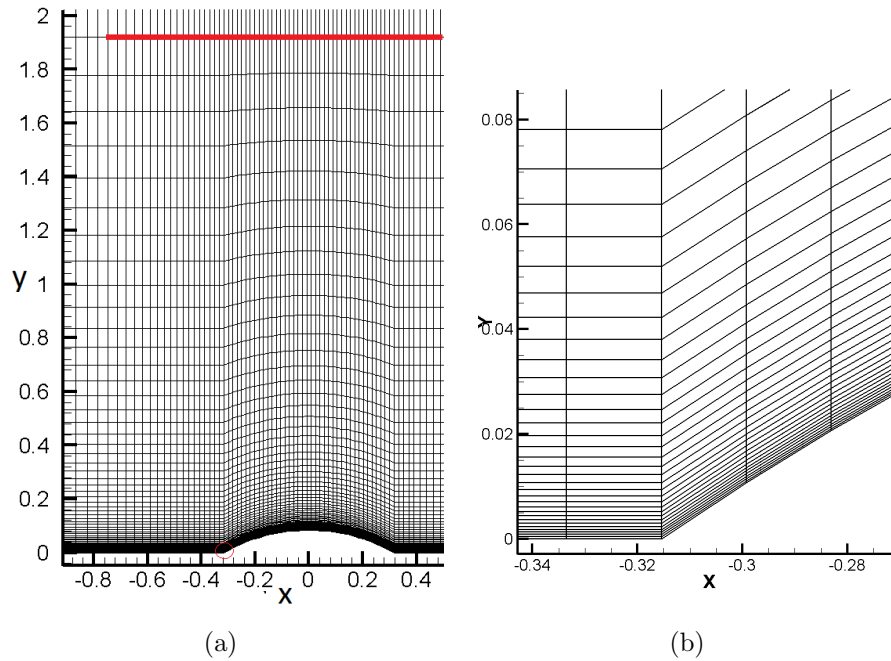
Figure 3.2: Moving mesh with an oscillating surface on the boundary wall. (a) The moving mesh zone. (b) Enlarged view of the boundary mesh.

defined moving zone rather than updating the whole computational domain, which reduces the computational cost. Therefore, for cases with simple geometry and small boundary deformations studied in this thesis, the geometry similarity is applied to construct the moving mesh.

3.8 Techniques on Hybrid RANS/LES Turbulence Modelling

3.8.1 Introduction

There are numerous turbulence modelling methods as discussed in Section 2.3. In the past decades, industrial applications have motivated investigations on unsteady dynamics of turbulent flows, such as flows around stalled wings, cavity flows and flows around landing gears. LES becomes widely used for these complex turbulent flows. However, an inevitable obstacle for LES is its requirements for mesh and time resolutions in near-wall regions. In order to resolve multi-scale turbulence near the wall, a quasi-DNS mesh is essential for LES, whereas this mesh resolution is still difficult to satisfy with foreseeable computational

71

resources for flows at high Reynolds numbers. Therefore, hybrid RANS/LES models have been extensively studied in recent years. These hybrid models combine the advantages of LES in resolving complex turbulent dynamics and the advantages of RANS in modelling the near-wall flows to avoid the requirements for high computational resources. The hybrid RANS/LES methods are the methods used in this study.

Regardless of physical meanings, the formats of RANS N-S and LES N-S equations are very similar. Applying an ensemble/time average to the N-S equations, the differential form of the N-S equations is

$$\frac{\partial(\rho \bar{u}_i)}{\partial t} + \frac{\partial(\rho \bar{u}_i \bar{u}_j)}{\partial x_j} = -\frac{\partial \bar{p}}{\partial x_i} + \frac{\partial \bar{\tau}_{ij}}{\partial x_j} - \frac{\partial \overline{u_i' u_j'}}{\partial x_j}, \tag{3.92}$$

where $\overline{u_i' u_j'} = \tau_{ij}^{\mathrm{R}}$, already given in Eq. (2.3), is an introduced additional term, called the Reynolds stress, which will be modelled via RANS models to close the equations. Applying a spatial average (spatial filter is defined explicitly by Pope [2000]) to the N-S equation, the differential form of the N-S equations is

$$\frac{\langle \partial \rho u_i \rangle}{\partial t} + \frac{\partial \langle \rho u_i u_j \rangle}{\partial x_j} = -\frac{\partial \langle p \rangle}{\partial x_i} + \frac{\partial \langle \tau_{ij} \rangle}{\partial x_j} - \frac{\partial(\langle u_i u_j \rangle - \langle u_i \rangle \langle u_j \rangle)}{\partial x_j}. \tag{3.93}$$

The last term of the right hand side is an additional term named sub-grid scale stress $\tau_{ij}^{\mathrm{S}} = \langle u_i u_j \rangle - \langle u_i \rangle \langle u_j \rangle$, given in Eq. (2.5), which needs to be closed via LES models.

Before discussing a specific turbulence model in details, some essential concepts and assumptions used in this study are addressed in advance.

For LES with an implicit filter, the spatial filter and differentiation is assumed to be commutative. For time average, the time average and the differential calculus are commutative, expressed as

$$\frac{\overline{\partial(\rho u_i u_j)}}{\partial x_j} = \frac{\partial(\overline{\rho u_i u_j})}{\partial x_j}. \tag{3.94}$$

However, for spatial average, strictly speaking, the spatial average and the differential calculus are noncommutative,

$$\left\langle \frac{\partial(\rho u_i u_j)}{\partial x_j} \right\rangle \neq \frac{\partial \langle \rho u_i u_j \rangle}{\partial x_j}. \tag{3.95}$$

Pope [2000] states that if the spatial filter is spatially uniform, the spatial filter and differentiation can commute. For an easier implementation, the assumption of commutativity is always assumed to be satisfied.

Boussinesq eddy viscosity assumption is applied to both RANS mode and

LES mode in the hybrid methods to relate the Reynolds/SGS stresses to the mean/filtered velocity gradients through the eddy viscosity. Analogy to a molecular viscosity, the concept of eddy viscosity is introduced artificially to describe the momentum transfer caused by turbulent eddies, just as the molecular viscosity is used to describe the momentum transfer caused by the molecular diffusion. Following the method of the Newton shear formula for isotropic fluid (Eq. (3.2)), the Boussinesq eddy viscosity hypothesis assumes

$$\tau_{ij}{}^{\mathrm{M}} - \frac{1}{3}\delta_{ij}\bar{\tau}_{kk}^{\mathrm{M}} = -2\mu_t \bar{S}_{ij} \tag{3.96}$$

where the superscribe "M" stands for modelled variables through either RANS or LES, μ_t is the eddy viscosity, and δ_{ij} is Kronecker's delta symbol.

The modelled stress $\bar{\tau}_{ij}$ is defined as Eq. (3.96). The resolved stress can be constructed through the equation $\overline{u_i u_j} - \bar{u}_i \bar{u}_j$, using the resolved velocities.

Hybrid of RANS and LES models rather than filters is used to achieve the hybrid RANS/LES methods. RANS with time averaging is derived based on a temporal filter, while LES with spacial averaging is based on a spacial filter. By contrast with the hybrid of filters (Germano [2004]; Rajamani and Kim [2010]; Sánchez-Rocha and Menon [2009]), directly combining the models/variables of these two types of modelling methods lacks theoretical fundamentals. However, the hybrid of the latter type has predicted satisfying results for many cases and achieved popular applications in both academia and industry. The possible reason that the time averaged variables and the spatial averaging variable can be blended is related to the characteristics of turbulence. The fact is that the sizes of eddies in turbulence is highly correlated with their life time, as well as the turbulence cascading property. This may make the hybrid RANS/LES feasible from physical point of view. Similar to most CFD solvers and commercial CFD software, the hybrid RANS/LES methods in DG-DES is a hybrid of models/variables rather than a hybrid of filters.

Several concepts, which are essential for turbulence modelling, are introduced now. The deformation tensor $\partial u_i / \partial x_j$ can be decomposed as

$$\begin{aligned}\frac{\partial u_i}{\partial x_j} &\equiv \frac{1}{2}\left(\frac{\partial u_i}{\partial x_j} + \frac{\partial u_j}{\partial x_i}\right) + \frac{1}{2}\left(\frac{\partial u_i}{\partial x_j} - \frac{\partial u_j}{\partial x_i}\right) \\ &= S_{ij} + \Omega_{ij},\end{aligned} \tag{3.97}$$

where S_{ij} is the rate of strain tensor, the symmetric part of $\partial u_i / \partial x_j$, and Ω_{ij} is the vorticity

tensor, the anti-symmetric part of $\partial u_i / \partial x_j$, which are

$$S_{ij} \equiv \frac{1}{2} \left(\frac{\partial u_i}{\partial x_j} + \frac{\partial u_j}{\partial x_i} \right), \quad \Omega_{ij} \equiv \frac{1}{2} \left(\frac{\partial u_i}{\partial x_j} - \frac{\partial u_j}{\partial x_i} \right). \tag{3.98}$$

The vorticity tensor can also be expressed as

$$\Omega_{ij} = \varepsilon_{ijk} \omega_k, \tag{3.99}$$

where ε_{ijk} is the Levi-Civita symbol, and ω is the angular velocity, defined as

$$\omega = \frac{1}{2} \nabla \times \mathbf{u}. \tag{3.100}$$

The basic turbulence model used in this study is the Spalart-Allmaras (S-A) turbulence model (Spalart and Allmaras [1992]). All the hybrid RANS/LES methods will be discussed based on the S-A model.

This section is organized as follows. Firstly, the S-A model will be described. Then, the hybrid methods DES, DDES and IDDES will be discussed and analysed respectively. Finally, the implicit LES will be briefly introduced.

3.8.2 Spalart-Allmaras turbulence model

The Spalart-Allmaras turbulence model is a one-equation turbulence model. It is a transport equation for a viscosity-like variable $\tilde{\nu}$. This model was derived by using empiricisms and arguments of dimensional analysis, Galilean invariance and the selected dependence on the molecular viscosity (Spalart and Allmaras [1992]). The most popular form of the S-A turbulence equation is given as

$$\underbrace{\frac{\partial \tilde{\nu}}{\partial t}}_{\text{I:time derivative}} + \underbrace{\frac{\partial (\tilde{\nu} u_j)}{\partial x_j}}_{\text{II:convective term}} - \underbrace{\frac{1}{\sigma_{\tilde{\nu}}} \frac{\partial}{\partial x_j} \left[(\nu + \tilde{\nu}) \frac{\partial \tilde{\nu}}{\partial x_j} \right]}_{\text{III:conservative diffusion}} - \underbrace{\frac{c_{\text{b2}}}{\sigma_{\tilde{\nu}}} \left(\frac{\partial \tilde{\nu}}{\partial x_j} \right)^2}_{\text{IV:nonconservative diffusion}} =$$

$$\underbrace{c_{\text{b1}} \tilde{S} \tilde{\nu}}_{\text{V: the basic production term}} - \underbrace{c_{\text{b1}} f_{\text{t2}} \tilde{S} \tilde{\nu}}_{\text{VI: Laminar limitation on production term}}$$

$$- \underbrace{c_{\text{w1}} f_{\text{w}} \left(\frac{\tilde{\nu}}{d_{\text{w}}} \right)^2}_{\text{VII: the basic destruction term}} + \underbrace{f_{\text{t2}} \frac{c_{\text{b1}}}{\kappa^2} \left(\frac{\tilde{\nu}}{d_{\text{w}}} \right)^2}_{\text{VIII: Damping of the laminar limitation}}$$

$$+ \underbrace{f_{\text{t1}} \Delta U^2}_{\text{IX:Tripping limitation on source term}} . \tag{3.101}$$

The subscripts in the S-A modelling are "b" for "basic", "w" for "wall" and "t" for "trip", which imply the main aspects of turbulence.

The eddy viscosity can be reconstructed from $\tilde{\nu}$ by the equation

$$\mu_t = \rho \cdot (f_{\nu 1} \tilde{\nu}), \tag{3.102}$$

and the modelled Reynolds stresses read

$$\tau_{ij}{}^{\mathrm{M}} = -2\mu_t \bar{S}_{ij}, \tag{3.103}$$

which neglects the turbulence kinetic energy term in Eq. (3.96).

Each term and function of this turbulence equation are summarized as follows.

- Term I and II comprise the material derivative for transport equations.

- Term III is a spatial derivative of $\tilde{\nu}$, working as the main diffusion term.

- Term IV is a nonconservative diffusion term involving the first derivatives of $\tilde{\nu}$, introduced by Spalart and Allmaras [1992] through an analogy to other two-equation models. This kind of diffusion term resembles the cross diffusion terms in $k-\epsilon$ models. This additional term breaks the conservation of the integral of $\tilde{\nu}$.

- Term V is the basic production term.

- Term VI is optional. It is a limitation on the basic production term in laminar region.

- Term VII is the destruction term, which involves a wall distance to reduce the eddy viscosity in the log layer and laminar sub-layer.

- Term VIII is optional. It is a damping of the limitation on the production in laminar region.

- Term XI is optional. It comes from a dimensional analysis for the flow transition by an actual trip.

The introduce of the nonconservative diffusion term IV destroys the conservation of $\tilde{\nu}$. Accordingly, the traditional turbulent Prandtl number σ changes to $\sigma_{\tilde{\nu}} = 2/3$. The other constant in Term IV is $c_{\mathrm{b2}} = 0.622$.

For the basic production term, some improvements have been made on the calculation of $\tilde{S}$. $\tilde{S}$ is a scalar parameter of the deformation tensor. For the original S-A, $\tilde{S}$ adopts the

magnitude of vorticity, which is

$$\tilde{S} = \Omega + \frac{\tilde{\nu}}{\kappa^2 d_{\mathrm{w}}^2} f_{\nu 2}, \tag{3.104}$$

where

$$\Omega = \sqrt{2\Omega_{ij}\Omega_{ij}}, \tag{3.105}$$

and

$$f_{\nu 2} = 1 - \frac{\chi}{1 + \chi f_{\nu 1}} \tag{3.106}$$

with

$$f_{\nu 1} = \frac{\chi^3}{\chi^3 + c_{\nu 1}^3}, \quad \chi = \frac{\tilde{\nu}}{\nu}. \tag{3.107}$$

Dacles-Mariani *et al.* [1995] proposed the so-called Dacles-Mariani correction to the deformation tensor, which is popularly used in turbulence models later. The Dacles-Mariani correction maintains the form of Eq. (3.104), but Ω is replaced with $\tilde{\Omega}$, which is defined as

$$\tilde{\Omega} \equiv ||\Omega_{ij}|| + C_{\mathrm{prod}} \min\left(0, ||S_{ij}|| - ||\Omega_{ij}||\right). \tag{3.108}$$

The merits of this correction is that the eddy viscosity is reduced in regions where the vorticity exceeds the strain rate ($|\Omega_{ij}| > |S_{ij}|$), such as in the vortex core where a pure rotation should suppress the turbulence. In vortex cores, the diffusion and dissipation effect (represented here by turbulent viscosity) should physically be suppressed by the stabilizing effects of rotation. The modification has little effect in thin shear layers, where $|\Omega_{ij}|$ and $|S_{ij}|$ are very close. Therefore, it does not interfere with the validation of the model. This modification represents an attempt to empirically adjust the production term for vortex-dominated flows. The factor C_{prod} is an arbitrary constant that can be adjusted depending on the amount of diffusion in a given turbulence model. $C_{\mathrm{prod}} = 2.0$ is usually used for the S-A model. Lee-Rausch *et al.* [2003] proposed another definition of $\tilde{S}$, which is

$$\tilde{S} = f_{\nu 3}\Omega + \frac{\tilde{\nu}}{\kappa^2 d_{\mathrm{w}}^2} \tilde{f}_{\nu 2}, \tag{3.109}$$

where

$$\tilde{f}_{\nu 2} = \frac{1}{\left(1 + \frac{\chi}{c_{\nu 2}}\right)^3} \tag{3.110}$$

and

$$\tilde{f}_{\nu 3} = \frac{(1 + \chi f_{\nu 1})(1 - f_{\nu 2})}{\chi}. \tag{3.111}$$

This form of $\tilde{S}$ tends to delay the boundary-layer transition relative to the original S-A at

moderately low Reynolds numbers. The constant is $c_{b1} = 0.1355$. In this study, Eq. (3.104) with the Dacles-Mariani correction (Eq. (3.108)) is used.

For Term VII the basic destruction term, d_w denotes the distance to the nearest wall. The constant c_{w1} is $c_{w1} = 3.24$. The most significant parameter in this term is f_w, which controls the damping of $\tilde{\nu}$ from the outer of boundary layer to the wall. f_w in the S-A model is expressed as

$$f_w(g) = g \left(\frac{1 + c_{w3}^6}{g^6 + c_{w2}^6} \right)^{1/6}, \tag{3.112}$$

where

$$g = r + c_{w3} \left(r^6 - r \right). \tag{3.113}$$

The variable r is defined as the ratio of the modelled mixing length to the wall distance, which indicates the blocking effect of the wall,

$$r = \frac{\tilde{\nu}}{\tilde{S} \kappa^2 d_w^2}. \tag{3.114}$$

The constants are

$$c_{w3} = 2.0, \quad c_{w2} = 0.3, \tag{3.115}$$

and κ is the von Karman constant $\kappa = 0.41$.

Three sources terms Term V, Term VIII and Term IX are introduced to deal with laminar regions and flow transition with tripping. For flows at high Reynolds numbers, effects of these three terms are negligible. f_{t2} in Term VI is

$$f_{t2} = c_{t3} \cdot e^{-c_{t4} \chi^2}, \tag{3.116}$$

where $c_{t3} = 1.1$, and $c_{t4} = 2.0$. Spalart and Allmaras [1992] suggested to set $c_{t3} = 0$ to leave Term VI and Term VIII out for turbulent boundary layer calculations. The aim of introducing Term IX is to obtain a flow transition. ΔU is the norm of the difference between the velocities at the trip. The trip function f_{t1} is

$$f_{t1} = c_{t1} g_t \cdot e^{\left[-c_{t2} \left(d_w^2 + g_t^2 d_t^2 \right) \frac{\omega_t^2}{(\Delta U)^2} \right]} \tag{3.117}$$

where $c_{t1} = 1.0$, $c_{t2} = 2.0$, and

$$g_t \equiv \min \left(0.1, \frac{\Delta U}{\omega_t \Delta x} \right), \tag{3.118}$$

where Δx is the grid spacing along the wall at the trip, and ω_t is the magnitude of vorticity at the trip point.

3.8.3 S-A model based DES, DDES and IDDES

For the hybrid methods DES, DDES and IDDES, the most popular basic turbulence model is the S-A model and the SST model (Menter [1994]). In our solver DG-DES, the S-A model is adopted to implement the hybrid methods.

3.8.3.1 DES

Transforming the S-A model for URANS to a LES SGS model is mathematically simple. The only change is the basic destruction term. In DES, the wall distance d_{w} in Eq. (3.101) is replaced by $\tilde{d}_{\mathrm{DES}}$, which reads

$$\tilde{d}_{\mathrm{DES}} = \min(d_{\mathrm{w}}, C_{\mathrm{SGS}}\Delta), \tag{3.119}$$

where $C_{\mathrm{SGS}} = 0.65$ is calibrated from the spectrum of decaying homogenous isotropic turbulence (Shur *et al.* [1999]), and Δ is the grid spacing, representing the implicit spatial filter.

There are several ways to calculate the grid spacing Δ (Shur *et al.* [2008]). A general form is to define it as the largest dimension of a local grid cell,

$$\Delta = \max(\Delta_i), \quad i = 1, 2, 3 \tag{3.120}$$

where Δ_i is usually the length of a cell edge. This form is most suitable for structured grids. For an unstructured mesh, with the same definition of the maximum length of cell edges, a brick cell may have a much larger volume (turbulence containing) than a tetrahedron. Therefore, for our unstructured-mesh solver, Δ_i is redefined as

$$\Delta_i = \max |\Delta \mathbf{r}_{i,n}|, \quad \forall n \in \mathbb{N}_i, \tag{3.121}$$

which means that for the cell i, the local grid spacing Δ_i is the maximum distance between its centroid and all neighbouring cells' centroid. $\mathbb{N}_i$ denotes all the neighbouring cells of the cell i. When the grids are structured with small spatial gradients, Eq. (3.121) restores to Eq. (3.120).
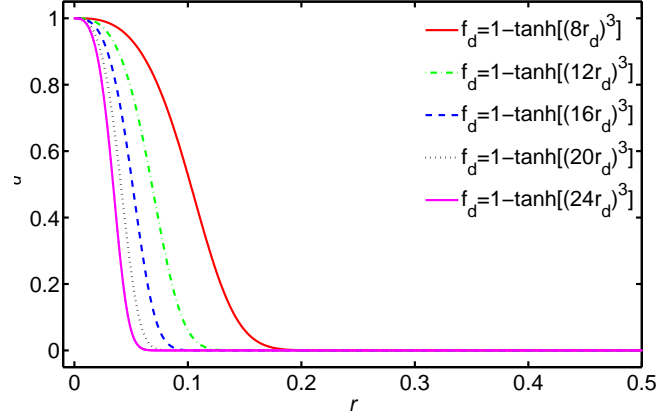
Figure 3.3: Graph of blending function f_d

3.8.3.2 DDES

Eq. (3.119) shows that the transition between RANS and LES for DES is pre-determined by wall-distances and grids. Therefore, mesh-refining may trigger the LES mode in attached boundary layers. Considering the other drawbacks of DES discussed in Section 2.3.4, DDES was proposed to provide a dynamic RANS/LES transition (Spalart *et al.* [2006]).

In DDES, the wall distance d_w in Eq. (3.101) is replaced by

$$\tilde{d}_{\mathrm{DDES}} = \min\left[d_\mathrm{w}, (1 - f_\mathrm{d})d_\mathrm{w} + f_\mathrm{d}C_{\mathrm{SGS}}\Delta\right], \tag{3.122}$$

where f_d is a blending function, dependent on instantaneous flow fields, which reads

$$f_\mathrm{d} \equiv 1 - \tanh[(C_1 r_\mathrm{d})^{C2}], \tag{3.123}$$

where

$$r_\mathrm{d} \equiv \frac{\nu_t + \nu}{\sqrt{S_{ij}S_{ij}}\kappa^2 d_\mathrm{w}{}^2}, \tag{3.124}$$

and $C_1 = 8$ and $C_2 = 3$ for the original S-A based DDES. These two variable C_1 and C_2 may vary in other blending methods (Gritskevich *et al.* [2012]). The graphs of the blending function f_d, with $C_1 = 8$, 12, 16, 20 and 24 and $C_2 = 3$ are shown in Fig.3.3, where $f_\mathrm{d} = 1$ corresponds to the LES mode, and $f_\mathrm{d} = 0$ to the RANS mode. The range $0 < f_\mathrm{d} < 1$ is the blending region. With an increasing value of C_1, the transition occurs in a smaller value of r and the transition becomes steeper.

3.8. Techniques on Hybrid RANS/LES Turbulence Modelling

3.8.3.3 IDDES

DDES is sensitive to the initial flow fields. If the initial flow field is far from a physical flow field, the flow-dependent blending function f_d may make the flow solutions further away from expected flow fields. Furthermore, DDES still suffer the LLM and MSD problems in some extent. With this background, an improved version of DDES was proposed by Shur *et al.* [2008]. The improvements mainly contain two aspects. One is the modification of the length scale for LES. The other is that it blends DDES with a wall-modelled LES, depending on whether the inflow conditions have any turbulent content or not.

Shur *et al.* [2008] discussed how to determine a reasonable sub-grid length scale. There are two extreme requirements for the sub-grid length scale. On one hand, the sub-grid length scale should be fairly isotropic far from the walls. On the other hand, in the very close vicinity of the wall, it should depend on wall-parallel grid spacing only. In regions in-between, it should be function of wall distance and grid spacing. Therefore, the new sub-grid length scale is defined as

$$\Delta = \min\left[\Delta_{\max}, \max\left(C_w d_w, C_w \Delta_{\max}, \Delta_{wn}\right)\right], \tag{3.125}$$

where $\Delta_{\max}$ is the same as Eq. (3.120), while in our study it is Eq. (3.121). Δ_{wn} is the grid step in the wall-normal direction, in order to reduce the computational cost, it adopts $\Delta_{\min}$. C_w is an empirical constant, and $C_w = 0.15$ based on a wall-resolved LES of channel flow. Then, the LES length scale is given in

$$l_{\text{LES}} = \Psi C_{\text{SGS}} \Delta, \tag{3.126}$$

where Ψ is a low-Reynolds number correction, originally proposed along with DDES in Spalart *et al.* [2006], which is defined as

$$\Psi^2 = \min\left\{10^2, \frac{1 - \frac{c_{b1}}{c_{w1}\kappa^2 f_w^*}\left[f_{t2} + (1 - f_{t2})f_{\nu2}\right]}{f_{\nu1}\max(10^{-10}, 1 - f_{t2})}\right\}, \tag{3.127}$$

where $f_w^* = 0.424$. The RANS length scale is the wall distance, the same as the original RANS model, which is

$$l_{\text{RANS}} = d_w. \tag{3.128}$$

In IDDES, the wall distance d_w in Eq. (3.101) is replaced by l_{hyb}, which is defined as

$$l_{\text{hyb}} = \tilde{f}_d(1 + f_e)l_{\text{RANS}} + (1 - \tilde{f}_d)l_{\text{LES}} \tag{3.129}$$

The main blending function $\tilde{f}_{\mathrm{d}}$ is

$$\tilde{f}_{\mathrm{d}} = \max\left(f_{\mathrm{B}}, 1 - f_{\mathrm{dt}}\right) \tag{3.130}$$

with

$$f_{\mathrm{dt}} \equiv 1 - \tanh[(C_1 r_{\mathrm{dt}})^{C2}], \tag{3.131}$$

and the empirical blending function f_{B}

$$f_{\mathrm{B}} = \min\left[1.0, 2 \cdot e^{-9\alpha^2}\right], \tag{3.132}$$

with

$$\alpha = \frac{1}{4} - \frac{d_{\mathrm{w}}}{\Delta_{\max}}. \tag{3.133}$$

The function f_{e} is the elevating function of the RANS component in Eq. (3.129), which is defined as

$$f_{\mathrm{e}} = \Psi f_{\mathrm{e}2} \cdot \max(0, 1 - f_{\mathrm{e}1}), \tag{3.134}$$

with

$$f_{\mathrm{e}1}(\alpha) = \begin{cases} 2 \cdot e^{-11.09\alpha^2}, & \text{if } \alpha \geq 0 \\ 2 \cdot e^{-9.0\alpha^2}, & \text{if } \alpha < 0 \end{cases} \tag{3.135}$$

and

$$f_{\mathrm{e}2} = 1.0 - \max(f_{\mathrm{t}}, f_{\mathrm{l}}). \tag{3.136}$$

$f_{\mathrm{e}2}$ controls the intensity of the elevating function f_{e} through the following two functions

$$f_{\mathrm{t}} \equiv 1 - \tanh[(C_{\mathrm{t}}^2 r_{\mathrm{dt}})^3], \tag{3.137}$$

$$f_{\mathrm{l}} \equiv 1 - \tanh[(C_{\mathrm{l}}^2 r_{\mathrm{dl}})^{10}], \tag{3.138}$$

where f_{t} and f_{l} are the turbulent and laminar analogues of Eq. (3.124), defined as

$$r_{\mathrm{dt}} \equiv \frac{\nu_t}{\kappa^2 d_{\mathrm{w}}^2 \cdot \max\left(\sqrt{S_{ij}S_{ij}}, 10^{-10}\right)}, \tag{3.139}$$

$$r_{\mathrm{dl}} \equiv \frac{\nu}{\kappa^2 d_{\mathrm{w}}^2 \cdot \max\left(\sqrt{S_{ij}S_{ij}}, 10^{-10}\right)}. \tag{3.140}$$

3.8.4 Implicit LES

In LES, the numerical discretization error in low accuracy numerical schemes can be as influential as the sub-grid scale model (Kravchenko and Moin [1997]), and it is difficult to disentangle the effects of the numerical schemes from that of the sub-grid scale (SGS) modelling. Therefore, without a SGS model, LES with the numerical discretization error working as a SGS dissipation can be regarded as a feasible approach to perform a large eddy simulation (Fureby and Grinstein [2002]). This approach is termed as Implicit LES (ILES) or Numerical LES (NLES). There are some applications of ILES to different flows and good results were achieved. For example, ILES successfully captured some complex jet dynamics in the free jet flows (Eastwood *et al.* [2012]; Grinstein [2007]). As with the majority of application-based solvers, our solver tends to be dissipative on the unstructured mesh. However, applications of the same solver with ILES to complex jets showed that omitting the sub-grid scale model can alleviate the excessive dissipation and improve the predictions, especially for unstructured mesh (Eastwood *et al.* [2012]).

For wall-bounded flows, there are numerous small flow structures, requiring a high mesh resolution (a quasi-DNS mesh) to resolve most of them in LES. In order to make accurate computations with a moderate mesh resolution, the wall-modelled ILES is used. The near-wall model is realized by using the improved delayed detached eddy simulation (IDDES) (Shur *et al.* [2008]) with the Spalart-Allmaras (S-A) model. IDDES can treat automatically different flow regions inside a complex geometry as natural (D)DES or wall modelled LES (Shur *et al.* [2008]). When the inflow does not contain any significant turbulence content, the DDES branch will be automatically activated, while when the inflow has turbulence information and the grid is fine enough to resolve the boundary layer dominant eddies, the WMLES branch will be turned on. Considering the excessive dissipation of the solver with unstructured meshes, ILES replaces the LES mode of IDDES. This means that for regions of the original RANS mode of IDDES, unsteady RANS works as a near-wall model, while for regions of original LES mode of IDDES, the turbulent viscosity ν_t is set to be zero, and ILES is switched on. The ILES with the S-A RANS model near the wall is referred to as SA-ILES hereafter.

3.8.5 Resolved and modelled fluctuations in LES

For LES and hybrid RANS/LES, part of the fluctuations is resolved, and the left modelled. In order to clearly distinguish the contributions from resolved or modelled part, several definitions is given, referring to Fadai-Ghotbi *et al.* [2010].

For a instantaneous flow field, the instantaneous velocity u_i can be decomposed into a resolved part $\widetilde{U}_i$, including the mean flow U_i and large-scale fluctuations U_i', and a residual fluctuating part u_i'', which is modelled via turbulence modelling methods. This relation is shown as

$$u_i = U_i + U_i' + u_i'', \tag{3.141}$$

where the resolved velocity $\widetilde{u}_i$ is

$$\widetilde{u}_i = U_i + U_i'. \tag{3.142}$$

The total fluctuation u_i' is the sum of the resolved large scale fluctuation U_i' and the modelled fluctuation u_i'', which is

$$u_i' = U_i' + u_i''. \tag{3.143}$$

Notice that this triple decomposition is different from the triple decomposition in Hussain and Reynolds [1970] shown in Section 2.4.2.1. The former is for the calculated variable from the viewpoint of numerical calculation, while the latter is based on the characteristics of a real flow signal.

For LES, the Reynolds stresses in the resolved flow structures (or the resolved Reynolds stresses) are given as

$$\tau_{ij}^{\text{res}} = \rho \left(\overline{\widetilde{U}_i \widetilde{U}_j} - U_i U_j \right), \tag{3.144}$$

and the modelled Reynolds stresses read

$$\tau_{ij}^{\text{mod}} = \rho \overline{u_i'' u_j''}. \tag{3.145}$$

For the S-A modelling equation, the only variable is the turbulent viscosity, and the turbulence kinetic energy term k is not explicitly calculated. Therefore, it is difficult to directly restore the modelled turbulent viscosity from Eq. 3.96. Durrani and Qin [2011] approximated the turbulence kinetic energy in the S-A model, based on the Bradshaw's hypothesis (Bradshaw and Ferriss [1967]). The turbulence kinetic energy k is elaborated as

$$k = \frac{\nu_t \sqrt{2 S_{ij} S_{ij}}}{\sqrt{C_\nu}}, \tag{3.146}$$

where S_{ij} is given in Eq. 3.98, and $C_\nu = 0.09$. With this restored turbulence kinetic energy and the resolved turbulent viscosity ν_t in the S-A model, the modelled Reynolds stresses can be calculated via Eq. 3.96.

Similar to the definition of the total fluctuations in Fadai-Ghotbi *et al.* [2010], the total

Reynolds stresses are defined as

$$\tau_{ij}^{\mathrm{tot}} = \tau_{ij}^{\mathrm{res}} + \tau_{ij}^{\mathrm{mod}}. \tag{3.147}$$

3.9   Summary

In this chapter, an elaborate description of the numerical methods and turbulence models implemented in the in-house code is presented. The general unsteady N-S equations and the ALE formulations are given to describe general turbulent flow with or without moving boundaries. Discretization both the time and spatial terms is presented, together with their low dissipation treatments. Dynamic grid techniques, which may be used in flow control, are described with details. Finally, the S-A based turbulence models, DES, DES, IDDES and implicit LES are discussed and implementation of these turbulence modelling to the in-house code is briefly introduced.

Chapter 4

Flow Control with Piezoelectric Actuators in Flow Around A Backward Facing Step

4.1 Introduction

Flow over a backward-facing step (BFS) has been widely investigated in both experiments (such as Armaly *et al.* [1983]; Driver and Seegmiller [1985]; Fessler and Eaton [1999]; Furuichi *et al.* [2004]; Jovic and Driver [1995]; Spazzini *et al.* [2001]) and simulations (for example, Barri *et al.* [2010]; Fadai-Ghotbi *et al.* [2008]; Le *et al.* [1997]; Panjwani *et al.* [2009]; Toschi *et al.* [2006]). This flow type is also established as a benchmark configuration to study turbulence models or other research topics on abruptly separated flows (Fadai-Ghotbi *et al.* [2008]; Gritskevich *et al.* [2012]; Shur *et al.* [2008]). In this study, flow over a BFS has been chosen to study flow control with oscillating surface of piezoelectric actuators. The experiments were carried out by the Aero-Physics Laboratory of The University of Manchester. In this study, simulations will provide more results and further understandings on flow control with piezoelectric actuators in BFS flow.

Figure 4.1 demonstrates the main features in flow over a backward facing step, which are described as follows (Emami-Naeini *et al.* [2005]). The attached boundary layer separates at the edge of the step, then the high-velocity flow leaving the upstream channel and the underlying low-velocity flow recirculating behind the step interact to form the mixing layer. Part of the mixing layer flow is reversed toward the step and re-entrained into the mixing layer, which results in the formation of a recirculating zone behind the step. Part of the shear layer re-attaches on the bottom wall, and a new boundary layer grows on the surface down-

stream of the reattachment point. The separation-reattachment process is characterized by a complex interaction between the separated shear layer and its adjacent flow.
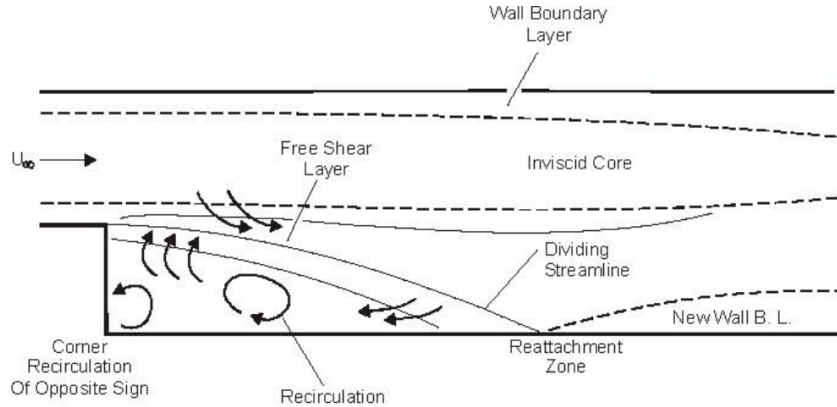
Figure 4.1: Schematic of streamlines in separation reattachement process of flows over a backward facing step (Kim [1978])

Flow separation from the step can affect heat/energy transfer, and bring about pressure loss, vibrations, and noise (Uruba *et al.* [2007]). By means of flow control, the recirculation region may increase or decrease, depending on the momentum transfer in this region. The control of the size of the separation region may also influence the pressure or skin friction distribution in the re-developing boundary layer, which makes the BFS and its control device become a whole to control the downstream re-developing flow. In this study, piezoelectric actuators are installed upstream of the step edge. The oscillating surface of these piezo-electric actuators replaces a certain part of the original fixed and solid wall. The motion of oscillation may change characteristics of the boundary layer before its separation from the step, affecting the flow instability and changing the size of the recirculation region. Investigating the control effect and the control mechanisms of oscillating surfaces in piezoelectric actuators are the main aims of this chapter.

In this chapter, a mostly studied backward facing step case (Driver and Seegmiller [1985]) is first simulated to validate mesh resolutions, numerical schemes and turbulence modelling. After obtaining reliable numerical configuration for this type of turbulent flow, the baseline BFS flow is simulated with the same flow and numerical setup as the experiments carried out by APL-UniMan. Then, piezoelectric actuators are simulated with the same control parameters in APL-UniMan's experiments. After analysing the control effect, some exploring simulations with different control parameters are investigated to study the influences of the control velocity.

4.2 Validation on flow over the BFS (Driver and Seegmiller)

4.2.1 Introduction

The BFS experiments carried out by Driver and Seegmiller [1985] and Driver *et al.* [1987] are chosen to be the validation case. In this section, firstly, influence of mesh resolutions on simulation results for the BFS flow is investigated. Then, numerical schemes are validated in this BFS case. After that, with a fixed numerical scheme, different hybrid turbulence modelling techniques (DES, DDES and IDDES) are applied to simulate the BFS flow, and their performances in this sharply separated flow are analysed.

4.2.2 Flow configuration

4.2.2.1 Computational domain

Figure 4.2 shows the experimental set-up of the BFS flow in Driver and Seegmiller [1985]. In experiments, a series of angles of the top-wall were studied, but in this study only the case with the angle of zero is investigated.
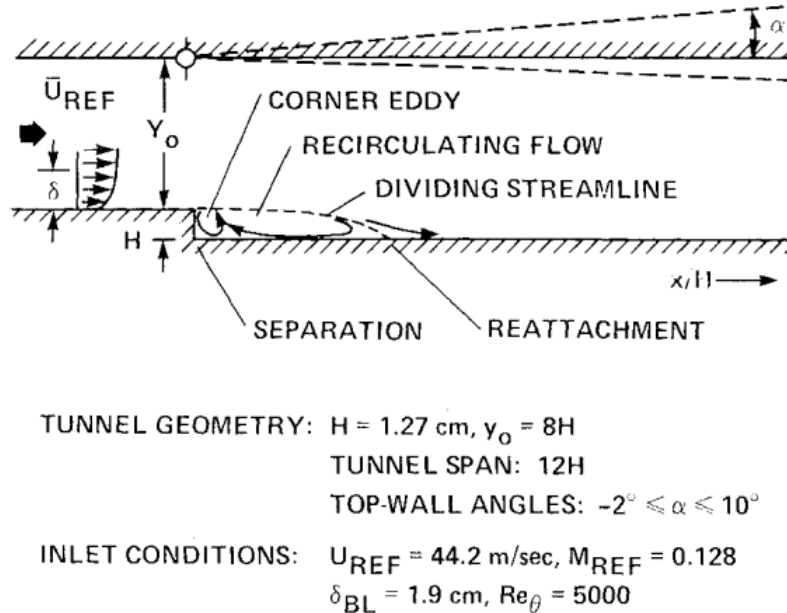
Figure 4.2: Experimental set up of the backward face step in Driver and Seegmiller [1985]

The same geometry and flow parameters as in experiments were set up in simulations.

4.2. Validation on flow over the BFS (Driver and Seegmiller)

The step height is $H = 1.27$ cm, and the inlet boundary layer thickness is $\delta = 1.5H$. The reference velocity is $U_\text{ref} = 44.2$ m s^{-1}. The Reynolds number based on the step height and the reference velocity is $Re_H = 37\,000$. The expansion ratio (the ratio of the outlet height to the inlet height) is $9H/8H = 1.125$. In the experiment, the width of span is $12H$, while in our simulation, a spanwise width of $L_z = 4H$ ($\approx 2.67\delta$) is chosen with a periodic boundary condition to save the computational cost. The location of the inlet is set to be $4H$ upstream of the step, and the distance downstream of the step is $40H$, which is the same as in Fadai-Ghotbi *et al.* [2008]. Figure 4.3 displays the computational domain in the $x - y$ plane. The three dimensional domain is generated by extruding this two dimensional domain in the spanwise direction (z-direction).
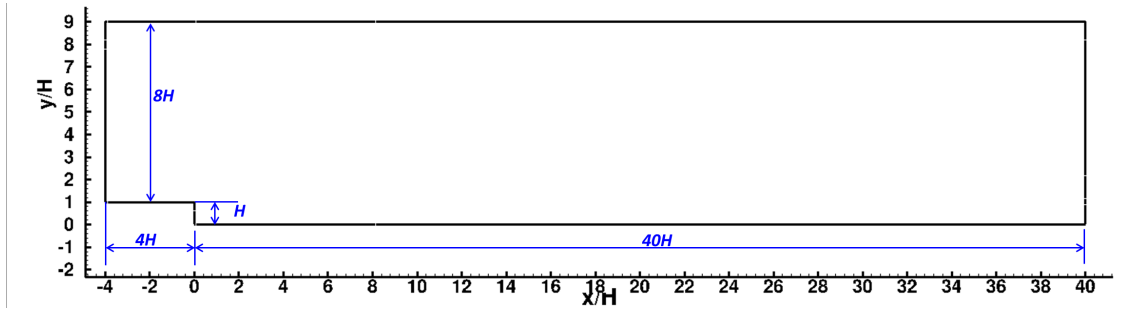
Figure 4.3: The computational domain in the $x - y$ plane

4.2.2.2 Boundary conditions and time steps

A non-reflecting convective boundary condition is used at the outlet. The span has a periodic boundary condition. The top and bottom wall is set to be no-slip wall. Velocity profiles obtained from experiments are specified at $x = -4H$ as the inlet boundary condition. In the current study, no unsteady fluctuations are superposed in the inlet velocity profiles. The main reason is that there are no effective methods to generate a spatially-developing turbulence boundary within such a short distance upstream of the step. Our experiences in using "random fluctuation inflow generation method" (Lund *et al.* [1998]) indicate that this method violates the separated shear layer. Actually, the unsteady inlet boundary condition by "random fluctuation inflow generation method" introduces artificial flow fluctuations in both the inviscid region and the recirculation region, which results in a much longer reattachment point. The main reason is that the random inlet fluctuations cannot satisfy the flow convection at inlet (which is highly influenced by the downstream step flow).

The time step is set to be $0.035H/U_\text{ref}$, which is between the LES study of the BFS case in Panjwani *et al.* [2009]($0.05H/U_\text{ref}$) and the LES study of the BFS case in Toschi *et al.*

[2006]$(0.01H/U_{\text{ref}})$. Time averages were calculated after the flow swept the computational domain three times to remove initial fields. (In the DES study of the same BFS case, Dietiker and Hoffmann [2009] ignored two flow-through time periods before statistical analysis.) In this study, time statistics were taken for a total duration of more than $700H/U_{\text{ref}}$, which is again between $500H/U_{\text{ref}}$ in Panjwani *et al.* [2009] and $1000H/U_{\text{ref}}$ in Toschi *et al.* [2006].

4.2.2.3 Mesh resolutions

A coarse mesh and a fine mesh were generated to study the effects of mesh resolution on simulation results. Figure 4.4 displays the resolution of the coarse mesh. The coarse mesh has a similar mesh resolution to the fine mesh in the DES study of the same BFS case in Dietiker and Hoffmann [2009]. The fine mesh in this study has a similar spanwise resolution to the coarse mesh, and the refinement was mainly implemented in the $x-y$ plane. The topology of the fine mesh is similar to the coarse mesh, not shown here. These two sets of mesh are both hybrid mesh, which use unstructured grids near the step to expand the clustered grids near the step. Table 4.1 lists the mesh resolutions for these two sets of mesh.
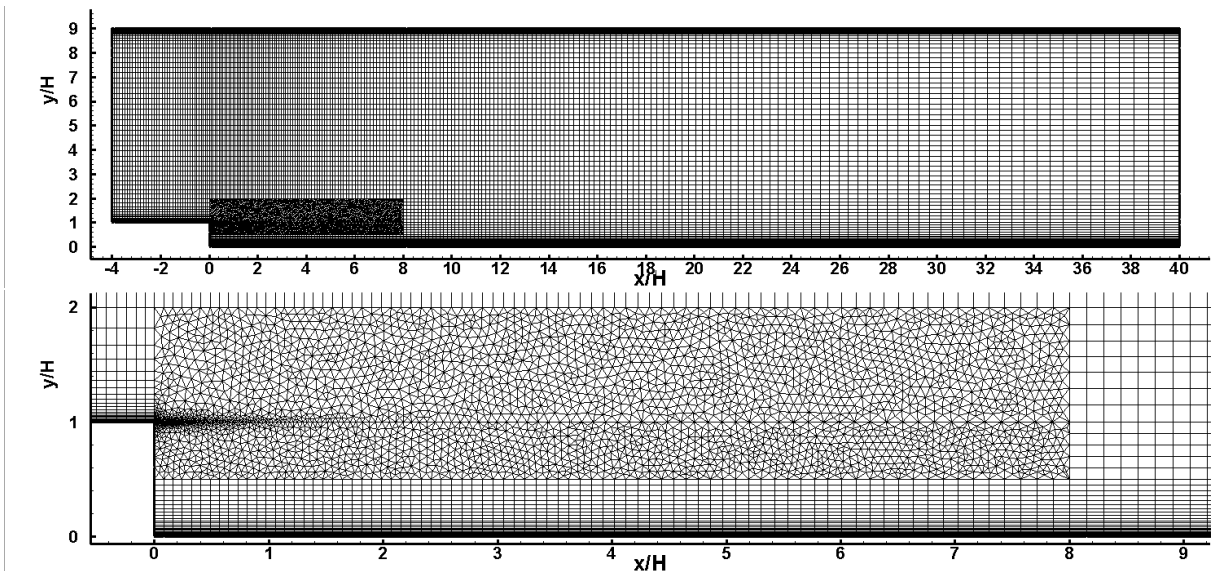
Figure 4.4: Computational mesh in the $x-y$ plane of the BFS flow. Top: the whole computational domain. Bottom: the drawing of a partial enlargement.

Table 4.1: Summary of mesh resolutions

Case	y_1^{+a}	Δx^{+b}	Δz^{+c}	$N_z{}^d$	N_{cell}
Baseline: Coarse	$0.2 - 0.98$	$72 - 144$	$25 - 60$	64	$2\,297\,408$
Baseline: Fine	$0.1 - 0.6$	$45 - 90$	$20 - 50$	70	$6\,181\,560$

[a]The non-dimensional grid spacing in the first layer above the bottom wall.
[b]The non-dimensional grid spacing in the streamwise direction ($x/H < 20$).
[c]The non-dimensional grid spacing in the spanwise direction.
[d]The cell number along the span.

4.2.3 Comparison of results simulated with different mesh resolutions

Turbulent flow properties, predicted by the two sets of mesh listed in above section, will be compared. The same turbulence model (DES) and the same numerical scheme (SLAU) were used. The only difference is the mesh resolution.

Figure 4.5 plots the streamwise velocity at different streamwise locations. The different mesh resolutions introduce little change of the velocity in the attached boundary layer before flow separation, as this region is dominated by RANS which is less sensitive to mesh resolutions. In the mixing layer, the fine mesh predicts a slightly smaller velocity than the coarse mesh, which may relate to a smaller dissipation in fine mesh. Overall, the coarse and fine mesh provides similar results, both in good agreements with the experimental measurement. The effect of mesh refinements in the BFS case is consistent with the statement in Dietiker and Hoffmann [2009], which also observed that for the BFS case, the first-order statistical results are practically grid-insensitive.

The modelled turbulent viscosity in different mesh resolutions is shown in Figure 4.6. As expected, the fine mesh, with a smaller spatial filter scale (indicating less modelled flow fluctuations), has a smaller turbulent viscosity, while the coarse mesh models more turbulent viscosity. Nevertheless, even for the coarse mesh, the modelled turbulent viscosity still meets $\nu_t/\nu < 10$ in the region $x/H < 10.0$. (After $x/H > 10.0$, the modelled turbulent viscosity becomes larger with a coarser mesh.) The value of ν_t/ν confirms the current coarse mesh resolution is feasible for the LES simulation (You and Moin [2007]). For the fine mesh, the high modelled turbulent viscosity congregates near the wall, which complements the near-wall LES mesh resolutions.

Figure 4.7 displays the Reynolds normal stress ($\langle u'u'\rangle/U_{\text{ref}}^2$ and $\langle v'v'\rangle/U_{\text{ref}}^2$) and the Reynolds shear stress ($\langle u'v'\rangle/U_{\text{ref}}^2$). The total Reynolds stresses are the sum of the modelled and the resolved Reynolds stress, as defined in Eq. 3.147. All these profiles of the three
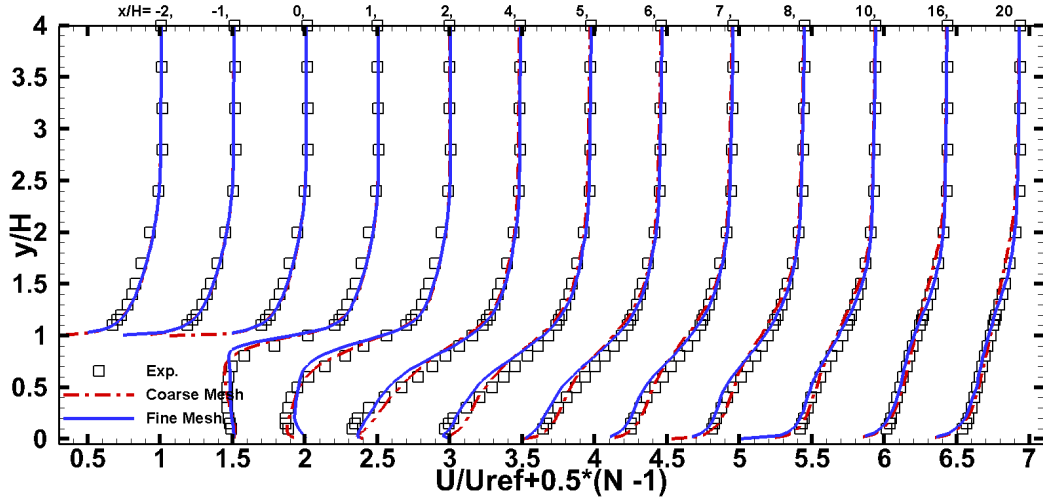
Figure 4.5: Comparison of streamwise velocity with different mesh resolutions
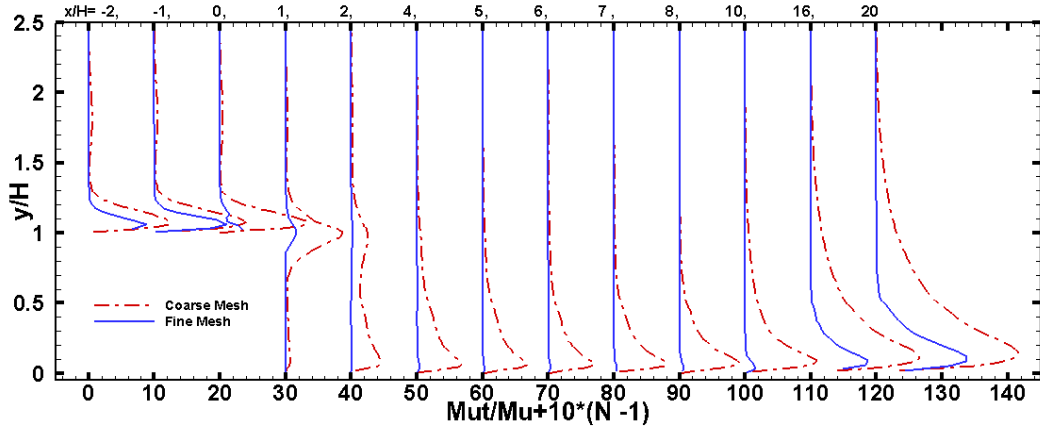
Figure 4.6: Comparison of modelled turbulent viscosity with different mesh resolutions.

Reynolds stress show that the contributions of the modelled stresses to the total Reynolds stresses are very small. Even though the modelled turbulent viscosity is distinctly different from each other in the two sets of mesh as show in Figure 4.6, considering the much smaller values of modelled Reynolds stresses than the resolved stresses, the differences between the modelled Reynolds stresses seem to be negligible for the total Reynolds stresses.

The resolved Reynolds stresses have some discrepancies with different mesh resolutions. The fine mesh provides relief from the over-perdition of Reynolds normal stress $\langle u'u'\rangle/U_{\text{ref}}^2$ (Figure 4.7(a)) and the Reynolds shear stress $\langle u'v'\rangle/U_{\text{ref}}^2$ (Figure 4.7(c)) in the both the primary recirculation and the re-developing regions. For the Reynolds normal stress $\langle v'v'\rangle/U_{\text{ref}}^2$ (Figure 4.7(b)), the fine mesh aggravates the over-prediction in the primary recirculation region, while in the re-developing region, it alleviates the over-perdition. Throughout the

4.2. Validation on flow over the BFS (Driver and Seegmiller)

main recirculation region, it is observed that $\langle u'u'\rangle > \langle v'v'\rangle$, which was also confirmed by Barri *et al.* [2010]. This relation implies the anisotropy of the recirculating flow, which may explain the different performances of mesh refinements in $\langle u'u'\rangle$ and $\langle v'v'\rangle$. Generally speaking, the mesh refinement indeed improves the prediction of the Reynolds stresses.

One of the objectives in this study is to observe the development of the flow structures. Mesh resolutions are expected to be a dominant factor. Figure 4.8 compares the resolved turbulence structures with these two sets of mesh. A shear layer is observed from the step in both sets of mesh, and then this shear layer breaks into small structures. Obviously, the fine mesh resolved more flow structures and it also resolved much smaller structures, especially in the recirculation region. The coarse mesh only captures eddies with large scales.

In conclusion, the mesh refinement resolves significantly more and smaller turbulence structures. It also improves the prediction of the Reynolds stresses to some extent, while there are no obvious improvements on the mean flow. Therefore, if evolutions and developments of turbulence structures are key points to be studies, a fine mesh resolution is necessary, while if only the statistical properties are concerned, a coarse mesh resolution can be chosen to save the computational cost. In this validation part, all simulations below are based on the coarse mesh to compare different methodologies.

(a)

(b)

(c)
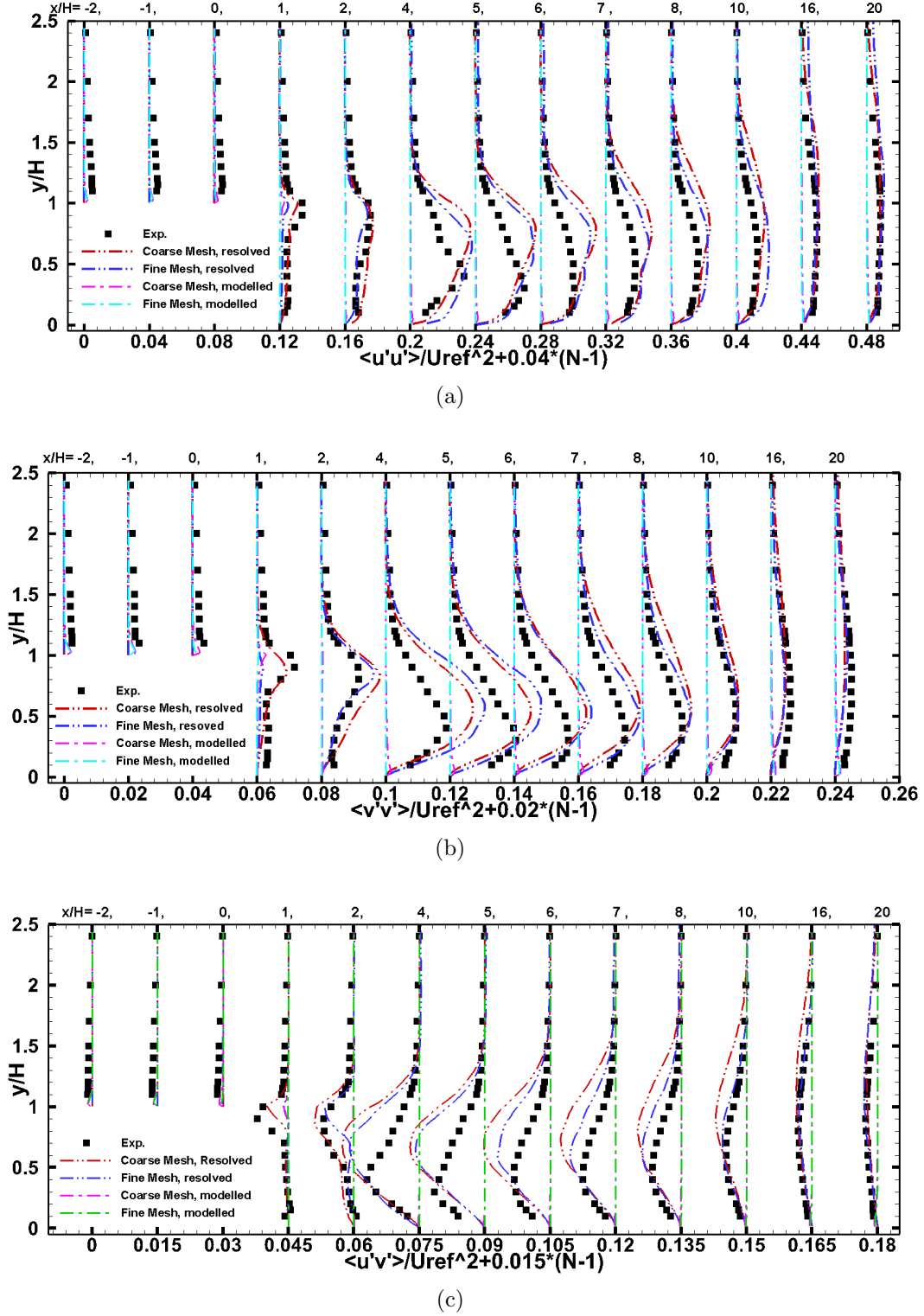
Figure 4.7: Comparison of both the modelled and the resolved Reynolds stresses with different mesh resolutions. (a) $\langle u'u'\rangle/U_{\mathrm{ref}}^2$; (b) $\langle v'v'\rangle/U_{\mathrm{ref}}^2$; (c) $\langle u'v'\rangle/U_{\mathrm{ref}}^2$

(a)

(b)
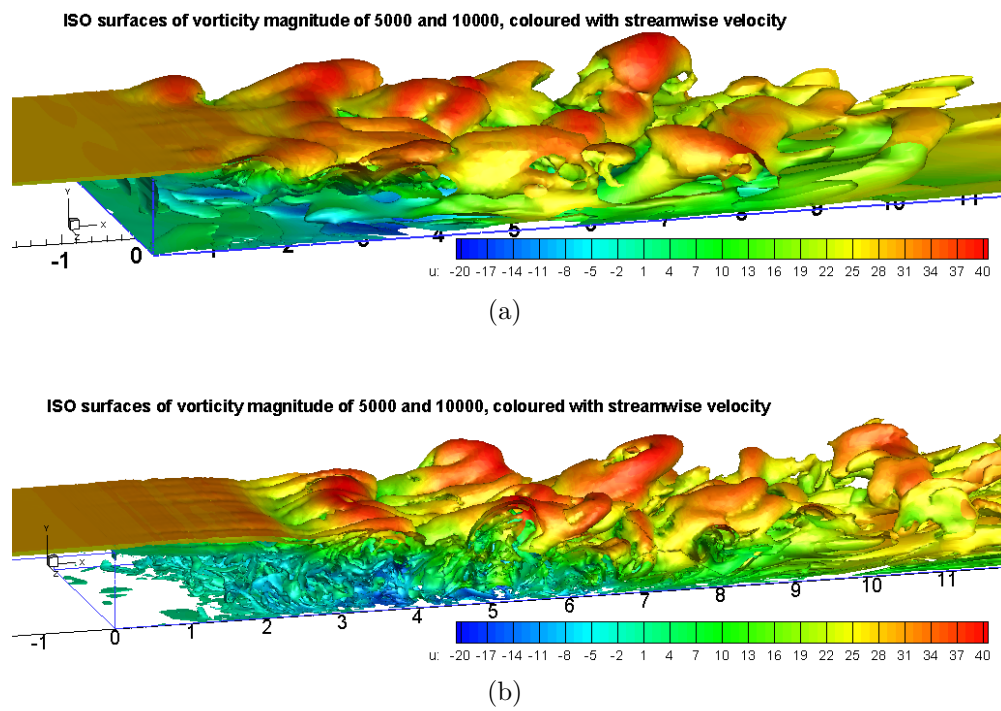
Figure 4.8: Iso-surface of instantaneous vorticity magnitude. (a) Coarse mesh; (b) Fine mesh

4.2.4 Comparison of results simulated with different flux difference splitting methods

In this validation, the mesh resolution (the coarse mesh) and the turbulence modelling method (DES) are fixed. The only change is different flux splitting schemes.

For this case with abruptly separated flow, it is observed that both the preconditioned Roe scheme and the low dissipation Roe scheme are unstable to run sufficient time for time average, due to large numerical oscillations in the recirculation region. As stated in Li and Gu [2011], except for extremely small time steps, the preconditioned Roe scheme is always found to be lack of robustness in flows with large fluctuations. Lessani *et al.* [2004] studied the preconditioning in LES with a proper small time step, and found that without the multigrid technique, there are few differences with or without the preconditioning in LES of flows with low Mach numbers (mainly due to the much smaller physical time step in LES than RANS). Therefore, we do not consider preconditioning in this study. As for the low dissipation Roe scheme, the unsteadiness of the solver mainly comes from the strong velocity gradient in the mixing layer. The low dissipation technique of Travin *et al.* [2002], in spite of successful application in SST based DES, seems to suffer from insufficient artificial dissipation in the S-A based DES. Therefore, in this study, only the classic Roe scheme and the SLAU scheme are compared to demonstrate their capability in abruptly separated flows.

Figure 4.9 (a) and (b) show the skin friction and the pressure coefficient along the bottom wall, respectively. The significant differences between the Roe and SLAU schemes locate in the recirculation region. The Roe scheme seems to predict smaller values both in C_f and $-C_p$.
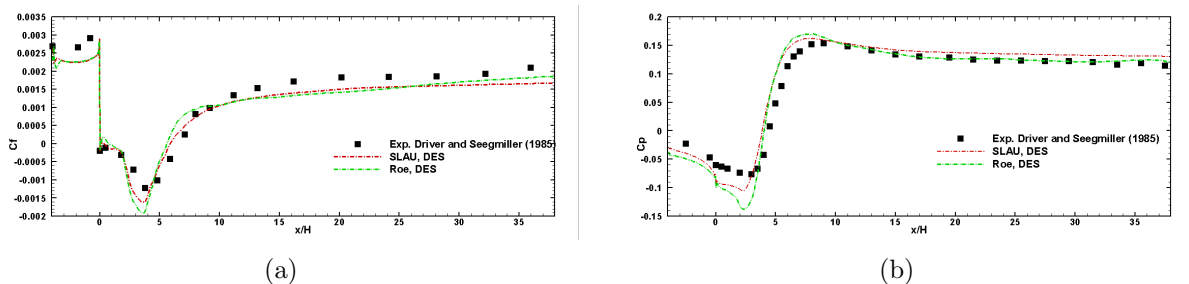
Figure 4.9: (a) C_f by different flux splitting methods, (b) C_p by different flux splitting methods

The Roe and SLAU schemes also predict very similar streamwise velocity profiles, as shown in Figure 4.10. As for the Reynolds shear stress, presented in Figure 4.11, in the shear layer far from the wall, the Roe scheme shows slightly better Reynolds shear stress.

4.2. Validation on flow over the BFS (Driver and Seegmiller)

However, results predicted by the SLAU scheme are slightly closer to the experimental data in the near-wall region, probably due to the low-speed treatment.
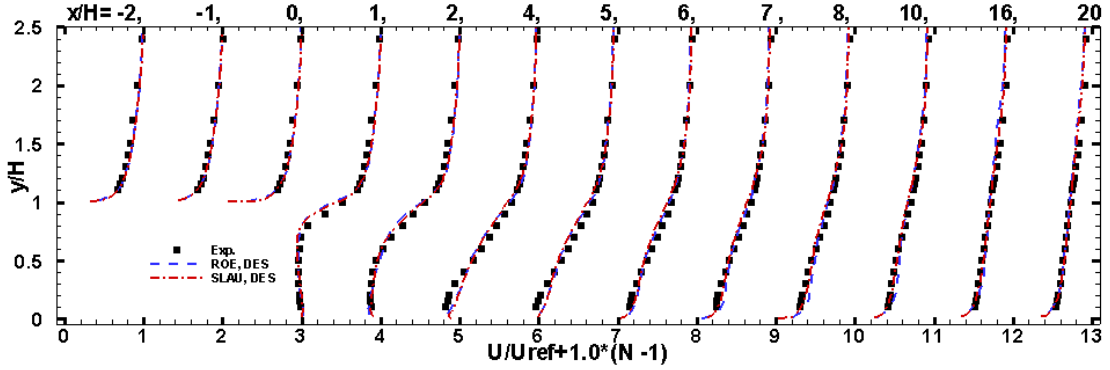
Figure 4.10: Comparison of streamwise velocity by different flux splitting methods.
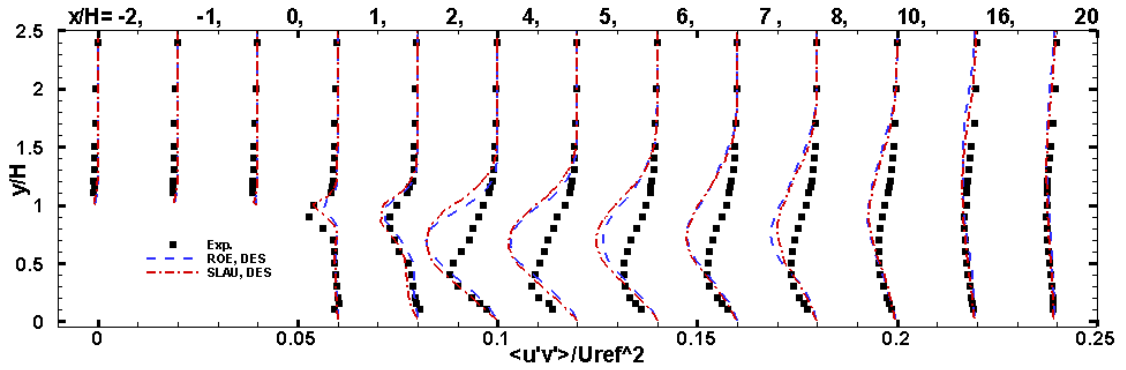
Figure 4.11: Comparison of the Reynolds normal stress $\langle u'v' \rangle/U_{\mathrm{ref}}^2$ by different flux splitting methods.

Overall, the classic Roe and SLAU schemes predict very similar results in DES for BFS (both the first-order and the second-order statistics), and no significant differences are observed. Thus, either one can be used. However, if the moving mesh is concerned, our tests show that when the ALE is considered in the flux splitting, the Roe scheme is more stable than the SLAU scheme. The SLAU scheme for ALE with a moving velocity produces numerical oscillation (not shown in this thesis). Therefore, for hybrid RANS/LES modelling of this BFS oscillating surface control case, the Roe scheme is adopted.

4.2.5 Comparison of results simulated with different hybrid RANS/LES turbulence modelling techniques

In this section, different hybrid turbulence modelling techniques (DES, DDES and IDDES) are compared in the abruptly separated flow. For all the simulations, except for the turbulence modelling techniques, all other setting up and numerical schemes are kept the same.

The primary differences from different turbulence models come from the modelled turbulent viscosity. Figure 4.12 shows the time-averaged contours of the turbulent viscosity by different modelling methods. Figure 4.13 plots the profiles of the turbulent viscosity μ/μ_t. Significant differences locate in the attached flow before the step, where DDES, covering the attach boundary layer with RANS, models the highest turbulent viscosity among these three methods. IDDES and DES modeled similar turbulent viscosity near the wall, while IDDES predicts slightly larger values in the whole boundary layer than DES, possibly due to the empirical configuration of the interface between RANS and LES in IDDES without incoming turbulent fluctuations. In the recirculation and recovering region, DES and DDES give similar turbulent viscosity. However, IDDES modelled less turbulent viscosity in the near-wall region. Because in this region, there is plenty of turbulent fluctuations fed to the IDDES model, which will make IDDES in the working mode of WMLES. In the central region of the recirculation, IDDES has slightly larger turbulent viscosity than DES and DDES, which may result from the introduced term of the low-Reynolds correction in the definition of the LES length scale. These behaviour of IDDES observed in the current study is consistent with the IDDES simulation of the backward facing step in Shur *et al.* [2008].

Figure 4.14 compares the friction coefficient and the pressure coefficient in simulations with different turbulence modelling techniques. Both C_p and C_f show IDDES predicted the most agreeable results to the experimental data, while DES and DDES predict similar results in the recirculation region and under-predict reattachment points. Nevertheless, DDES shows its improvement over DES in the redeveloping quasi-channel flow ($x/H > 12$) in the skin friction.

For the mean streamwise velocity, IDDES also gives slightly better simulation results than DES and DDES (see Figure 4.15). DES and DDES give similar velocity values, which are over-predicted in the backflow of the recirculation region. A similar over-prediction was also presented in Shur *et al.* [2008].

Both the modelled and the resolved Reynolds stresses are shown in Figure 4.16. Again, the modelled Reynolds stresses by all these three techniques contributes little to the total Reynolds stresses. For the Reynolds stress $\langle u'u'\rangle/U_{\text{ref}}^2$ and $\langle u'v'\rangle/U_{\text{ref}}^2$, IDDES slightly alleviates the over-predictions in the recirculation region, but the improvement is not significant.

4.2. Validation on flow over the BFS (Driver and Seegmiller)
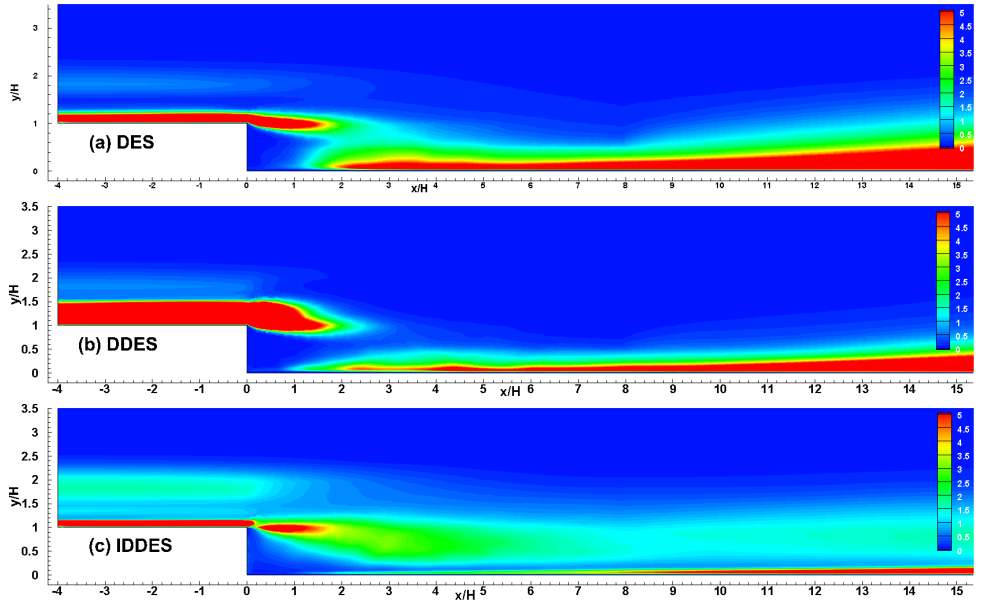
Figure 4.12: Comparison of time-averaged modelled turbulent viscosity simulated with different turbulence modelling. (a) DES, (b) DDES and (c) IDDES
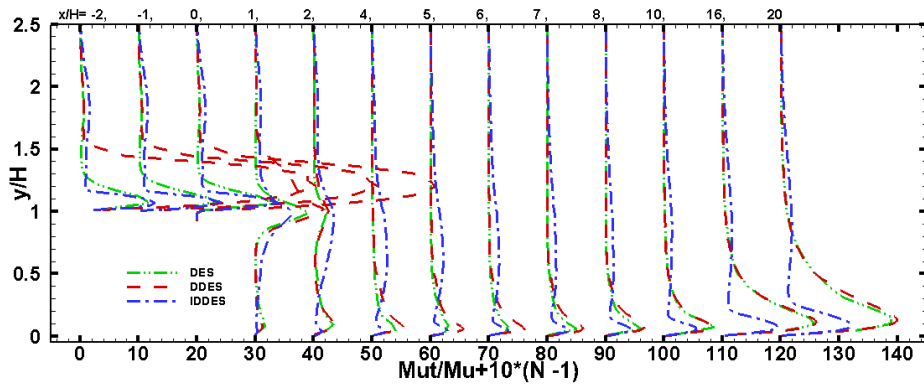
Figure 4.13: Profiles of modelled turbulent viscosity with different turbulence modelling.

For $\langle v'v' \rangle / U_{\text{ref}}^2$, the over-prediction by IDDES seems to be exacerbated in the recirculation region away from the wall, and the under-predictions occur near the wall.

Figure 4.17 displays the instantaneous vorticity magnitude at the section cut from the centre of the span. With the same mesh, the contours of magnitude of vorticity by these three methods all display the breaking-down of the shear layer and the reattachments towards the bottom wall. The vorticity predicted by DES and DDES do not have significant differences, while IDDES seemly resolves smaller and more detailed turbulent fluctuations in the recirculation region.

Based on all above analysis, IDDES improves the prediction of the mean velocity and
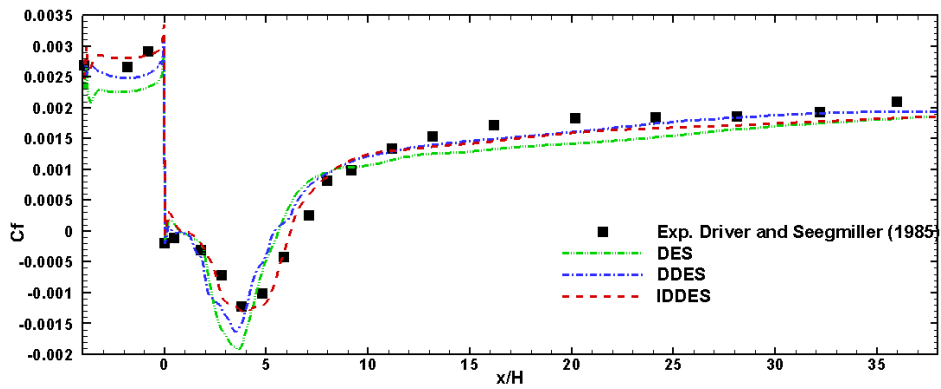
(a)
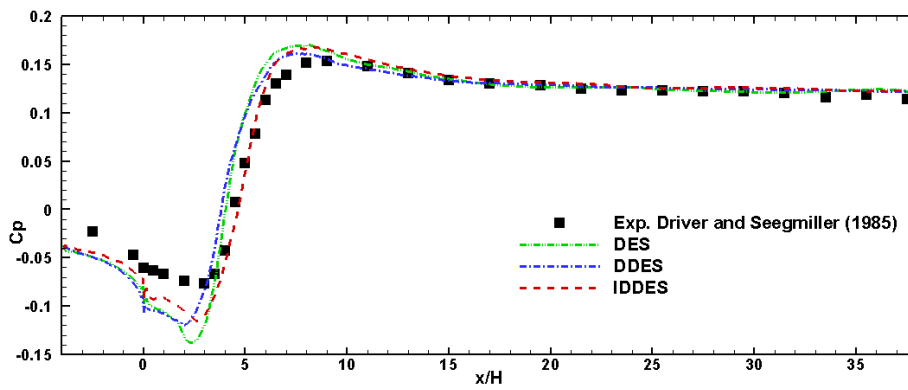
(b)

Figure 4.14: (a) C_f simulated with different turbulence modelling, (b) C_p simulated with different turbulence modelling
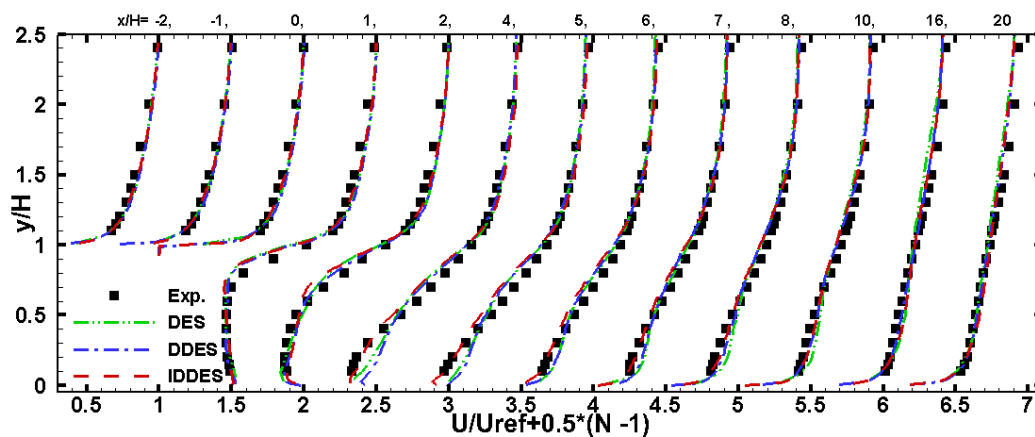
Figure 4.15: Comparison of profiles of the streamwise velocity predicted with different turbulence modelling techniques

4.2. Validation on flow over the BFS (Driver and Seegmiller)

Reynolds stresses in the recirculation region. The reason may be that IDDES can "sense" the turbulence content upstream, and correspondingly adjust its transition between RANS and LES. Shur *et al.* [2008] also showed that IDDES improves the prediction of the reattachment point in the backward facing step case. Therefore, IDDES is adopted in the following numerical simulations.
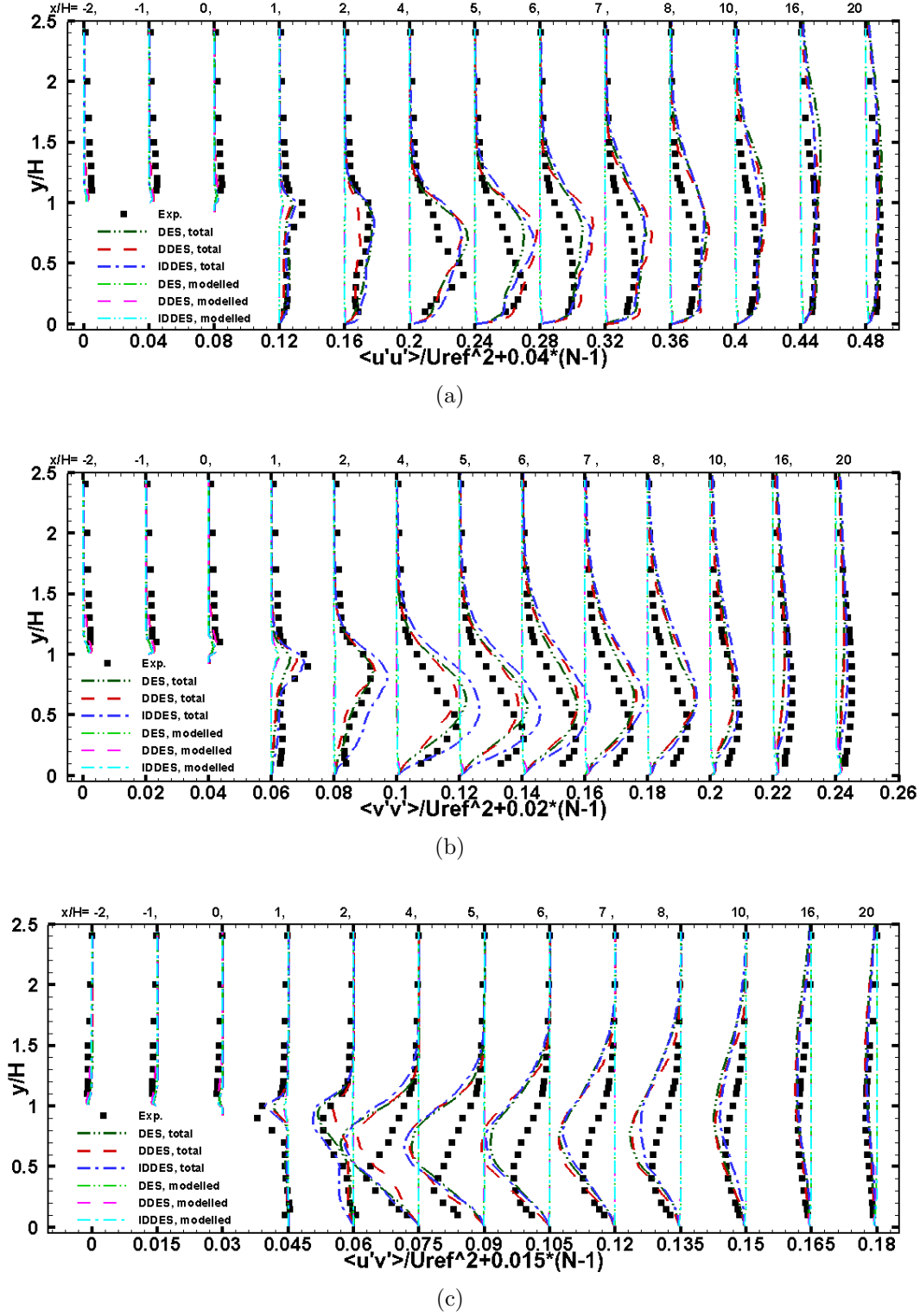
Figure 4.16: Comparison of both the modelled and the resolved Reynolds stresses with different turbulence modelling. (a) $\langle u'u' \rangle/U_{\text{ref}}^2$; (b) $\langle v'v' \rangle/U_{\text{ref}}^2$; (c) $\langle u'v' \rangle/U_{\text{ref}}^2$

(a)

(b)

(c)
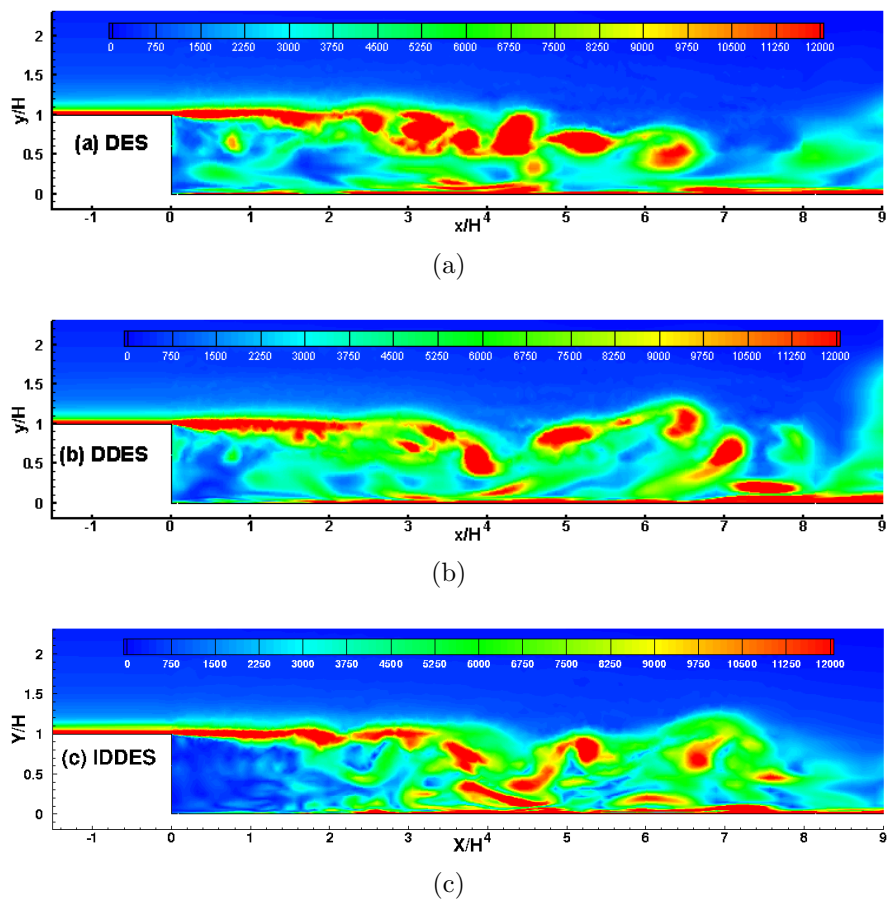
Figure 4.17: The instantaneous vorticity magnitude at the central slice of the span. (a) DES, (b) DDES and (c) IDDES.

4.2.6 Summary

Through the study of validations of the BFS case on three aspects, the conclusions are summarized as follows.

(1) In the geometry-introduced separation, the flow statistics are less insensitive to mesh resolutions as long as they are proper LES mesh resolution, and the improvements on the time averaged velocity and Reynolds stresses are not significant. However, a fine mesh can resolve much smaller and much more turbulence structures than a moderate LES mesh resolution. Considering our interests on flow control of coherent structures, a fine mesh is recommended in the following BFS investigations.

(2) The preconditioning Roe scheme and the low dissipation treatment of the Roe scheme both behave unstabe in this geometry-induced large flow separation. The classic Roe and SLAU schemes predict similar results. When the ALE is applied with moving wall, the Roe scheme is more stable than the SLAU scheme. As a result, the Roe scheme is chosen for the following BFS investigation, both the baseline and the flow controlled case.

(3) In this case, IDDES gives overall best predictions both in the near wall region (skin friction) and the recirculation region (velocity and Reynolds stresses). This is also confirmed by other studies in the BFS cases. In the following simulation of BFS, IDDES is chosen as the turbulence modelling method.

4.3 Flow control with piezoelectric actuators in flow over the BFS (APL-UniMan)

4.3.1 Introduction

Flexible composite surface, in the form of a $50 - 100$ μm thick micro-flexural tape, shows its potential in separation control on aerofoils since it was developed by Sinha [1999] and Sinha and Zou [2000]. Piezoelectric actuators are one of the micro-oscillating membrane devices. Experiments, carried out by Choi *et al.* [2002] and Amir and Kontis [2008], both showed the piezoelectric actuators installed on the suction side of aerofoils effectively increased the lift force at high angles of attack by delaying separations. Although application of the piezoelectric actuators on aerofoil has gained positive control effect, their applications on other flow types are hardly seen. APL-UniMan and our group cooperate in the study of flow control with piezoelectric actuators installed on the step wall in turbulent flow over a backward facing step. Experiments were conducted by APL-UniMan, and simulations were carried out in our group. The piezoelectric actuators installed on the step wall replace the solid wall with oscillating surface (flexible membrane). The oscillating surface may change the boundary layer before its separation from the step, and furthermore, it may influence the flow downstream. The aim of this chapter is to investigate the influences of the piezoelectric actuators to flows in the recirculation region and the recovering region in the BFS case.

Simulations were conducted as follows. Firstly, a baseline case without any control was simulated. Then, the piezoelectric actuators, with the same configurations as the experiments, were carried out. After analysing the control effect, other configurations of the oscillating surface were studied to investigate the influences of different control parameters.

4.3.2 Flow configuration

4.3.2.1 Description of the geometry

The experiment was carried out in the wind tunnel in APL-UniMan. The wind tunnel has a squared cross section of 0.9 m $\times$ 0.9 m, and the length of the test section is 5.5 m. Figure 4.18 shows the BFS model in the wind tunnel. The height of the step is $H = 0.065$ m. The upstream length before the step is $53.85H$, and the downstream length behind the step is $30.77H$. The expansion ratio (outlet height/inlet height) is about 1.07. Considering this small expansion ratio, the top wall effect is negligible for the BFS flow. In simulations, the top wall is set to have a symmetry boundary condition.

The computational domain is shown in Figure 4.19. Simulations cannot afford to calculate the whole length of the wind tunnel, and therefore the numerical inlet is set to be $5H$ upstream of the step, which is not too far away from the step to increase computational cost, neither too near to be influenced by the separated flow downstream. The outlet is $46.4H$ downstream of the step, which is longer than the experiments in order to provide a proper outlet flow convection. Two piezoelectric actuators with a central interval of 0.045 m are simulated with the periodic boundary condition in the two ends of the span. The span has a length of 0.09 m ($\approx 1.38H$).
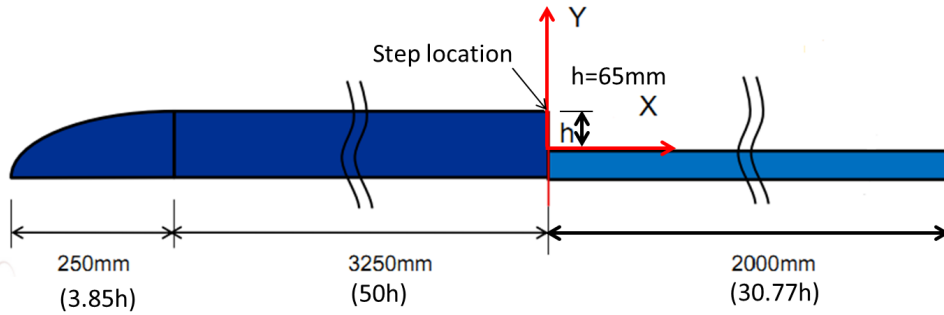
Figure 4.18: Wind tunnel model in APL-UniMan.
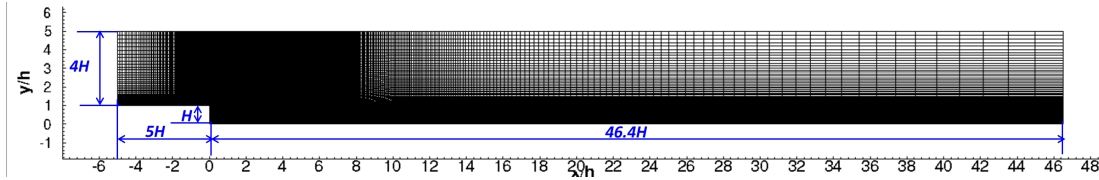
Figure 4.19: Computational domain in the $x - y$ plane.

4.3.2.2 Boundary conditions and time steps

The experiments have a reference velocity of 15 m s^{-1}. The Reynolds number based on the step height and the reference velocity is approximately 64 000. At inlet, the given experimental velocity profiles (in the streamwise and vertical directions) are specified as the inflow conditions. Due to the same reasons as the validation case in the last section, no unsteady fluctuations are superposed on the inlet velocity profiles. The lack of incoming fluctuations upstream of the step may make it difficult to observe the interaction between the generated turbulence and the resolved boundary layer structures. Nevertheless, with IDDES modelling of the near-wall region and with such small oscillations, turbulence flow structures near the wall are expected to be less resolved. A non-reflecting convective boundary condition is used

4.3. Flow control with piezoelectric actuators in flow over the BFS (APL-UniMan)

Table 4.2: Mesh resolutions for the BFS (APL-UniMan)

Case	y_1^+	Δx^{+a}	Δz^+	N_z	N_{cell}
Case	$0.1 - 0.5$	$38 - 70$	$16 - 36$	84	$7\,685\,496$

[a]The non-dimensional grid spacing in the streamwise direction ($x/H < 20$).

at the outlet. The span has a periodic boundary condition. The bottom wall is set to be no-slip wall. The oscillating surface is set to be moving wall.

Similar to the validation case, the time step is set to be $0.0023H/U_{\text{ref}}$, which is 0.001 times of the experimental control time interval of 0.01 s (the control frequency is 100 Hz). Time averaging is calculated after five flow-through periods to remove initial fields. The time average is carried on for a total duration of about $200H/U_{\text{ref}}$.

4.3.2.3 Mesh resolution

A mesh resolution similar to the fine mesh in the validation case of the BFS (Driver and Seegmiller) is generated for this case. The mesh in the $x - y$ plane is shown in Figure 4.20. Above validation case employs an unstructured mesh to expand clustered grids near the step. However, the high skewness ratio of unstructured mesh may introduce high unexpected-numerical-dissipation. Therefore, in this study, the structured mesh is used for the whole domain, both upstream of the step and the recirculation region. The clustered structured mesh above the step wall is expanded and mapped to the downstream domain. Inevitably, some grids with a high stretching ratio exist in the mixing layer region for the expanded structured mesh. Nevertheless, the current mesh with structured mesh expanding in a longer distance is a compromise between a dissipative unstructured mesh and a high stretching-ratio mesh.

Table 4.2 summaries the mesh resolution in three dimensions. As oscillating surface will be simulated, a finer spanwise resolution (compared with the fine mesh of the BFS (Driver and Seegmiller)) is generated, and the grids near the oscillating surface in the streamwise direction are also refined. Overall, this mesh resolution is comparable and finer than the fine mesh in the validation case.

4.3.2.4 Numerical schemes and turbulence modelling

As stated in the above validation case, the classic Roe scheme and the SLAU scheme predict similar results in this type of flows. However, the classic Roe scheme is more stable in numerical simulation with moving surfaces. Therefore the classic Roe scheme is applied to
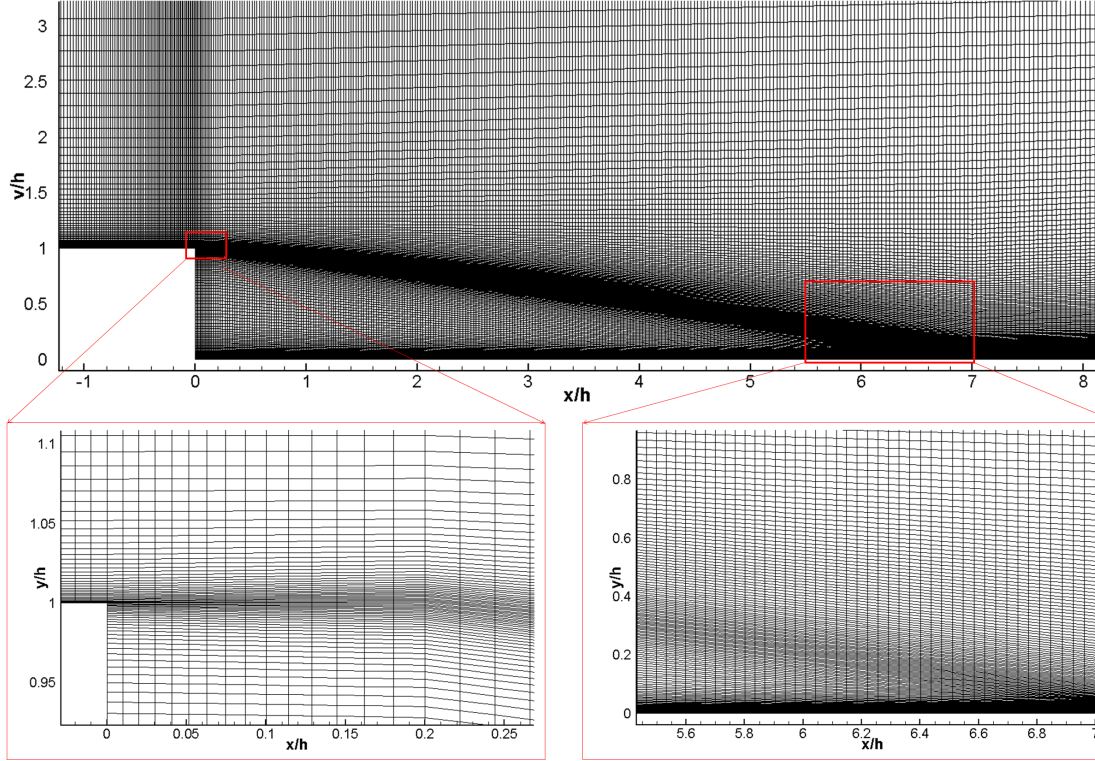
Figure 4.20: Diagram of the mesh in the $x - y$ plane.

all below simulations.

IDDES has advantages in simulating flows in the recirculation region and the recovery region, because it takes the high flow fluctuations in these regions into account to resolve more turbulence structures. Thus, IDDES is used for below simulations.

4.3.3 Setup of the oscillating surface in simulation

4.3.3.1 Numerical configuration of the oscillating surface

For the flow control case, the piezoelectric actuators are arrayed in the span upstream of the step. Figure 4.21 displays the setup of the piezoelectric actuators in experiments. The piezoelectric actuator has a circular shape with a diameter of 0.041 m. The distance between two neighbouring actuators is 0.045 m. The centroid of the circular actuators locates at $x = -0.095$ m $(-1.462H)$ upstream of the step, and at $z \approx \pm 0.3462H$ in the spanwise direction. (The origin of x-coordinate locates at the step, the origin of y-coordinate locates at the bottom wall, and the origin of z-coordinate locates at the middle of two adjacent actuators.) Figure 4.22(a) lists the main specifications of the piezoelectric actuators, extracted from the manual of the piezoelectric actuators. Figure 4.22(b) demonstrates the oscillation motion of

4.3. Flow control with piezoelectric actuators in flow over the BFS (APL-UniMan)

an actuator.
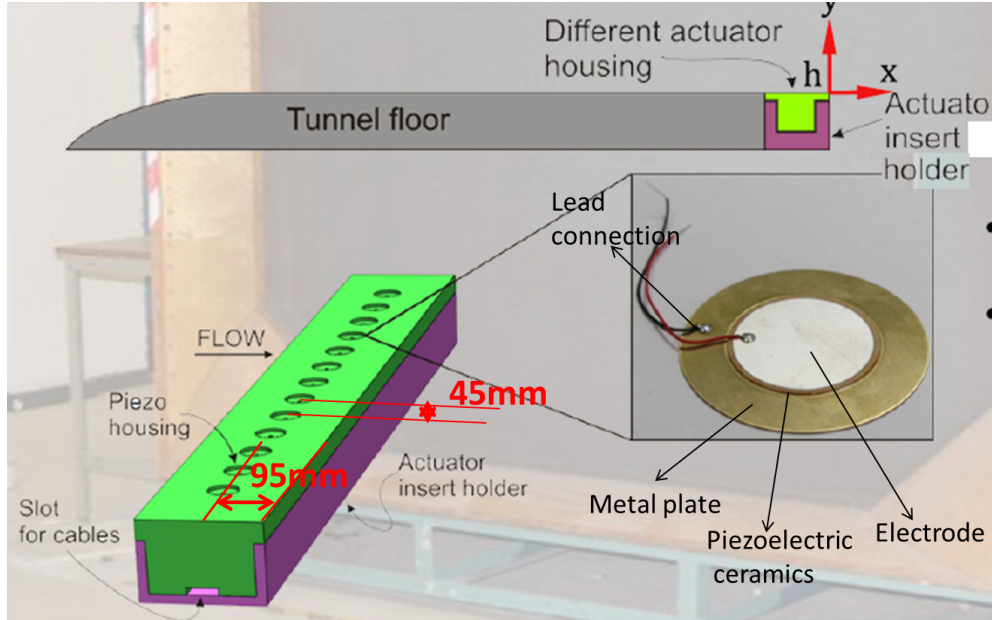
Figure 4.21: Experimental setup of the piezoelectric actuators.

Diaphragm Specifications	
Resonant Frequency	2.2 kHz + 0.3 kHz
Plate Size	41.0 mm
Plate Thickness	0.40 mm
Element Size	25.5 mm
Electrode Size	23.0 mm
Thickness	0.63 mm
Plate Material	Brass with lead wire

(a)

(b)
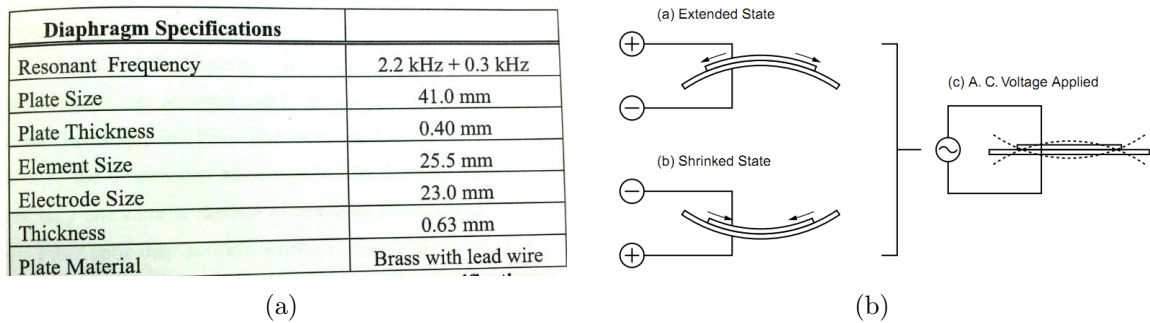
Figure 4.22: (a) Specification of the piezoelectric actuator. (b) Diagram of the oscillating system in operation

In order to simulate the oscillating motion of the piezoelectric actuators, the trajectory of the whole oscillating surface should be described. Considering that the maximum displacement of the oscillating surface of the piezoelectric actuators is in the order of micrometer, it is reasonable to assume that the deformed shape of this oscillating surface follows the shape of a spherical crown. The oscillation in time obeys a sinusoid wave, with the maximum displacement at its stagnation point. The apex of the surface of spherical crown oscillates following the function

$$y_a = A_a \sin(2\pi f t + \phi), \tag{4.1}$$

where A_a is the maximum displacement of the apex, f is the oscillating frequency, t is the real physical time, ϕ is an arbitrary initial phase angle, and the subscript a means the apex. Correspondingly, the velocity profile at this apex is derived as

$$V_a = \frac{dy_a}{dt} = 2\pi f A_a \cos(2\pi f t + \phi). \tag{4.2}$$

For other points on the oscillating surface except the apex, their movements and locations can be derived based on the assumption of the sphere and the movement of the apex point. In simulation, the actuation is generated by assigning a vertical displacement on the piezoelectric surface. Assume (x, y, z) as the coordinates of an arbitrary point on the surface, then its x and z coordinates maintain the same as the neutral position and the y-coordinates of the deformed surface is given by

$$y(x, z, t) = \begin{cases} y_0 - \frac{R^2 - [A_a \sin(2\pi f t)]^2}{2 A_a \sin(2\pi f t)} + \text{sign}\left[A_a \sin(2\pi f t)\right] \cdot \\ \sqrt{\{\frac{[A_a \sin(2\pi f t)]^2 + R^2}{2 A_a \sin(2\pi f t)}\}^2 - \left[(x - x_0)^2 + (z - z_0)^2\right]}, & \sin(2\pi f t) \neq 0 \\ \\ 0, & \sin(2\pi f t) = 0 \end{cases} \tag{4.3}$$

where (x_0, y_0, z_0) is the coordinate of the central apex in the neutral position, and R is the radius of the circular surface in the neutral position.

An example of the deformed surface is given in Figure 4.23. In this example, the maximum movement of the apex is $0.1H$, which is much larger than the real oscillating surface to clearly demonstrate the surface deformation. This example also shows that even with such a large motion, the dynamic grid method with geometry similarity is stable and effective, and the mesh quality is also acceptable.

4.3.3.2 Control parameters

The experiments of flow control with the piezoelectric actuators were carried out in APL-UniMan. The control parameters in the experiments correspond to the case name OS1 and OS2 in Table 4.3. Experimental result shows that there is little control effect on the reattachment point with these control configurations. As the amplitude of the piezoelectric actuator is in the order of micrometer, even with a frequency of 500 Hz, the maximum velocity is about 0.03 m s^{-1}, which is only 0.2% of the edge velocity of the boundary layer. In contrast to flows separated with a gradual adverse pressure gradient, the flow with an abrupt separation in this case has less sensitivity to the upstream flows (Sagaut *et al.* [2006]).

4.3. Flow control with piezoelectric actuators in flow over the BFS (APL-UniMan)
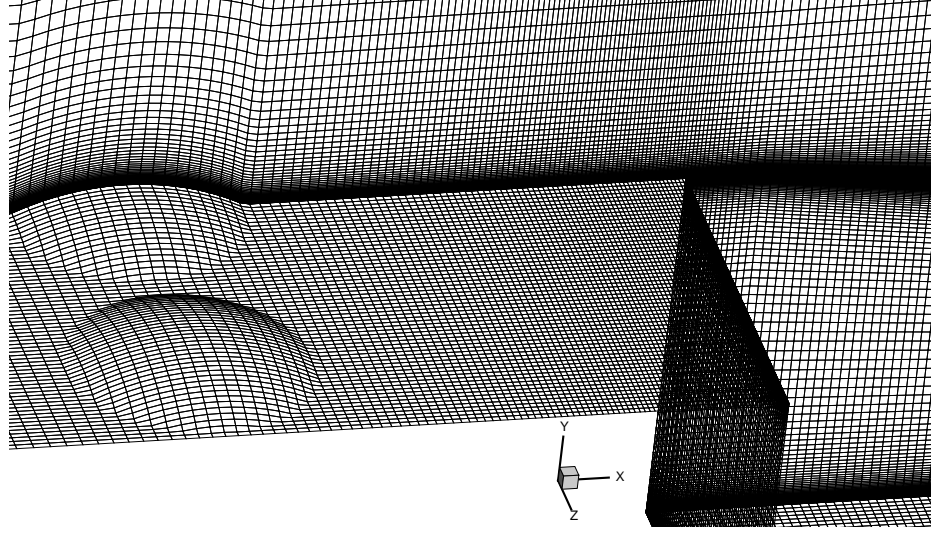
Figure 4.23: An example of the geometry of the oscillating surface.

Table 4.3: Control parameters of the oscillating surface

Case	f^a (Hz)	$A_a{}^b$ (m)	$V_a{}^c$ (m/s)
Baseline	0	0	0
OS1	100	$9.55 \times 10^{-6} \approx 1.47 \times 10^{-4} H$	$0.006 \approx 4.0 \times 10^{-4} U_{\text{ref}}$
OS2	500	$9.55 \times 10^{-6} \approx 1.47 \times 10^{-4} H$	$0.03 \approx 2.0 \times 10^{-3} U_{\text{ref}}$
OS3	360	$2.21 \times 10^{-3} \approx 3.39 \times 10^{-2} H$	$5.0 = 1/3 U_{\text{ref}}$
OS4	360	$4.41 \times 10^{-3} \approx 6.78 \times 10^{-2} H$	$10.0 = 2/3 U_{\text{ref}}$
OS5	360	$6.63 \times 10^{-3} \approx 1.02 \times 10^{-1} H$	$15.0 = U_{\text{ref}}$

[a]The oscillating frequency.
[b]The displacement amplitude of the central apex.
[c]The velocity amplitude of the central apex

As a result, experiments with the configuration OS1 and OS2 both display little control effect on the flow reattachment. Therefore, only the control case with control parameters of OS1 (Table 4.3) was carried out in simulation to study the influences of the flow control.

Regardless of the physical realizability of piezoelectric actuators, more values of the control parameters in the oscillating surface are investigated to study the control effect of the oscillating surface, which are cases OS3-OS5 in Table 4.3. These exploring cases have a control velocity in the order of the free stream velocity.

4.3.4 Results and discussion on the baseline flow and the oscillating surface controlled flow

This section validates the simulation results of the baseline flow, compared with available experimental data. It also compares the baseline flow and the control flow with the exact control parameters as the experiment (Case OS1). The baseline flow is a benchmark to investigate the controlled flow, thus it will be repeatedly referred to in the following sections. Rather than repeating the baseline flow, the simulation results of the baseline flow are only shown in this section.

4.3.4.1 Coherent vortices

Several vortex identification criteria (the λ_2 criterion and the vorticity Ω_x, Ω_y and Ω_z) are used to visualise turbulent flows. Details on the vortex identification criteria were given by Jeong and Hussain [1995].

Figure 4.24 displays iso-surfaces of the three vorticity components at the value of ± 500 for the baseline flow. It is observed that at the specified values, there is a large sheet of the spanwise vorticity Ω_z over the step and this sheet breaks into small structures just downstream of the step and still keeps the same rotation direction. For the other two vorticity components, they mostly locate in the recirculation region of the step flow. Le *et al.* [1997] also reported the dominant role of the spanwise vorticity in flow over the BFS. A popular flow control on BFS is to break these spanwise vortices. For example, Neumann and Wengle [2003] studied the vortex generators of control fences installed on the step (a passive flow control method), and showed that the main contribution of the vortex generators is to generate streamwise vorticity, which aims to break the quasi-two dimensional spanwise vortices, and then to enhance the mixing in the recirculation region.

The instantaneous flow structures for the baseline flow and the flow control case OS1 are shown in Figure 4.25. The baseline flow and the control case OS1 show some common features in the flow structures, which are typical for flow over a BFS. Figure 4.25 shows that in the region near the step and above the secondary recirculation, quasi-two dimensional vortex tubes are generated from the step edge, and shed from the step. When the primary reversing flow goes up to mix with the separated shear layer, the quasi-two dimensional vortex tubes interact with the reversing flow, break down, and form hairpin-like structures. It is observed that the lower parts of these large hairpin-like structures form the separated shear layer, breaking into smaller vortex and moving towards the wall. The above part of the mixing layer is observed to still be large-scale hairpin-like eddies. These phenomena of
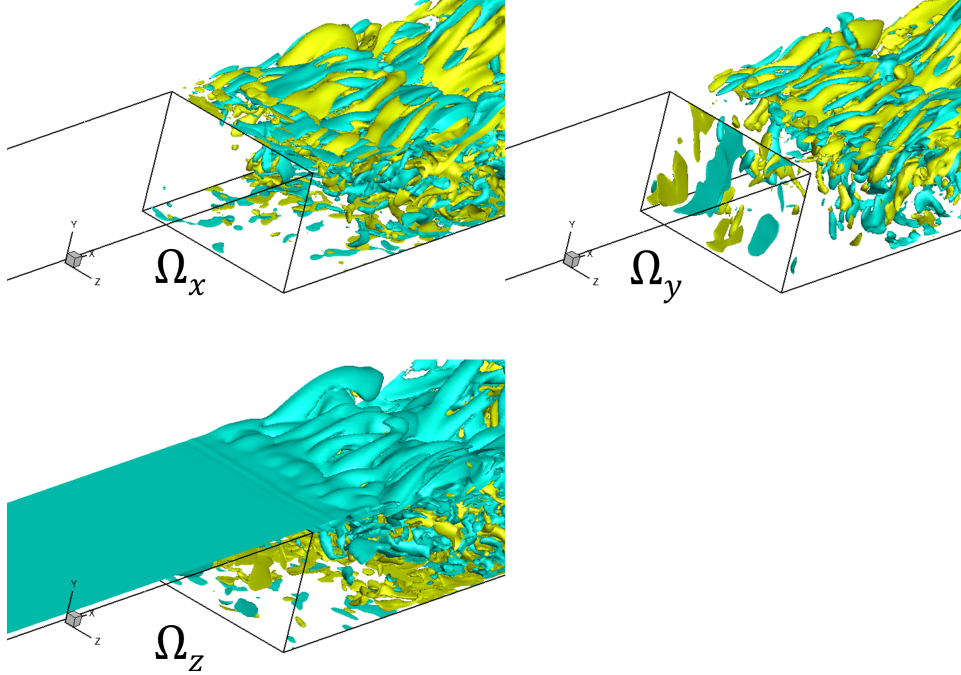
Figure 4.24: Instantaneous baseline flow: the iso-surface of the three vorticity components, Ω_x, Ω_y and Ω_z. (The light orange colour for the value of 500, and the light blue colour for the value of -500 for all these three vorticity.)

turbulent structures in BFS flow are also observed in the BFS study in Koken and Constantinescu [2009]. There are some differences in the vortex structures in the controlled case OS1 from the baseline case. The differences in downstream of the step may come from the different stages of the vortex shedding period. However, the flow control case OS1 (Figure 4.25(b)) displays some vortex tubes in the vicinity of the oscillating surfaces before the flow separation from the step edge, while for the baseline case (Figure 4.25(a)), there is no tube-structures observed before the step edge (in any stage of the vortex shedding period). The generation of tube-like structures upstream of the step edge is also observed in flows with a control fence upstream of the step of the BFS (Neumann and Wengle [2003]), although these quasi-two dimensional tubes generated by the oscillating surface is much weaker than those generated by a control fence.

In order to clearly observe these structures near the actuators, the iso-surfaces of the streamwise vorticity (Ω_x) at a very small number ($\Omega_x = \pm 0.1$) is shown in Figure 4.26. For the flow control case OS1, vortices are generated in pairs around each actuator. These vortice-pairs generated around the actuators influence the flow structures around the step edge, making large structures break down. The contours of the streamwise vorticity are

(a)

(b)
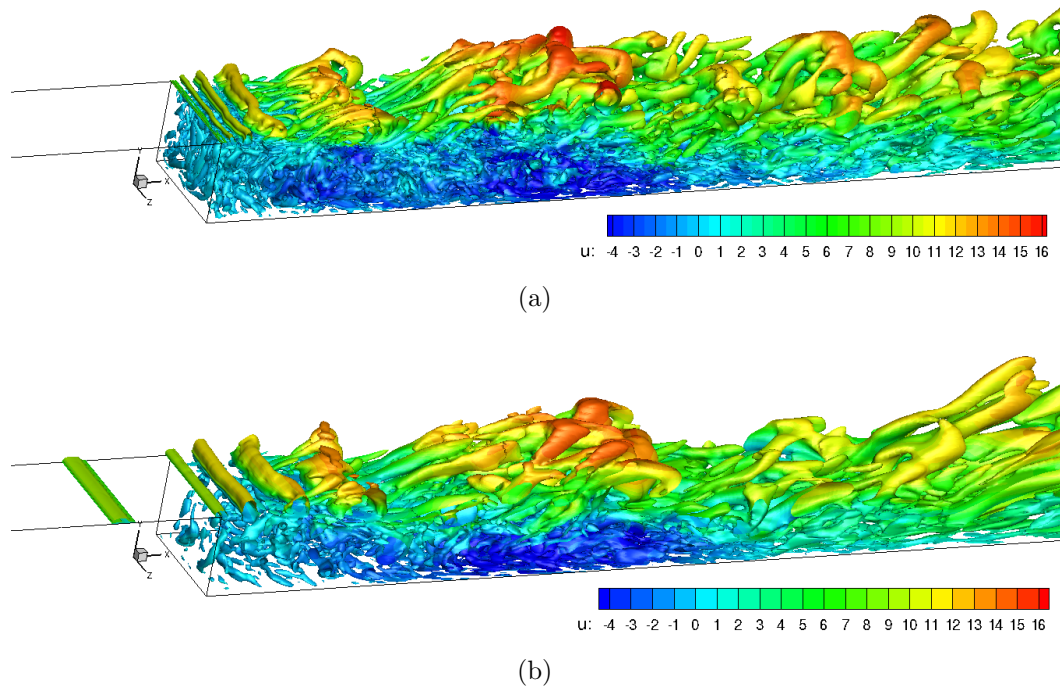
Figure 4.25: The iso-surface of λ_2 equal to -5000 for instantaneous flow. (a) Baseline flow, and (b) OS1. (The colour coding in these iso-surfaces corresponds to the streamwise velocity.)

compared in Figure 4.27 for the baseline flow and Figure 4.28 for the control case OS1. Firstly, the baseline flow displays two adjacent Ω_x in opposite directions at $x/H = -0.5$ due to the downstream flow with spanwise variations, while each actuator in the control case OS1 introduces a pair of two streamwise vortices in opposite directions. Secondly, for the baseline flow, the streamwise vortex downstream of the step extends to the upstream of the step, while for the flow control case OS1, the extended streamwise vortex from downstream interacts with the oscillation-generated vortex, and much smaller streamwise vortex is formed at downstream of the step, for example, at $x/H = 1.0$ shown in Figure 4.28. The large values of the Ω_x shown in the case OS1 in Figure 4.28 also occupy a large region in the free stream flow downsteam of the step. (Note that in order to display the effect of oscillating surfaces, the legend in the contours of streamwise vorticiy is limited to a very small range, much smaller than the other two vorticity. The current legend for Ω_x is from -0.1 to 0.1. If the legend for the controlled flow OS1 becomes 500, just as shown in Figure 4.24 for the baseline flow, there are no obvious differences observed in the iso-surface of Ω_x from the baseline flow.)

The instantaneous flow structures show that the flow controlled case OS1 introduces tube-

4.3. Flow control with piezoelectric actuators in flow over the BFS (APL-UniMan)

(a)

(b)
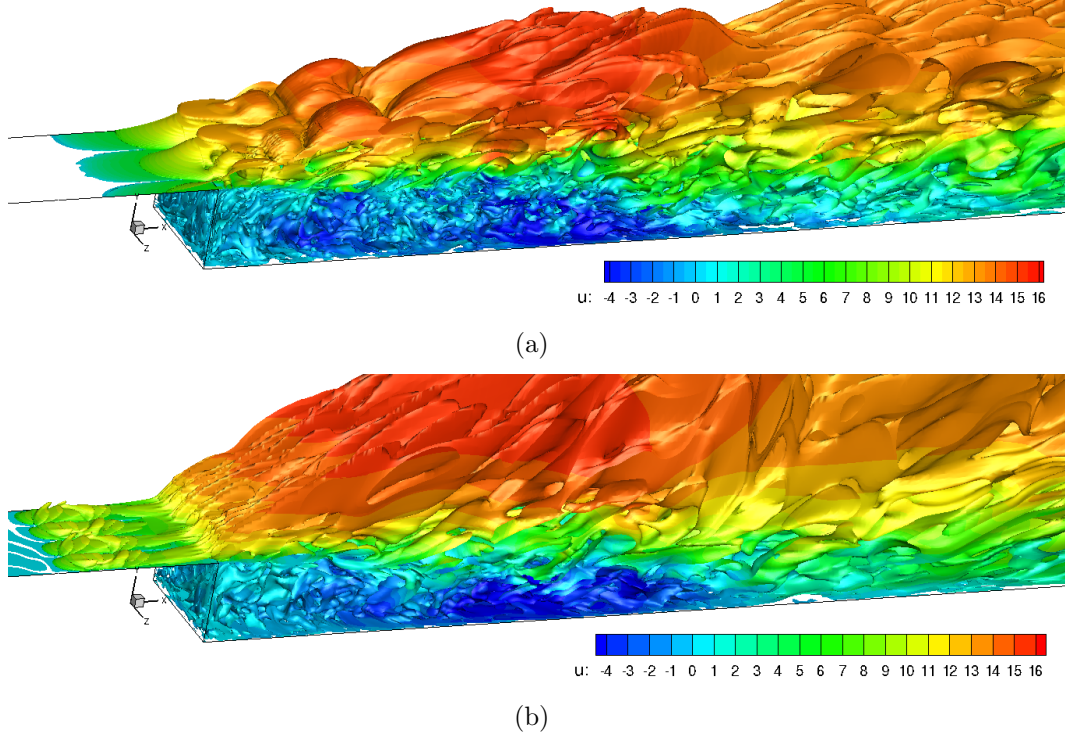
Figure 4.26: The iso-surface of the streamwise vorticity Ω_x equal to ± 0.1 for instantaneous flow. (a) Baseline flow, and (b) OS1. (The colour coding in these iso-surfaces corresponds to the streamwise velocity.)

like vortices upstream of the step, but the influences to the downstream flow are limited. The generated streamwise vorticity is also in a very limited scale. In order to study the influences of actuators in the whole energy spectral, power spectral density (PSD) of the pressure probed on the wall at $x/H = 6.5$ is displayed in Figure 4.29. A hamming window with an overlap of 50% is used to filter the signals. The comparison of frequencies shows the simulation of the baseline flow provide a similar dominant Strouhal number to the experiment, which are both approximately $St = 0.056$. This Strouhal number is similar to the reported Strouhal number of 0.06 in the DNS study of a BFS case by Le *et al.* [1997].

PSD analysis of another three points in the mixing layer, which are at $(x, y, z) = (0.2H, 0.95H, 0)$, $(x, y, z) = (3H, 1H, 0)$ and $(x, y, z) = (5.5H, 0.4H, 0)$, are also compared in Figure 4.30. For the pressure signal at the point $(x, y, z) = (0.2H, 0.95H, 0)$ very near the step edge, the baseline flow and the control case OS1 both show a distinct peak Strouhal number. The dominant Strouhal number for the controlled case OS1 ($St = 0.172$) is slightly higher than the baseline flow ($St = 0.152$), which are both higher than the dominant Strouhal number calculated from the wall near the reattachment point. For the Strouhal numbers larger than the peak values, the flow control case OS1 displays a higher PSD values than
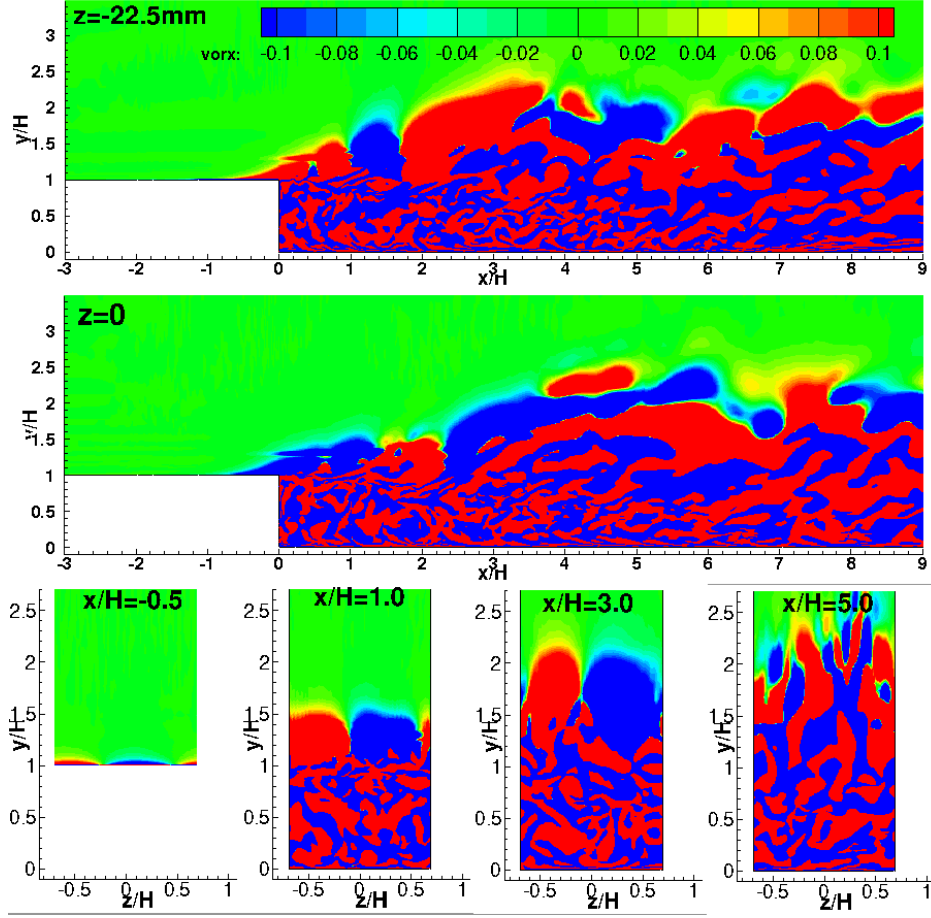
Figure 4.27: Baseline flow: contours of the streamwise vorticity Ω_x at the sections $z/H = -0.346$, $z/H = 0$, and the cross-sections $x/H = -0.5$, 1.0, 3.0 and 5.0

the baseline flow, which may corresponds to the high fluctuations introduced by the smaller structures just downstream of the step shown by the streamwise vorticity in Figure 4.26. The control frequency (corresponding to a Strouhal number of $St = 0.43$) cannot be observed from this point (Figure 4.30(a)). Further downstream at the points in the recirculation region $(x, y, z) = (3H, 1H, 0)$ and $(x, y, z) = (5.5H, 0.4H, 0)$, the control frequency is still not observed from the PSD plots. In the region of high Strouhal numbers, the flow control case OS1 displays a lower PSD values than the baseline flow.

115

4.3. Flow control with piezoelectric actuators in flow over the BFS (APL-UniMan)
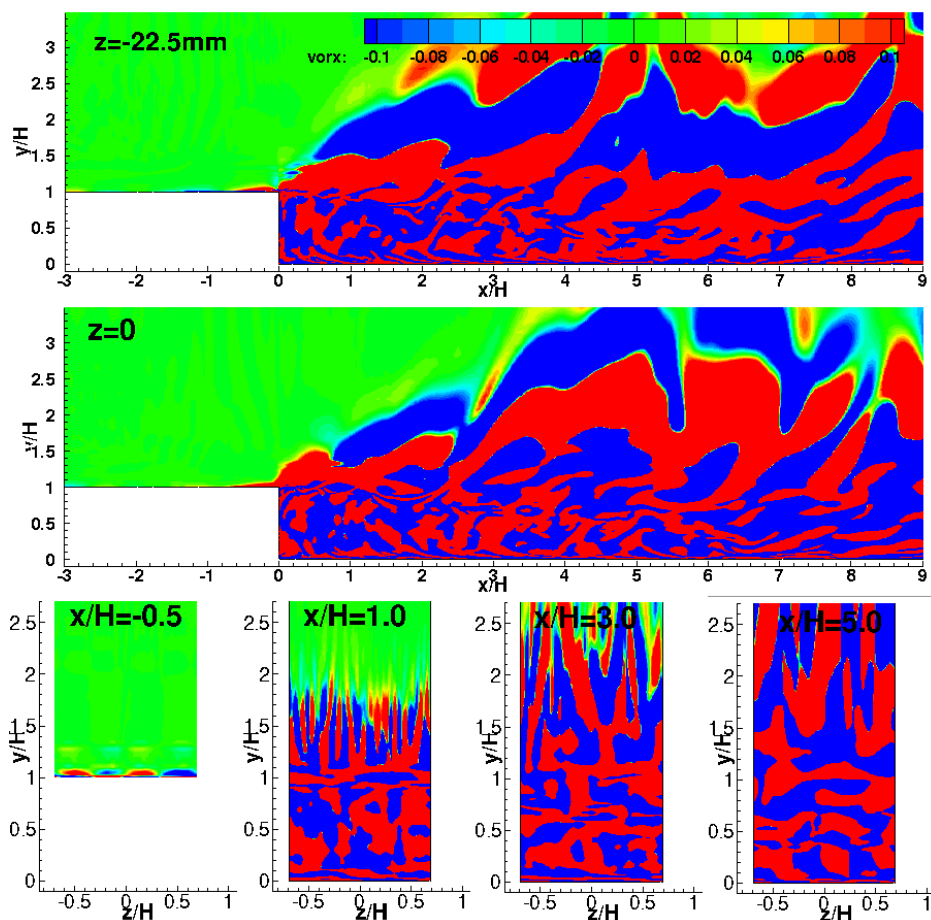
Figure 4.28: The controlled flow OS1: contours of the streamwise vorticity Ω_x at the sections $z/H = -0.346$, $z/H = 0$, and the cross-sections $x/H = -0.5$, 1.0, 3.0 and 5.0

(a)   (b)
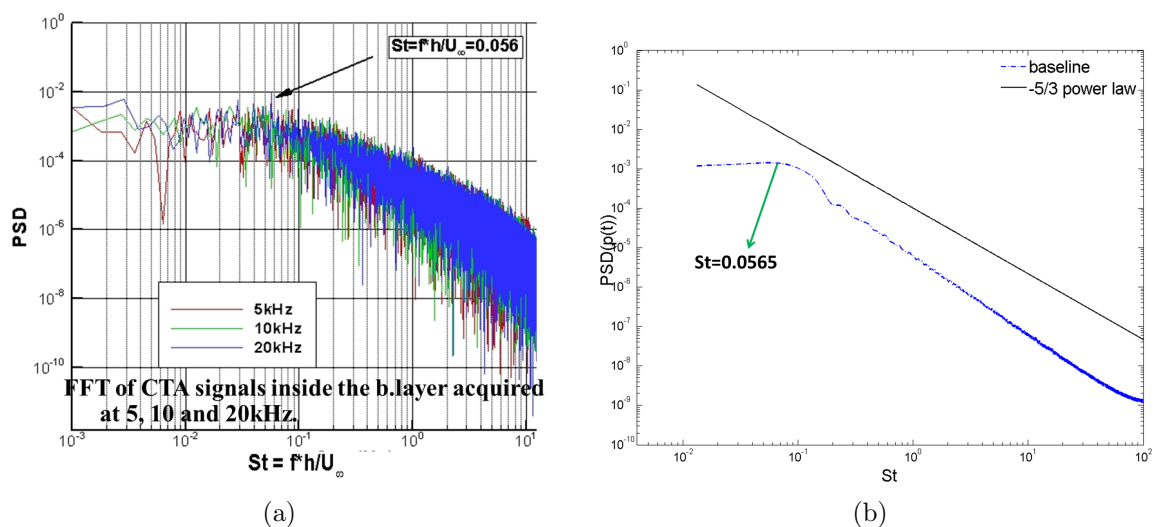
Figure 4.29: Power spectral density of the instantaneous pressure $p(t)$ at $(x, y, z) = (6.5, 0, 0)$ for the baseline case. (a) Experimental result of the baseline flow. (b) Simulation result
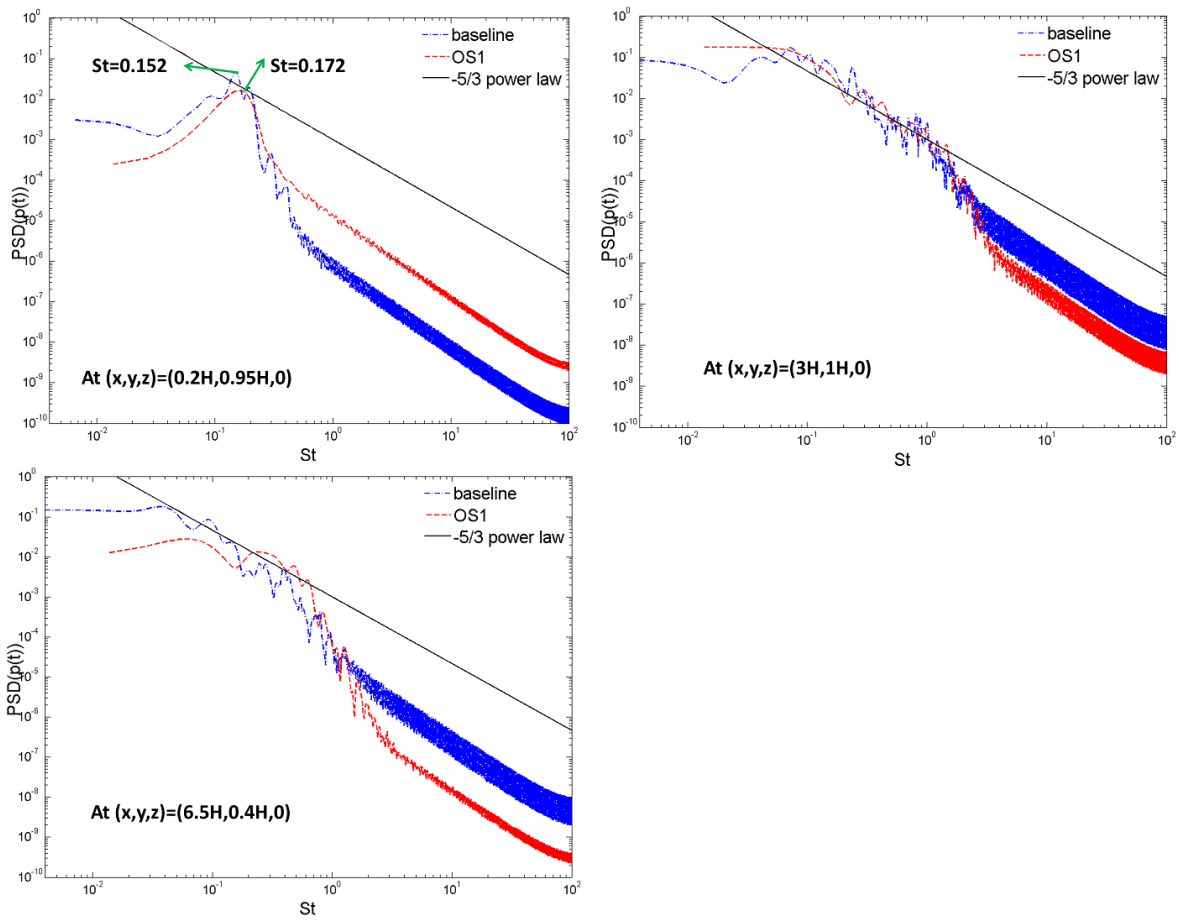
Figure 4.30: Power spectral density of the instantaneous pressure $p(t)$ at $(x, y, z) = (0.2H, 0.95H, 0)$, $(x, y, z) = (3H, 1H, 0)$ and $(x, y, z) = (5.5H, 0.4H, 0)$.

4.3. Flow control with piezoelectric actuators in flow over the BFS (APL-UniMan)

4.3.4.2   The motion of oscillation

One period of the oscillation motion is studied to investigate the control mechanisms. Figure 4.31 shows the probed time-dependent locations of the apex of the control surface, and corresponding vertical velocities. It can be seen that the maximum movement is less than $0.015\% H$, and maximum velocity is $0.04\% U_\text{ref}$. Considering this small control parameters, the iso-surfaces and the vorticitiy contours shown below are displayed in a very small scale to highlight the structures generated by the actuators.
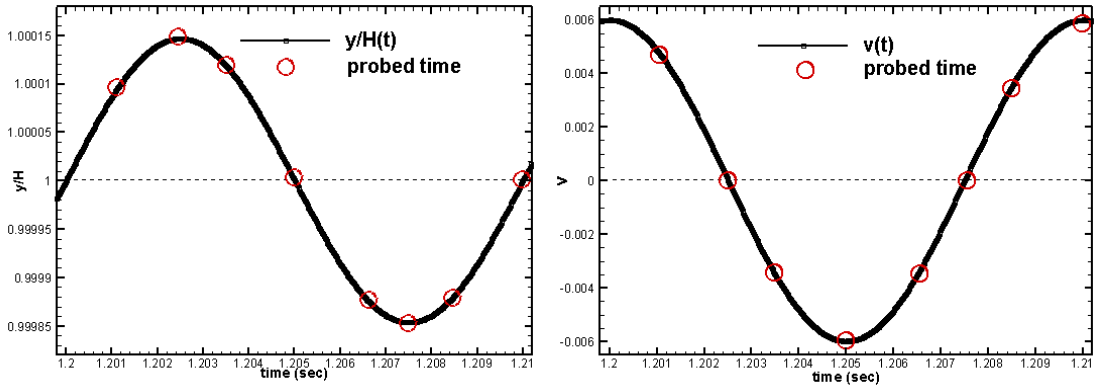
Figure 4.31: Time-dependent motion of oscillation in one oscillating period of the control case OS1. Left: displacement of the apex of the surface. Right: vertical velocity on the apex of the surface. (The probed location and velocity are recorded every other time step)

Figure 4.33 displays the instantaneous streamwise velocity, vertical velocity and the spanwise velocity on the first layer of cells above the wall around the actuator in one control period (τ). The probed time-sequence (or phase angle in one period) follows the circled points in Figure 4.31. An obvious periodicity of the vertical velocity and the spanwise velocity obeying the control period is observed. As expected, the contours of the vertical velocity form concentric circles. However, the vertical velocity outside the region of actuators is scarcely affected by the oscillating motion, which means the vertical oscillating motion transfer little momentum towards its surroundings. The streamwise velocity also shows periodicity in some extent, but not as distinct as the vertical velocity. The affected regions by the actuators displayed by these three velocities are different. The affected region of the vertical and spanwise velocity revolves around the location of the actuators. However, the affected streamwise velocity is mainly in the region from the central of the oscillating surface towards the edge of the step. The contours of spanwise velocity seems to shift between four phases, and the four phases are defined in Figure 4.32. The four phases are divided into two groups, the left group with Phase II and Phase III, and the right group with Phase IV

118

and Phase I. It is observed that the first-order derivative of the vertical velocity affect the shift of the spanwise velocity in different phases. Take the left group for example, from the phase angle $2\tau/20$ to $10\tau/20$, where the vertical velocity decrease, the negative spanwise velocity in Phase II increases and expands towards Phase III, while the region in Phase III with the positive spanwise velocity shrinks. The right group shows an opposite trend. From the phase angle $13\tau/20$ to τ, the vertical velocity increase from the valley value to its peak value, the spanwise velocity in Phase II become positive and becomes higher and tends to occupy the whole region in the left group. The alternative of the spanwise velocity results in squamous structures stacked above the oscillating surface, which will be discussed in the following.
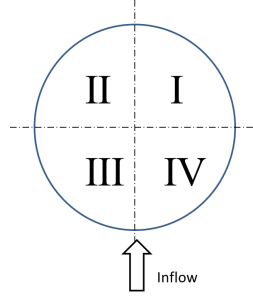
Figure 4.32: Four phases in the oscillating surface of one actuator

In order to study the generation of streamwise vortices around the actuators and their impact on the downstream flow, Figure 4.34 displays the iso-surface of the streamwise vorticity at $\Omega_x = \pm0.05$. Figure 4.35 display the contours of the streamwise vorticity in the sections cut from $x/H = -0.5$. Figure 4.34 shows that the motion of oscillation generates squamous structures stacked above the oscillating surface. In addition, the evolution of the structures shown by the streamwise vorticity is highly related to the shifting of the spanwise velocity in Figure 4.33. The motion of oscillation generates vortex with different directions in the four phases. These vortices stack layer by layer on the surface (can also be seen in Figure 4.35), and tilts towards the streamwise direction. The shapes of the vortex generated directly by the oscillation of the surface are different from those generated by synthetic jets driven by piezoelectric actuators, in which the vortex are usually blown away from the wall, and not stacked together (Qin and Xia [2008]; Xia and Qin [2005]). The forms of vortices generated in the control case OS1 are not only related with the motion of oscillation, but also relevant to the control parameters. The low control magnitude results in the vortex to develop in the very near wall region.
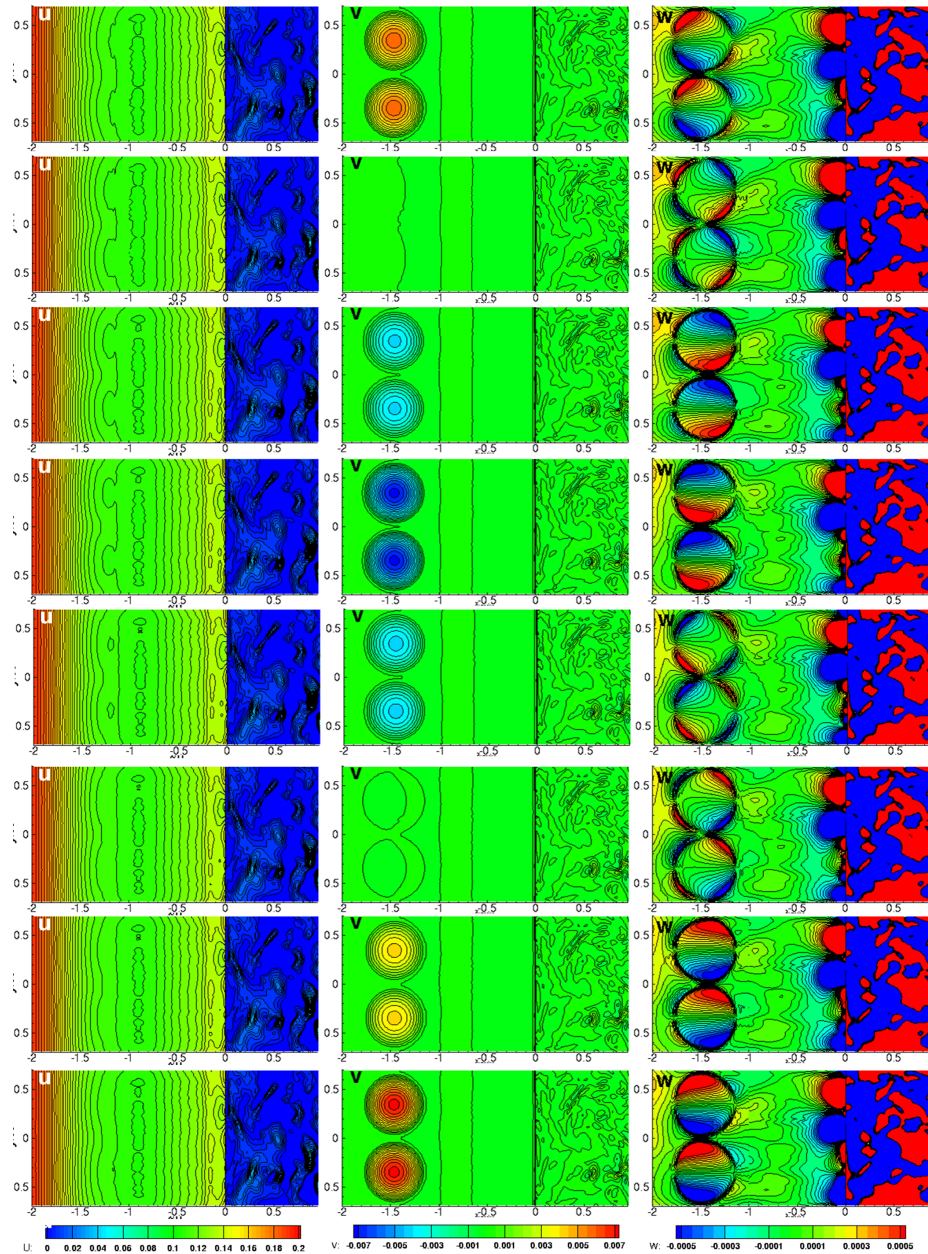
Figure 4.33: Instantaneous velocity at the first cell above the wall in one control period. Left column: streamwise velocity u. Middle column: vertical velocity v. Right column: spanwise velocity w. The phase angle from top to bottom: $2\tau/20$, $5\tau/20$, $7\tau/20$, $10\tau/20$, $13\tau/20$, $15\tau/20$, $17\tau/20$ and τ (or 0). (Note that the legends for u, v and w is different.)
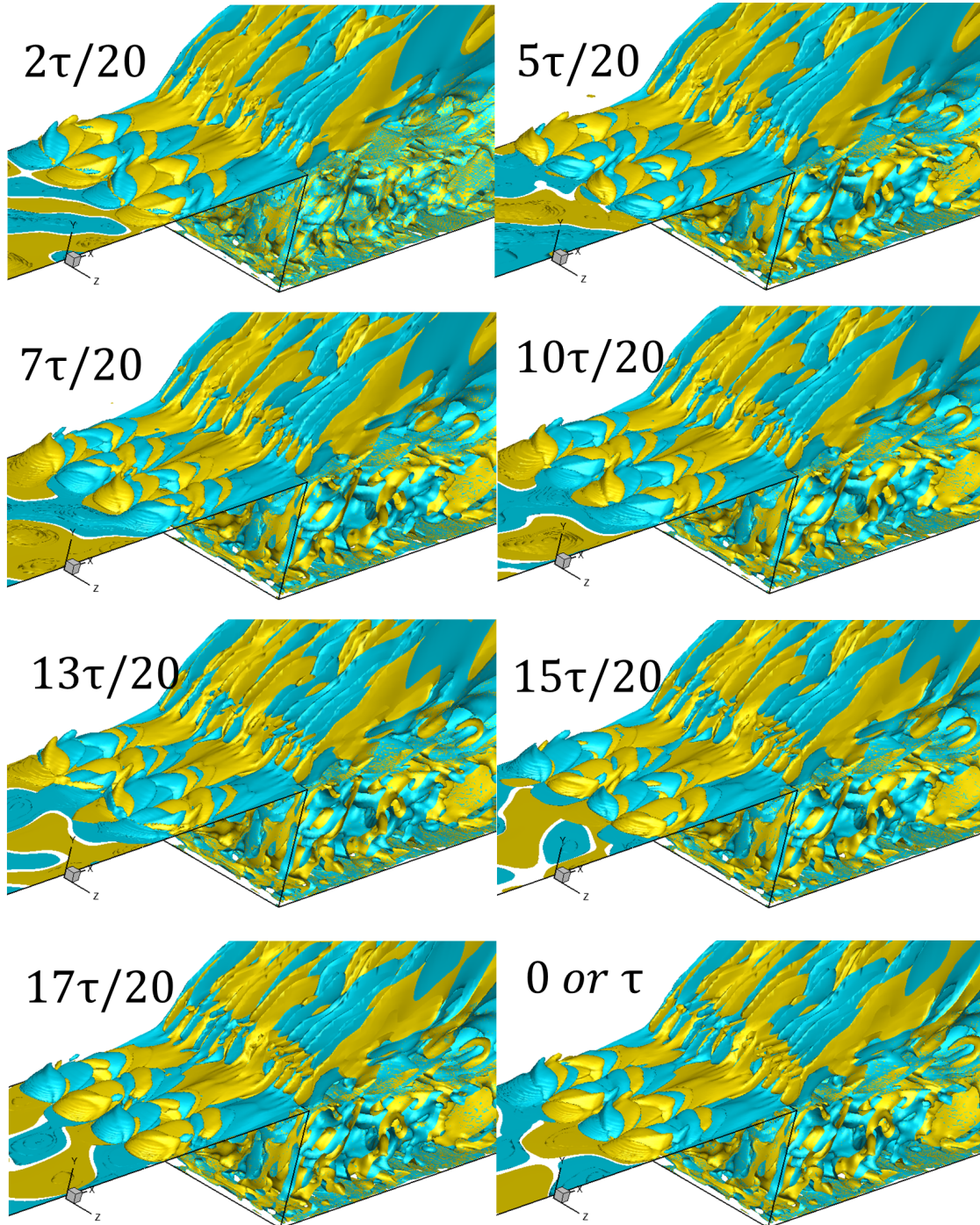
Figure 4.34: OS1: The iso-surface of the streamwise vorticity Ω_x equal to ± 0.05. (The light orange colour for the value of 0.05, and the light blue colour for the value of -0.05.)

4.3. Flow control with piezoelectric actuators in flow over the BFS (APL-UniMan)
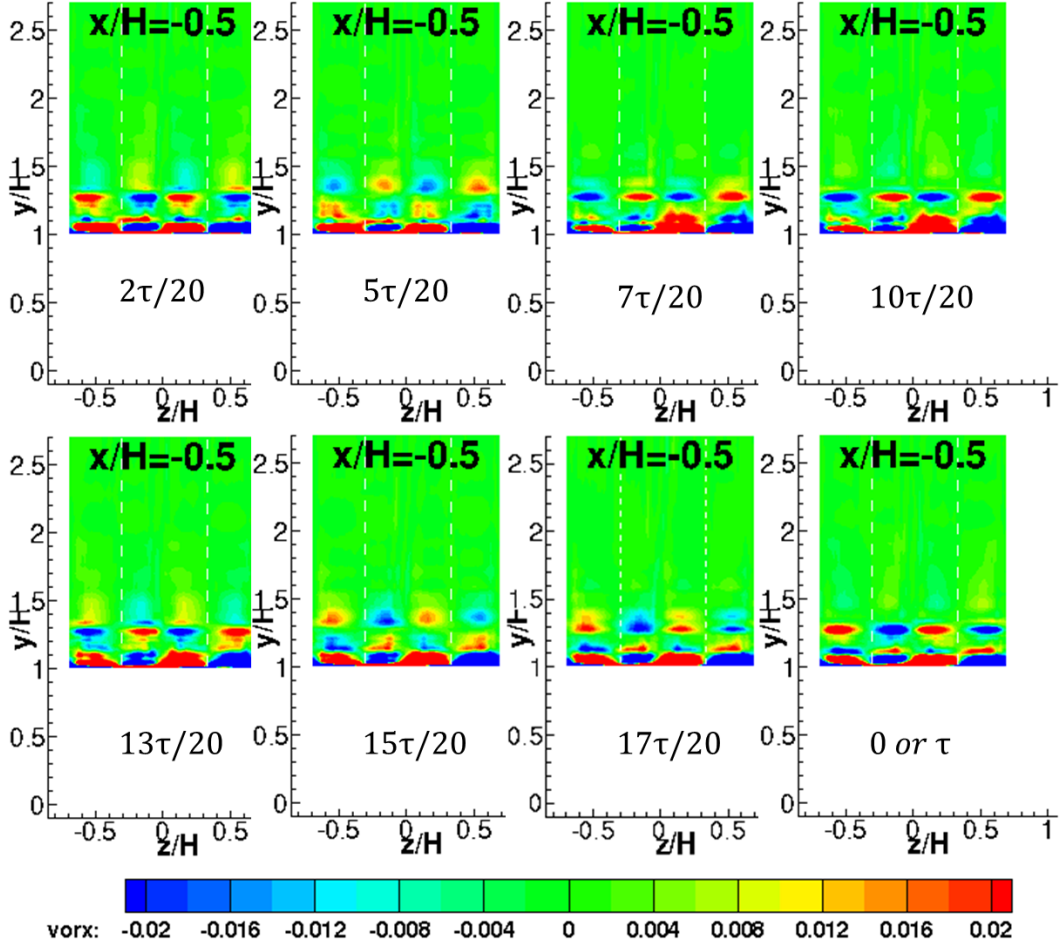
Figure 4.35: OS1: Contours of the streamwise vorticity Ω_x

Figure 4.36 demonstrates the shifting of the counter-rotating directions of vortices generated by a single actuator. During the vertical oscillating velocity $v < 0$ ($5\tau/20$, $7\tau/20$, $10\tau/20$ and $13\tau/20$ in Figure 4.31), the streamwise vorticity in Phase I and II is counter-rotating (highlighted in Figure 4.36(a)), transferring low-momentum flows generated by the actuators outwards to region above the surface, which may reduce the velocity in flows away from the wall. On the contrary, the counter-rotating streamwise vorticity in Phase III and IV energises the flow near the wall by transferring the high momentum from the free stream flow to the surface. Meanwhile, the different rotation direction in the Phase II and Phase III (or Phase I and Phase IV) enhances the shear stress in the interfaces of structures with different rotation directions. During the vertical oscillating velocity $v > 0$, Figure 4.36 (b) shows a similar but opposite procedure in vortices rotations.

The turbulence structures shown above are observed to be similar to the flow control with tabs in Park *et al.* [2007] in some extent. The common feature is that each actuator
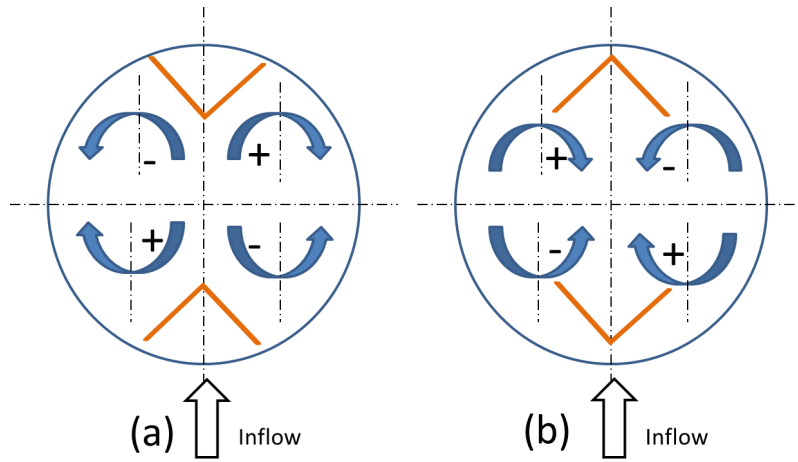
Figure 4.36: Schematic of the flow control. (a) During the vertical oscillating velocity $v < 0$. (b) During the vertical oscillating velocity $v > 0$

or tab introduces counter-rotating vortices, moving downwards. There are two main different aspects. Firstly, the vortex generated by tabs keeps the rotating directions, while the oscillation of actuators introduce the shift of rotation directions, as a result, the generated vortices with opposite directions pile up along the streamwise direction. A schematic of the differences can be seen from Figure 4.37. Secondly, the vortex generated by tabs is much stronger than that generated by the piezoelectric oscillation, thus for the latter, the generated counter-rotating vortices cannot be observed in the downstream flow. However, even without explicit observation, the rotating vortex affects the downstream momentum transfer, which will be analysed quantificationally in the next section.
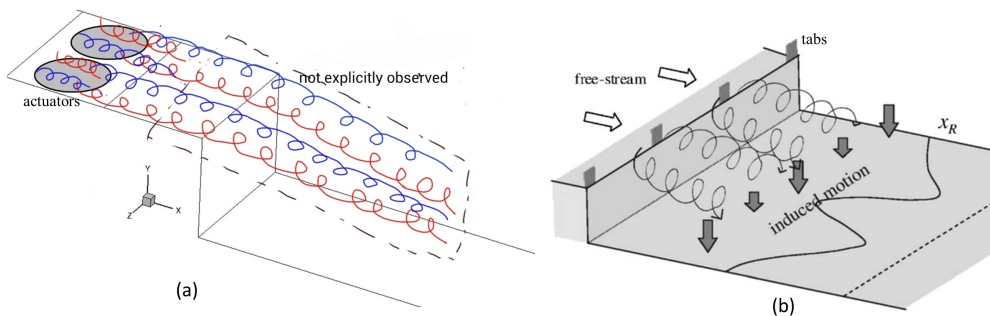
Figure 4.37: Schematic of the flow control. (a) Piezoelectric actuators in this study. (b) Passive flow control with tabs in Park *et al.* [2007]

4.3. Flow control with piezoelectric actuators in flow over the BFS (APL-UniMan)

4.3.4.3   Flow reattachment and skin friction

Experiments show a flow reattachment at $X_R^{\text{exp}} \approx 6.5H$ and a secondary recirculation at $X_{SR}^{\text{exp}} \approx 1.8H$ for the baseline flow. Figure 4.38(a) displays the time and spanwise averaged flow field with streamlines. The predicted reattachment of the baseline flow is at $X_R \approx 6.7H$, an over-prediction of about 3%, and the predicted secondary recirculation has a length of $1.2H$, which seems to be squeezed by the primary recirculation. Compared with experiments, simulation of the baseline flow provides a slightly longer reattachment point and a shorter secondary recirculation. A possible reason is that the high-ratio stretching grids (shown in Figure 4.20) hinder the mixing of the high-free stream flow to the recirculating low-momentum flow, thus the velocity near the wall cannot be accelerated. Nevertheless, generally speaking, the simulations provide reasonable primary and secondary recirculation. By contrast with the baseline flow, both the primary and the secondary recirculation in the flow control case OS1 slightly shrink, which are respectively $X_R \approx 5.8H$ and $X_{SR} \approx 1.0H$ (see the C_f profile shown in Figure 4.40). The centre of the primary recirculation decreases from $x/H \approx 3.4$ in the baseline flow to $x/H \approx 3.1$ in OS1.

(a)

(b)
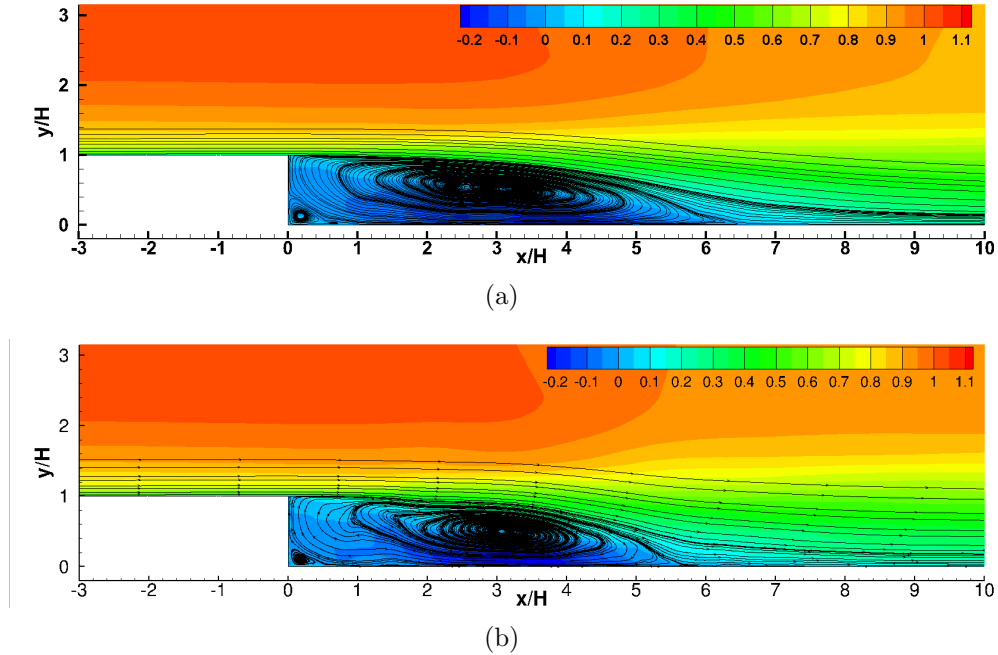
Figure 4.38: Time and spanwise averaged streamlines of the flow field. (a) the baseline flow and (b) OS1

Figure 4.39 displays the instantaneous skin friction. The spanwise distribution of C_f does not display a regular spanwise variation related to the actuators, just as the tabs did in Park *et al.* [2007]. This is due to the control velocity is too small to affect a large region.

Lack of regular C_f distribution along the span can also be derived from the nearly-uniform spanwise distribution of the instantaneous streamwise velocity, shown in Figure 4.33.

The coefficient of the skin friction, averaged both in time and in the spanwise direction, is given in Figure 4.40. For the baseline flow, there is a reduction of the skin friction on the step wall, followed by an increase near the step edge. A similar reduction (about 12%) is also observed in the validation case by Driver and Seegmiller [1985], but in this case the reduction is more serious (more than 20%). The reduction of the C_f in OS1 before the step separation is about 50%, which may be caused by the oscillating surface, resulting in the decrease of the streamwise velocity near the wall (see Figure 4.33).

For the baseline flow, the C_f at $-1H$ compares to the experiments very well, which are both around $C_f = 0.0022$. Therefore, the boundary layer properties before separation are comparable to the experimental boundary layer. Around $C_f = 0$, the control case OS1 shows a zigzag profile in spite of small fluctuations even with a long time average. Compared with the baseline flow, C_f of the control case OS1 has a larger valley value of the negative C_f at around $x/H = 4.0$, which corresponds to the reduced recirculation region observed from the streamlines. After the flow reattachment, the baseline flow and the control case OS1 show very similar recovered C_f. The study on C_f illustrates that the flow control with OS1 decrease the skin friction before flow separation, but the influence on the recirculation region and the recovered region is little, except for a slightly reduced reattachment.

(a)

(b)
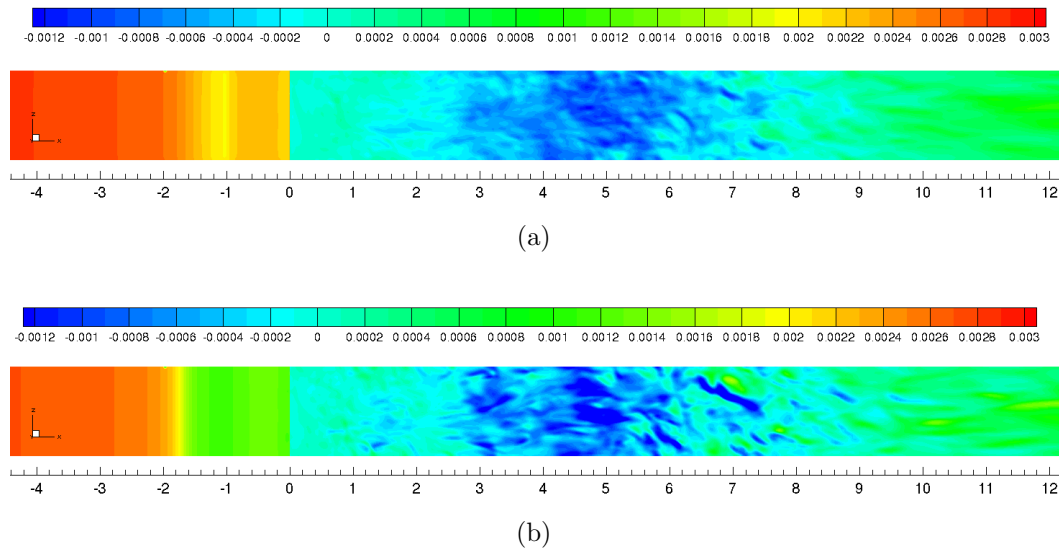
Figure 4.39: Contours of skin friction. (a) The baseline flow (b) OS1
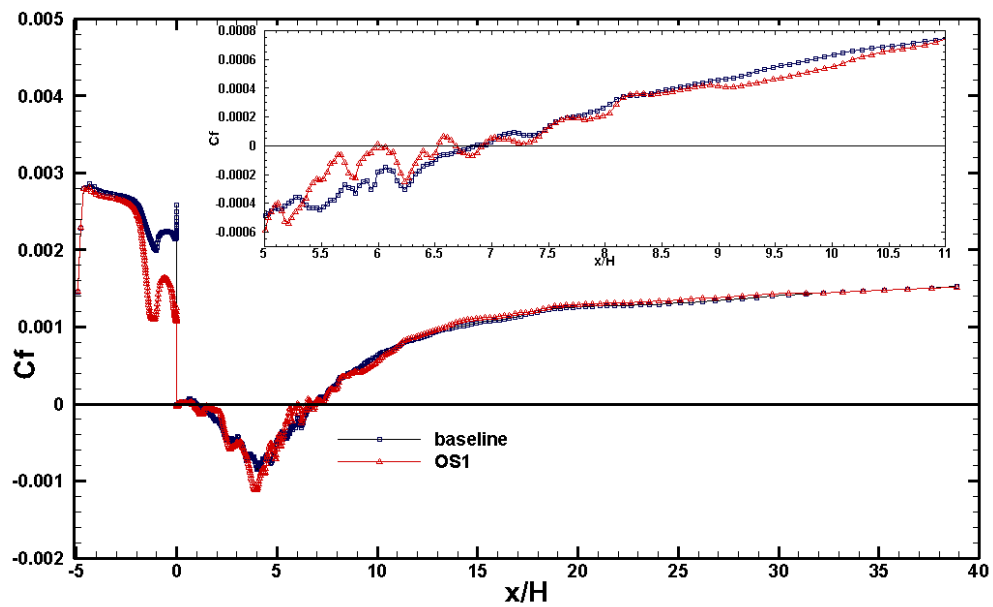
Figure 4.40: Time and spanwise averaged skin friction coefficient.

4.3.4.4   Velocity

Experimental data are only available for the baseline flow, and there are no any experimental measurements of the velocity and Reynolds stresses for the controlled flow. Therefore, only the baseline flow is compared with the experimental measurements to assess the reliability of the simulations.

Figure 4.41 compares the streamwise and the vertical velocity with the experimental data for the baseline flow. Corresponding to a slightly longer X_R in the simulation, the streamwise velocity is under-predicted in the near wall region. The vertical velocity gives a good comparison in the near wall region, and in the free flow region, it has some disparities.

(a)   (b)
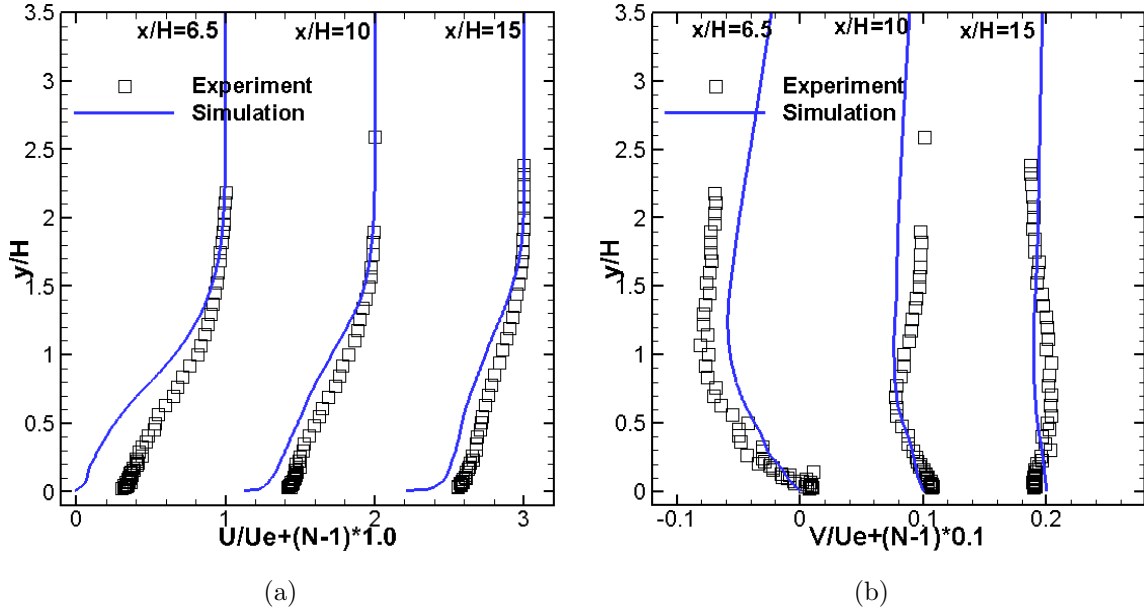
Figure 4.41: Time and spanwise averaged velocities. (a) The scaled streamwise velocity U/U_e. (b) The scaled vertical velocity V/U_e

For the flow control case OS1, the velocity varies in the spanwise direction. Figure 4.42 compares the streamwise velocity profiles with the baseline flow at $z = 0$ (middle of two adjacent actuators) and $z = 0.0225$ m (centre of the actuator). At upstream stations $x/H = -1.0$ and $x/H = 0$, the boundary layer velocity profile of the control case OS1 is quite similar to the baseline, and the differences concentrate on the near-wall region (too small to be shown in Figure 4.42), which corresponds a smaller skin velocity (See Figure 4.39). At the location of the centre of the actuator ($z = 0.0225$ m) shown in Figure 4.42(b), the mean velocity decreases slightly, especially from $x/H = 5.0$ to $x/H = 10.0$, implying the de-energisation of the recirculation region. At the middle of two adjacent actuators, shown in

4.3. Flow control with piezoelectric actuators in flow over the BFS (APL-UniMan)

Figure 4.42(a), from $x/H = 3.0$, the control case OS1 has a larger streamwise velocity than the baseline in the recirculation region. The acceleration of the mean streamwise velocity is more inclined to the bottom wall as flow moves downstream, resulting in a reduction of the reattachment. Interestingly, similar streamwise velocity changes are observed in flow control by tabs on a BFS (Park *et al.* [2007]), although in the flow control by tabs in Park *et al.* [2007], the generated streamwise vorticity is obviously stronger than the current actuators.

(a)

(b)
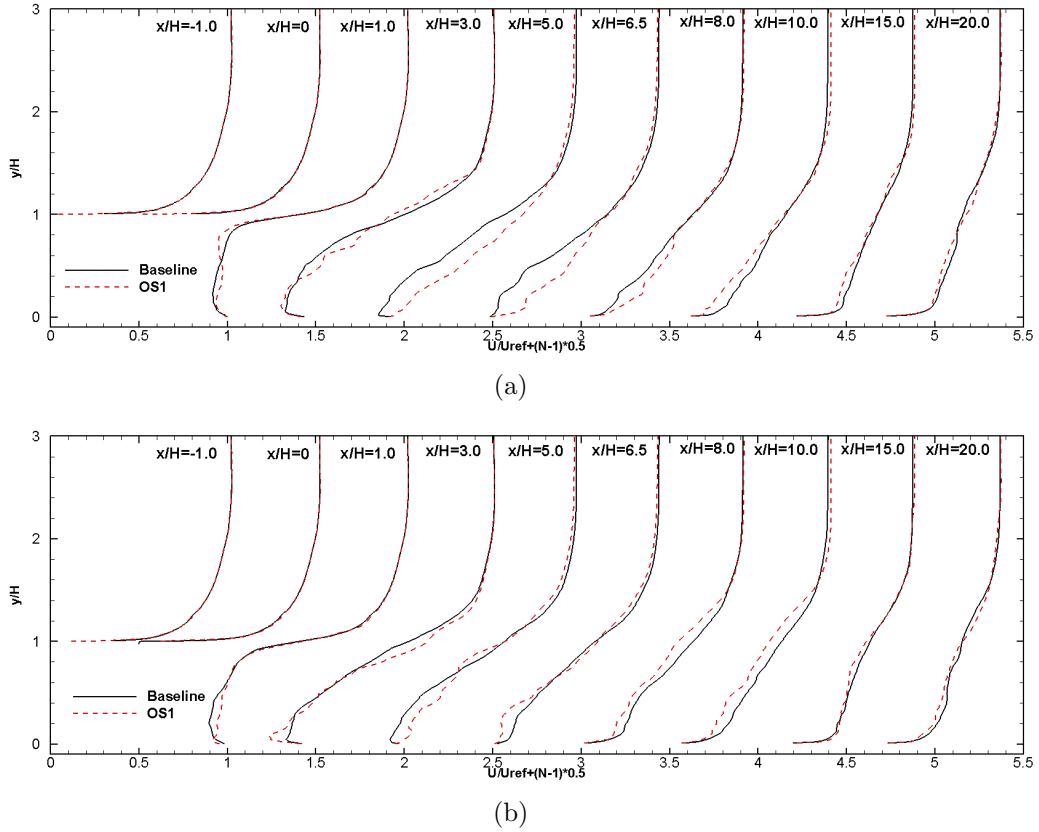
Figure 4.42: Time and spanwise averaged streamwise velocity. (a) at $z = 0$, (b) at $z = 0.0225$ m

Actually, the distribution of the streamwise velocity along the span in Park *et al.* [2007] and in the current study are very similar. Figure 4.43 compares the streamwise velocity along the span. At $x/H = 1.0$ near the step, there are no obvious changes of the controlled velocity. However, at $x/H = 3.0$ and $y/H = 1.0$, the streamwise profiles along the span show an acceleration behind the two actuators, and there is a deceleration in the region in-between two adjacent actuators. At $x/H = 5.0$, the two peaks behind the actuators merge to one at the middle of two adjacent actuators, which may imply that the generated streamwise vortices interact with each other and merged together from $x/H = 5.0$.

The variation of the streamwise velocity along the span indicates that even though the
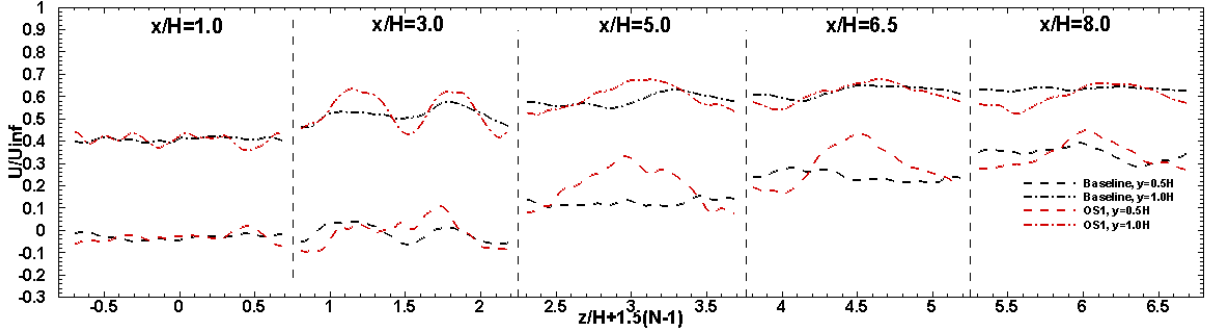
Figure 4.43: Time averaged streamwise velocity.

oscillating surface has a much smaller control magnitude and generates weak streamwise vorticity, the induced motion of pairs of rotating streamwise vortices changes the flow mixing in the downstream flow.

4.3.4.5 Reynolds stress

For the baseline flow, flow fluctuations of the streamwise and vertical velocities are compared with the experiments in Figure 4.44. Figure 4.44(a) shows an under-prediction of the streamwise velocity fluctuations near the wall and an over-prediction in the free flows at $x/H = 6.5$ and $x/H = 10.0$. The over-prediction of the Reynolds stresses in the mixing layer seems to be a common issue suffered by hybrid RANS/LES methods (Gritskevich *et al.* [2012]; Sainte-Rose *et al.* [2008]; Shur *et al.* [2008]). Gritskevich *et al.* [2012] studied the IDDES and DDES based on the SST model in a BFS case, which both over-predict the Reynolds stresses in the mixing layer (around $y/H = 1.0$). Reasons for the over-prediction are still under investigated, and there is no effective method to correct this issue. At $x/H = 15.0$, where the turbulent boundary layer is recovered, both the streamwise and vertical flow fluctuations are in good agreement with the experimental data. Overall, both the streamwise and the vertical velocity fluctuations are acceptably good, compared with the experimental measurements.

The profiles of the Reynolds normal stress $\langle u'u' \rangle / U_{\mathrm{ref}}^2$ at different streamwise locations are shown in Figure 4.45. (The Reynolds stress displayed here is the sum of the resolved and modelled Reynolds stresses.) Upstream of the step, both at $z = 0$ and $z = -0.0225$ m, the control case OS1 has much less Reynolds normal stress $\langle u'u' \rangle / U_{\mathrm{ref}}^2$ than the baseline flow. At $z = 0$, middle of two adjacent actuators, the Reynolds normal stress $\langle u'u' \rangle / U_{\mathrm{ref}}^2$ increase near the bottom wall in the recirculation region ($x/H < 6.5$). At $x/H = 1.0$ and $x/H = 3.0$, it has a slight increase in the mixing layer, and then there is an obvious decrease in the mixing layer from $x/H = 5.0$ to $x/H = 8.0$. The decrease of the Reynolds

4.3. Flow control with piezoelectric actuators in flow over the BFS (APL-UniMan)
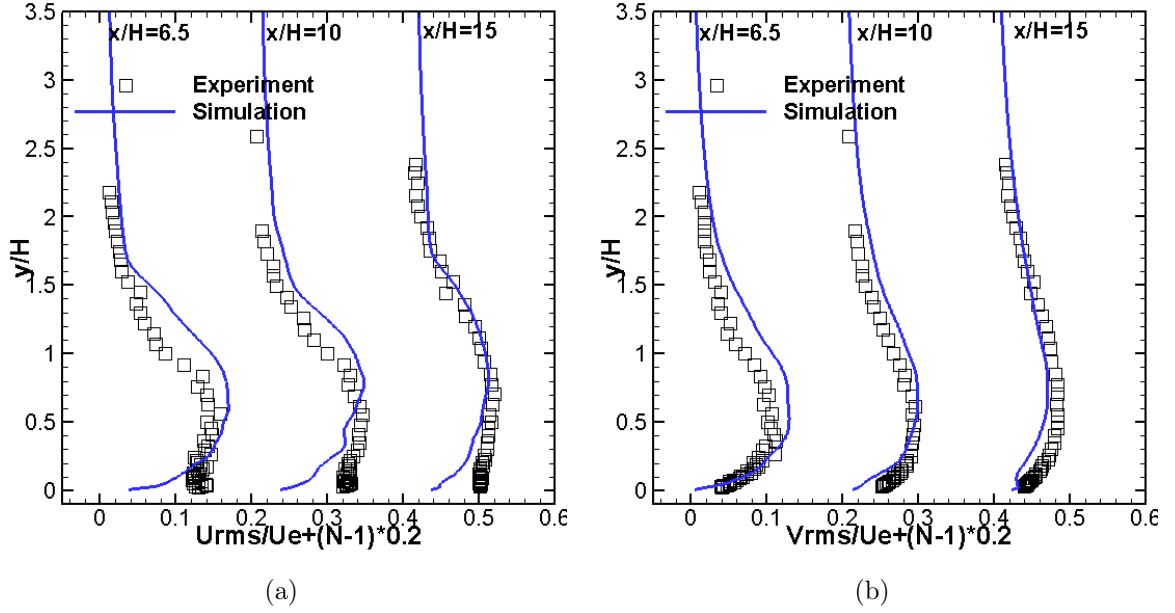
Figure 4.44: Time and spanwise averaged flow fluctuations. (a) The scaled streamwise velocity fluctuations U_{rms}/U_e. (b) The scaled vertical velocity fluctuations V_{rms}/U_e

stress may be related to the acceleration of the streamwise velocity. This may indicate that the interaction between the shifting counter-rotating vortices generated by the two adjacent actuators tends to bend the momentum transfer towards the wall. As a result, the near-wall region has larger fluctuations, and leaves smaller fluctuations away from the wall. At $z = -0.0225$ m, where the centre of one actuator locates, the Reynolds normal stress $\langle u'u'\rangle/U_{\mathrm{ref}}^2$ decrease compared with the baseline flow near the bottom wall, while in the mixing layer, $\langle u'u'\rangle/U_{\mathrm{ref}}^2$ does not differ a lot from the baseline flow except for $x/H = 3.0$, where there is a rapid increase around $y/H = 1.0$. For the section $z = -0.0225$ m, at the centre of the actuator, the counter-rotating vortices generated by a single actuator tends to move away from each other. Actually, the vortices pairs generated by two adjacent actuators seem to have stronger interaction than those generated by a single actuator, as shown in Figure 4.34. This may result in the stronger control effect at the in-between region of the two adjacent actuators than those regions behind the actuators. This may explain the reason why both the velocity and the Reynolds stresses has more significant changes at $z = 0$ than at $z = -0.0225$ m. The trends of the distribution of the Reynolds normal stresses in these two sections are also similar to the BFS with a tab flow control in Park *et al.* [2007]. It is noted that the tab in Park *et al.* [2007] has a height of $0.1H$, while the current maximum displacement of oscillation is only about $0.0147\%H$. Besides, the vortices generated tabs are stronger than those generated by the motion of oscillation. Actually, this similarity may

come from the fact that the regular shifting rotation of the counter-rotating vortices seem to enhance the mixing procedure.

(a)

(b)
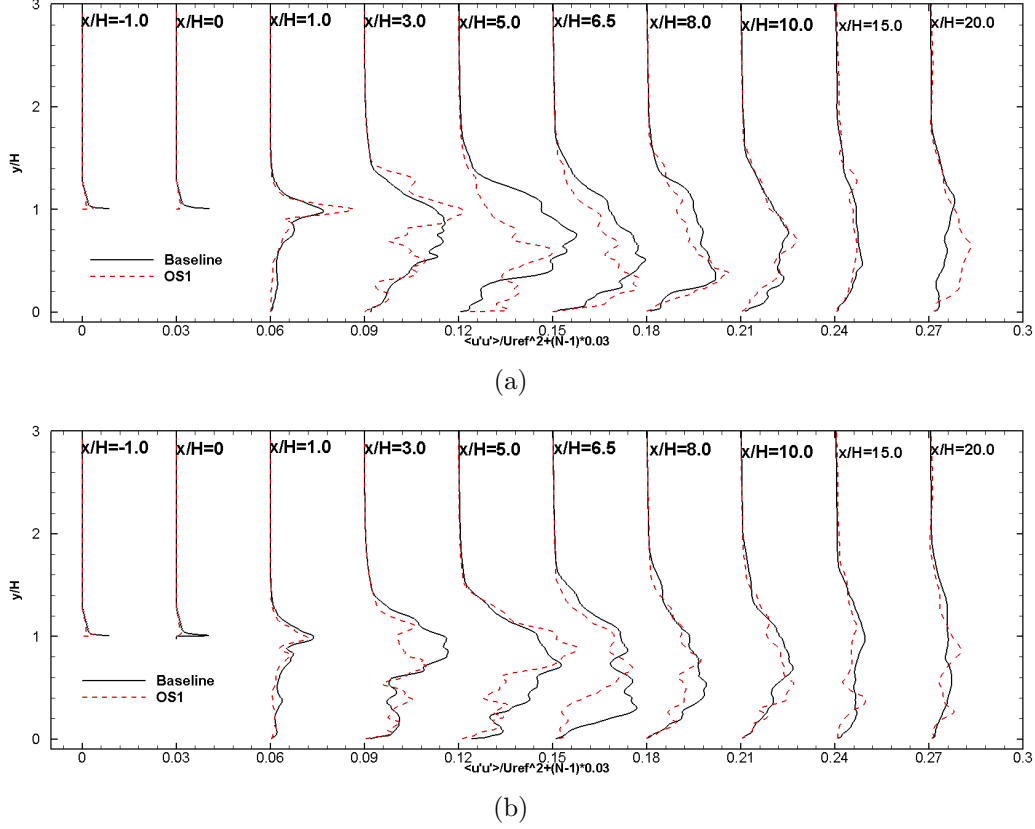
Figure 4.45: Reynolds stress $\langle u'u' \rangle / U_{\text{ref}}^2$. (a) at $z = 0$, (b) at $z = 0.0225$ m

Figure 4.46 displays the distribution of $\langle u'u' \rangle / U_{\text{ref}}^2$ at the mixing layer $y/H = 1.0$ along the span. Even with such a long time average, there are still some irregularities along the span. Nevertheless, the affected trends by the motion of oscillation can still be clearly observed. In the secondary recirculation region ($x/H < 3.0$), the middle of two adjacent actuators has a peak of $\langle u'u' \rangle / U_{\text{ref}}^2$, while the centre of each actuators has a valley of $\langle u'u' \rangle / U_{\text{ref}}^2$. This is caused by structures of the generated vortices shown in Figure 4.35, where the streamwise vortices generated by one actuator depart from each other and grows towards the edge of the actuators. The interaction between these counter-rotating vortices generated by one actuator seems to only last to $x/H = 3.0$, and further downstream, the interaction between the adjacent vortices generated by two adjacent actuators just overwhelms it. Actually, the adjacent vortices generated by two adjacent actuators moves towards each other, finally merge with each other, and form a large valley of $\langle u'u' \rangle / U_{\text{ref}}^2$ after $x/H = 5.0$. This indicates that the interaction of the weak vortex generated by the motion of oscillation manipulates

the downstream Reynolds stress, and after a distance, the merging effect of two adjacent vortices generated by two adjacent actuators becomes strong and finally results in a reduced flow reattachment.
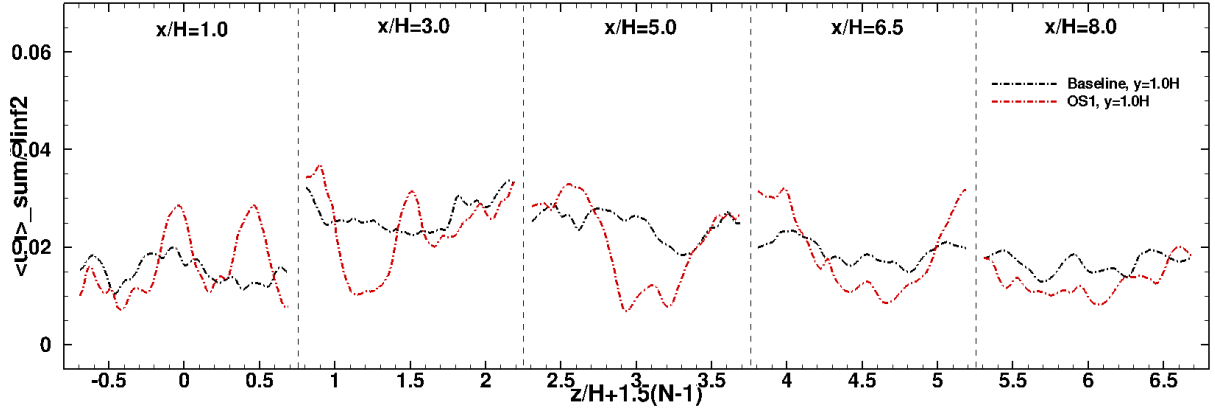
Figure 4.46: Reynolds stress $\langle u'u'\rangle/U_{\mathrm{ref}}^2$ in the cross sections.

Figure 4.47 displays the Reynolds normal stress $\langle v'v'\rangle/U_{\mathrm{ref}}^2$. The influences of the piezoelectric actuators on the Reynolds normal stress $\langle v'v'\rangle/U_{\mathrm{ref}}^2$ are quite similar to $\langle u'u'\rangle/U_{\mathrm{ref}}^2$. Upstream of the step, the control case OS1 has less Reynolds normal stress $\langle v'v'\rangle/U_{\mathrm{ref}}^2$ than the baseline flow. For the region near the step $x/H < 3.0$, $\langle v'v'\rangle/U_{\mathrm{ref}}^2$ increases at the middle of two adjacent actuators ($z/H = 0$), and it decreases in the centre of the actuator ($z = 0.0225$ m). Further downstream from $x/H = 5.0$, there is a deficiency of $\langle v'v'\rangle/U_{\mathrm{ref}}^2$ at $z/H = 0$, and an increase at $z = 0.0225$ m, just the same as $\langle u'u'\rangle/U_{\mathrm{ref}}^2$. What is different from $\langle u'u'\rangle/U_{\mathrm{ref}}^2$ is the profiles of $\langle v'v'\rangle/U_{\mathrm{ref}}^2$ do not show obvious changes near the wall. Figure 4.48 shows the spanwise distribution of the Reynolds normal stress $\langle v'v'\rangle/U_{\mathrm{ref}}^2$ in the mixing layer. Similar to the Reynolds normal stress $\langle u'u'\rangle/U_{\mathrm{ref}}^2$, at the near-step region ($x/H < 3.0$), there is a shape of "W" for the Reynolds normal stress $\langle v'v'\rangle/U_{\mathrm{ref}}^2$, with peak values in the middle of two adjacent actuators, and with valley values in the centre of each actuator. At $x/H = 5.0$, a shape of "V" is formed in the distribution of $\langle v'v'\rangle/U_{\mathrm{ref}}^2$, which valley values at the middle of two adjacent actuators. These trends are all similar to $\langle u'u'\rangle/U_{\mathrm{ref}}^2$. The different shapes of distribution may be the different interactions between vortices generated by a single actuator or by two adjacent actuators. After the reattachment, the Reynolds stress $\langle v'v'\rangle/U_{\mathrm{ref}}^2$ does not show the affected shape of spanwise distributions, while for the Reynolds stress $\langle u'u'\rangle/U_{\mathrm{ref}}^2$, it is from $x/H = 8.0$ that the variations along the span become small.

Figure 4.49 and Figure 4.50 display the spanwise Reynolds normal stress $\langle w'w'\rangle/U_{\mathrm{ref}}^2$. The Reynolds normal stress $\langle w'w'\rangle/U_{\mathrm{ref}}^2$ of the control case OS1 has similar trends of altering

(a)

(b)
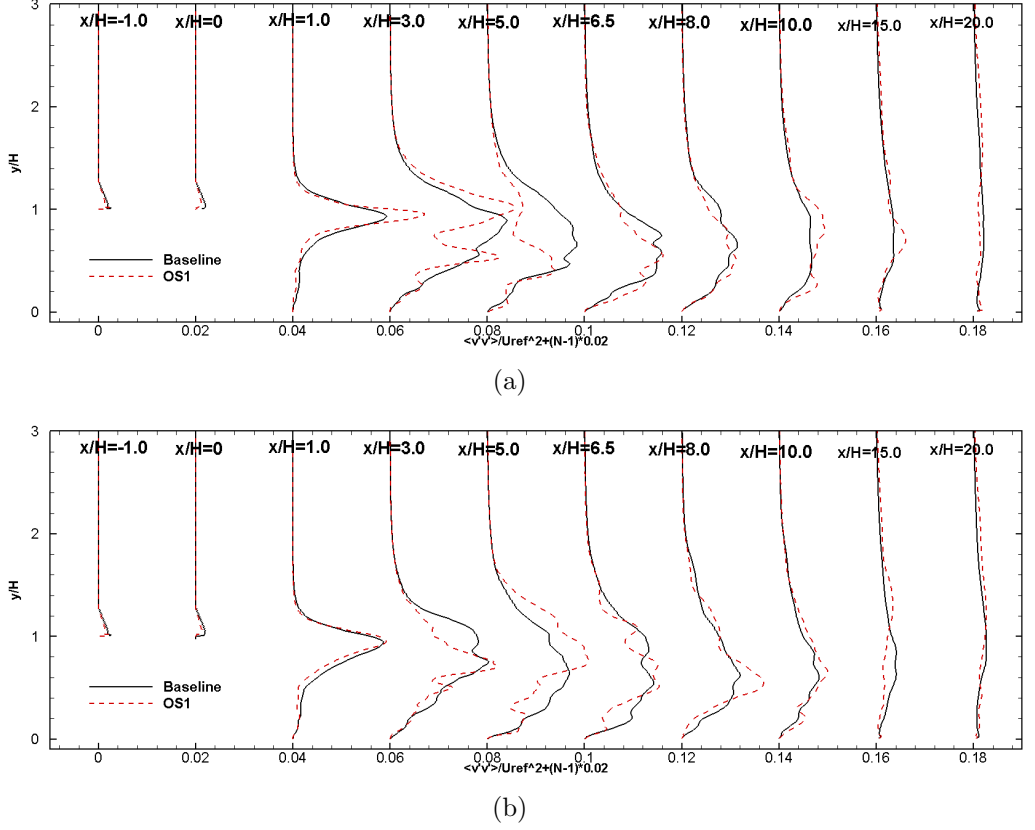
Figure 4.47: Reynolds stress $\langle v'v' \rangle / U_{\text{ref}}^2$. (a) at $z = 0$, (b) at $z = 0.0225$ m
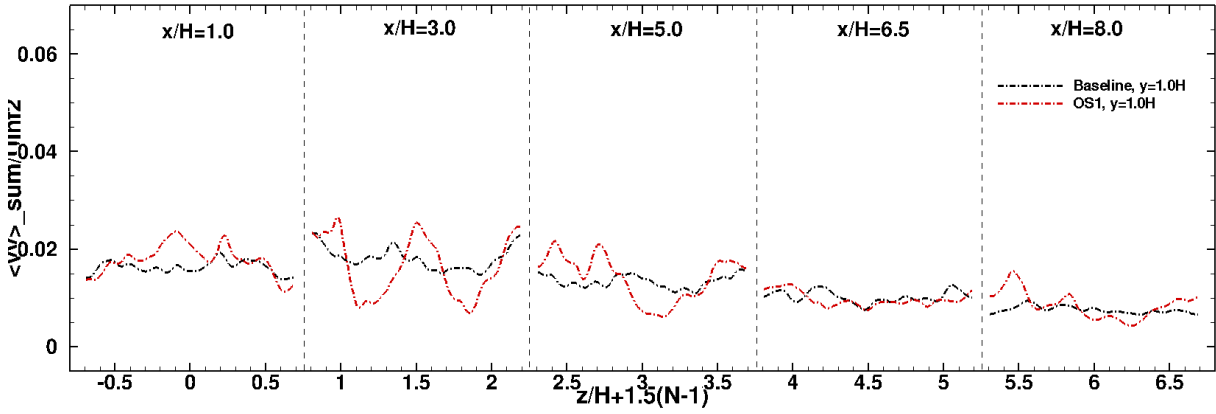
Figure 4.48: Reynolds stress $\langle v'v' \rangle / U_{\text{ref}}^2$ in the cross sections.

to the other two normal stress. However, although the generated vortex are primarily the streamwise vorticity, the control effect on $\langle w'w' \rangle / U_{\text{ref}}^2$ is weaker, compared with $\langle u'u' \rangle / U_{\text{ref}}^2$ and $\langle v'v' \rangle / U_{\text{ref}}^2$. This is related with the much smaller spanwise velocity introduced by the motion of oscillation shown in Figure 4.33.

The Reynolds shear stress $\langle u'v' \rangle / U_{\text{ref}}^2$ is shown in Figure 4.51 and Figure 4.52. The

4.3. Flow control with piezoelectric actuators in flow over the BFS (APL-UniMan)

(a)

(b)
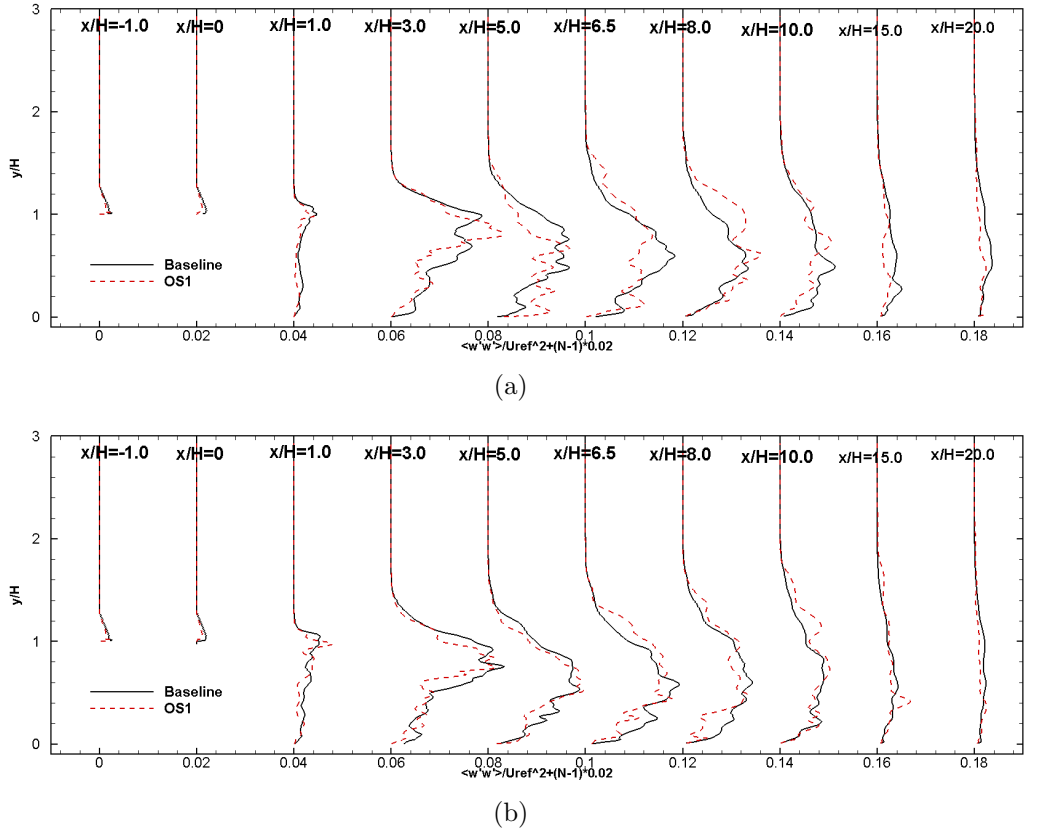
Figure 4.49: Reynolds stress $\langle w'w' \rangle / U_{\mathrm{ref}}^2$. (a) at $z = 0$, (b) at $z = 0.0225$ m
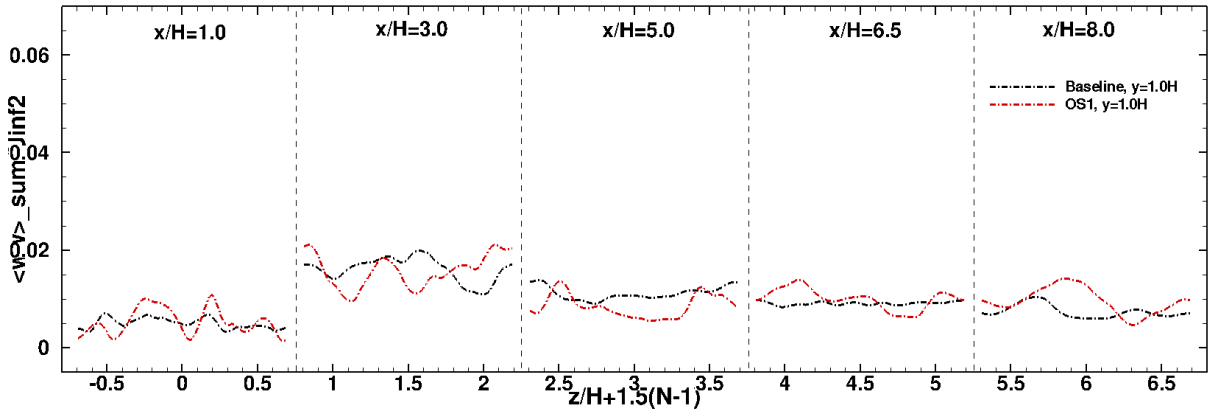
Figure 4.50: Reynolds stress $\langle w'w' \rangle / U_{\mathrm{ref}}^2$ in the cross sections.

shapes of the Reynolds shear stress $\langle u'v' \rangle / U_{\mathrm{ref}}^2$ in the distribution along the span seem to be opposite of the Reynolds normal stresses. At $x/H = 3.0$, the shape of $\langle u'v' \rangle / U_{\mathrm{ref}}^2$ looks like "M", and the peaks occur in the centres of the actuators, and the valley values locates at the middle of two adjacent actuators. At $x/H = 5.0$, it is a shape of "Λ", with low values near the middle of two adjacent actuators.

(a)

(b)
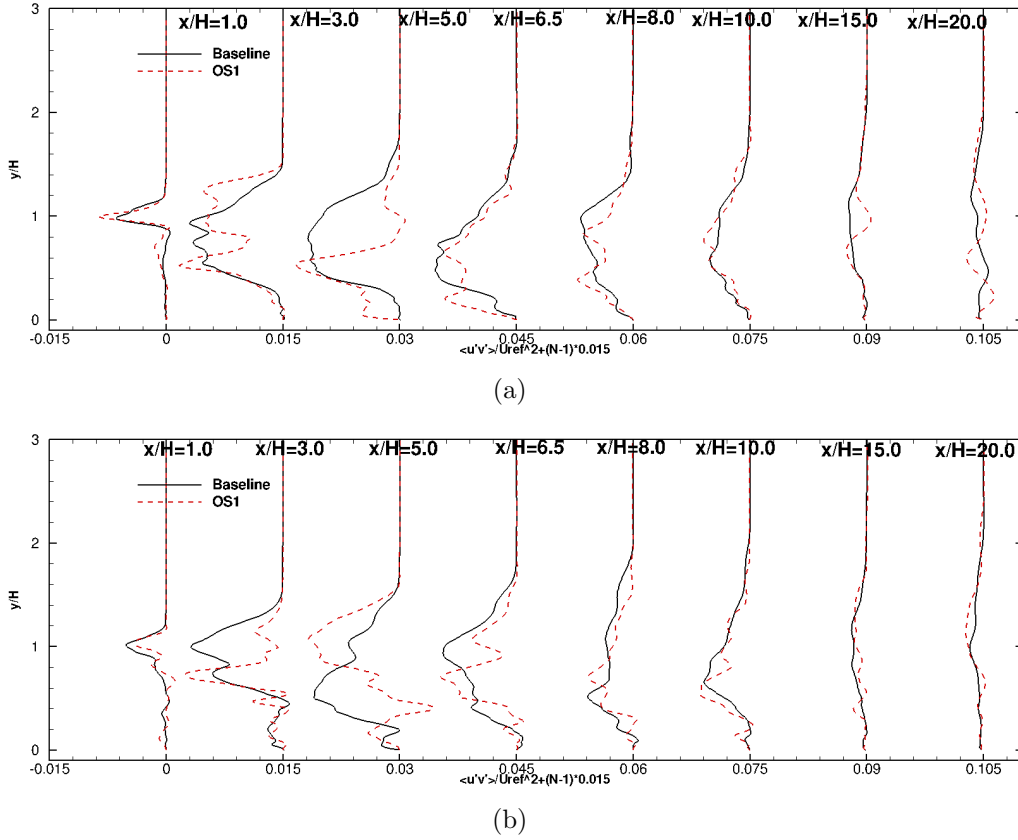
Figure 4.51: Reynolds stress $\langle u'v' \rangle / U_{\text{ref}}^2$. (a) at $z = 0$, (b) at $z = 0.0225$ m
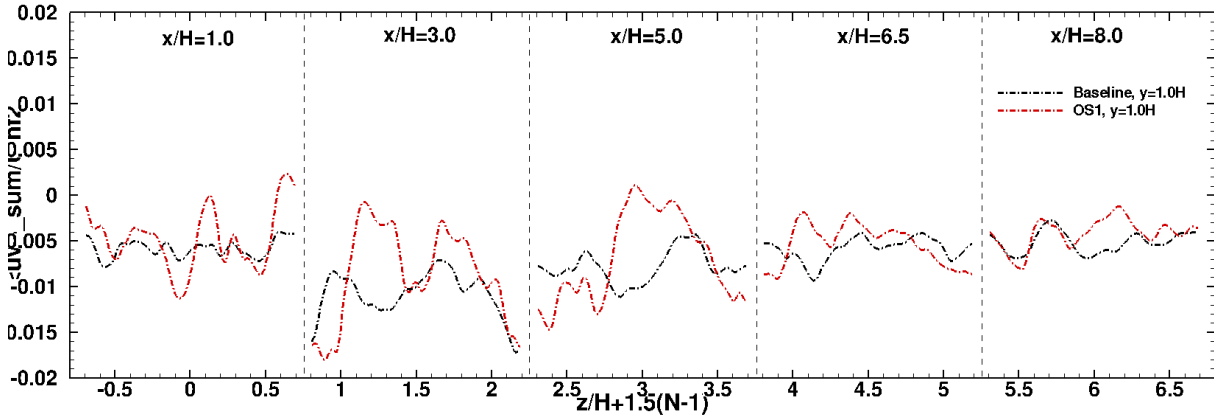
Figure 4.52: Reynolds stress $\langle u'v' \rangle / U_{\text{ref}}^2$ in the cross sections.

For the recovery region $x/H > 10.0$, there are few differences for these Reynolds stresses between the control case OS1 and the baseline. The high Reynolds stresses for both of these two cases damp out in the recovery region. The main differences come from the recirculation region.

Conclusively, the oscillating surface on the step introduces variations of Reynolds stresses

in the spanwise direction. Although the vortices near the oscillating surface, generated by the four phases, has opposite counter-rotating directions, when these generated vortices interacts with the flow recirculation in the downstream flow, a preferred rotation direction is observed from profiles of the stream velocity and the Reynolds stress. A schematic of shapes of the streamwise velocity along the span, and the preferred rotating directions (deduced from the velocity shapes) of the streamwise vortices are shown in Figure 4.53. When the piled vortices with opposite rotating directions generated by a single actuator interact with the clockwise spanwise vortices near the step, the main trend near the step seems to transfer the high-momentum flow towards the wall, resulting in a peak value of the velocity and Reynolds shear stress near the centre of each actuator. The energised flow suppresses the flow fluctuations, and then the Reynolds normal stresses have opposite shapes of the spanwise distribution, compared with the streamwise velocity. When flow goes down to around $x/H = 5.0$, the interaction in the mixing layer becomes more complicated, which may include the generated streamwise vortices, the interaction between the generated vortices and the spanwise vortices by the step, and the interaction with the recirculation flows. The procedure of the interaction is very sophisticated, but the dominant interaction seems to be the merging of vortices generated by two adjacent actuators. As a result, the streamwise velocity and the Reynolds shear stress have peak values in-between two actuators, while the Reynolds normal stresses has valley values. One issue to be mentioned is in the current study, even though there is a "Λ" shaped streamwise velocity in the mixing layer near the reattachment, the skin friction or the reattachment lines does not show a clear shape of "Λ", which is observed in the tab flow control in Park *et al.* [2007].
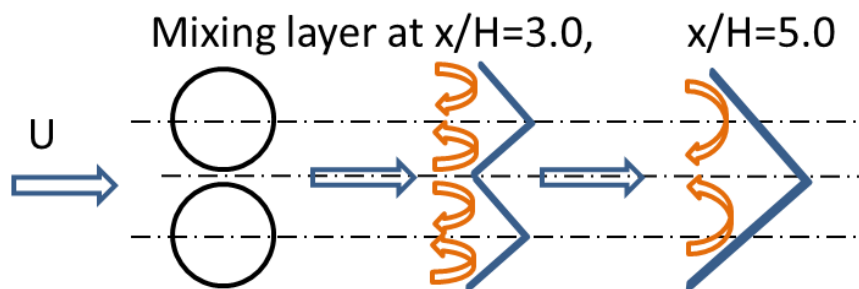
Figure 4.53: Schematic of the flow statistics in the mixing layer.

4.3.5 Summary

The validation of the baseline flow shows a good comparison in both the first order and second order statistics with the available experimental results. The study on the energy

spectra in simulation also gives good agreements with the experiments for the baseline flow.

The comparison of the control case OS1 and the baseline flow shows some results as follows.

(1) The time and space streamlines and the C_f distribution show that the control case OS1 has a reduction of the primary recirculation region from $6.8H$ in the baseline flow to $6.0H$. Although C_f shows a near-zero value from $x/H = 6.0$, there is a zigzag shape until $x/H \approx 6.5$.

(2) Power spectral density analysis of the pressure signals near the reattachment in the baseline flow shows a very similar Strouhal number to the experimental measurement. Compared with the baseline flow, the control case OS1 has a slightly higher Strouhal number peak in the mixing layer near the step. The control frequency cannot be extracted from the PSD of the pressure signals.

(3) Streamwise vortices with different counter-rotating directions are generated with the motion of oscillation, and these vortices pile up to move downstream, and interact with the downstream recirculating flow structures. The counter-rotating vortices generated by a single actuators have a trend to depart from each other and their interaction with the shear layer near the step ($x/H < 3.0$) tends to draw high-momentum flow inwards. Further downstream, the interaction of vortices generated by two adjacent actuators seems to overwhelm the interaction in a single actuator. The merging of the adjacent vortices energises the flow in-between two adjacent actuators. In these energised flow, the three Reynolds normal stresses are suppressed.

4.4 An exploration on the control parameters of oscillating surface

4.4.1 Introduction

The simulation of flow control OS1 shows that the control effect on the reattachment is limited due to the small control magnitude. (The maximum control velocity in the control case OS1 is only 0.04% of the reference velocity.) In order to enhance the interaction between the generated vortices with the shedding shear layer, oscillating surface flow control with higher control velocities is simulated as an exploring study.

The same mesh, boundary conditions, numerical schemes, turbulence modelling and the other numerical set-up are used to explore the influences of the control velocity in the oscillating surface. The position of the actuators is also fixed, as described in the above

section. The only variations are the three parameters, control amplitude, control velocity and control frequency, only two of which are independent. Herein, the frequency and velocity are chosen to be the two independent control parameters. The control cases OS3, OS4 and OS5 with the same control frequency are compared to investigate the influences of the control velocity amplitude, and the velocity amplitude at the centre of the circular oscillating surface are 5 m s^{-1} ($= 1/3U_{\mathrm{ref}}$), 10 m s^{-1} ($= 2/3U_{\mathrm{ref}}$) and 15 m s^{-1} ($= U_{\mathrm{ref}}$).

It is noted that these control cases are simulated to provide an exploring study on the oscillating surface control of BFS flow, which are irrespective of physical realizability by devices. Besides, because of the large amount of control parameters, it would be unrealistic to perform optimal configurations, and control optimization is out of scope of this thesis.

4.4.2 Results and discussion on influence of velocity amplitude

4.4.2.1 The motion of oscillation

One period of the oscillation in the flow control case OS3 is studied to investigate the flow control mechanisms. The probed velocity and displacement at the centre of an actuator during a control period are plotted in Figure 4.54. Seven time points with a time interval of 5×10^{-4} s circled in Figure 4.54 are investigated.
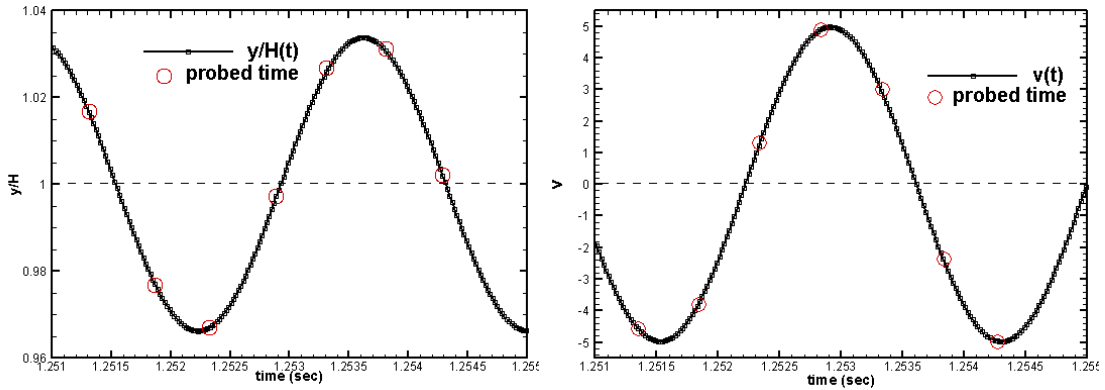
Figure 4.54: Time-dependent motion of oscillation in one oscillating period of the control case OS1. Left: displacement of the apex of the surface. Right: vertical velocity on the apex of the surface. (The probed location and velocity are recorded every other time step.)

Figure 4.55 shows the instantaneous streamwise, vertical and spanwise velocities on the first cell above the wall at the probed seven time points in the flow control case OS3. In the study of the flow control OS1, it is observed that the affected streamwise and vertical velocities are in the same order, but the spanwise velocity is much smaller than the other velocity components. However, with the control velocity magnitude of 5 m s^{-1} in OS3,

the three affected velocities are of the same order of magnitude, as shown in Figure 4.55. Similar to the control case OS1, the vertical velocity v displays a periodicity following the given control frequency. Different from the control case OS1, the spanwise velocity does not change directions during the control period. Each actuator produces a pair of "kidney-type" region with high spanwise velocity gradients. This pair of regions locates in the left and right side of the centre line of the actuator in the streamwise direction, and this pair of regions has spanwise velocity with opposite directions away from each other. A schematic of the spanwise velocity distribution above the actuator is shown in Figure 4.56 (b). For the streamwise velocity, the affected region is divided by the centreline of the actuator in the spanwise direction into two regions, which have streamwise directions towards each other, as demonstrated in Figure 4.56 (a). In spite of not as distinct as the vertical velocity, the magnitudes of the streamwise and spanwise velocity also display some cyclical variations. The magnitudes are slightly smaller with a smaller gradient during the period with the negative vertical velocity and slightly larger with a higher gradient during the period of the positive vertical velocity. Overall, the variations of the streamwise and spanwise velocity in one period are totally different for the control case OS1 and OS3. Figure 4.55 illustrates that when the oscillating velocity goes up to the same order of the freesteam velocity, the interactions between the vertical oscillating velocity and the incoming streamwise velocity produce a quasi-steady state of the streamwise and spanwise velocity components, which both have opposite velocity directions, and are respectively towards and away from each other.

Figure 4.57 display the instantaneous three vorticity Ω_x, Ω_y and Ω_z at the probed seven time points during one control period. The three vorticity components all keep the same rotation directions during the process of the actuator oscillation, and the magnitudes also do not have significant changes. With the quasi-steady streamwise and spanwise velocity shown in Figure 4.55, these quasi-steady vorticity components are anticipated. The quasi-steady distributions of the affected velocities influence the rotation directions of different vorticity components. For the streamwise vorticity Ω_x, the actuator generates a pair of counter-rotating vortices apart from each other. For the vorticity Ω_y, the actuator generates two pairs of vortices. The pair of primary vortices are counter-rotating towards each other, while the secondary pair of vortices are embedded by the primary vortices with different rotation directions. The spanwise vorticity Ω_z displays two pairs of co-rotating vortices (left and right) above the wall at $x/H = -0.5$. The near-wall pair co-rotates in the direction of z, and the other pair is just above the near-wall pair and co-rotates in the direction of $-z$. The near-wall vortices and the vortices above them form counter-rotating vortices (up and
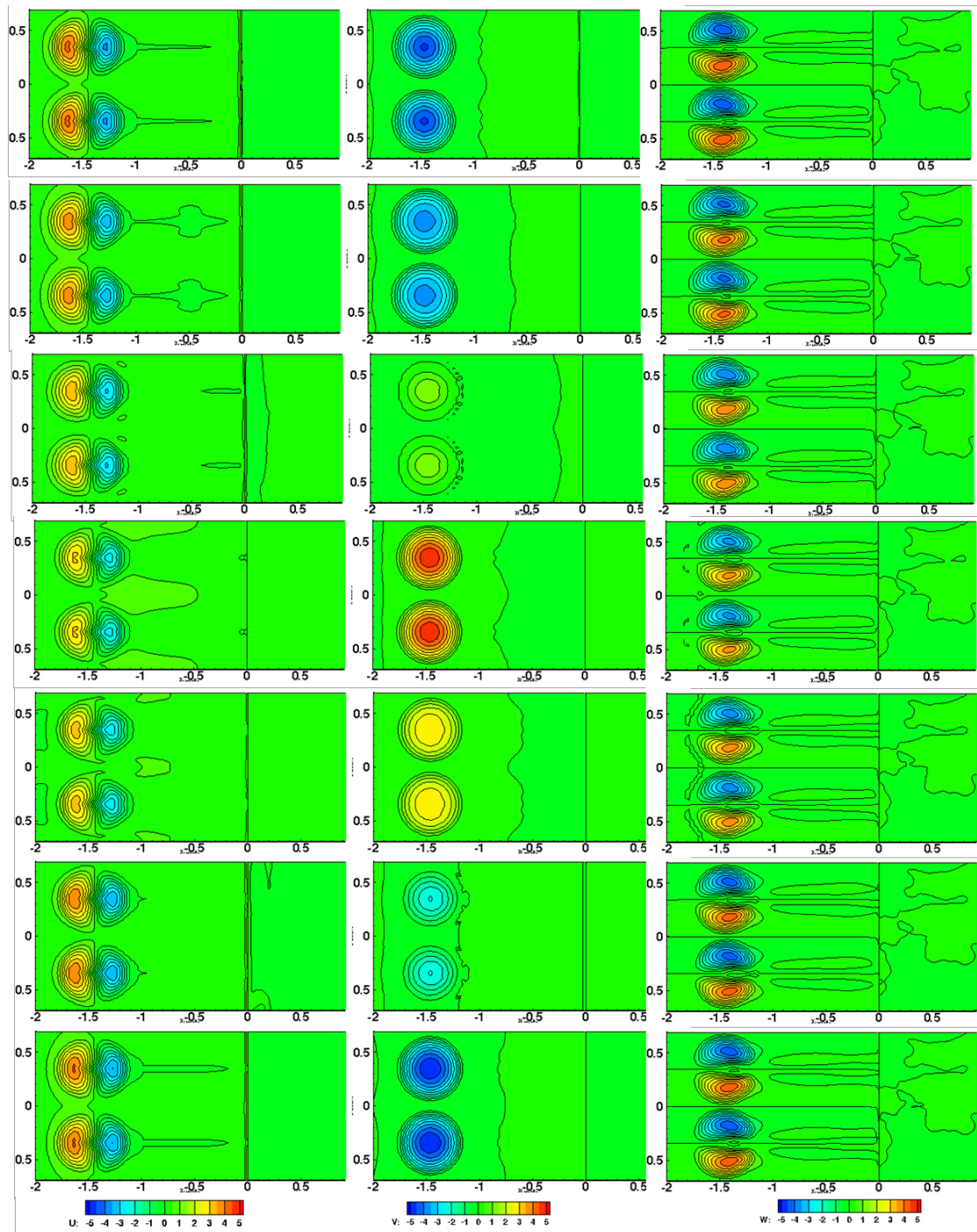
Figure 4.55: Instantaneous velocity at the first cell above the wall in one control period. Left column: streamwise velocity u. Middle column: vertical verlocity v. Right column: spanwise velocity w. The phase angles from top to bottom follow the time point circled in Figure 4.54.
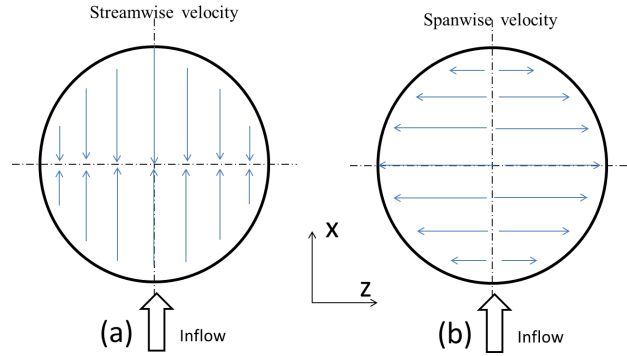
Figure 4.56: Schematic of the velocity distribution on the first layer of cells above the actuators. (a) Schematic of the streamwise velocity. (b) Schematic of the streamwise velocity.

down).
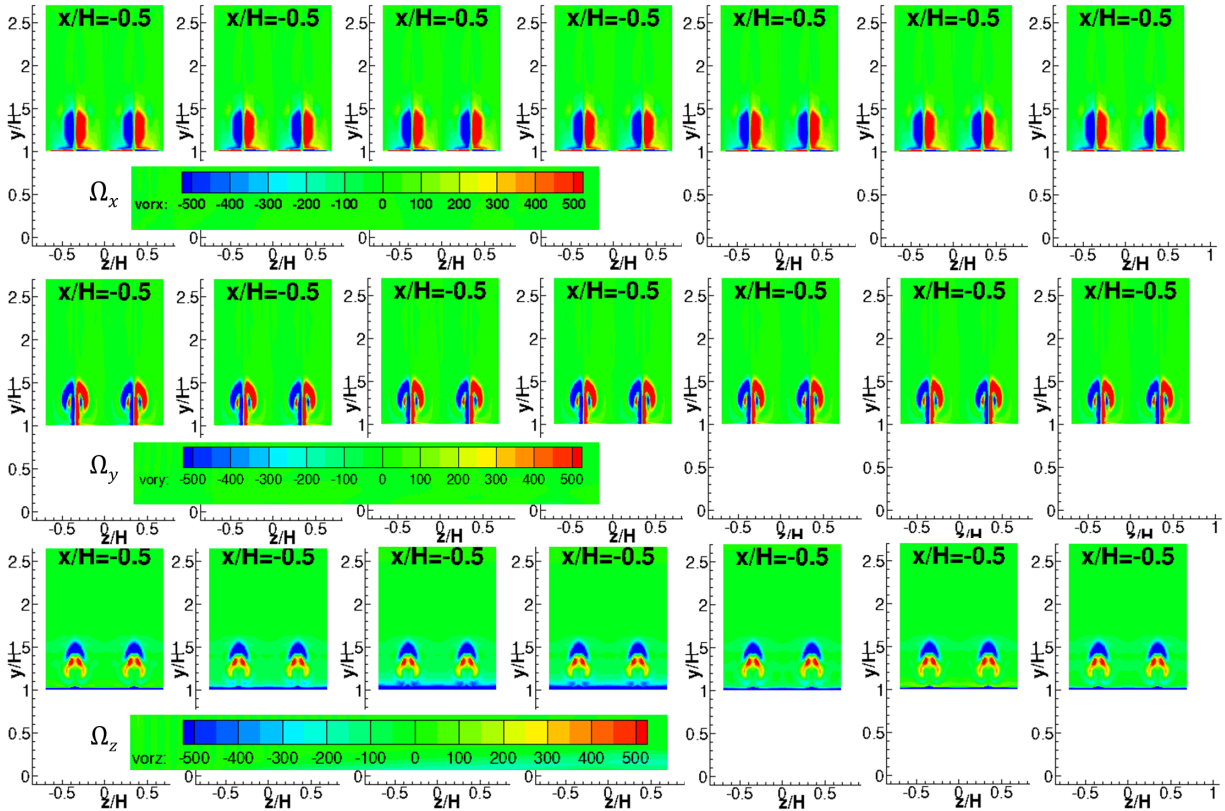
Figure 4.57: Instantaneous vorticity contours at $x/H = -0.5$ in one control period. The phase angles from left to right follow the time point circled in Figure 4.54. The top row for the streamwise vorticity Ω_x, the middle row for the vorticity Ω_y and the bottom row for the spanwise vorticity Ω_z.

Conclusively, the oscillating surface of the piezoelectric actuators in the control case OS3

generates quasi-steady vortices near the wall upstream of the step.

4.4.2.2   Coherent vortices

As the vortices are quasi-steady near the wall upstream of the step, instantaneous vortices generated by different control parameters in OS3, OS4 and OS5 at arbitrary time points are compared. Figure 4.58 displays the iso-surface of the three vorticity near the actuators in the control cases OS3, OS4 and OS5. The generated vortices displayed by the streamwise vorticity Ω_x form a counter-rotating vortex pair, growing towards downstream, just like jets in cross flows (Fric and Roshko [1994]; Kolář *et al.* [2003]; Salewski *et al.* [2008]). Typical vortical structures of the jet in the crossow are shown in Figure 4.59. Besides these similarities, unlike the Ω_x structures in Salewski *et al.* [2008] with jets in cross flow, the current flow control case OS3, OS4 and OS4 all display another counter-rotating vortex pair attached on the wall upstream of the primary counter-rotating vortex pair, which is very thin and underneath the primary pair. These unique structures may be introduced by the motion of the oscillating surface. With a higher control velocity, the counter-rotating vortex pair becomes stronger at a higher angle and the diameter of the vortex tube also becomes larger. The structures presented by the vorticity Ω_y develop from the central region of the actuator, and no obvious structures are observed on the wall. Besides, the high control velocity in the case OS5 produces larger structures represented by the vorticity Ω_y, and the mixing in the vortex pair is enhanced. The spanwise vorticity Ω_z displays a pair of counter-rotating horseshoe vortices. With a higher control velocity, the counter-rotating horseshoe vortices become stronger. Nevertheless, when the control velocity goes up the same as the inflow velocity, bifurcate vortices with positive spanwise rotation are observed in the flow control case OS5.

Figure 4.60 displays the iso-surface of λ_2 criterion for the control cases OS3, OS4 and OS5. There are some common features of the generated vortices by the oscillating surface and jets. By comparing the structures in Figure 4.60 and the jets structures in Figure 4.59, the vortices generated by the oscillating surface and the jets have these typical flow structure, which are the jet shear-layer vortices, the counter-rotating vortex pair and the horseshoe vortices near the wall. A typical turbulence structure generated by jets also includes wake vortices connecting the counter-rotating vortex pair to the turbulent boundary layer flow, however these types of vortices are not observed in the control cases. The reason may be that the magnitude of the control velocity is less than the free stream velocity, and a majority of the cases with jets in cross flow have a jet velocity several times of the freestream velocity. Due to the same reason, the interaction between the counter-rotating vortex pair is very
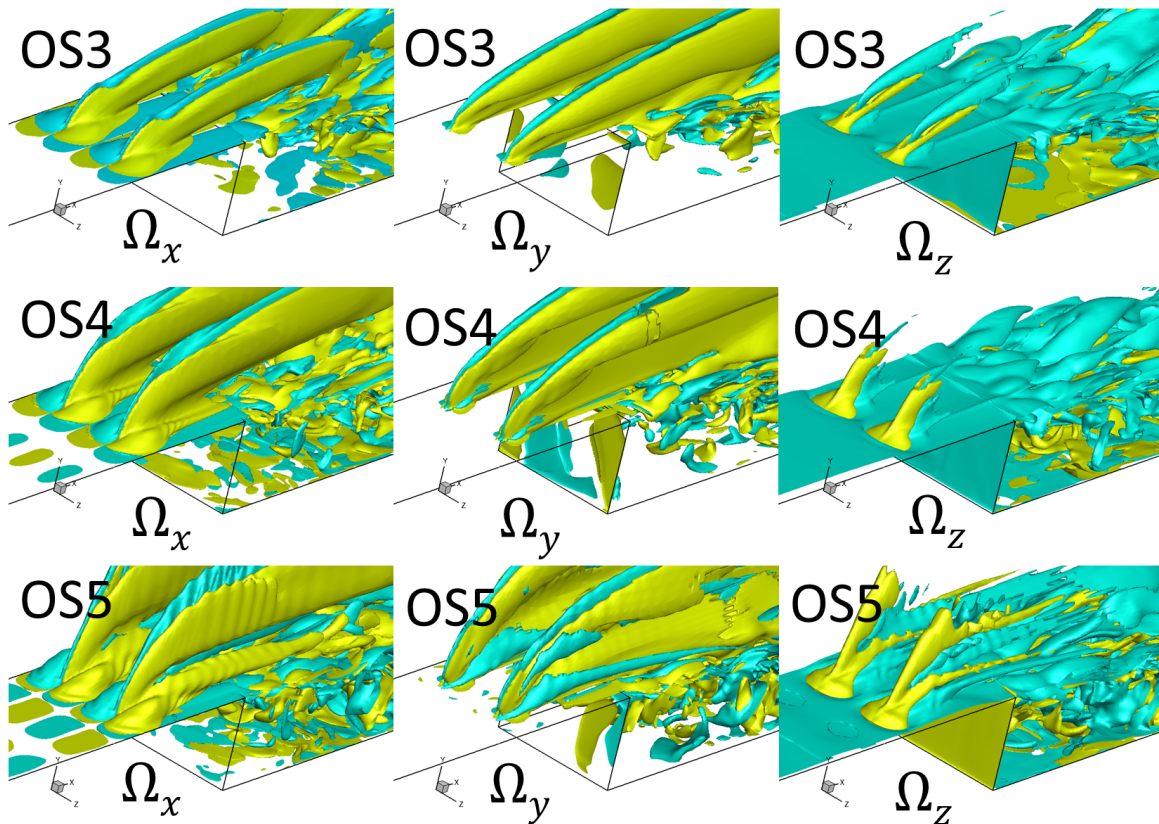
Figure 4.58: The iso-surface of Ω_x, Ω_y and Ω_z (from left to right) for OS3, OS4 and OS5 (from top to bottom). The light orange colour for the value of 500, and the light blue colour for the value of -500 for all these three vorticity components.
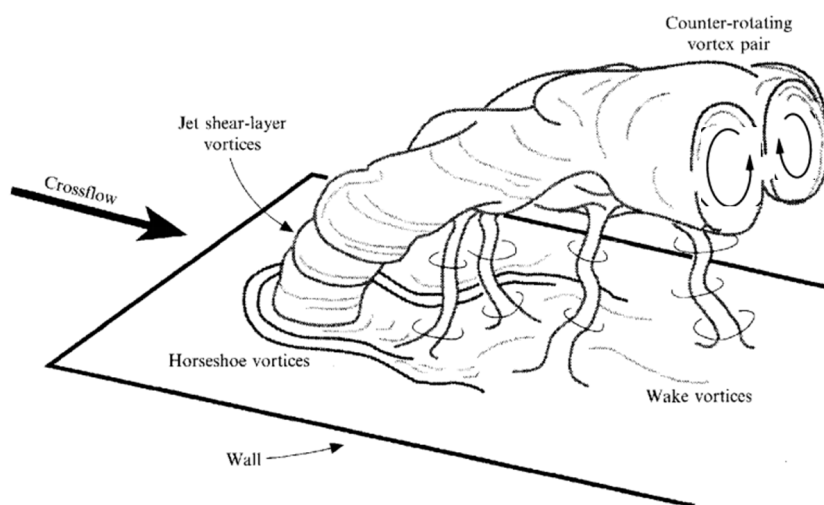
Figure 4.59: The vortical structures of the jet in the cross ow in Fric and Roshko [1994]

4.4. An exploration on the control parameters of oscillating surface

weak upstream of the step. In addition, the interaction between two counter-rotating vortex pairs generated by the adjacent actuators is also very weak. Another unique feature of the vortices generated by the oscillating surface is bulge structures upstream of the horseshoe vortices, which is the outcome of the motion of oscillation. With a larger control velocity, these bulge structures shrink.

With different control velocities in the control case OS3, OS4 and OS5, the generated vortices by the oscillating surface show some different characteristics. The control flow with a higher control velocity has a resultant velocity vector downstream further away from the wall on the oscillating surface (or a higher elevation angle). The generated counter-rotating vortex pair by the oscillating surface in the control case OS3 has the smallest angle of elevation, which makes the vortex tubes closer to the wall, easier merging with the separated shear layer near the step. A higher angle elevation seems to blow the counter-rotating vortex pair further away from the separated shear layer, so that the interaction between the vortex pair and the separated shear layer may not be enhanced, compared with the case with a smaller control velocity. Take the control case OS3 and OS4 as examples, although the control case OS4 generates stronger vortices, with a higher elevation angle, the interaction between the counter-rotating vortex pairs and the separated shear layer shown in OS4 (Figure 4.60(b)) seems to be weaker than the control case OS3 shown in Figure 4.60(a). Nevertheless, when the control velocity is further increased to the same magnitude of the free streamwise velocity in the control case OS5, the interactions both in one counter-rotating vortex pair and between two adjacent counter-rotating vortex pairs become stronger and the high velocity makes the generated vortex tubes unsteady and bifurcate, as shown in Figure 4.60(c). The low part of the bifurcated vortex is near to the wall and the interaction between the separated shear layer and the generated counter-rotating vortex pairs is enhanced, compared with the control case OS3 and OS4.

The contours of the three vorticity components at the section $z = 0$ (middle of two adjacent actuators) and the section $z = 0.0225$ m (centre of one actuator) are respectively shown in Figure 4.61. The interactions between the separated shear layer and the generated counter-rotating vortex pairs are clearly observed in these contours. The contour of the streamwise vorticity shown in Figure 4.61 (a) displays that for all these three control cases, the section at the centre of the actuator ($z = 0$) has a larger/higher flow mixing region than the section at the middle between two actuators ($z = 0.0225$ m). Besides, when the control velocity increases, the mixing regions both at $z/H = 0$ and $z = 0.0225$ m become larger, especially above the recirculation region. The vorticity Ω_y in Figure 4.61(b) show similar features to Ω_x, and the vorticity Ω_y in the mixing region at $z = 0.0225$ m is much stronger

(a)

(b)

(c)
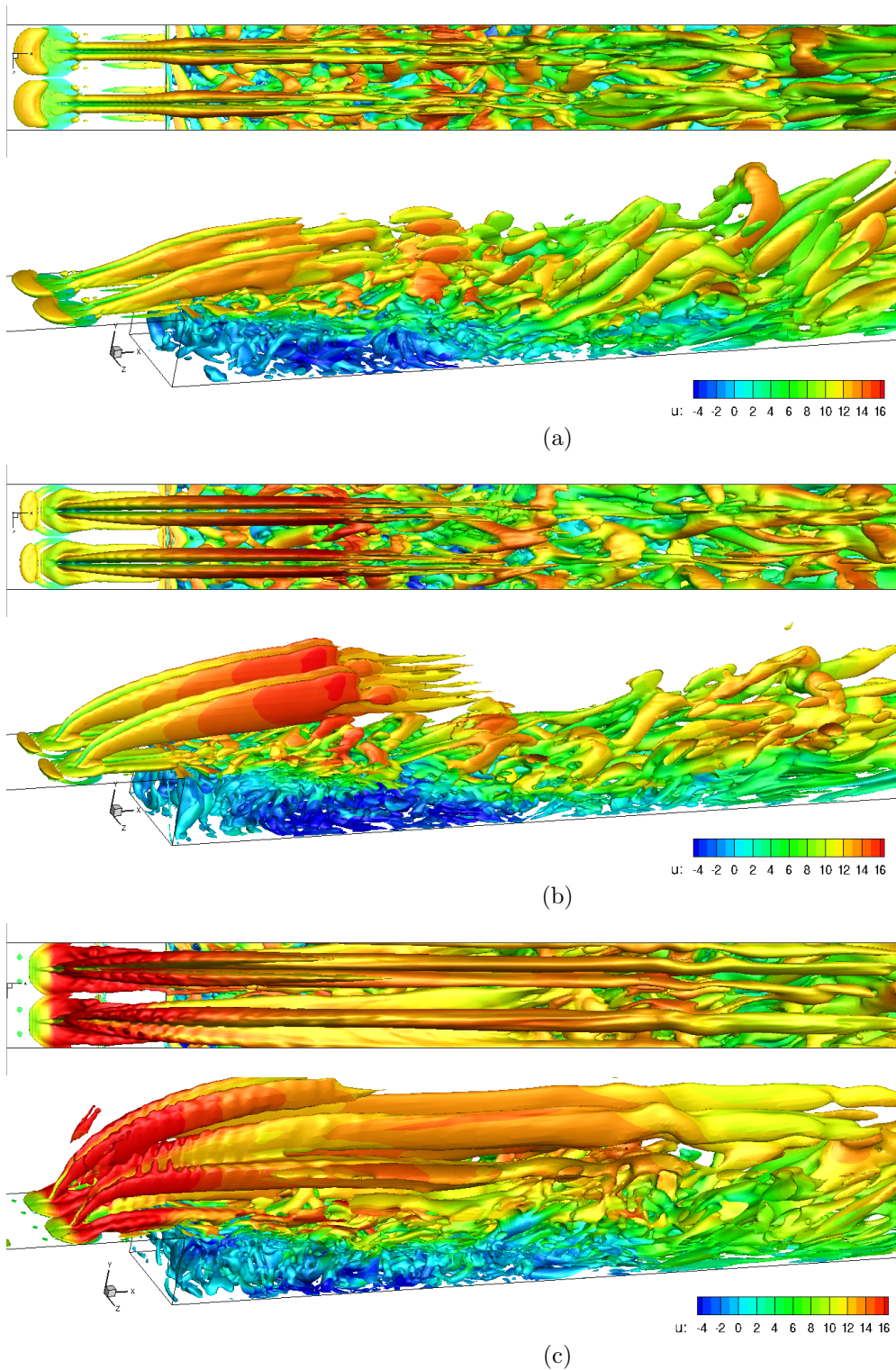
Figure 4.60: Iso-surfaces of λ_2 equal to -5000 for the instantaneous flow (top view and three dimensional view). (a) OS3 (5 m s^{-1}), (b) OS4 (10 m s^{-1}) and (c) OS5 (15 m s^{-1}).

than the streamwise vorticity Ω_x, which enhances the interaction with the recirculation region. The spanwise vorticity at $z = 0.0225$ m clearly show the vortex rings rotating in the spanwise direction. The vortex rings at the centre of actuator shown in Figure 4.61(c) are continuous in the case OS3 and OS4, while for the control case OS5, the rings become discrete, similar to structures in jet flows with a high velocity ratio. An interesting feature is that at the centre of the actuator ($z = 0.0225$ m), when the control velocity increases, the concomitant spanwise vorticity with an opposite rotating direction, upstream of the primary spanwise vorticity rings, becomes stronger, and the primary spanwise vorticity become bifurcate. Although the high control velocity blows the generated vortices away from the mixing layer in the downstream, the bifurcate vortices near the wall in the case with high control velocity enhances the interaction with the mixing layer flow. The contours of the three vorticity components at different cross sections in Figure 4.62 confirm that when the control velocity is $1/3U_{\mathrm{ref}}$ in the case OS3, the generated vortices move downwards and interact with the recirculating flows, while the control case OS4 with the control velocity of $2/3U_{\mathrm{ref}}$ generates vortices at a high angle and began to move downwards to interact with the mixing layer in a longer distance. For the control case OS5, the high oscillating velocity makes the vortices bifurcate and enhances the mixing from the step to downwards. From this point of view, the mixing of the generated vortices and the recirculating flow is not in a linear relation with the control velocity.
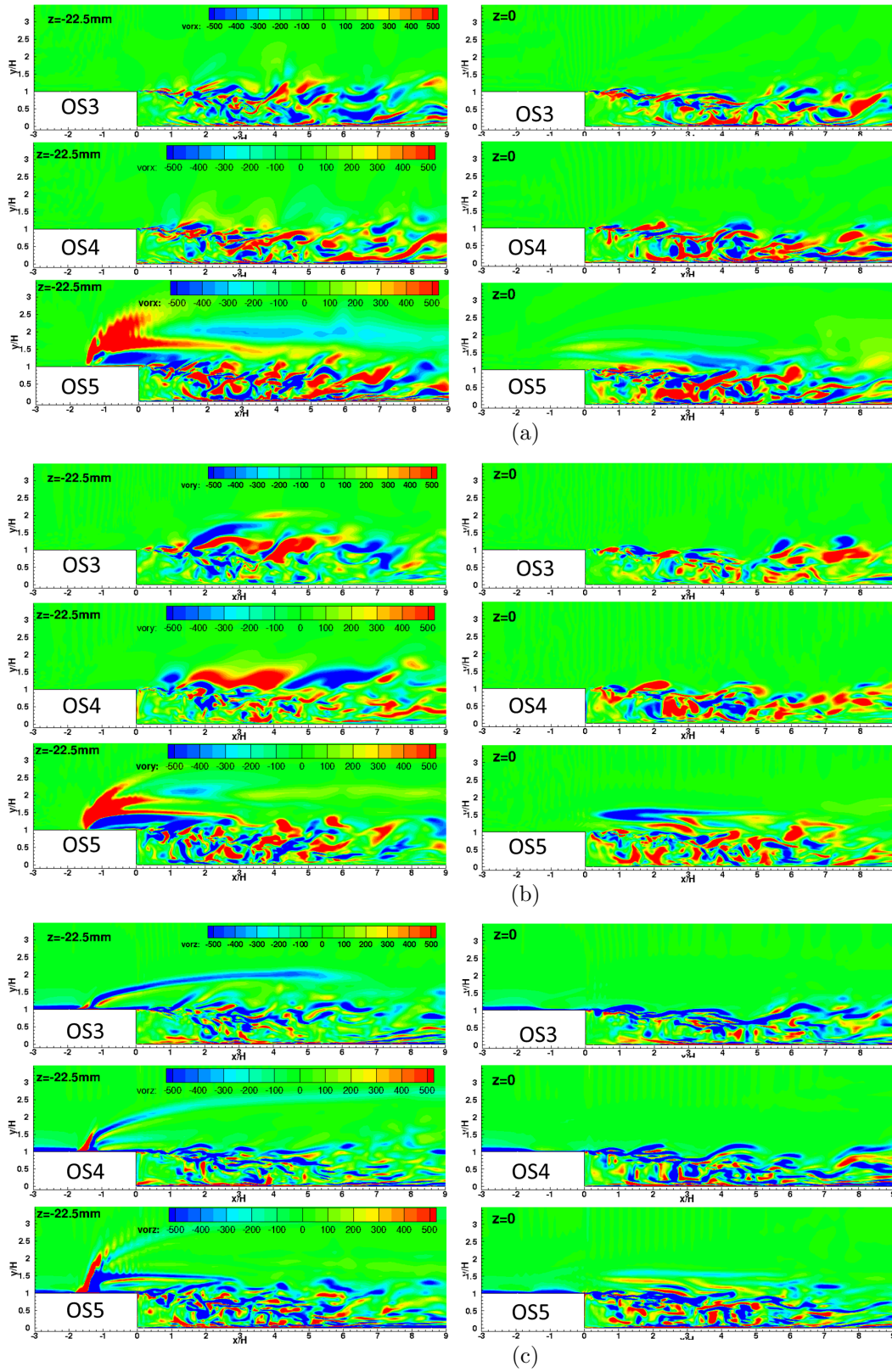
Figure 4.61: The iso-surface of the vorticity at the section $z = 0.0225$ m (left column) and $z/H = 0$ (right column). (a) the streamwise vorticity Ω_x, (b) the vorticity Ω_y and (c) the spanwise vorticity Ω_z.
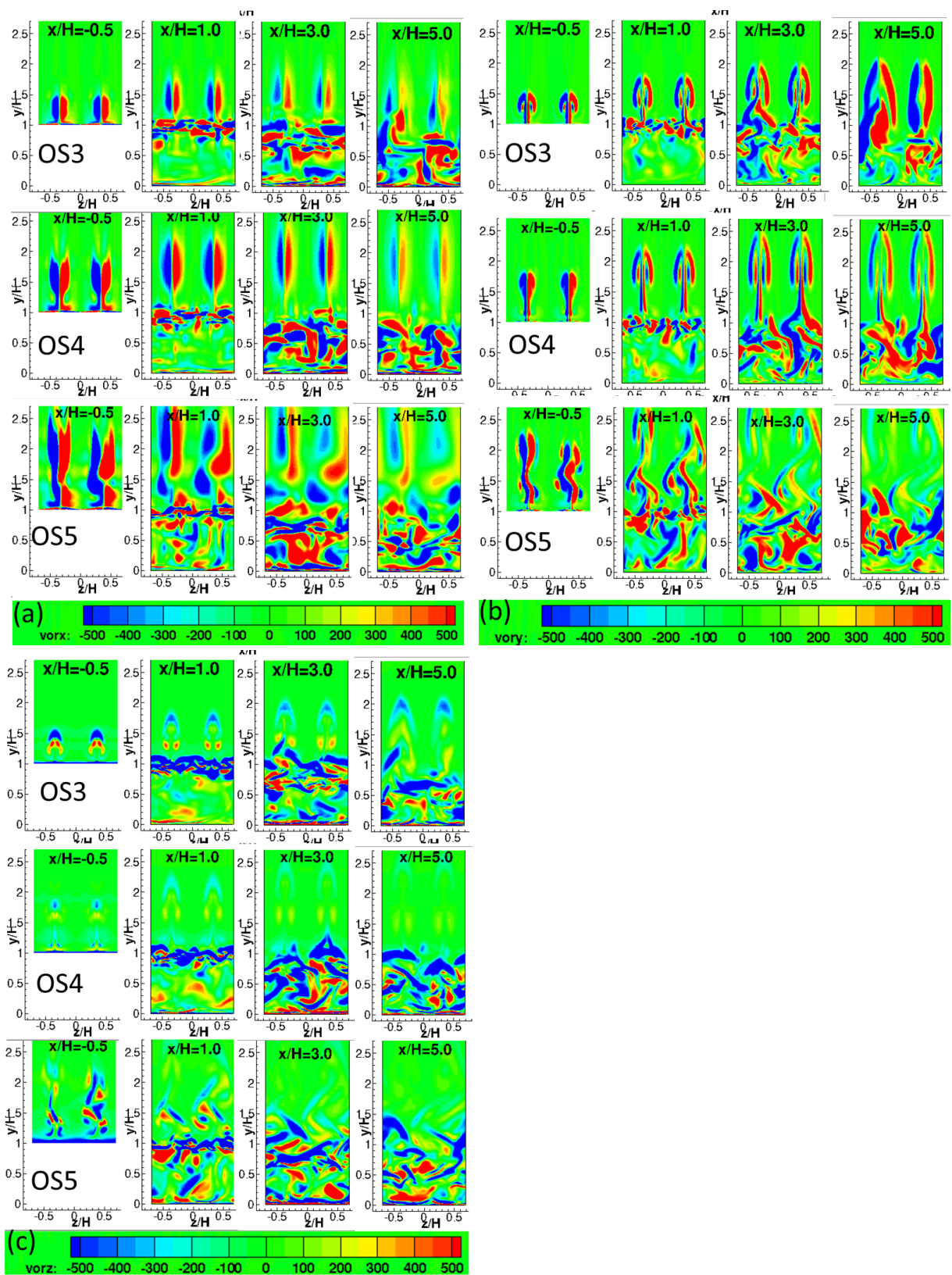
Figure 4.62: (a) The iso-surface of the streamwise vorticity Ω_x at the cross sections. (b) The iso-surface of the vorticity Ω_y at the cross sections.(c) The iso-surface of the spanwise vorticity Ω_z at the cross sections.

Power spectra density of the pressure signals on the wall at $x/H = 6.5$ is plotted in Figure 4.63. Again, the hamming window with an overlap of 50% is used to filter the signals. The control frequency 360 Hz corresponds to a Strouhal number of $St_0 = 1.56$. In the control case OS1, the control frequency cannot be observed from the pressure signal. For these three control cases OS3, OS4 and OS5, all the three control cases capture this basic frequency in the PSD of the pressure signals, which illustrates the increased control velocity has an enhanced effect on the whole recirculation region and large eddies generated by the oscillating surface upstream of the step leave "footprint" on the bottom wall near the reattachment point. Besides the control frequency, all of the three control cases also display a dominant frequency at around $St \approx 0.82 = 0.52St_0$. In addition, both OS4 and OS5 predict dominant frequencies at around $St = 3.12 = 2St_0$ and $St = 4.67 = 3St_0$. These frequencies higher than the control frequency may be related with break-down of the structures generated from the oscillating surface. The control cases OS4 and OS5 have another peak frequency at $St = 6.24 = 4St_0$.
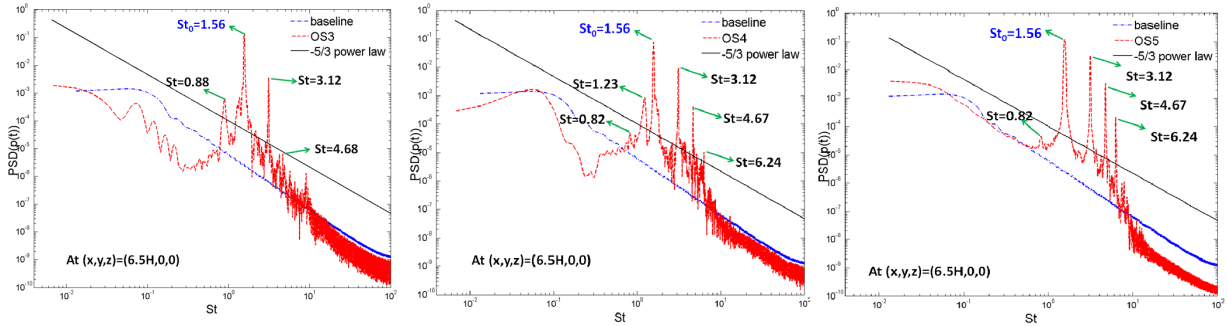
Figure 4.63: Power spectral density of the instantaneous pressure $p(t)$ at $(x, y, z) = (6.5, 0, 0)$. From left to right: OS3, OS4 and OS5

4.4.2.3 Flow reattachment and skin friction

Figure 4.64 shows the time and space averaged flow fields and streamlines. It is noted that even with a long time average, some small eddies still exist after the primary shear layer reattaches the wall. Without regard to these small eddies, the control case with a higher control velocity shows a smaller size of the primary recirculation and a larger size of the secondary recirculation. Compared with the baseline flow, all these three control cases give a smaller primary recirculation region.

Figure 4.65 displays the skin friction along the bottom wall for all these three control cases. All the three cases have a region with large negative C_f in the area where the oscillating surface locates ($x/H \in [1.146, 1.178]$) and a larger positive C_f in its surroundings.

4.4. An exploration on the control parameters of oscillating surface
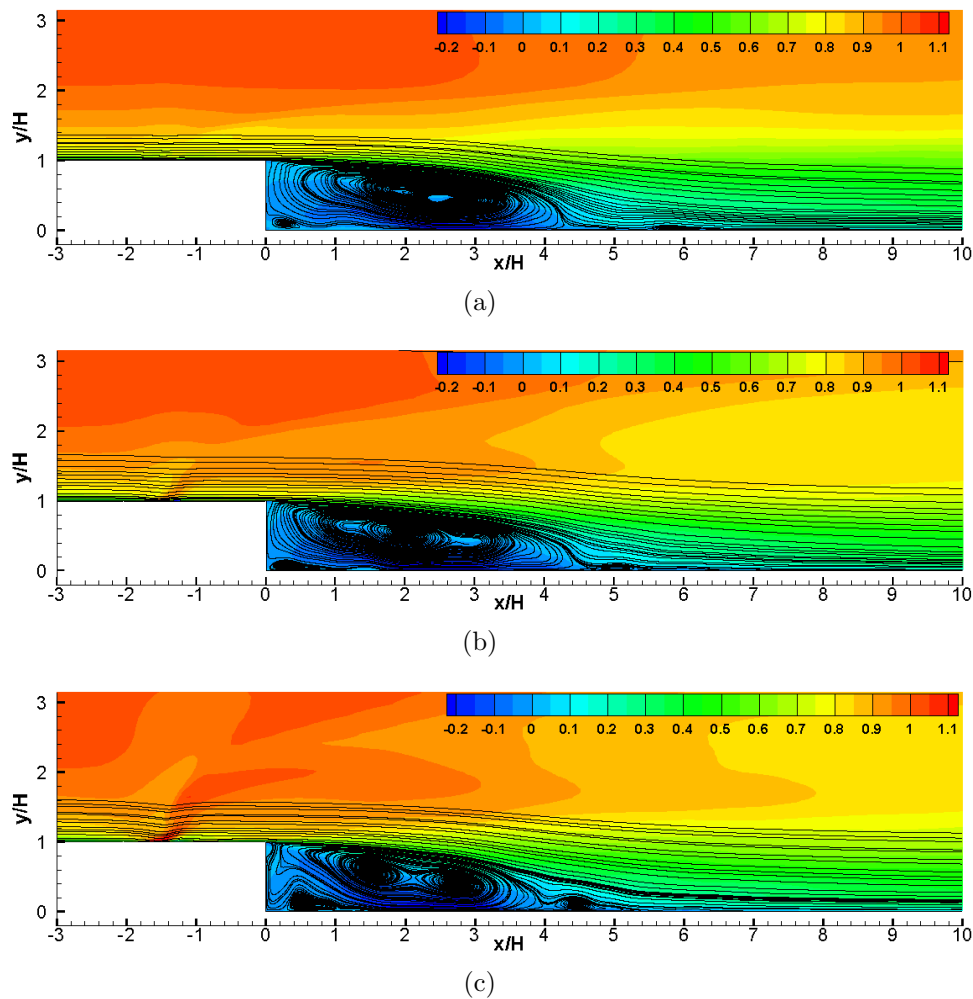
Figure 4.64: Time and spanwise averaged streamlines of the flow field. (a) OS3 (5 m s^{-1}), (b) OS4 (10 m s^{-1}) and (c) OS5 (15 m s^{-1})

An interesting point is even though the actuators are symmetric about the centreline of the surface, a biased distribution of negative C_f around the oscillating surfaces is presented by all the control cases. The spanwise averaged skin friction in Figure 4.66 confirms that OS5 has the largest magnitude of $-C_f$, while OS3 has the smallest value on the oscillating surface, as a result of the smallest velocity gradient in the oscillation. In all these three control cases, the large negative C_f leaves tracks when the flow approaches towards the step edge, which is not observed in OS1. The control case with the largest control velocity has the strongest tracks. However, the "footprint" of the oscillating surface is not clearly observed in the C_f distribution downstream of the step.

From the time and space averaged skin friction shown in Figure 4.66, it can be seen that the control case OS5 with the largest control velocity has the largest negative peak value of

C_f in the recirculation region, which may result from the fact that the large control velocity enhances the momentum transfer in the recirculation region. Although the streamlines in Figure 4.64 shows the larger control velocity results in a smaller primary recirculation, the C_f near zero displays zigzag profiles. Even with large differences in the recirculation regions, the three control cases have similar recovered C_f after $x/H = 12.0$, which is an about 18% reduction from the baseline flow.
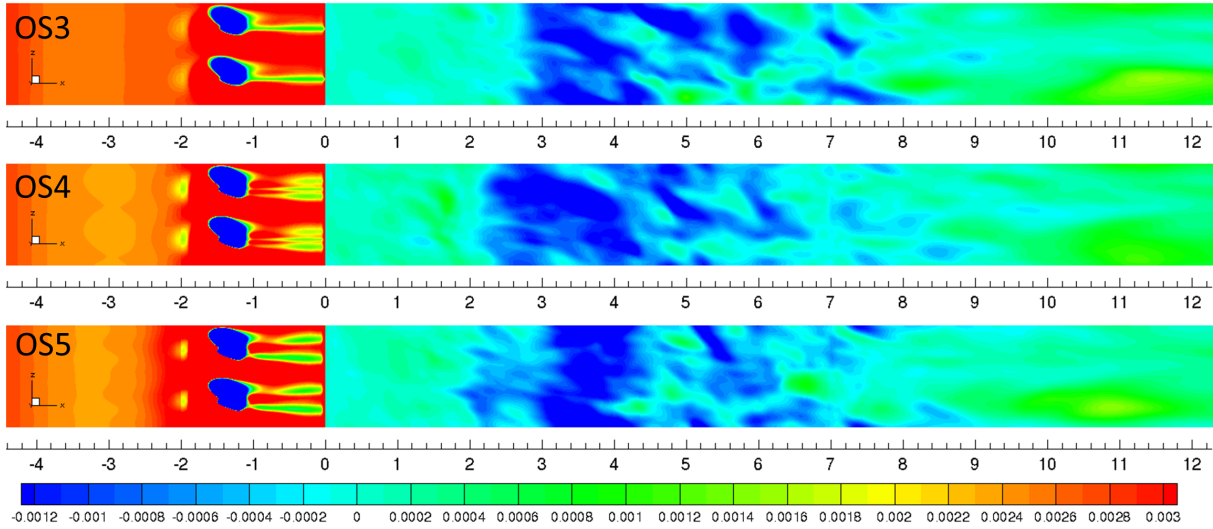
Figure 4.65: Contours of skin friction. From top to bottom: OS3 (5 m s^{-1}), OS4 (10 m s^{-1}) and OS5 (15 m s^{-1})

4.4.2.4   Velocity

Figure 4.67 compares the streamwise velocity profiles at $z = 0$ and $z = 0.0225$ m for the baseline case and these three control cases. The velocity contours at these sections are shown in Figure 4.68. At the section $z = 0.0225$ m in Figure 4.68, all these three control cases show the oscillating surface has a trend to "decelerate" flow along its motion path with an angle of elevation. It can also be observed that OS3 with the smallest control velocity and the smallest angle of elevation has the smallest influenced region in the free stream. The decreased velocity region around the actuators in the control case OS5 has a much larger elevation angle and it reduces the free stream flow in a larger region downstream of the step. Figure 4.67(b) confirms that the larger the control velocity, the larger (or higher) the velocity-decreased region is observed. Nevertheless, due to a smaller elevation angle, the region with decreased velocity in the control case OS3 is much near to the mixing layer, and furthermore, it reduces the velocity in the recirculation region. On the contrary, in spite of
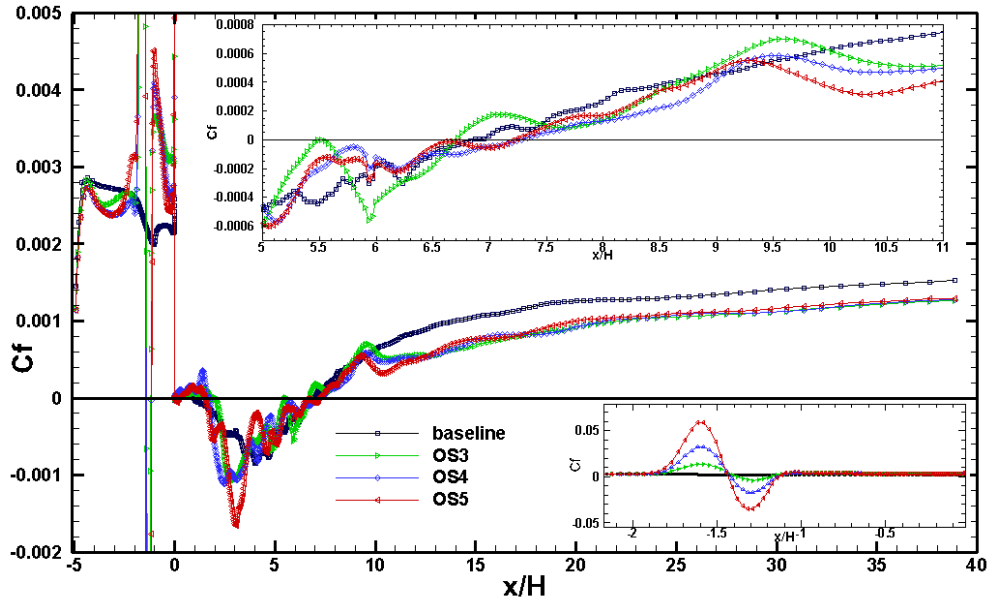
Figure 4.66: Time and spanwise averaged skin friction coefficient.

a larger affected region in the control case OS5, regions with the most decreased velocity are far from the mixing layer. Actually, the streamwise velocity in the recirculation region at $z = 0.0225$ m in the control case OS5 is energised, and the section via the centre of the actuator in Figure 4.68 displays a smaller recirculation region in the control case OS5. The reason is for the control case OS4 and OS5, due to the higher angles of elevation, a large velocity region exist between the primary velocity-decreased region and the recirculation region (see Figure 4.68), and this large velocity region and the enhanced mixing in the recirculation region result in the increase of the streamwise velocity. On the contrary, the generated low-velocity vortices by the control case OS3 has a smaller angle of elevation, and directly de-energise the flow in the mixing layer.

For the section between two actuators at $z = 0$, all these three cases energise the flow in the recirculation region. The control case OS3 has the smallest increase of the velocity, but the differences between these three cases are not significant. Interestingly, after $x/H = 8.0$ in the recovery region, the velocity becomes de-energised, and the control case OS3 decrease the recovered flow most. The reason is the generated vortices with low-velocity begin to move downwards and interact with each other, which can be observed from the velocity contours in the cross sections in Figure 4.69. Figure 4.69 shows that the higher the control velocity, the generated low-velocity vortices have higher velocity, which results in the energised flow in the recirculation region in the region near the centre of the actuators. It is observed that the low-velocity region produced by the actuators in the control case OS3 merges with the

(a)

(b)
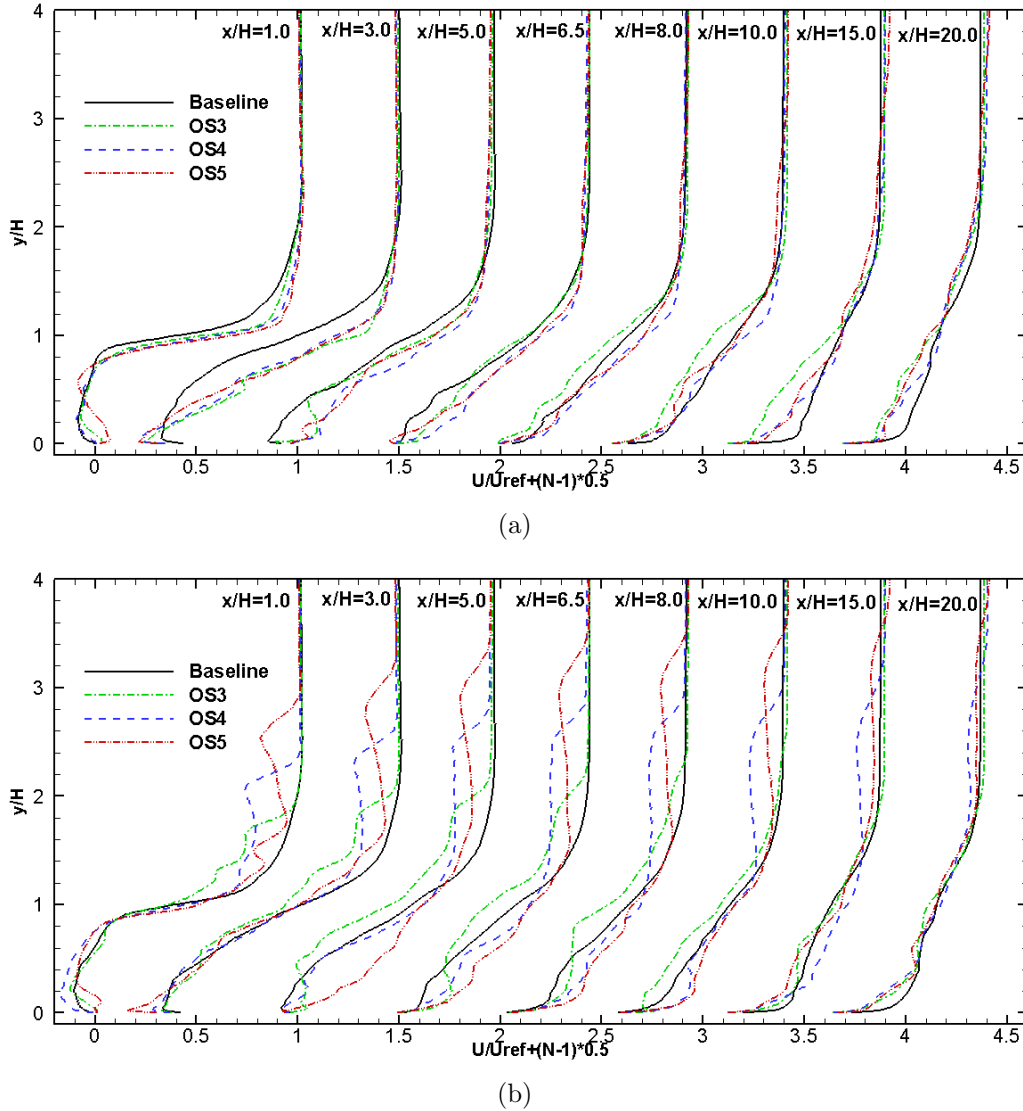
Figure 4.67: Time and spanwise averaged streamwise velocity. (a) at $z = 0$, (b) at $z = 0.0225$ m

downstream recirculation region from $x/H = 1.0$, and the merging of these two regions is stronger downstream. For the control case OS4, the interaction between these two regions is weak at $x/H = 1.0 \sim 3.0$, and begins to be obvious from $x/H = 5.0$. The control case OS5 has a stronger interaction than the control case OS4, regardless of a higher angle of elevation, due to the bifurcate low-velocity regions near the wall (See Figure 4.69).

Generally speaking, the oscillating surface generates low-velocity vortices, which move downstream at a certain angle of elevation, and the larger the control velocity, the higher the angle of elevation and the higher the velocity of the vortices. Vortices of the lowest velocity in the flow control case OS3 merges with the mixing flow just downstream of the step due
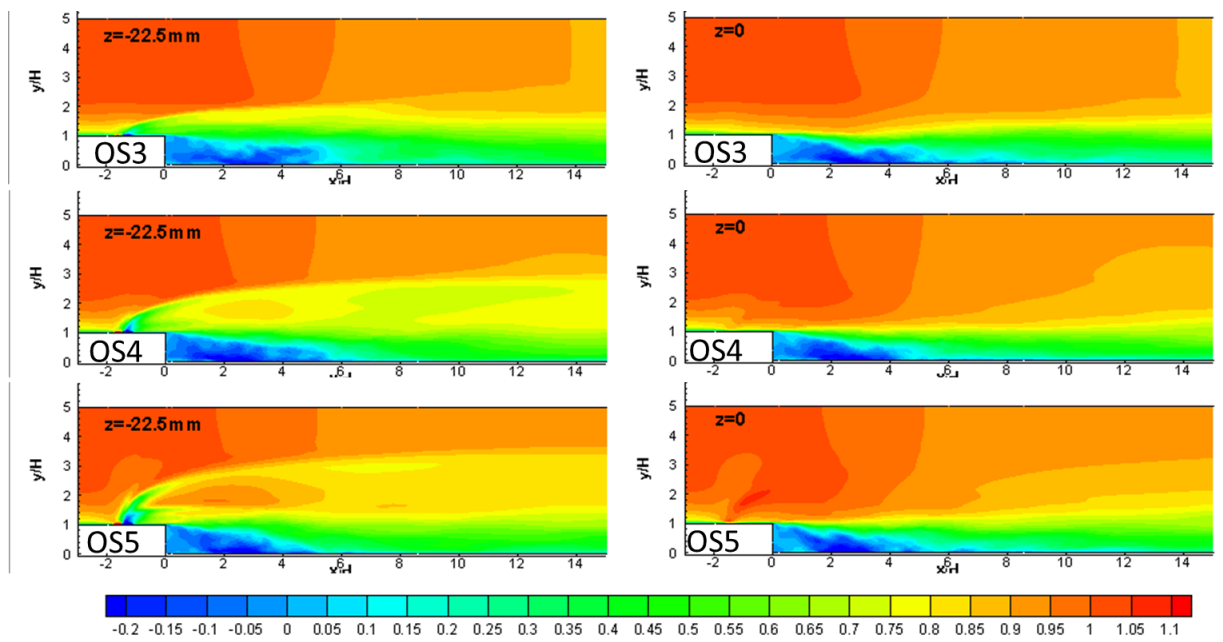
Figure 4.68: Contours of time averaged streamwise velocity the streamwise section $z = -0.0225$ m and $z = 0$. From top to bottom: OS3, OS4 and OS5

to the smallest angle of elevation. This interaction decreases the velocity in the mixing layer, especially along the centre of the actuators. The control case OS4 and OS5 have a similar process. However, the velocity of the vortices is higher than the control case OS3, and there is a high-velocity region between the main region of the low-velocity vortices and the mixing layer, due to the higher angle elevation. The momentum transfer between this high-momentum region and the recirculation region energises the flow in the recirculation region in the whole span, resulting in a near reattachment.
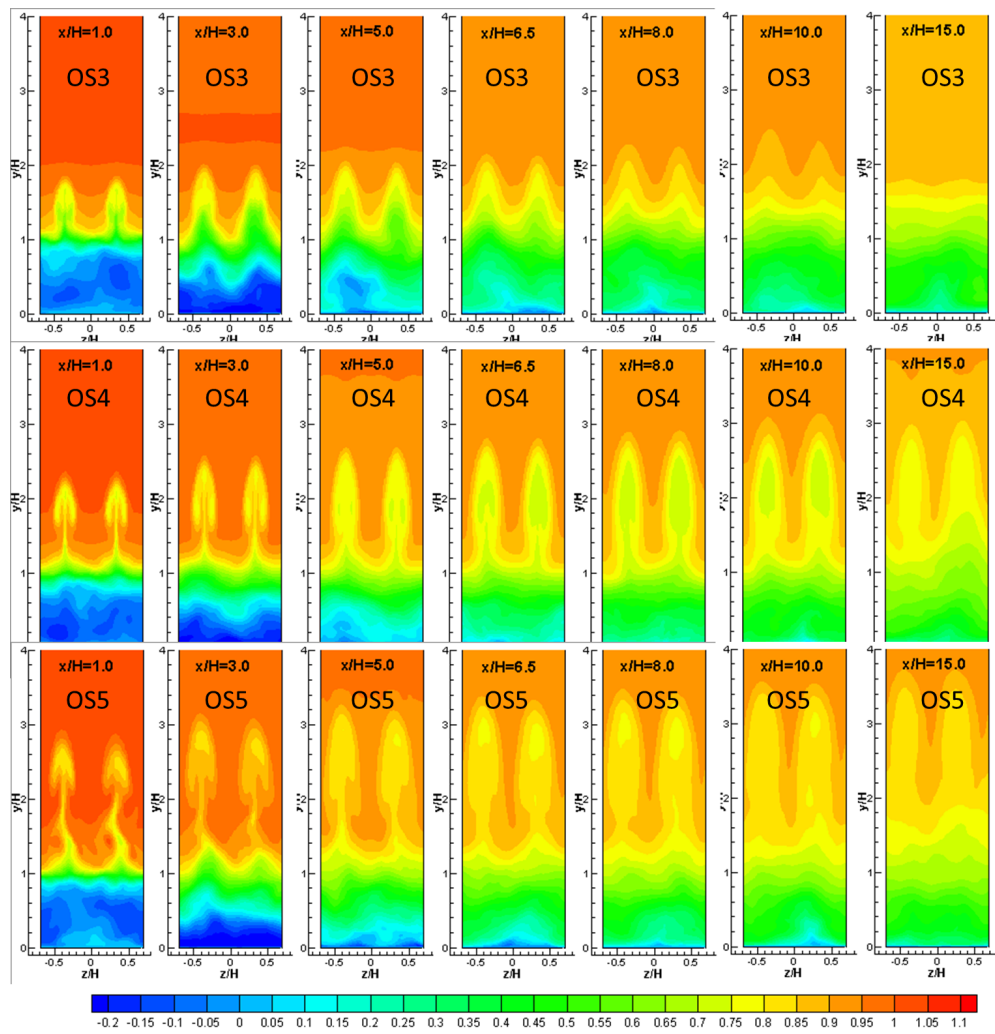
Figure 4.69: Contours of time averaged streamwise velocity at the cross section $x/H = 1.0$, 3.0, 5.0, 6.5, 8.0, 10.0 and 15.0. From top to bottom: OS3, OS4 and OS5

4.4. An exploration on the control parameters of oscillating surface

4.4.2.5 Reynolds stress

Figure 4.70 compares profiles of the Reynolds normal stress $\langle u'u' \rangle / U_{\mathrm{ref}}^2$. Figure 4.71 displays contours of $\langle u'u' \rangle / U_{\mathrm{ref}}^2$ for the control case OS3, OS4 and OS5 at the sections $z = 0$ and $z = 0.0225$ m. The contours in Figure 4.71 show that the influences of different control velocity on the Reynolds normal stress are different. The oscillating surface in the flow control case OS3 produces high Reynolds normal stress $\langle u'u' \rangle / U_{\mathrm{ref}}^2$ further above the recirculation region at $z = 0.0225$ m, and the influences to the free stream flow is small. By contrast, when the control velocity increases, the motion of oscillation produces more Reynolds stress $\langle u'u' \rangle / U_{\mathrm{ref}}^2$ near the oscillating surface, and affects almost the whole domain. Due to the wide spreading towards the free stream flow, the control case OS4 and OS5 do not have an obvious high-Reynolds stresses layer above the recirculation region, but the enhanced mixing increases the Reynolds normal stress $\langle u'u' \rangle / U_{\mathrm{ref}}^2$ in the recirculation region. Figure 4.70 displays that for the area where the vortex tube locates in the free stream filed, the control case OS3 has the largest Reynolds normal stress $\langle u'u' \rangle / U_{\mathrm{ref}}^2$, while in the recirculation region, the control case OS3 displays the smallest value. Similar to the velocity, the section in-between two actuators at $z = 0$ has a smaller region with the high-Reynolds stress than the section at $z = 0.0225$ m, which address the momentum transformation between vortices generated by adjacent actuators are weak.

Figure 4.72 displays the contours of the Reynolds normal stress $\langle u'u' \rangle / U_{\mathrm{ref}}^2$ at the cross sections. It is observed that for all these three cases, at regions near the step ($x/H = 1.0 \sim 6.5$), the streamwise velocity fluctuations are higher near the centres of the actuators than the in-between region of two actuators. The distribution of the high $\langle u'u' \rangle / U_{\mathrm{ref}}^2$ along the span shows a shape of "M". However, further downstream with more interactions between two adjacent actuators, the high $\langle u'u' \rangle / U_{\mathrm{ref}}^2$ occurs towards the middle of the two actuators. Further downstream, the low $\langle u'u' \rangle / U_{\mathrm{ref}}^2$ near the wall and the high $\langle u'u' \rangle / U_{\mathrm{ref}}^2$ away from the wall both forms a shape of Λ. Beside, when the control velocity increases, the high Reynolds stress $\langle u'u' \rangle / U_{\mathrm{ref}}^2$ spreads towards the wall and occupies a larger region.

Figure 4.73 compares the profiles of the Reynolds normal stress $\langle v'v' \rangle / U_{\mathrm{ref}}^2$. Figure 4.74 displays the contours of $\langle v'v' \rangle / U_{\mathrm{ref}}^2$ for the control case OS3, OS4 and OS5 at the sections $z = 0$ and $z = 0.0225$ m. The Reynolds normal stress $\langle v'v' \rangle / U_{\mathrm{ref}}^2$ shows similar features to the Reynolds normal stress $\langle u'u' \rangle / U_{\mathrm{ref}}^2$. The higher the control velocity, the larger the Reynolds normal stress $\langle v'v' \rangle / U_{\mathrm{ref}}^2$ in the whole domain, both the free stream regions and the recirculation region. The higher Reynolds normal stress $\langle v'v' \rangle / U_{\mathrm{ref}}^2$ implies an enhanced momentum transfer in the wall-normal direction. Furthermore, energised flows in the recirculation and reduced size of the primary recirculation. This may explain why the OS5
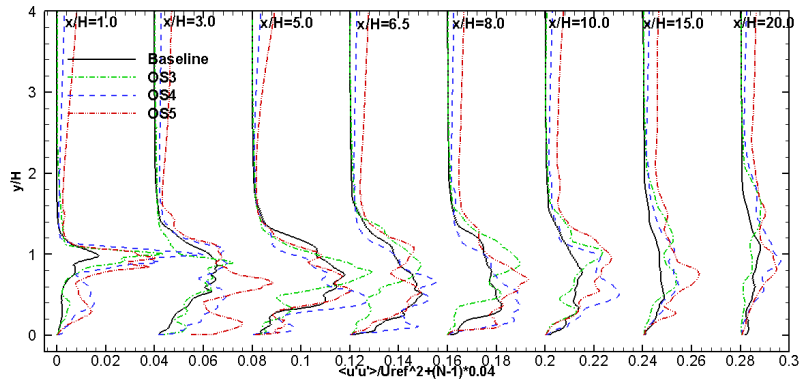
(a)
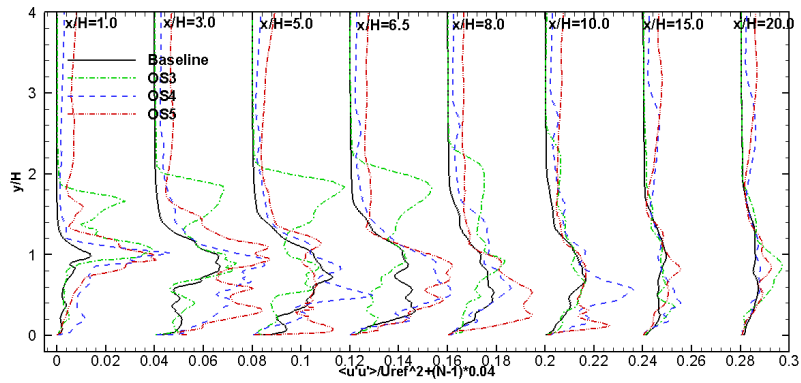
(b)

Figure 4.70: Reynolds stress $\langle u'u' \rangle / U_{\text{ref}}^2$. (a) at $z = 0$, (b) at $z = 0.0225$ m
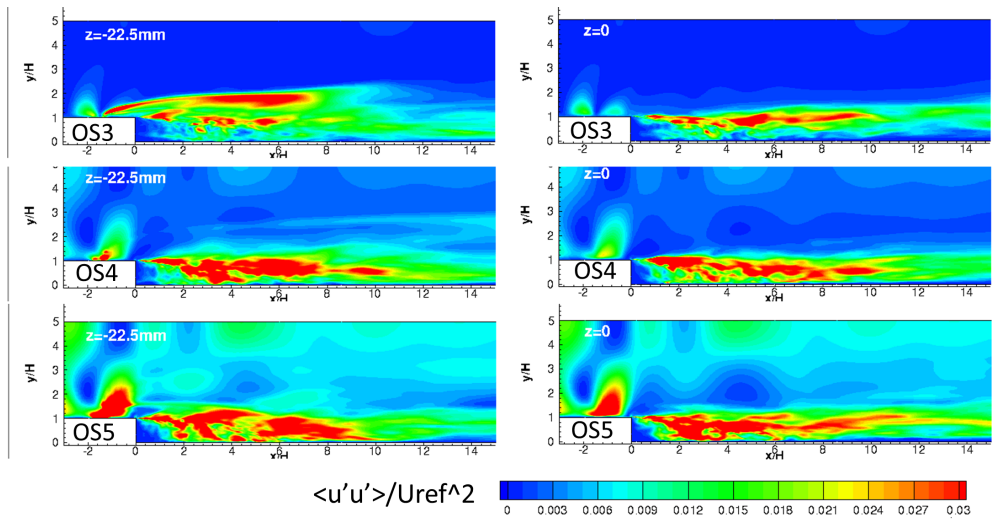
Figure 4.71: Reynolds stress $\langle u'u' \rangle / U_{\text{ref}}^2$ at the streamwise section $z = -0.0225$ m and $z = 0$. From top to bottom: OS3, OS4 and OS5

157

4.4. An exploration on the control parameters of oscillating surface
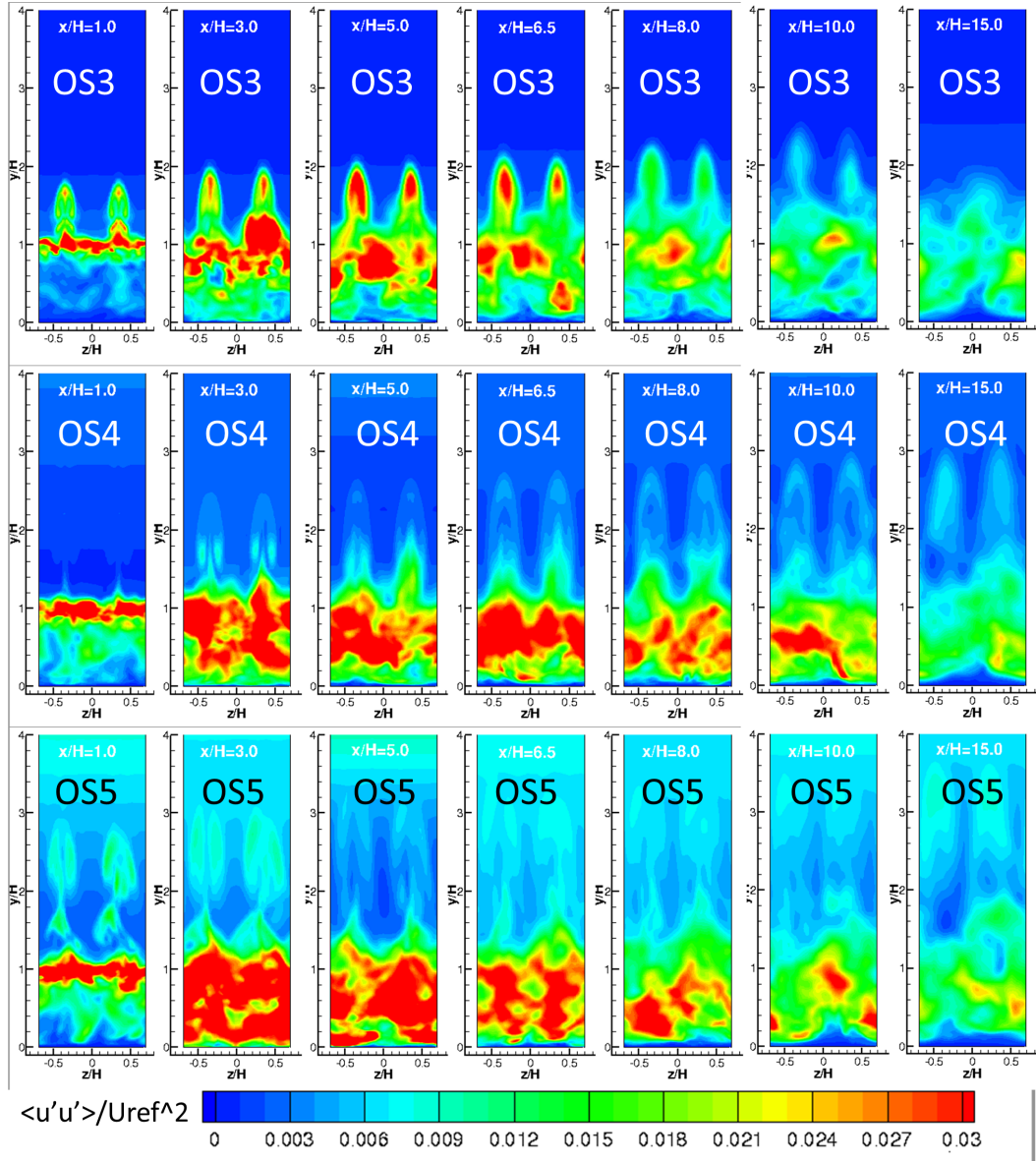
Figure 4.72: Reynolds stress $\langle u'u'\rangle/U_{\text{ref}}^2$ at the cross section $x/H = 1.0$, 3.0, 5.0, 6.5, 8.0, 10.0 and 15.0. From top to bottom: OS3, OS4 and OS5

has the smallest primary recirculation region. Interestingly, a region with high $\langle v'v'\rangle/U_{\text{ref}}^2$ exists in the middle of the channel above the recirculation region in the control case OS3 and OS4, which may highly relates with influences to the free stream flow. Unlike the Reynolds normal stress $\langle u'u'\rangle/U_{\text{ref}}^2$, the variations of $\langle v'v'\rangle/U_{\text{ref}}^2$ along the span are not that distinct in the recirculation region.

Figure 4.75 shows the contours of the Reynolds normal stress $\langle v'v'\rangle/U_{\text{ref}}^2$ in the cross sections. The Reynolds normal stress $\langle v'v'\rangle/U_{\text{ref}}^2$ again shows similar spanwise distributions

158

to the Reynolds normal stress $\langle u'u'\rangle/U_{\mathrm{ref}}^2$. The difference is that the influences of the normal velocity fluctuations to the free stream flow are higher in the region near the step, which reduces downstream. This is just opposite of the distribution of the Reynolds normal stress $\langle u'u'\rangle/U_{\mathrm{ref}}^2$. The reason is the normal velocity fluctuations are directly determined by the vertical oscillation of the surfaces, which damps with going downstream. However, the streamwise fluctuations are highly related with the moving of the vortex pairs along the incoming flow. When flow goes downstream, the generated vortices begin to lose "control" from the upstream oscillating motion, but have more interactions with the free stream flows.

Figure 4.76 compares the profiles of the Reynolds normal stress $\langle w'w'\rangle/U_{\mathrm{ref}}^2$. Figure 4.77

(a)

(b)
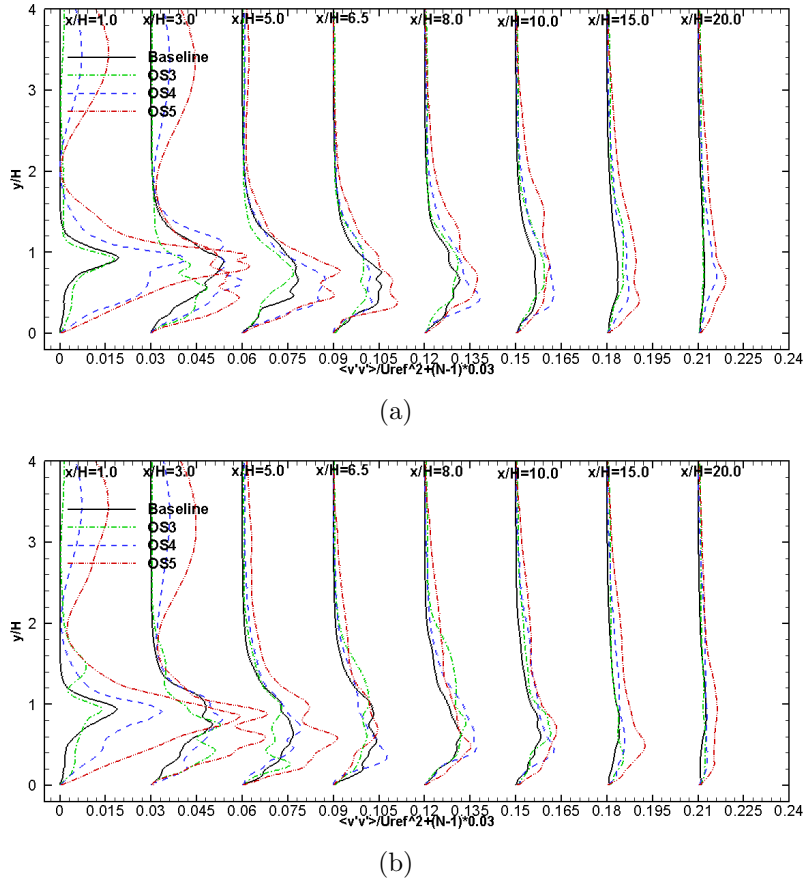
Figure 4.73: Reynolds stress $\langle v'v'\rangle/U_{\mathrm{ref}}^2$. (a) at $z = 0$, (b) at $z = 0.0225$ m

displays the contours of $\langle w'w'\rangle/U_{\mathrm{ref}}^2$ for the control case OS3, OS4 and OS5 at the sections $z = 0$ and $z = 0.0225$ m. Obviously, the Reynolds normal stress $\langle w'w'\rangle/U_{\mathrm{ref}}^2$ are generally smaller than the other two Reynolds normal stresses. Thus, even with high control velocity and strong streamwise vorticity, the turbulence downstream of the step are still highly anisotropic. Unlike the Reynolds normal stress $\langle u'u'\rangle/U_{\mathrm{ref}}^2$ and $\langle v'v'\rangle/U_{\mathrm{ref}}^2$, the influences of

4.4. An exploration on the control parameters of oscillating surface
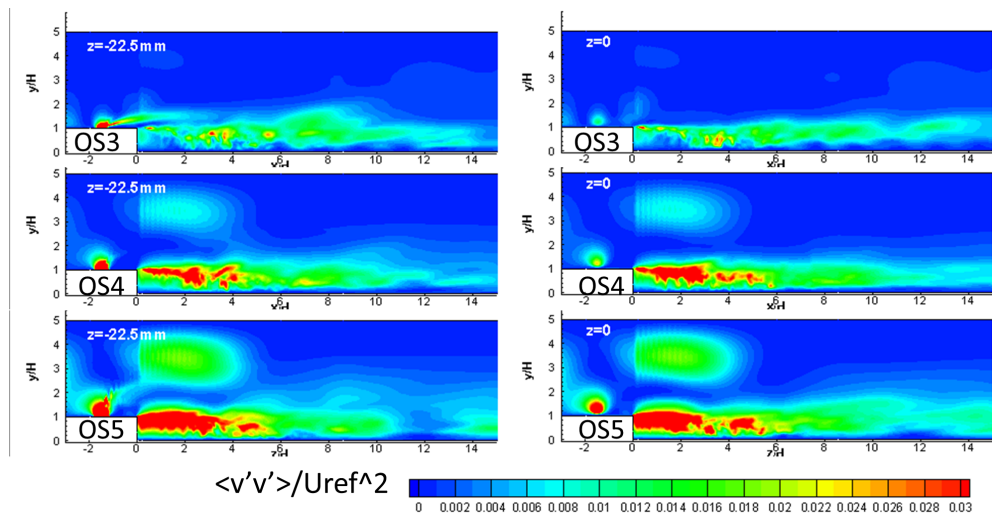
Figure 4.74: Reynolds stress $\langle v'v' \rangle/U_{ref}^2$ at the streamwise section $z = -0.0225$ m and $z = 0$. From top to bottom: OS3, OS4 and OS5

the spanwise fluctuations to the free stream are almost negligible. Similar to the vertical fluctuations, the Reynolds normal stress $\langle w'w' \rangle/U_{ref}^2$ also displays a larger region with high values in the middle of two adjacent actuators than the section along the centre of the actuators. In addition, the control case OS5 displays large spanwise fluctuations, ejecting from the oscillating surface, which are not observed in the case OS3 and OS4.

Figure 4.78 shows the contours of the Reynolds normal stress $\langle w'w' \rangle/U_{ref}^2$ in the cross section. Unlike the velocity fluctuations in the other two directions, the contours of the spanwise fluctuation display weak links with the generated vortices. When the control velocity increases, the links begin to become stronger. This may be due to the weak interaction in the spanwise vorticity shown in Figure 4.61.
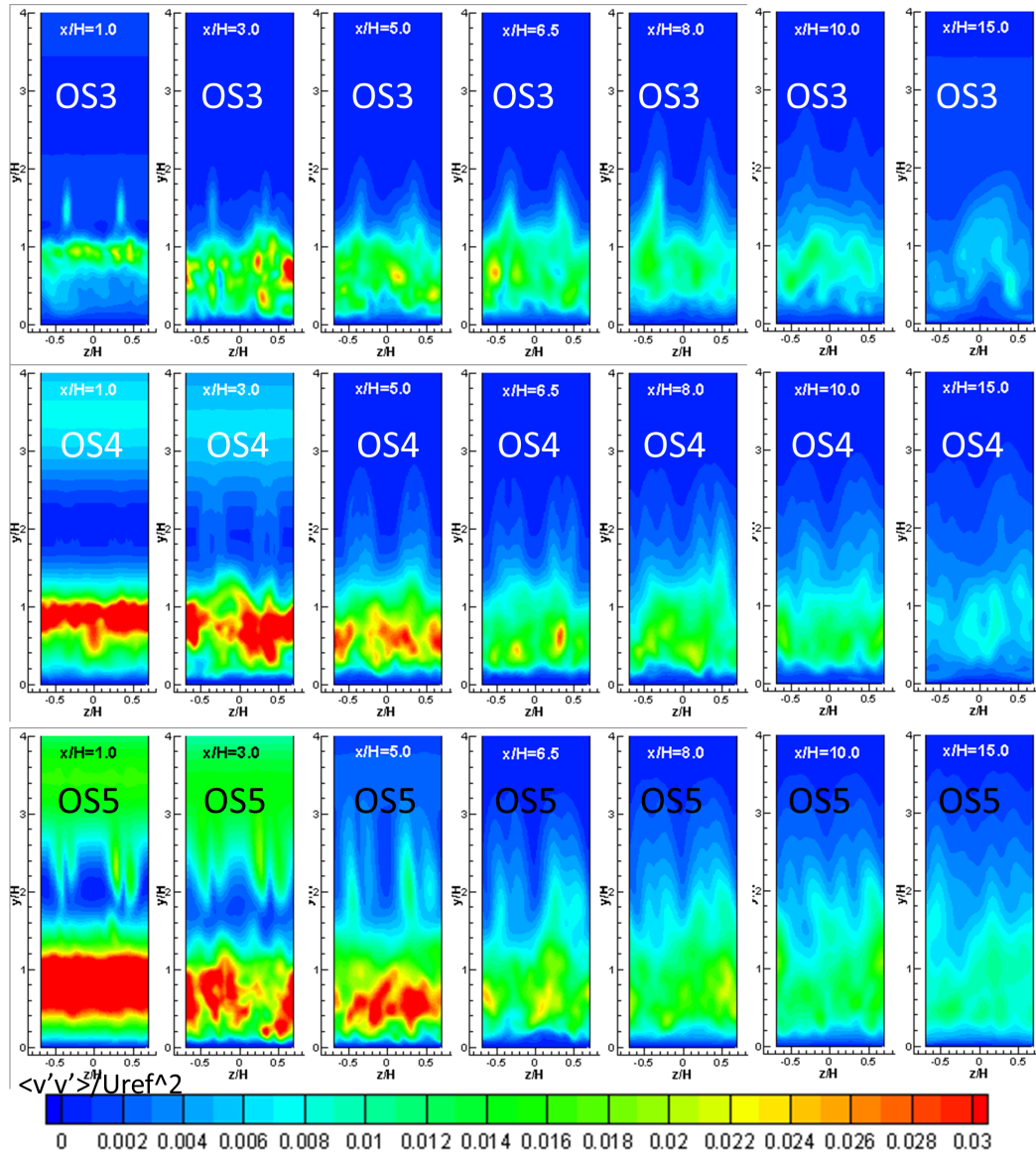
Figure 4.75: Reynolds stress $\langle v'v' \rangle / U_{\mathrm{ref}}^2$ at the cross section $x/H = 1.0, 3.0, 5.0, 6.5, 8.0, 10.0$ and 15.0. From top to bottom: OS3, OS4 and OS5
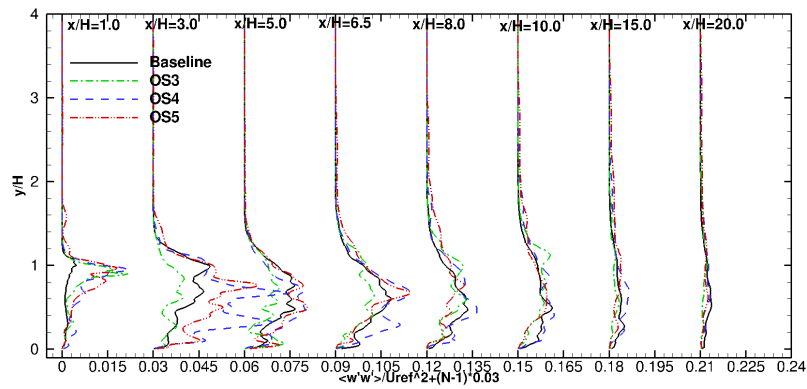
(a)
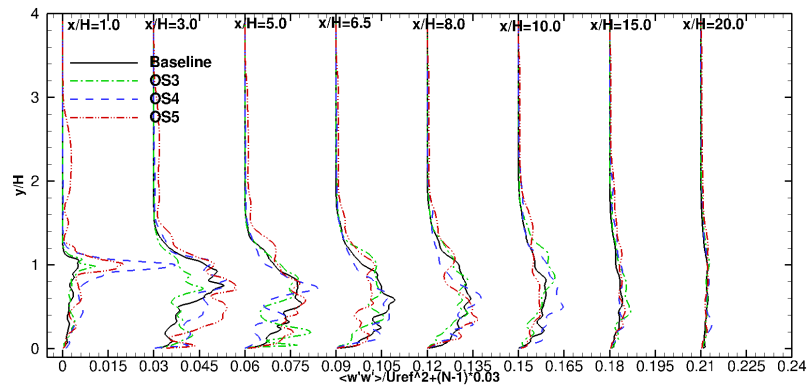
(b)

Figure 4.76: Reynolds stress $\langle w'w' \rangle / U_{\text{ref}}^2$. (a) At $z = 0$, (b) at $z = 0.0225$ m.
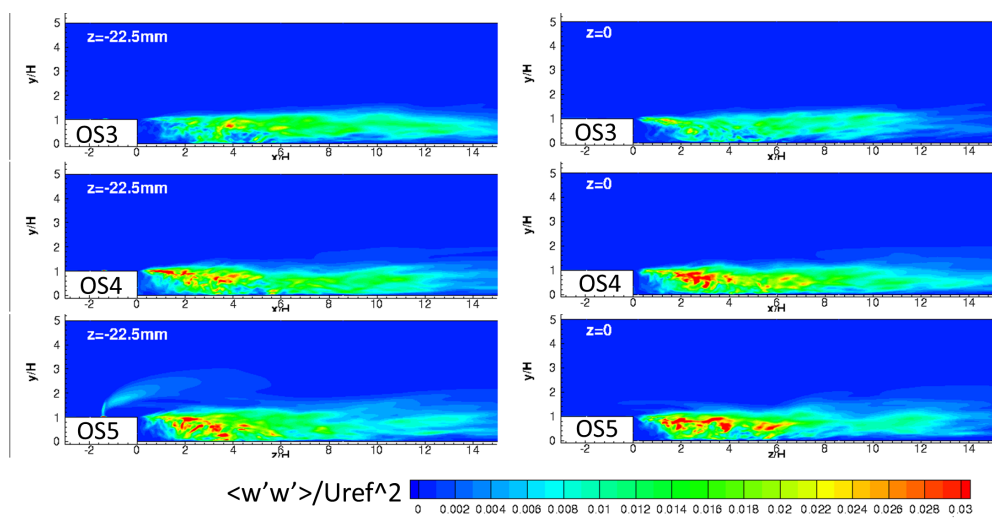
Figure 4.77: Reynolds stress $\langle w'w' \rangle / U_{\text{ref}}^2$ at the streamwise section $z = -0.0225$ m and $z = 0$. From top to bottom: OS3, OS4 and OS5
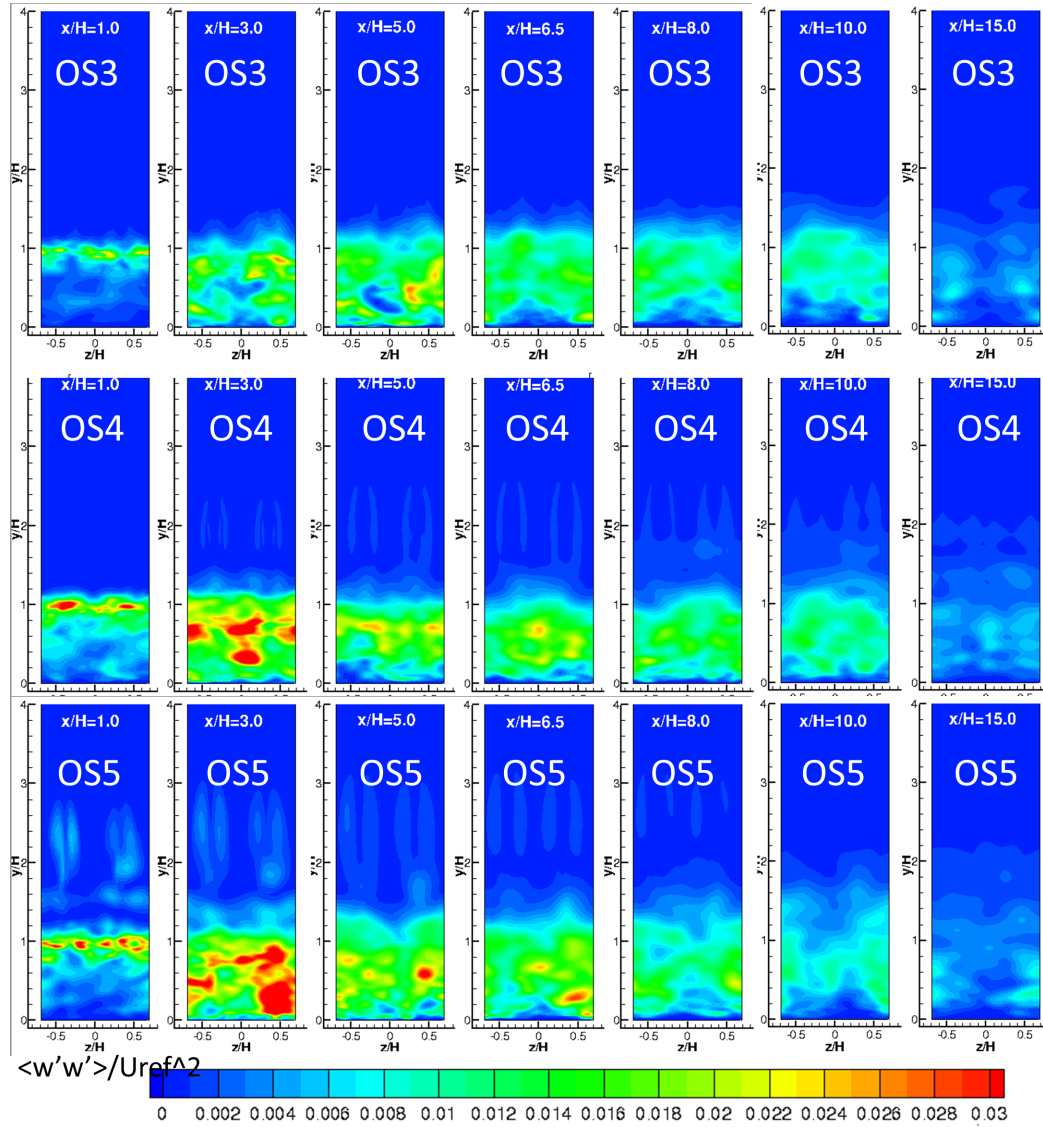
Figure 4.78: Reynolds stress $\langle w'w' \rangle / U_{\text{ref}}^2$ at the cross section $x/H = 1.0$, 3.0, 5.0, 6.5, 8.0, 10.0 and 15.0. From top to bottom: OS3, OS4 and OS5

4.4. An exploration on the control parameters of oscillating surface

4.4.3 Summary

The oscillating surface flow control with a control velocity with a magnitude in the order of the free stream is investigated in this subsection. The study of the amplitudes of the control velocity, in the three flow control cases OS3-OS5, explores more flow phenomena in the oscillating surface flow control, which are summarized as follows.

(1) When the control velocity becomes similar to the free stream flow, the motion of oscillating generates quasi-steady vortices upstream of the step. Oscillating surface produces counter-rotating vortex pairs which have some common features to the vortex pairs generated by jets. The larger the control velocity, the wider the vortex pairs in the spanwise direction and the larger the angle of elevation. The generated vortices by the control case OS3, OS4 and OS5 are very different from the control case OS1. (With a very small control velocity, the OS1 generates piled vortices with shifting directions.)

(2) The power spectra density of the pressure on the wall near the reattachment point shows that all the three cases capture the control frequency. With a larger control velocity, more peak frequencies with multiples of the control frequency are observed. These dominant frequencies extracted from the flow spectra indicate the flow structures near the reattachment are obviously influenced by the oscillating surfaces on the step, although no "track" of actuators can be observed in the contours of the skin friction.

(3) From the viewpoint of time and spanwise averaged C_f, all these three cases give similar reattachment points as the baseline flow. However, the primary recirculation becomes smaller and smaller with a larger control velocity. Even without significant reduction of the reattachment point, the three controlled cases have a reduction of the skin friction by 18% in the recovered region, compared with the baselines.

(4) Due the deceleration effect from vortices-rings generated by the oscillating surface, the flow, in the area where these vortex tubes locate, has a reduced velocity and increased Reynolds stresses. The larger control velocity has a larger velocity-decelerated region in the free stream flow field. Compared with the area where oscillating surface locates, the area in-between two actuators is less influenced by the vortex tubes.

Generally speaking, when the control velocity is increased to the same order of the free stream flow, the generation of vortices is different from the control case OS1 and looks like jets in cross flows. Besides, a larger control velocity gives a stronger control effect on the flow recirculation downstream of the step.

4.5 Summary

This chapter presents the investigation on the oscillating surface flow control with piezoelectric actuators.

Firstly, validations of the mesh resolution, flux splitting schemes and turbulence models were carried out in the backward facing step case of Driver and Seegmiller [1985]. The validation shows that the high resolution mesh does not give significant improvements on the statistical results, only with more and smaller resolved turbulence structures, which benefits the study focusing on the manipulation of turbulence structures. The classic Roe scheme and the SLAU scheme predict similar results for this no-control case, while the classic Roe scheme seems to be more stable than the SLAU scheme when solving the moving boundaries. The turbulence model IDDES gives the overall best simulation results, compared with DES and DDES.

Then, the backward facing step with an oscillating surface with the same control configuration as the experiments carried out by APL-UniMan is carried out. The baseline flow shows good agreements with the available experimental results. The oscillating surface increases the fluctuation of the vertical velocity in the recirculation region, which enhances the momentum transfer between the affected shear layer and the recirculating flow, which leads to a reduction of the primary recirculation by about 12%. However, the power spectral density analysis of the pressure cannot capture any information of the control frequency at the current study.

Finally, regardless of physical realizability, three control velocities with a magnitude in the order of the free stream flow were investigated. The control velocities in these three cases are increased by three orders of magnitudes compared with the experimental setup, and the size of the primary reattachment has an about 35% reduction from the baseline flow. In addition, the secondary recirculation becomes larger with a larger control velocity. Furthermore, the recovered skin friction has a 18% reduction compared with baseline flow. With the large control velocity, the control frequency and its multiples are observed from the pressure signal near the reattachment point.

Chapter 5

Flow Control with Pulsed Jets in Flows around NACA0015

5.1 Introduction

Lift enhancement and drag reduction have a great significance for aircraft in fuel efficiency, flight performance and manoeuvrability. Various control methods were proposed to realize a common aim to force the separated flow reattached with low energy input from actuators (Greenblatt and Wygnanski [2000]).

The objective of this study is to analyse the influence of pulsed jets on flow separation. The case NACA0015 to be studied in this chapter corresponds to the configurations in the experiments carried out by Siauw [2008]. Experiments show that for the uncontrolled baseline flow around NACA0015 at an angle of attack 11°, there is a trailing edge separation at around 0.7 times of the chord length from the leading edge, and after switching on the jets, the separation becomes smaller and finally cannot be observed (Siauw [2008]). Although the flow control jets in the experiments are so-called pulsed jets, actually the jets behave more likely to continuous jets, because the control frequency (1 Hz) is much lower than the vortex shedding frequency. More specifically, experiments show that after the jets have been switched on for around 0.1 s, the flow has been attached, and the attached flow has little change in the remaining 0.4 s (1 Hz with a 50% work duty) during the jet-working period. Therefore, there is some space to optimize the frequency and duty cycle to achieve a better control energy efficiency.

There are two objectives for numerical simulations in this study. The first one is to demonstrate the effectiveness of pulsed jets flow control and to compare the flow characteristics at the statically steady state of the baseline case and the jets controlled flow.

Simulation results will be compared with available experimental data to validate the numerical simulations. The other objective is to investigate the transient process from jet-off to jet-on, in which the baseline trailing edge separation flow is forced to be attached. A brief description of the transient process from jet-on to jet-off is also given.

5.2 Flow configuration

5.2.1 Description of the geometry

The experiments on jets flow control of the NACA0015 ware carried out by Siauw *et al.* [2009] in their wind tunnel. The NACA0015 model in the experiments has a chord length of $c = 0.35$ m and an angle of attack 11°. The experimental test section has a span of 2.4 m ($\approx 6.86c$), a transverse length of 2.6 m ($\approx 7.43c$) and a streamwise length of 6.0 m ($\approx 17.14c$). The computational domain in the transverse and streamwise directions are the same as the wind tunnel, while the length of the span is reduced to 0.06 m ($\approx 0.1714c$) with a periodic boundary condition to save computational cost. The computational domain is shown in Figure 5.1.

In experiments (Siauw *et al.* [2009]), an array of 44 holes were deployed at $0.3c$ downstream of the leading edge of the aerofoil. This array of holes occupied the central one third spanwise portion of the aerofoil and was spaced apart in the span with an interval of $\lambda = 0.015$ m ($\approx 0.04286c$). The spanwise length of the computational domain (0.6 m) were designed for four holes to be uniformly distributed. The locations of the four jets can be seen in Figure 5.1(b), and the centres of jets are at $z = \lambda \cdot \pm n/2, n \in \{\pm1, \pm3\}$. In experiments, the blowing jets were realized by blowing air into tubes connecting to the holes distributed on the aerofoil surface. The experimental setup is shown in Figure 5.2. The tubes have an diameter of $\phi = 0.001$ m, and the jet flow from the tubes has a pitch angle of 30° and a skew angle of 60°, as shown in Figure 5.3. The flow area at the jet exit on the aerofoil surface is an ellipse with a major axis length of 0.002 m and a minor axis length of 0.001 m, shown in Figure 5.3.

5.2.2 Boundary condition and time step

In experiments, the inlet velocity was 40 m s^{-1} with a turbulence intensity below 0.5%. The turbulence intensity is too small to be maintained numerically before the flow reaches the aerofoil, and therefore no turbulence intensity was superposed on the uniform inlet velocity in the simulations. The Reynolds number based on the chord and the inlet velocity is

5.2. Flow configuration

(a)

(b)
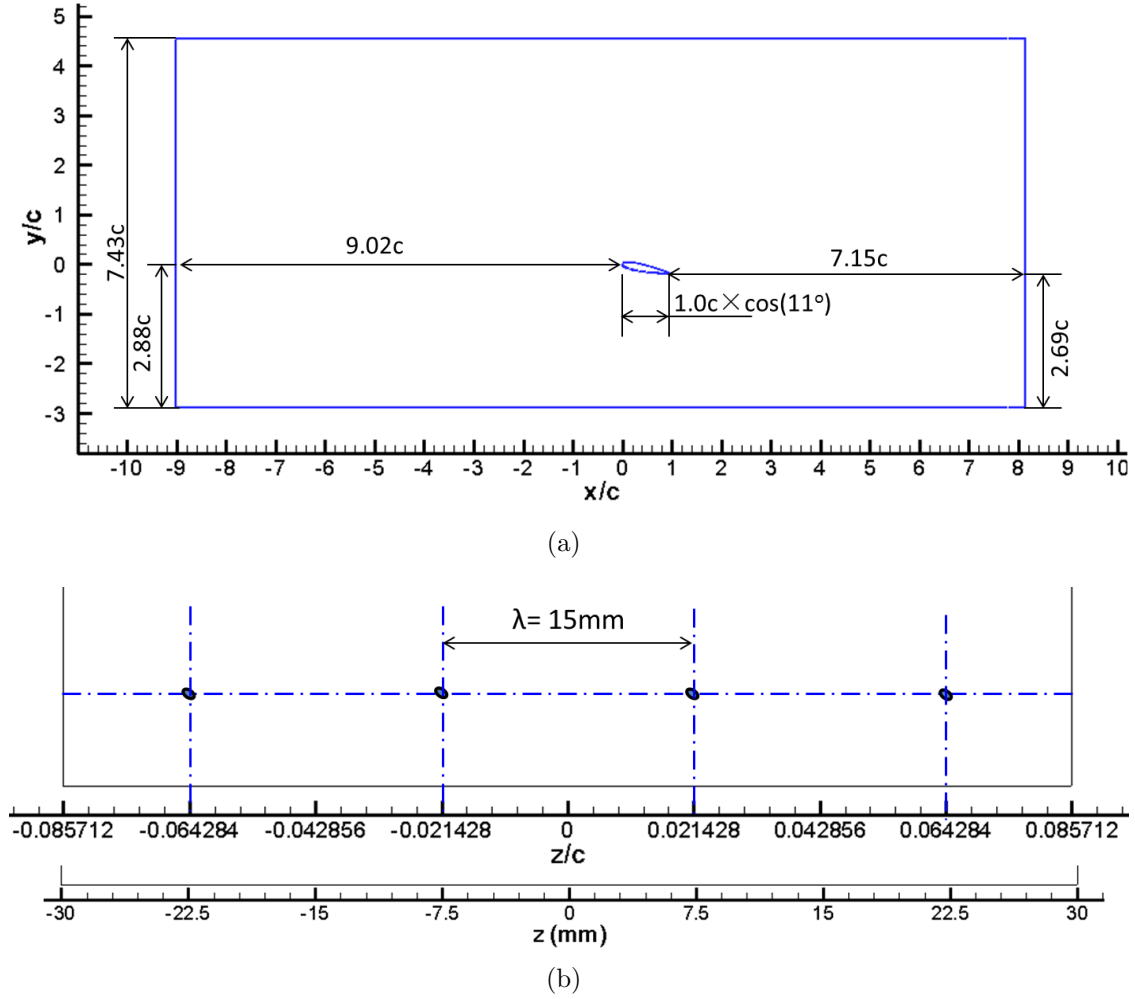
Figure 5.1: Computational domain of NACA0015 (a) The x-y plane; (b) the z-y plane to demonstrate the locations of jets

$Re_c = 9.33 \times 10^5$. In the numerical simulation, the outlet is set to be a convective outlet, the wind tunnel walls are set to be no-slip wall, and the span has a periodic boundary condition. In experiments, roughness elements (a carborundum size of 80 micron) were applied to trigger transition and to eliminate the laminar bubble which exists at $0.06c$ from the leading edge. In the simulation, no particular transition treatments are implemented, which means all the flow field is treated as turbulence.

In the simulation, the blowing jets are realized by specifying the jet velocity at the area of jets exit on the wall of the aerofoil surface. The peak velocity of the jet is around 200 m s^{-1} in the experiments (Siauw [2008]), corresponding to a momentum coefficient $C_\mu = 0.67\%$
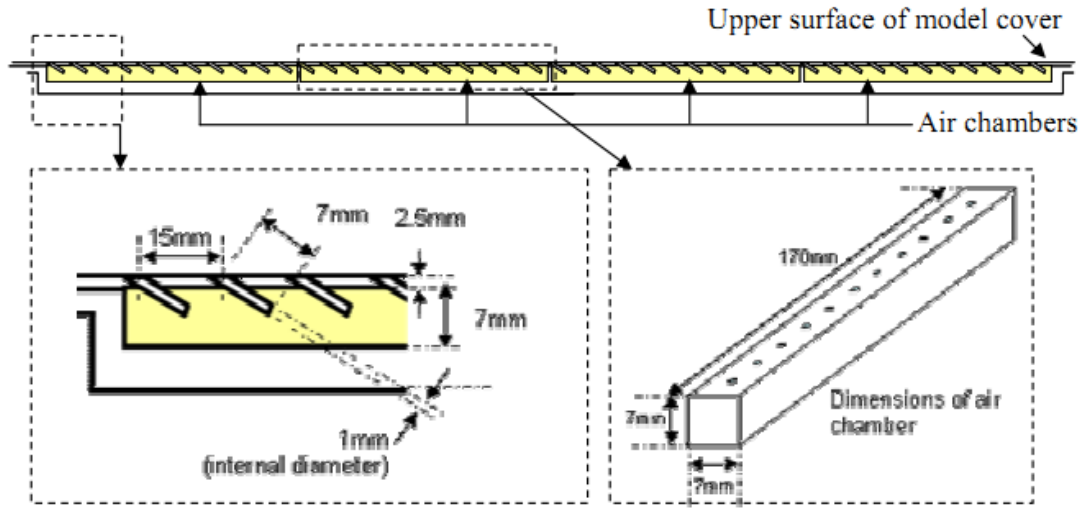
Figure 5.2: Schematic of the experimental configuration on pulsed jets (Siauw [2008])
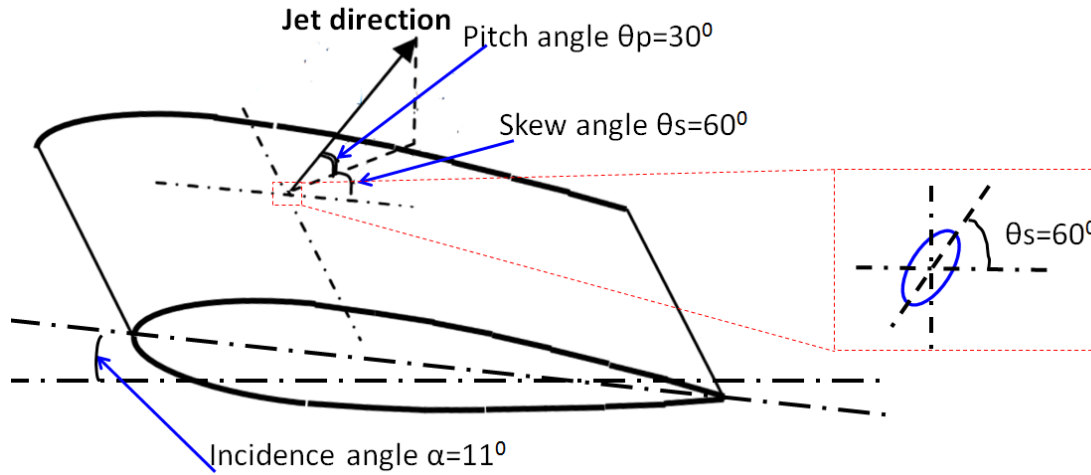
Figure 5.3: Schematic of pulsed jets orientation relative to the aerofoil.

and a control velocity ratio $VR = 5.0$. The momentum coefficient C_μ is defined as

$$C_\mu = \frac{1}{2} \frac{\rho_{\text{jet}} U_{\text{jet}}^2 A_{\text{jet}}}{\rho_\infty U_\infty^2 A_{\text{s}}}, \tag{5.1}$$

where A_{jet} is the area of jet holes, and A_{s} is the wing planform area spanned by the jets. The control velocity ratio is defined as

$$VR = \frac{U_{\text{jet}}}{U_\infty}, \tag{5.2}$$

Table 5.1: Flow phenomena

Conditions	Area/jet (m^2)	U_{jet} (m s^{-1})
Reference	1.57×10^{-6}	200.0
Experiment(Siauw [2008])	1.57×10^{-6}	204.0 ± 6.67
Simulation	1.50×10^{-6}	209.3

If the exact elliptical geometry of the jet-exit is fitted with numerical grids, the mesh will be very complicated to generate. Even if these grids representing the exact jet exit geometry are generated, they may deteriorate the grid quality in other computational domains because of the complicated topology. Therefore, in this simulation, the geometry of the jets exit does not follow the exact shape of ellipses, but it is determined by the real grid topologies generated for a typical aerofoil case. As a result, the jet exit area may be slightly larger or smaller than the exact elliptic area. In order to keep the same momentum coefficient, the jet velocity is adjusted according to the real jet area in the computation. The comparison of the given control parameters and the real ones used in the simulations according to the grid topology is given in Table 5.1. The control velocity in the simulation is about 4% increase of the experimental control velocity, but the momentum coefficient is kept the same.

The time step for all calculations for this NACA0015 case was set to be $2.3 \times 10^{-3} c/U_\infty$. For the baseline case, physical solutions were achieved after around 40 flow-through periods, and then another 40 flow-through periods were carried out for statistical sampling. The flow-through period is defined as

$$T_{\text{ft}} = \frac{c}{U_\infty}. \tag{5.3}$$

After obtaining a statistically converged baseline flow, the jets were switched on. In the experiments, the control frequency is 1 Hz, and the duty circle is 50%. Therefore, a time interval of 0.5 s were carried on in the control state. After this controlled 0.5 s, the jets were switched off. As mentioned before, the experiments show the pulsed jets with a control frequency of 1 Hz behave similar to a continuous jets, and therefore only one control period is simulated in the present study.

5.2.3 Mesh resolution

There is no mesh convergence theoretically for numerical simulations involving solving turbulent structures using LES. In order to assess the effect of spatial resolution on the simulation results, three sets of meshes (coarse, medium and fine) were carried out for the baseline case.

With the same aerofoil geometry as the experiments, the NACA0015 aerofoil in simula-

Table 5.2: Summary of mesh resolutions

Case	N_z [a]	N_{cell} [b]	y_1^+ [c]	Δx^+ [d]	Δz^+ [e]
Baseline: Coarse	40	3 513 960	$0.6 \sim 1.2$	$68 \sim 113$	$60 \sim 120$
Baseline: Medium	40	8 511 000	$0.4 \sim 1.0$	$52 \sim 98$	$40 \sim 100$
Baseline: Fine	88	12 675 600	$0.2 \sim 0.7$	$30 \sim 76$	$18 \sim 37$

[a]The cell number along the span.

[b]The total cell number.

[c]The non-dimensional maximum grid spacing in the wall-normal direction along the aerofoil.

[d]The non-dimensional grid spacing in the streamwise direction in the region from the leading edge to two chord downstream of the trailing edge.

[e]The non-dimensional grid spacing in the spanwise direction.

tions has a blunt trailing edge with a thickness of 0.5 mm. The H-C-H grid topology was used to generate the mesh around the aerofoil in the numerical domain. The fine mesh for the streamwise section at a fixed spanwise location is shown in Figure 5.4. (The coarse and medium meshes, working as auxiliary meshes, have similar mesh topology and mesh stretching ratios to the fine mesh, which will not be shown). The blunt trailing edge contains 24 elements, with smooth transition to the near-wall grid resolution on the aerofoil (Figure 5.4(d)). In order to reconstruct the geometry of jets exits on the aerofoil, the mesh near the jets was refined (Figure 5.4(e)). This mesh refinement in the attached boundary layer may harm the accuracy of hybrid RANS/LES (Spalart [2001]), but it is a price worth paying for the simulation of jets control on aerofoils. The span, with a length of 60 mm and 4 jets, has 84 grid cells uniformly distributed. The mesh resolutions for these three sets of meshes are listed in Table 5.2.

Simulations of the baseline case were carried out with these three sets of meshes. The IDDES turbulence modelling technique was used. The pressure and skin friction are used to validate the mesh convergence for this case. Figure 5.5(a) shows the pressure coefficients with the three sets of meshes. The differences between the pressure coefficient is less than 3% for the three sets of mesh, and the fine mesh gives the best agreements to the experimental data. The differences of the skin friction for these three sets of mesh are less than 5%, while the most discrepancy occurs in the separated region, where the coarse mesh seems to slightly over-predict the flow separation. Overall, simulation results by these three sets of meshes provide very close C_p distributions. (The prediction on the second order statistics improves with a finer mesh, which is not shown). Following the mesh study criteria for LES (Klein [2005]), the three sets of simulations achieve an acceptable mesh convergence in the first order statistics. In order to achieve the best flow resolution, all simulations in the following sections on both the baseline flow and the controlled flow are carried out with the fine mesh,
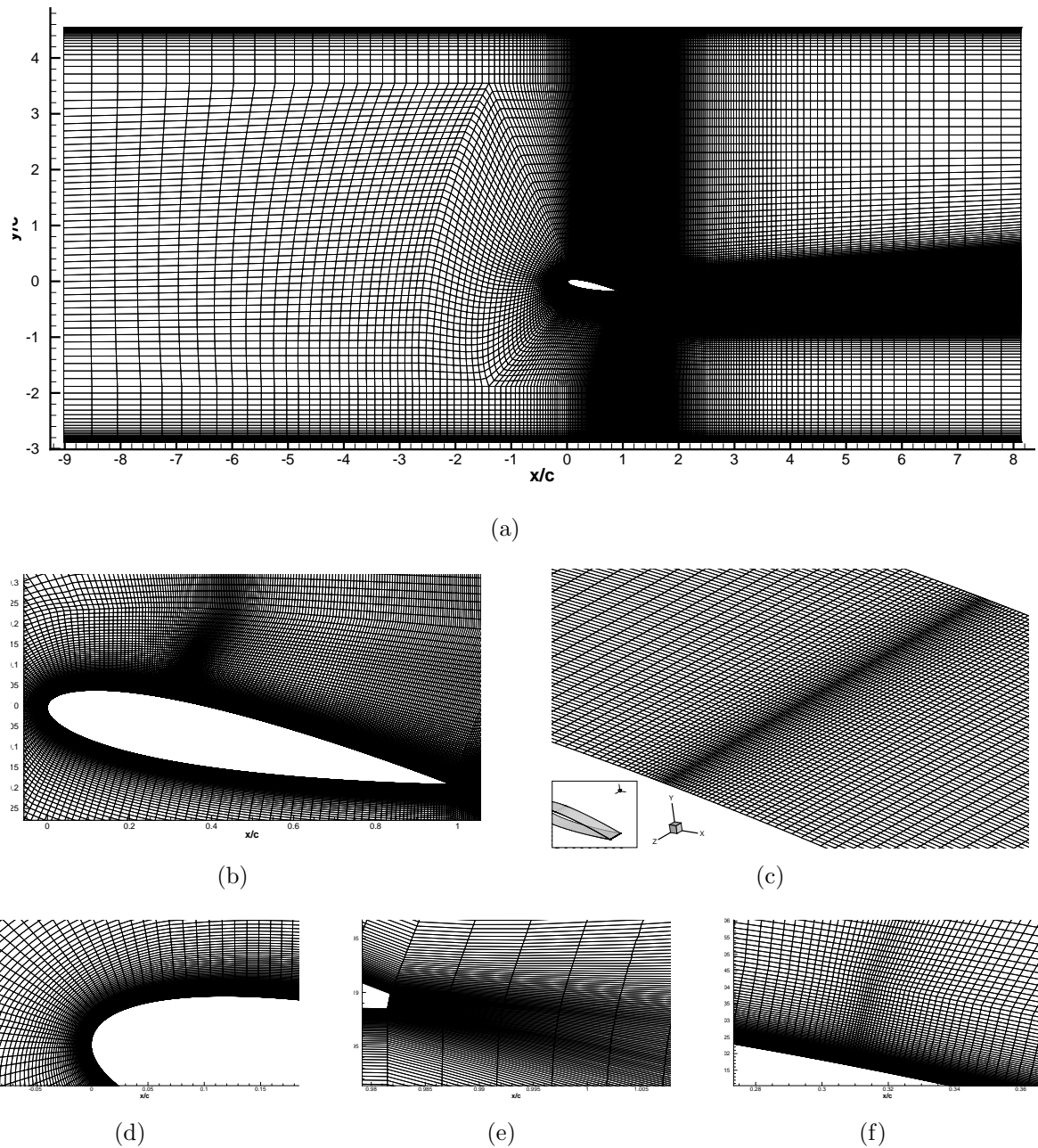
Figure 5.4: Computational mesh for NACA0015 simulation. (a) 2D mesh in the whole domain; (b) 2D mesh near the aerofoil; (c) 3D mesh on the aerofoil near the jets' locations; (d) 2D mesh near the leading edge; (e) 2D mesh near the trailing edge; (f) 2D near the jets' locations.

unless otherwise stated.
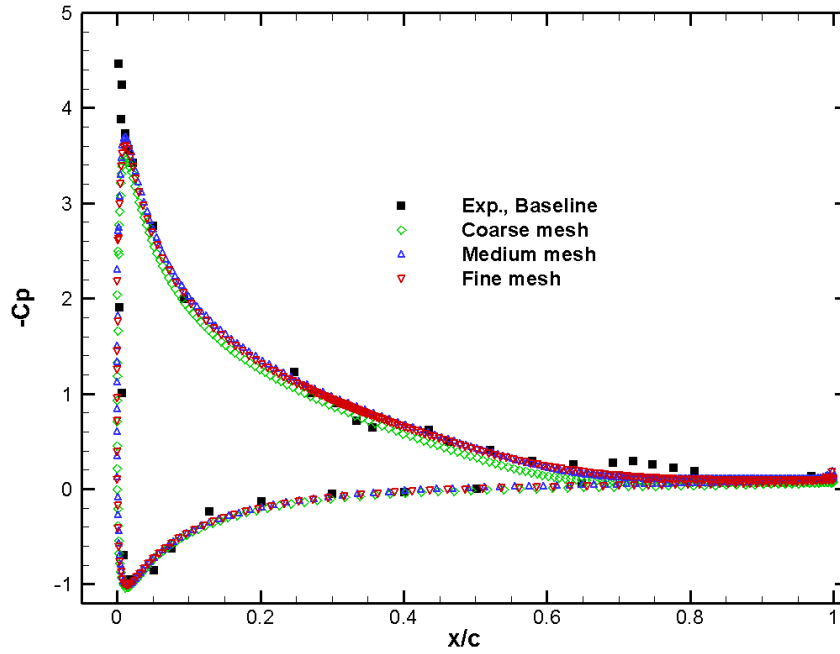
(a)
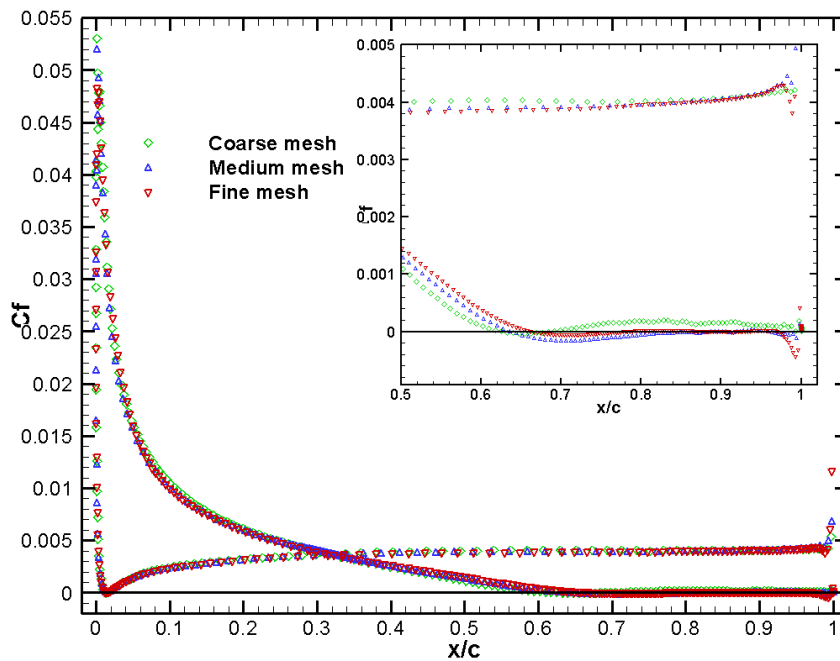
(b)

Figure 5.5: Comparison of the first-order statistics from different mesh resolutions. (a)Time averaged C_p; (b) Time averaged C_f.

5.3 Validation of turbulence models in the baseline flow of NACA0015

5.3.1 Introduction

Our previous study (Wang and Qin [2012]) on DES and its variations shows that DES usually predicts a larger separation due to the "MSD" problem (Spalart [2009]), while DDES can alleviate it, especially for a mild separation flow. However, DDES has a tendency to suppress the resolved flow fluctuations in the separated region due to its "delayed" properties. IDDES is a recently proposed promising hybrid RANS/LES method. The validation of IDDES both in attached flows and in separated flows in Shur *et al.* [2008] shows its advantages over DDES. In a mild separation flow, IDDES works like DDES in the attached boundary layer and like WM-LES in the separated region.

For this case, initially, DDES and IDDES ware applied to the coarse mesh. However, only IDDES predicts a separation similar to the experiments. DDES cannot capture any flow separation. In order to study the behaviours of DDES in this particular case, after the statistically steady state of the baseline flow was achieved by IDDES (with the fine mesh), DDES was switched on to replace IDDES. After a certain number of time steps, DDES forced the separated flow originally predicted by IDDES to be attached again, which is consistent with the conclusion in initial simulations with the coarse mesh that DDES cannot predict any separations.

In order to study the failure of DDES, the transient process from the separated flow predicted by IDDES to the attached flow by DDES will be investigated in the following subsection.

5.3.2 Comparison of DDES and IDDES in the baseline flow

Figure 5.6 compares the instantaneous results by IDDES and DDES at different time steps. It is observed that DDES, which replace the original IDDES, introduces high modelled turbulent viscosity and extends it in the streamwise direction until it finally covers the whole trailing edge. Correspondingly, the instantaneous streamlines (Figure 5.6(b)) shows the separated shear layer bends towards the wall and finally removes the separation.

Durrani and Qin [2011] also observed the incapability of DDES in capturing a mild separation. In this literature, DDES just behaves like URANS, which produce excessive turbulent viscosity to resist the flow separation. Wang and Qin [2012] gave some explanations on why DDES produces large modelled turbulent viscosity in the originally separated region.

On the whole, the transition between RANS and LES in DDES highly depends on the initial turbulent viscosity. This dependence may produce much more modelled turbulent viscosity by a mechanism similar to a positive feedback in the region where there should be separated. If the separation region, in itself, has small flow fluctuations, the drawback of DDES will arise and become obvious, which generates unnecessarily high modelled turbulent viscosity to resist the flow separation. (These drawbacks of DDES are summarized in Wang and Qin [2013] submitted to a journal with formulation derivations and validations in more cases.) As for IDDES, it has three different types of modelling modes (RANS, DDES and WMLES), depending on the flow properties, and it can "inherit turbulent content" from the upstream region (Shur *et al.* [2008]). The IDDES streamlines in Figure 5.6 show that even though the flow has been separated, the flow fluctuations near the separation point are weak. These weak fluctuations may be sensed by IDDES to produce less modelled turbulent viscosity, while DDES may not take the weak fluctuations into account in producing the modelled turbulent viscosity. Thus, DDES has higher modelled turbulent viscosity, which in turn hampers the development of turbulence fluctuations, and finally leads to a much smaller separation region.

What is interesting is that the drawback of DDES is much more obvious in this case than other cases with mild separations, for example, the A-aerofoil with $0.83c$ separation (Wang and Qin [2012]). In addition, for flows with larger separations, DES and DDES give very similar results, both for flows over an aerofoil (Durrani and Qin [2012]) and for flows over a geometry-induced sudden separation (Section 4.2.5). Therefore, the current NACA0015 case with an angle of attack 11° seems to be very special, and may become a useful case to further analyse different hybrid RANS/LES turbulence models.

5.3.3 Summary

With current configurations, only IDDES can provide a flow separation similar to the experimental measurement. The failure of DDES may come from the excessive turbulent viscosity and small flow fluctuations in the separated region. For all following simulations, IDDES is chosen to realize the turbulence modelling.

(a) streamlines

(b) ν_t
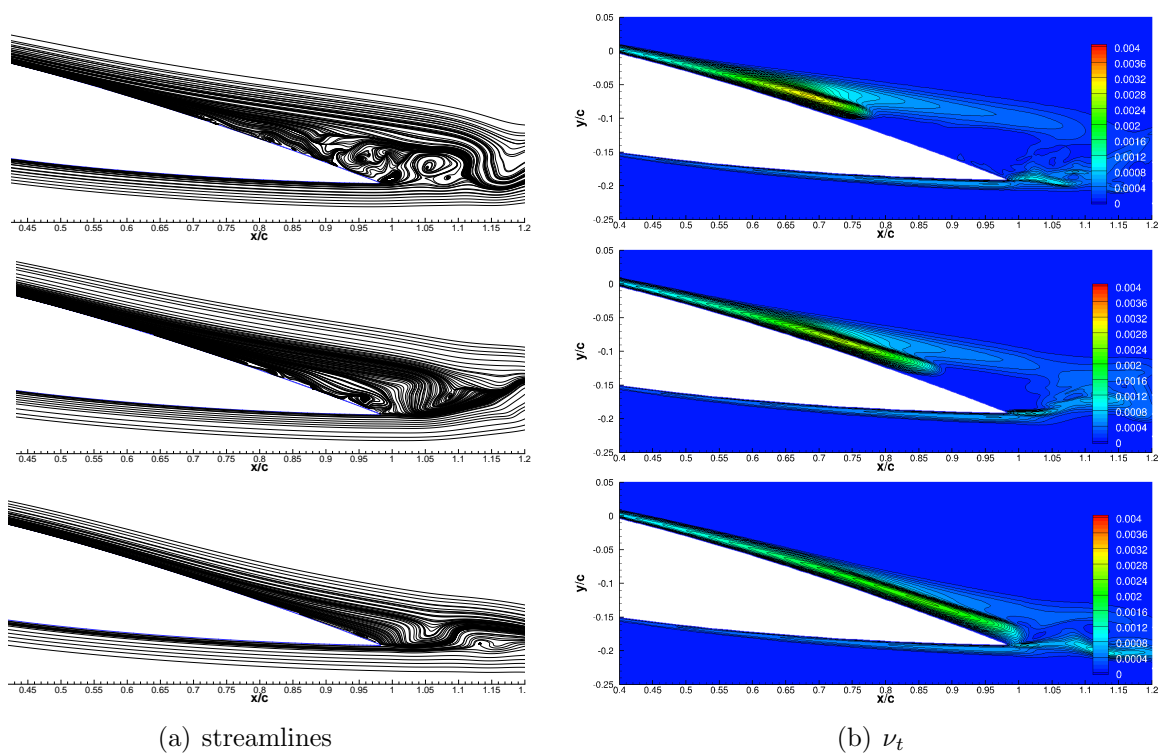
Figure 5.6: (a) Instantaneous $2D$ streamlines at z=0. (b) Instantaneous modelled turbulent viscosity, and the legend stands for ν_t. From top to bottom: IDDES, DDES after 0.006 s, DDES after 0.02 s.

5.4 Comparative study of flow characteristics in the statistically steady state of the baseline and controlled flow

After switching on the jets for about 0.1 s, the originally separated flow in the baseline case become attached. In this section, the statistically averaged baseline flow and the controlled attached flow are compared.

5.4.1 Coherent vortices

The generated vortices by the jets are first investigated. The instantaneous flow for the baseline is arbitrarily chosen, while the instantaneous flow for the jet-controlled flow is chosen from the time step at 0.44 s after switching on the jets, which is statistically steady for the attached flow.

The instantaneous flow structures in the baseline flow are shown in Figure 5.7, which shows clear vortex shedding. Figure 5.8 displays the instantaneous visualization of the controlled flow after the jets switching on for 0.44 s. The flow is locally fully-attached, and small vortices near the trailing edge in regions between two jets can still be observed. Nevertheless, no obvious vortex shedding can be observed in the wake for the jet-controlled flow (Figure 5.8). Jets-manipulated shear layer dominates the whole chord of the aerofoil, and even expands to the wake flow.
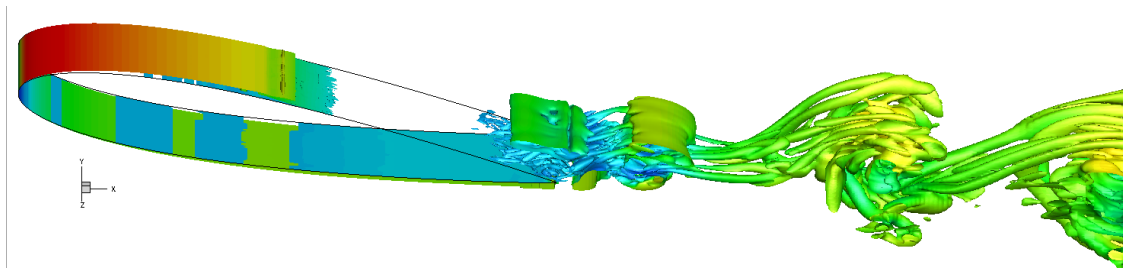
Figure 5.7: Baseline flow: the λ_2 criterion, coloured with the streamwise velocity.

The three vorticity components Ω_x, Ω_y and Ω_z for the baseline flow is given in Figure 5.9, and Figure 5.10 presents these vorticity components for the controlled flow. It is observed that for the baseline flow, the spanwise vorticity Ω_z overwhelms the other two vorticity components upstream of the trailing edge. The separated shear layer is obviously observed from the iso-surfaces of the spanwise vorticity Ω_z. Figure 5.10 shows that in addition to the

5.4. Comparative study of flow characteristics in the statistically steady state of the baseline and controlled flow
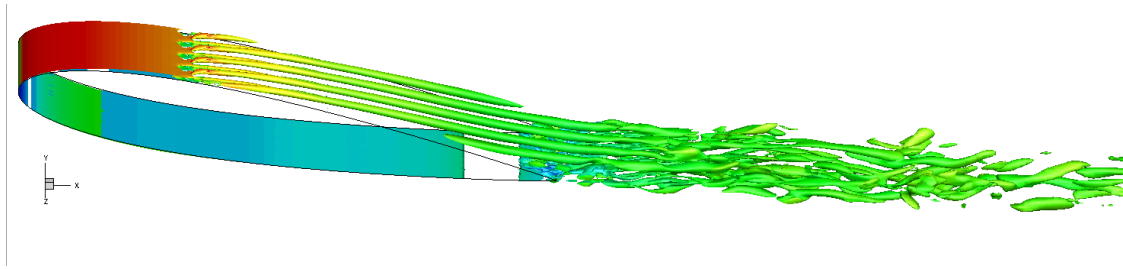
Figure 5.8: Jets controlled flow at $t = 0.44$ s after switching on the jets: the λ_2 criterion, coloured with the streamwise velocity.

spanwise vorticity, the jet-blowing introduces strong vorticity Ω_x and Ω_y around the aerofoil.
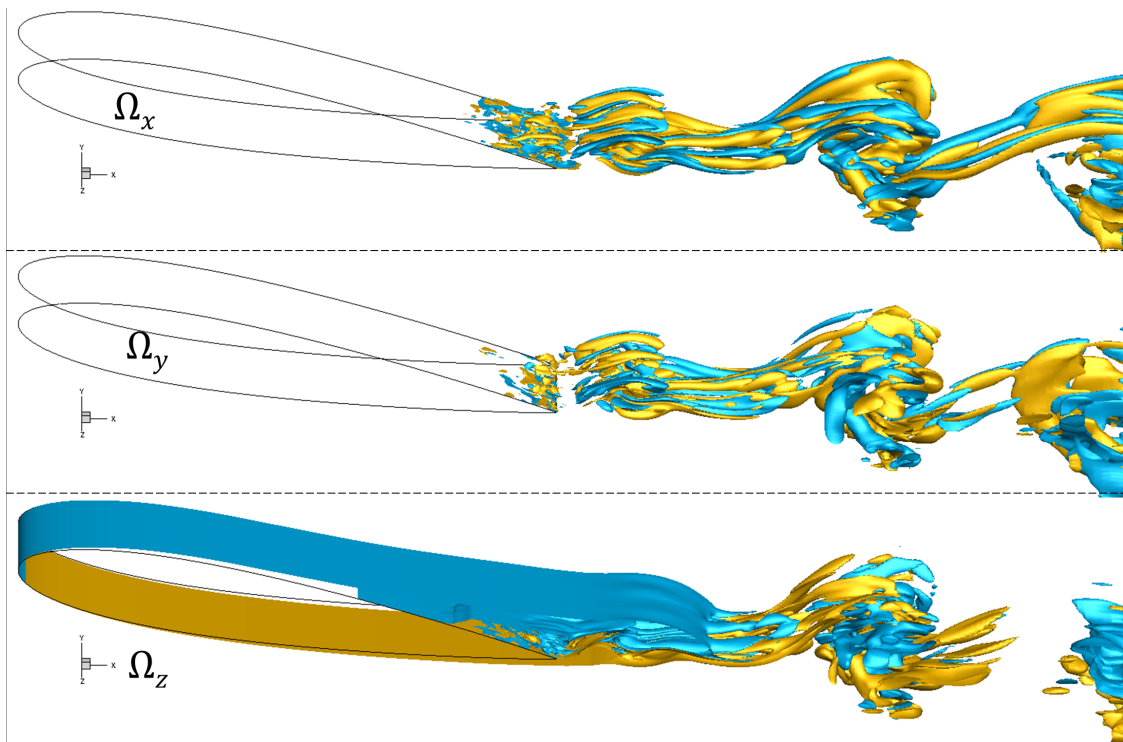
Figure 5.9: Baseline flow: iso-surface of the vorticity components at ± 1000 (The colour of yellow for 1000, and the colour of blue for -1000). From top to bottom: Ω_x, Ω_y and Ω_z.

Figure 5.11 presents the contours of the three components of the vorticity at different cross sections. Figure 5.10 and Figure 5.11 display features of the generated vortices as follows. From the streamwise vortices, it is observed that the generated vortices in the focal region has a rotation direction of clockwise viewed downstream along the $+x$ axis (This is the default viewed direction, which will not be repeated when mentioning the rotation directions.). The rotation direction is determined by the direction of skew angle. Johnston
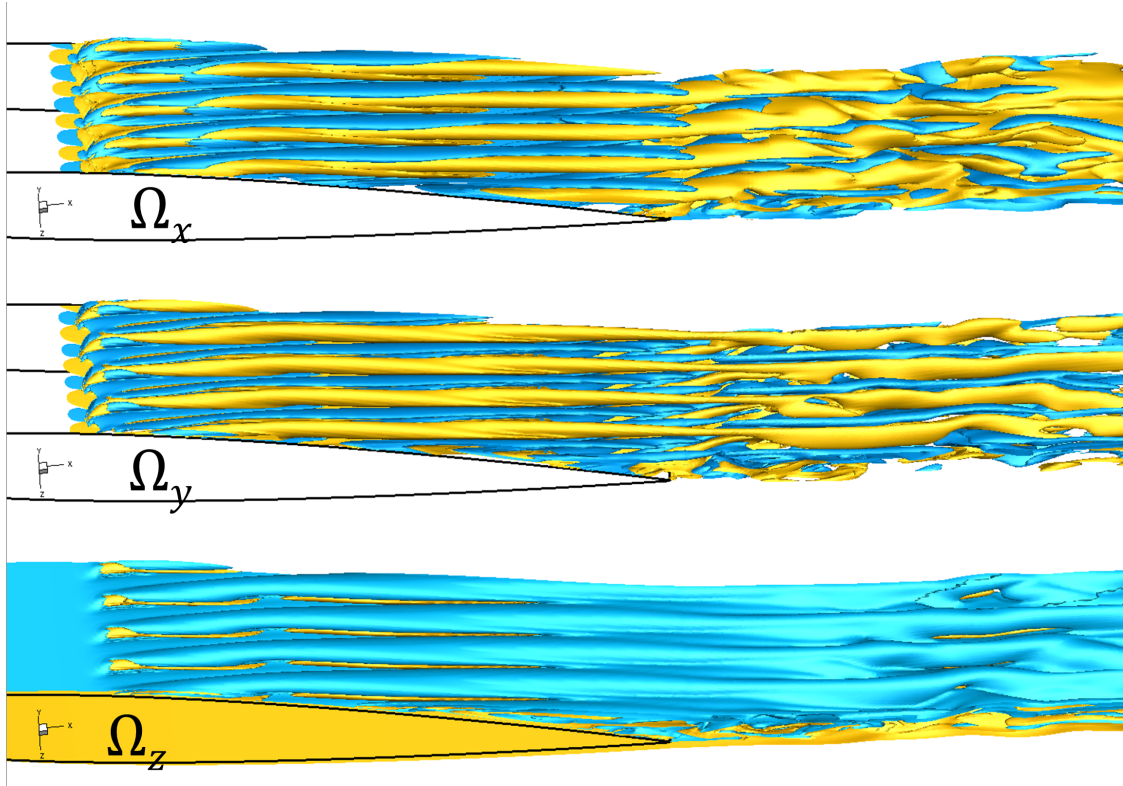
Figure 5.10: Jets controlled flow at $t = 0.44$ s after switching on the jets: iso-surface of the vorticity components at ± 1000 (The colour of yellow for 1000, and the colour of blue for -1000). From top to bottom: Ω_x, Ω_y and Ω_z.

and Nishi [1990] discussed the relation between the skew angle and the streamwise rotation direction of generated vortices. Our simulation results confirmed this relation. In addition, a region with a negative sign of the streamwise voriticiy Ω_x exists around the focal region of positive Ω_x from the side of skewed direction and roots in the wall. These vortices with opposite streamwise rotation directions form a counter-rotating vortex pair. However, this counter-rotating vortex pair is not symmetrically side by side, as observed in jet-flow with a large jet diameter (See Figure 4.59 extracted from Fric and Roshko [1994]). The skewness and the small jet diameter make counter-rotating vortex pair strongly biased. A similar phenomenon is also observed in Kostas *et al.* [2007]. From $x/H = 0.7$, the streamwise vortices generated by two adjacent jets begin to merge, and this interaction weakens the vortices with the rotation of anti-clockwise direction. The spanwise vorticity Ω_z shows that the jet shear layer of the vortices (the outer region of the vortices) rotates from the upstream towards the downstream, which is determined by the incoming flow direction. However, inside of the jet shear layer, vortices have the opposite direction, and counter-rotating vortex pairs exist inside of the jet shear layer.
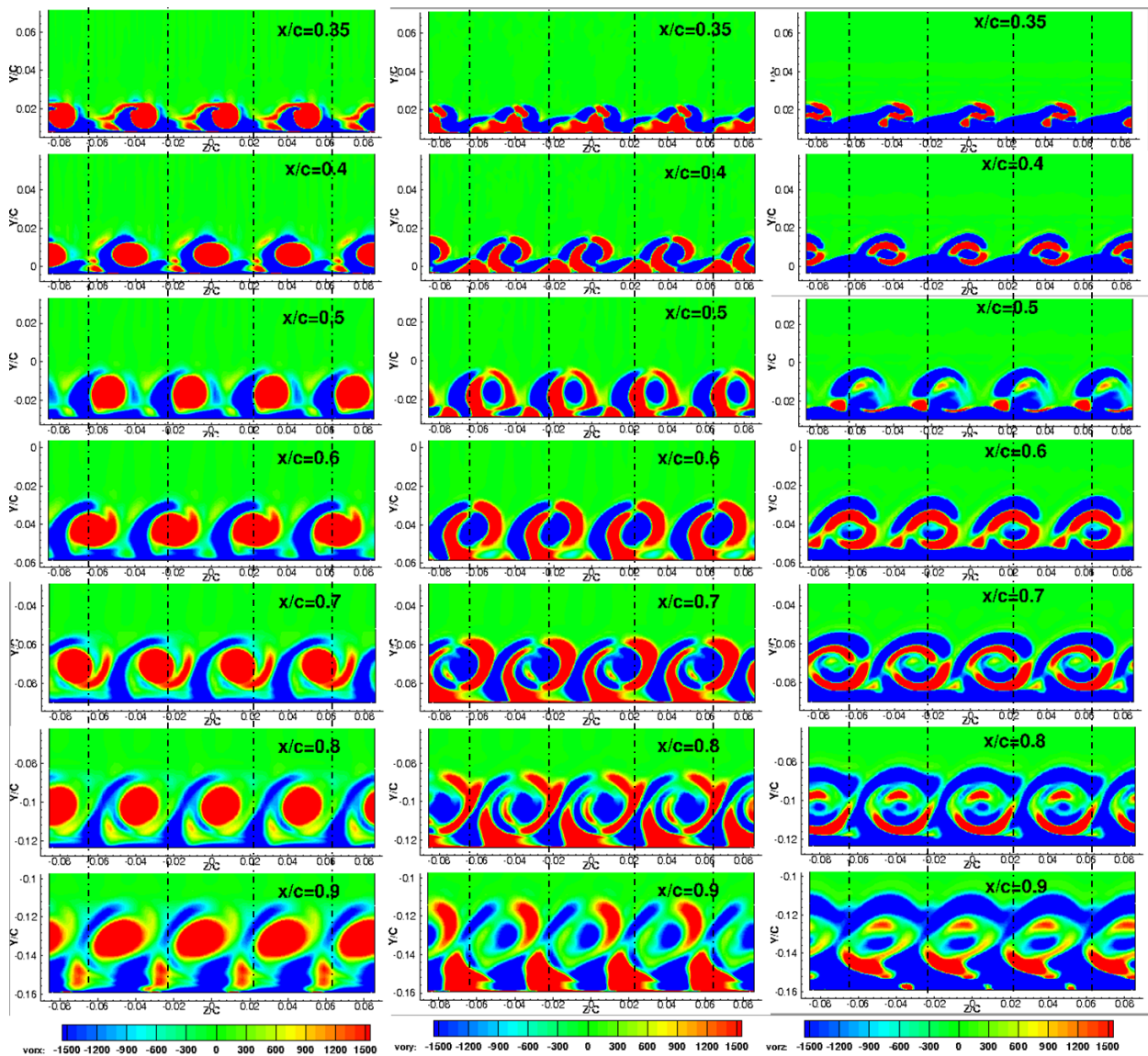
Figure 5.11: Contours of the vorticity components at ± 1000 at the cross sections $x/c = 0.35$, 0.4, 0.5, 0.6, 0.7, 0.8 and 0.9. The left column for the streamwise vorticity Ω_x, the middle column for the vorticity Ω_y and the right column for the spanwise vorticity Ω_z.

5.4.2 Pressure and skin friction along the aerofoil

5.4.2.1 The lift and drag coefficient

In simulations, the lift (C_L) and drag (C_d) coefficients are calculated in their original definitions, which are:

$$C_L = \frac{2L}{\rho U_\infty^2 A}, \quad C_d = \frac{2D}{\rho U_\infty^2 A}, \tag{5.4}$$

where L is the lift force, and D is the drag force, which both are integrals of the skin friction and pressure in the direction of normal/parallel to the inlet velocity along the whole span, and A is the reference area. In experiments, the drag coefficient was estimated indirectly from the wake profiles (Siauw *et al.* [2009]). The different methods on calculating the coefficients in simulations and experiments may introduce some disparities.

The simulated lift and drag coefficients both in the baseline and the control flow are listed in Table 5.3. By contrast to the baseline, the jets controlled aerofoil has an increased lift coefficient and a reduced drag coefficient, predicted both by experiments and simulations. For the jet controlled flow, the simulation provides a 16.7% increase in the lift coefficient, compared with a 11.5% increase in experiments. For the drag coefficient, a reduction of 28.4% is obtained by simulations, while the experiments gave a 28.6% reduction. Overall, simulation results give good agreements with the experiments. Simulations confirm the effectiveness of pulsed jets in increasing the lift-to-drag ratio, which is desirable for aircraft design.

Table 5.3: Lift and drag coefficients

Conditions	C_L		C_d	
	baseline	controlled	baseline	controlled
Experiment	0.920 ± 0.0017	1.026 ± 0.0017	0.0280 ± 0.0014	0.0200 ± 0.0014
Simulation	0.912	1.065	0.0275	0.0197

5.4.2.2 The skin friction coefficient

The lift and drag coefficients only represent the integral effects. Comparisons of the skin friction and the pressure between the baseline case and the controlled case will provide more details on the control effect. Considering the skew angle in the controlled flow, the direction of the force of skin friction varies depending on the flow properties. For simplicity, the skin friction shown below is defined as: the magnitude of C_f is the magnitude of the skin friction along the aerofoil surface, and the sign of C_f is determined by the sign of the x-component of the skin friction vector.

5.4. Comparative study of flow characteristics in the statistically steady state of the baseline and controlled flow

Figure 5.12 gives a comparison of the time and spanwise averaged skin friction coefficient C_f between the baseline and the controlled flow (There are no available experimental data on skin friction). If the zero-C_f is used to define the separation point, the baseline case shows a separation at $x = 0.68c$, and the pulsed jets controlled aerofoil has a separation at $x = 0.99c$. In experiments, the baseline case has a $x \approx 0.7c$ separation and the controlled aerofoil has a fully-attached flow. The separations in experiments were estimated by oil flow visualization, not by a zero-C_f. In spite of slight differences, we think the simulations provide good agreements on the separation points both for the baseline and the controlled flow to the experiments. A distinct conclusion on the effect of pulsed jets drawn from both the experiments and simulations is that pulsed jets force the separated flow to be attached.

Besides separation points, Figure 5.12 shows more details on C_f along the controlled flow around the aerofoil. Near the jets location ($x = 0.3c$), an abrupt change of C_f occurs for the controlled flow. This is introduced by the imposed high velocity from jets. Downstream of the jets' location to $x \approx 0.48c$, C_f in the controlled flow is slightly smaller than the baseline flow. This may imply that the jets blow the flow out and extract energy from the boundary layer outwards when the pitched vortex is very close to the boundary layer. However, from $x \approx 0.5c$ to the trailing edge, the controlled flow has a much larger C_f than the baseline flow. This trend illustrates that the boundary layer is energised by the jets and the velocity gradient is much larger than the baseline flow, which will resist flow separation. For the pressure side, the change of C_f introduced by the pulsed jets along most of the aerofoil is small, around 5% reduction, and the largest difference exists near the trailing edge, which is around 18% reduction from the baseline flow.

As the jets have a skew angle, the C_f distribution in the spanwise direction will not be uniform. Figure 5.13 displays the instantaneous contours of C_f both for the baseline and the controlled flow. For the baseline flow, shown in Figure 5.15(a), the zero-C_f locates around $x = 0.7c$, and before this location, the attached flow behaves like $2D$ flow with little variation along the span, just the same as the observation in experiments. In comparison with the baseline flow, the jets introduced strong spanwise variations on C_f, shown in Figure 5.15(b). There are several phenomena observed in C_f contours of the jets controlled flow. Firstly, near the jets, large positive and negative C_f associatively exist and incline to the skew angle. This may relate to the fluidic obstacles from the blowing jets, which force the flow to rotate. Secondly, a region with lower C_f have formed at around $x \approx 0.4c - 0.45c$ between the large C_f trajectories. Thirdly, near the trailing edge at around $x = 0.75c$, low C_f strips begin to grow alternating with the high C_f, and then they expand in the spanwise directions and develop towards the trailing edge. Downstream of this location, the interaction of the adjacent jets
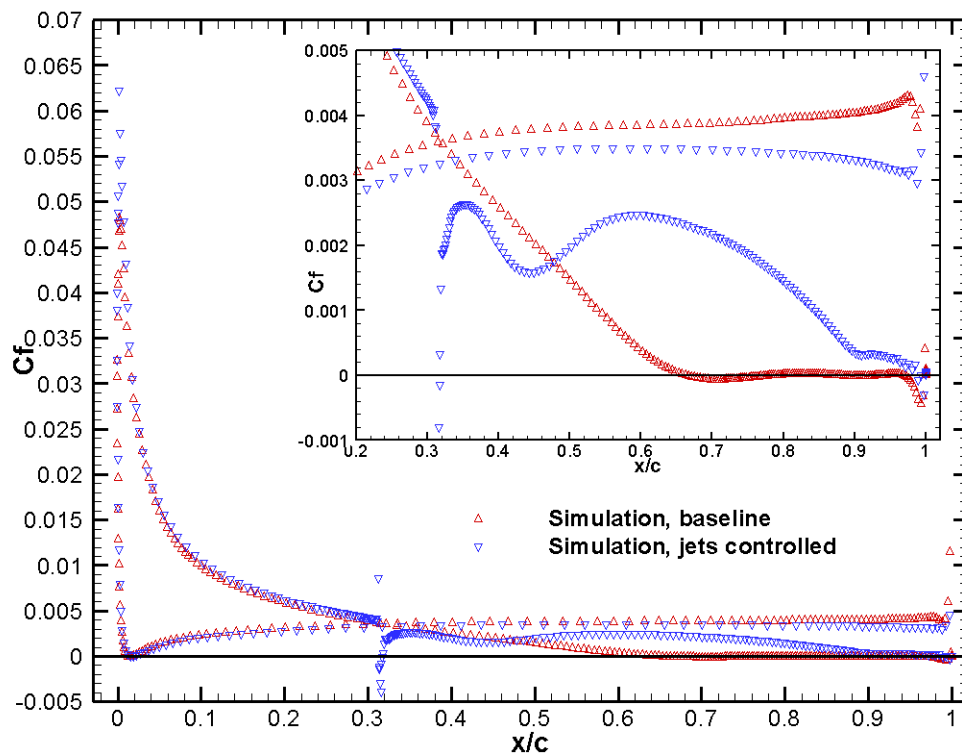
Figure 5.12: Comparison of the skin friction in the baseline flow and the jets controlled flow.

becomes significant. Very near the trailing edge, it is difficult to distinguish the lower and higher C_f strips, because of the intense interaction between jets. Although the time and spanwise averaged C_f (Figure 5.12) shows a $0.99c$ separation point in the controlled flow, the instantaneous C_f displays that flow may begin to separate at upstream of $x = 0.99c$ in some narrow regions along the span. More explanations on the distribution of the skin friction will be given in the next subsection together with the velocity distributions.

5.4. Comparative study of flow characteristics in the statistically steady state of the baseline and controlled flow
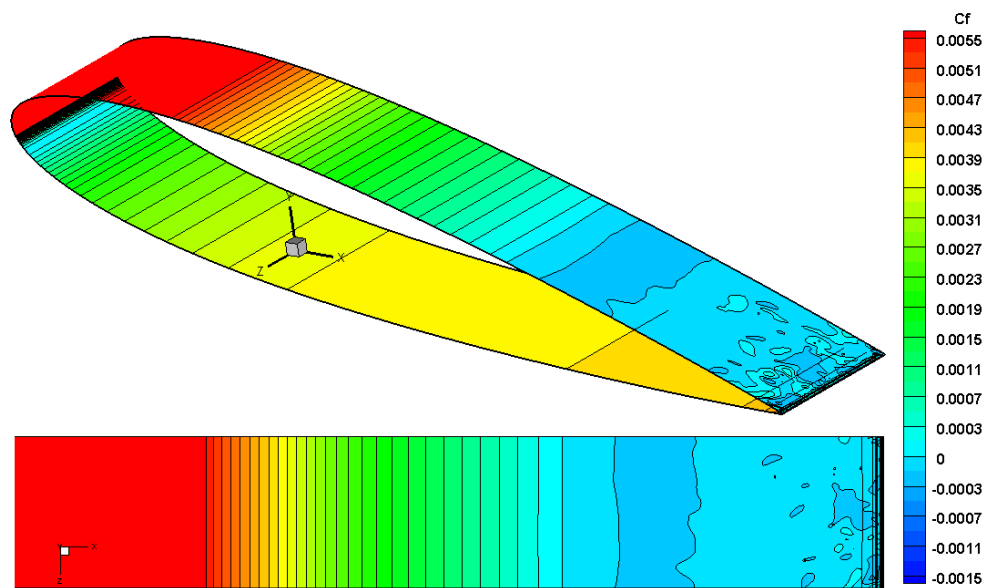
(a)
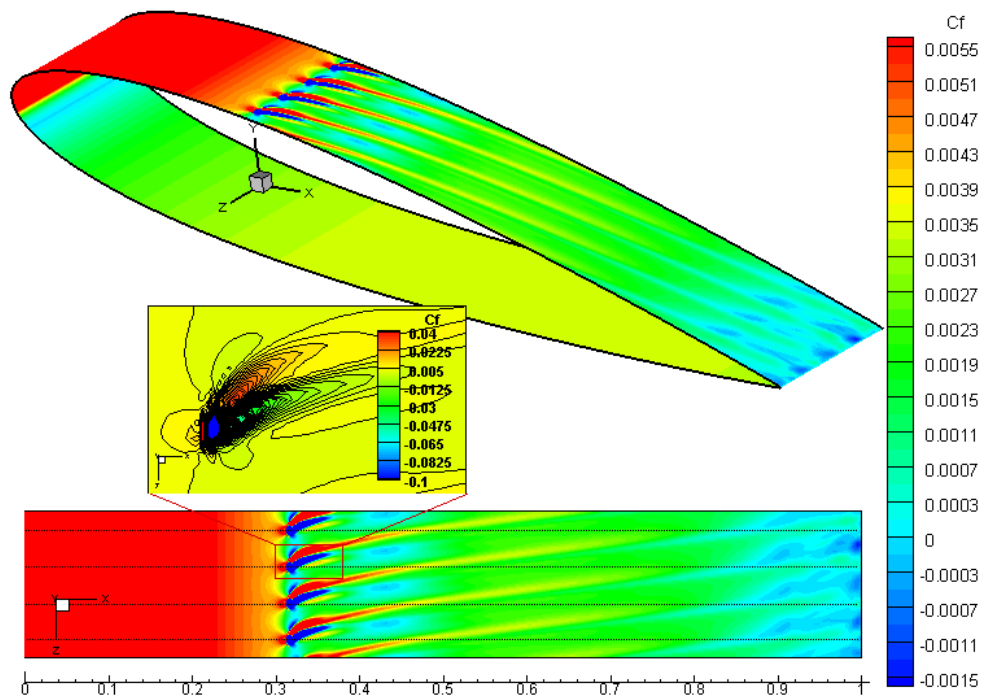
(b)

Figure 5.13: Instantaneous contours of skin friction coefficient C_f in a statistically steady state. (a) The baseline case (the top figure for a 3D view and the bottom figure for a 2D top view); (b) The jets controlled case (the top figure for a 3D view, the bottom figure for a 2D top view and the middle figure is an enlarged view of one single jet). Note: (1) the legend of the middle figure of (b) has a different scale from others to display a clear visualization near the jets; (2) the dash line in the bottom figure of (b) represents the spanwise locations of jets.

5.4.2.3   The pressure coefficient

The pressure distribution contributes the most to the lift enhancement. The simulations predict a very similar pressure distribution to the experimental data, both for the baseline and the controlled flow, as shown in Figure 5.14.

For the jets controlled flow, the time and spanwise averaged pressure coefficient $(-C_p)$ along the suction side of the aerofoil (shown in Figure 5.14) becomes smaller than the baseline flow at the region $x/c < 0.7$, and is higher than the baseline flow downstream of $x/c \approx 0.7$. For the pressure side, the jets controlled aerofoil always provides higher C_p. These changes in the controlled flow contribute to a larger lift coefficient than the baseline flow. At $x/c = 0.3$, where the jet-centres locate, an abrupt change of the pressure coefficient occurs. This steep pressure bump may be introduced by the rapid change of velocity, due to the jets blowing effect.
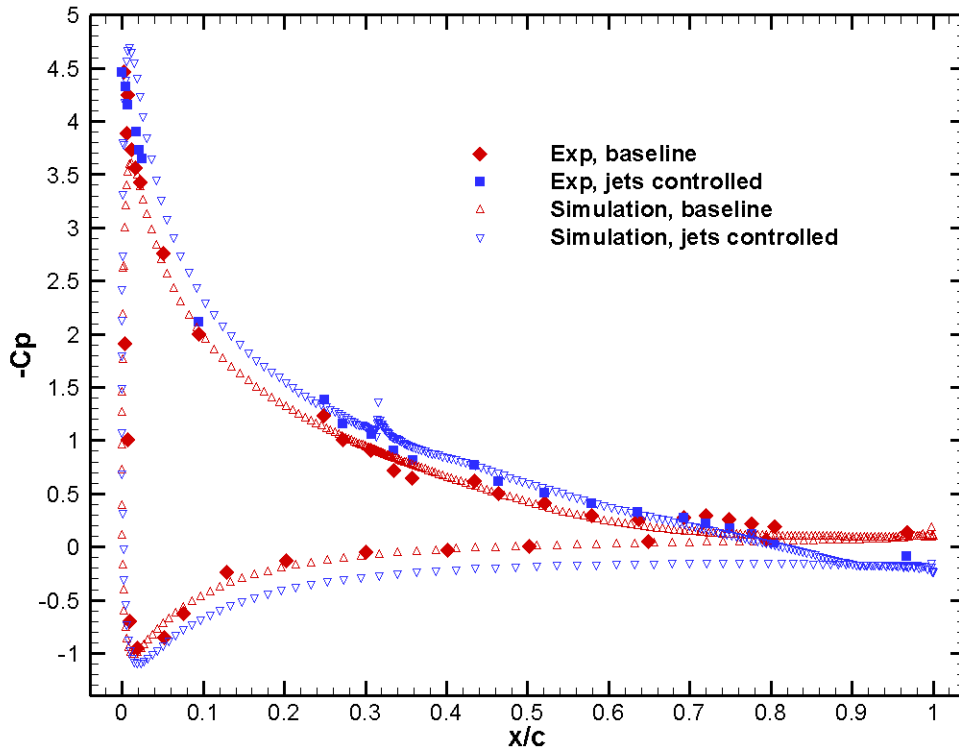
Figure 5.14: Comparison of the pressure coefficients (both time and spanwise averaged) in the baseline flow and the jets controlled flow.

Instantaneous C_p contours on the baseline and controlled aerofoil surface are given in Figure 5.15 at the same time step as the C_f shown in Figure 5.13. Again, for the baseline flow, there is little variation of C_p along the span before the separation point (shown in Fig-

5.4. Comparative study of flow characteristics in the statistically steady state of the baseline and controlled flow

ure 5.15(a)). The pulsed jets introduce tremendous changes of C_p around the jets locations in the spanwise direction (shown in Figure 5.15(b)). The pressure coefficient C_p around the jet is very regular for the four jets, and the entanglement between jets in terms of C_p is weak, which may be due to a small ratio of the jet diameter ϕ to the jet spanwise spacing λ ($\phi/\lambda = 1/15$). The regular trajectories of the jets-influenced C_p extend to the trailing edge and fade out. The dash-lines in Figure 5.15(b) show that when flow approaches to the trailing edge, the regular spanwise spacing between the peak C_p maintains the original jets' spanwise spacing, which implies weak interaction between jets. Although the skew angle is set to be 60°, the trajectory of C_p has a much smaller skew angle owing to the rectification from the inlet streamwise flow.
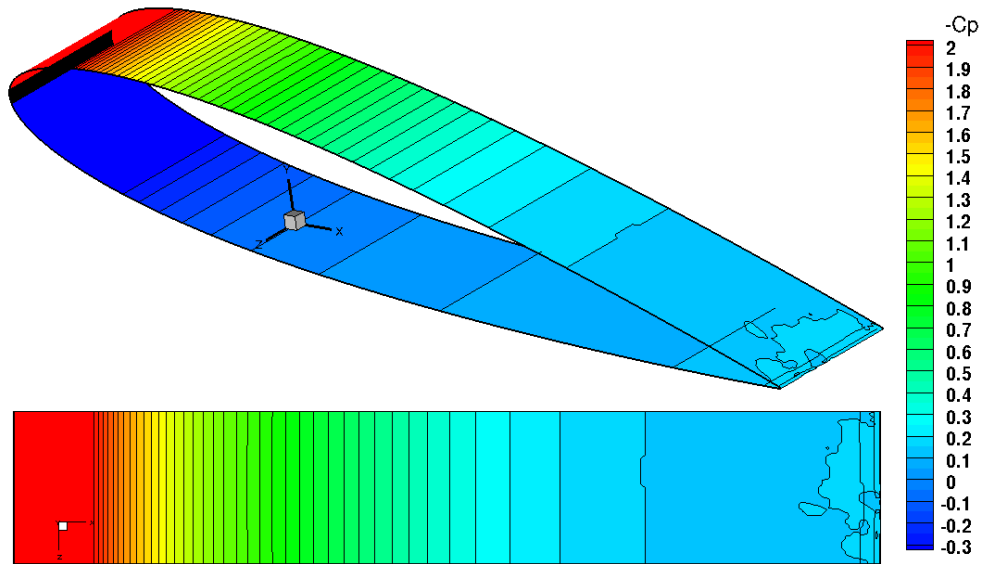
(a)
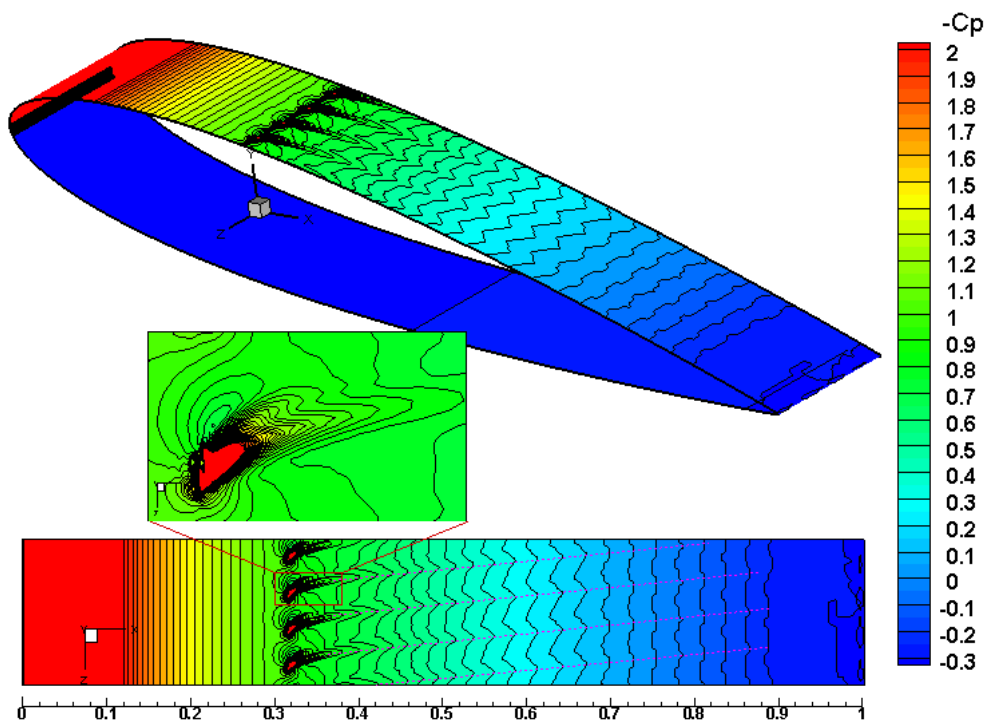
(b)

Figure 5.15: Instantaneous contours of pressure coefficients in a statistically steady state. (a) The baseline case (the top figure for a 3D view and the bottom figure for a 2D top view); (b) The jets controlled case (the top figure for a 3D view, the bottom figure for a 2D top view and the middle figure is an enlarged view of one single jet). Note: the dash-lines are trajectories.

5.4.3 Controlled turbulent boundary layer

The effect of pulsed jets in forcing the separated flows to be attached is directly related to behaviours of the boundary layer. In this section, the streamwise velocity and velocity perturbation (Reynolds stresses) in both the baseline and the controlled flow are compared and analysed. The survey direction for the velocity and perturbation profiles follows the same as the experimental measurements (Siauw [2008]), shown in Figure 5.16(a). As shown in the skin friction that the pulsed jets introduce strong spanwise variations. Since profiles cannot provide a whole picture of flow developing, contours are also displayed to investigate the development of boundary layers. The time averaged contours in sections extracted from the computational domain are investigated, and the survey directions are shown Figure 5.16(b).
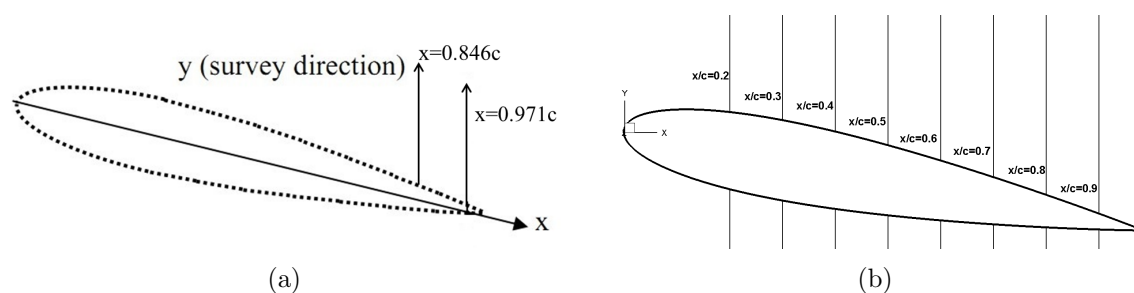
Figure 5.16: Schematic of boundary layer survey direction. (a) Profile survey direction in experiments; (b) Contour survey direction

5.4.3.1 Velocity

Figure 5.17 compares the velocity distributions of the baseline and controlled flow at $x/c = 0.846$ and $x/c = 0.971$ with the available experimental results. The experiments were carried out at three positions in the spanwise direction ($z = \lambda/2$, $7\lambda/2$ and $13\lambda/2$), and these three survey locations are all on the planes where the jet centres locate. In addition to the sections where the jets centres go through, the simulated velocity profiles in the plane of in-between two jets are also shown in Figure 5.17. At these two locations $x/c = 0.846$ and $x/c = 0.971$, the velocity profiles predicted by simulations agree well with experimental profiles for the outer boundary layer. In the near-wall region, the simulated velocity is under-predicted for the baseline flow. Considering the starting point in the single hotwire was 3 mm above the aerofoil surface in experiments and the uncertainty is much higher in the near-wall measurements, the simulations generally provide reasonably good comparisons with the experiments both for the baseline and the controlled flow.

5.4. Comparative study of flow characteristics in the statistically steady state of the baseline and controlled flow

Compared with the baseline flow, the controlled flow has augmented velocity profiles, and they vary in different spanwise positions. At $x/c = 0.846$, the baseline flow shows a small negative velocity near the wall, which implies the flow has been separated. For the controlled flow, the velocity profiles display "S" shapes at $x/c = 0.846$ and $x/c = 0.971$. This "S" shape is related to streamwise and spanwise development of jets-introduced vortex structures, which will be shown in the velocity contours. Figure 5.18 shows how the jets flow influences its surrounding flows from $x/c = 0.3$ to $x/c = 0.39$. The velocity contours in the baseline flow at the same locations are displayed in Figure 5.19. By contrast with the baseline flow, there are two main significant changes for the controlled flow. In the boundary layer, the high velocity flow blowing from jets destroys the original spanwise-uniform boundary layer, and spanwise vortex structures generate due to velocity disparity (or pressure gradient). In the region of the outter of boundary layer and the free stream field, the velocity in the controlled flow is obviously higher than that in the baseline flow owing to the high velocity blown by jets. This means the blowing jets improve the momentum of free stream flow near the aerofoil, which contributes significantly to energise the boundary layer.

The spiral of vortex near the boundary surface can be clearly observed from $x/c = 0.33$ to downstream. After superposing the free stream flow and the blowing flow, the real flow direction is smaller than the given skew angle. The above section about the coherent vortices has confirmed the rotation direction (which agrees with the study of Johnston and Nishi [1990]). This spiral rotation explains why the jets can energise the boundary layer: as flow spirally rotates in the clockwise direction, it brings the high momentum flow blowing from jets and its surrounding high free stream flow towards the wall, and this rotation also push the original low boundary layer flow outwards. Whether the boundary layer is energised or de-energised is based on the net momentum transfer towards the boundary layer. For the effect of blowing flow outwards or drawing flow inwards, the one, which dominates the momentum transfer, determines the fullness or deficiency of the boundary layer.

The velocity profiles near the jets shown in Figure 5.20 display deficient velocity profiles. This means, in regions very near to the jets, the effect of rotation in drawing the boundary layer flow outwards seems to play a more dominant role than transferring the high-momentum outer flow towards the wall, as a result, the net energy is extracted from the boundary layer, decreasing the skin friction. In combination with the C_f distribution in Figure 5.12, from $x/c = 0.5$, the energy transfer from high-momentum flow towards the wall becomes predominant.

The streamwise velocity profiles at regions far from the jets ($x/c = 0.52$, 0.60, and 0.714) are given in Figure 5.21. The velocity contours, displaying more details in flow structures

5.4. Comparative study of flow characteristics in the statistically steady state of the baseline and controlled flow
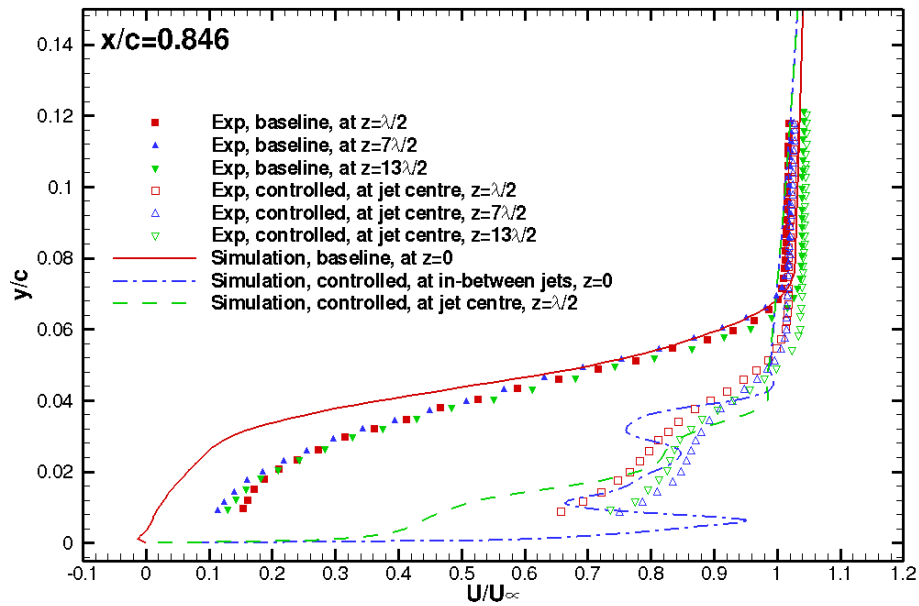
(a)
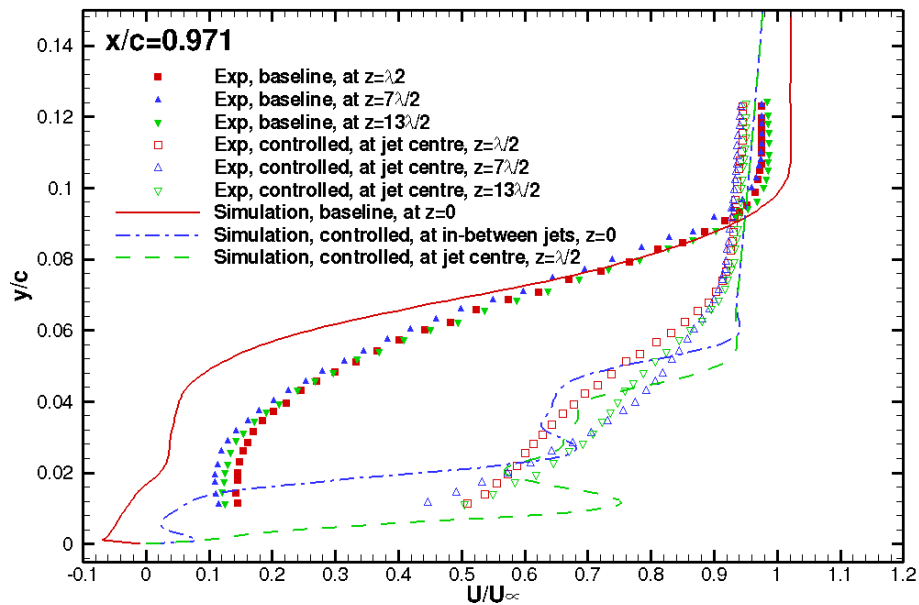
(b)

Figure 5.17: Time averaged velocity profiles both for the baseline and the controlled cases at (a) $x = 0.846c$ and (b) $x = 0.971c$.

and developments, are shown in Figure 5.22 and Figure 5.23 for the baseline and controlled flow, respectively. Figure 5.21 shows that at all these three locations, the boundary layer is augmented in the whole span, which is different from the region near the jets.
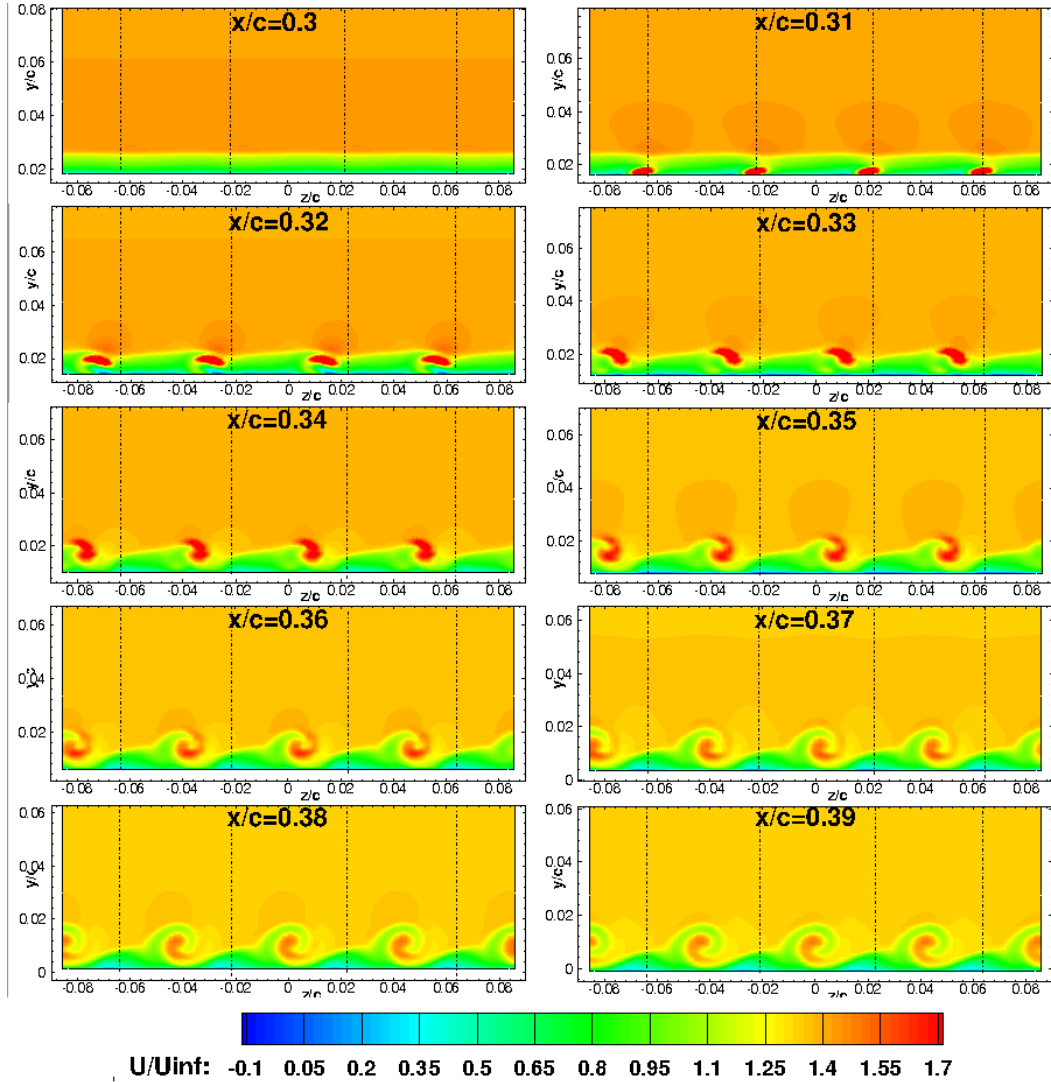
Figure 5.18: Contours of time-averaged streamwise velocity U for the pulsed jets controlled flow at 10 streamwise sections from $x/c = 0.30$ to $x/c = 0.39$. (The dash lines represent the jet locations in the spanwise direction.)

At a longer distance downstream from the jets, the projected distance from the high jet velocity to the wall become longer, thus the flow rotation has less impact on the wall and the boundary layer in the spanwise direction has less variation in most of the span. This can be seen by comparing the flow contours at $x/c = 0.4$ and $x/c = 0.7$ in Figure 5.23. The former shows that the rotation downwards suppresses the boundary layer, while for the latter, the boundary layer is more uniform. Another observation is that the size of spirally rotating vortex becomes larger and larger when the flow approaches towards the trailing edge. At around $x/c = 0.75$, the two adjacent rotating vortex meet each other and from this location downstream, the interaction between adjacent vortex structures began to

5.4. Comparative study of flow characteristics in the statistically steady state of the baseline and controlled flow
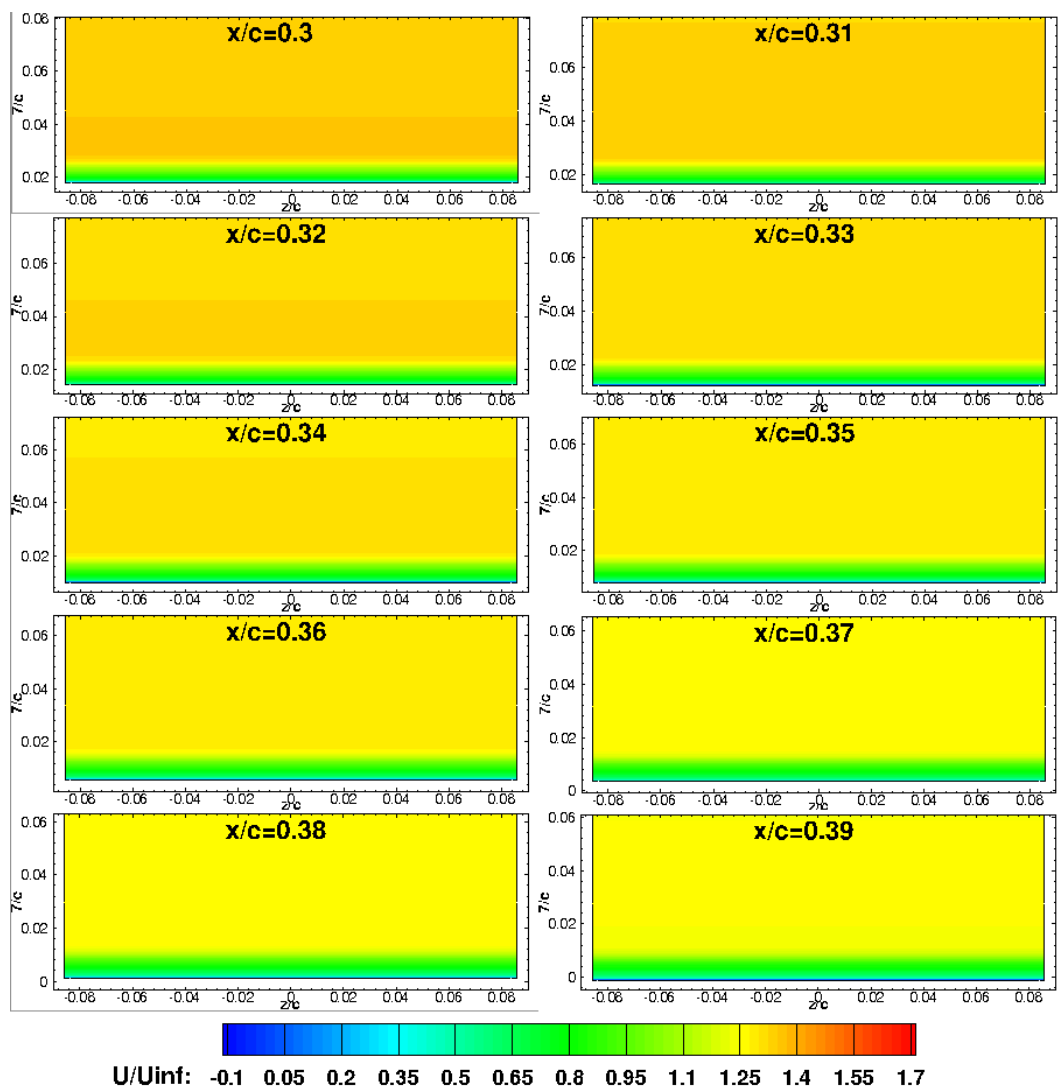
Figure 5.19: Contours of time-averaged streamwise velocity U for the baseline flow at 10 streamwise sections from $x/c = 0.30$ to $x/c = 0.39$.

play a more important role. At around $x/c = 0.9$, the adjacent vortex structures squeeze with each other and become extruded in the wall-normal direction. At $x/c = 0.95$, the longitudes vortex structures begin to depart from the surface. Although most of the region at $x/c = 0.95$ has a positive velocity, alternative narrow zones begin to have slightly negative velocity, which means small separations occur locally.
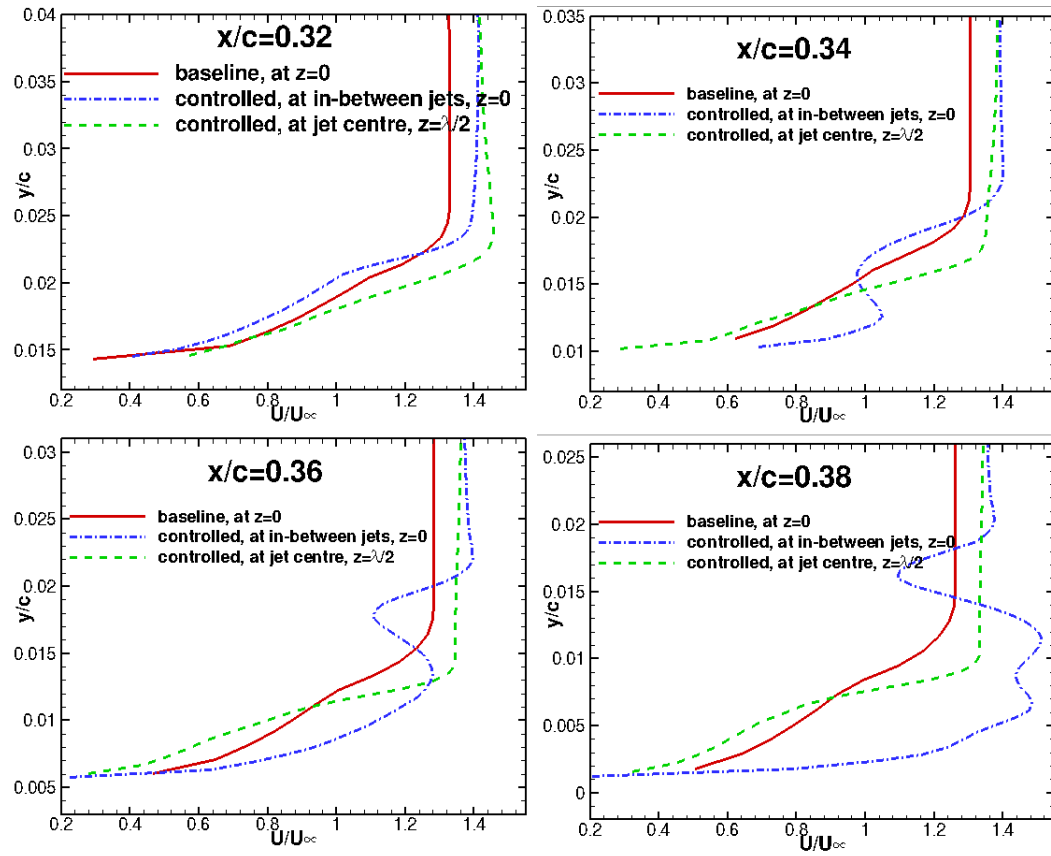
Figure 5.20: Time averaged velocity profiles at $x/c = 0.32$, 0.34, 0.36 and $x/c = 0.38$.
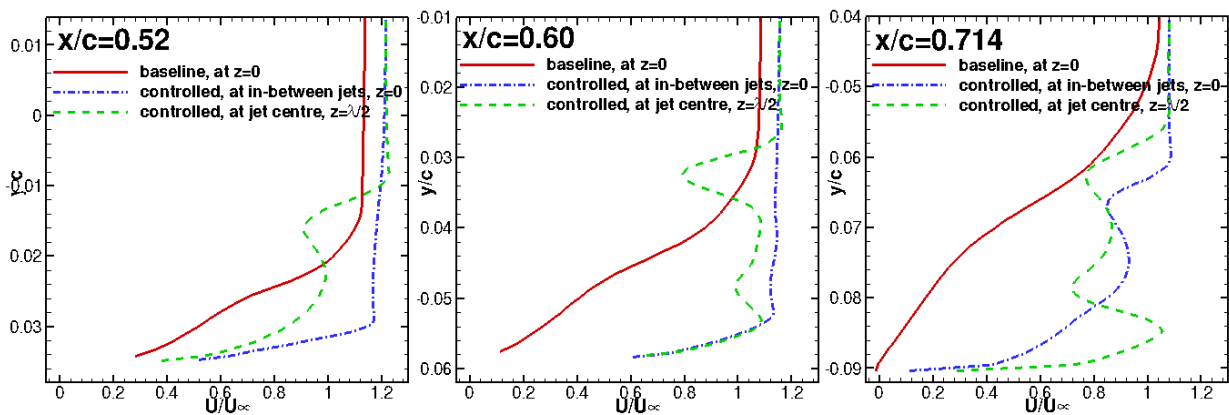
Figure 5.21: Time averaged velocity profiles at $x/c = 0.52$, 0.60 and $x/c = 0.714$.
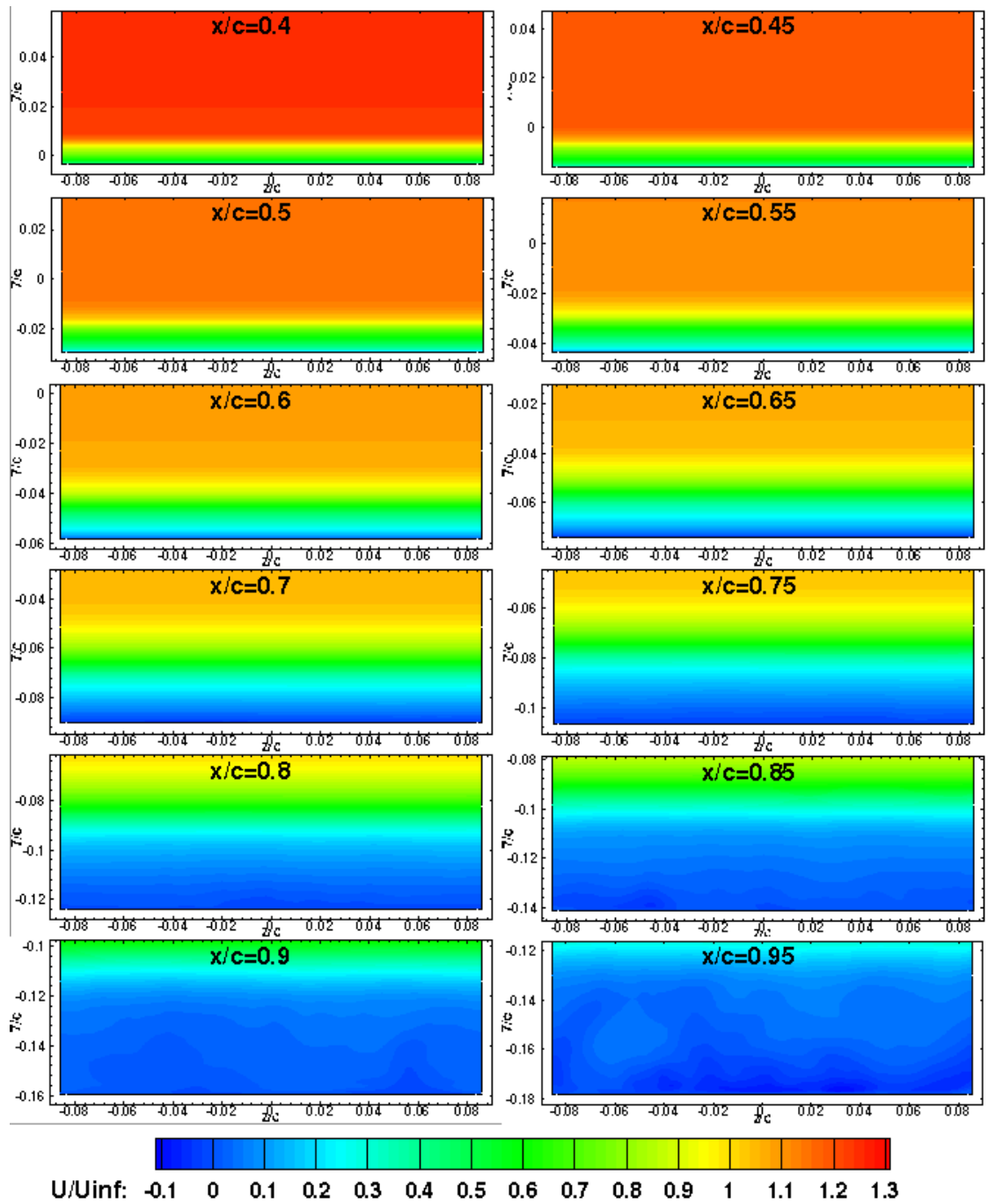
Figure 5.22: Contours of time-averaged streamwise velocity U for the baseline flow at 12 streamwise sections from $x/c = 0.4$ to $x/c = 0.95$.
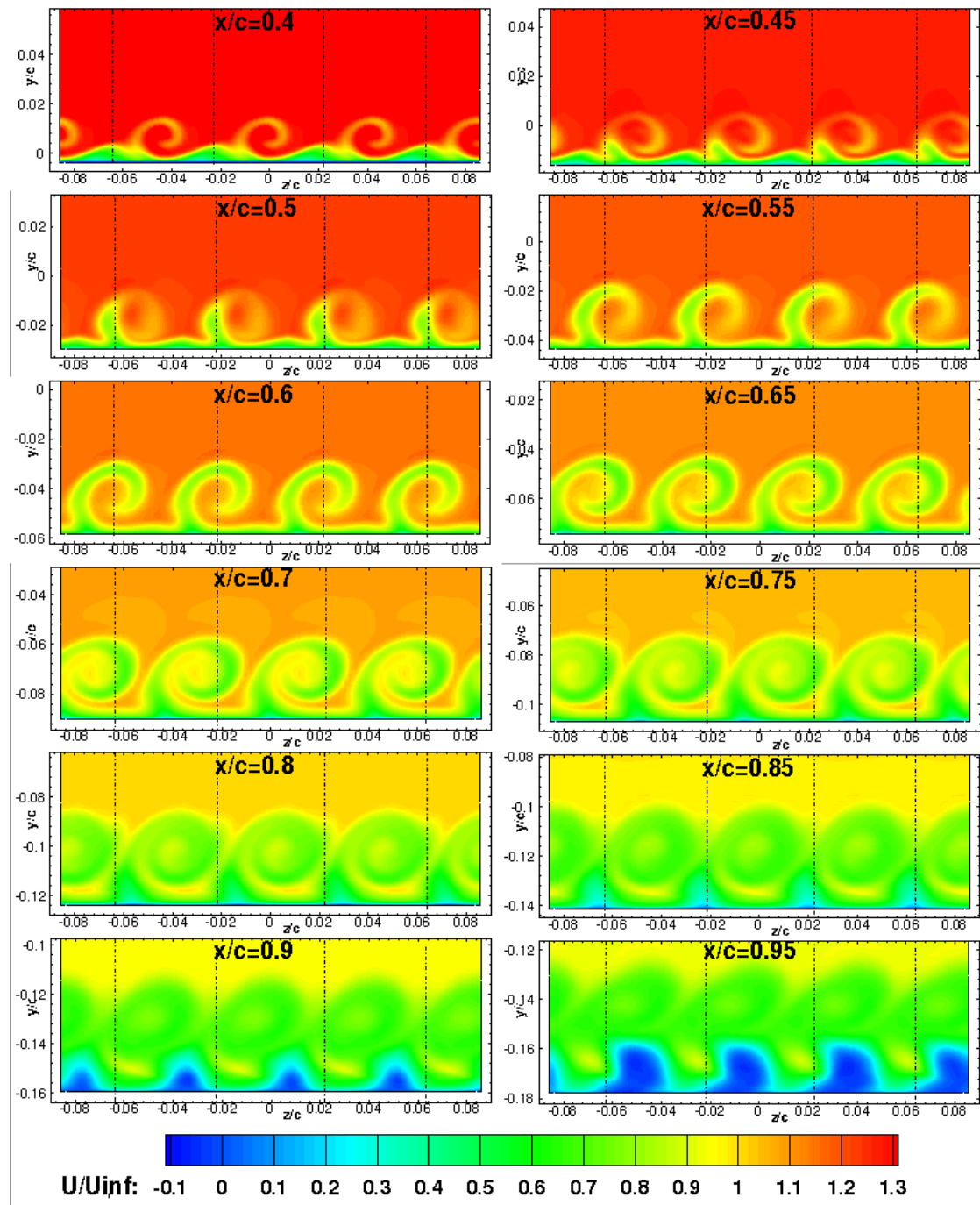
Figure 5.23: Contours of time-averaged streamwise velocity U for the pulsed jets controlled flow at 12 streamwise sections from $x/c = 0.4$ to $x/c = 0.95$. (The dash lines represent the jet locations in the spanwise direction.)

After analysing the skin friction and the streamwise velocity separately in the above two sections, the relation between these two primary parameters can be observed by comparing Figure 5.13 and Figure 5.24. Figure 5.24 shows the time averaged C_f distribution along

5.4. Comparative study of flow characteristics in the statistically steady state of the baseline and controlled flow

the span. By comparison, it can be qualitatively concluded that in the process of the vortex rotating from the wall to the outer boundary layer, in which the boundary layer is drawn outwards and has smaller velocity, the skin friction decreases. Correspondingly, in the process of rotation from the outer boundary layer to the wall, in which the rotating vortex structures entrain high-momentum fluid towards the wall, the skin friction increase. The controlled flow at $x/c = 0.4$, much near to the jets, has a large "blowing-outwards" region, and the energy transferring from high-speed free stream towards the wall is weak, thus there is a large low C_f region. This corresponds the smaller C_f than the baseline, given in Figure 5.24. This phenomenon can be used to design novel control devices to control skin frictions.
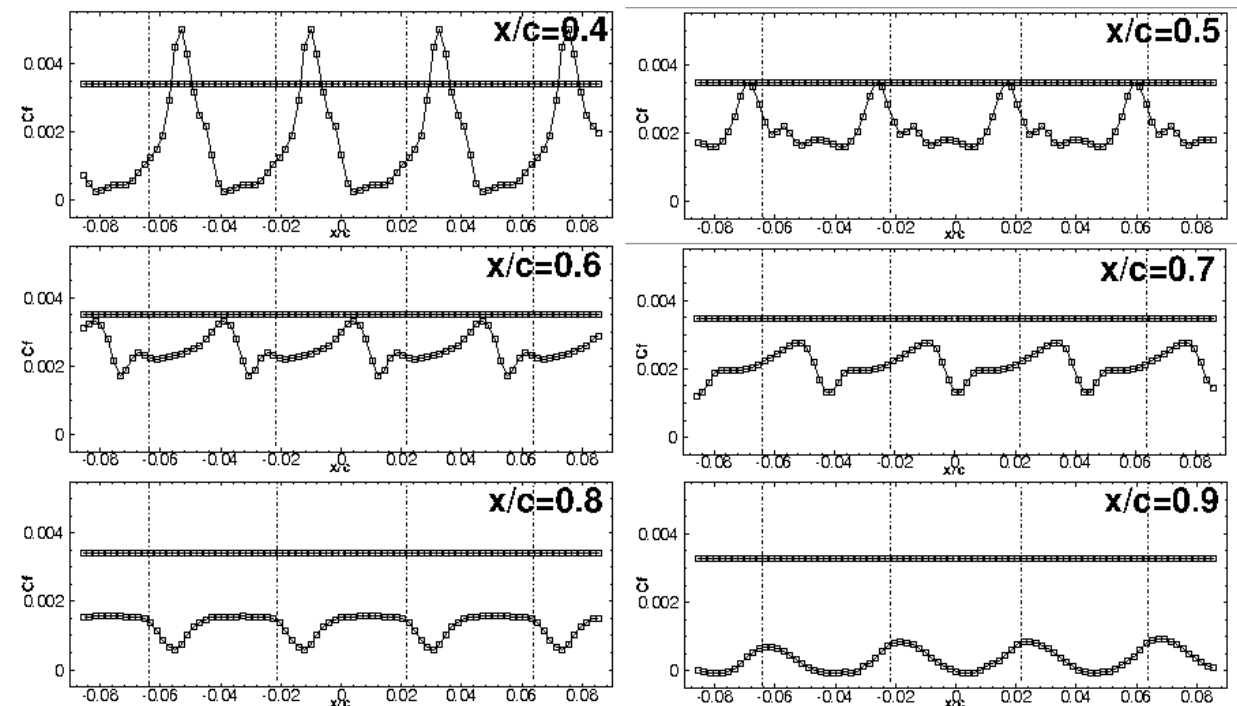
Figure 5.24: Profiles of time averaged C_f distribution in the spanwise direction at $x/c = 0.4$, 0.5, 0.6, 0.7, 0.8 and 0.9. (the constant line is for the pressure side)

5.4.3.2 Reynolds stress

The Reynolds stresses in the boundary layer will be discussed in this section. All Reynolds stress herein are the sum of the resolved Reynolds stress and the Reynolds stress modelled by turbulence models.

Figure 5.25 compares the streamwise normal stress $\langle u'u' \rangle$ at $x/c = 0.846$ and $x/c = 0.971$ in the baseline and controlled flow field. The simulation predicts agreeable Reynolds stresses at the outer region of the boundary layer for the baseline flow, while at the near-wall region, simulation under-predicts it. For the controlled flow, the Reynolds stress in the simulation has the same distribution trends as that in the experiments, but the absolute magnitude is under-predicted at $x/c = 0.846$ and slightly over-predicted at $x/c = 0.971$. Because of the limitation of measurements with only one single hotwire and the turbulence modelling errors, explanations on these disparities are not easy. Although there are some gaps between the results by the simulations and experiments, the consistent distribution trends, like the two peaks and kinks in the controlled flow, still benefit the understandings the control effect and flow developments by simulations.

Figure 5.26 displays the three normal stresses at $x/c = 0.44$, 0.52, 0.60 and 0.714. In the baseline flow, sharp peaks exist in the streamwise normal stress, and the wall-normal locations of peak values of $\langle u'u' \rangle$ moves further away from the aerofoil surface from $x/c = 0.44$ to $x/c = 0.971$ as a result of the separated share layer. However, no sharp peaks are observed in $\langle v'v' \rangle$ and $\langle w'w' \rangle$ in the baseline flow. Furthermore, in the baseline flow, $\langle w'w' \rangle$ and $\langle v'v' \rangle$ have similar values (the former is slightly larger), which are smaller than the Reynolds normal stress $\langle u'u' \rangle$. This illustrates in the baseline flow, the Reynolds normal stress $\langle u'u' \rangle$ contributes the most to turbulence kinetic energy. Different from increasing peak values of Reynolds stress in the baseline flow, the peak values in Reynolds stress for the controlled flow at $z = 0$ becomes smaller and smaller in regions further away from the jets. However, at $z/c = \lambda/2$ they become slightly larger from $x/c = 0.44$ to $x/c = 0.714$. The reduction of Reynolds stress at $z = 0$ and increase at $z = \lambda/2$ may imply that the flow fluctuations introduced by jets expand in the spanwise direction. Comparing the baseline and the controlled flow, at the region near the jets, the controlled flow has a larger flow fluctuation than the baseline flow due to the forced energy transfer, while near and after the separation, the baseline flow has a much larger fluctuation due to the separated shear layer shedding. These phenomena in the controlled flow were also observed in studying pulsed jets on a bump (Kostas *et al.* [2007]). From $x/c = 0.52$, secondary peaks are observed at $z = \lambda/2$ in far-field from the wall for all three normal stresses. These two peaks may correspond to the shape of the rotating vortex structures. Among all these three normal stresses in the

5.4. Comparative study of flow characteristics in the statistically steady state of the baseline and controlled flow
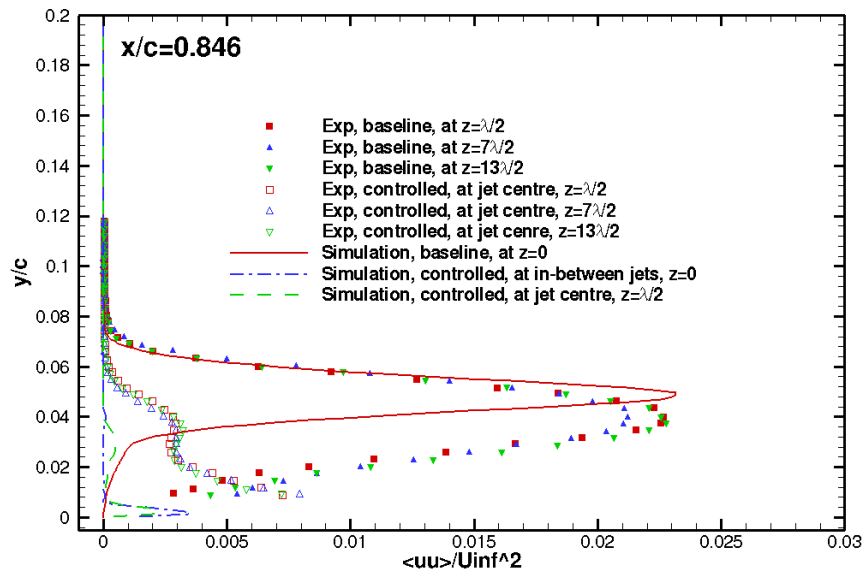
(a)
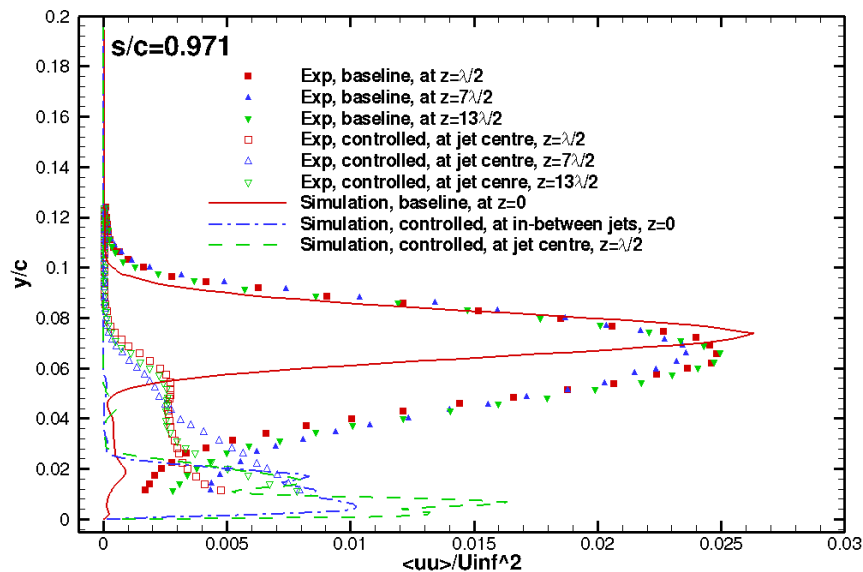
(b)

Figure 5.25: Mean profiles of $\langle u'u' \rangle / U_\infty^2$ both for the baseline and the controlled cases at (a) $x = 0.846c$ and (b) $x = 0.971c$.

controlled flow, $\langle v'v' \rangle$ is higher than the other two normal stresses at most regions, but the differences of magnitudes of all these three normal stresses are not significant. It can be inferred that for the baseline flow, the instability of the shear layer separating from the aerofoil makes the streamwise flow fluctuations outstanding, while for the controlled flow with attached boundary layer, the most significant fluctuation is in the vertical direction

due to the jets blowing from the surface to the free streams. For the controlled flow, the normal stresses at $z/c = 0$ and $z/c = \lambda/2$ vary a lot, which will be further illustrated in Reynolds stress contours.
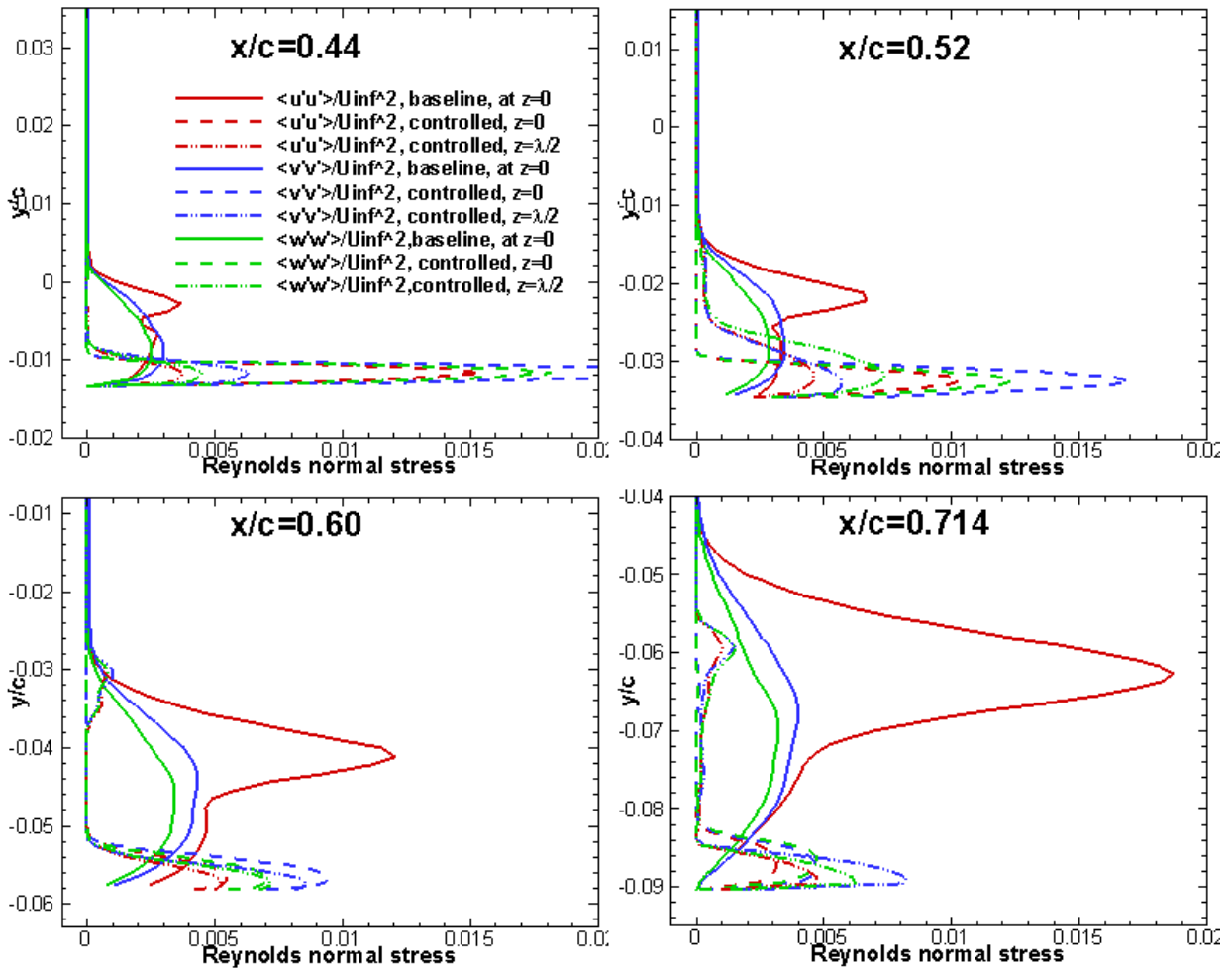
Figure 5.26: Mean profiles of the Reynolds normals stresses $\langle u'u' \rangle/U_\infty^2$, $\langle v'v' \rangle/U_\infty^2$ and $\langle w'w' \rangle/U_\infty^2$ both for the baseline and the controlled cases at $x/c = 0.44$, 0.52, 0.60 and 0.714.

Figure 5.27 displays the three shear stresses at $x/c = 0.44$, 0.52, 0.60 and 0.714. The shear stress $\langle u'v' \rangle$ shrinks with longer distance from the jet and the peak values are much nearer to the wall in the controlled flow, with similar trends to the normal stresses shown in Figure 5.26. The other two shear stresses $\langle u'w' \rangle$ and $\langle v'w' \rangle$ are almost zero in the baseline flow, while they play a part in the controlled flow, which has strong spanwise fluctuations.

Considering the spanwise variations on the Reynolds stresses for the controlled flow, contours of the six Reynolds stress $\langle u'u' \rangle$, $\langle v'v' \rangle$, $\langle w'w' \rangle$, $\langle u'v' \rangle$, $\langle u'w' \rangle$ and $\langle v'w' \rangle$ are given in Figure 5.29 - Figure 5.34 respectively. For the baseline flow, only the middle section ($z/c = 0$)

5.4. Comparative study of flow characteristics in the statistically steady state of the baseline and controlled flow
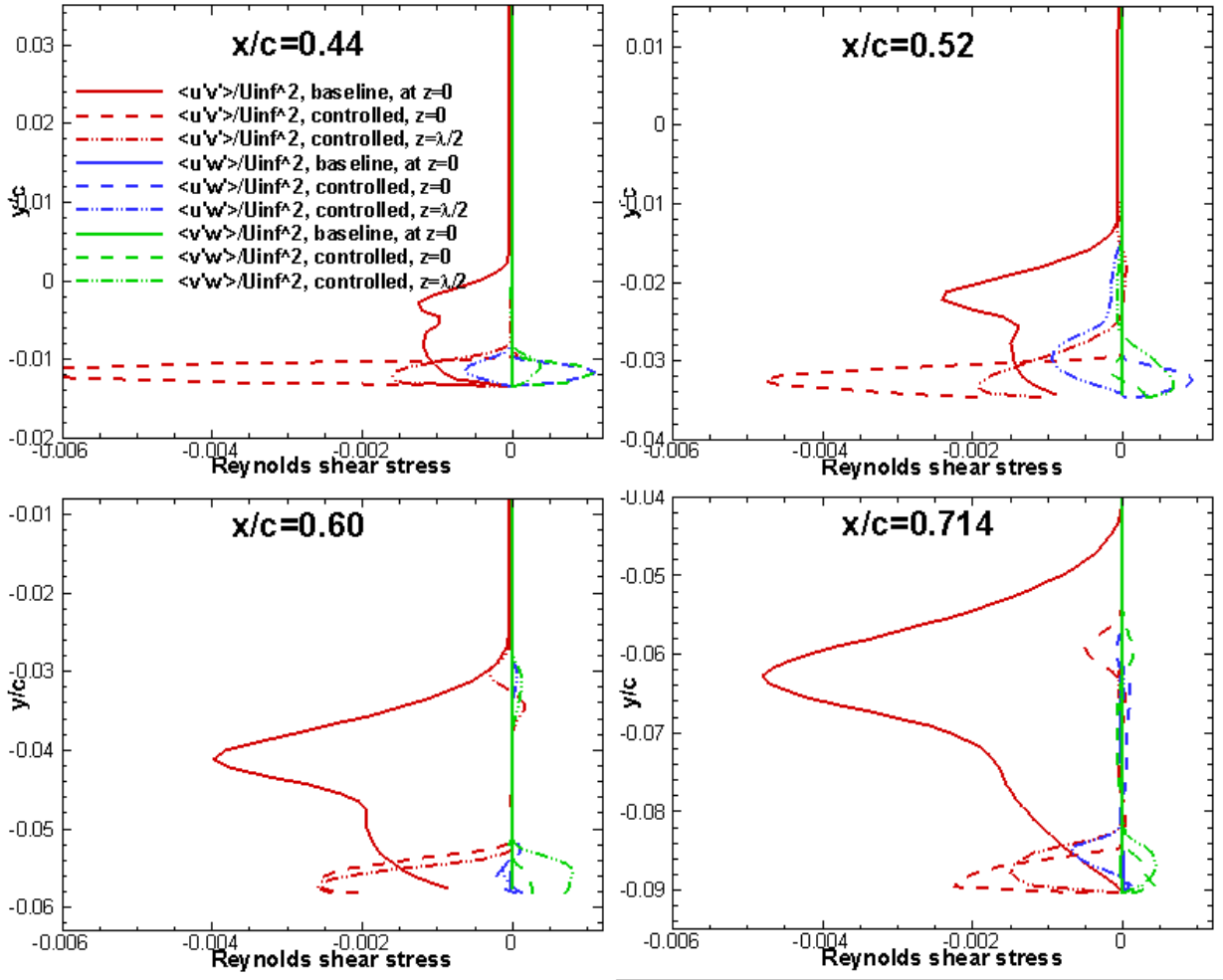
Figure 5.27: Mean profiles of the Reynolds shear stresses $\langle u'v' \rangle / U_\infty^2$, $\langle u'w' \rangle / U_\infty^2$ and $\langle v'w' \rangle / U_\infty^2$ both for the baseline and the controlled cases at $x/c = 0.44$, 0.52, 0.60 and 0.714.

is given in Figure 5.28 to compare with the controlled flow, as the spanwise variations are much weaker. Besides, for the baseline flow, $\langle u'w' \rangle$ and $\langle v'w' \rangle$ are much smaller than the other Reynolds stresses as shown in Figure 5.27, thus they are not shown in contours.

By contrast with the baseline flow, Reynolds stresses in the controlled flow display some characteristics as follows. (1) For the Reynolds normal stresses, there are two prominent regions with high stresses, the near-wall region and the outer edge of rotating vortex structures. These two regions with high Reynolds stresses correspond to the two peaks in the profiles shown in Figure 5.25 and Figure 5.26. Moreover, compared with the near-wall region, the outer edges of vortex structures have smaller values. (2) All the three normal stresses have very similar distributions. At the near-wall region, flow field with vortex rotating outwards has smaller Reynolds normal stresses than that with vortex rotating towards the wall. At

the outer of boundary layer, the high stresses follow the outer edge of vortex structures. This phenomenon is also observed in Kostas *et al.* [2007], where the high levels of turbulent stresses are generated at the extremities of vortex structures. (3) Similar to what is shown in Figure 5.26, $\langle v'v' \rangle$ and $\langle w'w' \rangle$ is higher than $\langle u'u' \rangle$ at the same location, and the high level of the first two normal stress extends longer distance than $\langle u'u' \rangle$. This is an important difference from the baseline, in which $\langle u'u' \rangle$ plays a dominant part in the turbulent fluctuation. (4) The baseline flow has very small $\langle u'w' \rangle$ and $\langle v'w' \rangle$, but the controlled flow have much larger levels of these two shear stresses, and their distributions are also related with the vortex structures.
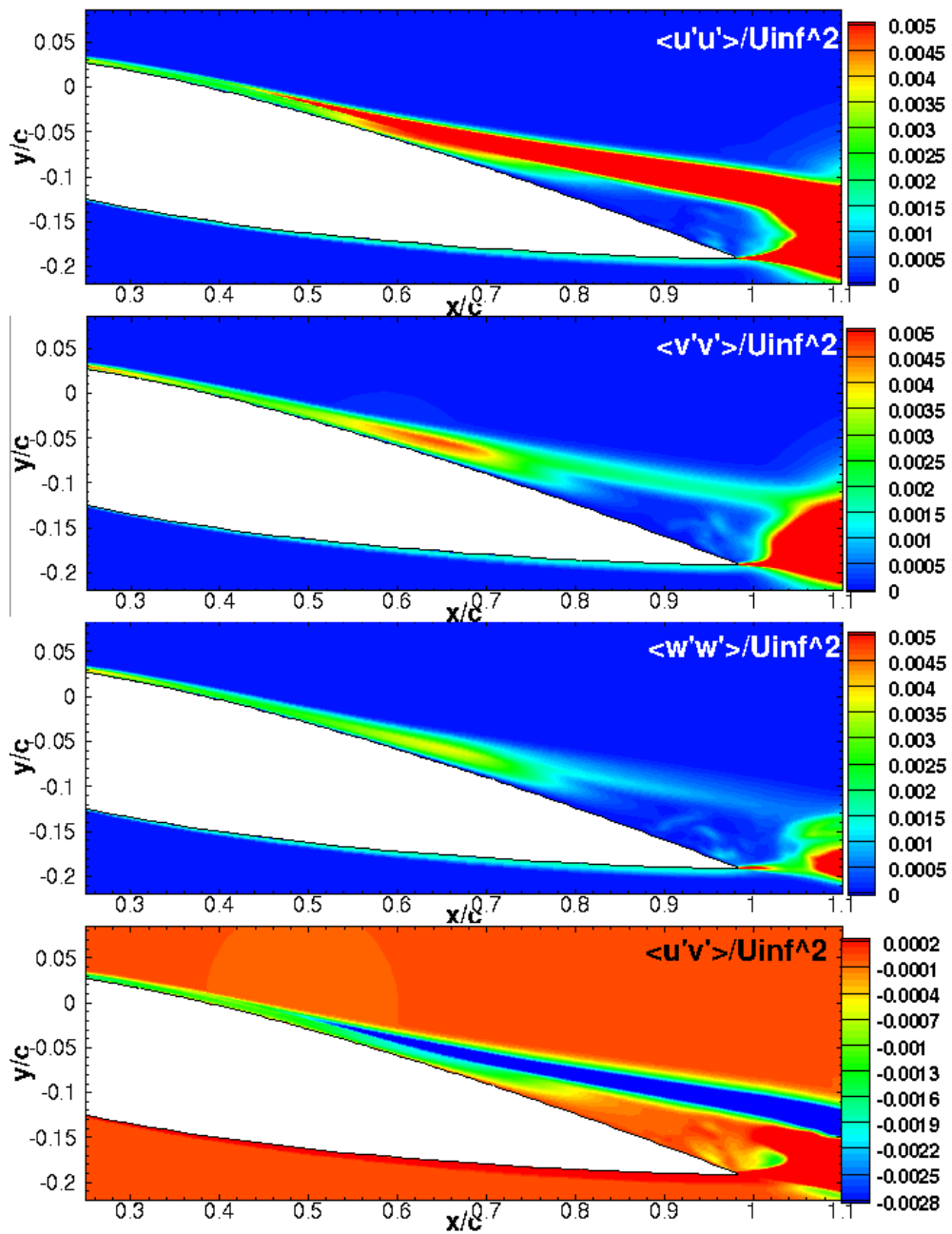
Figure 5.28: Contours of Reynolds stresses for the baseline flow at $z/c = 0$. From top to bottom, $\langle u'u' \rangle/U_\infty^2$, $\langle v'v' \rangle/U_\infty^2$, $\langle w'w' \rangle/U_\infty^2$ and $\langle u'v' \rangle/U_\infty^2$.
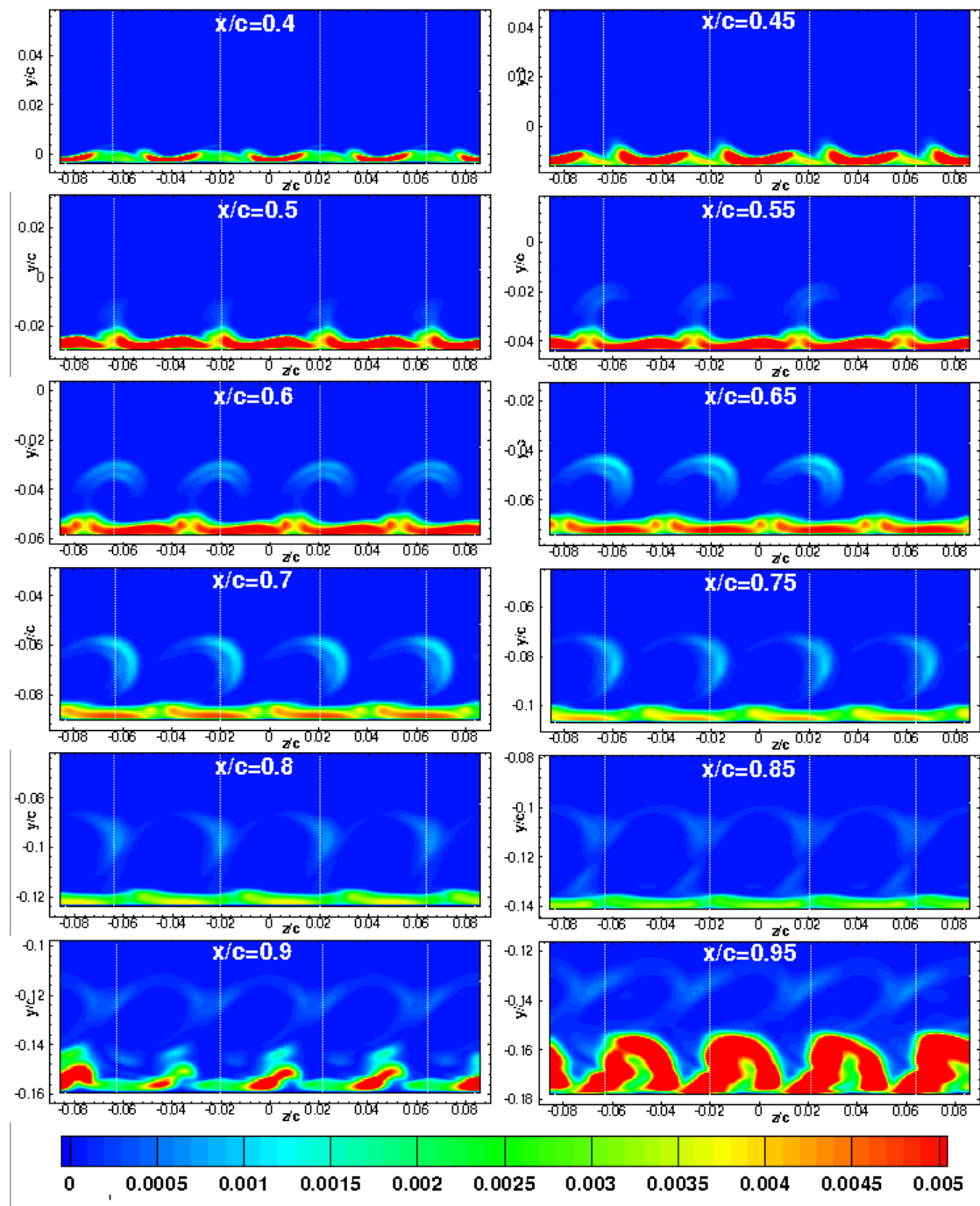
Figure 5.29: Contours of Reynolds stress $\langle u'u' \rangle / U_\infty^2$ for the controlled flow at 12 streamwise sections from $x/c = 0.4$ to $x/c = 0.95$.

Figure 5.30: Contours of Reynolds stress $\langle v'v' \rangle / U_\infty^2$ for the controlled flow at 12 streamwise sections from $x/c = 0.4$ to $x/c = 0.95$.

Figure 5.31: Contours of Reynolds stress $\langle w'w' \rangle / U_\infty^2$ for the controlled flow at 12 streamwise sections from $x/c = 0.4$ to $x/c = 0.95$.

Figure 5.32: Contours of Reynolds stress $\langle u'v' \rangle / U_\infty^2$ for the controlled flow at 12 streamwise sections from $x/c = 0.4$ to $x/c = 0.95$.

Figure 5.33: Contours of Reynolds stress $\langle u'w' \rangle / U_\infty^2$ for the controlled flow at 12 streamwise section from $x/c = 0.4$ to $x/c = 0.95$.

5.4. Comparative study of flow characteristics in the statistically steady state of the baseline and controlled flow
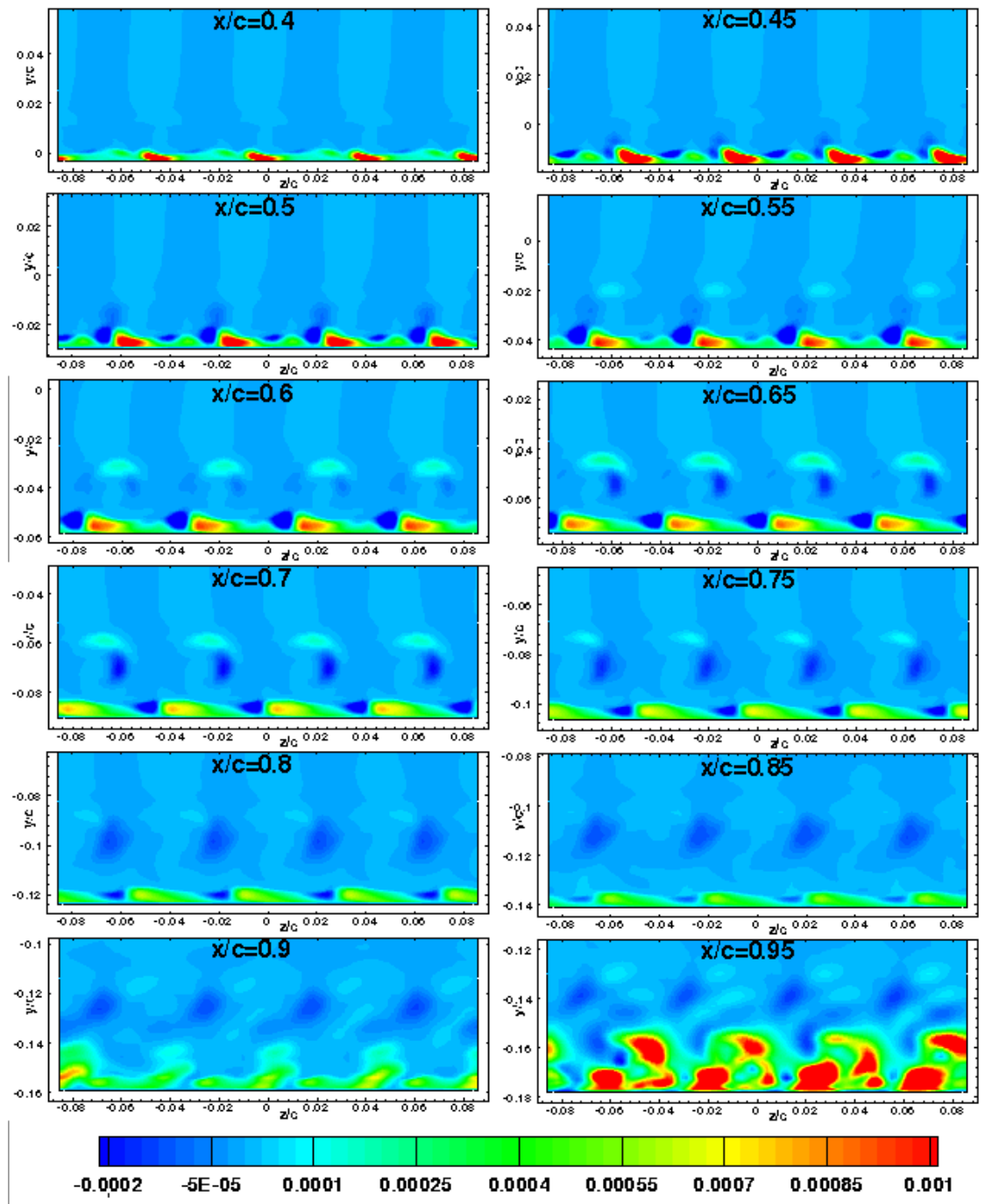
Figure 5.34: Contours of Reynolds stress $\langle v'w' \rangle / U_\infty^2$ for the controlled flow at 12 streamwise section from $x/c = 0.4$ to $x/c = 0.95$.

Conclusively, the flow development process in the state of jets control can be depicted as follows. The blowing jets augment both the boundary layer and the free stream flow around the aerofoil. The jets-induced disparities of velocity in the span lead to spiral rotation for the flow to generate streamwise vortices. These vortices rotate and grow in the streamwise, which

entrains high-momentum flow towards the wall to energise the boundary layer. This results in an increased skin friction, delaying/suppressing flow separation. From $x/c = 0.75$ to the downstream, structures of the primary vortices rotating towards the wall and structures of their adjacent vortices rotating outwards from the wall begin to merge and squeeze the vortices more elongated in the wall-normal direction. With the vortices departing from the wall, small local separations begin to occur at regions very near the trailing edge.

In combination with the skin friction in Figure 5.24, velocity distribution in Figure 5.23 and Reynolds stresses in Figure 5.29 - Figure 5.32, the relation between vortex structures, skin friction and Reynolds stresses can be drawn as follows. In the region where structures of the primary vortices rotate outwards and depart from the wall, the boundary layer energy is extracted and blown outwards, which make the boundary layer thicker than its surroundings. These thicker boundary layers correspond to a higher velocity gradient and a higher skin friction. The flow rotates outwards also has fewer fluctuations than other regions in the span, which leads to smaller Reynolds normal stresses and shear stress near the wall. When flow goes downstream and gets further from the jets, vortices grow and most of the boundary layer are influenced by structures rotating from the high-momentum free stream towards the wall. These regions have energised boundary layer and more fluctuations. Therefore, they have higher Reynolds stresses and higher skin friction, which suppress the flow separation.

5.4.4   Wake flow

5.4.4.1   Velocity

Figure 5.35 displays the wake velocity at $x/c = 1.98$. For the baseline flow, the simulation slightly over-predicts the wake width compared with the experiments. Nevertheless the general comparison is acceptable, considering the slightly larger separation provided by simulation. For the controlled flow, the simulation velocity agrees very well with the experimental data. Figure 5.36 shows the contours of the streamwise velocity in the wake at locations $x/c = 1.1$ to 1.9. Obviously, the controlled flow with an attached boundary layer has a smaller wake width. It is also observed that the vortex structures merge and interact with adjacent structures and the trajectories of the four jets last downstream to $x/c = 1.6$ before they are totally merged together.

5.4.4.2   Reynolds stress

The Reynolds stresses $\langle u'u' \rangle$ and $\langle v'v' \rangle$ are also compared with the experiments, shown in Figure 5.37. Simulations for the baseline flow over-predicted the two normal stresses, but the

5.4. Comparative study of flow characteristics in the statistically steady state of the baseline and controlled flow
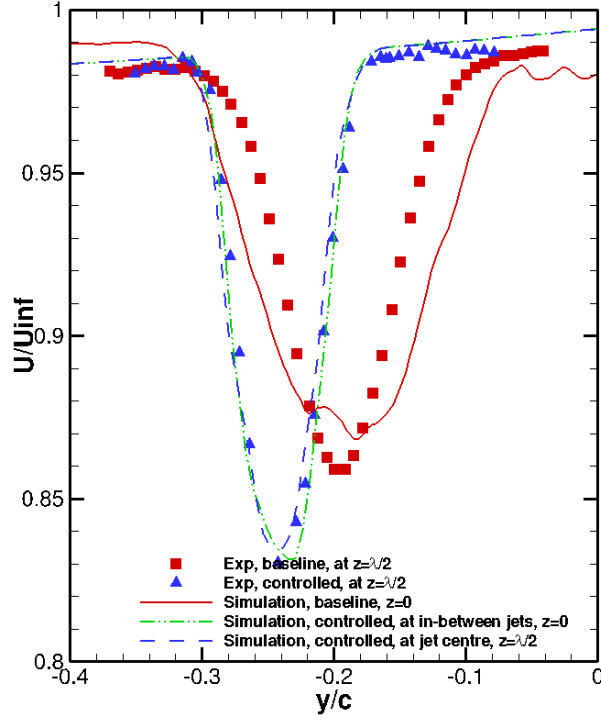
Figure 5.35: Profiles of time averaged streamwise velocity in the wake at $x/c = 1.98$.

distribution trend is consistent with the experiments. For the controlled flow, the simulation predicts very agreeable Reynolds stresses to the experiments. With an attached boundary layer, the controlled flow has much smaller Reynolds stresses than the baseline flow in the wake. As it is far from the jets, the variations at different span locations are smaller than around the aerofoil.

Figure 5.38 and Figure 5.39 display the three Reynolds stresses for the baseline and controlled flow. For the baseline flow, the main contribution to the turbulence kinetic energy is from the streamwise ($\langle u'u' \rangle/U_\infty^2$) and vertical fluctuations ($\langle v'v' \rangle/U_\infty^2$), just like the boundary layer, but the vertical fluctuations player a larger part than that in the boundary layer. The spanwise fluctuation ($\langle w'w' \rangle/U_\infty^2$) for the baseline flow is still much smaller than the other two components, similar to the boundary layer. For the controlled flow, the streamwise flow fluctuations play a dominant role in the turbulence kinetic energy, different from the boundary layer, in which the vertical fluctuation has a higher level. For the controlled flow, the spanwise flow fluctuations are much larger than the baseline and similar to the vertical flow fluctuations, which may be due to the skew and pitch angles enhancing the spanwise flow transport. For the Reynolds shear stress, $\langle u'v' \rangle/U_\infty^2$ is higher than the other two components in both the baseline and the controlled flow. As the baseline flow has a trailing edge separation, all of these three Reynolds shear stresses are much larger than

(a)

(b)
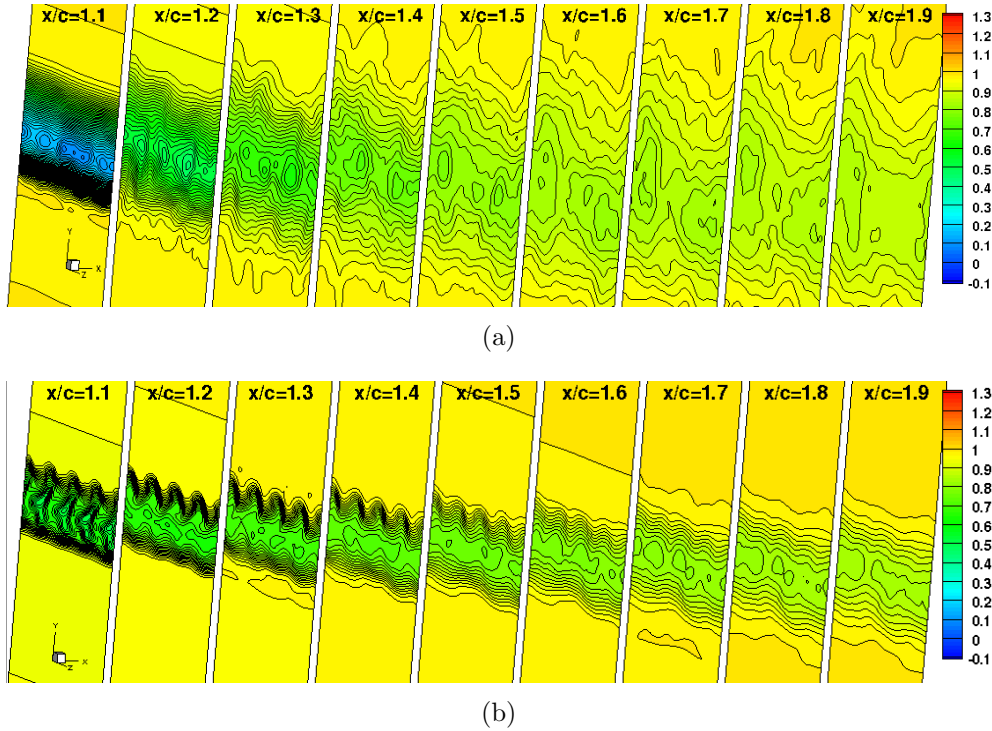
Figure 5.36: Contours of streamwise velocity in the wake. (a) The baseline flow (b) The controlled flow

in the controlled attached flow. For the controlled attached flow, due to larger spanwise fluctuations, the values in the three Reynolds shear stresses have few differences from each other.

Figure 5.40 presents the Reynolds stress distribution in the spanwise direction for the controlled flow. As observe in Figure 5.39, the Reynolds normal stress $\langle u'u' \rangle / U_\infty^2$ dominates the turbulence kinetic energy, and $\langle v'v' \rangle / U_\infty^2$ and $\langle w'w' \rangle / U_\infty^2$ have similar contributions. In addition, all the Reynolds normal stresses show four high-value regions in each x/c section, which is highly related with the blowing jets on the aerofoil. With a longer distance away from the trailing edge, the interaction between adjacent high-value regions becomes stronger and from $x/c = 1.7$, the boarders between two adjacent high-value regions become blurred. The Reynolds shear stress $\langle u'v' \rangle / U_\infty^2$ also displays the tracks of the four jets, and the upper part with negative values of the wake seems to have weaker interaction between two adjacent regions than the lower part with the positive values. This actually can also be observed in $\langle u'u' \rangle / U_\infty^2$.

5.4. Comparative study of flow characteristics in the statistically steady state of the baseline and controlled flow

(a)   (b)
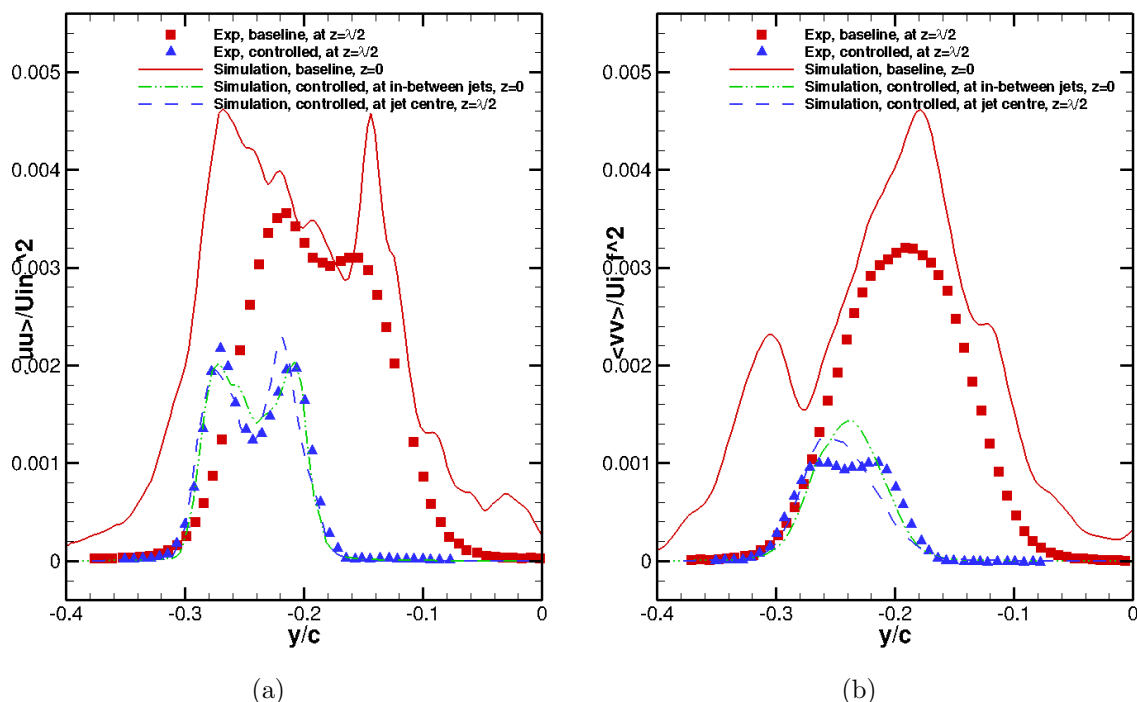
Figure 5.37: Reynolds stress profiles in the wake at $x/c = 1.98$. (a)$\langle u'u' \rangle/U_\infty^2$, (b) $\langle v'v' \rangle/U_\infty^2$
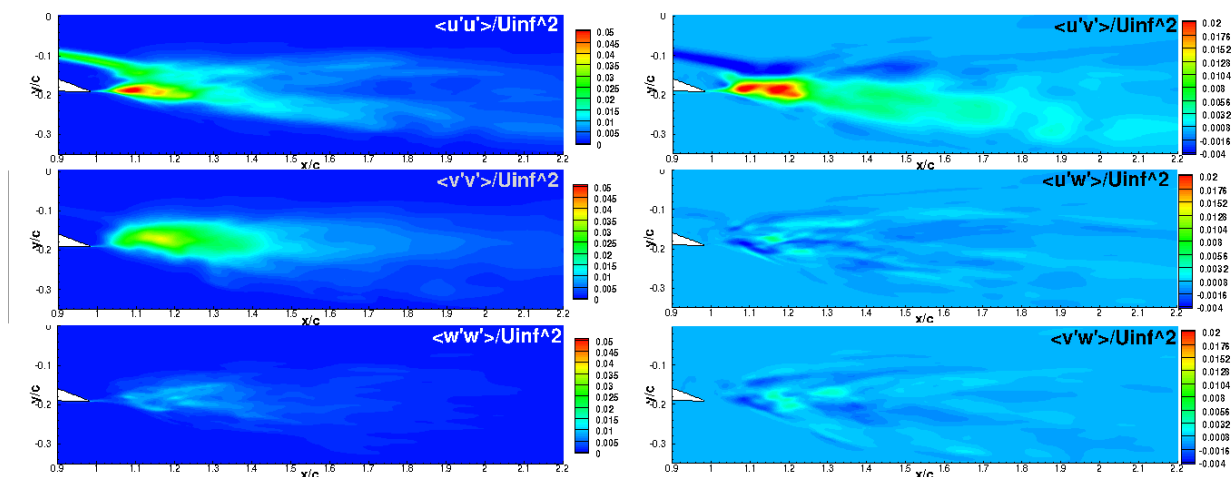
Figure 5.38: Contours of Reynolds stress in the wake for the baseline flow at $z/c = 0$.

5.4.5   Summary

This section compares the baseline flow and the jets controlled flow. The comparison between experiments and the simulations indicates that numerical simulations slightly over-predict the separation, thus there are some gaps between the Reynolds stress near the trailing edge predicted by simulations and experiments. However, the simulations give reasonably good agreements to the experiments in velocity profiles, C_p distribution, the lift and drag

5.4. Comparative study of flow characteristics in the statistically steady state of the baseline and controlled flow
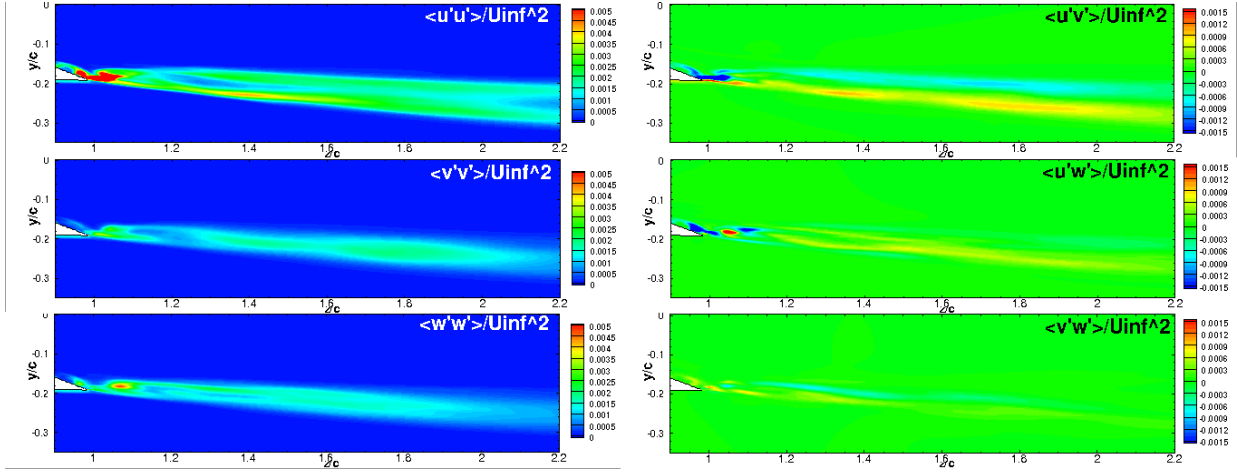
Figure 5.39: Contours of Reynolds stress in the wake for the controlled flow at $z/c = 0$.

coefficients. From an overall point of view, the simulation of the baseline flow gives good comparisons to the experiments. For the controlled flow, simulations obtain even better comparisons with the experimental data, especially in the wake region.

Compared with the baseline flow, the controlled flow has below features.

(1) Strong rotating vortices are formed in the jets controlled flow. The rotation of these vortices entrains the high momentum free stream flow to the boundary layer in most regions downstream of the jets. For the controlled flow, the skin friction C_f has been enlarged over the whole span at most regions downstream of the jets. The energised boundary layer resists flow separation. Thus, the controlled flow is almost fully attached, while the baseline flow has a trailing edge separation at $0.3c$ from the trailing edge.

(2) The jets controlled flow, with an attached boundary layer, has an increased lift coefficient and reduced drag coefficient. Due to the pitch and skew angles of jets, the distributions of the pressure and skin friction coefficients along the span are periodic, and closely related to the direction of vortex generated by jets.

(3) The study on the flow velocity and skin friction shows that when jets-induced vortex rotates from the wall to the outer boundary layer, the boundary layer is drawn outwards and has smaller momentum. The skin friction decreases. When the vortex rotates towards the wall and draws high momentum flow towards the wall, the boundary layer is energised and has a larger C_f. In regions near the jets, the former process dominates, while from $x/c = 0.45$ to the trailing edge, the latter process plays a key role, which contributes most to the attachment of the shear layer.

(4) Along the aerofoil, for the baseline flow, the streamwise Reynolds normal stress is the dominating component in the turbulence kinetic energy, while for the controlled flow,

213

5.4. Comparative study of flow characteristics in the statistically steady state of the baseline and controlled flow
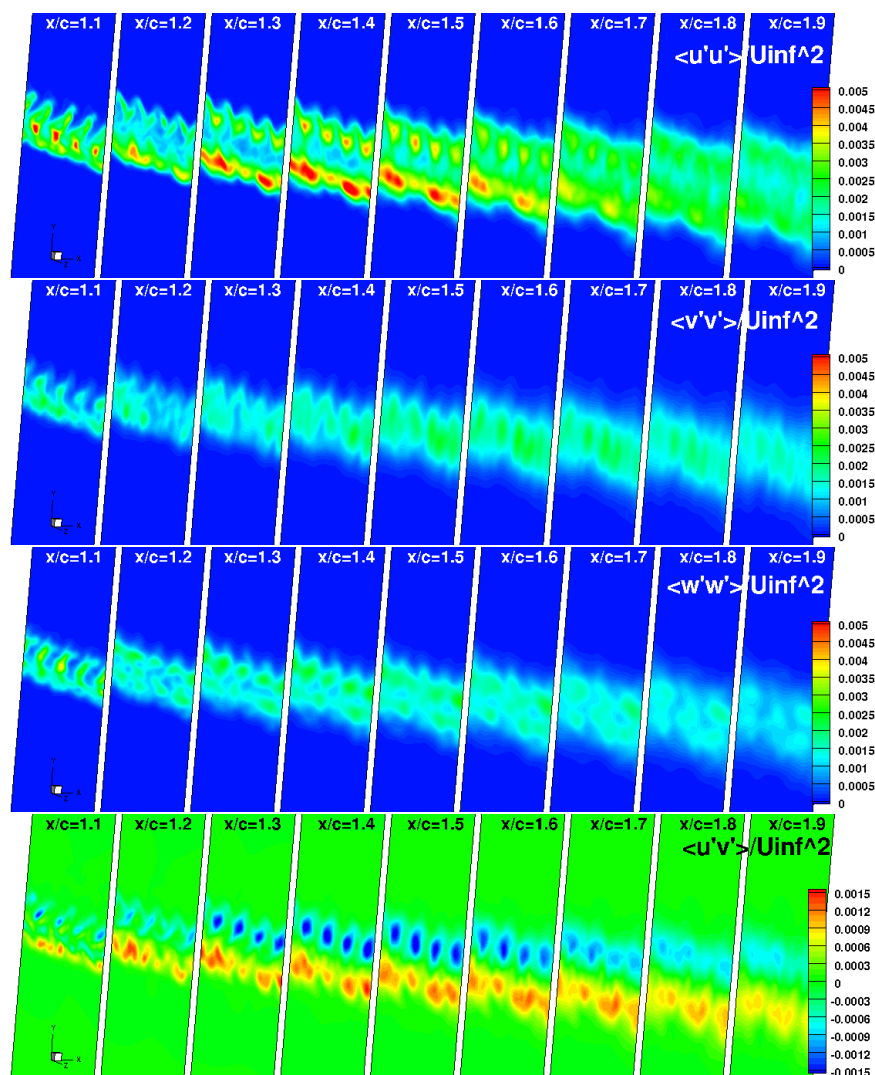
Figure 5.40: Contours of Reynolds stress in the wake for the controlled flow flow at different streamwise sections. From left to right at $x/c = 1.1$, $x/c = 1.2$, $x/c = 1.3$, $x/c = 1.4$, $x/c = 1.5$, $x/c = 1.6$, $x/c = 1.7$, $x/c = 1.8$ and $x/c = 1.9$. From top to bottom for $\langle u'u' \rangle$, $\langle v'v' \rangle$, $\langle w'w' \rangle$ and $\langle u'v' \rangle$

due to a pitch and a skew angle, the other two Reynolds normal stress play as important roles as the streamwise fluctuation.

(5) In the wake region, for the baseline flow, the two dominating components in the turbulence kinetic energy are the streamwise and vertical flow fluctuations. For the controlled flow, even though the streamwise flow fluctuations are higher than the other two directions, the spanwise flow fluctuations are comparable to the vertical fluctuations.

(6) Even at about $0.6c$ downstream of the trailing edge, the traces of the jets can still be observed both in velocity and Reynolds stress contours. Further downstream, the interaction

between the jets influenced flow in the span becomes stronger and stronger. At around $x/c = 1.0$ downstream of the trailing edge, the traces of jets damp out.

5.5 Transient process of deploying and removing the jets from the baseline flow

5.5.1 Introduction

The frequency of pulsed jets in experiments is set to be 1 Hz. Considering the higher computational resources required for more control cycles, the simulation in this study was carried out as follows. Firstly, a baseline case was simulated from a uniform initial flow field. After a statistically steady flow field was achieved, the jets were switched on (this time is set to be 0.). Then, the jets worked for 0.5 s, after that, the jets were switched off, just as the experiment did. With the jets off, another 0.2 s was simulated, and by then a baseline flow was recovered.

During the whole simulation, the development of drag coefficient as a function of time is plotted in Figure 5.41. The sampling frequency of C_d recorded in Figure 5.41 is 2 000 Hz. It is worthy to note that C_d obtained in experiments was based on wake survey techniques, while in the simulation it is directly calculated from pressure and skin friction. This may explain the simulated C_d has a larger perturbation than the experimental measurements. In spite of some discrepancies between experiments and simulations in the transition from baseline flow to controlled flow, generally speaking, the simulation predicts the same C_d development trends, and after $t = 0.2$ s, the differences on the absolute values between experiments and simulations are less than 10%.

According to the C_d development, the time history after deploying jets is roughly divided into below time zones.

(I) The C_d lag zone ($t = 0 - 0.02$ s), during which C_d still keeps similar values to the baseline flow.

(II) The transition zone (off-on) with large C_d perturbations ($t = 0.02 - 0.1$ s), during which C_d goes through decaying perturbations until reaching a final statistically steady state.

(III) The C_d steady zone ($t = 0.1 - 0.5$ s), during which C_f has regular small perturbations and is statistically converged.

(IV) The transition zone from jets-on to jets-off.
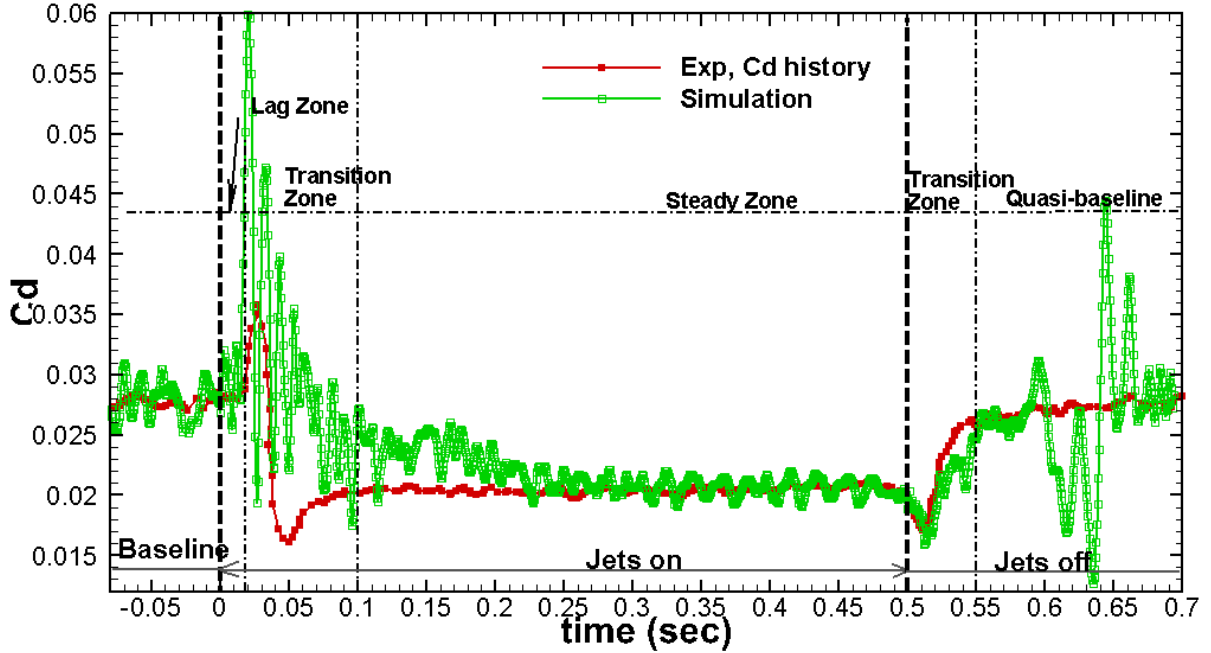
Figure 5.41: The drag coefficient C_d during the whole simulation.

(V) Another statistically steady zone (quasi-baseline) for jets-off flow.

As the pulsed jets behave like continuous jets with such a low frequency observed in experiments, the transition from the baseline flow to the controlled flow will be focused on and the study on the jets-on to off transition will only focus on the transient time, which is essential for the optimization of the control frequency and the duty cycle in the future.

As the previous section has already discussed the statistically steady flow in the controlled state, in this section, the steady zone will not be a key point of discussion. In the following sections, the other zones will be investigated in more details.

5.5.2 The C_d lag zone during the transition from the baseline to jets-on

Figure 5.42 is an enlarged view of time-dependent C_d in the time lag zone. The marked points are the time steps which will be sampled to study this transition process. There are two main questions to be answered in the time lag zone: (1) why this time lag zone exists, and (2) why C_d increases after this time lag zone.

In order to study the relation between flow structures and the drag coefficient, Figure 5.43 displays the vortex structures represented by the λ_2 criterion. When the jets have just been switched on for $t = 0.0005$ s, small vortices were generated around the jets. At $t = 0.003$ s,
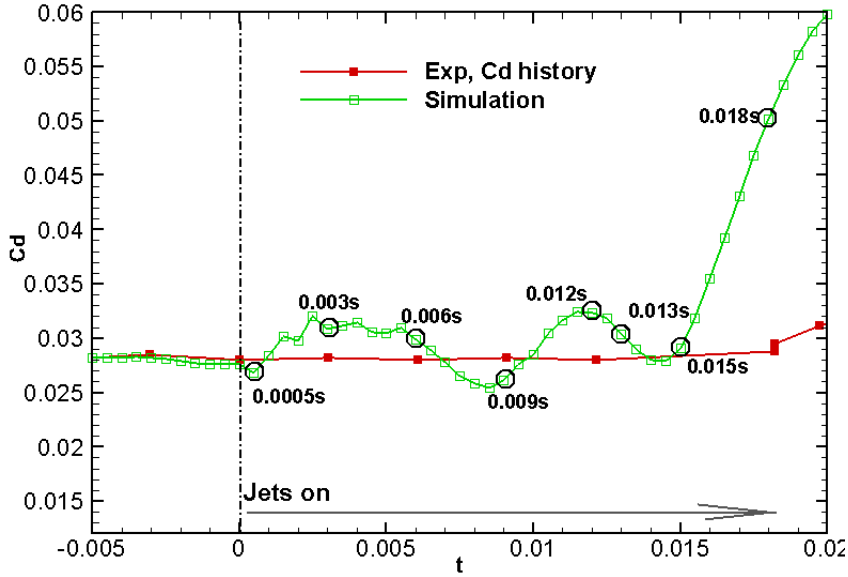
Figure 5.42: The drag coefficient C_d during the transient process of deploying and removal of jets.

it is observed that the vortices upstream of the jets become weak, and the vortices trend to develop associated with the skew angle in the streamwise direction. From the colour coding in Figure 5.43, it can also be observed that the vortices have smaller pressure (larger $-C_p$) than the ambient flow. These pressure differences may result in the formation of the rotating vortices. Combined with the interaction between jets-induced vortices with the free stream velocity, vortices rotate spirally and stretched downwards, as time marches.

At around $t = 0.012$ s, the elongated vortices reach the originally separated shear layer and begin to interact with the separated shear layer. Figure 5.44 shows the original separated flow beneath the shear layer becomes organized, and resembles the locations of jets. Besides, these underneath vortices have stronger spanwise interactions than their upstream flow. At $t = 0.015$ s, the separated shear layer is obviously changed by these elongated vortices. Referring to Figure 5.42, this time $t = 0.015$ s is when C_d begins to increase. This illustrates that only after the generated vortices meeting with the originally separated flow, their influences on the drag coefficient become remarkable. The lagged time is the time period during which the jets vortices moves downstream to merge with the separated shear layer. It is observed that the separation size (or flow type) is highly associated with the drag coefficient, and therefore the process before jets-induced vortices meets the originally separated flow and begins to manipulate the separated shear layer, a C_d lag zone exists. Hence, the first question is answered.

From $t = 0.015$ s to $t = 0.018$ s, the jets-vortices occupied the whole chord of the aerofoil,

217
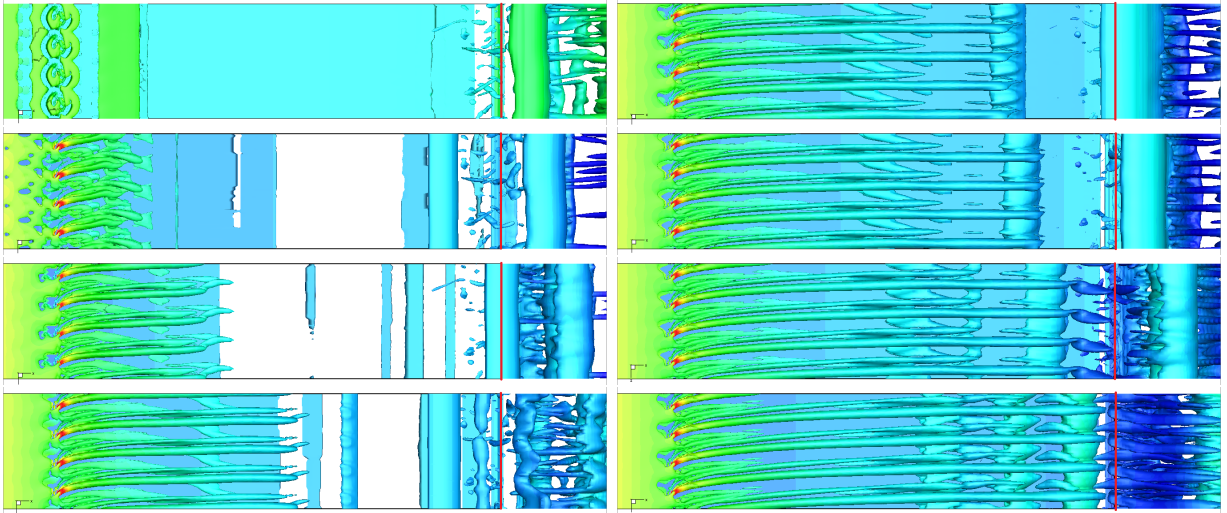
Figure 5.43: Top view of the flow structures represented by the λ_2 criterion, coloured with $-C_p$. (The red line marks where the trailing edge locates.) Left column from top to bottom: $t = 0.000\,5$ s, 0.003 s, 0.006 s and 0.009 s. Right column from top to bottom: 0.012 s, 0.013 s, 0.015 s and 0.018 s
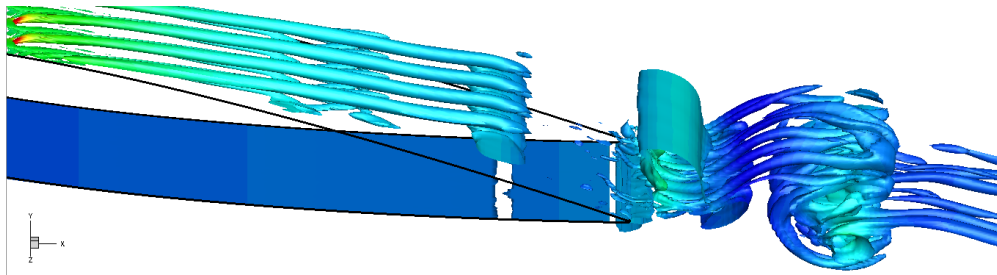
Figure 5.44: Enlarged view of the flow structures represented by the λ_2 criterion, coloured with $-C_p$ at $t = 0.013$ s.

and the wake flow is also apparently affected by these jets-induced vortices. The underneath vortices moves towards the trailing edge and merge with the shedding vortex on the trailing edge to become the new-manipulated shedding vortex (Kuethe and Chow [1986]). The period from $t = 0.015$ s to $t = 0.018$ s corresponds to the increase of C_d (Figure 5.42). From the pressure distribution shown in Figure 5.45(b), it seems at this initial stage of jets-on, after the jets-induced vortices merges with the shear layer, it enlarges the flow wake, and the similar phenomenon was observed in the experiments (Siauw [2008]). Compared with $t = 0.015$ s, C_p at $t = 0.018$ s has shown a larger area between the upper and lower curves, and C_f has a larger negative values near the trailing edge. The initial interaction between the jets-induced vortex and the shear layer enhances the vortex shedding, which makes a larger pressure difference and skin friction difference thus the drag coefficient increases. This

answers the second question.

(a)   (b)
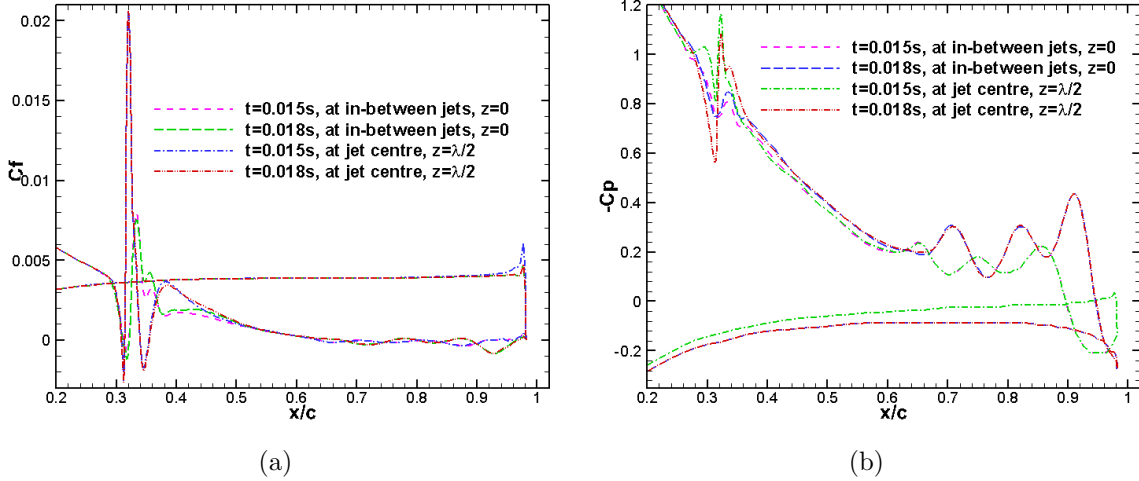
Figure 5.45: The controlled flow at $t = 0.015$ s and $t = 0.018$ s: (a) The skin friction C_f (b) The pressure coefficient $-C_p$

5.5.3 The large C_d fluctuations zone during the transition from a baseline flow to a controlled flow

The transition process of C_d from an highly increased value to the small value in the attached steady state, and the drag coefficient C_d fluctuations with a smaller and smaller amplitude are observed in simulation, while experiments show a smooth reduction rather than fluctuations. Experimental analysis on vortex shedding during the transition process hints the existence of these C_d fluctuations, however, interestingly, the C_d fitted from the wake velocity profile in experiments does not show them. Why these fluctuations exist will be discussed from the instantaneous flow visualization.

The large C_d fluctuations zone begins from the increasing C_d at $t = 0.015$ s to the statistically steady C_d state at $t = 0.1$ s. Figure 5.46 is a view of this transition zone. Five time points during a complete C_d oscillating cycle are selected as marked in Figure 5.46. The experimental drag coefficient indicates a transient time interval of about 0.1 s (a slow increase from $t = 0.06$ s to 0.1 s in Figure 5.41), and our simulation results displays similar transient time interval regardless of the high fluctuations. The fluctuations with high frequencies may be not resolved, and the fluctuations here correspond to the vortex shedding in the wake. In Siauw [2008], some contradictory results about the time interval during jet deployment were given. On one side, the table on Page 163 of Siauw [2008] shows an time interval of 0.03 s, on the other hand, the referred figure (on Page 162 of Siauw [2008]) by this table displays an

5.5. Transient process of deploying the jets from the baseline flow

transient time interval about 0.09 s. Considering the fact that the forces in the experiments were estimated from the parameters of the wake flow in about one chord downstream of the trailing edge, this estimation may introduce some disparities, especially for the fluctuations of forces.
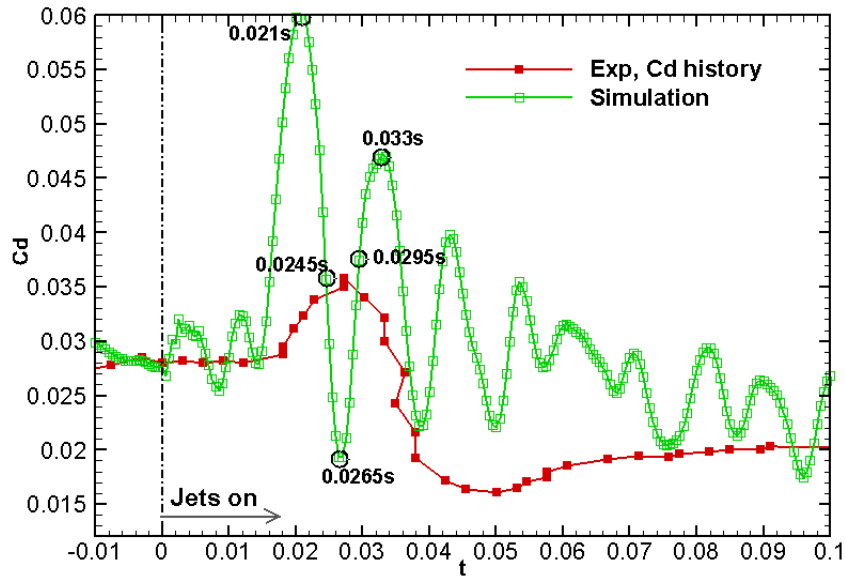
Figure 5.46: The drag coefficient C_d during the transient process of deploying jets. The circled points are the sampled time steps.

Figure 5.47 shows the turbulent flow structures at the six sampled time steps during one cycle of C_d perturbation. Figure 5.48 displays the instantaneous pressure profiles along the aerofoil at these six time steps. At $t = 0.021$ s, the shedding vortices becomes the largest size before their shedding from the trailing edge, as shown in Figure 5.47, which corresponds to the largest pressure differences between the suction and pressure side near the trailing edge. The shedding vortex begins to move off the trailing edge from $t = 0.021$ s, and at $t = 0.0265$ the vortex structures shown in Figure 5.47 seem to be completely off the edge. During this process, the pressure differences between the pressure and suction side become smaller and smaller. After this period, another vortex generates beneath manipulated shear layer, grows and moves towards the trailing edge. During this process, the pressure differences get larger and larger. When it arrives at the trailing edge, the C_p differences is the largest, but smaller than the last same shedding stage at $t = 0.021$ s. This vortex shedding process makes up a cycle of C_d fluctuation, and under the affection of controlled jets, the magnitude of fluctuations becomes smaller.

Besides, the large changes of the pressure near the trailing edge, Figure 5.49 also displays a gradual change of C_p and C_f in other regions. In spite of the large fluctuation of C_p and C_f
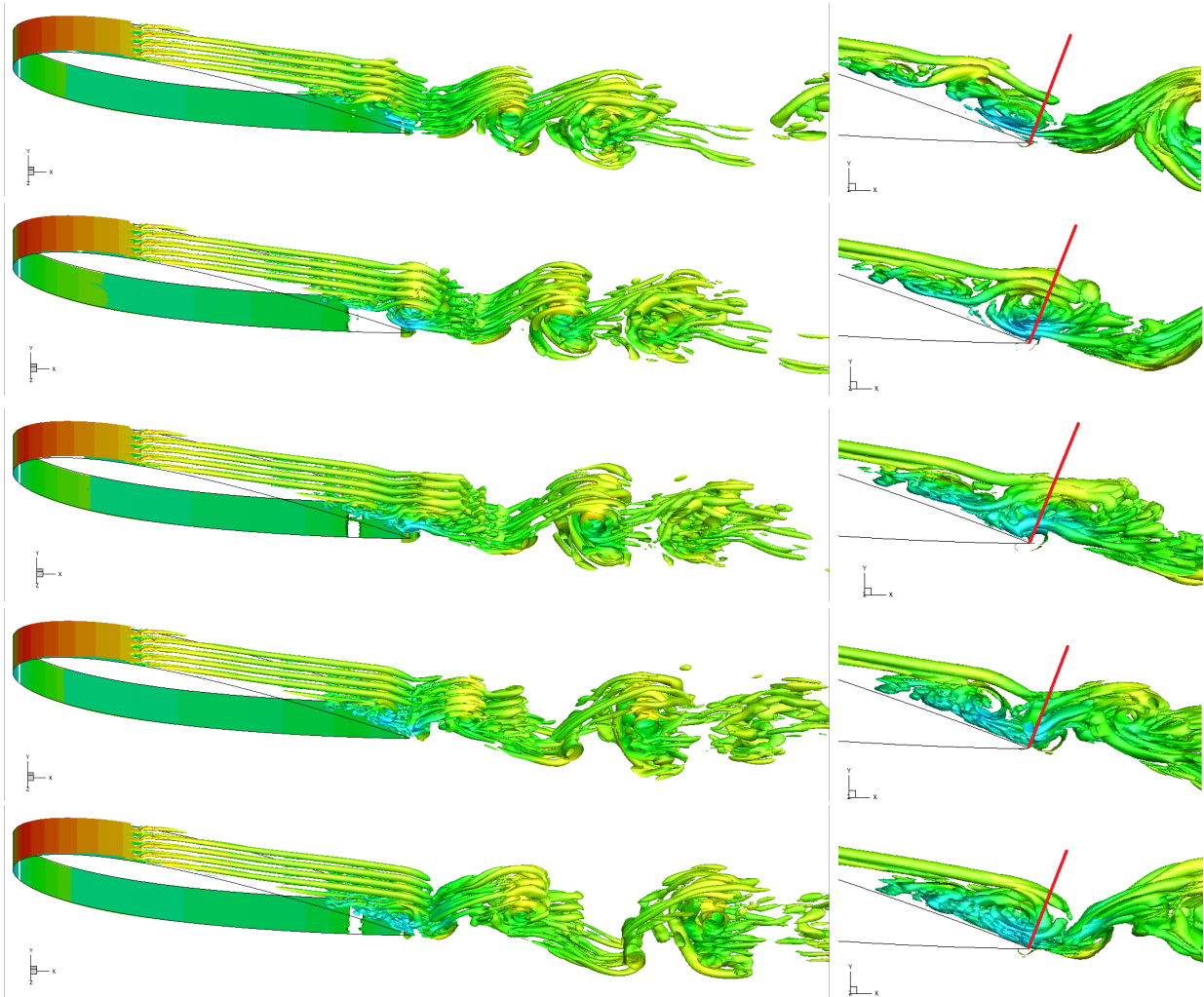
Figure 5.47: The λ_2 criterion, coloured with the streamwise velocity at (from top to bottom) $t = 0.021$ s, 0.0245 s, 0.0265 s, 0.0295 s and 0.033 s. The left column is $3D$ view, and the right column is an enlarged side view (the red lines are references, which are perpendicular to the trailing edge surface).

near the trailing edge, the high $-C_p$ and high C_f induced by jets are steadily approaching in the steamwise direction in the region before the flow separation. On one hand, it implies the jets manipulation on the flow structures moves faster than the change of the flow properties on the wall in the initial transition stage. On the other hand, it also illustrates these high $-Cp$ and C_f moving towards the trailing edge in turn affects the formation and shedding of vortex, especially with a smaller and smaller separation region.

The shrinking separation region can be further quantitatively compared in the profiles of the skin friction C_f shown in Figure 5.50. As time marches, the change of skin friction induced by the jets propagates downstream slowly. At both the sections $z = 0$ and $z = \lambda/2$,
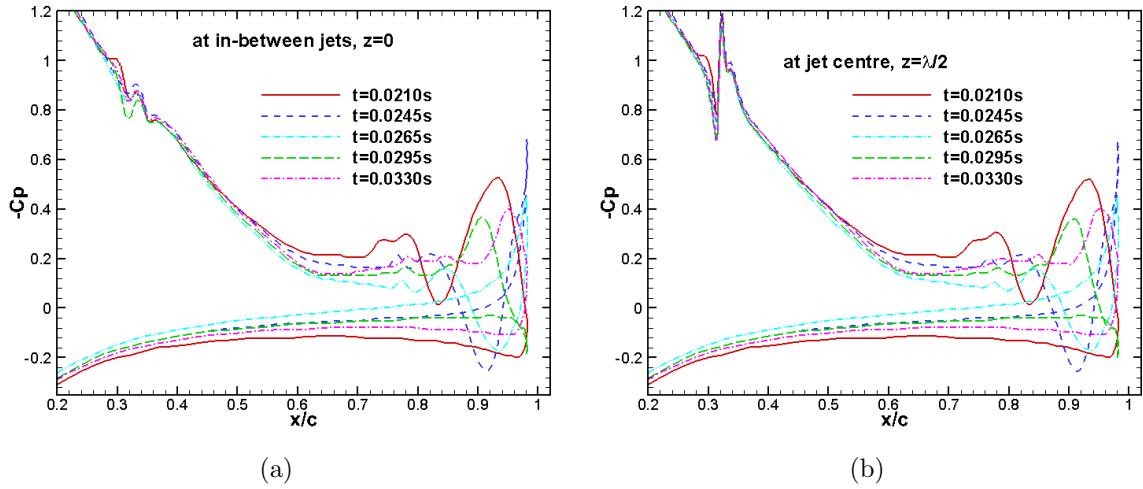
Figure 5.48: Pressure coefficients during the time marching. (a) at in-between jets, $z = 0$, (b) at jet centre, $z = \lambda/2$

the original monotonic decrease of C_f gradually becomes a shape of "$\sim$", with a C_f reduction near the jets and an increase after $x/c = 0.45$. In spite of C_f fluctuations near the trailing edge, the overall trend of C_f becomes larger and larger around the original separation point, which indicates the flow separation region becomes smaller and smaller. It seems that the vortex shedding corresponds to the fluctuation of C_d, and regardless of the stage in the period of the vortex shedding, the jet flow shrinks the flow separation, and reduces the C_d fluctuation magnitude.

5.5.4 The steady zone during the transition from a baseline flow to a controlled flow

With the high skin friction induced by jets approaching towards the trailing edge, the flow separation becomes smaller and smaller, as discussed above. When the generated vortices dominates the whole chord and removes the original separated shear layer, the flow becomes almost fully attached and the unsteadiness becomes weak. A final steady state is achieved.

Statistically averaged flow field in this steady zone reflects the final control effect, which has been discussed in Section 5.4. Instantaneous distributions of C_p and C_f have also been presented in Section 5.4. Thus, details on the controlled flow in this stage will not be repeated.

(a) -C_p

(b) C_f
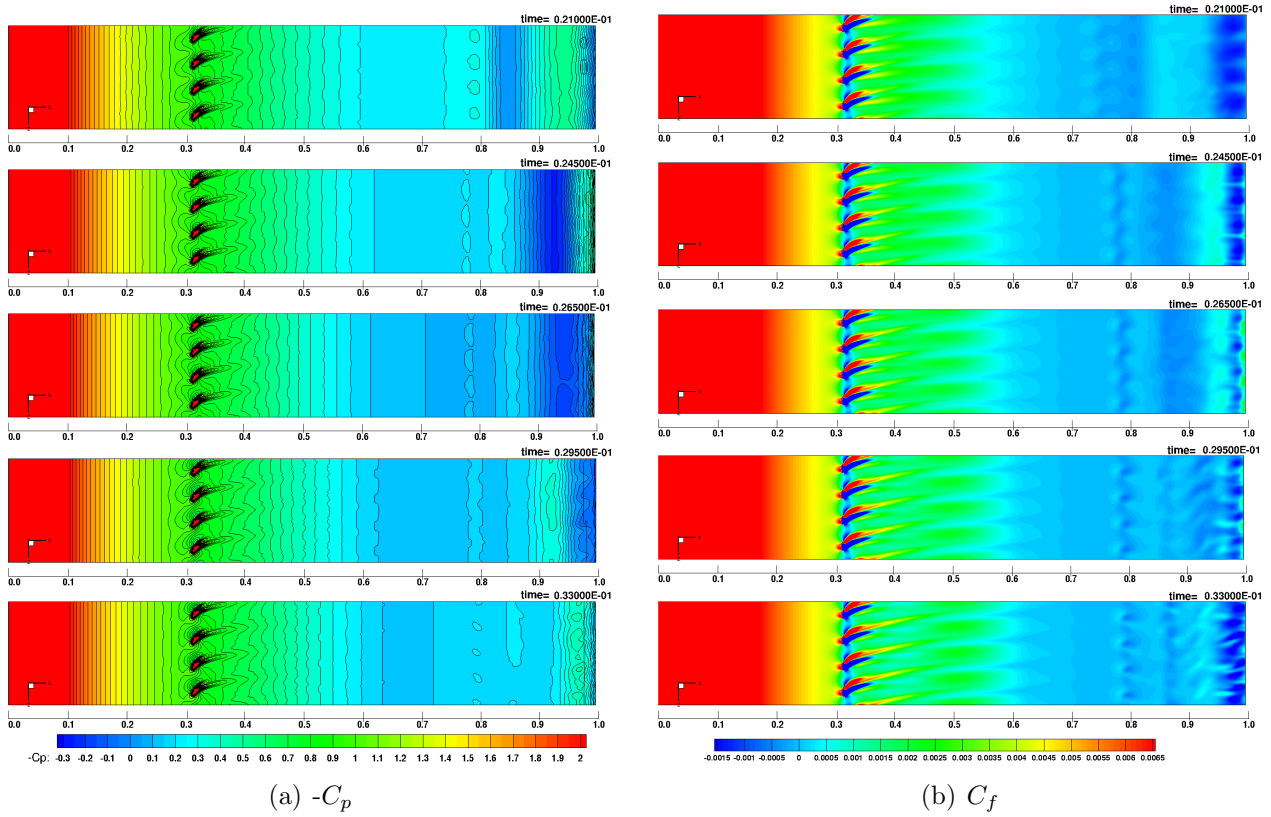
Figure 5.49: The contours of (a) pressure coefficient $-C_p$ and (b) skin friction C_f, at $t = 0.021$ s, 0.0245 s, 0.0265 s, 0.0295 s and 0.033 s (from top to bottom).
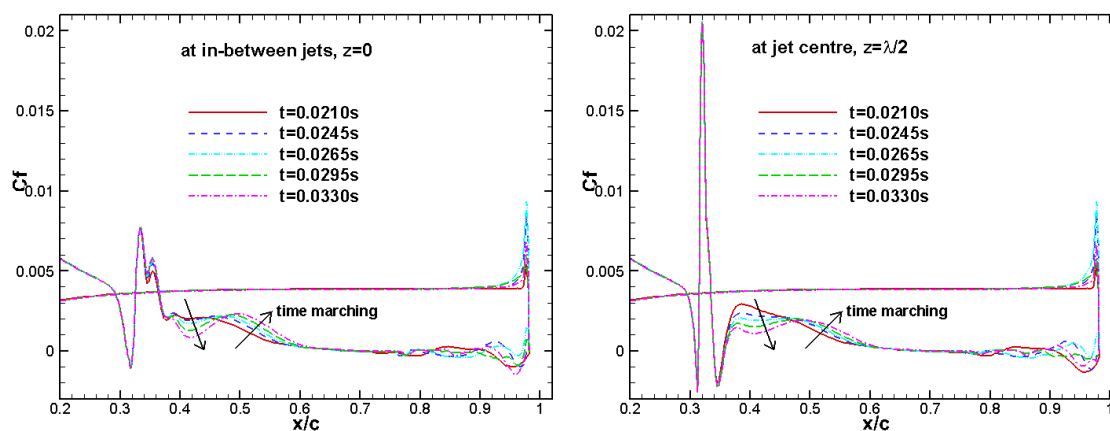
Figure 5.50: Skin friction during the time marching. Left: at in-between jets, $z = 0$. Right: at jet centre, $z = \lambda/2$

5.5.5 The transition zone from jets-on to jets-off

Figure 5.51 displays the time-dependent C_d during the transition from removal of the jets. The circled points are sampled to study the transient process. Figure 5.51 shows that from the removal of the jets at $t = 0.5$ s to 0.58 s, the simulation results of the drag coefficient agree reasonably well with the experimental measurements. However, from $t = 0.59$ s to 0.67 s, the numerical results encounter large fluctuations. Besides, both the experiments and the simulations display a slight increase from the recovered region $t = 0.55$ s to $t = 0.7$ s.
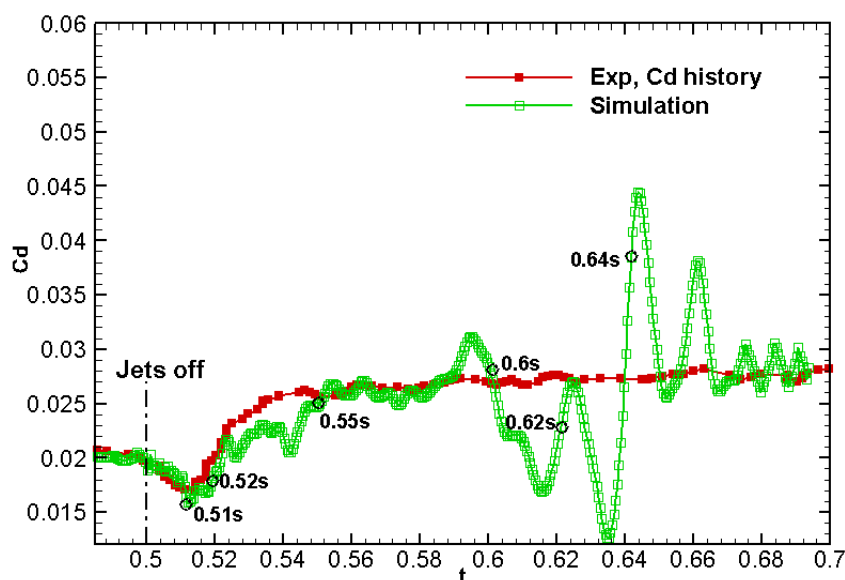
Figure 5.51: The drag coefficient C_d during the transient process of removal of jets. The circled points are the sampled time steps.

Figure 5.52 displays the iso-surface of the λ_2 criterion to show the turbulent structures. It is observed that although the drag coefficient has recovered to the quasi-steady state from $t = 0.51$ s to 0.55 s (see Figure 5.51), the effect from the previous jets on the turbulent structures are still observed. Nevertheless, the previous controlled vortices shrink from the original locations of the jets. From $t = 0.6$ s to 0.64 s, Figure 5.52 shows that the trailing edge separation becomes larger and larger and eventually recovers to similar separation region to the baseline flow. In addition, vortex shedding becomes obvious in the wake flow from $t = 0.62$ s. The initial recovered vortex shedding and the developments of the shedding vortices near the trailing edge and in the wake may be related with the high fluctuations of the drag coefficient.

For the transient time interval of the process of jet removal, the experiments also presented some contradictory results. From the drag coefficient shown in Figure 5.51, the experiment displays a transient time interval of about 0.05 s, however, the figure in Page 162 of Siauw [2008] showed an transient time interval of about 0.15 s. The drag coefficient by the simulation shown in Figure 5.51 displays a transient time interval of about 0.17 s.

Conclusively, the experiments of Siauw [2008] declared a transient time interval for the jet deployment of about 0.03 s and a transient time interval for the jet removal of about 0.05 s. The figures about the evolution of the lift coefficient fluctuations in Siauw [2008] correspond to a transient time interval for the jet deployment of about 0.09 s and a transient time interval for the jet removal of about 0.15 s. The simulated drag coefficients in this study predict a transient time interval for the jet deployment of about 0.1 s and a transient time interval for the jet removal of about 0.17 s, which are similar to the results shown by the mentioned figures in Siauw [2008]. Nevertheless, all these results show that the transient time for the jet removal is about 70% longer than the transient time interval for the jet deployment.

5.5.6   Summary

Numerical simulation predicts reasonably good transition process of the development of C_d, and the flow developments during the transition process are further analysed via instantaneous C_p, C_f distributions and flow structures.

After the jets on, there is a C_d lag zone of about 0.015 s. During this time, the jets-induced rotating vortex generates from the jets and grows towards the originally separated shear layer, before these vortices merging and interacting with the shear layer, the C_d varies little. After that, the growing vortex and the shear layer produce large shedding vortex. The shedding process of the vortex corresponds to the large fluctuations of C_d. Along with

5.5. Transient process of deploying the jets from the baseline flow
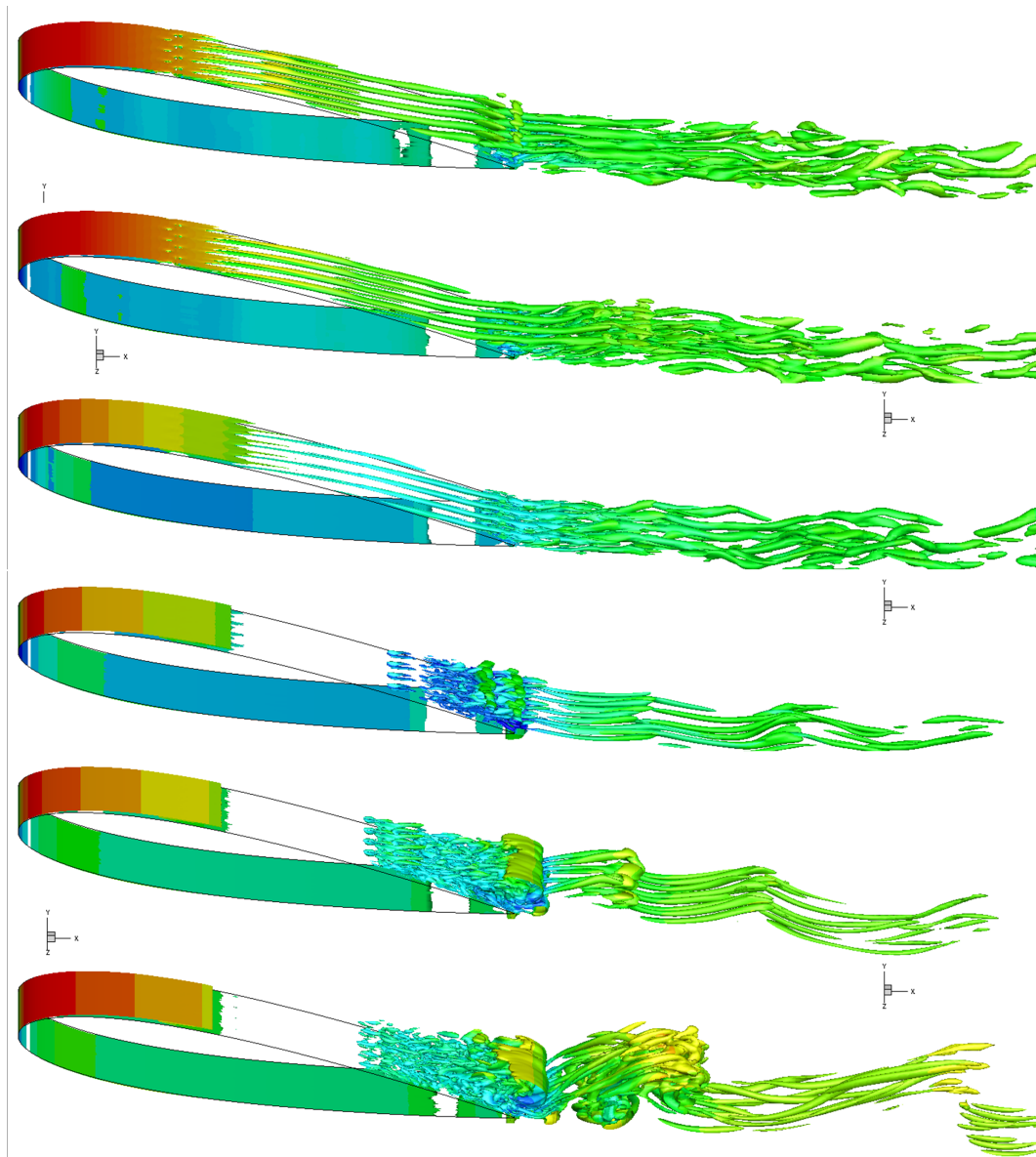
Figure 5.52: The λ_2 criterion, coloured with the streamwise velocity at (from top to bottom) $t = 0.51$ s, 0.52 s, 0.55 s, 0.6 s, 0.62 sand 0.64 s.

time, the vortex with high momentum becomes dominant, which forces the separated shear layer smaller and smaller. Finally, the flow becomes almost fully attached, and there is no more vortex shedding from the trailing edge. Thus, the C_d becomes steady. The transition process last about 0.1 s. Flow changes little during the remained 0.4 s during the jets-on duty. After switching off the jet, the simulation results show an transient time interval of about 0.17 s. Both the experiments and the simulations display an about 70% longer of the transient time for the jet removal than that for the jet deployment.

5.6 Summary

Simulations on the pulsed jets flow control employed on NACA0015 with an original mild separation were carried out in this chapter. The baseline case validation was first conducted to study the different performance of different hybrid RANS/LES methods. Interestingly for this case, only IDDES gives proper separation, while DDES cannot predict any flow separation.

IDDES simulations of the baseline flow and the controlled flow agree well with the experimental data. Besides the comparison on profiles in particular locations, spatial distributions of pressure, skin friction, velocity and Reynolds stress are provided by the simulation to study the affected flow field. The transition process from the baseline flow to the jets controlled steady flow is also investigated.

Chapter 6

Passive Flow Control with Fractal Orifices in Pipe Flows

6.1 Introduction

Traditional attempts at understanding the multi-scale facet of turbulence rely on turbulent flows generated by simple geometries, such as flat plates, pipes and steps. In the recent decade, new approaches to generate turbulent flows have emerged. In these approaches, turbulent flows are generated by multi-scale/fractal objects. The properties of turbulent flows, such as the turbulence evolution, its dissipation, decay and the cascade process, were better understood by studying the interaction between the flow intrinsic multi-scales and the boundary geometric scales of the fractal objects. In addition, some unique mechanisms (e.g. the space-scale unfolding mechanism (Laizet and Vassilicos [2012])) in the mixing process of fractal-generated turbulence were also observed and discussed. The purpose of this chapter is to provide further understanding of turbulent flows through fractal orifices with numerical simulations to predict flows at relatively high Reynolds numbers.

To generate fractal-forced turbulent flows, various fractal objects have been used by different research groups, as documented in Chapter 2. In this chapter, we concentrate on the orifices with fractal perimeters (Nicolleau [2013]; Nicolleau *et al.* [2011]). Fractal orifices in pipes can be related to engineering applications such as optimal flow meters, industrial mixing, combustion, cooling in nuclear power stations and flow control devices. Unlike the flows generated by regular or square fractal grids, the fractal orifice flow is a wall-bounded pipe flow, involving the interaction between the fractal-forced turbulence structures and the near-wall turbulence structures. On the other hand, because the size of forced turbulence structures highly depends on the fractal geometric length scales, flows through the fractal

orifices also distinguishes themselves from flows through classical non-circular orifice jets (Gutmark and Grinstein [1999]; Mi *et al.* [2010]).

A majority of the published papers on the fractal-generated turbulence focus on experimental studies. There are also a few Direct Numerical Simulations, but they were usually conducted at a reduced Reynolds number compared with the experiments. To understand multi-scales of fractal-forced turbulent flows, resolving turbulence structures is necessary. Reynolds Averaged Navier-Stokes approaches cannot deliver on this because of their incapability in modelling massively separated flows involving large adverse pressure gradients (Sagaut *et al.* [2006]). Therefore, DNS and the Large Eddy Simulation become the primary considerations for investigating these multi-scale flows. However, with current computational resources, the Reynolds numbers are limited for DNS in comparison with the laboratory experiments. Nagata *et al.* [2008] applied DNS to the grid-generated turbulence and used the immersed boundary method to construct the complex grids. The Reynolds number in their DNS was 1250. Geurts [2012] applied DNS to simulate flows through fractal orifice pipes, and in his simulations laminar flows were at a Reynolds number of 1 and turbulent flows were at a Reynolds number of 4300. Laizet *et al.* [2010] and Laizet and Vassilicos [2011] provided a numerical strategy to apply a high-order DNS combined with the immersed boundary method to simulate their fractal grids. Even with an extraordinary powerful high performance computing system, Laizet *et al.* [2010] had to reduce the Reynolds number (based on an effective grid length and defined in Laizet *et al.* [2010]) for the cross grid fractal flows from the experimental $Re_{\text{exp}} = 87\,400$ to $Re_{\text{DNS}} = 1860$ and from $Re_{\text{exp}} = 20\,800$ to $Re_{\text{DNS}} = 4430$ for the square grid fractal flows to make DNS achievable. These DNS results with reduced Reynolds numbers can only be compared qualitatively with the available experimental data. Besides DNS, Chester *et al.* [2007] and Chester and Meneveau [2007] used a new technique called renormalized numerical simulation to model the drag of the branches of a fractal tree. However, as commented by Laizet and Vassilicos (Laizet and Vassilicos [2011]), this approach cannot resolve the actual turbulent flow structures. There is no doubt that DNS with high-order schemes is the best choice to study the flow details and turbulence mechanisms for the fractal-generated turbulence if computing resources allow. Considering the motivations driven by engineering applications, LES can provide a more practical approach for simulations of fractal-generated orifice flows in the same Reynolds number ranges as those in the experiments. LES resolves the large-scale structures contributing the most to the turbulent transport process and models the statistically isotropic and universal small scales (Sagaut *et al.* [2006]). Even though LES lacks the capability of providing the whole spectra of turbulent flows, considering that it can resolve

most of the energy-carrying large structures at a more affordable computational cost, it becomes a balanced choice. In the present study, referring to the experiments by Nicolleau *et al.* [2011], the large eddy simulations of turbulent flows through snowflake fractal-type orifices were carried out to improve our understandings of the experimental results and to reveal more physics of fractal-generated turbulence. These flow characteristics revealed in the simulations can also provide some guidance on the design of control devices and flow management.

The chapter is organized as follows. Firstly, the geometries of the fractal orifices and the flow configuration are described. A mesh study is also presented in this section. Then, instantaneous flow visualisations are shown and discussed. After that, the statistical results are presented and compared with the available experimental data, and more detailed analyses of the underlying flow physics are given. Finally, concluding remarks are drawn.

6.2 Validation of turbulence models in flow through a circular orifice pipe

Flow through a circular orifice has a geometry-fixed separation. Meanwhile, it is wall-bounded flow. The turbulent boundary layers along the pipe may interact with each other, which challenges the application of hybrid RANS/LES methods. In this validation section, flow through the circular orifice was simulated with different treatments of hybrid RANS/LES methods. One of the aims is to find a proper turbulent viscosity treatment and numerical parameter configuration with in-house code DG-DES before further research on passive flow control with fractal orifices in pipes.

6.2.1 Flow configuration

Nicolleau *et al.* [2011] and Nicolleau [2013] conducted an experimental study on flows through a circular and fractal orifices in a pipe with a diameter (D) of 0.14 m for different fractal levels of orifices. The computational domain simulates the same geometry as the experiment, including the ramps supporting the orifice plate. The schematic of the computational domain is shown in Figure 6.1. The thickness of the orifice plate is 0.002 m. The coordinates are defined as: $x - y$ plane is the cross section and the pipe section is defined as the main cross section, y is the vertical direction and z is the streamwise direction. The diameter of the circular orifice is $d = 0.08$ m. The orifice beta ratio (the ratio of the orifice diameter to the pipe diameter) is 0.57. The Reynolds number based inflow velocity and the pipe diameter

is 38,900.

Figure 6.1: Computational domain of the fractal-orifice pipe. Unit: meter

6.2.2 Boundary condition and time step

A bell-mouth inlet was used in the pipe to ensure a uniform inlet velocity in experiments. The same uniform velocity $U_\infty = 5$ m s^{-1} was applied at the inlet in the computation. The Reynolds number based on the pipe diameter and the inlet velocity is $Re = 38\,900$. Because of a very small turbulent intensity at the inlet (less than 1%) in the experiments, no turbulence was superposed on the uniform inlet velocity in the simulations. The convective outlet boundary condition was used at the outlet. A no-slip condition was enforced at all the pipe and plate walls.

The Strouhal number, defined as

$$St = \frac{L}{U_e} f, \tag{6.1}$$

was used to determine the computational time step in the orifice pipe flow. In Eq. (6.1), the variable L is the equivalent diameter for the fractal orifices and is chosen to be the diameter of the circular orifice. The variable f is the frequency of the vortex shedding. The variable U_e is the centreline velocity at the exit of the orifice. Strouhal numbers in different jet facilities at Reynolds numbers above 10^4 vary from 0.24 to 0.64 (Gutmark and Ho [1983]). Beavers and Wilson [1970] studied the Strouhal numbers in the orifice pipe flows, which were around 0.63 to 0.66 for Reynolds numbers up to $15\,000$. Herein a Strouhal number of 0.5 was chosen to calculate a vortex shedding period $T = L/(St \cdot U_e)$. This led to a time step of $\Delta t = 0.012\,T$. Physical solutions were achieved after $100\,T$ and then statistical sampling could be started. The flow was calculated for a further $50\,T$ to compute the various

statistical properties.

All these configurations on computational domain, boundary conditions and time step maintain the same for flows through fractal orifices, which will not be repeated in the following sections.

6.2.3 Comparison of hybrid RANS/LES turbulence modelling techniques

In order to study the turbulent flow through pipes with orifices, there are two important issues to delivery: one is to reasonably simulate the boundary layer in the region before flow reaching the orifice plate and the region where it redevelops after reattaching to the pipe wall, the other is to resolve the flow structures and predict the recirculation region as good as possible. Considering these two requirements, DES was chosen to be the primary modelling method. (In this geometry-fixed turbulent flow, DDES was validated not to provide significant improvements (Shur *et al.* [2008]).) Considering the strong anisotropic characteristics of geometry-induced shear layer and the anisotropic unstructured grids, the numerical dissipation and the turbulence modelling may strongly interact with other, and this interaction may jeopardize the accuracy of LES methods which were usually designed with assumptions of isotropic flow and isotropic grids. Therefore, implicit LES, which makes use of the numerical dissipation to represent the modelled turbulent viscosity, is also considered a promising turbulence modelling method in this study. In consideration of the boundary layer mesh which may be not fine enough for LES, a wall-modelling ILES (SA-ILES) is used. Details on SA-ILES were already described in Chapter 3.

DES, iLES and SA-iLES on the circular orifice flow are compared in this study to provide some guidance on the applications of turbulence modelling for this particular type of flow.

6.2.3.1 RANS and LES zones in DES and SA-iLES

Simulations are carried out in two types of mesh, the coarse mesh and the fine mesh. The differences between these two sets of mesh are mainly in the out of the boundary layer region and the stretching ratio in the streamwise direction. Differences in the near-wall mesh resolutions are not significant. Details on the mesh resolution are listed in Table 6.2 (Some of the circular mesh information will be given in Secretion 6.3 to make a clear comparison to the fractal orifices. Therefore, some figures referred in this section may have to look in Secretion 6.3). The coarse and fine mesh in the cross section are shown in Figure 6.2. The first layer y^+ distribution for the coarse mesh is plotted in Figure 6.3, in which there are

(a)   (b)
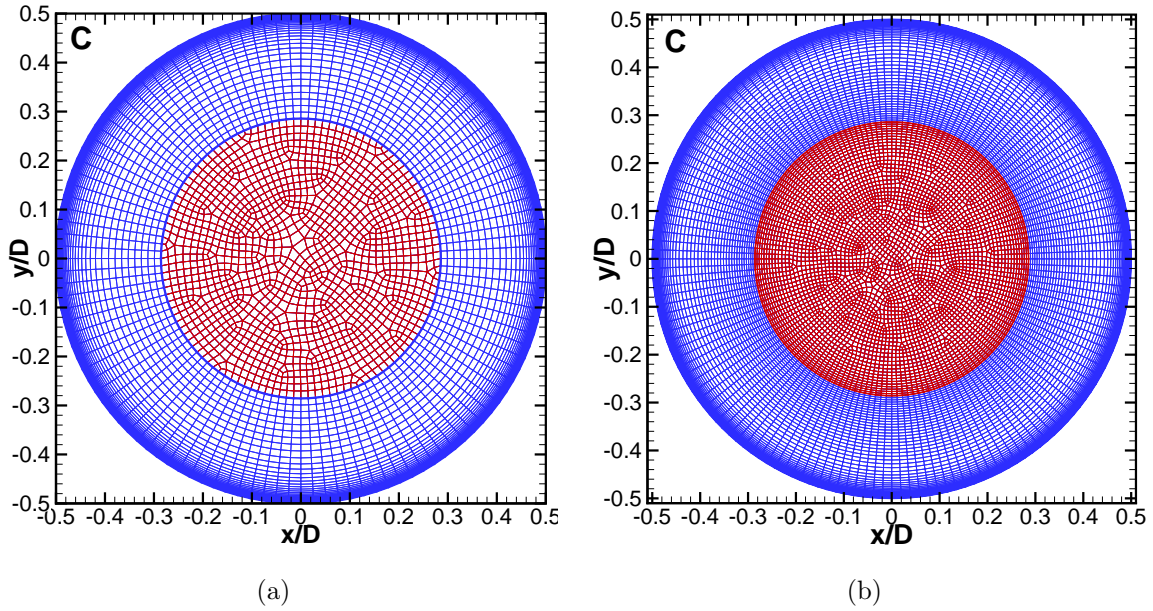
Figure 6.2: The mesh on the cross section for the circular orifice. (a) The coarse mesh (b) The fine mesh

two lines representing two intersection lines of a plane via the central axis with the pipe surface. The abrupt increase of y^+ near the orifice plate represents the first layer grid on the orifice plate, which is less important compared with the boundary layer first cell thickness. Generally, the near-wall mesh with $y^+<1$ is considered reasonable for the S-A method.
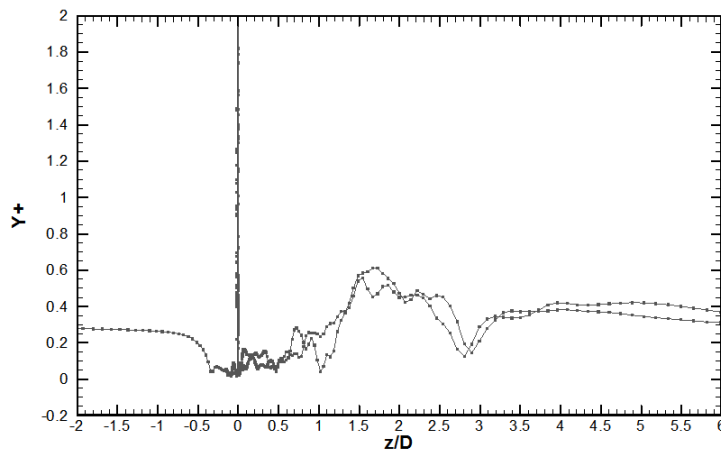
Figure 6.3: The first layer y^+ (for the coarse mesh) along the pipe wall.

According to relation of the wall distance and grid spacing, DES or SA-iLES divide the whole domain into RANS region and LES (or iLES) region (shown in Figure 6.4). The RANS region covers about half of the whole boundary layer thickness for the turbulent boundary

layer region, and it covers a much thinner region in the flow recirculation region.
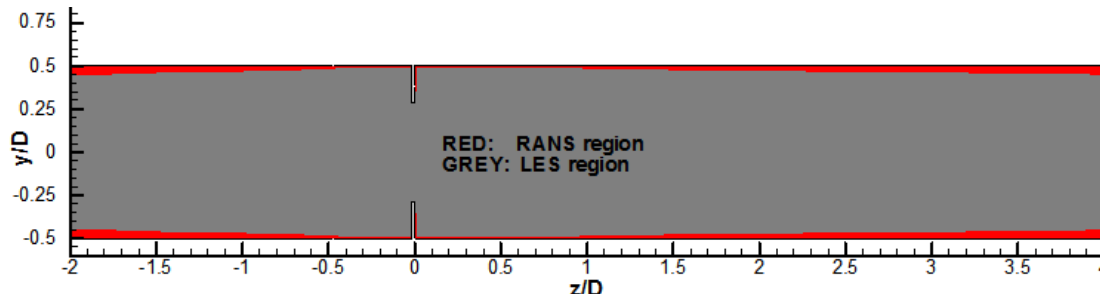
Figure 6.4: RANS and LES regions in DES.

6.2.3.2 Boundary layer

To illustrate the capability of different treatments on turbulence modelling in simulation of the turbulent boundary layer, velocity profiles at $z/D = -2.0$ in the coarse mesh is shown in Figure 6.5. It can be seen that ILES cannot predict accurately the boundary layer, while SA-ILES and DES capture similar boundary layer velocity profiles to the empirical formula in Spalding [1961]. The possible reason for the failure of ILES in predicting boundary layer is that with current mesh resolution, in near-wall region ILES cannot provide sufficient eddy viscosity only from numerical dissipation, thus the momentum transfer is far less sufficient, and then the boundary layer is thinner that those predicted by DES and SA-ILES, as shown in Figure 6.5. As a conclusion, for the mesh resolutions designed for the hybrid RANS/LES, the near wall region has to be wall-modelled, and ILES cannot work well in this region without any wall treatment.

6.2.3.3 Flow recirculation

After through the orifice, flow is forced separated, and strong shear layer is generated from the edge of the orifice. A large flow recirculation region is formed downstream of the orifice plate.

Figure 6.6 compares the velocity distribution in the radial direction to investigate the momentum transfer. For the coarse mesh, SA-ILES and ILES give very similar velocity profiles, which implies the failure of ILES in simulating the boundary layer before the orifice has little effect on the recirculation region. In other words, flow in the recirculation region is more affected by the orifice effect than by the upstream velocity profiles. Compared SA-ILES, DES in the coarse mesh over-predicts the velocity near the central core of the pipe, and under-predict the velocity near the wall from $z/D = 2.0$ to 4.0. These velocity profiles
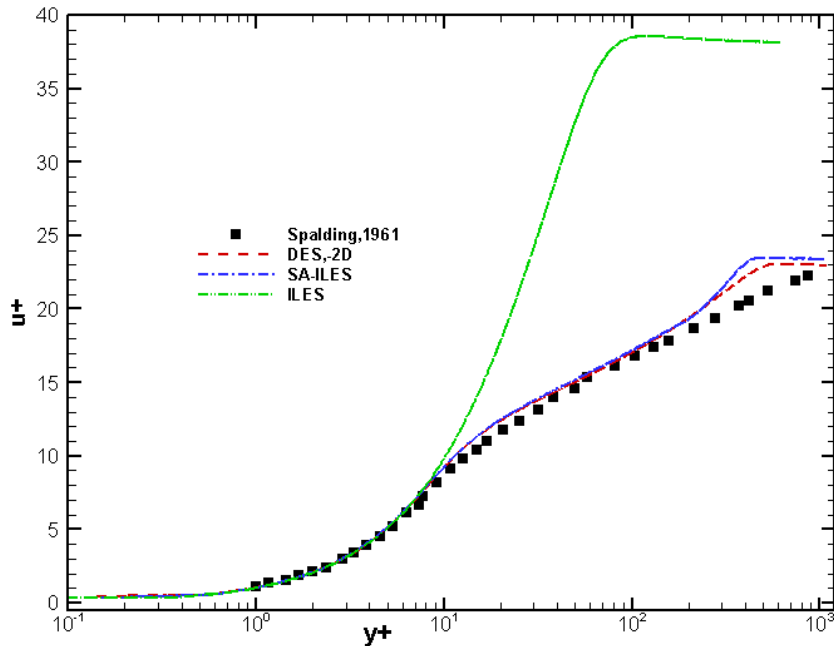
Figure 6.5: The velocity profiles at $z/D = -2$ for the coarse mesh.

by DES imply the total viscosity is far more than that for a reasonable momentum transfer. This is also confirmed in Figure 6.7. For the fine mesh, differences between SA-ILES and DES are slight. The only obvious discrepancies exist in the central region of the pipe at $z/D = 2.0$ and 2.5, where DES seemly transfer more momentum from the pipe axis towards the wall to make the velocity in the centre smaller. This corresponds a larger turbulent viscosity near the central region, as shown in Figure 6.7.

From Figure 6.7, it can be seen that in the recirculation region, the mesh resolution significantly changes the modelled turbulent viscosity for DES. With a similar mesh resolution for the coarse and fine mesh near the wall, SA-ILES for these two sets of mesh gives similar wall-modelling function. Comparing DES and SA-ILES in the fine mesh, in the recirculation region, DES actually models very small turbulence fluctuations (less than 10 times of the molecular viscosity), which results in a very similar simulation to SA-ILES. For DES and SA-ILES, most of the flow fluctuations are resolved in this region.

6.2.4 Summary

Compared with DES, SA-ILES with different mesh resolutions give few differences in the predicted velocity distributions. Considering the fact that much smaller forced turbulence structures will be produced in the fractal orifices, the generation of proper mesh resolutions
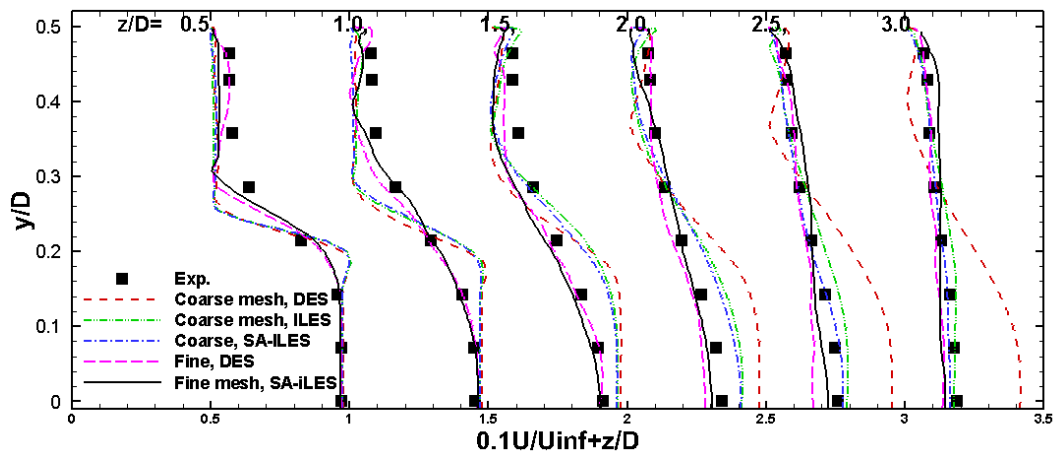
Figure 6.6: The streamwise velocity along the centreline.

for DES is challenging. If unstructured anisotropic mesh will be used it may increase the numerical dissipation, which may aggravate turbulent transport, in addition to the possible increased turbulent viscosity due to a relatively coarse mesh in DES. SA-ILES, without modelled turbulent viscosity may reduce the suffering from high numerical dissipation with unstructured anisotropic mesh. Besides, SA-ILES also predict good boundary layer flow due to the wall modelling. Conclusively, in the wall-bounded orifice flow with complex fractal geometries, SA-ILES seems to be the best choice of the turbulence modelling.
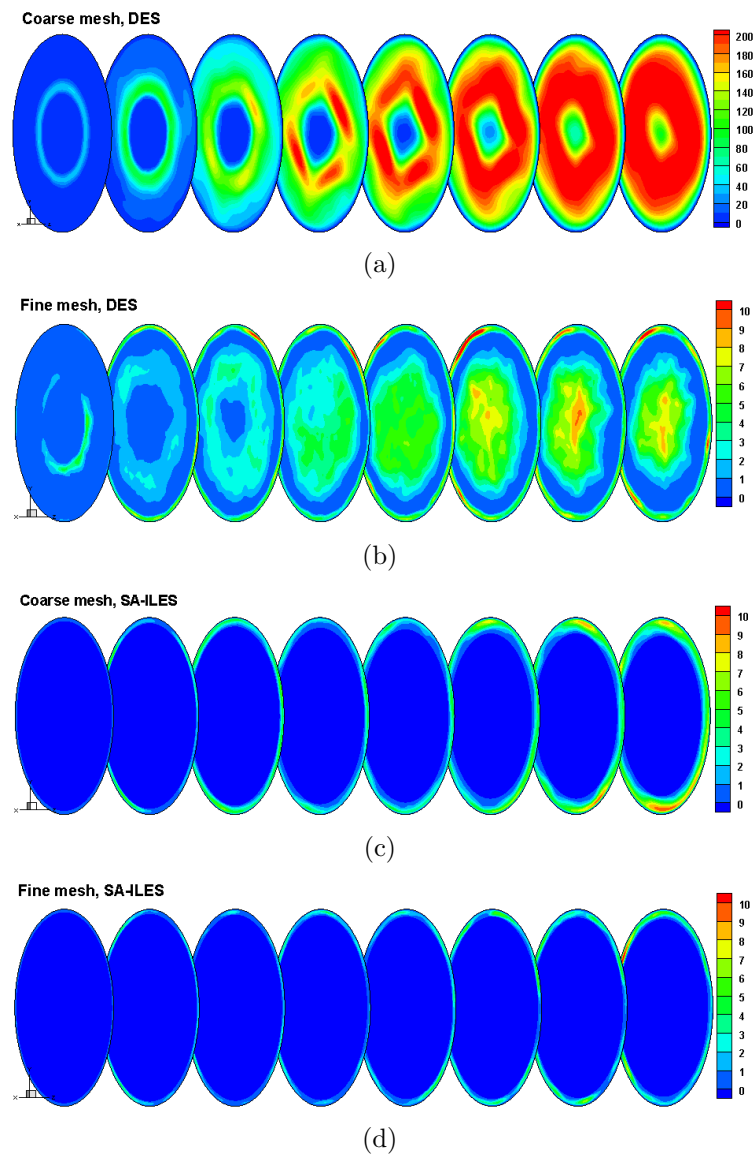
Figure 6.7: The modelled turbulent viscosity μ_t/μ at $z/D = 0.5$, 1.0, 1.5, 2.0, 2.5, 3.0, 3.5 and 4.0. (a) Coarse mesh, DES (b) Fine mesh, DES (c) Coarse mesh, SA-ILES (d) Fine mesh, SA-ILES

Table 6.1: Geometric parameters of the fractal orifices

Levels	C	F0	F1	F2	F3
L_{s}[a]	$0.571D$	$0.770D$	$0.222D$	$0.071D$	$0.023D$
L_{w}[b]	$0.214D$	$0.055D$	$0.114D$	$0.134D$	$0.142D$
ϕ[c]	$0.571D$	$0.444D$	$0.444D$	$0.422D$	$0.411D$
L_{min}- Scaling[d]	0.743	$1.000 \times (\frac{1}{3})^0$	$0.866 \times (\frac{1}{3})^1$	$0.822 \times (\frac{1}{3})^2$	$0.802 \times (\frac{1}{3})^3$

[a]The length of the shortest side of the fractals. For the circular orifice, it is the diameter of the orifice.
[b]The shortest distance from the pipe wall to the vertexes of the polygon fractals.
[c]The diameter of the circle inscribed within the fractal flow area.
[d]The scaling factor of L_{min} to L_{min0} (for the zero level, $L_{\mathrm{min0}} = 1$).

6.3 Flow through fractal orifices

6.3.1 Description of the geometry of fractal orifices

Fractal patterns of the orifices are based on the von Koch snowflake. First, keeping the same flow area as the circular orifice, an equilateral triangle orifice, named the zero level (labelled as F0) is generated, and the edge length of this equilateral triangle is the fractal generator length. Then a hexagram (the first level fractal, labelled as F1) is constructed by splitting each segment of the fractal perimeter in the last level into three equal segments and replacing the middle segment with two edges of an equilateral triangle pointing outwardly. Fractal orifices with higher levels are constructed by recursively altering each segment following above processes. The schematics of the fractal orifices in this study are shown in Figure 6.8. For constructing the fractal geometries, only one geometry parameter can be conserved for all the fractal levels, either the fractal generator length or the flow area. When the fractal generator length is kept constant, the flow area grows with the fractal level. As discussed by Nicolleau *et al.* [2011], fixing the fractal generator length means comparing orifices with different flow areas, which makes the analysis difficult. Therefore, the flow areas are conserved at all fractal levels, the same as that in the experiments (Nicolleau *et al.* [2011]). A summary of the geometry parameters of the fractal orifices is listed in Table 6.1.

6.3.2 Mesh resolution

Because of the interaction between the numerical dissipation and the sub-grid scale modelling, the mesh study for LES is more difficult than that for RANS. Strictly speaking, a grid-independent solution cannot be achieved in approaches with the implicit spatial filter-
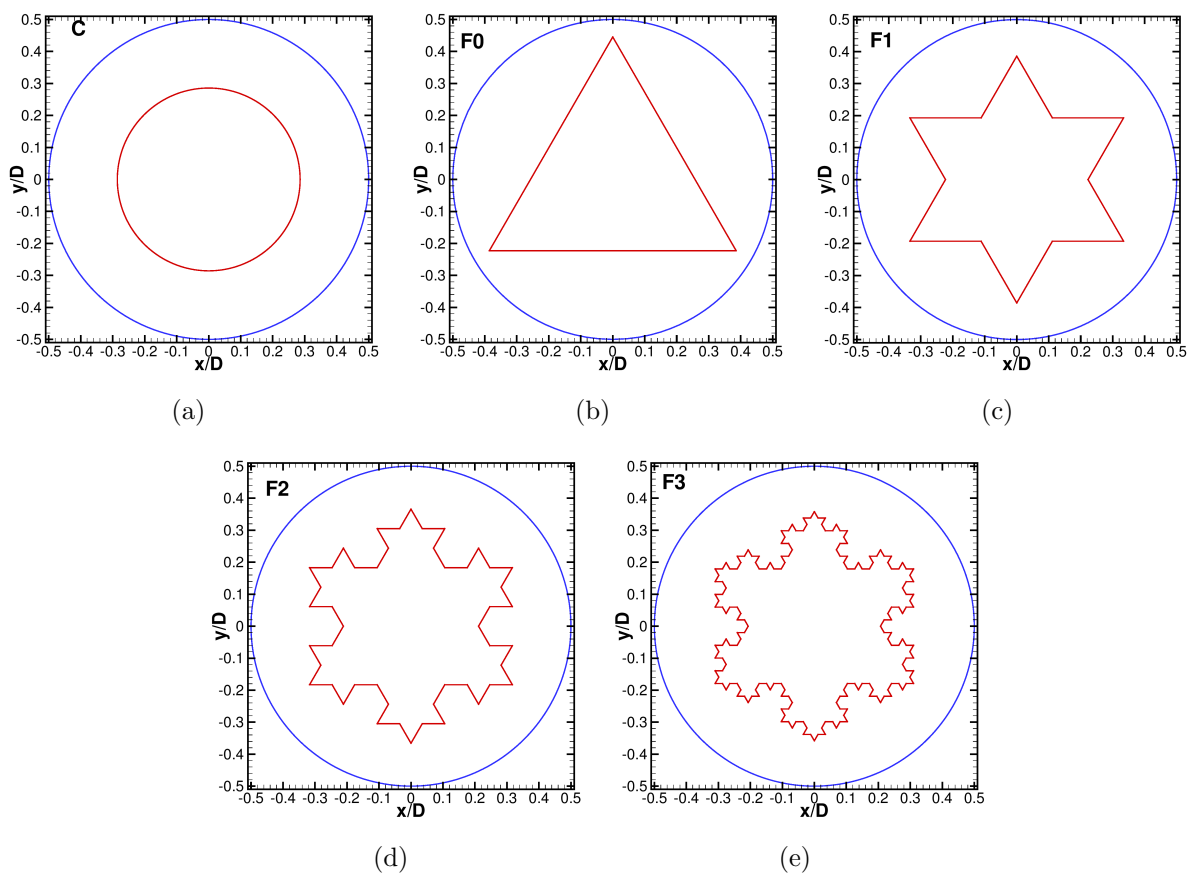
Figure 6.8: Geometry of the fractal orifices for (a) C, (b) F0, (c) F1, (d) F2 and (e) F3.

ing, as the sub-grid scale models highly rely on the grid resolution. An accepted criterion of the mesh convergence for LES is that the differences of the first order statistics with different mesh resolutions are within a tolerance level. In order to study the mesh convergence in LES, Celik *et al.* [2005] recommended at least three sets of meshes with refinements based on the Richardson extrapolation.

To assess the mesh convergence, three sets of meshes (coarse, medium and fine) were simulated with SA-ILES for each fractal orifice pipe flow. Figure 6.9 shows the fine mesh in the main cross section for all five cases. The coarse and medium meshes are not shown here, as their topologies are similar to the corresponding fine mesh. Table 6.2 summarizes the mesh resolutions of these three sets of mesh. The mesh refinements were carried out mainly on the stretching factors in the cross section besides a slight increase in the cell number along the segments of the fractal perimeter. In all these five orifice pipes, the mesh topologies of the main cross sections are maintained and extruded in the streamwise direction with a stretching factor of 1.08 in the region near the orifice plate ($z \in [-1D, 4D]$) and with a stretching factor of 1.18 towards the two ends of the pipe. The grids in the main cross section are structured near the pipe-wall and unstructured in the core region of the pipe.

The profiles of time-averaged streamwise velocity along the centreline of the pipe are compared to perform the mesh study. The velocity profiles are shown in Figure 6.10. For the circular orifice C, differences of the velocity with different meshes mainly locate at $z/D \geq 2$. For the triangular shape F0 and the fractal orifice F2, the differences are very small, less than 5%. For the fractal orifices F1 and F3, with finer mesh, the predicted centreline velocity decreases, closer to the experimental measurements (Measured data will be shown in the next subsection.), and the differences are below 15%. Following the mesh study criteria for LES (Klein [2005]), the three sets of simulations achieve an acceptable mesh convergence. All simulation results shown below are given by SA-ILES with the fine mesh unless otherwise noted.

Table 6.2: Summary of mesh resolutions

Case	$L_{\text{cell}}{}^{a}$	$N_{\text{cell}}{}^{b}$	$r_1{}^{+c}$	$\Delta r_{\max}^{+}{}^{d}$	$\Delta C_{\max}^{+}{}^{e}$	Δz^{+f} in $z \in [-1D, 4D]$
C: Coarse	120	1 767 900	$0.4 - 1.5$	56	70	$10 - 62$
C: Medium	140	2 677 366	$0.2 - 1.2$	48	62	$10 - 56$
C: Fine	160	4 521 316	$0.1 - 1.0$	37	54	$8 - 48$
F0: Coarse	60	2 671 110	$0.2 - 2.0$	40	104	$14 - 105$
F0: Medium	60	3 212 046	$0.2 - 1.7$	38	96	$12 - 95$
F0: Fine	60	5 324 349	$0.1 - 1.1$	36	84	$9 - 80$
F1: Coarse	20	2 580 570	$0.2 - 2.4$	56	106	$16 - 110$
F1: Medium	24	3 744 820	$0.2 - 1.8$	53	90	$14 - 102$
F1: Fine	28	5 970 912	$0.1 - 1.6$	50	60	$10 - 70$
F2: Coarse	14	3 819 622	$0.4 - 2.5$	69	50	$12 - 72$
F2: Medium	14	5 219 542	$0.3 - 2.0$	62	48	$10 - 68$
F2: Fine	16	7 587 562	$0.1 - 1.6$	56	45	$8 - 63$
F3: Coarse	10	4 584 819	$0.2 - 1.7$	64	70	$15 - 74$
F3: Medium	10	7 255 689	$0.2 - 1.6$	60	50	$11 - 69$
F3: Fine	12	13 179 756	$0.2 - 1.2$	48	30	$5 - 60$

[a]The cell number on each segment of the perimeter.

[b]The total cell number.

[c]The non-dimensional maximum thickness of the first layer on the wall.

[d]The non-dimensional maximum grid spacing in the radial direction.

[e]The non-dimensional maximum grid spacing in the circumferential direction.

[f]The non-dimensional grid spacing in the axial direction.

(a)

(b)

(c)

(d)
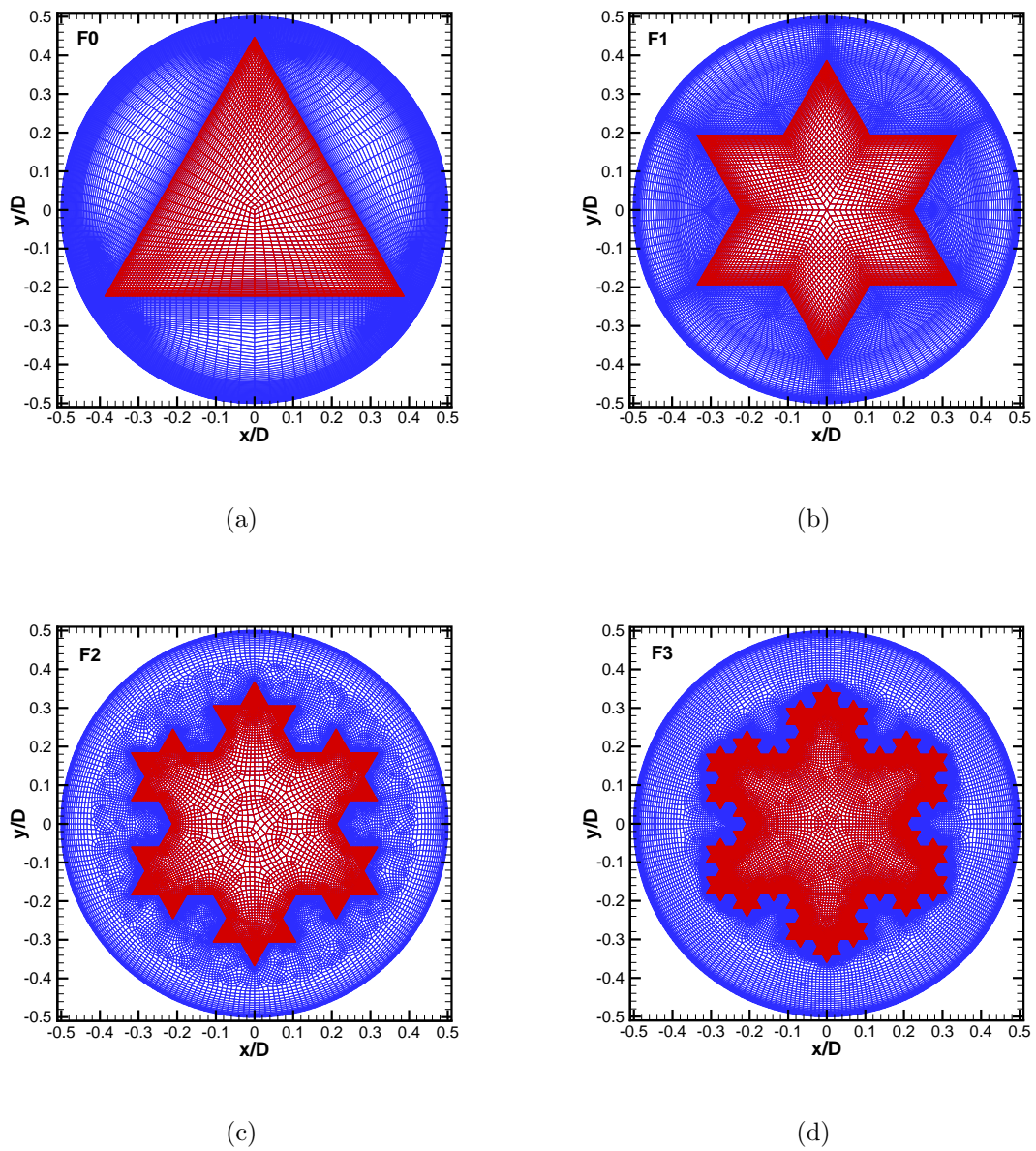
Figure 6.9: Mesh in the main cross section for (a) F0, (b) F1, (c) F2 and (d) F3
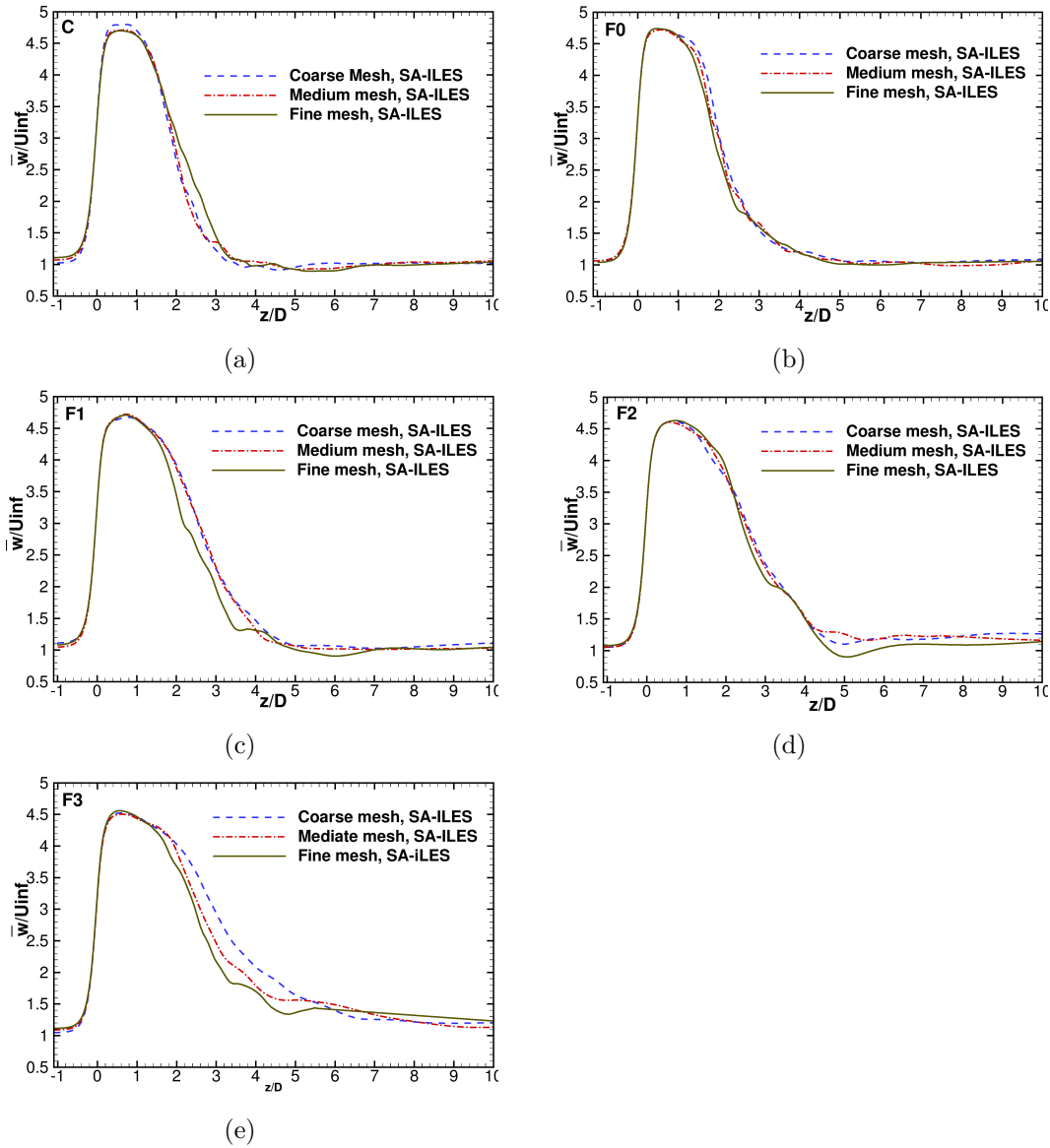
Figure 6.10: Time average streamwise velocity at the centreline for (a) C, (b) F0, (c) F1, (d) F2 and (e) F3. Blue $---$ for the coarse mesh, Red $-\cdot-\cdot-$, for the medium mesh and brown solid line for the fine mesh.

6.3.3 Instantaneous flow visualisations

Two vortex identification criteria (the λ_2 criterion and the z-vorticity) are used to visualise the turbulent flows generated by the fractal orifices. Details on the vortex identification criteria were given by Jeong and Hussain [1995].

The streamwise component of the vorticity vector, z-vorticity (Ω_z), plays a dominating role in dynamics of coherent structures during vortex generation through orifices (Zaman [1996]). The streamwise vorticity at the orifice location $z/D = 0$ is presented in Figure 6.11. The red and blue colours represent the two opposite rotating directions of vortex elements. It is observed that at the orifice location $z/D = 0$, the z-vorticity reflects a distinct pattern of the fractal orifice geometry, and these fractal orifices display some common patterns in rotation directions of vortices. In order to clearly study the streamwise coherent structures forced by these fractal geometries, Figure 6.12 demonstrates the rotation directions of the streamwise vortices just downstream of the orifice. It is observed that the fractal orifices F0, F1, F2 and F3 generate counter-rotating vortex pairs around the sharp corner of the flow-through area in the cross section. Figure 6.13 displays the streamwise velocity contours at $z = 0$, and it can be seen that the sharp corners have higher velocity than both the inside high-velocity region and the outside region. Therefore, these counter-rotating vortices around the sharp corners transfer the high momentum inside of the sharp corner towards the low-momentum region out of the flow-through area. As a result, at downstream, the high velocity at the sharp corner will shrink, and the velocity in the outer surroundings of the sharp corner will increase. The velocity contours in Figure 6.18 of the next section confirmed this conclusion. Another interesting point is that for the circular orifice and the triangular orifice, even at $z = 0$ just downstream of the orifice, the vortices are not continuous along the segments of the orifice perimeter. Actually, there are several counter-rotating vortex pairs with different directions along the segments of these two orifices. For the other fractal orifices, the counter-rotating vortex pairs are generated by two adjacent segments which consist of the flow area in the sharp corners, and along the orifice segments, no vortex pairs are observed, and there is only a single piece of vortices with a fixed rotation angle. The differences between the vortices generated by different fractal levels may be related to the instability of the generated vortices with different sizes. It can also be explained from the point view of the rotation directions of vortices. The rotation direction of vortices generated by orifices is related with the velocity differences, and usually the flow with a high velocity prefers to rotate towards the area with low velocity in its surroundings (Zaman [1996]). It is observed from Figure 6.13 that the velocity along the edge at the high level fractal orifices has little differences, while the circular and the triangular orifices with longer segments have
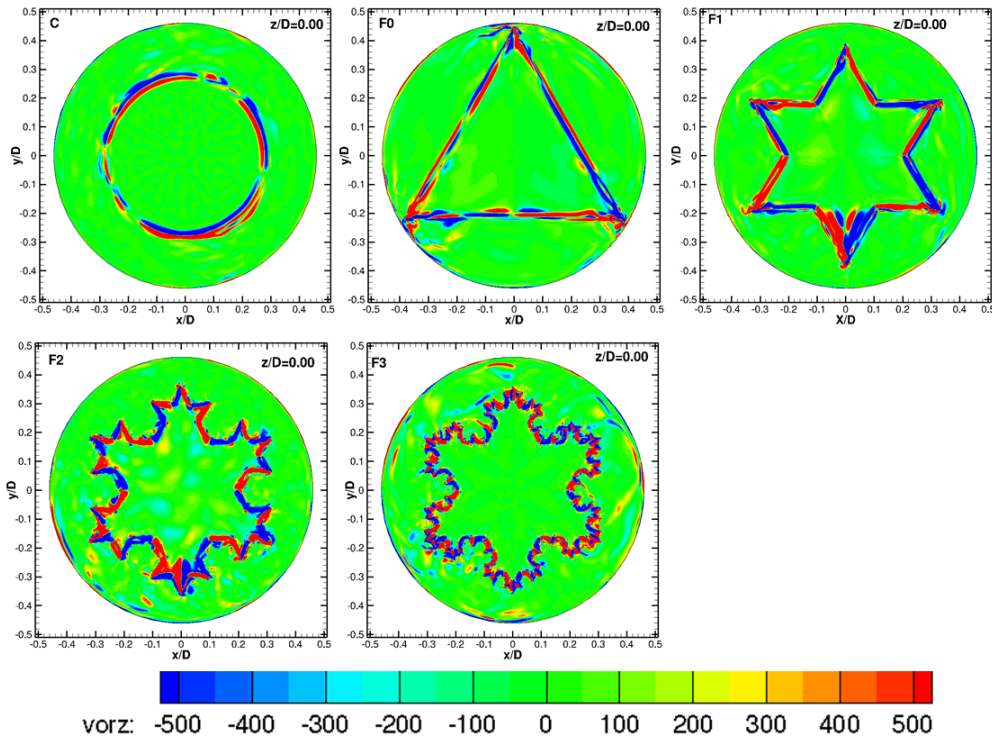
Figure 6.11: Contours of the instantaneous streamwise vorticity Ω_z at $z/D = 0$. From left to right: C, F0, F1, F2 and F3.

larger velocity difference along the segments. Therefore, for the high level fractal orifices, the streamwise vortices along one segment usually rotates in one direction from the high velocity flow to the outer region of the flow area. However, for the circular and the triangular orifices, the vortices moves faster near the corner than near the middle of the segments, and the different moving velocity forces the vortices breaking into several pairs. Overall, smaller segments in the high fractal level introduce smaller vortices with counter-rotating between two adjacent segments, which are very regular and organized near the orifice plate. Although the circular and triangular orifices introduce larger vortices, the large velocity differences force these vortices broken down to form several counter-rotating vortex pairs with different rotation directions along the segments. Therefore, the decay of these vortices in different fractal levels may be much more complicated rather than a linear relation with the size of initial sizes of the forced vortices.

Figure 6.14 shows the contours of the streamwise vorticity Ω_z at cross sections away from the orifice plate. At $z/D = 0.50$, the large vortices generated in the circular and triangular orifices have broken into smaller vortices compared with the location of $z = 0$, but these broken vortices in the circular orifice C and the triangular orifice still seem to be larger than those in the other fractals. For these two orifices, from $z/D = 0.25$ to $z/D = 0.75$, the
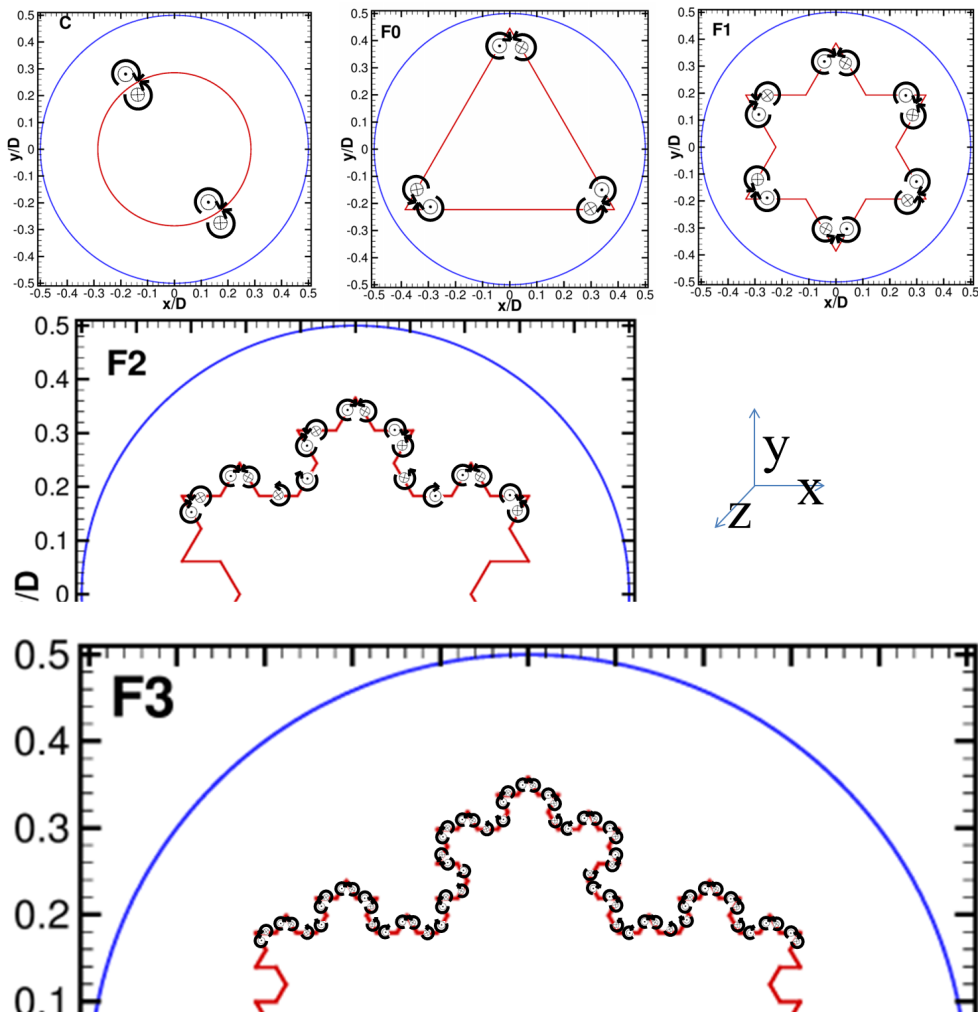
Figure 6.12: The rotation directions of the streamwise vortices just downstream of the orifice plate (about $z/D = 0$)
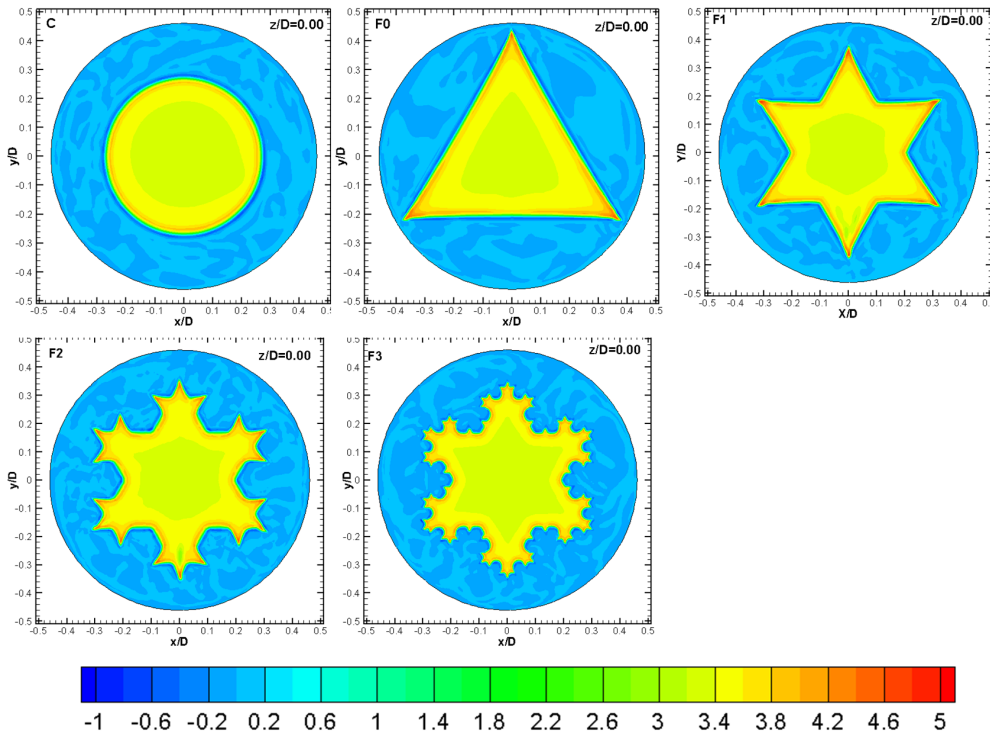
Figure 6.13: Contours of the instantaneous streamwise velocity w/U_∞ at $z/D = 0$. From left to right: C, F0, F1, F2 and F3.

generated large vortices become smaller and smaller through the process of the breaking-down. On the contrary, the fractal orifices F1, F2 and F3, which have shorter segments in their geometries, generate vortices of smaller sizes. From $z/D = 0.25$ to $z/D = 1.0$, these small vortices interact with each other and merge together to form larger vortex structures. At $z/D = 0.5$, an interesting observation is that the vortices gathers in the corner of two adjacent segments with the obtuse angle, rather than the sharp corner as in $z = 0$. Actually, this change may correspond to the phenomenon of the axis-switching, which will be discussed in details later. In regions from $z/D = 0.25$ to $z/D = 1$, a common feature for all these fractal orifices is a "ring-shaped" region of z-vorticity which develops around the orifice perimeter and most of which remains concentrated in this annular region. The z-vorticity then spreads preferentially towards the pipe-wall and it remains small at the pipe-centre. In addition, the spreading trend seems that the higher the fractal orifice level, the slower the z-vorticity transfers to the pipe's central core. This phenomenon can be explained from the vortex rotation in Figure 6.12. For all these fractal orifices, the generated streamwise vortices near the orifice plate have primary trends to rotate from inside to outside of the core region, and the interaction between these vortices is mainly in the outside merging process. Therefore, as Figure 6.14 shown, the vortex dynamics are much stronger outside of

the annular region than the pipe's central core. From $z/D = 1$ to further downstream, the small broken-down vortices in the circular orifice C and triangular orifice F0 begin to merge and extend to cover the whole cross section of the pipe, while for the fractal orifices F1, F2 and F3, it seems to take longer distance for the z-vorticity to cover the central region of pipe and gradually to become uniform. This is understandable, as the more counter-rotating vortex pairs with different rotation directions in the circular and triangular orifices introduce enhanced momentum transfer.

Figure 6.15 shows the iso-surfaces of λ_2. For the sake of clarity, only a half cylinder $(x/D < 0)$ is shown. It is observed that the characteristic sizes of the forced turbulence structures near the orifice plates are similar to the lengths of the segments of the fractal perimeters. Actually, the shorter the segments of the fractal perimeter in a higher fractal level, the smaller the forced turbulence structures. However, further downstream of the orifice plates, the differences in the turbulent length scales are less pronounced between the different fractal levels due to turbulent mixing and breaking-down. Flow evolutions for the fractal orifices, shown in Figure 6.15, can be described as follows. First, downstream near the orifice plate, turbulence structures, with similar sizes of the fractal geometric segments, are compulsively generated for all these orifices. Then, the following developments of these forced structures in downstream flows become different for different fractal orifices. For the circular orifice C and the triangular orifice F0, these forced large structures shed from the forced shear layers. Clear intermittency effects are displayed for these two orifices. The shedding structures break down into smaller structures when they go downstream. For the fractal orifices F2 and F3, because the fractal-generated turbulence structures are originally much smaller, the vortex shedding from the forced shear layers is not as distinct as those for the circular and triangular orifices, and there is no observation of clear structures breakdown of these shedding vortices near the orifice plates. Instead, the most significant effect downstream is the mixing and merging of these forced small structures. Further downstream, these merged structures begin to break down and decay. The flow evolution for the fractal orifice F1 lies in-between above two situations. The vortex shedding for the fractal orifice F1 is recognizable, but the breakdown of these shedding structures is obscure. It seems that the turbulent breaking-down, mixing and merging of these forced turbulence structures play equivalent roles together for the orifice F1.

Conclusively, the smaller segments of the higher level fractal orifice generate smaller size of vortices near the orifice plate. Because of the smaller sharp-corner areas, the generated vortices by these smaller segments along the edge initially rotate with a fixed direction and the vortices from the adjacent segments forms a counter-rotating vortex pair, which
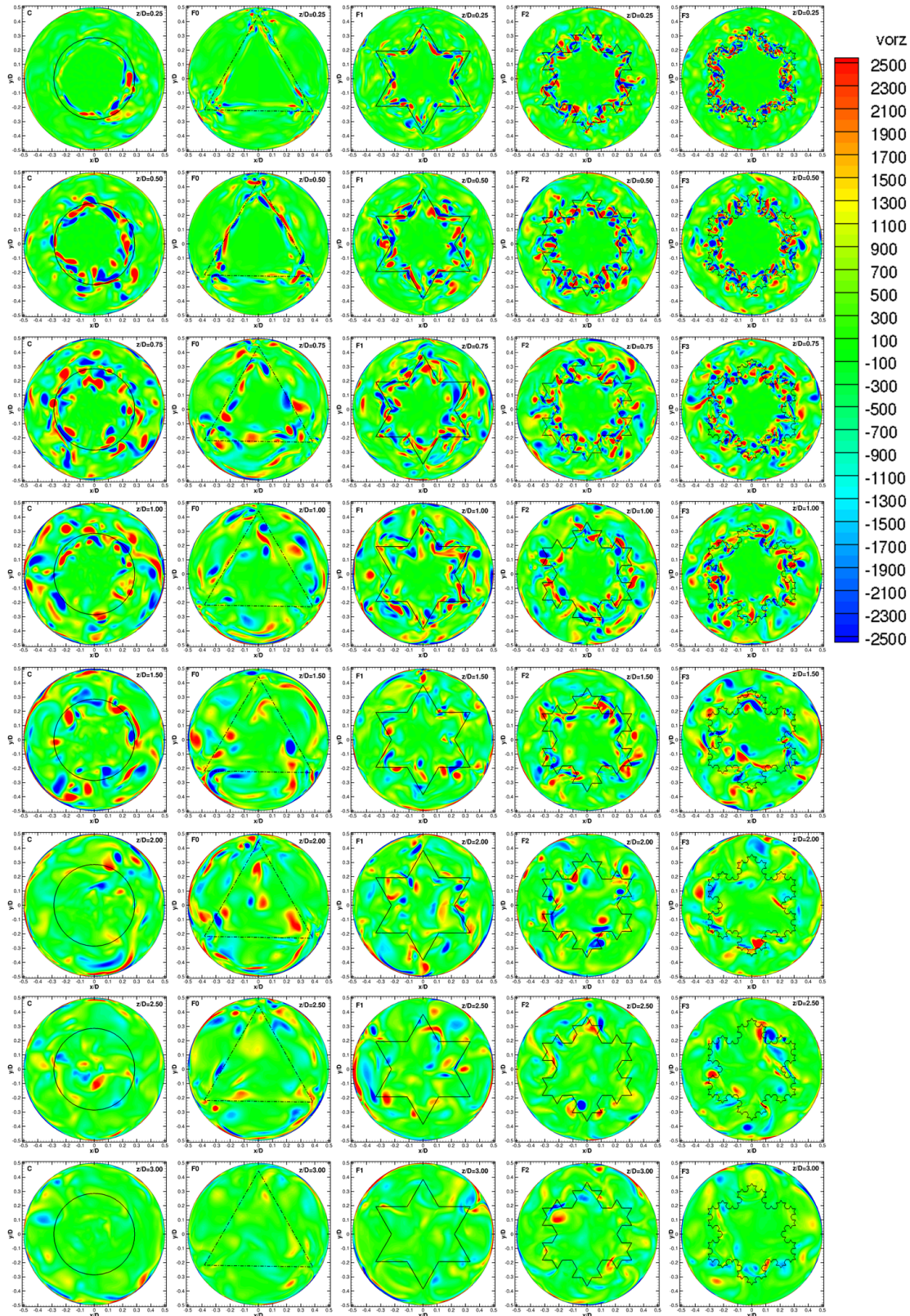
Figure 6.14: Contours of the instantaneous z-vorticity. From left to right: C, F0, F1, F2 and F3. From top to bottom $z/D = 0.25, 0.5, 0.75, 1, 1.5, 2, 2.5$, and 3.
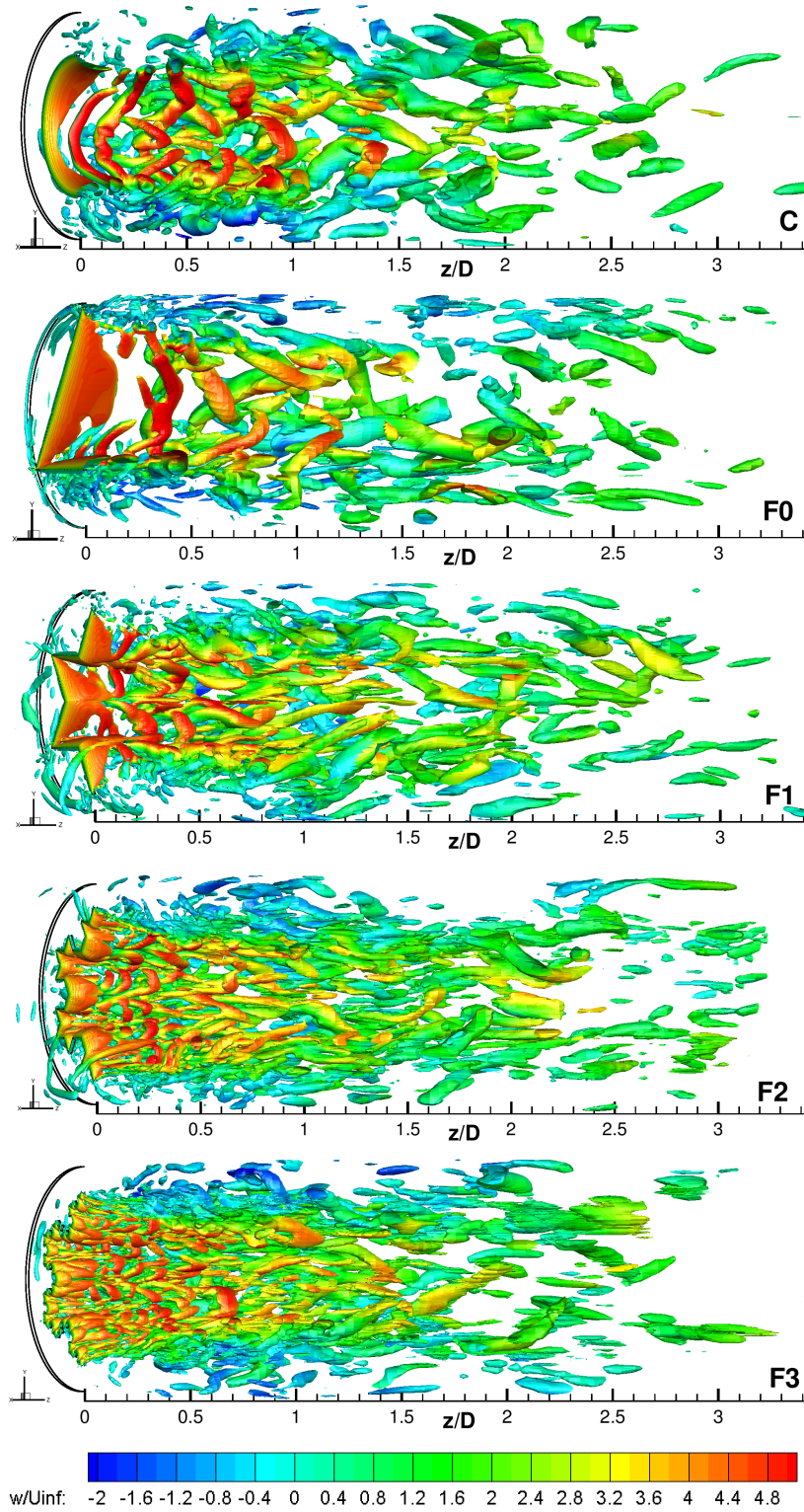
Figure 6.15: Isosurfaces of λ_2 equal to $-500\,000$ for the instantaneous flows (only the half part with $x < 0$ is shown), the colour coding corresponds to the steamwise velocity. From top to bottom: C, F0, F1, F2 and F3.

promotes the vortex mixing outside of the core region. The axis-switching can be observed in the fractal cases F1, F2 and F3. The longer segments in the circular orifice generate several large vortices, and even along one edge in F0, there are several counter-rotating vortices, which enhance the mixing of vortex structures. Overall, the smaller segments forces the generated vortices more organized, and the lack of strong interaction with flows in the pipe core makes these organized vortices last long distance before their decay.

6.3.4 Results and discussion of statistical results

In current flow configurations, the entrance length for a fully developed boundary layer as calculated by the empirical formulation $L_{\mathrm{e}} = 4.4Re^{1/6}$ would be $25.6D$. Therefore, the present entrance length before the orifice plate (which is the same for both the experiments and simulations) cannot provide a fully developed turbulent flow before the orifice. The turbulent boundary layer thickness at $z = -1D$ for the circular orifice can be empirically estimated as approximately $0.15D$. As a result of influences from the downstream flows, the boundary layer thicknesses vary with the different fractal geometries, however they all remain around $0.1D$ to $0.15D$ except for the triangular orifice F0. Considering the shortest distance from the pipe wall to the vertexes of the fractal orifices (L_{w} in Table 6.1), the flow downstream of the orifices is barely influenced by the boundary layer developed upstream before the orifice. This is less true for the triangular shape F0, which has a skewed flow area, making the downstream flows interact with the upstream boundary layer.

The main results that are presented and discussed in this section are as follows. (1) The simulation results are compared with the available experimental measurements. (2) The contours of the velocity and the turbulence kinetic energy are shown to provide further understanding of the flow evolutions for the different fractal orifices. (3) The energy spectra of the streamwise velocity are discussed.

6.3.4.1 Velocity

As a single hotwire was used to measure the velocity in the experiments, the measured velocity u_{m}, containing the streamwise velocity w and the vertical velocity v, reads

$$u_{\mathrm{m}} = \sqrt{w^2 + v^2}. \tag{6.2}$$

The fluctuation of the measured velocity u_{m} is defined as

$$u_{\mathrm{m}}^{'} = u_{\mathrm{m}} - \overline{u}_{\mathrm{m}}, \tag{6.3}$$

where $\overline{u}_\mathrm{m}$ is the time averaged velocity and the symbol $\overline{\cdot}$ stands for the time average.

Figure 6.16 shows the average velocity $\overline{u}_\mathrm{m}$ as a function of the radial r from the pipe centre to the pipe wall, compared with the measurements at six stations $z/D = 0.5$, 1, 1.5, 2, 2.5 and 3. The numerical results follow the same trends as the experimental data. The maximum difference between the experimental points and numerical results is less than 8% for all orifices. Generally speaking, the velocities predicted by the simulations agree reasonably well with the experimental results.

Figure 6.17 is presented to compare the fractal scaling effects on the velocity profiles at the centreline. To make a clearer comparison of the different fractal levels, the experimental data and the simulations are separated into two pictures. Although the simulations slightly over-predict the velocities at the centreline, (as shown in Figure 6.16), both the experiments (Figure 6.17(a)) and the simulations (Figure 6.17(b)) illustrate the same trends of flow evolutions and the scaling effects from different fractal levels, which are described as follows. (1) In the region near the orifice plate ($z/D < 1$), the orifice with a higher fractal level has a smaller velocity in the centreline. This is consistent with the pressure drop profiles, which show that higher fractal levels lead to a smaller pressure drop. (2) When the flows go further downstream, the centreline velocities begin to recover from the peak values at the vena contracta. The velocity for the higher level fractal orifice decreases more slowly, even with a smaller peak value. The triangular orifice F0 distinguishes itself from the other cases, having the smallest velocity after $z/D > 1.2$. (3) In spite of small differences between the velocities for the fractal orifices F1, F2 and F3, it can also be seen that in the region $z/D > 2$, the velocity of a higher fractal level is larger than that of a lower fractal level. This phenomenon, shown in both the experiments and the simulations, is interesting and different from the classic orifice pipes in which a smaller vena contracta velocity usually goes with a faster flow recovery. In general, the fractal orifice with a higher level has a smaller vena contracta velocity but a slower recovery in the streamwise direction and a slightly longer recovery length. The same recovery trends were also present in the pressure drop profiles shown in Figure 6.20.

In order to investigate the velocity evolutions in the cross section, the contours of the time averaged streamwise velocity ($\overline{w}/U_\infty$) at $z/D = 0, 0.25, 0.5, 0.75, 1, 1.5$ and 2 are presented in Figure 6.18. At $z/D = 0$, just downstream of the orifice plate, sharp images of the orifice geometries are imprinted on the velocity contours. Furthermore, the velocity in the flow area of the orifice is nonuniform but higher near the sharp corners and smaller near the central region. At $z/D = 0.25$, the geometric patterns imprinted on the velocity contours begin to shrink and become blurred. They can still be observed from the velocity contours for C, F0
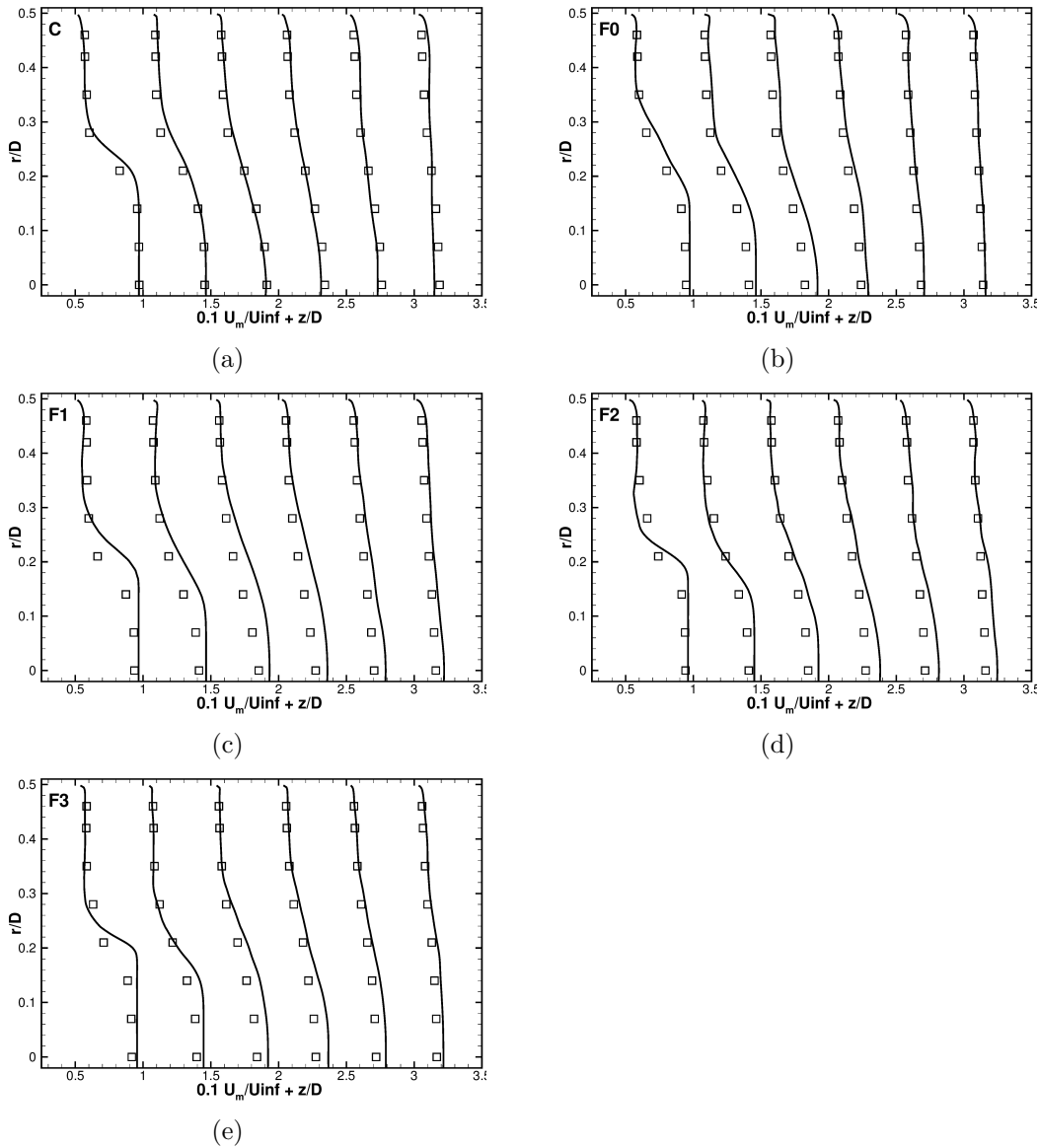
Figure 6.16: Time and space averaged velocity $\overline{u}_{\mathrm{m}}/U_\infty$ at different stations: $z/D = 0.5$, 1, 1.5, 2, 2.5 and 3 for (a) C, (b) F0, (c) F1, (d) F2 and (e) F3. $\square$, experimental data; —, simulated results. For the sake of clarity, scaling multipliers and translations have been implemented to separate the profiles in a given figure.
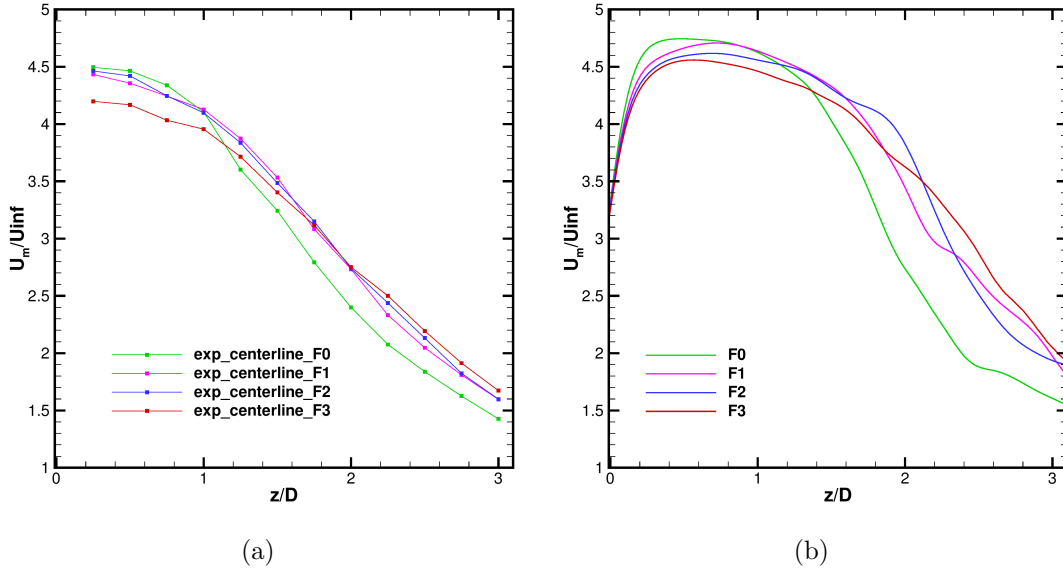
Figure 6.17: Fractal scaling effect on the centreline velocity $\overline{u}_{\mathrm{m}}/U_{\infty}$. (a) Experiment data (b) Simulation results

and F1, while the smallest geometric length scales cannot be recognized for the higher level orifices F2 and F3. In fact, axis-switching is observed at $z/D = 0.25$ for the orifice F2 and F3. (Details of axis-switching will be given later.) At $z/D = 0.5$, the triangular orifice F0 still shows the initial geometry pattern in the velocity contours, although it begins to lose its sharp details. For the fractal orifice F1, F2 and F3, the regions of high velocities shrink at the concave corners of the original fractal orifice, while at the convex corners the high velocity region erupts towards the periphery. (It is worthy to be noted that the terms "concave" and "convex" refer to the solid orifice plate rather than the flow area of the orifice.) As a result, a "zigzag" circle of the high velocity forms as a transient status between the fractal pattern at $z/D = 0.25$ and the pattern of a regular hexagon at $z/D = 0.75$. At $z/D = 0.75$, the fractal orifices F1, F2 and F3 shows very similar geometric patterns of velocity contours, exhibiting the shape of a regular hexagon. In order words, there is "rotation" of an angle of $\pi/3$ in the velocity contours from at $z/D = 0.25$ to the section at $z/D = 0.75$, regardless of the disappearance of the smallest scales. At $z/D = 1$, the geometric pattern of the velocity contour for F0 "rotate" by an angle π to an inverted triangle. Further downstream, the velocity contours of the triangular orifice F0 still keeps the shape of an inverted triangle. However, another weak "rotation" of the angle of $\pi/3$ seems to happen for the orifices F1, F2 and F3 from $z/D = 0.75$ to $z/D = 1.5$. It is so-called secondary switch-over in the literatures on axis-switching (Zaman [1996]). The secondary switch-over is much faint, and not easy

to detectable and recognized. Even more switch-over may occur for some particular cases, but mechanisms for the number of switch-over in axis-switching are still under investigation. Further downstream after $z/D = 1.5$, all the orifices show similar shapes of the high velocity like an irregular circle. These irregularities of the quasi-circles may come from further switch-overs. The experiments in Zaman [1996] also show similar irregularity even with long time average.

Figure 6.19 displays the time average iso-contours of the streamwise velocity $\overline{w}/U_\infty$. What differentiates the triangular orifice F0 from the other cases is its small value of L_w shown in Table 6.1, which introduces a stronger impact from the pipe wall. The wall effect results in a flow oscillation about the pipe axis in a gyroscopic fashion (Xu and Mi [2010]). Figure 6.19 shows results as follows. (1) The higher level fractal orifice has a smaller velocity downstream of the orifice plate in the range of $0 < z/D < 1D$. As mentioned before, the higher level fractal orifice has a longer perimeter with high velocity, thus the central velocity is smaller due to the same flow area (almost the flow volume rate). (2) The higher level fractal has a longer and slightly thinner region of high velocities (or a recovery region). These phenomena may come from the different roles that the segment L_s of the perimeter and the inscribed circle diameter ϕ play in the evolutions of the orifice flows. A longer perimeter with more and smaller fractal segments breaks down the mixing layer near the orifice plate, enhances the flow mixing and then reduces the velocity in the vicinity of the vena contracta. The smaller inscribed circle diameter ϕ for the higher fractal level may contribute to the longer and thinner high velocity region further downstream. Figure 6.14 shows that the generated small structures by the higher level fractal orifices develop mostly in a "ring-shape" and these forced coherent structures last longer in the streamwise direction. This may also explain why the higher level fractal orifice has a longer recovery length of both the velocity and the pressure. The study on the mean velocity contours corroborates the conclusions drawn for flows forced through fractal grids by Laizet and Vassilicos [2011] that the smaller geometric scales (e.g. the segments of the fractal perimeter) of the fractal object play an important role close to the plate, while the larger geometric scales (e.g. the inscribed circle diameter of the fractal orifice) influence the flow further downstream.

6.3.4.2 Pressure drop

The pressure drop is a key factor in designing pressure differential flowmeters. Three pressure drop parameters are defined here. A normalized pressure drop p^* is defined as

$$p^* = \frac{p - p_\mathrm{in}}{\frac{1}{2}\rho U_\infty^2}, \tag{6.4}$$
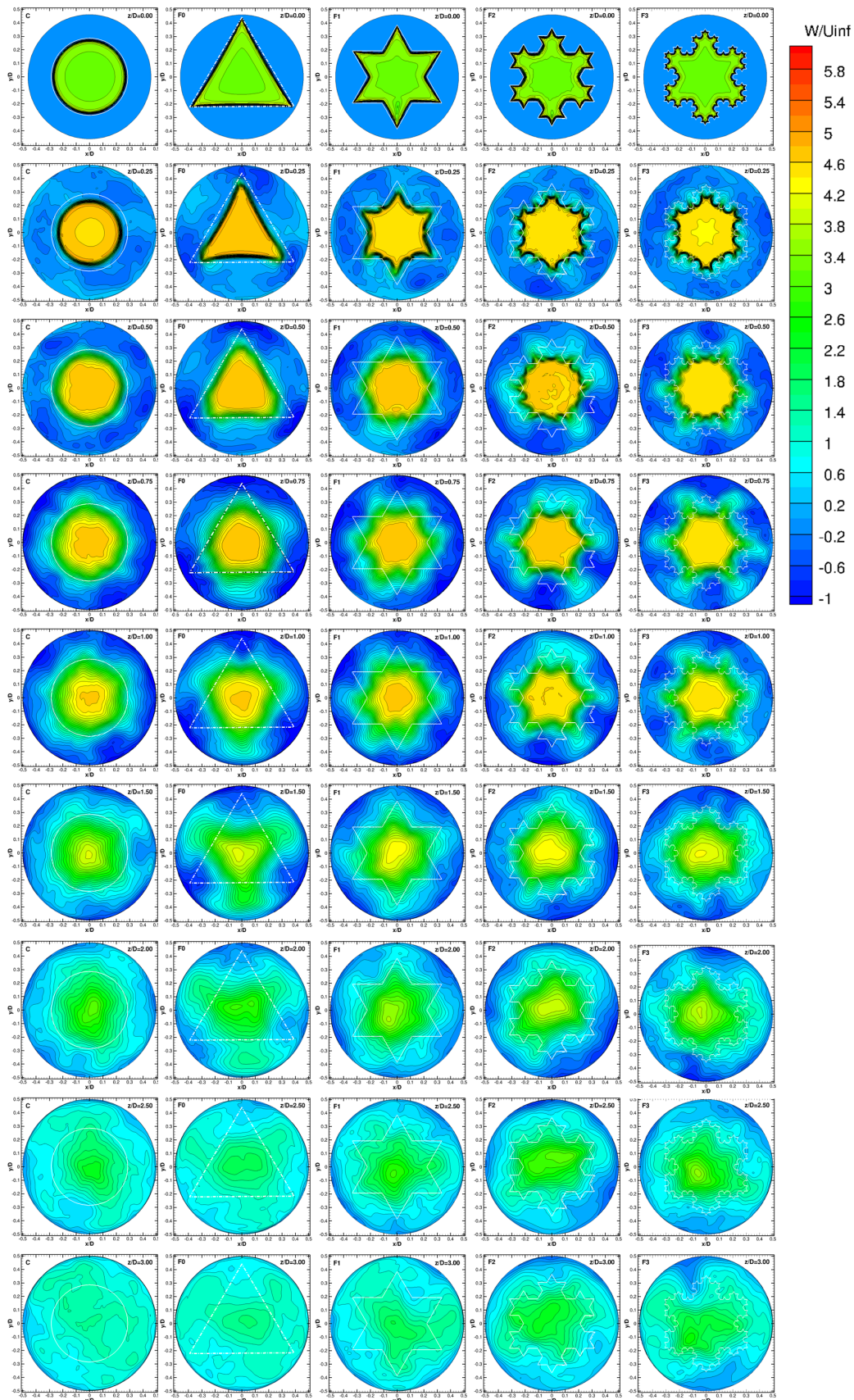
Figure 6.18: Contours of time-averaged normalized streamwise velocity $\overline{w}/U_\infty$ for (a) C, (b) F0, (c) F1, (d) F2 and (e) F3. From top to bottom $z/D = 0$, 0.25, 0.5, 0.75, 1, 1.5, 2, 2.5, and 3.
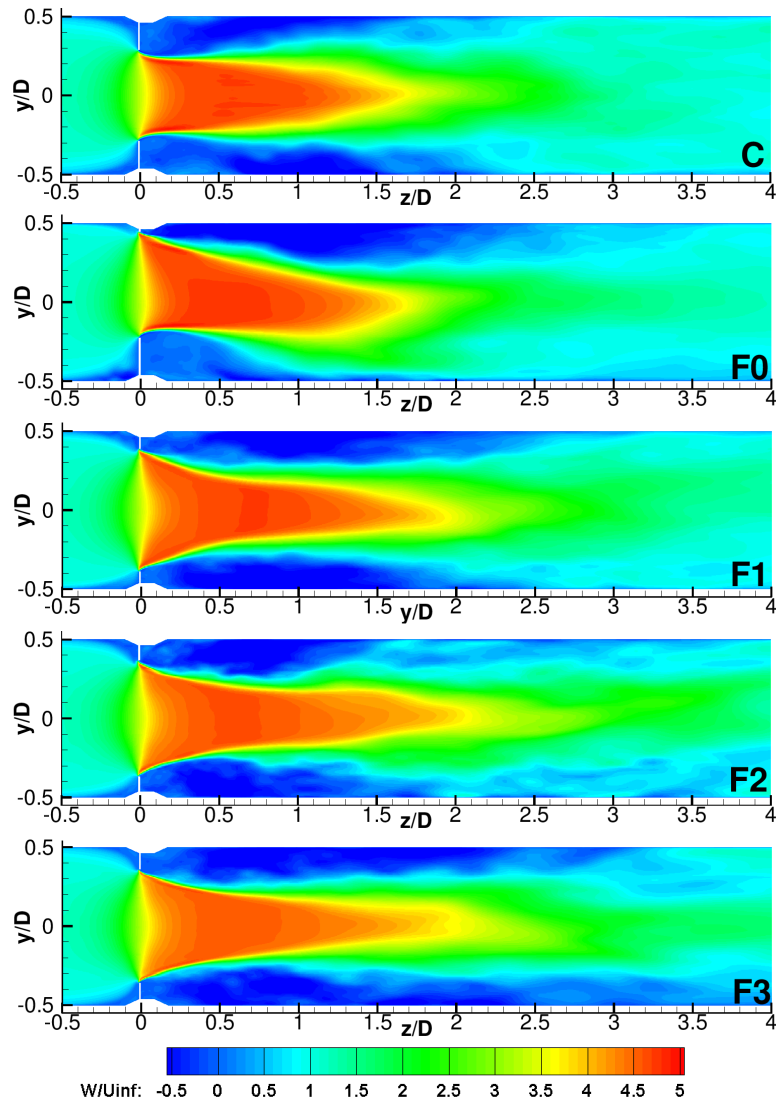
Figure 6.19: Iso-contours of the time averaged streamwise velocity $\overline{w}/U_\infty$ in the z-y plane. From top to bottom: C, F0, F1, F2 and F3.

6.3. Flow through fractal orifices

Table 6.3: The unrecoverable pressure loss and the pressure recovery rate

Cases	C	F0	F1	F2	F3
Δp^*	12.33	12.14	11.89	11.68	11.51
r_{p}	0.651	0.650	0.652	0.654	0.661

where p is the pressure at the probed station and p_{in} is the inlet pressure. The unrecoverable pressure loss Δp^* is defined as the difference between the inlet pressure drop and the pressure drop after the flow recovery, expressed as

$$\Delta p^* = p_{\mathrm{in}}^* - p_{\mathrm{rec}}^*, \tag{6.5}$$

where p_{in}^* is the pressure drop at the inlet, usually zero, and p_{rec}^* is the recovered p^*, which has reached an asymptotic value towards the end of the pipe (if neglecting the pressure drop introduced by the skin friction). The pressure recovery rate r_p, defined as the ratio of the unrecoverable pressure drop to the maximum pressure drop, reads

$$r_p = \frac{p_{\mathrm{in}}^* - p_{\mathrm{rec}}^*}{p_{\mathrm{in}}^* - p_{\mathrm{min}}^*}, \tag{6.6}$$

where p_{min}^* is the minimum value of p^* in the pressure valley after the orifices.

The normalized pressure drop along the pipe wall in the streamwise direction is shown in Figure 6.20. Figure 6.20(b) is an enlarged view of the recovery region. In the upstream region where z is less than $-1D$, p^* is quite similar for all levels of the fractal geometries and it decreases slightly owing to the skin friction. Just before the orifice plate ($-1D < z < 0$), p^* has a small peak for all fractal levels. This phenomenon, also reported by Morrison *et al.* [1993], usually goes with the increasing velocity when the flow squeezes through the orifice. For all orifices, the lowest pressure values are reached within one diameter downstream from the orifice plate. Meanwhile, the higher the fractal level, the closer the streamwise location of the minimum p^* to the orifice plates, and as the fractal level increases, the absolute value of the minimum p^* becomes smaller and smaller. In fact, the absolute value of the minimum p^* is highly relevant to the vena contracta. The fractal with a higher level has a longer circumference with high velocity, therefore, with the same flow area, the central of the orifice exit seems to have smaller velocity than the lower fractal level (Next section will show the velocity comparison to discuss it). Thus, the absolute value of the minimum p^* in higher fractal level is smaller.

The unrecoverable pressure losses Δp^* in Table 6.3 were calculated from Figure 6.20. The circular orifice C has the largest value of Δp^*, which means all the fractal orifices have

(a)

(b)
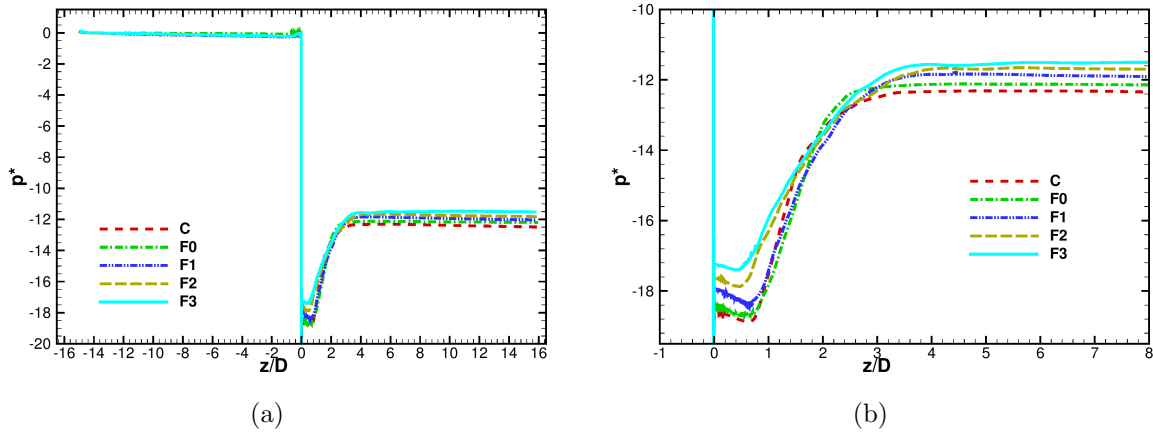
Figure 6.20: Evolution of the normalized pressure drop p^* at the pipe wall distributed in the streamwise direction: (a) the pressure drop along the whole pipe wall, (b) enlarged view of the pressure drop in the recovery region

less unrecoverable pressure drop than the classic circular orifice. This is consistent with the experiments and other studies on non-circular orifices. In addition, the simulations show a clear trend that the higher the fractal level, the smaller the unrecoverable pressure loss, though the difference between the largest and the smallest pressure loss is less than 7%. In experiments, the measurements were carried out only over a length of three diameters downstream of the orifice plate. Both the small differences of pressure drops between orifices and a short measured distance may explain why the experiments did not capture a clear trend of the pressure drop in the different fractal levels.

The pressure recovery rate $r_{\rm p}$ represents the pressure capability to recover from the lowest values. Table 6.3 shows that the higher level fractal orifice has a higher pressure recovery rate, but the difference of the pressure recovery rates $r_{\rm p}$ (approximately 1.6%) is much smaller than the difference of pressure drops (approximately 7%) between these orifices. In spite of higher pressure drops and smaller recovery rates, the recovery lengths for the circular C and the triangular shape F0 are shorter than those for the fractal orifices F1, F2 and F3. Furthermore, the recovery length becomes slightly longer for the orifice with a higher fractal level. Actually, the longer recovery length in the higher fractal level is due to the weaker interaction between the generated vortices with the central high velocity flow, as shown in Figure 6.14. In general, the fractal orifice with a higher level has a smaller unrecoverable pressure drop, a higher pressure recovery rate and a longer recovery length.
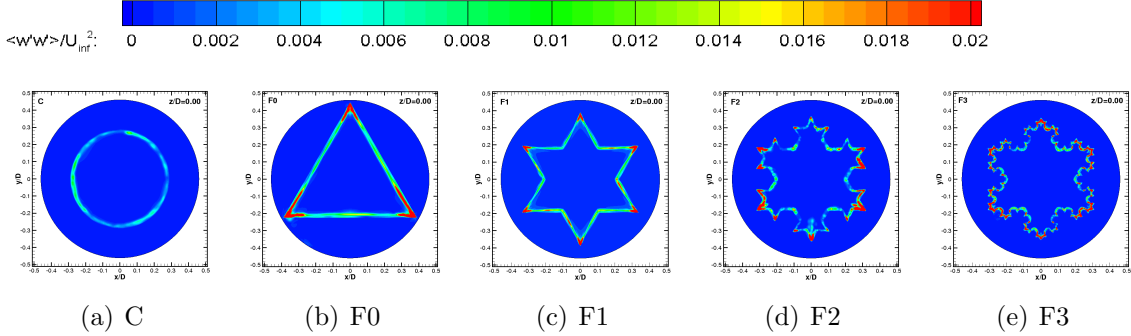
(a) C   (b) F0   (c) F1   (d) F2   (e) F3

Figure 6.21: Contours of the kinetic energy associated to the velocity fluctuation in the streamwise direction, $\overline{w'^2}/U_\infty^2$ at the section $z/D = 0$, for (a) C, (b) F0, (c) F1, (d) F2 and (e) F3.

6.3.4.3 Turbulence kinetic energy

Turbulence kinetic energy (TKE) is defined as

$$k = \frac{1}{2}(\overline{u'^2} + \overline{v'^2} + \overline{w'^2}), \tag{6.7}$$

where $u' = u - \overline{u}$, $v' = v - \overline{v}$ and $w' = w - \overline{w}$ are the fluctuations of the velocities. $\overline{w'^2}/U_\infty^2$ is the Reynolds normal stress in the streamwise direction or can be interpreted as the turbulence kinetic energy associated to the fluctuation of the streamwise velocity w.

Figure 6.21 shows $\overline{w'^2}/U_\infty^2$ at the section $z/D = 0$. The high values of $\overline{w'^2}/U_\infty^2$ forms the edges of the orifice geometries. The values near the sharp concave fractal corners are much higher than those at other locations, as is the case for the streamwise velocity in Figure 6.18. This means that sharp concave corners in the fractal orifices display a stronger blockage effect than the convex corners, inducing both a higher velocity and a higher turbulence kinetic energy in the streamwise direction.

The velocity variance $\overline{u_\mathrm{m}'^2}/U_\infty^2$ is compared with the experimental measurements in Figure 6.22. For the circular orifice C and the fractal orifices F2 and F3, the simulations are in good agreement with the statistics from the experiments. For the triangular orifice F0, under-predictions of $\overline{u_\mathrm{m}'^2}/U_\infty^2$ occur near the central core at $z/D = 0.5$ and 1.0, and over-predictions exists in the mixing layer at $z/D = 1.5$ and 2. The simulation results for the fractal orifice F1 generally agree reasonably well with the experiments, with the some discrepancies occurring in the central region at $z/D = 1$ and 1.5.

Figure 6.23 presents the TKE evolutions for different fractal orifices in the radial direction at different stations. At $z/D = 0.25$, the orifices C, F0 and F1 retain blurred patterns from the orifice geometries. The fractal orifice F2 and F3 follow the same trends of the
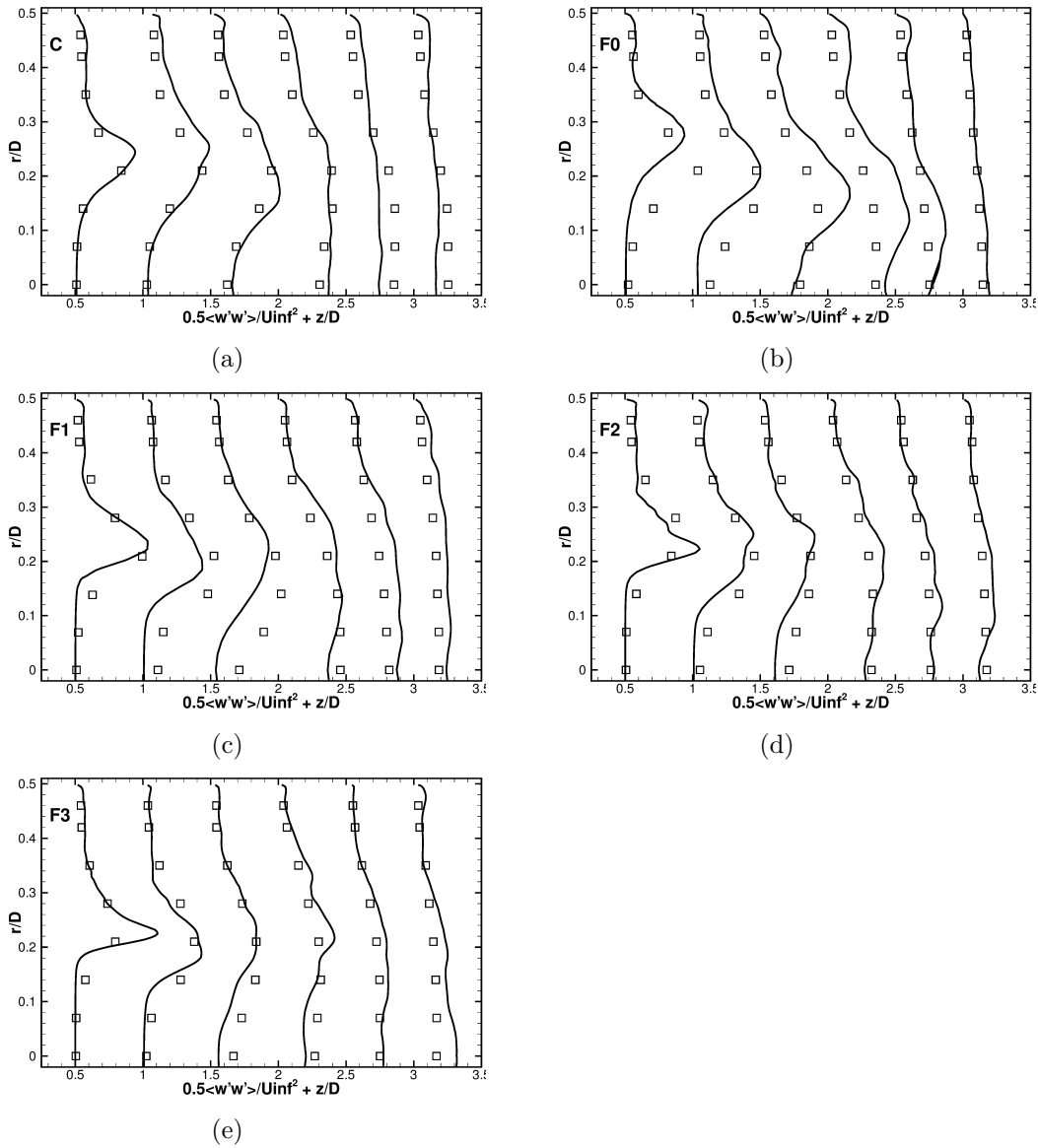
Figure 6.22: The turbulence kinetic energy, $\overline{u_\mathrm{m}'^2}/U_\infty^2$, related with the measured velocity fluctuations at five sections $z/D = 0.5$, 1, 1.5, 2, 2.5 and 3 for (a) C, (b) F0, (c) F1, (d) F2 and (e) F3. $\square$ experimental data; —, simulation results. Note that for the sake of comparison of the variations, scaling multipliers an translations are used at all stations.

velocity development in Figure 6.18: the high TKE region shrinks at the concave corners of the original fractal orifices and the convex corners have high TKE developing towards the periphery, to form a transient high TKE distribution in a "zig-zag" circle. At $z/D = 0.5$ and 0.75, the contours of the TKE for the fractal orifices F1, F2 and F3 have rotated by the angle $\pi/3$ from their initial geometries to form an hexagonal shape with high TKE near the edges. Apparently, the circular and triangular orifices have large TKE at these studied cross-sections near the orifice plates than the other orifices. As discussed in the spanwise vorticity, the long segments in the circular and triangular orifices generate several pairs of counter-rotating vortex pairs along each segment, which may enhance the vortex dynamics, and a high turbulence kinetic energy. On the contrary, for the high level fractal orifice with short segments, each segment usually generates vortices with the same rotation direction, and the counter-rotating vortex pair is generated by two adjacent segments at the sharp corners. Therefore, the vortex dynamics for these high fractal orifices are more regular, and have fewer fluctuations. Besides, the vortex pairs are all from the inside of the flow area to the outside, thus, the flow mixing mostly occurs outside of the pipe core. This is why a clear trend of the TKE diffusion is mostly towards the pipe-wall and little to the central core. From $z/D = 1$ to downstream, the high TKE transfers both centrifugally and centripetally, but obviously the higher fractal orifices have a weaker transfer towards the central region at the same streamwise distance. The axis-switching phenomenon can also be observed in the contours of the turbulence kinetic energy for the fractal orifices F0, F1, F2 and F3.

Figure 6.24 displays the evolution of the total turbulence kinetic energy (TKE), expressed in Eq. (6.7). The region of low turbulence kinetic energy forms a conical shape (shown as a triangle shape in the 2D view) downstream of the orifice plate. This is associated with the development of the turbulence structures. As shown in the instantaneous contours of z-vorticity (Figure 6.14), the forced structures mostly merge, mix and decay in the regions between the pipe wall and the original locations of the fractal orifices. Expansion of flow structures towards the central core is slower, and interactions of flow structures with the central core are weaker. Figure 6.24 shows that from the fractal orifice F0 to F3, the higher level fractal orifice has a slightly longer cone of the low TKE. This means the turbulence kinetic energy in the central region increases more slowly from the low values near the orifice plate for the higher fractal levels. This phenomenon can also be explained from the contours of the z-vorticity shown in Figure 6.14. The smaller forced turbulence structures in flows through the higher level fractal orifice are more organized and merge and mix outside of the flow area, then break down and decay in a longer distance from the orifice plate, while the breaking-down and turbulence decay occur in a shorter distance for larger forced turbulence
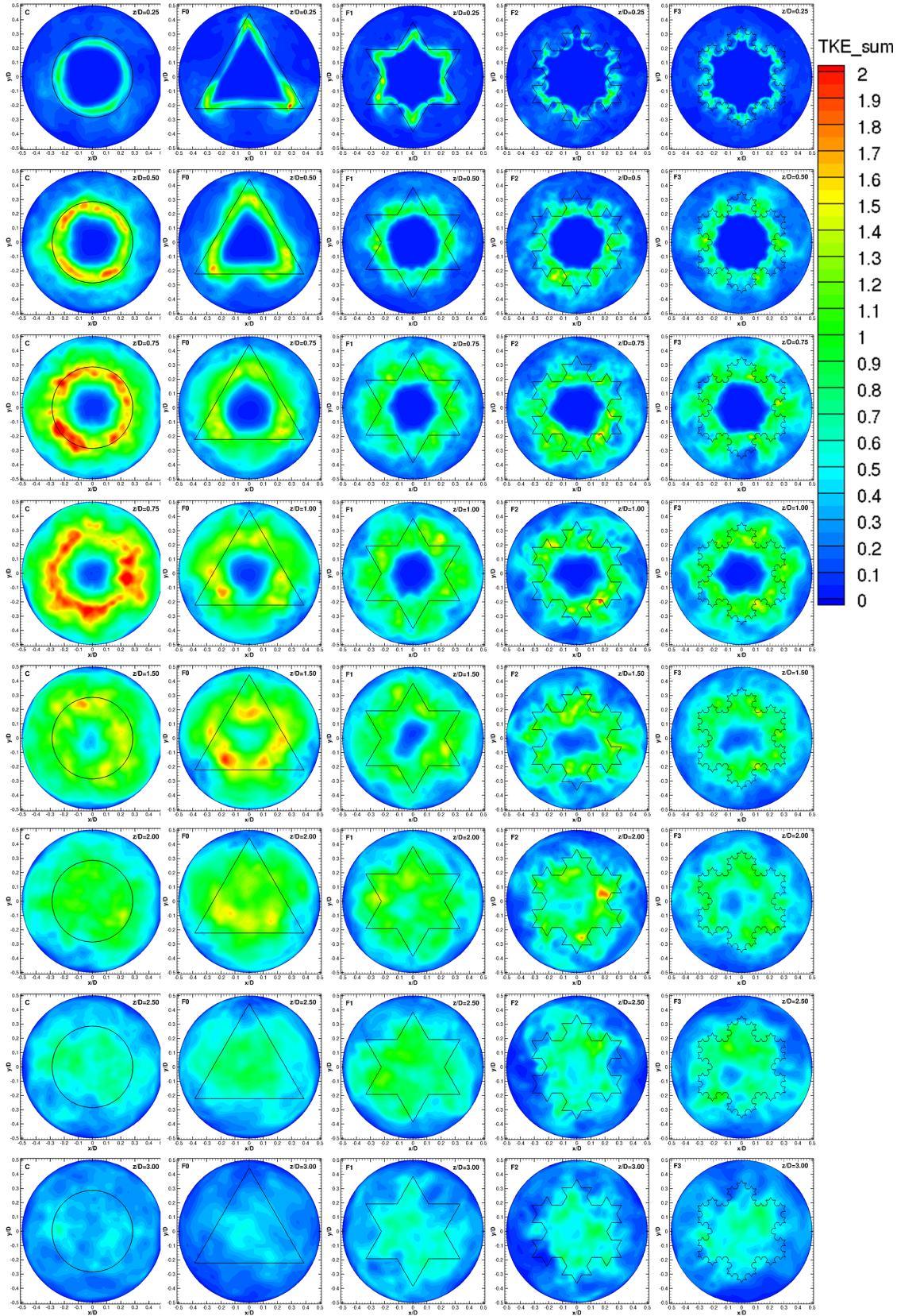
Figure 6.23: Contours of the turbulence kinetic energy for (a) C, (b) F0, (c) F1, (d) F2 and (e) F3 at fives sections $z/D = 0.25, 0.5, 0.75, 1, 1.5, 2, 2.5$ and 3 (from top to bottom).

structures in the lower fractal levels. Therefore, the turbulence kinetic energy for the high fractal levels increases progressively in a longer distance, and a longer low TKE region forms. The triangular orifice $F0$ has a bias distribution of the turbulence kinetic energy, the same bias direction as the velocity.

6.3.4.4 Axis-switching

Axis-switching is often observed in the investigation of non-circular jets, such as the rectangular or elliptic orifices. (Gutmark and Grinstein [1999]; Mi *et al.* [2010]). Axis-switching was described in Zaman [1996] as "a phenomenon in which the cross section of an asymmetric jet evolves in such a manner that, after a certain distance from the nozzle, the major and minor axes are interchanged." It is also clarified by Zaman [1996] that axis-switching is not because of a helical turning of the jet volume, instead, it is the flow-expansion in the direction of the minor axis and contracting in the direction of the major axis due to the vortices dynamics generated by the orifices. Above study on the fractal orifices F0, F1, F2 and F3 all displays axis-switching, which is clearly observed from the contours of the velocity and the turbulence kinetic energy.

The mechanism of axis-switching was discussed by Hussain and Husain [1989] from the point of view in the azimuthal vorticity in the flow through elliptic jets. From Figure 6.25, it can be briefly described as follows. Flow through the asymmetric jet becomes to roll up into vortex rings similar to the exit geometry. Due to the differences in the azimuthal curvature, the vortex rings near the ends of the major axis with high curvature have higher velocity than those near the ends of the minor axis. As a result, the vortice segments near the geometry with high curvature convect faster and curl up, which shrinks the major axis and expands the minor axis. Quinn [1992], Grinstein and DeVore [1996] and Zaman [1996] analysis the mechanism of the first axis switch-over from the point-view of the streamwise vorticity (The streamwise vorticity and the azimuthal vorticity are relevant and not two in-dependent vorticity.) Quinn [1992] studied the streamwise vorticity in flow through a rectangular jet, as shown in Figure 6.26. The adjacent segments of the rectangular orifice generate counter-rotating vortex pairs, which transfer the low-momentum inwards and spread the high momentum outwards. As a result, there is a rotation of the angle of $pi/2$ downstream.

The streamwise vorticity shown in the fractal orifices in this study has the same rotation directions near two adjacent segments as that in Quinn [1992]. From $z/D = 0.25$ to $z/D = 1$, the velocity contours for the triangular orifice F0 "rotate" from a regular triangle to an inverted triangle. The patterns of velocity contours for the triangular orifice F0 at $z/D =$
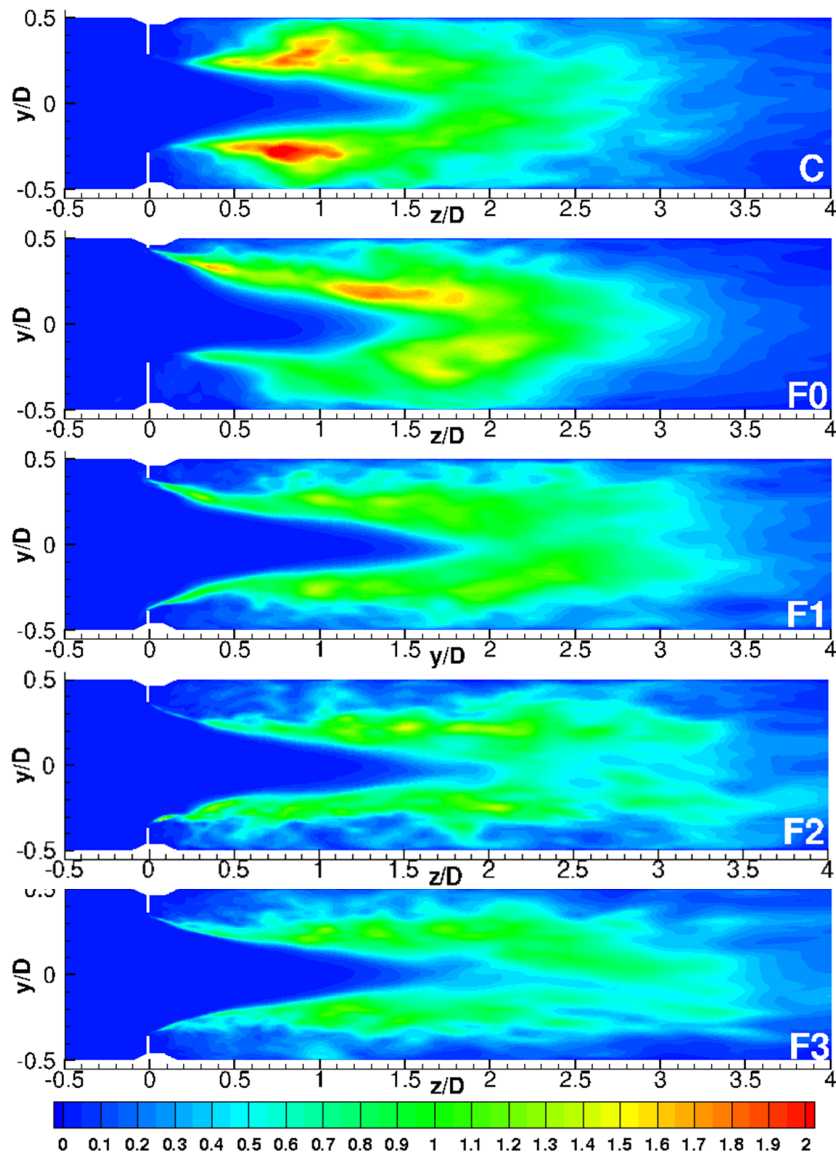
Figure 6.24: Contours of the turbulence kinetic energy in the z-y plane From top to bottom: C, F0, F1, F2 and F3.
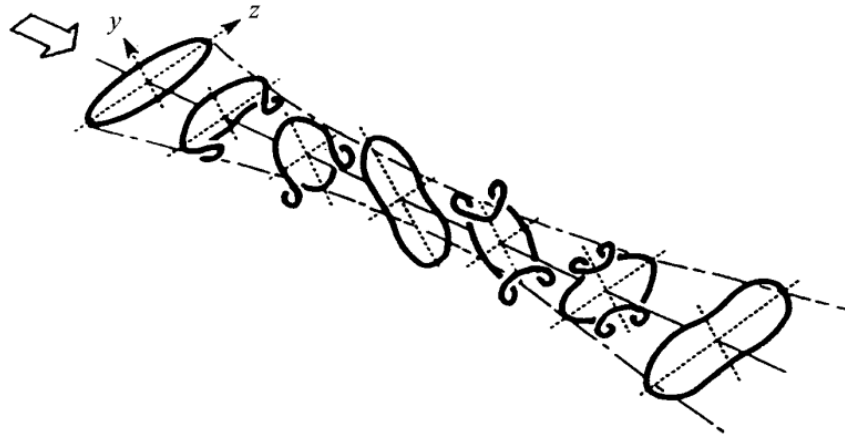
Figure 6.25: Dynamics of the azimuthal vorticity in the deformation of an elliptical ring leading to axis switching in Hussain and Husain [1989].
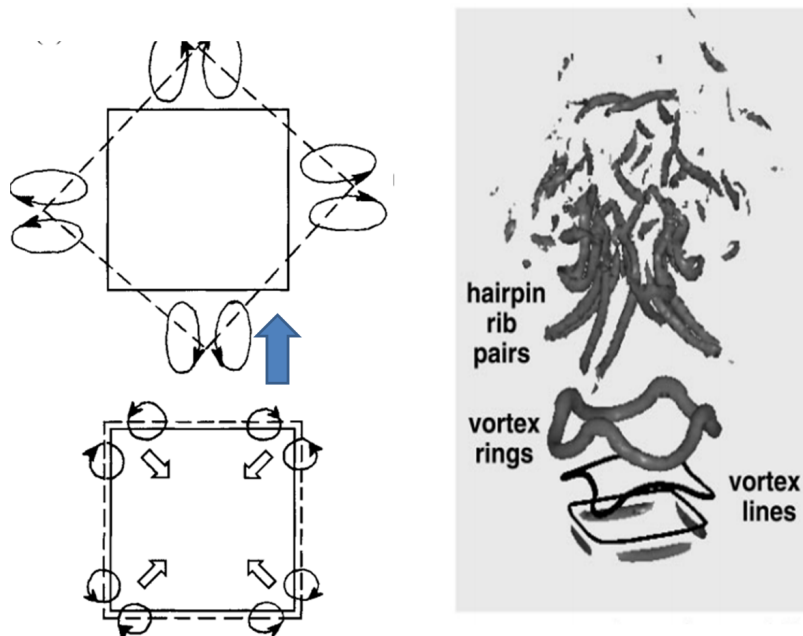
Figure 6.26: Left: schematic of vorticity distribution in a rectangular jet (Quinn [1992]). Right: vortices by iso-surface of the vorticity magnitude flow through a rectangular jet. (Grinstein and DeVore [1996]).

0.5, 0.75 and 1 (shown in Figure 6.18(b)) are quite similar to the three patterns during the "rotation" for the triangular orifice presented in Gutmark and Grinstein [1999]. In spite of different Reynolds numbers and flow area ratios, the lengths for a complete "rotation" of an angle π for our triangular orifice F0 and the triangular orifice in Gutmark and Grinstein [1999] are both around one diameter downstream of the orifice plate. The simulations also show that the velocity contours of the fractal orifices F1, F2 and F3 "rotates" by an angle of $\pi/3$ after $0.75D$ downstream of the orifice, and then the shape of a regular hexagon seems to have another secondary switch-over, and gradually recovers to a classic pipe flow further downstream. Although the phenomenon of the axis-switching was reported in some non-circular jet flows (Gutmark and Grinstein [1999]; Mi *et al.* [2010]), this is the first time it is reported for flows through thin fractal orifices at a relatively high Reynolds number.

6.3.4.5 Energy spectra

The energy spectra of the streamwise velocity fluctuations w' were computed at four stations $z/D = 0.5$, 1, 1.5 and 2 along the centreline. They are displayed in Figure 6.27. These spectra were calculated using the Welch algorithm with a Hamming window.

The circular orifice C and the triangular orifice F0 both capture distinct vortex shedding frequencies at the station $z/D = 0.5$. The dominant frequencies for the orifice C and F0 are very similar, approximately 155 Hz and very close to the experimental measurement (around 152 Hz). These vortex shedding frequencies in the simulations correspond to a Strouhal number around 0.53, which is similar to the assumed Strouhal number for determining the time step. Distinct frequency peaks exist in these two orifices, because the forced large turbulence structures roll around the segments of the orifice and are easier to shed, split and break down to smaller structures. For the fractal orifices F1, F2 and F3, the frequency peaks are much smoother than those observed for the circular and triangle orifices. A possible reason is that with a higher fractal level, the turbulence structures that are produced by the fractal perimeter of the orifices are already small (as observed earlier in Figure 6.15) so that there is no vortex shedding as distinct as for the circular and triangular orifices. For the circular orifice C and the triangular orifice F0, the peak of the frequency is still recognisable until $z/D = 1$, then it is smoothed out to give way to a small range (100 Hz - 300 Hz) of the Kolmogorov-type $f^{-5/3}$ power law at stations further downstream. The short inertial range may be related to the relatively coarse mesh resolutions. The same trend can also be observed for the fractal orifice F1, though the frequency peak is less pronounced. By contrast, the higher level fractal orifices F2 and F3 seem to reinforce the peak frequency at around 160 Hz at $z/D = 1$ and downstream, and they do not exhibit yet the Kolmogorov-
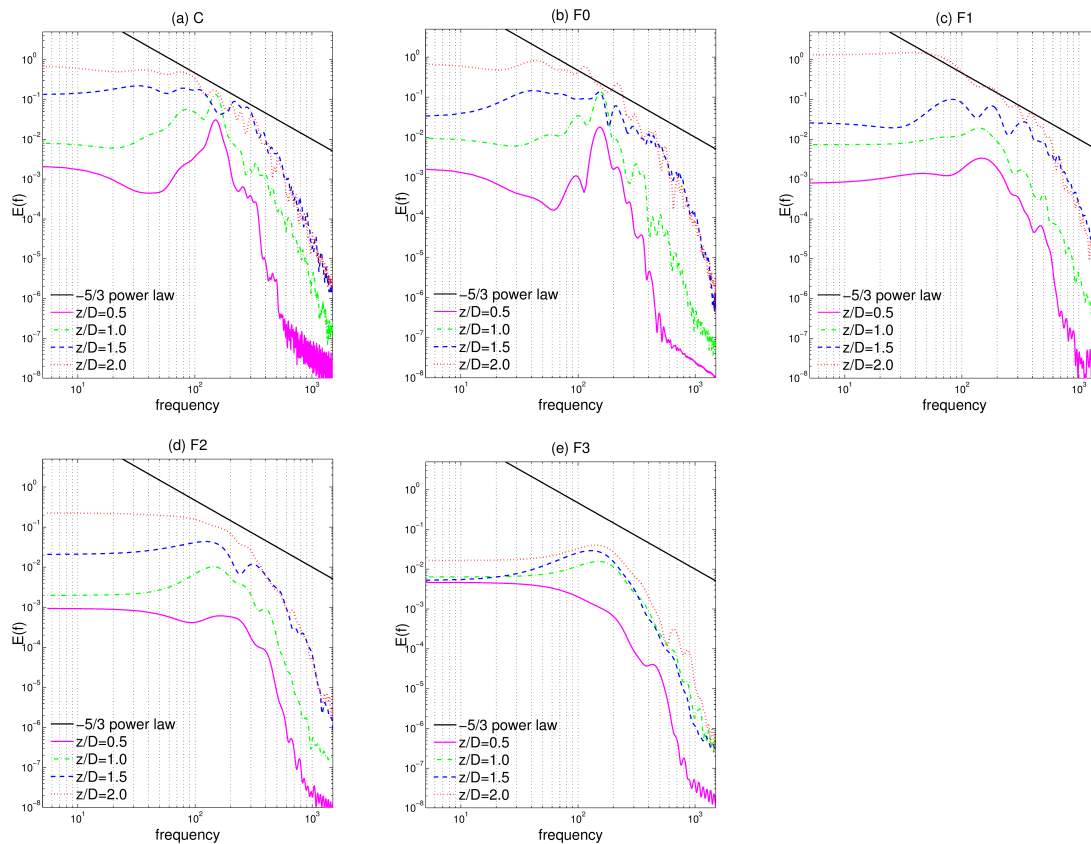
Figure 6.27: Energy frequency-spectra for the streamwise velocity fluctuations at four stations: $z/D = 0.5$, 1, 1.5 and 2 in the centreline for (a) C, (b) F0, (c) F1, (d) F2 and (e) F3.

type power law at $z/D = 2$.

6.3.5   Summary

Spatially evolving turbulent flows generated by four levels of snowflake fractal-orifices and a circular orifice have been investigated with a wall-modelled implicit LES approach. The simulation results of both the velocity and the kinetic energy agree reasonably well with available data provided by laboratory experiments. More results and further understanding of the fractal-forced turbulent flows have been obtained from the numerical simulations. Some conclusions may be drawn here.

(1) Instantaneous flow visualisations imply that the size of the turbulence structures near the orifice plate is dominated by the segments of the orifice perimeter. For the fractal orifice of a higher level with shorter segments, the structures breakdown near the orifice becomes less significant and the dominant process becomes vortex merging and mixing.

(2) The higher level fractal orifice has a smaller unrecoverable pressure loss and a higher pressure recovery rate but a slightly longer recovery length, corresponding to the protracted region of the turbulent mixing and decay.

(3) At the centreline of the pipe, the higher level fractal orifice has a smaller vena contracta velocity but a slower velocity recovery. In the whole flow region, the higher level fractal orifice has a longer and thinner high velocity region, because of a smaller scribed circle of the flow area of the orifice.

(4) The axis-switching phenomenon is observed in the contours of both the velocity and the turbulence kinetic energy for the triangular orifice F0 and the other fractal orifices. The triangular orifice has a rotation angle of π, while the fractal orifices F1, F2 and F3 have a rotation angle of $\pi/3$. The axis-switching phenomenon is reported for the first time for flows through thin fractal orifices at a relatively high Reynolds number.

(5)The higher level fractal orifices with smaller segments generate more organized vortices, and adjacent segments produce a counter-rotating streamwise vortex pair, which maintains the high turbulence kinetic energy in the annular region for a longer distance and a slower decay. The higher level fractal orifice has a longer region of the low turbulence kinetic energy downstream. It also has a slower increase of the turbulence kinetic energy along the centreline. The flow mixing mostly occurs outside of the central cone, and the energy transfer to the pipe wall is more significant than that to the central region.

(6) The energy spectra of the fluctuation of the streamwise velocity show that near the orifice plate, the circular orifice C and the triangular orifice F0 capture distinct vortex shedding frequencies similar to those of the experiments. The fractal orifices F2 and F3 with much smaller forced structures do not show a distinct vortex shedding frequency.

6.4   Summary

With moderate LES mesh resolution in an unstructured mesh, the current study shows that the implicit LES with S-A modelling as the wall-modeling predicts better results than DES. The simulations of the circular orifice and four level fractal orifices are in good agreement with the experimental results. The passive control effect of the orifice geometries in flow mixing and decay is studied through statistical results and instantaneous flow features.

Chapter 7

Conclusions

7.1   Summary of work, achievements and findings

The objective of this study is to study the flow control effect with different control methods in different flow types (the geometry-induced sharp edge flow separation, adverse pressure gradient induced flow separation from smooth surface, and sharp edge induced flow separation in a wall-bounded domain.), using hybrid RANS/LES methods. The main achievements are addressed in the following sections.

7.1.1   Performances of hybrid RANS/LES turbulence modelling in complex turbulent flow

The S-A based hybrid RANS/LES turbulence modelling techniques (DES, DDES, IDDES and SA-iLES) are investigated in three types of flows.

For the BFS case, the main difference of the turbulent viscosity predicted by DES and DDES locates at the attached boundary layer upstream of the step. As the flow separation is driven by the sharp geometrical edge, the calculated upstream flow has limited influences to the downstream recirculation region. Thus, simulation results in the recirculation region do not have significant differences. IDDES, which takes the upstream fluctuation into account in calculating the turbulent viscosity, gives slightly improved results in the recirculation region and the recovery region. For flows separated from a smooth surface due to an adverse pressure gradient (like, NACA0015 at the angle of attack of 11° degree), DES has its famous "MSD" problem due to its fixed interface between RANS and LES in the inner region of the attached boundary layer. DDES, which was designed to postpone the RANS region to cover the whole attached boundary layer, seems to have a strong "delay" effect, so that the

originally separated region seems to shrink or even disappear, due to the large dissipation in the RANS mode. IDDES gives the best simulation result in this kind of flow. In simulations with fractal geometries, even with a moderate LES mesh solution, complex objects in the flow may deteriorate the mesh quality, and sometimes unstructured mesh topology has to be used. In such a scenario, the LES mode in the hybrid RANS/LES methods seems to be over-dissipative due to irregular spatial filter scales and a large numerical dissipation. A wall-modelled implicit LES may be a good choice in these cases.

7.1.2 Achievements in the piezoelectric oscillating surface control of flow over a backward facing step

Both experiments and the numerical simulations show that the control effect of piezoelectric actuators installed on the step far from the sharp edge is limited for the downstream recirculation region. This conclusion is consistent with literatures, which states the wall-based control strategies in altering near-wall turbulence are less effective.

In order to significantly change downstream flow properties, either the attach boundary layer is obviously affected or the flow instability is obviously altered at the edge. For the current flow control with the piezoelectric actuators, the introduced motion with a velocity of less than 0.2% of the free stream has limited manipulation to the boundary layer. Nevertheless, even without a significant change of the reattachment point, the simulation of the controlled flow leads to several findings. Spanwise variations of the velocity and Reynolds stresses are introduced. The controlled flow has a slightly smaller primary recirculation region especially for the in-between region of two actuators, resulting from the enhanced momentum transfer in the wall-normal direction, which is observed in the distribution of the vertical Reynolds normal stresses.

Exploring studies of three flow control cases, with the oscillating surface of the control velocities in the order of the free stream, were carried out. Numerical simulations show that the distribution of the time and spaced averaged C_f has a reduction of 18% in the recovered flow for all the three controlled cases. The primary recirculation becomes much smaller with a larger control velocity. Counter-rotating vortex pairs are generated from the oscillating surfaces. The vortex tubes extend towards downstream of the step and interact with the shear layer. It is also found that the larger the control velocity, the higher the elevation angle. When the control velocity is up to the same as the free stream, the generated vortex tubes significantly influence the whole flow domain. Bifurcation of vortices was observed in this case, which seems to enhance the interaction between the generated vortex and the

shear layer.

Overall, this investigation displays the limits of piezoelectric actuators in flow control. The exploring study on the oscillating surface may provide some hints on designing novel control devices.

7.1.3 Achievements in the flow control with jet vortex generators in NACA0015

Both experiments and simulations in flow over NACA0015 with an angle of attack of 11° demonstrate that the jet vortex generators are effective in forcing a natural separated flow to be attached. As a result, the lift coefficient is enhanced, and the drag coefficient is reduced, which are desirable to improve the performances of aircraft.

The comparison of the statistical steady states of both the baseline flow and the controlled flow by jet vortex generators leads to some useful conclusion as follows. For the controlled flow, there is almost no flow separation observed. The blowing jets, installed at $0.3c$ from the leading edge, improve the flow momentum around the aerofoil in the suction side. The "footprints" of these jets can be distinguishingly observed in distributions of pressure and skin frictions. The controlled flow is far from a quasi-2D flow as in the baseline case. Due to the velocity and pressure gradients near the jets, rotating vortices are generated and extend to the wake flow. Along most region in the streamwise direction, the rotation of the vortices brings the high momentum flow in the free stream towards the wall. The boundary layer is energised, and has fuller boundary velocity profiles. This high-momentum boundary layer overcomes the adverse pressure gradient and resists flow separating. Correspondingly, the attached boundary layer has less velocity fluctuations (or Reynolds stresses). In the baseline flow, because of a trailing edge separation, the streamwise Reynolds normal stress contributes the most to the turbulence kinetic energy. While for the controlled flow, the three Reynolds normal stresses have similar contributions to the turbulence kinetic energy because of the pitch and skew angles.

During the transient process of deploying jets, the drag coefficient initially maintains the same as the uncontrolled state, during which the jets vortices are generated but have not yet reached the separated shear layer. When the jets-generated vortices move downstream and interact with the originally separated shear layer, the drag coefficient goes through sharp fluctuations. In this process, the interaction suppresses the flow separation. After the high momentum vortices remove the original separation off the trailing edge, a statistical steady state of the drag coefficient is achieved, which corresponds to a fully-attached flow. When

the jets are switched off, the previous fully attached flow recovers to the original baseline flow. Both the experiments and simulation illustrate that the jet-removal process has about 70% longer transient time than the jet-deployment process.

7.1.4 Achievements in the fractal orifice passive flow control in pipes

A circular orifice is widely investigated either as flow measurement devices or as an exit of jet flows. In flow control with jets, the geometry of jets play an important role in control optimization. In this study, the orifice with fractal geometries in a pipe flow is investigated, using wall-modelled implicit LES.

For all the four levels of fractal orifices, simulation results are in good agreement with the experimental measurements in the velocity and Reynolds stresses. The statistical results show that the higher level fractal orifice also has a smaller vena contracta velocity, a smaller unrecoverable pressure loss and a higher pressure recovery rate. The lower pressure loss is desirable, especially for flows with several orifice meters. Instantaneous flow visualisations show that the length scale of the turbulence structures near the orifice plate is dominated by the segments of the orifice perimeter. For the fractal orifice of a higher level with shorter segments, the structures breakdown near the orifice becomes less significant and the dominant process becomes vortex merging and mixing. The higher level fractal orifices with smaller segments generate more organized vortices, and adjacent segments produce a counter-rotating streamwise vortex pair, which maintains the high turbulence kinetic energy in the annular region for a longer distance and a slower decay. The energy spectra of the fluctuation of the streamwise velocity show that near the orifice plate, the circular orifice and the triangular orifice capture distinct vortex shedding frequencies similar to those of the experiments, while other high level fractal orifices do not have distinct shedding frequencies observed. The axis-switching phenomenon is observed in the contours of both the velocity and the turbulence kinetic energy for the triangular orifice F0 and the other fractal orifices.

The properties of the fractal orifices in flow mixing and axis-switching may inspire new concepts in flow control and flow measurement devices.

7.2 Suggestions for future work

Furthering the findings from the current study, some future research work is recommended to extend the current study in flow control methods and control optimization using hybrid RANS/LES methods.

Firstly, for the backward facing step case, some other control methods are recommended to be investigated. This topic can extend to the flow control of sharp separation flow, which is not so sensitive to the upstream boundary layer. Two control methods in this case seem to be promising. The first one is to use the spanwise vortex generators near the step to change the flow instability, in which the spanwise vortex generators are suggested to locate in the buffer layer to enhance their effect on flow instability. The other is to use plasma actuation in the whole attached boundary layer before separation. Some experiments on this study provide promising control effect, while there is a lack of numerical investigation. These two control methods are highly recommended to be used in this case.

Secondly, for the NACA0015 case with jet vortex generators, pulsed jets with a certain duty cycle are promising, as it improves the control efficiency. For current study, the control frequency 1 Hz is far too small, as the flow already becomes attached in the first about 20% of the jets-on time, and after the jets-off, it takes only about 35% of the current off-time to recover to the baseline flow. Therefore, an optimization on the flow control frequency and duty circles deserves further research to improve the control performance and efficiency.

Thirdly, for the fractal orifices flow, as the current LES study damps the flow fluctuations below the filter size, which makes it impossible to investigate the energy dissipation and cascading in full spectra, impeding further understanding on the fractal forced flow separation mechanisms. Therefore, a DNS study with a scaled Reynolds number may be interesting.

Finally, a combination of passive flow control and active flow control is also promising work. For example, for the pulsed jets, the current geometry of the jet exit is elliptical, and other exit geometries (triangular, rectangular, and fractal geometries) may be studied.

List of Published/Submitted Papers

Wang, W. and Qin, N., 2012. Balancing Destruction and Production in SA Model-Based Hybrid RANS-LES for Flow around an Aerofoil with Mild Separation. *In: Progress in Hybrid RANS-LES Modelling*, 379–388.

Wang, W. and Qin, N., 2013. A new blended destruction term for the Spalart-Allmaras model based detached eddy simulation. *(To be submitted)*.

Wang, W., Qin, N., and Nicolleau, F., 2013a. Large eddy simulation for turbulent flows through snowflake fractal orifice pipe. *(To be submitted)*.

Wang, W., Siouris, S., and Qin, N., 2013b. Hybrid RANS-LES for active flow control. *Aircraft Engineering and Aerospace Technology(Under Revison)*.

References

Amir, M. and Kontis, K., 2008. Application of piezoelectric actuators at subsonic speeds. *Journal of Aircraft*, 45 (4), 1419–1430.

Anderson, D.A., Tannehill, J.C., and Pletcher, R.H., 1984. *Computational Fluid Mechanics and Heat Transfer*. Washington, USA: Hemisphere Publishing Corp.

Angland, D., Zhang, X., and Goodyer, M., 2012. The use of blowing flow control to reduce bluff body interaction noise. *AIAA Journal*, 50 (8), 1670–1684.

Armaly, B.F., *et al.*, 1983. Experimental and theoretical investigation of backward-facing step flow. *J. Fluid Mech*, 127 (473), 20.

Badry, B.M. and Badarudin, A., 2007. Synthetic Turbulence Generation for LES on Unstructured Cartesian Grids. Thesis (PhD). Cranfield University.

Baggett, J., 1998. On the feasibility of merging LES with RANS for the near-wall region of attached turbulent flows. *Annual Research Briefs*, Center for Turbulent Research, Stanford Univ./NASA Ames Reseach Center, 267–278.

Bai, K., Meneveau, C., and Katz, J., 2012. Near-Wake Turbulent Flow Structure and Mixing Length Downstream of a Fractal Tree. *Boundary-Layer Meteorology*, 143, 285–308.

Barri, M., *et al.*, 2010. DNS of backward-facing step flow with fully turbulent inflow. *International Journal for Numerical Methods in Fluids*, 64 (7), 777–792.

Batina, J.T., 1990. Unsteady Euler airfoil solutions using unstructured dynamic meshes. *AIAA journal*, 28 (8), 1381–1388.

Batten, P., Chakravarthy, S., and Goldberg, U., 2004. Interfacing statistical turbulence closures with large-eddy simulation. *AIAA Journal*, 42, 485–492.

Beavers, G.S. and Wilson, T.A., 1970. Vortex growth in jets. *Journal of Fluid Mechanics*, 44, 97–112.

Berland, J., Bogey, C., and Bailly, C., 2006. Low-dissipation and low-dispersion fourth-order Runge-Kutta algorithm. *Computers and Fluids*, 35 (10), 1459–1463.

Blazek, J., 2001. *Computational Fluid Dynamics: Principles and Applications: Principles and Applications*. Oxford, UK: Elsevier Science.

Bobonea, A., 2012. Impact of pulsed blowing jet on aerodynamic characteristics of wind turbine airfoils. *In: AIP Conference Proceedings*, Vol. 1493, p. 170.

Bons, J.P., Sondergaard, R., and Rivir, R.B., 2002. The fluid dynamics of LPT blade separation control using pulsed jets. *Journal of Turbomachinery*, 124 (1), 77–85.

Bradshaw, P. and Ferriss, D. H.and Atwell, N.P., 1967. Calculation of boundary layer development using the turbulent energy equation. *J. Fluid Mech*, 28 (3), 593–616.

Bui, T.T., 2000. A parallel, finite-volume algorithm for large-eddy simulation of turbulent flows. *Computers & fluids*, 29 (8), 877–915.

Cattafesta, L.N., *et al.*, 1997. Active control of flow-induced cavity resonance. *In: AIAA 97-1804*.

Cattafesta, L.N., Garg, S., and Shukla, D., 2001. The Development of Piezoelectric Actuators for Active Flow Control. *AIAA paper*, 39 (8), 1562–1568.

Cattafesta, L.N. and Sheplak, M., 2011. Actuators for active flow control. *Annual Review of Fluid Mechanics*, 43, 247–272.

Cattafesta, L.N., *et al.*, 2008. Active control of flow-induced cavity oscillations. *Progress in Aerospace Sciences*, 44 (7), 479–502.

Cattafesta, L.N., *et al.*, 2003. Review of active control of flow-induced cavity resonance. *AIAA paper*, 3567.

Celik, I.B., Cehreli, Z.N., and Yanuz, I., 2005. Index of Resolution Quality for Large Eddy Simulations. *J. Fluids Eng.*, 127, 949–959.

Chen, W., Hu, H., and Li, H., 2013. Suppression of Vortex Shedding from a Circular Cylinder by using a Suction Flow Control Method. *In: 51st AIAA Aerospace Sciences Meeting*

REFERENCES

Including the New Horizons Forum and Aerospace Exposition, January., Grapevine, Taxas, USA.

Chester, S. and Meneveau, C., 2007. Renormalized numerical simulation of flow over planar and non-planar fractal trees. *Environ Fluid Mech*, 7, 289–301.

Chester, S., Meneveau, C., and Parlange, M.B., 2007. Modeling turbulent flow over fractal trees with renormalized numerical simulation. *J. Comput. Phys.*, 225 (1), 427–448.

Choi, J., Jeon, W.P., and Choi, H., 2002. Control of flow around an airfoil using piezoceramic actuators. *AIAA journal*, 40 (5), 1008–1010.

Compton, D.A. and Johnston, J.P., 1992. Streamwise vortex production by pitched and skewed jets in a turbulent boundary layer. *AIAA journal*, 30 (3), 640–647.

Crittenden, T., *et al.*, 2001. Combustion-driven jet actuators for flow control. *AIAA Paper*, 2768.

Dacles-Mariani, J., *et al.*, 1995. Numerical/experimental study of a wingtip vortex in the near field. *AIAA Journal*, 33 (9), 1561–1568.

Dandois, J., Garnier, E., and Sagaut, P., 2007. Numerical simulation of active separation control by a synthetic jet. *Journal of Fluid Mechanics*, 574 (1), 25–58.

Darbandi, M. and Fouladi, N., 2011. A reduced domain strategy for local mesh movement application in unstructured grids. *Applied numerical mathematics*, 61 (9), 1001–1016.

Davidson, L., 2009. Hybrid LES-RANS: back scatter from a scale-similarity model used as forcing. *Phil. Trans. R. Soc. A*, 367, 2905–2915.

Davidson, L. and Dahlström, S., 2005. Hybrid LES-RANS: An approach to make LES applicable at high Reynolds number. *International Journal of Computational Fluid Dynamics*, 19, 415–427.

Deck, S., 2012. Recent improvements in the Zonal Detached Eddy Simulation (ZDES) formulation. *Theoretical and Computational Fluid Dynamics*, 26, 523–550.

Deng, S., Jiang, L., and Liu, C., 2007. DNS for flow separation control around an airfoil by pulsed jets. *Computers & fluids*, 36 (6), 1040–1060.

Dietiker, J.F. and Hoffmann, K.A., 2009. Predicting Wall Pressure Fluctuation over a Backward-Facing Step Using Detached Eddy Simulation. *Journal of Aircraft*, 46 (6), 2115–2120.

Donea, J., *et al.*, 2004. Chapter 14 Arbitray Lagriangian-Eulerian Methods. *In*: E. Stein, R. Borst and T.J.R. Hughes, eds. *Encyclopedia of Computational Mechnics, Volume 1, Fundamentals.*, England, U.K.

Driver, D.M. and Seegmiller, H.L., 1985. Features of a reattaching turbulent shear layer in divergent channel flow. *AIAA Journal*, 23, 163–171.

Driver, D.M., Seegmiller, H.L., and Marvin, J.G., 1987. Time-dependent behavior of a reattaching shear layer. *AIAA Journal*, 25, 914–919.

Durrani, N.I., 2009. Hybrid RANS-LES simulations for separated flows using dynamic grids. Thesis (PhD). The University of Sheffield.

Durrani, N.I. and Qin, N., 2011. Behaviour of detached-eddy simulations for mild trailing-edge separation. *Journal of Aircraft*, 48 (1), 193–202.

Durrani, N.I. and Qin, N., 2012. Comparison of Hybrid RANS-LES Methods for Massively Separated Flows. *Progress in Hybrid RANS-LES Modelling.*, 257–266.

Dwight, R.P., 2006. Time-Accurate Navier-Stokes Calculations with Approximately Factored Implicit Schemes. *In*: C. Groth and D.W. Zingg, eds. *Computational Fluid Dynamics 2004.*, 211–217.

Eastwood, S., Xia, H., and Tucker, P.G., 2012. Large-eddy simulation of complex geometry jets. *Journal of Propulsion and Power*, 28, 235–245.

Egorov, Y., *et al.*, 2010. The Scale-Adaptive Simulation Method for Unsteady Turbulent Flow Predictions. Part 2: Application to Complex Flows. *Flow Turbulence and Combustion*, 85 (1), 139–165.

El-Askary, W.A., El-Mayet, M., and Balabel, A., 2012. On the performance of sudden-expansion pipe without or with cross-flow injection: experimental and numerical studies. *International Journal for Numerical Methods in Fluids*, 69 (2), 366–383.

Emami-Naeini, A., *et al.*, 2005. Active control of flow over a backward-facing step. *In*: *Decision and Control, 2005 and 2005 European Control Conference. CDC-ECC'05. 44th IEEE Conference on*, 7366–7371.

REFERENCES

England, G., *et al.*, 2010. The effect of density ratio on the near field of a naturally occurring oscillating jet. *Experiments in fluids*, 48 (1), 69–80.

Fadai-Ghotbi, A., *et al.*, 2010. A Hybrid RANS-LES Model Based on Temporal Filtering. *In*: S.H. Peng, P. Doerffer and W. Haase, eds. *Progress in Hybrid RANS-LES Modelling.*, Vol. 111 of *Notes on Numerical Fluid Mechanics and Multidisciplinary Design*, 225–234.

Fadai-Ghotbi, A., Manceau, R., and Borée, J., 2008. Revisiting URANS computations of the backward-facing step flow using second moment closures. Influence of the numerics. *Flow, Turbulence and Combustion*, 81 (3), 395–414.

Farhat, C., Geuzaine, P., and Grandmont, C., 2001. The discrete geometric conservation law and the nonlinear stability of ALE schemes for the solution of flow problems on moving grids. *Journal of Computational Physics*, 174 (2), 669–694.

Ferziger, J.H. and Peric, M., 2002. *Computational methods for fluid dynamics.* Berlin, Heidelberg, New York, Barcelona, Hong Kong, London, Milan, Paris, Tokyo: Springer.

Fessler, J.R. and Eaton, J.K., 1999. Turbulence modification by particles in a backward-facing step flow. *Journal of Fluid Mechanics*, 394 (1), 97–117.

Fric, T.F. and Roshko, A., 1994. Vortical structure in the wake of a transverse jet. *Journal of Fluid Mechanics*, 279 (1), 47.

Friederich, T.A. and Kloker, M.J., 2011. Direct Numerical Simulation of Swept-Wing Laminar Flow Control Using Pinpoint Suction. *In*: *High Performance Computing in Science and Engineering'10*, 231–250.

Fröhlich, J. and von Terzi, D., 2008. Hybrid LES/RANS methods for the simulation of turbulent flows. *Progress in Aerospace Sciences*, 44, 349–377.

Fureby, C. and Grinstein, F.F., 2002. Large Eddy Simulation of High-Reynolds-Number Free and Wall-Bounded Flows. *Journal of Computational Physics*, 181 (1), 68–97.

Furuichi, N., Hachiga, T., and Kumada, M., 2004. An experimental investigation of a large-scale structure of a two-dimensional backward-facing step by using advanced multi-point LDV. *Experiments in fluids*, 36 (2), 274–281.

Gad-el Hak, M., 2007. *Flow control: passive, active, and reactive flow management.* Cambridge University Press.

Geipel, P., Henry Goh, K.H., and Lindstedt, R.P., 2010. Flow control with noncircular jets. *Flow Turbulence Combust*, 85, 397–419.

Germano, M., 2004. Properties of the hybrid RANS/LES filter. *Theoretical and Computational Fluid Dynamics*, 17, 225–231.

Germano, M., *et al.*, 1991. A dynamic subgrid-scale eddy viscosity model. *Physics of Fluids A: Fluid Dynamics*, 3 (7), 1760–1765.

Geurts, B.J., 2012. Simulation of turbulent flow through a fractal orifice in a pipe. *In: 2nd UK-Japan Bilateral Workshop*, London.

Gilarranz, J.L., Traub, L.W., and Rediniotis, O.K., 2005. A new class of synthetic jet actuators: Part I: Design, fabrication and bench top characterization. *Journal of fluids engineering*, 127 (2), 367–376.

Glezer, A., 2011. Some aspects of aerodynamic flow control using synthetic-jet actuation. *Philosophical Transactions of the Royal Society A: Mathematical, Physical and Engineering Sciences*, 369 (1940), 1476–1494.

Glezer, A. and Amitay, M., 2002. Synthetic jets. *Annual Review of Fluid Mechanics*, 34 (1), 503–529.

Godnunov, S.K., 1959. A difference scheme for numerical computation of discontinuous solutions of equations of fluid dynamics. *Mat. Sb.*, 47, 271–290.

Gomes-Fernandes, R., Ganapathisubramani, B., and Vassilicos, J.C., 2012. Particle image velocimetry study of fractal-generated turbulence. *Journal of Fluid Mechanics*, 711, 306–336.

Goodarzi, M., Rahimi, M., and Fereidouni, R., 2012. Investigation of Active Flow Control over NACA0015 Airfoil Via Blowing. *International Journal of Aerospace Sciences*, 1 (4), 57–63.

Greenblatt, D. and Wygnanski, I.J., 2000. The control of flow separation by periodic excitation. *Progress in Aerospace Sciences*, 36 (7), 487–545.

Grin, V., 1967. Experimental study of boundary-layer control by blowing on a flat plate at M=2.5. *Fluid Dynamics*, 2 (6), 79–80.

Grinstein, F.F., 2007. Recent Progress on Monotone Integrated Large Eddy Simulation of Free Jets. *JSME International Journal Series B*, 49, 890–898.

REFERENCES

Grinstein, F.F. and DeVore, C.R., 1996. Dynamics of coherent structures and transition to turbulence in free square jets. *Physcis of Fluids*, 8, 1237–1252.

Gritskevich, M.S., *et al.*, 2012. Development of DDES and IDDES Formulations for the $k-\omega$ Shear Stress Transport Model. *Flow Turbulence and Combustion*, 88 (3), 431–449.

Gusakov, E.Z. and Kosolapova, N.V., 2011. Fluctuation reflectometry theory and the possibility of turbulence wave number spectrum reconstruction using the radial correlation reflectometry data. *Plasma Physics and Controlled Fusion*, 53 (4), 045012.

Gutmark, E. and Grinstein, F.F., 1999. Flow control with noncircular jets. *Annual Review of Fluid Mechanics*, 31, 239–272.

Gutmark, E. and Ho, C., 1983. Preferred modes and the spreading rates of jets. *Physcs of fluids*, 26 (10), 2932–2938.

Hamba, F., 2003. A Hybrid RANS/LES Simulation of Turbulent Channel Flow. *Theoretical and Computational Fluid Dynamics*, 16 (5), 387–403.

Hamba, F., 2006. A hybrid RANS/LES simulation of high-Reynolds-number channel flow using additional filtering at the interface. *Theoretical and Computational Fluid Dynamics*, 20, 89–101.

Hamba, F., 2009. Log-layer mismatch and commutation error in hybrid RANS/LES simulation of channel flow. *International Journal of Heat and Fluid Flow*, 30 (1), 20–31.

Han, X. and Krajnovic, S., 2012. An efficient very large eddy simulation model for simulation of turbulent flow. *International Journal for Numerical Methods in Fluids*.

Harlow, F.H. and Fromm, J.E., 1965. Computer experiments in fluid dynamics. *Scientific American*, 212 (3), 104.

Harten, A., 1983. High resolution schemes for hyperbolic conservation laws. *Journal of Computational Physics*, 49 (3), 357–393.

Harten, A. and Hyman, J.M., 1983. Self adjusting grid methods for one-dimensional hyperbolic conservation laws. *Journal of Computational Physics*, 50, 253–269.

Hasegawa, H. and Kumagai, S., 2008. Adaptive separation control system using vortex generator jets for time-varying flow. *Journal of Applied Fluid Mechanics*, 1 (2), 9–16.

Hasse, C., Sohm, V., and Durst, B., 2009. Detached eddy simulation of cyclic large scale fluctuations in a simplified engine setup. *International Journal of Heat and Fluid Flow*, 30 (1), 32–43.

Heinz, J.C., 2010. Investigation of piezoelectric flaps for load alleviation using CFD. Technical report.

Hong, G., 2012. Numerical Investigation to Forcing Frequency and Amplitude of Synthetic Jet Actuators. *AIAA journal*, 50 (4), 788–796.

Hsieh, K.J., Lien, F.S., and Yee, E., 2010. Towards a unified turbulence simulation approach for wall-bounded flows. *Flow Turbulence Combust*, 84, 193–218.

Hurst, D. and Vassilicos, J.C., 2007. Scalings and decay of fractal-generated turbulence. *Physics of fluids*, 19, 035103.

Hussain, A.K.M.F. and Reynolds, W.C., 1970. The mechanics of an organized wave in turbulent shear flow. *J. Fluid Mech.*, 41, 241–258.

Hussain, F. and Husain, H.S., 1989. Elliptic jets. Part 1. Characteristics of unexcited and excited jets. *Journal of Fluid Mechanics*, 208 (1), 257–320.

Iio, S., *et al.*, 2006. Vortex behavior of pulsating jets from a rectangular nozzle. *JSME International Journal*, 49 (4), 988–994.

Ishihara, T., Gotoh, T., and Kaneda, Y., 2009. Study of High Reynolds Number Isotropic Turbulence by Direct Numerical Simulation. *Annual Review of Fluid Mechanics*, 41 (1), 165–180.

Jahanmiri, M., 2010. Active flow control: a review. Technical report 2012:12, Division of Fluid Dynamics, Department of Applied Mechanics, Chalmers University of Technology, Goteborg, Sweden.

Jakirlić, S., *et al.*, 2009. LES, zonal and seamless hybrid LES/RANS: rationale and application to free and wall-bounded flows involving separation and swirl. *Numerical Simulation of Turbulent Flows and Noise Generation.*, 253–282.

Jameson, A., 1991. Time dependent calculations using multigrid, with applications to unsteady flows past airfoils and wings. *In: AIAA-Paper 91-1596, Proc. 10th Comp. Fluid Dyn. Conf.*, June., Onolulu, HI, USA.

REFERENCES

Jameson, A., Schimidt, W., and Turkel, E., 1981. Numerical solution of the Euler Equations by finite volume methods using runge-kutta time-stepping schemes.. *In: Fluid And Plasma Dynamics Conference*, Palo Alto, USA, 81–1259.

Jarrin, N., *et al.*, 2006. A synthetic-eddy-method for generating inflow conditions for large-eddy simulations. *International Journal of Heat and Fluid Flow*, 27 (4), 585–593.

Jeong, J. and Hussain, F., 1995. On the identification of a vortex. *Journal of Fluid Mechanics*, 285, 69–94.

Jewkes, J.W. and Chung, Y.M., 2010. Low Velocity-Ratio Pitched and Skewed Jet in a Turbulent Boundary Layer. *In:* G.D. Mallinson and J.E. Cater, eds. *17th Australasian Fluid Mechanics Conference*, Auckland, New Zealand.

Johnston, J.P. and Nishi, M., 1990. Vortex generator jets-means for flow separation control. *AIAA journal*, 28 (6), 989–994.

Jovic, S. and Driver, D., 1995. Reynolds number effect on the skin friction in separated flows behind a backward-facing step. *Experiments in fluids*, 18 (6), 464–467.

Kamakoti, R. and Shyy, W., 2004. Evaluation of geometric conservation law using pressure-based fluid solver and moving grid technique. *International Journal of Numerical Methods for Heat & Fluid Flow*, 14 (7), 851–865.

Kamnis, S. and Kontis, K., 2004. Numerical Studies on the Application of Synthetic Jets for the Active Control of Subsonic Flow Configurations. *AIAA paper 2004-2609*.

Kang, H.S. and Dennis, D., 2011. Flow over fractals: drag forces and near wakes. *Fractals*, 19, 387–399.

Kawai, S. and Lele, S.K., 2009. Large-eddy simulation of jet mixing in a supersonic turbulent crossflow. *AIAA Paper*, 3795.

Keating, A. and Piomelli, U., 2006. A dynamic stochastic forcing method as a wall-layer model for large-eddy simulation. *Journal of Turbulence*, 7, 12.

Kermani, M.J. and Plett, E.G., 2001. Modified Entropy Correction Formula for the Roe Scheme. *AIAA paper*, 2001-0083.

Keylock, C.J., *et al.*, 2012. The flow structure in the wake of a fractal fence and the absence of an inertial regime. *Environ Fluid Mec.*, 12.

Kim, J.J., 1978. Investigation of separation and reattchement of a turbulent shear layer: flow over a backward facing step. Thesis (PhD). Stanford University.

Kim, S.E., 2004. Large eddy simulation using unstructured meshes and dynamic subgrid-scale turbulence models. . *In: Technical Report AIAA-2004-2548, American Institute of Aeronautics and Astronautics, 34th Fluid Dynamics Conference and Exhibit.*

Kim, W.W. and Menon, S., 1997. Application of the localized dynamic subgrid-scale model to turbulent wall-bounded flows. *In: Technical Report AIAA-97-0210, American Institute of Aeronautics and Astronautics*, 35th Aerospace Sciences Meeting, Reno, NV, USA.

Kitamura, K., Shima, E., and Fujimoto, K., 2011. Performance of Low-Dissipation Euler Fluxes and Preconditioned LU-SGS at Low Speeds. *Commun. Comput. Phys.*, 10 (1), 99–119.

Klein, M., 2005. An Attempt to Assess the Quality of Large Eddy Simulations in the Context of Implicit Filtering. *Flow, Turbulence and Combustion*, 75, 131–147.

Koken, M. and Constantinescu, G., 2009. An investigation of the dynamics of coherent structures in a turbulent channel flow with a vertical sidewall obstruction. *Physics of Fluids*, 21, 085104.

Kolář, V., *et al.*, 2003. Vorticity transport within twin jets in crossflow. *Experimental thermal and fluid science*, 27 (5), 563–571.

Kosin, R.E., 1965. Laminar flow control by suction as applied to the x-21a airplane. *Journal of Aircraft*, 2 (5), 384–390.

Kostas, J., Foucaut, J.M., and Stanislas, M., 2007. The flow structure produced by pulsed-jet vortex generators in a turbulent boundary layer in an adverse pressure gradient. *Flow, turbulence and combustion*, 78 (3-4), 331–363.

Kral, L.D., 1999. Active flow control technology. *ASME Fluids Engineering Division Newsletter*, 3–6.

Kral, L.D., *et al.*, 1997. Numerical simulation of synthetic jet actuators. *AIAA Paper 97-1824*.

Kravchenko, A.G. and Moin, P., 1997. On the Effect of Numerical Errors in Large Eddy Simulations of Turbulent Flows. *Journal of Computational Physics*, 131 (2), 310–322.

REFERENCES

Krogstad, P.A. and Davidson, P., 2011. Homogeneous Turbulence Generated by Multi-scale Grids. *J. Phys.: Conf. Ser.*, 318, 032042.

Kuethe, A.M. and Chow, C.Y., 1986. *Foundation of Aerodynamics: Bases of Aerodynamic Design*. John Wiley & Sons.

Laizet, S., Lamballais, E., and Vassilicos, J.C., 2010. A numerical strategy to combine high-order schemes, complex geometry and parallel computing for high resolution DNS of fractal generated turbulence. *Computers and Fluids*, 39, 471–484.

Laizet, S. and Vassilicos, J.C., 2011. DNS of Fractal-Generated Turbulence. *Flow Turbulence Combust*, 87, 673–705.

Laizet, S. and Vassilicos, J.C., 2012. Fractal space-scale unfolding mechanism for energy-efficient turbulent mixing. *Phys. Review E.*, 86, 046302.

Laval, J.P., *et al.*, 2010. Large-eddy simulations of control of a separated flow over a 2D bump by means of pulsed jets. *Journal of Turbulence*, 11, N52.

Le, H., Moin, P., and Kim, J., 1997. Direct numerical simulation of turbulent flow over a backward-facing step. *Journal of Fluid Mechanics*, 330 (1), 349–374.

Lee, C.Y. and Goldstein, D.B., 2002. Two-dimensional synthetic jet simulation. *AIAA journal*, 40 (3), 510–516.

Lee, Y. and Setoguchi, T., 2008. Passive Control Techniques to Alleviate Supersonic Cavity Flow Oscillation. *Journal of Propulsion and power*, 24 (4), 697–703.

Lee-Rausch, E.M., *et al.*, 2003. CFD sensitivity analysis of a drag prediction workshop wing/body transport configuration. *AIAA Paper*, 2003-3400.

Leschziner, M.A. and Lardeau, S., 2011. Simulation of slot and round synthetic jets in the context of boundary-layer separation control. *Philosophical Transactions of the Royal Society A: Mathematical, Physical and Engineering Sciences*, 369 (1940), 1495–1512.

Lesoinne, M. and Farhat, C., 1996. Geometric conservation laws for flow problems with moving boundaries and deformable meshes, and their impact on aeroelastic computations. *Computer methods in applied mechanics and engineering*, 134 (1), 71–90.

Lessani, B., Ramboer, J., and Lacor, C., 2004. Efficient large-eddy simulations of low Mach number flows using preconditioning and multigrid. *International Journal of Computational Fluid Dynamics*, 18 (3), 221–233.

LeVeque, R.J., 1999. *Numerical Methods for Conservation Laws (Lectures in Mathematics)*. Second Edition Basel, Boston, Berlin: Birkhauser.

Li, X., Gu, C., and Xu, J., 2009. Development of Roe-type scheme for all-speed flows based on preconditioning method. *Computers and Fluids*, 38 (4), 810–817.

Li, X.s. and Gu, C.w., 2011. On the Mechanism of Roe-type Schemes for All-Speed Flows. *arXiv preprint arXiv:1107.3744*.

Lin, J.C., 2002. Review of research on low-profile vortex generators to control boundary-layer separation. *Progress in Aerospace Sciences*, 38, 389 – 420.

Lin, S., Chen, Y., and Shih, S., 1997. Numerical study of MUSCL schemes for computational aeroacoustics. *AIAA97-0023*.

Liou, M.S., 1996. A Sequel to AUSM: AUSM. *Journal of computational Physics*, 129 (2), 364–382.

Liou, M.S., 2006. A sequel to AUSM, Part II: AUSM+-up for all speeds. *Journal of Computational Physics*, 214 (1), 137–170.

Liou, M.S. and Steffen, C.J., 1993. A new flux splitting scheme. *Journal of computational physics*, 107 (1), 23–39.

Liscinsky, D.S., True, B., and Holdeman, J.D., 1996. Crossflow mixing of noncircular jets. *Journal of Propulsion and Power*, 12 (2), 225–230.

Liu, N.S. and Shih, T.H., 2006. Turbulence modelling for very large eddy simulation. *AIAA Journal*, 44, 687–697.

Liu, X., Qin, N., and Xia, H., 2006. Fast dynamic grid deformation based on Delaunay graph mapping. *Journal of Computational Physics*, 211 (2), 405–423.

Liu, Y. and Vinokur, M., 1989. Upwind algorithms for general thermo-chemical nonequilibrium flows. *AIAA paper*, 89-0201.

Lu, F.K., *et al.*, 2011. Review of Micro Vortex Generators in High-Speed Flow. *In: 49th AIAA Aerospace Sciences Meeting including the New Horizons Forum and Aerospace Exposition*, Orlando, Florida, USA.

Luedke, J., *et al.*, 2005. Characterization of steady blowing for flow control in a hump diffuser. *AIAA journal*, 43 (8), 1644–1652.

REFERENCES

Lund, T.S., Wu, X., and Squires, K.D., 1998. Generation of Turbulent Inflow Data for Spatially-Developing Boundary Layer Simulations. *Journal of Computational Physics*, 140 (2), 233–258.

Maddalon, D.V., *et al.*, 1990. *Transition flight experiments on a swept wing with suction*. Springer.

Mandelbrot, B.B. and Blumen, A., 1989. Fractal Geometry: What is it, and What Does it do?. *Proceedings of the Royal Society of London. A. Mathematical and Physical Sciences*, 423 (1864), 3–16.

Mane, P., Mossi, K., and Bryant, R., 2005. Synthetic jets with piezoelectric diaphragms. *In*: *Smart Structures and Materials*, 233–243.

Mathew, J., *et al.*, 2006. Optimized design of piezoelectric flap actuators for active flow control. *AIAA journal*, 44 (12), 2919–2928.

Mavriplis, D.J. and Jameson, A., 1990. Multigrid solution of the Navier-Stokes equations on triangular meshes. *AIAA Journal*, 28, 1415–1425.

Mavriplis, D.J. and Yang, Z., 2006. Construction of the discrete geometric conservation law for high-order time-accurate simulations on dynamic meshes. *Journal of Computational Physics*, 213 (2), 557–573.

Mazellier, N. and Vassilicos, J.C., 2010. Mean velocity and turbulence fields inside a beta = 0. 50 orifice flowmeter. *American Institute of Chemical Engineers Journal*, 22, 075101–075101–25.

Melson, N.D., Sanetrik, M.D., and Atkins, H.L., 1993. Time-accurate Navier-Stokes calculations with multigrid acceleration. *In*: *6th Copper Mountain Conference on multigrid methods*, 423–439.

Meneveau, C., Lund, T.S., and Cabot, W.H., 1996. A Lagrangian dynamic subgrid-scale model of turbulence. *Journal of Fluid Mechanics*, 319, 353–385.

Menter, F.R., 1994. Two-equation eddy-viscosity turbulence models for engineering applications. *AIAA Journal*, 32, 1598–1605.

Menter, F.R. and Egorov, Y., 2010. The Scale-Adaptive Simulation Method for Unsteady Turbulent Flow Predictions. Part 1: Theory and Model Description. *Flow Turbulence and Combustion*, 85 (1), 113–138.

Menter, F.R. and Kuntz, M., 2004. Adaptation of eddy-viscosity turbulence models to unsteady separated flow behind vehicles. *In: Symposium on the aerodynamics of heavy vehicles: trucks, buses and trains*, Berlin.

Menter, F.R., Kuntz, M., and Langtry, R., 2003. Ten years of experience with the SST turbulence model. *In: 4th International Symposium on Turbulence Heat and Mass Transfer*, 625–632.

Merzari, E., Khakim, A., and Ninokata, H., 2009. Unsteady Reynolds-averaged Navier-Stokes: toward accurate prediction of turbulent mixing phenomena. *Int. J. Process Systems Engineering*, 1 (1), 100–123.

Messing, R. and Kloker, M.J., 2010. Investigation of suction for laminar flow control of three-dimensional boundary layers. *Journal of Fluid Mechanics*, 658 (1), 117–147.

Mi, J., Kalt, P., and Nathan, G.J., 2010. On Turbulent Jets Issuing from Notched-Rectangular and Circular Orifice Plates. *Flow Turbulence and Combustion*, 84, 565–582.

Milanovic, I.M. and Zaman, K.B.M.Q., 2004. Fluid dynamics of highly pitched and yawed jets in crossflow. *AIAA journal*, 42 (5), 874–882.

Mittal, R., Rampunggoon, P., and Udaykumar, H.S., 2001. Interaction of a synthetic jet with a flat plate boundary layer. *AIAA paper*, 2773 (200), 1.

Mohamed, M.A., 2011. Dynamic grid detached-eddy simulation of wing flows beyond stall and its control using synthetic jet actuators. Thesis (PhD). The University of Sheffield.

Moin, P. and Mahesh, K., 1998. Direct numerical simulation: a tool in turbulence research. *Annual Review of Fluid Mechanics*, 30 (1), 539–578.

Moreau, E., 2007. Airflow control by non-thermal plasma actuators. *Journal of Physics D: Applied Physics*, 40 (3), 605.

Morrison, G.L., *et al.*, 1993. Mean velocity and turbulence fields inside a $\beta = 0.50$ orifice flowmeter. *American Institute of Chemical Engineers*, 39, 745–756.

Nagata, K., *et al.*, 2008. Direct numerical simulation of turbulent mixing in grid-generated turbulence. *Phys. Scr.*, T132, 014054.

Nani, D.J. and Smith, B.L., 2012. Effect of orifice inner lip radius on synthetic jet efficiency. *Physics of Fluids*, 24 (11), 115110–115110.

REFERENCES

Nastase, I. and Meslem, A., 2007. Passive control of jet flows using lobed nozzle geometries. *Mecanique and Industries*, 8, 101–09.

Neumann, J. and Wengle, H., 2003. DNS and LES of Passively Controlled Turbulent Backward-Facing Step Flow. *Flow, Turbulence and Combustion*, 71, 297–310.

Nicolleau, F.C.G.A., 2013. Return to axi-symmetry for pipe flows generated after a fractal orifice. *Fluid Dynamics Research*, In Press.

Nicolleau, F.C.G.A., Salim, S.M.M., and Nowakowski, A.F., 2011. Experimental study of a turbulent pipe flow through a fractal plate. *Journal of Turbulence*, 12 (44), 1–20.

Nicoud, F. and Ducros, F., 1999. Subgrid-scale modelling based on the square of the velocity gradient tensor. *Flow, Turbulence and Combustion*, 62, 183–200.

Ortmanns, J. and Kähler, C.J., 2004. Investigation of pulsed actuators for active flow control using phase locked stereoscopic particle image velocimetry. *In*: *12th Intl. Symposium on Application of Laser Techniques to Fluid Mechanics, Lisbon*.

Ovenden, N.C. and Smith, F.T., 2005. Vortices and flow reversal due to suction slots. *Philosophical Transactions of the Royal Society A: Mathematical, Physical and Engineering Sciences*, 363 (1830), 1199–1208.

Oyewola, O.M., 2012. Manipulation of Near-wall Structure in a Boundary Layer Subjected to Concentrated Suction and Roughness Strip . *International Journal of Scientific and Engieering Research*, 3, 1–4.

Panjwani, B., *et al.*, 2009. Large eddy simulation of backward facing step flow. *In*: *Fifth National Conference on Computational Mechanics, MekIT*, Vol. 9.

Park, H., *et al.*, 2007. Mixing enhancement behind a backward-facing step using tabs. *Physics of Fluids*, 19, 105103.

Park, N. and Choi, H., 2006. A dynamic subgrid-scale eddy viscosity model with a global model coefficient. *Physics of Fluids*, 18, 125109–24.

Piomelli, U., *et al.*, 2003. The inner-outer layer interface in large-eddy simulations with wall-layer models. *Int. J. Heat Fluid Flow*, 24, 538–550.

Poletto, R., *et al.*, 2011. Divergence free synthetic eddy method for embedded LES inflow boundary conditions. *In*: *Seventh International Symposium On Turbulence and Shear Flow Phenomena (TSFP-7), Ottawa*.

Pope, S.B., 2000. *Turbulent Flows*. Cambridge University Press.

Prandtl, L., 1904. Fluid motion with very small friction. *In: Third international mathematics congress, Heidelberg*, 484–491.

Prasad, R.R. and Sreenivasan, K.R., 1990. The measurement and interpretation of fractal dimensions of the scalar interface in turbulent flows. *Physics of Fluids*, 2, 792–807.

Prince, S.A., Khodagolian, V., and Gaind, R., 2012. An experimetnal study of a pulsed air jet and an acoustic synthetic jet on a low speed turbulent boundary layer. *In: 28th Congress of the International Concil of the Aeronautical Sciences*, Brisbane, Australia.

Qin, N. and Xia, H., 2008. Detached eddy simulation of a synthetic jet for flow control. *Proceedings of the Institution of Mechanical Engineers, Part I: Journal of Systems and Control Engineering*, 222 (5), 373–380.

Quinn, W., 1992. Streamwise evolution of a square jet cross section. *AIAA journal*, 30 (12), 2852–2857.

Rajamani, B. and Kim, J., 2010. A hybrid-filter approach to turbulence simulation Flow. *Turbulence and Combustion*, 85, 421–441.

Ravi, B.R., Mittal, R., and Najjar, F.M., 2004. Study of three-dimensional synthetic jet flowfields using direct numerical simulation.. *AIAA paper*, 51, 61801.

Reynolds, O., 1895. On the dynamical theory of incompressible viscous fluids and the determination of the criterion. *Philosophical Transactions of the Royal Society of London. A*, 186, 123–164.

Roe, P.L., 1981. Approximate Riemann solvers, parameter vectors, and difference schemes. *Journal of Computational Physics*, 43 (2), 357 – 372.

Rumsey, C.L., 2009. Successes and challenges for flow control simulations. *International Journal of Flow Control*, 1 (1), 1–27.

Sagaut, P. and Deck, S., 2009. Large eddy simulation for aerodynamics: status and perspectives. *Royal Society of London Philosophical Transactions Series A*, 367, 2849–2860.

Sagaut, P., Deck, S., and Terracol, M., 2006. *Multiscale and multiresolution approaches in turbulence*. Imperial College Press.

REFERENCES

Sainte-Rose, B., *et al.*, 2008. Delayed Detached Eddy Simulation of a Premixed Methane-Air Flame behind a Backward-Facing Step. *AIAA Paper*, 5134.

Salewski, M., Stankovic, D., and Fuchs, L., 2008. Mixing in circular and non-circular jets in crossflow. *Flow, Turbulence and Combustion*, 80 (2), 255–283.

Sánchez-Rocha, M. and Menon, S., 2009. The compressible hybrid RANS/LES formulation using an additive operator. *J. Comput. Phys.*, 228 (6), 2037–2062.

Sau, R. and Mahesh, K., 2008. Dynamics and mixing of vortex rings in crossflow. *Journal of Fluid Mechanics*, 604, 389–410.

Sau, R. and Mahesh, K., 2010. Optimization of pulsed jets in crossflow. *Journal of Fluid Mechanics*, 653, 365.

Sawant, S.G., *et al.*, 2012. Modeling of Electrodynamic Zero-Net Mass-Flux Actuators. *AIAA journal*, 50 (6), 1347–1359.

Scholz, P., *et al.*, 2006. Leading edge separation control by means of pulsed jet actuators. *In: AIAA Flow Control Conference, San Francisco, California*.

Schumann, U., 1975. Subgrid scale model for finite difference simulations of turbulent flows in plane channels and annuli. *Journal of Computational Physics*, 18 (4), 376 – 404.

Seifert, A., *et al.*, 1998. Use of piezoelectric actuators for airfoil separation control. *AIAA journal*, 36 (8), 1535–1537.

Seoud, R.E. and Valente, P.C., 2007. Dissipation and decay of fractal-generated turbulence. *Physcis of fluids*, 19, 105108–105108–11.

Sergent, E., 2002. Vers une methodologie de couplage entre la Simulation des Grandes Echelles et les modeles statistiques. Thesis (PhD). Ecole Central de Lyon.

Shima, E., 1997. Role of CFD in aeronautical engineering (No. 14)-AUSM type upwind schemes. *In: 14th NAL Symposium on Aircraft Computational Aerodynamics, 1997*.

Shima, E. and Kitamura, K., 2009. On new simple low-dissipation scheme of AUSM-Family for all speeds. *In: AIAA Aerospace Sciences Meeting Including The New Horizons Forum and Aerospace Exposition*, AIAA 2009–136.

Shur, M., *et al.*, 2011. A rapid and accurate switch from RANS to LES in boundary layers using an overlap region. *Flow, turbulence and combustion*, 86 (2), 179–206.

Shur, M., *et al.*, 1999. Detached-eddy simulation of an airfoil at high angle of attack. *In: roceedings of the fourth international symposium on engineering turbulence modelling and measurements*, Amsterdam, 669–678.

Shur, M., *et al.*, 2008. A hybrid RANS-LES approach with delayed-DES and wall-modelled LES capabilities. *International Journal of Heat and Fluid Flow*, 29, 1638–1649.

Siauw, W.L., 2008. Transient process of separation and attachment over a NACA 0015 airfoil controlled by fluidic vortex generators. Thesis (PhD). University of Poitiers.

Siauw, W.L., *et al.*, 2009. Physics of Separated Flow over a NACA 0015 Airfoil and Detection of Flow Separation. *In: 47th AIAA Aerospace Sciences Meeting, AIAA Paper*, Vol. 144, p. 2009.

Siauw, W.L., *et al.*, 2010. Transient dynamics of the flow around a NACA 0015 airfoil using fluidic vortex generators. *International Journal of Heat and Fluid Flow*, 31 (3), 450–459.

Sinha, S.K., 1999. System for efficient control of flow separation using a driven flexible wall. *In:* US Patent 5,961,080, October.

Sinha, S.K. and Hyvärinen, J., 2008. Flexible Wall Turbulence Control for Drag Reduction on Streamlined and Bluff Bodies. *AIAA Paper 2008-4207*, 23–26.

Sinha, S.K. and Ravande, S.V., 2006a. Drag Reduction of Natural Laminar Flow Airfoils with a Flexible Surface Deturbulator. *AIAA Paper*, 3030, 5–8.

Sinha, S.K. and Ravande, S.V., 2006b. Sailplane Performance Improvement Using a Flexible Composite Surface Deturbulator. *AIAA Paper*, 447, 9–12.

Sinha, S.K. and Zou, J., 2000. On controlling flows with micro-vibratory wall motion. *AIAA Paper*, 4413.

Smagorinsky, J., 1963. General circulation experiments with the primitive equations. *Monthly Weather Review*, 91, 99.

Smith, B.L. and Glezer, A., 1998. The formation and evolution of synthetic jets. *Physics of fluids*, 10, 2281.

Spalart, P.R., 2001. Young-person's guide to Detached-Eddy Simulation grids. *NASA Langley Technical Report Server*.

REFERENCES

Spalart, P.R. and Allmaras, S.R., 1992. A one-equation turbulence model for aerodynamic flows. *In: Proceedings of the 30th AIAA Aerospace Sciences Meeting and Exhibit*, AIAA paper 92–0439.

Spalart, P.R., *et al.*, 2006. A new version of detached-eddy simulation, resistant to ambiguous grid densities. *Theoretical and Computational Fluid Dynamics*, 20, 181–195.

Spalart, P.R., Jou W-H., S.M., and Allmaras, S.R., 1997. Comments on the feasibility of LES for wings and on a Hybrid RANS/LES approach. *In: Advances in DNS/LES, 1st AFOSR Int. Conf. on DNS/LES*.

Spalart, R.P., 2009. Detached-Eddy Simulation. *Annual Review of Fluid Mechanics*, 41, 181–202.

Spalding, D., 1961. A single formula for the "law of the wall". *Journal of Applied Mechanics*, 28, 455.

Spazzini, P.G., *et al.*, 2001. Unsteady behavior of back-facing step flow. *Experiments in fluids*, 30 (5), 551–561.

Speziale, C.G., 1998. Turbulence Modeling for time-dependent RANS and VLES: a review. *AIAA J.*, 36, 173–184.

Staicu, A., *et al.*, 2003. Turbulent wakes of fractal objects. *Phys. Rev. E*, 67, 066306.

Strelets, M., 2001. Detached eddy simulation of massively separated flows. *AIAA 2001-0879*.

Suzuki, H., *et al.*, 2010. Direct numerical simulation of turbulent mixing in regular and fractal grid turbulence. *Physica Scripta*, 142, 014065.

Swanson, R.C., Turkel, E., and Rossow, C.C., 2007. Convergence acceleration of Runge-Kutta schemes for solving the Navier-Stokes equations. *J. Comput. Phys.*, 224 (1), 365–388.

Tabor, G.R. and Baba-Ahmadi, M.H., 2010. Inlet conditions for large eddy simulation: A review. *Computers & Fluids*, 39 (4), 553–567.

Thomas, A.M. and Abraham, J.P., 2010. Numerical simulation of circular synthetic jets with asymmetric forcing profiles. *Open Mechanical Engineering Journal*, 4, 1–7.

Thomas, F., 1965. Boundary layer control for increasing lift by blowing. *AIAA Journal*, 3 (5).

Thomas, P.D. and Lombard, C.K., 1979. Geometric conservation law and its application to flow computations on moving grids. *AIAA journal*, 17 (10), 1030–1037.

Tilly, A. and Sousa, J.M., 2008. Kelvin-Helmholtz Instability Due to Slot Blowing in Laminar Boundary Layers. *AIAA Journal*, 46 (6), 1562–1565.

Tilmann, C.P., *et al.*, 2003. Characterization of pulsed vortex generator jets for active flow control. Technical report, DTIC Document.

Toschi, F., *et al.*, 2006. Backward-facing step calculations using the shear improved Smagorinsky model. *In*: *Proceedings of the Summer Program*, 87–97.

Travin, A., *et al.*, 2002. Physical and numerical upgrades in the detached-eddy simulation of complex turbulent flows. *Advances in LES of complex flows*, 239–254.

Travin, A.K., *et al.*, 2006. Improvement of delayed detached-eddy simulation for LES with wall modelling. *In*: *European Conference on Computational Fluid Dynamics*.

Travnivcek, Z., *et al.*, 2003. Aerodynamic and mass transfer characteristics of an annular bistable impinging jet with a fluidic flip–flop control. *International journal of heat and mass transfer*, 46 (7), 1265–1278.

Uruba, V., Joáš, P., and Mazur, O., 2007. Control of a channel-flow behind a backward-facing step by suction/blowing. *International Journal of Heat and Fluid Flow*, 28 (4), 665 – 672.

Valente, P.C. and Vassilicos, J.C., 2011. The decay of turbulence generated by a class of multiscale grids. *J. Fluid Mech*, 687, 300–340.

Valente, P.C. and Vassilicos, J.C., 2012. Universal Dissipation Scaling for Nonequilibrium Turbulence. *Physical Review Letters*, 108 (21), 214503.

Vijayan, P. and Kallinderis, Y., 1994. A finite-volume scheme for the euler equations on adaptive tetrahedral grids. *J. Computational Physics*, 113, 249–267.

Von Koch, H., 1904. On a Continuous Curve without Tangent Constructible from Elementary Geometry. *Classics on Fractals (Westview Press, 2004)*, 25, 45.

Vreman, A. and Mahesh, K., 2012. A Lagrangian subgrid-scale model with dynamic estimation of Lagrangian time scale for large eddy simulation of complex flows. *Physics of Fluids*, 24, 085101–24.

REFERENCES

Vreman, A.W., 2004. An eddy-viscosity subgrid-scale model for turbulent shear flow: Algebraic theory and applications. *Physics of Fluids*, 16 (10), 3670–3681.

Wang, H., *et al.*, 2012a. A dynamic pressure-sink method for improving large eddy simulation and hybrid Reynolds-averaged Navier–Stokes/large eddy simulation of wall-bounded flows. *Proceedings of the Institution of Mechanical Engineers, Part G: Journal of Aerospace Engineering*, 226 (9), 1107–1120.

Wang, L., *et al.*, 2012b. Review of actuators for high speed active flow control. *Science China Technological Sciences*, 55 (8), 2225–2240.

Wang, W. and Qin, N., 2012. Balancing Destruction and Production in SA Model-Based Hybrid RANS-LES for Flow around an Aerofoil with Mild Separation. *In: Progress in Hybrid RANS-LES Modelling*, 379–388.

Wang, W. and Qin, N., 2013. A new blended destruction term for the Spalart-Allmaras model based detached eddy simulation. *(to be submited)*.

Watson, M., Jaworski, A.J., and Wood, N.J., 2003. A study of synthetic jets from rectangular and dual-circular orifices. *The Aeronautical Journal*, 427–434.

Weaver, D., McAlister, K., and Tso, J., 2004. Control of VR-7 dynamic stall by strong steady blowing. *Journal of Aircraft*, 41 (6), 1404–1413.

Weiss, J.M. and Smith, W.A., 1995. Preconditioning applied to variable and constant density flows. *AIAA Journal*, 33, 2050–2057.

Wilcox, D.C., 2006. *Turbulence Modeling for CFD*. Third Edition DCW Industries Inc.

Wright, M.C. and Nelson, P.A., 2000. Four-channel suction distribution optimization experiments for laminar flow control. *AIAA journal*, 38 (1), 39–43.

Xia, H., 2005. Dynamic grid detached eddy simulation for synthetic jet flows. Thesis (PhD). The University of Sheffield.

Xia, H. and Qin, N., 2005. Detached-eddy simulation for synthetic jets with moving boundaries. *Modern Physics Letters B*, 19, 1429–1434.

Xia, H. and Qin, N., 2008. DES Applied to an Isolated Synthetic Jet Flow. *In: Advances in Hybrid RANS-LES Modelling*, 252–260.

Xu, M. and Mi, J., 2010. Large eddy simulation of a partially-confined triangular jet with self-excited low-frequency oscillation. *In: 17th Australasian Fluid Mechanics Conference*, Auckland, New Zealand.

You, D. and Moin, P., 2006. Large-eddy simulation of flow separation over an airfoil with synthetic jet control. *Center for Turbulence Research Annual Research Briefs*, 337–346.

You, D. and Moin, P., 2007. A dynamic global-coefficient subgrid-scale eddy-viscosity model for large-eddy simulation in complex geometries. *Physics of Fluids*, 19, 065110.

You, D. and Moin, P., 2007. Study of flow separation over an airfoil with synthetic jet control using large-eddy simulation. *Annual Research Briefs, Center for Turbulence Research, Stanford University*, 311–321.

Zaman, K., 1996. Axis switching and spreading of an asymmetric jet: the role of coherent structure dynamics. *Journal of Fluid Mechanics*, 316 (1), 1–27.

Zha, G. C.and Carroll, B.F., *et al.*, 2007. High-performance airfoil using coflow jet flow control. *AIAA journal*, 45 (8), 2087–2090.

Zhang, X., 2003. The evolution of co-rotating vortices in a canonical boundary layer with inclined jets. *Physics of Fluids*, 15, 3693.

Zhang, X., Zhang, H.L., and Collins, M., 1996. Some aspects of streamwise vortex production using air jets. *AIAA paper*, 96–0209.

Zheng, H., Nicolleau, F.C.G.A., and Qin, N., 2012. Detached eddy simulation for turbulent flows in a pipe with a snowflake fractal orifice. *In:* F.C.G.A. Nicolleau, C. Cambon, J.M. Redondo, J.C. Vassilicos, M. Reeks and A.F. Nowakowski, eds. *New Approaches in Modeling Multiphase Flows and Dispersion in Turbulence, Fractal Methods and Synthetic Turbulence.*